

Robert Barthorpe *Editor*

Model Validation and Uncertainty Quantification, Volume 3

Proceedings of the 37th IMAC, A Conference and
Exposition on Structural Dynamics 2019



@Seismicisolation

Springer

The Springer logo consists of a stylized horse head icon followed by the word "Springer" in a white, serif font.

Conference Proceedings of the Society for Experimental Mechanics Series

Series Editor

Kristin B. Zimmerman, Ph.D.
Society for Experimental Mechanics, Inc.,
Bethel, CT, USA

The Conference Proceedings of the Society for Experimental Mechanics present early findings and case studies from a wide range of fundamental and applied work across a broad range of fields that comprise experimental solid mechanics and structural dynamics. This series volume represents a collection of early findings and case studies on fundamental and applied aspects of Model Validation and Uncertainty Quantification.

More information about this series at <http://www.springer.com/series/8922>

Robert Barthorpe
Editor

Model Validation and Uncertainty Quantification, Volume 3

Proceedings of the 37th IMAC, A Conference and Exposition on Structural Dynamics 2019



@Seismicisolation

Editor

Robert Barthorpe
Department of Mechanical Engineering
University of Sheffield
Sheffield, UK

ISSN 2191-5644 ISSN 2191-5652 (electronic)
Conference Proceedings of the Society for Experimental Mechanics Series
ISBN 978-3-030-12074-0 ISBN 978-3-030-12075-7 (eBook)
<https://doi.org/10.1007/978-3-030-12075-7>

© Society for Experimental Mechanics, Inc. 2020

This work is subject to copyright. All rights are reserved by the Publisher, whether the whole or part of the material is concerned, specifically the rights of translation, reprinting, reuse of illustrations, recitation, broadcasting, reproduction on microfilms or in any other physical way, and transmission or information storage and retrieval, electronic adaptation, computer software, or by similar or dissimilar methodology now known or hereafter developed.

The use of general descriptive names, registered names, trademarks, service marks, etc. in this publication does not imply, even in the absence of a specific statement, that such names are exempt from the relevant protective laws and regulations and therefore free for general use.

The publisher, the authors, and the editors are safe to assume that the advice and information in this book are believed to be true and accurate at the date of publication. Neither the publisher nor the authors or the editors give a warranty, express or implied, with respect to the material contained herein or for any errors or omissions that may have been made. The publisher remains neutral with regard to jurisdictional claims in published maps and institutional affiliations.

This Springer imprint is published by the registered company Springer Nature Switzerland AG.
The registered company address is: Gewerbestrasse 11, 6330 Cham, Switzerland



Preface

Model Validation and Uncertainty Quantification represents one of eight volumes of technical papers presented at the 37th IMAC, A Conference and Exposition on Structural Dynamics, organized by the Society for Experimental Mechanics and held in Orlando, Florida, January 28–31, 2019. The full proceedings also include volumes on Nonlinear Structures & Systems; Dynamics of Civil Structures; Dynamics of Coupled Structures; Special Topics in Structural Dynamics & Experimental Techniques; Rotating Machinery, Optical Methods & Scanning LDV Methods; Sensors and Instrumentation, Aircraft/Aerospace, Energy Harvesting & Dynamic Environments Testing; and Topics in Modal Analysis & Testing.

Each collection presents early findings from experimental and computational investigations on an important area within structural dynamics. Model Validation and Uncertainty Quantification (MVUQ) is one of these areas.

Modeling and simulation are routinely implemented to predict the behavior of complex dynamical systems. These tools powerfully unite theoretical foundations, numerical models, and experimental data, which include associated uncertainties and errors. The field of MVUQ research entails the development of methods and metrics to test model prediction accuracy and robustness while considering all relevant sources of uncertainties and errors through systematic comparisons against experimental observations.

The organizers would like to thank the authors, presenters, session organizers, and session chairs for their participation in this track.

Sheffield, UK

Robert Barthorpe

Contents

1 Nondestructive Consolidation Assessment of Historical Camorcanna Ceilings by Scanning Laser Doppler Vibrometry	1
M. Martarelli, P. Castellini, and A. Annessi	
2 The Need for Credibility Guidance for Analyses Quantifying Margin and Uncertainty	11
Benjamin B. Schroeder, Lauren Hund, and Robert S. Kittinger	
3 Failure Behaviour of Composites Under Both Vibration Loading and Environmental Conditions	25
Georgios Voudouris, Dario Di Maio, and Ibrahim Sever	
4 Verification and Validation for a Finite Element Model of a Hyperloop Pod Space Frame	33
Vignesh Jayakumar, T. S. Indraneel, Rohan Chawla, Sudeshna Mohanty, Shishir Shetty, Dhaval Shiyani, and Shabaan Abdallah	
5 Investigating Nonlinearities in a Demo Aircraft Structure Under Sine Excitation	41
S. B. Cooper, S. Manzato, A. Borzacchiello, L. Bregant, and B. Peeters	
6 Sensor Placement for Multi-Fidelity Dynamics Model Calibration	59
G. N. Absi and S. Mahadevan	
7 Application of Cumulative Prospect Theory to Optimal Inspection Decision-Making for Ship Structures ...	65
Changqing Gong, Dan M. Frangopol, and Minghui Cheng	
8 Establishing an RMS von Mises Stress Error Bound for Random Vibration Analysis	75
David Day, Moheimin Khan, Michael Ross, and Brian Stevens	
9 A Neural Network Surrogate Model for Structural Health Monitoring of Miter Gates in Navigation Locks	93
Manuel Vega, Ramin Madarshahian, and Michael D. Todd	
10 Model Validation Strategy and Estimation of Response Uncertainty for a Bolted Structure with Model-Form Errors	99
Huijie Li, Qintao Guo, Ming Zhan, and Yanhe Tao	
11 Characteristic Analysis of Modified Dolly Test: A Sensitivity Study of Initial Conditions on Rollover Outcomes	107
Mohammad Reza Seyed, Sungmoon Jung, and Jerzy Wekezer	
12 Input Estimation of a Full-Scale Concrete Frame Structure with Experimental Measurements	117
Xi Liu and Yang Wang	
13 Bayesian Estimation of Acoustic Emission Arrival Times for Source Localization	127
Ramin Madarshahian, Paul Ziehl, and Michael D. Todd	
14 Quantification and Evaluation of Parameter and Model Uncertainty for Passive and Active Vibration Isolation	135
Jonathan Lenz and Roland Platz	

15 Bayesian Model Updating of a Five-Story Building Using Zero-Variance Sampling Method	149
Mehdi M. Akhlaghi, Supratik Bose, Peter L. Green, Babak Moaveni, and Andreas Stavridis	
16 Input Estimation and Dimension Reduction for Material Models	153
Sam Myren, Emilio Herrera, Andrew Shoats, Earl Lawrence, Emily Casleton, D. J. Luscher, and Saryu Fensin	
17 Augmented Sequential Bayesian Filtering for Parameter and Modeling Error Estimation of Linear Dynamic Systems	163
Mingming Song, Hamed Ebrahimian, and Babak Moaveni	
18 On-Board Monitoring of Rail Roughness via Axle Box Accelerations of Revenue Trains with Uncertain Dynamics	167
V. K. Dertimanis, M. Zimmermann, F. Corman, and E. N. Chatzi	
19 Bayesian Identification of a Nonlinear Energy Sink Device: Method Comparison	173
Alana Lund, Shirley J. Dyke, Wei Song, and Ilias Bilionis	
20 Calibration of a Large Nonlinear Finite Element Model of a Highway Bridge with Many Uncertain Parameters	177
Rodrigo Astroza, Nicolás Barrientos, Yong Li, and Erick Saavedra Flores	
21 Deep Unsupervised Learning for Condition Monitoring and Prediction of High Dimensional Data with Application on Windfarm SCADA Data	189
C. Mylonas, I. Abdallah, and E. N. Chatzi	
22 Influence of Furniture on the Modal Properties of Wooden Floors	197
Lars Vabbersgaard Andersen, Christian Frier, Lars Pedersen, and Peter Persson	
23 Optimal Sensor Placement for Response Reconstruction in Structural Dynamics	205
Costas Papadimitriou	
24 Finite Element Model Updating Accounting for Modeling Uncertainty	211
Rodrigo Astroza, Andres Alessandri, and Joel P. Conte	
25 Model-Based Decision Support Methods Applied to the Conservation of Musical Instruments: Application to an Antique Cello	223
R. Viala, V. Placet, S. Le Conte, S. Vaiedelich, and S. Cogan	
26 Optimal Sensor Placement for Response Predictions Using Local and Global Methods	229
Costas Argyris, Costas Papadimitriou, and Geert Lombaert	
27 Incorporating Uncertainty in the Physical Substructure During Hybrid Substructuring	237
Connor Ligeikis and Richard Christenson	
28 Applying Uncertainty Quantification to Structural Systems: Parameter Reduction for Evaluating Model Complexity	241
Robert Locke, Shyla Kupis, Christopher M. Gehb, Roland Platz, and Sez Atamturktur	
29 Non-unique Estimates in Material Parameter Identification of Nonlinear FE Models Governed by Multiaxial Material Models Using Unscented Kalman Filtering	257
Mukesh Kumar Ramancha, Ramin Madarshahian, Rodrigo Astroza, and Joel P. Conte	
30 On Key Technologies for Realising Digital Twins for Structural Dynamics Applications	267
D. J. Wagg, P. Gardner, R. J. Barthorpe, and K. Worden	
31 Hygro-mechanical Modelling of Wood and Glutin-based Bond Lines of Wooden Cultural Heritage Objects	273
Michael Kaliske and Daniel Konopka	
32 Modelling of Sympathetic String Vibrations in the Clavichord Using a Modal Udwadia-Kalaba Formulation	277
J.-T. Jiolat, J.-L. Le Carrou, J. Antunes, and C. d'Alessandro	

33 Modeling and Stochastic Dynamic Analysis of a Piezoelectric Shunted Rotating Beam	281
Zhenguo Zhang, Ningyuan Duan, Jiajin Tian, and Hongxing Hua	
34 On Digital Twins, Mirrors and Virtualisations.....	285
K. Worden, E. J. Cross, P. Gardner, R. J. Barthorpe, and D. J. Wagg	
35 Applications of Reduced Order and Surrogate Modeling in Structural Dynamics	297
Alexandros A. Taflanidis, Jize Zhang, and Dimitris Patsialis	



Chapter 1

Nondestructive Consolidation Assessment of Historical Camorcanna Ceilings by Scanning Laser Doppler Vibrometry

M. Martarelli, P. Castellini, and A. Annessi

Abstract This paper presents a procedure for the evaluation of the conservation state and the restoration efficiency of nineteenth century camorcanna vaults based on the analysis of objective features extrapolated from nondestructive vibration testing data. As example of application has been chosen the camorcanna vault of the “salone grande” in the nineteenth century Villa Greppi in Monticello Brianza near to Milan, Italy. Non-contact scanning laser Doppler vibrometry has been exploited for the evaluation of the dynamic behavior of the vault before and after rehabilitation. At the first, the structure where frescoes are attached, a cannulated loft spread with mortar, and related aging problem, e.g. painting detachment, are explained. Thus, usual and innovative non-invasive diagnostic techniques are listed, focusing attention on Laser Doppler Vibrometry. Then, Villa Greppi case study is considered, reporting on site equipment and how measurements were taken. Therefore, processed data results are shown, and objective feature indices defined.

Keywords Camorcanna · Frescoes · Restoration · Scanning laser Doppler vibrometry · Modal analysis

1.1 Introduction

Nowadays, Cultural Heritage (e.g. artwork and historical buildings) diagnostics and conservation state assessment using various non-contact techniques is more and more conventional. Several techniques have been successfully exploited to evidence typical defects in artworks, as delamination, detachment of frescoes, wooden icons or mosaics, i.e. Scanning Laser Doppler vibrometry (SLDV [1, 2]), Electronic Speckle Pattern Interferometry (ESPI, [3, 4]), Infrared Thermography (IRT, [5–7]), acoustic and ultrasound imaging techniques ([8, 9]). In the present paper, the conservation state and the restoration efficiency of thin camorcanna vaults made with wooden beams, mats of reeds and mortar is assessed. Studies regarding camorcanna vaults show that differential settlements of light vaults may cause cracking on the lower surface, damaging stuccoes and frescoes. Thus, it is necessary to understand the causes for this to happen and find interventions to prevent cracks [10, 11]. To investigate the conservation state on camorcanna vaults, traditionally restorer use visual inspection and percussion techniques. Nowadays, Non-Destructive Testing (NDT) could be adopted using LDV and IRT [12]. The former seems to be one of the most promising diagnostic techniques, especially due to its nondestructive nature, high spatial resolution and frequency range [13]. It allows to measure vibrational frequency response of the structure in terms of mobility functions, which allow to evidence areas of detachment between frescoes and wooden structure. The latter is capable of identifying and characterizing imperfections over a large area. This can be achieved only if there is a sufficient temperature gradient between the flawed and sound area that is appreciable by the IRT sensor [14]. Also ultrasonic techniques are successful in evaluating camorcanna detachments. Defect localization and dimensions could be estimated [15].

M. Martarelli
Faculty of Engineering, Università degli Studi eCAMPUS, Novedrate (CO), Italy

P. Castellini (✉) · A. Annessi
Industrial Engineering and Mathematical Sciences Department, Università Politecnica delle Marche, Ancona, Italy
e-mail: p.castellini@univpm.it

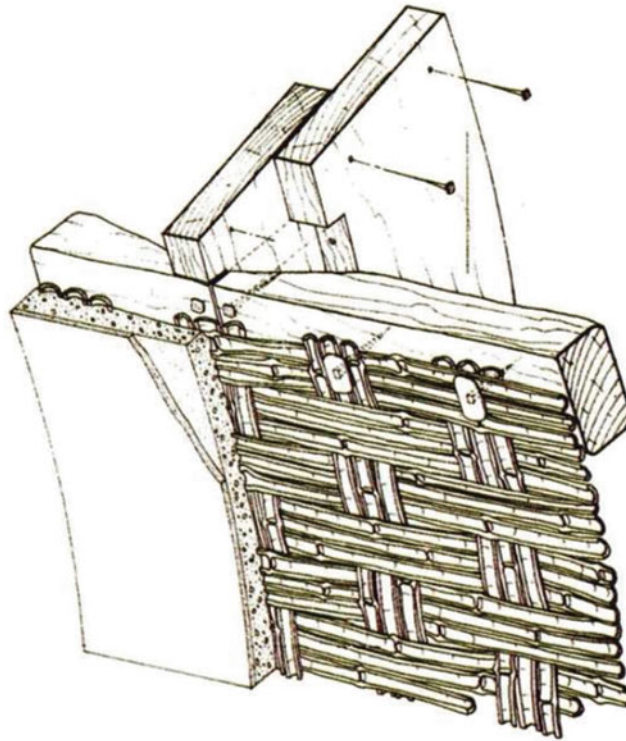


Fig. 1.1 Carmorcanna vault portion with intertwined reeds [16]

1.2 Camorcanna Vaults Structure

In many theaters, churches and historical buildings between the sixteenth and nineteenth century, vaults were made by mats consisting of stitched thin cane and mortar fixed on a wooden framework. This kind of structure is usually called camorcanna. These vaults were cheap, lightweight and easy to built up, thus really popular. They were often decorated with precious frescoes and stuccoes that give them historical, artistic and architectural value.

Camorcanna is composed by mats of reeds, constructed linking together thin canes with strings (see Fig. 1.1). Reed mats are fixed on a wooden supporting structure and mortar is spread on them. When it is dry, the surface is ready to be decorated with frescos and stuccoes.

Nowadays, many camorcanna vaults are left in deterioration due to many factors linked with constructive system problems or external issues. The former may be errors in ribs sizing, inadequate link between the elements or wood inner defects. The latter are caused by accidental events e.g. subsidence, earthquakes, water infiltration, variation in thermo-hygrometric loads or attacks from fungi and insects [16]. The mortar detachment is one of the usual defect in paintings on described structures due to improper installation. During construction, the mortar has to be quite liquid so it can wrap straws properly. In fact, it has to penetrate the straw layer to create a mechanical connection (by interference and adhesion). If the mortar is too solid when given, the connection between it and the straws is only by adhesion. Hence, the joint is not resistant enough and the painting falls under his own weight.

Another usual issue of cannulated vaults is straws detachment from the wooden support they are linked with. It can yield to a coat brake and a consequent fall of a vault portion. Both the indicated faults are not visible from the outside and are detectable only afterwards.

1.3 Case Study: Paintings in Greppi's Manor Vault

Villa Greppi is a nineteenth century manor located in Monticello (LC), Italy. The plan detail of Fig. 1.2a shows the frescoed coffered ceiling hall under study. In Villa Greppi's case, the camorcanna panels were made as follow:

1. The first structure consists of thick chestnut wooden beams supporting the floor (about 40 by 40 cm in size).
2. Smaller transverse beams (about 8 by 10–15 cm in size), called ribs, are used to link together the latter beams.

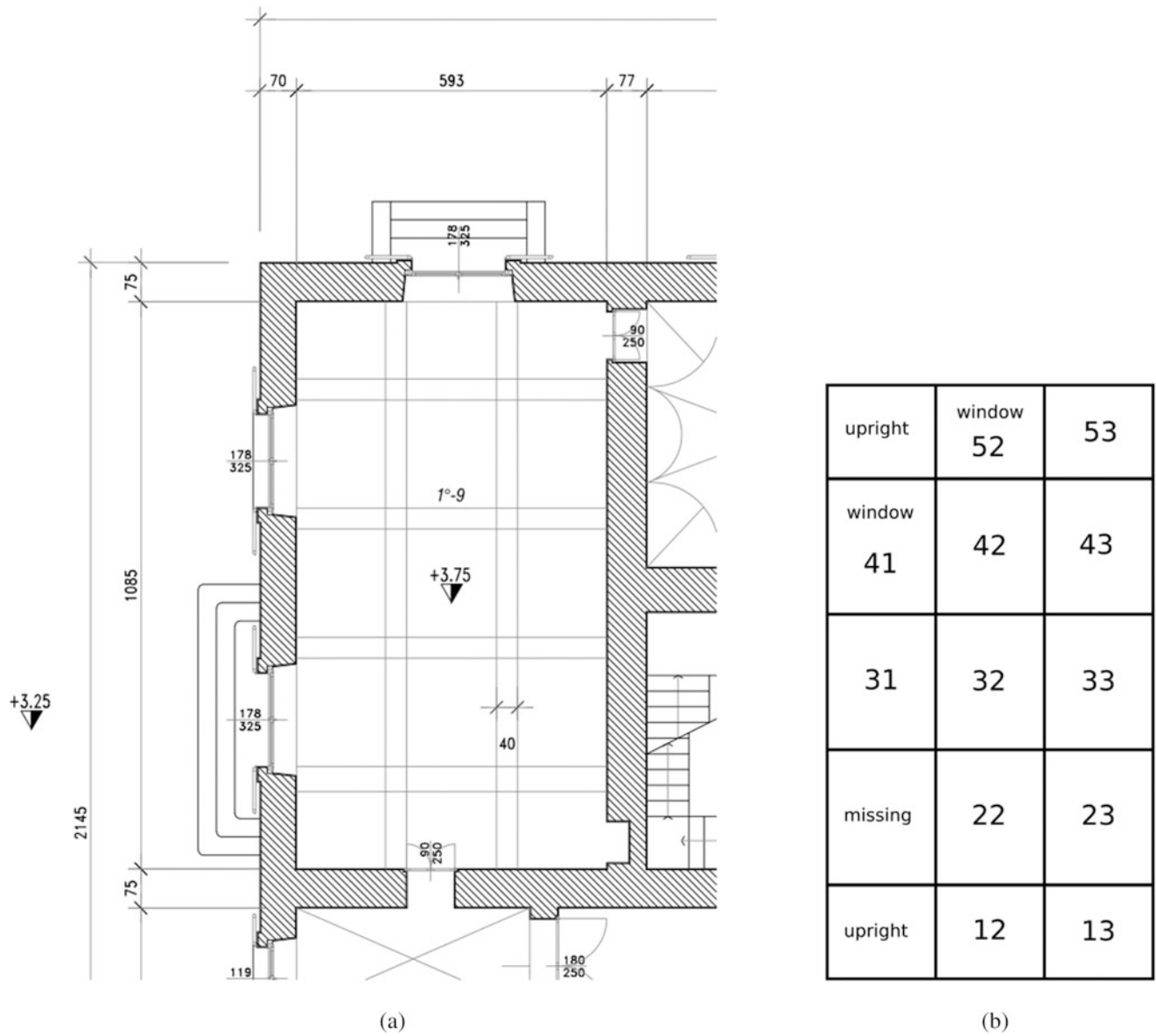


Fig. 1.2 Frescoed hall scheme. (a) Plan detail of the frescoed hall. (b) Panels measurement labels scheme

3. Mat of reeds (5–10 mm in diameter) are fixed to ribs lower part by at head nails.
4. The mortar (made by plaster, lime or a mixture of both) is then spread on the straws.

A painted panel and one missing the fresco and the mortar are shown in Fig. 1.3. The main hall has an area of $66 m^2$ and the coffered loft is 5 m high. It is divided in 15 painted panels (square or rectangular). A visualization scheme is shown in Fig. 1.2b. Panel names are arranged in a matrix form.

1.4 Testing Equipment and Measurement Set-Up

The objective of this study is the assessment of the structural behavior improvement due to restoration process. The damage occurred to some parts of the ceiling were due to detachment of whole panels, and this suggest the need to verify the stiffness of the connection between the frescos structure and the supporting reeds, but also the behavior of the whole ceiling, which movements could stress the panels in a dangerous way.



Fig. 1.3 Villa Greppi's painted loft. **(a)** Frescos on camorcanna. **(b)** Damaged camorcanna without mortar and painting

For these reasons, vibration measurements were performed before and after the restoration following two approaches:

1. The vibration response measurement at local level, with a dense spatial sampling on each panel (where the fresco was present), that can be considered a panel level investigation.
2. The vibration response measurement at global level, for the entire vault where one measurement point for each panel was taken, that can be considered a ceiling level investigation.

The vibration response of the structure was measured in both cases in terms of velocity by means of an LDV that gives mobility Frequency Response Function (FRF). The measurement was performed on the frescoes surface in the vertical direction with a frequency range of 0–512 Hz and a frequency resolution of 312.5 mHz. Measurement points were selected to highlight the local and the global behavior respectively.

The panel analysis was performed on all ceiling coffers except to the number 11, 12 and 51, see scheme in Fig. 1.2b, since the frescoes were missing on those panels. Each coffer was forced into vibration by means of an electrodynamic shaker operating as an inertial vibrodyne. As shown in Fig. 1.4b, the shaker was leaning on the vault structural beam of the ceiling and it was pushing an inertial mass of 500 g. The reaction force was acting as excitation of the structure. A load cell was measuring the force applied on the mass, which corresponded to the sum of dynamic forces applied, as a reaction force, by the shaker on the beam. The panel vibration response was measured by the LDV pointing on a regular grid of points on the fresco surface. A grid of 6×7 points was sat for the square panel and 8×7 points grid for rectangular one.

The measured data set is made of FRF functions, obtained as ratio between the vibration velocity response of the panel and the force imparted in input by the electrodynamic shaker. Each FRF is weighted by the transmission path from the shaker to each measurement point and indicates how the energy travels through the different supporting elements (beams, panel, fresco). Therefore, diagnostics is possible: loss of signal amplitude could be due to a structural problem, e.g. fresco detachment.

The global behavior of the ceiling has been estimated by performing an additional test. Excitation was provided by an instrumented hammer on the ceiling beam while response was measured by LDV on the central point of each panel. The vibration velocity was measured by the LDV that was sequentially moved at the central position of all the panels.



Fig. 1.4 Test setup. **(a)** LDV during measurements. **(b)** Shaker position during measurements

Table 1.1 Loft mode shapes

N. modes	Type	Frequency (Hz)	
		Before restoration	After restoration
Mode 1	2nd flexural	10.72	11.53
Mode 2	3rd flexural	12.96	15.00
Mode 3	1st torsional	28.80	32.01

1.5 Experimental FRF Analysis

In order to assess the effectiveness of the restoration on the health status of the structure, an analysis of the measured FRFs has been performed at both ceiling and panel level. First, a modal analysis has been done on the FRFs set in order to identify the dynamic behavior of the structure before and after the restoration in terms of resonance frequencies, damping loss factor and mode shapes. Then FRFs measured at each panel have been processed in order to extract quantitative features correlated to the structural modification produced by the restoration. Finally, signal features were extracted from FRFs in order to obtain synthetic set of scores that could assess effectiveness of restoration accomplished.

1.6 Modal Analysis

The modal analysis carried out on the impact testing FRFs set allowed estimating the resonance frequencies before and after the restoration at global level (listed in Table 1.1). Structure stiffening and frequency shift could be noticed in Fig. 1.5, particularly in the phase graph. The corresponding mode shapes are shown in Fig. 1.6, only for the configuration before the restoration, the shape of the mode is not experiencing variation after the intervention. The modal analysis carried out on the FRFs computed on panel level dataset allowed to estimate the resonance frequencies before and after the restoration of each panel. The resonance frequencies before and after restoration are reported in Table 1.2, specifically for panel 42. The corresponding mode shapes calculated for the configuration after the restoration are shown in Fig. 1.7. Panel irregularities (concerning materials, structure) and non-linear behavior increase the analyses complexity. The restoration intervention

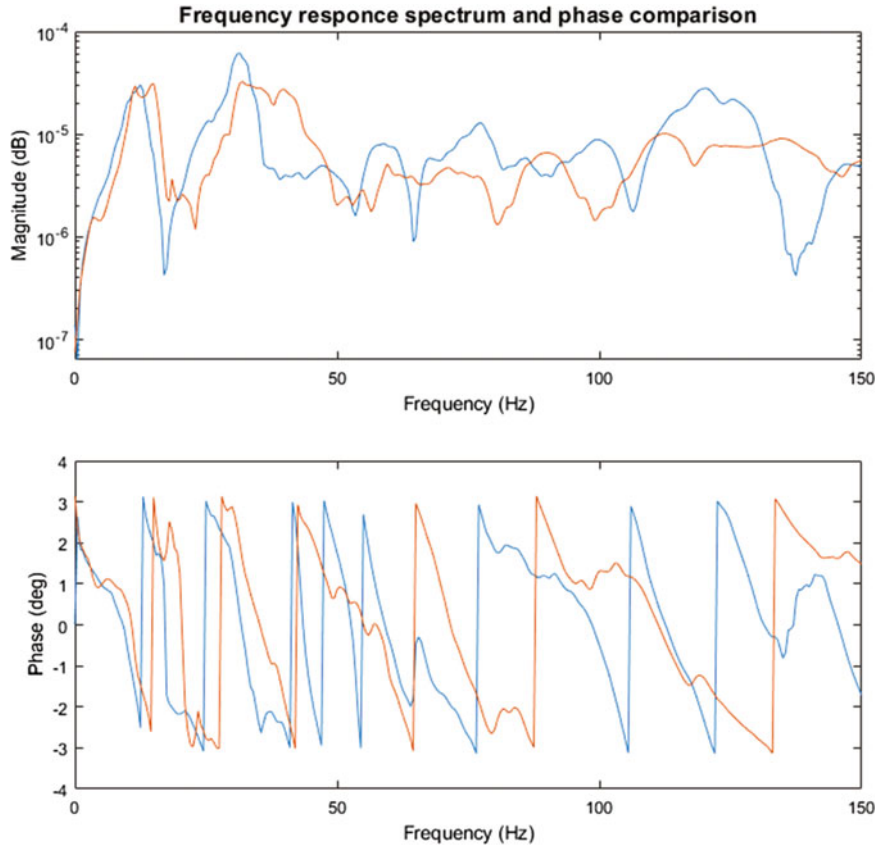


Fig. 1.5 Comparison between FRFs before (blue curves) and after (red curves) therestoration on a loft representative point

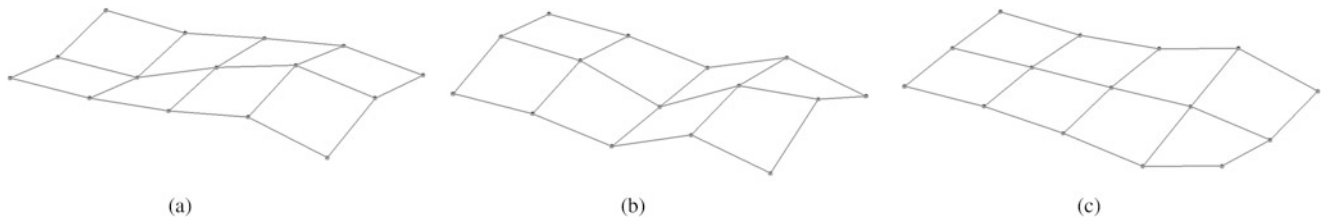


Fig. 1.6 Loft mode shapes. (a) Loft 2nd flexural mode. (b) Loft 3rd flexural mode. (c) Loft 1st torsional mode

Table 1.2 Single panel mode shape

N. modes	Type	Frequency (Hz)	
		Before restoration	After restoration
Mode 1	Rigid mode	11.34	12.64
Mode 2	Rigid mode	13.76	15.90
Mode 4	1st flexural	31.84	42.50
Mode 6	2nd flexural	43.28	64.51

added mass and stiffened the panel structure changing the boundary conditions; thus, the disposition of the nodal lines, which previously coincided with possible cracks, has changed. Furthermore, the first panel modes, that looks like rigid body motion, at panel level, correspond to global modes of the loft.

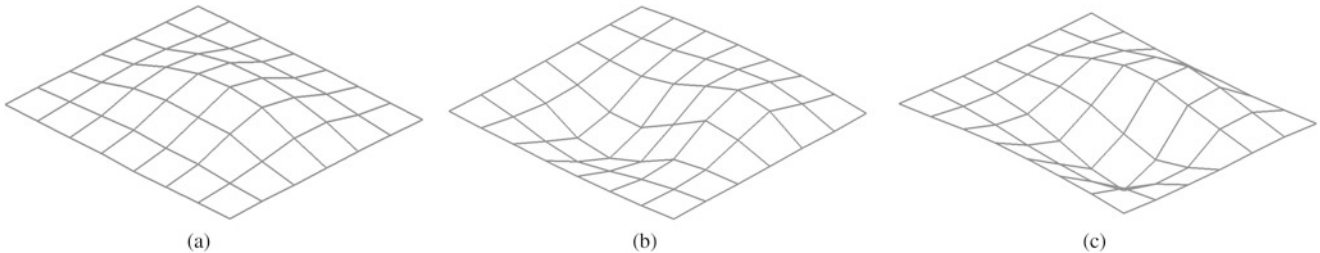


Fig. 1.7 Loft mode shapes. (a) 1st flexural mode. (b) 2nd flexural mode. (c) 12th flexural mode

1.7 FRF Analysis

Modal analysis does not provide correct and stable information due to the marked variability of the structure under test (between different panels and before/after restoration). In order to catch the effects of the restoration on each panel, obtaining a “score scale” related to the efficiency of the intervention, synthetic parameters that could condense all the collected measures were searched. This can be tackled by observing the averaged FRF obtained from the mean of all the FRFs measured on each panel. The averaged FRF for each panel, before and after restauration are reported in Fig. 1.8; it is evident a stiffening effect after the intervention.

By observing the average FRF plots it has been deducted that a significant feature representing the effect of the restauration is the stiffening of the structure, i.e. the shift at the highest frequency range of the panel resonances. This frequency shift can be straightforwardly identified by cross-correlating corresponding average FRFs before and after intervention. Cross-correlation functions are reported in Fig. 1.9; they show a frequency lag (on the x-axis) that is always positive, thus a frequency shift towards high frequencies is present and is consistent for all panels.

1.8 Conclusions

In the present paper, camorcanna ceilings consolidation is assessed using LDV. The aim of this work is to method to evaluate the restoration efficiency of frescoed panels (by means of its vibrational characteristics). Villa Greppi’s case study is presented. From the modal analysis of global ceiling and the single coffer, it has been possible to demonstrate that the restauration increases the stiffness of the entire ceiling that is evident from frequency resonance shift in the high range and from mode shapes modification. By analyzing the FRF data sets for each panel this frequency shift is evident at global level for the entire FRF. It was possible therefore to extract a feature representing this stiffening effect, which is the consequence of the restauration. Even if the stiffening is consistent on all the panels (there is an average frequency increase of 14 Hz) it is very variable between one panel to another: it goes from values around 30 Hz to values of about 3 Hz (with a standard deviation of 10 Hz). This demonstrates the inhomogeneity of the intervention: observe the map of the frequency shift according to the arrangement of the coffers, Fig. 1.10.

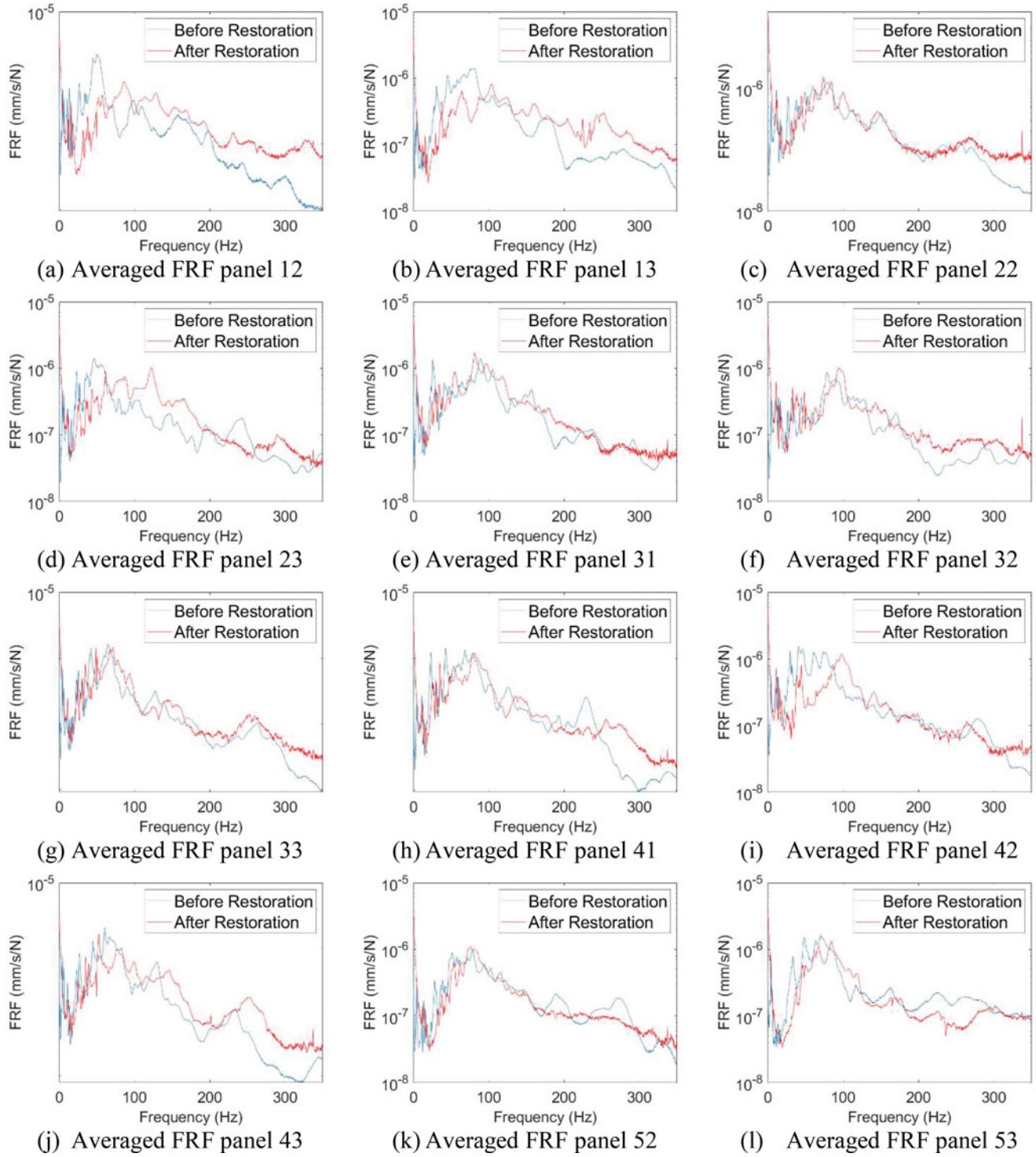


Fig. 1.8 Averaged FRF for each panel. (a) Averaged FRF panel 12. (b) Averaged FRF panel 13. (c) Averaged FRF panel 22. (d) Averaged FRF panel 23. (e) Averaged FRF panel 31. (f) Averaged FRF panel 32. (g) Averaged FRF panel 33. (h) Averaged FRF panel 41. (i) Averaged FRF panel 42. (j) Averaged FRF panel 43. (k) Averaged FRF panel 52. (l) Averaged FRF panel 53

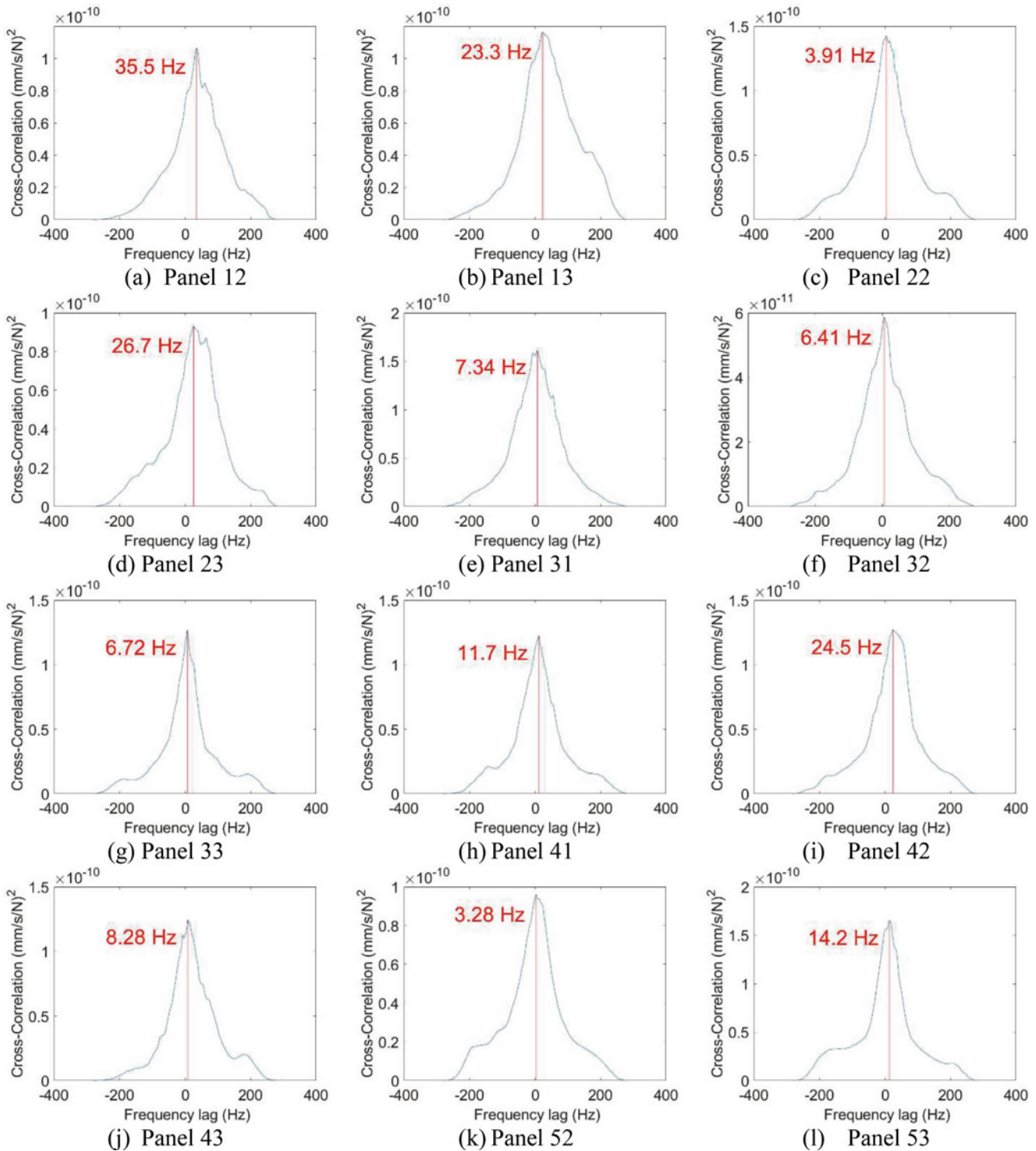
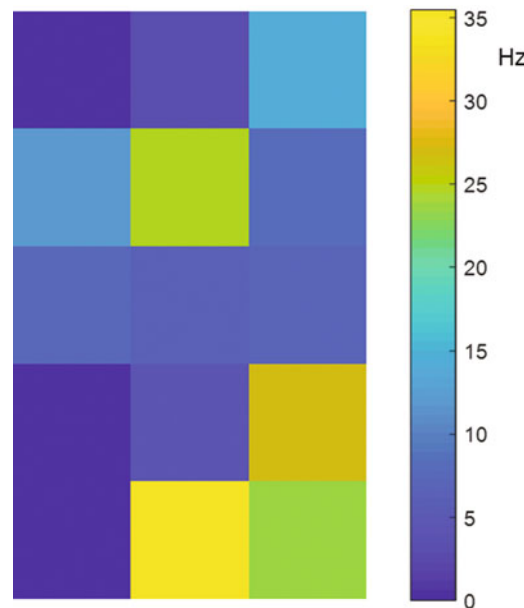


Fig. 1.9 Cross-correlation curves for each panel. (a) Panel 12. (b) Panel 13. (c) Panel 22. (d) Panel 23. (e) Panel 31. (f) Panel 32. (g) Panel 33. (h) Panel 41. (i) Panel 42. (j) Panel 43. (k) Panel 52. (l) Panel 53

Fig. 1.10 Frequency increase map over the coffers disposition



References

1. Castellini, P., Revel, G.: Damage detection and characterization by processing of laser vibrometer measurement results: application on composite materials. **3411**, 458–468 (1998). <https://doi.org/10.1111/12.307732>
2. Castellini, P., Esposito, E., Legoux, V., Paone, N., Stefanaggi, M., Tomasini, E.: On field validation of non-invasive laser scanning vibrometer measurement of damaged frescoes: Experiments on large walls artificially aged. *J. Cult. Herit.* **1**(2), S349–S356., cited By 16 (2000). [https://doi.org/10.1016/S1296-2074\(00\)00145-X](https://doi.org/10.1016/S1296-2074(00)00145-X)
3. Castellini, P., Abaskin, V., Achimova, E.: Portable electronic speckle interferometry device for the damages measurements in veneered wood artworks. *J. Cult. Herit.* **9**(3), 225–233, cited By 16 (2008). <https://doi.org/10.1016/j.culher.2008.05.002>
4. Sfarra, S., Ibarra-Castanedo, C., Tortora, M., Arrizza, L., Cerichelli, G., Nardi, I., Maldague, X.: Diagnostics of wall paintings: a smart and reliable approach. *J. Cult. Herit.* **18**, 229–241 (2016). <https://doi.org/10.1016/j.culher.2015.07.011>
5. Meola, C., Carlomagno, G.M.: Recent advances in the use of infrared thermography. *Meas. Sci. Technol.* **15**(9), R27–R58 (2004). <https://doi.org/10.1088/0957-0233/15/9/r01>
6. Pucci, M., Cicero, C., Orazi, N., Mercuri, F., Zammit, U., Paoloni, S., Marinelli, M.: Active infrared thermography applied to the study of a painting on paper representing the Chigi's family tree. *Stud. Conserv.* **60**(2), 88–96 (2013). <https://doi.org/10.1179/2047058413y.0000000117>
7. Cadelano, G., Bison, P., Bortolin, A., Ferrarini, G., Peron, F., Giroto, M., Volinia, M.: Monitoring of historical frescoes by timed infrared imaging analysis. *Opto-Electron. Rev.* **23**(1), 102–108 (2015). <https://doi.org/10.1515/oere-2015-0012>
8. Calicchia, P., Cannelli, G.B.: Detecting and mapping detachments in mural paintings by non-invasive acoustic technique: measurements in antique sites in Rome and Florence. *J. Cult. Herit.* **6**(2), 115–124 (2005). <https://doi.org/10.1016/j.culher.2004.11.001>
9. Kloiber, M., Reinprecht, L., Hrvínak, J., Tippner, J.: Comparative evaluation of acoustic techniques for detection of damages in historical wood. *J. Cult. Herit.* **20**, 622–631 (2016). <https://doi.org/10.1016/j.culher.2016.02.009>
10. Quagliarini, E., Lenci, S., Seri, E.: On the damage of frescoes and stuccoes on the lower surface of historical at suspended light vaults. *J. Cult. Herit.* **13**(3), 293–303 (2012). <https://doi.org/10.1016/j.culher.2011.11.008>
11. Quagliarini, E., D’Orazio, M., Stazi, A.: Rehabilitation and consolidation of high-value camorcanna vaults with FRP. *J. Cult. Herit.* **7**(1), 13–22 (2006). <https://doi.org/10.1016/j.culher.2005.09.002>
12. Quagliarini, E., Esposito, E., del Conte, A.: The combined use of IRT and LDV for the investigation of historical thin vaults. *J. Cult. Herit.* **14**(2), 122–128 (2013). <https://doi.org/10.1016/j.culher.2012.01.004>
13. Martarelli, M., Castellini, P., Quagliarini, E., Seri, E., Lenci, S., Tomasini, E.P.: Nondestructive evaluation of plasters on historical thin vaults by scanning laser Doppler vibrometers. *Res. Nondestruct. Eval.* **25**(4), 218–234 (2014). <https://doi.org/10.1080/09349847.2014.896964>
14. Tavares, S., Agnani, A., Esposito, E., Feligiotti, M., Rocchi, S., de Andrade, R.: Comparative study between infrared thermography and laser Doppler vibrometry applied to frescoes diagnostic. In: Proceedings of the 2006 International Conference on Quantitative InfraRed Thermography, QIRT Council, 2006. <https://doi.org/10.21611/qirt.2006.039>
15. Quagliarini, E., Revel, G.M., Lenci, S., Seri, E., Cavuto, A., Pandarese, G.: Historical plasters on light thin vaults: state of conservation assessment by a hybrid ultrasonic method. *J. Cult. Herit.* **15**(2), 104–111 (2014). <https://doi.org/10.1016/j.culher.2013.04.008>
16. Quagliarini, M.D.E.: Recupero e Conservazione di volte in “Camorcanna”, Alinea Editrice, 2005



Chapter 2

The Need for Credibility Guidance for Analyses Quantifying Margin and Uncertainty

Benjamin B. Schroeder, Lauren Hund, and Robert S. Kittinger

Abstract Current quantification of margin and uncertainty (QMU) guidance lacks a consistent framework for communicating the credibility of analysis results. Recent efforts at providing QMU guidance have pushed for broadening the analyses supporting QMU results beyond extrapolative statistical models to include a more holistic picture of risk, including information garnered from both experimental campaigns and computational simulations. Credibility guidance would assist in the consideration of belief-based aspects of an analysis. Such guidance exists for presenting computational simulation-based analyses and is under development for the integration of experimental data into computational simulations (calibration or validation), but is absent for the ultimate QMU product resulting from experimental or computational analyses. A QMU credibility assessment framework comprised of five elements is proposed: requirement definitions and quantity of interest selection, data quality, model uncertainty, calibration/parameter estimation, and validation. Through considering and reporting on these elements during a QMU analysis, the decision-maker will receive a more complete description of the analysis and be better positioned to understand the risks involved with using the analysis to support a decision. A molten salt battery application is used to demonstrate the proposed QMU credibility framework.

Keywords Credibility · Margin · Uncertainty · QMU · Guidance

2.1 Introduction

The purpose of this paper is to describe the need for credibility guidance in quantification of margins and uncertainty (QMU) analyses and provide a potential structure for such guidance. Credibility is defined as “the quality or power of inspiring belief” [1], so credibility guidance should assist in the consideration of belief-based aspects of an analysis. A QMU credibility assessment framework comprised of five elements is proposed: requirement definitions and quantity of interest (QoI) selection, data quality, model uncertainty, calibration/parameter estimation, and validation. Through considering and reporting relevant aspects of these elements during a QMU analysis, the decision-maker will receive a more complete description of the analysis and be better positioned to understand the risks involved with using the analysis to support a decision.

This paper will be structured as follows. The remainder of this section will provide a history of QMU, motivation for why a credibility assessment framework is needed, and highlight similar efforts in the CompSim domain. Next will be a section outlining the proposed framework for gathering and organizing QMU credibility evidence. How to use the evidence to evaluate analysis credibility is then discussed. A demonstration of the process applied to a molten salt battery example problem is provided in the next section. Lastly, a summary of the paper is provided.

2.1.1 What Is QMU

QMU originated at the national laboratories in the early 2000s to address risk in nuclear weapon stockpile stewardship in the absence of full system testing [2]. QMU was originally posed as a risk assessment framework for nuclear weapons, addressing the three elements of the risk triplet (what can occur? how likely is it? and what are the consequences?) [3]; this

B. B. Schroeder (✉) · L. Hund · R. S. Kittinger
Sandia National Laboratories, Albuquerque, NM, USA
e-mail: bbschro@sandia.gov

QMU formulation also included a fourth element, credibility, defined as the answer to the question ‘how much confidence do we have in our risk assessment?’ [4]. Historically at Sandia National Laboratories (Sandia), QMU was largely applied to experimental data-based problems, but it appears likely that an integration of computational simulation (CompSim) results and experimental data will be the paradigm of the future. While processes for conducting QMU have developed over time (e.g., [5, 6]), there are still no formal processes for evaluating the credibility of a QMU analysis.

QMU entails comparing a performance measure to a performance requirement to determine the likelihood of functioning as intended, considering all relevant uncertainties. Implementing a QMU analysis requires building a team with the relevant expertise; identifying performance measures and requirements; assimilating relevant data; running an analysis; and communicating the results. Considering these steps of a QMU analysis, a corresponding QMU credibility assessment should address many of the inherent aspects of the analysis such as relevance of the performance measure and requirement, data quality, and analysis limitations.

2.1.2 Why Measure Credibility?

There is currently a gap in guidance within Sandia National Laboratories (Sandia) for assessing the credibility of QMU analyses. New guidance for QMU was recently released as internal documents within Sandia in two sections: (1) an overview of high-level QMU concepts and processes and (2) descriptions of statistical tools that can be used to derive QMU results, with a focus on QMU for experimental data. This new guidance pushed for broadening the analyses supporting QMU results beyond extrapolative statistical models and advocated for a more holistic picture of risk, including information garnered from both experimental and CompSim campaigns. Although this new guidance improves the informational basis of QMU analyses, it does not provide a consistent framework for communicating the credibility of analysis results.

Credibility assessment guidance for QMU is needed because:

- Decision-makers are increasingly asking for credibility assessments when being provided analysis results. Decision-makers are learning that they must understand the level of confidence they should invest in the results to better utilize the analysis that they commissioned.
- Failing to provide guidance for communicating credibility may lead to overconfidence in results. A question that should be posed to QMU analysts is, “What is the credibility of your results?” Without asking this question, the decision-maker may believe results are more reliable than is warranted and make ill-informed decisions.
- A unified QMU credibility framework would result in greater consistency in information presentation. When credibility results are analyst-specific and/or analysis-specific, decision-makers will interpret results differently depending on who conducted the analysis.
- Streamlined documentation of important auxiliary information (e.g., metadata, methods) is integral to understanding and reproducing QMU results. Summary QMU results (for example, margin over uncertainty ratios) always rely on auxiliary supporting information about the QMU process and supporting experimental data.

Without a consistent credibility assessment framework, decision-makers must rely on source credibility, or their belief in the source of the information. Although not specific to the reception of QMU results, psychological research has explored the role of source credibility in other information distribution areas. Across the psychology literature, source credibility is typically attributed to a person providing a message. Key aspects of source credibility include the source’s trustworthiness and expertise [7]; to a lesser degree, composure, dynamism, sociability [8] and even accents of voices [9]. Chaiken and Maheswaran found source credibility can affect decisions in two ways: (1) by serving as a peripheral cue for simple acceptance or rejection of an argument, and (2) by biasing the strength of the decision-maker’s argument processing [10].

While biasing the belief in results based on the source is potentially problematic in itself, Heesacker et al. found that as source credibility increases, persuasion also increases [11]. They attribute this phenomenon to more credible sources eliciting greater thinking about the message (improved information presentation, not informational content).

Across psychological research a theme persists: human judgment is persuaded and biased by a variety of minute factors. As humans participate in high stakes decision making, it is important to understand how small changes in presentation of the message (or data) can unintentionally bias the decision-maker. To mitigate such bias, credibility frameworks may help through providing consistency, transparency, and structure.

2.1.3 *History of Credibility in CompSim*

The concepts of credibility continue to be developed for presenting CompSim results as evidence to support a decision as well as for the incorporation of experimental data into CompSim analyses. Reviewing the progress of credibility guidance for these fields provides a starting point for the analogous guidance for QMU analyses.

For institutions that utilize CompSim to support decisions regarding complex engineering questions such as national laboratories, the aerospace and defense industries, and space agencies, the credibility associated with CompSim predictions must be understood. Methods for assessing and communicating the credibility of CompSim based evidence are being developed by many organizations [12]. As an example, the Predictive Capability Model Maturity (PCMM) [13] has been developed at Sandia over the last decade to provide a consistent framework for evaluating CompSim credibility. PCMM was developed as a method of directing discussion about and communication of the many assumptions, errors, biases, and uncertainties ever present in CompSim predictions. A broad spectrum of CompSim activities are covered by elements of PCMM including code verification, physics and material model fidelity, representation and geometric fidelity, solution verification, validation, and uncertainty quantification. Those elements are perceived to encompass the majority of error/uncertainty sources that may impact a CompSim analysis. An approach for grading a simulation's performance in the different elements is also provided, which includes guidance describing the expected attributes needed to achieve a specific maturity level for each element. This grading is meant to foster gap identification and resource allocation.

PCMM can be used as a results credibility communication tool as well as an initial analysis planning aid. Applications using PCMM as a prediction credibility assessment tool have been demonstrated [14, 15].

In the CompSim community, experimental credibility is currently being developed from the perspective of using experimental data for model validation and calibration [16, 17]. Through providing structure for the assessment of experiments used for CompSim and experimental integration activities, consistency between modeling activities can be increased. A common difficulty when comparing experimental and CompSim results is ensuring that the scenarios captured by each are similar enough to not be the cause of significant discrepancy. When such discrepancies occur, it may be difficult to determine the source. Through capturing information about the experimental setup from the perspective of how that information will be used in CompSim analyses, more information can be gained from the comparisons. This same framework can be used to increase an experimental campaign's value through incorporating knowledge about how the data will be utilized into the test planning process. Outcomes of these experimental credibility processes include characterization of experimental uncertainties, assessment of model validation or calibration quality, and assessment of experimental alignment with modeling goals.

2.2 Important Elements for QMU Credibility

Following the strategy for developing a credibility framework laid out by the CompSim community, potential sources of error, uncertainty, bias, or assumptions that could impact a QMU analysis are categorized into elements. It is proposed that QMU credibility can be assessed using the following five elements.

QMU Credibility Elements

1. Requirement Definition and QoI Selection

Defining the requirement against which performance is compared and selecting the appropriate quantity of interest that can be used to represent performance

2. Data Quality

Evaluating the available data and its attributes

3. Model Uncertainty

Describing any models used to analyze the data and associated assumptions

4. Calibration/Parameter Estimation

Considering how the model is fit or calibrated

5. Validation

Determining if the model is a sufficient representation of the data with respect to making the prediction of interest

The five elements are described in more detail in the subsections below. At the end of each element-specific section, suggested documentation is provided that would support credibility statements for each element.

2.2.1 Requirement Definition and QoI Selection

Requirements may sometimes be clearly specified and the mapping from available data to that requirement may be simple, but this is not strictly true. Requirements may need interpretation that comes from consultation with a subject matter expert or simply from the QMU analyst. Available data often requires additional assumptions and/or processing to be comparable with the requirement. The quantity compared against the requirement is referred to as the QoI. QoIs are typically physical quantities, while requirements may be functions of these physical quantities. Determining how the requirement and QoI definitions will be compared is a necessary step of a QMU analysis.

Suggested Documentation What is the requirement? Are there any perceived ambiguities in the requirement definitions? What is the QoI? What is the relevance of the QoI relative to the requirement?

2.2.2 Data Quality

A great deal of qualitative information lives with the dataset that may impact the value of the dataset. Specifically, metadata about a dataset should be documented and preserved, so that important information about the data-generating mechanism can be evaluated when the data are analyzed. Metadata may include:

- When was the data gathered?
- What method was used to capture the measurements?
- How well developed was the measurement/experimental method?
- Where was the test conducted?
- Who conducted the test?
- What tester(s) was used?
- How well characterized are the experimental conditions?

Transparently evaluating metadata reduces the risk of omitting information that may impact the conclusion of the analysis. The following four categories are common categories of such auxiliary data (but should not be considered all-encompassing).

- Sparsity** The amount of data available impacts how much sampling uncertainty will exist in an estimate. Further, some estimates require more data than others to avoid extrapolative inferences; for instance, estimating a mean typically requires much less data than estimating an extreme percentile or rare exceedance probability to avoid extrapolation. Issues with presenting distributional tail extrapolation have been highlighted in [18].

Suggested Documentation How much data is available? Is the data sufficient to empirically validate any estimates being made?

- Representativeness** The QoI often cannot be directly measured given the available data. Therefore, the analyst must consider how the available data map onto the QoI. For example, are we interested in environment A, but only have data tested in a similar, but less stressing environment B?

Suggested Documentation What is the representativeness of the data relative to the application space (including tested environments, age, etc.), as defined by the QoI?

- Noisiness/Measurement uncertainty** Most measurements contain some error. This error can arise from many different sources. A common source of error is the tester or instrument's measurement error. In addition, errors can be introduced during data processing steps to convert a signal captured by a measurement device to a physical quantity. Uncertainty in the measurement can also be injected into the data through uncertainty about what is truly being measured. For example, measurement devices may be placed in orientations and exposed to boundary conditions that deviate from those specified for the experiment.

Suggested Documentation What are the magnitudes and hypothesized sources of the measurement errors?

- Bad data/Outliers** Rejection of bad (inaccurate) data or non-physical outliers is an aspect of data analysis. Omitting outliers is often acceptable, but only when the root cause of the outlier is known. Understanding the root cause of impactful outliers often requires investigation into manufacturing and/or measurement process.

Suggested Documentation How much data was rejected (not included in the final analysis)? Why it was rejected?

2.2.3 Model Uncertainty

Models, whether physics-based or statistical, are an important aspect of QMU analyses, particularly when data are sparse or are not representative. Information about the types of models, underlying assumptions, and additional uncertainties associated with modeling activities must be considered and communicated. If the model is purely physics-based, then existing predictive maturity methods like PCCM [13] can be used to assess the model credibility. If the model is empirical or statistical, then the credibility for these types of models should be evaluated, though we are not aware of any formal frameworks for evaluating model credibility. Goodness-of-fit methods are not sufficient metrics for evaluating model credibility [19], due to only testing if the distribution form hypothesis can be rejected. A typical means of assessing a statistical model's prediction capabilities is to demonstrate the model's ability to predict data not used to train the model. While such activities may be used to support model validation (as will be address later in the validation subsection), this does not probe the underlying model uncertainties we deem to be essential to model credibility. We recommend assessing two components of model credibility: the causal structural and functional assumptions of the model.

- Causal structural assumptions** The inability to accurately represent the collected data in the empirical model will introduce bias in QoI estimates. Causal structural assumptions concern whether causal or physics-based relationships can be learned from the available data by comparing how the data were generated to an underlying causal model for the data. Specifically, causal analysis concerns establishing underlying causal relations between variables and then determining if the collected data are sufficient to infer the QoI under these causal relations [20]. Common sources of bias include [21]:

- Omitted variable bias: important variables were not measured in the dataset that should be included in the model to accurately capture the physics in the empirical model.
- Selection bias: the data are not a random sample from the population, but the model assumes a random sample.

Suggested Documentation Was the causal structure of the model considered? Is the fitted model consistent with an underlying causal model for the data? Is selection or omitted variable bias present? To what fidelity is the causal structure understood?

2. Functional assumptions Given a set of causal structural assumptions, statistical models are then specified to represent the empirical relationship between the inputs and outputs. Functional assumptions specify this relationship, conditioning on the set of causal assumptions. Stated differently, causal assumptions pertain to whether all of the necessary inputs are included in the modeling to address biases in the data; functional assumptions pertain to whether the empirical model is correct, conditioning on having the correct inputs in the model. Examples of functional assumptions include normality or other distributional assumptions, linearity between inputs and outputs, and no interaction between inputs on the output, i.e., independence of effects. The complexity of the selected model is often limited by the available data. Further, the importance of the functional assumptions often varies. For instance, normality assumptions will often have minimal impact when estimating means, but can have a significant impact on tail extrapolations, which are common in reliability and QMU analyses. If multiple model forms provide similar fits to the data, this model form uncertainty should be considered.

Suggested Documentation What functional assumptions were made? Were the assumptions tested empirically, based on subject matter data, or required due to lack of data? To what fidelity are the functional relationships understood? How sensitive is the QoI estimate to the functional assumptions?

2.2.4 Calibration/Parameter Estimation

The act of updating model parameters using data (including both estimating and quantifying uncertainty in the parameters) is called calibration when models are physics-based and parameter estimation when models are empirical/statistical. These definitions are not universally accepted, but will be used within this framework. When data are sparse, calibration and statistical estimation procedures can perform poorly (e.g., maximum likelihood, bootstrapping), and limitations to calibration procedures should be addressed. Bayesian calibration processes incorporate additional knowledge into parameter estimates in the form of prior distributions. When using Bayesian techniques, the sensitivity of the calibration result to the prior should be considered and acknowledged if significant.

Additionally, not all calibration parameters are equally important to consider; specifically, the degree of consideration paid to an updated parameter should scale with the model's sensitivity to that parameter. Model sensitivity analysis typically refers to evaluating the magnitude of change in a prediction caused by changes to an input parameter's value.

Suggested Documentation What is the accuracy of the selected calibration/estimation procedure for important model parameters in the application? Was additional information incorporated into the parameter estimates? What is the sensitivity to updated and non-updated parameters?

2.2.5 Validation

Once the dataset is understood, the model selected, and the model fit to best represent the data, the model's validity should be judged with regards to the prediction of interest (quantity deemed comparable to requirement). Comparing model predictions with experimental data allows for the model's predictive capability, in regards to the prediction quantities of interest, to be quantitatively assessed. Model validation should occur when using physical-based models or statistical models [6]. Model validation has become a major area of emphasis in the CompSim domain [22, 23], and is well developed for statistical cross-validation of models [24–26]. It should be noted that validation cannot prove a model's predictive capability, only provide supporting evidence. If data sufficiently relevant to the requirement was available, then this data would be used to make the QMU assessment, and models would not be needed.

Suggested Documentation How well does the model predict the available data? Can the model be compared to an ‘external test set,’ i.e., data that were not used to build or calibrate the model? If so, what is the fidelity of the validation data? Are the model predictions consistent with subject matter knowledge? How relevant to the requirement is the validation?

2.3 Evaluating Credibility

Once these elements of credibility have been evaluated, then these elements can be assimilated to provide an overall assessment of credibility. Each of the five elements should undergo a **peer review** of the analysis decisions and **documentation** of those decisions so that the analysis can be fully understood at a later date. Both peer review and documentation are also included in the aforementioned experimental [17] and CompSim credibility approaches [13]. When presenting QMU results to a decision-maker, overviews of these five elements should be included in order to allow the decision-maker to better understand the value of information contained.

Whether to develop a quantitative scale for scoring analysis credibility remains an open question. Many ‘predictive maturity’ frameworks assign numeric scores to sub-elements and combine the sub-scores to create an overall score. For instance, in PCMM, sub-elements are assigned an ordinal score from 0 to 3, and the PCMM authors suggest methods for combining sub-element scores into a single overall score, though advise against this collapsing of information due to interpretability issues [13]. Zeng et al. score the ‘trustworthiness’ of methods using a decision model based on the analytic hierarchy process [27]. Hemez et al. developed a predictive maturity index, emphasizing the need to go beyond goodness of fit and consider a more wholistic picture of credibility when evaluating the predictive maturity of modeling and simulation based results [19].

We do not score credibility herein, instead favoring a more qualitative synopsis of the credibility supporting evidence. Following [13], we argue that there is not a natural ‘weighting’ of the subelements that can produce a meaningful overall score. Further, our experience suggests that quantitative scoring can become highly politicized and arbitrary. When presenting credibility results, we recommend that, instead of collapsing information into a quantitative score, information should be collapsed into a set of key points. Specifically, the sensitivity of the QMU predictions to the model assumptions should be qualitatively or quantitatively assessed. Elements with particularly low credibility and potentially high impact should be highlighted. In areas of concern, sensitivity studies [28] can be conducted to determine the potential quantitative impact of an assumption. If the QoI results hinge on assumptions that are highly uncertain, then the analysis naturally lacks credibility.

2.4 Example Application

To demonstrate our concept of QMU credibility, the proposed framework is applied to a simulated molten-salt battery dataset. The example is meant to resemble a real-world equivalent that could be generated from a production facility. Conditions varied within the dataset are the environmental temperature (-35°C to 65°C), intensity of the current loading profile (characterized as varying intensities between 0 and 1), and production lot number (1 through 7). Typical means of visualizing this dataset against a requirement are shown in Fig. 2.1. The performance requirement specified for this dataset is for the baseline voltage to remain above 30 V for a specified time. The dataset is comprised of observed baseline voltages at the required time. Examination of the plots would seem to show that the requirement would be met, but it is also difficult to know how useful the information provided is in answering the question “what is the margin to the requirement and what are the associated uncertainties in that estimate?”

In order to better answer this margin and uncertainty question, suggested documentation from the proposed QMU credibility assessment framework when applied to the molten salt battery example is now provided.

2.4.1 Requirement Definition and QoI Selection

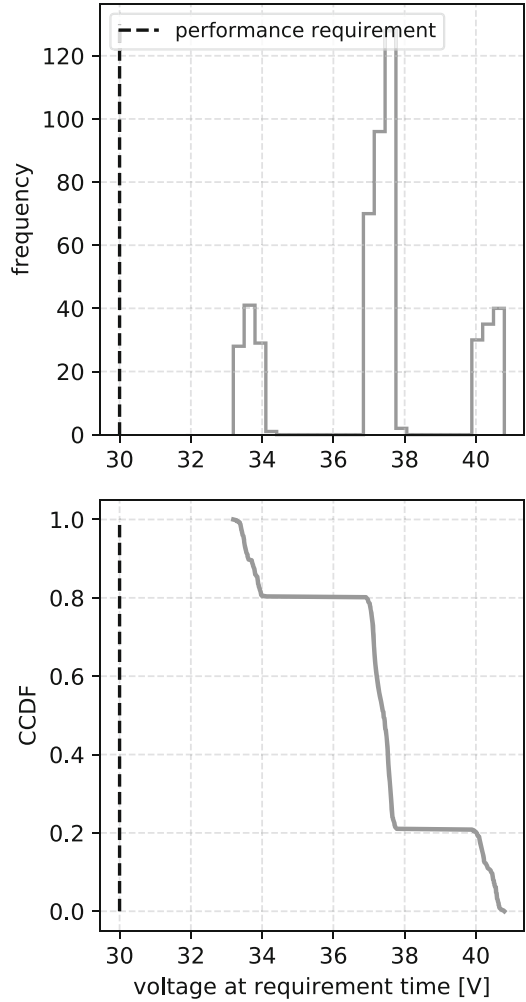
Requirement: Once activated, 99.5% of batteries must maintain a baseline voltage above 30 V for YY seconds.

QoI: Predict the baseline voltage at the requirement time, in the battery population at their harshest temperature and loading conditions at end of life.

Rationale: The requirement must be met in the current battery stockpile for all application environments. Therefore, environments that impact battery voltage, such as temperature, loading profile, and age, must be considered.

Uncertainties: The QoI is defined at the worst-case load and temperature, but the requirement is ambiguous about those effects. It is improbable that the battery will ever experience these environmental extremes in use-environments. Therefore, predictions to the worst-case setting may be too conservative and sensitivity studies should explore the impact of this conservatism. The requirement specifies a 0.995 reliability, so variability in the battery population must be considered to reach comparable terms.

Fig. 2.1 Raw battery performance data (500 samples) available for comparison to requirement. The top figure shows data's battery performance measure as a frequency density, where the three subpopulations come from the three testing temperatures. A cumulative complementary density function of the same performance measure is shown in the second plot as an example of another common method of visualizing QMU datasets



2.4.2 Data Quality

Metadata/Source: The data was gathered during production 15 years ago and captured using two high quality testers by three operators (equally distributed). The measurement method was developed during battery design process.

Uncertainty: Uncertainty in the data primarily stems from the lack of representativeness. Individual sources of uncertainty are detailed below.

Sparsity: 500 units were tested at different environmental conditions. The quantity of data was deemed sufficient, but may require extrapolation from a statistical model to characterize tail behavior and estimate the percentile of interest and corresponding uncertainty.

Representativeness: Tested units were randomly sampled from all produced units and are therefore representative of all production lots. Tested units span the full temperature and loading conditions of interest, but were tested immediately after production and therefore do not provide any information about battery aging.

Noisiness/Measurement uncertainty: Loading and voltage measurements are sufficiently precise. Experimental temperature conditions are within $\pm 0.5^\circ\text{C}$. Unit to unit variability is expected due to manufacturing tolerances of components, but will need to be characterized.

Bad data/Outliers: No outliers found.

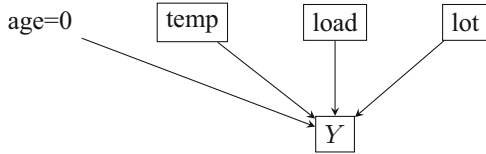


Fig. 2.2 Causal network for molten salt battery. Boxes indicate observed variables. In causal language the boxes would be known as interventions due to those variable values being manipulable for a single battery test. Age is believed to potentially have a causal relationship with the QoI (Y , voltage), but is always 0 in the available data

2.4.3 Model Uncertainty

Type of model: For this dataset a statistical model is used, so causal and functional assumptions can be assessed.

Causal structural assumptions: An underlying causal model for the molten-salt battery system was elicited from experts and shown below in a causal network format (Fig. 2.2).

Age, temperature, loading conditions, and manufacturing lot number are all covariates that have a causal relationship with voltage. This causal structure assumes that the covariates are not confounders (no association between inputs).

To estimate the QoI (the voltage at the worst-case temperature and load) using the data, we define the QoI of interest as:

$$Y_Q(lot) = (Y|age, load, temp, lot) \quad (2.1)$$

$$Y_Q = (Y|age, load, temp) \quad (2.2)$$

$$= \int Y_Q(lot) P(lot) dlot \quad (2.3)$$

An omitted variable bias exists, because all production data was collected on un-aged batteries. Expert judgement can be leveraged to determine the potential impact of this bias. To estimate the QoI, we assume:

$$Y_Q(lot) = (Y|age = 0, load, temp, lot) + \delta_A \quad (2.4)$$

where δ_A is an additive shift due to age that is elicited from experts or an auxiliary source of information.

Selection bias may also be present in the dataset due to a great number ($\approx 60\%$) of the samples coming from room temperature tests versus the tests at temperature extremes ($\approx 20\%$ each). Because we condition on temperature in the QoI, this selection bias should not impact the ability to make inference about the QoI, though it does increase the variance of the estimated effect of temperature on voltage.

Functional assumptions: To model $Y_Q(lot)$, a linear model is assumed to be an appropriate method of representing the input-output relationships:

$$Y_Q(lot) = \alpha_0 \times temp. + \alpha_1 \times load + \sum_{i=1}^{lots} \alpha_{1+i} I(i = lot) + \epsilon \quad (2.5)$$

$$\epsilon \sim N(0, \sigma^2) \quad (2.6)$$

This model assumes linear relationships between the input parameters and output; and assumes that interactions between parameters are insignificant. Further, residual variability due to manufacturing tolerances is modeled using a normal distribution. Because age = 0 in the dataset, age-effects cannot be estimated in the fitted statistical model.

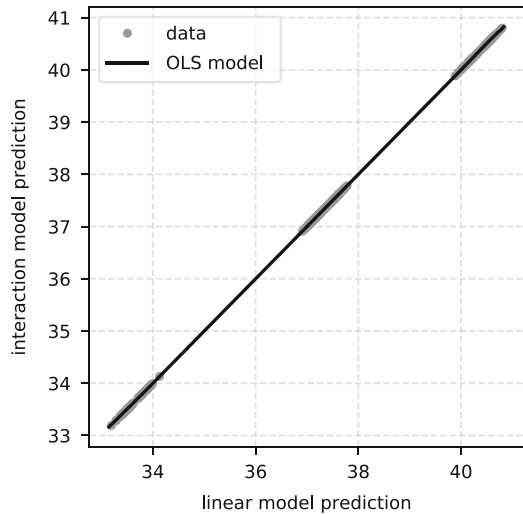
2.4.4 Calibration/Parameter Estimation

Parameter estimation procedure: Ordinary least-squares (OLS) minimization is used to fit the statistical model. Because the sample size is large ($n = 500$) and model is simple, there are no meaningful uncertainties associated with the parameter estimation procedure. Fit results are shown below with standard errors and manufacturing variability captured as the model residual (Table 2.1).

Table 2.1 OLS model parameter fits and standard errors

Parameter	OLS fit	Std. err.
α_0	0.067	9.9E-5
α_1	-0.784	0.013
α_2	36.48	0.012
α_3	36.56	0.014
α_4	36.60	0.013
α_5	36.63	0.014
α_6	36.57	0.013
α_7	36.63	0.013
α_8	36.71	0.012
σ	0.0734	-

Fig. 2.3 Validating linear assumption by comparing an OLS fit containing no-interaction terms to one with first order interactions



Parameter sensitivities: Variability due to lot number is found to be differentiable through calibration, but the major model sensitivities are due to the load and temperature. Sensitivity to aging cannot be inferred from the data, leaving an unknown in the analysis.

2.4.5 Validation

Prediction performance: With ample data the functional assumptions of linearity and no interaction can be evaluated from the data, as shown in Fig. 2.3. Comparing the data fit of the model without any interactions to one with all possible interactions demonstrates that no improvement in fit occurred.

Prediction assessment: The model's predictions are consistent with behaviors anticipated by subject matter experts. The normal-residuals assumption can be empirically checked for inaccuracy. However, because we are using the model to predict a 99.5th percentile from data collected at multiple loads and temperatures, we cannot directly confirm this assumption for the temperature/load condition where we are predicting (50 out of 500 samples were at the worst-case conditions).

2.4.6 Summary of Credibility Assessment

Key assumptions that were identified include: relevance of the QoI, normality of the residuals, and no battery aging. Sensitivity studies can be conducted to evaluate the impact of these assumptions. For instance, worst case temperature (-35°C) and loading conditions (1) have been assumed for the QoI. Figure 2.4 compares the calibrated model's prediction battery performance uniformly sampled across all conditions of interest with the predictions only for the worst case scenario, demonstrating how this QoI assumption significant impacts on our QMU conclusions. Model predictions for the worst-case

Fig. 2.4 Illustration of potential QoI bias from using most strenuous conditions to define performance, as compared to general population. Shaded regions show 95% confidence intervals

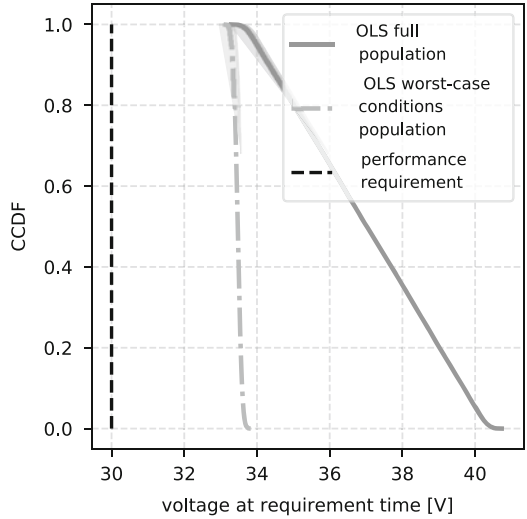
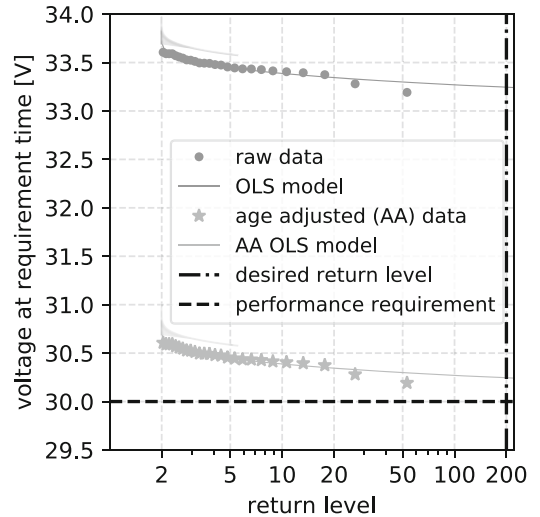


Fig. 2.5 Comparison of return level trends for raw experimental data at most strenuous temperature and loading conditions with (asterisk) and without (filled circle) inclusion of worst case aging impact. Estimates of percentiles based on the raw data with 95% confidence intervals (shaded regions) are compared with those based on the fitted model (line). Variability in predictions is due to lot differences and unit-to-unit variability



scenario are still a distribution, due to including lot and unit-to-unit variability. Comparing the worst-case distribution with the full potential distribution shows the degree of conservatism being added to the analysis. Experts may also have some knowledge about the appropriateness of a normal approximation to represent unit to unit variability in battery performance; to elicit such information, analysts can inquire about subpopulations or non-linearities in manufacturing tolerances that would result in a multi-modal, skewed, or heavy tailed distribution. Subject matter experts can be consulted to determine the impact of age on voltage over time, resulting in sensitivity information such as: aging will reduce the performance in a linear manner by at worst 3 V by the end of lifetime of the battery population.

In order to estimate the 99.5th percentile of the battery population at the worst case conditions, extrapolation using the model is needed due to only limited data available for those conditions. Figure 2.5 illustrates both the sensitivity to aging and the extent of extrapolation through plotting the experimental data and model predictions in terms of return level [29]. Return level is $\frac{1}{1 - \text{percentile}}$; for instance, a return-level of 200 can be interpreted as the average number of units necessary to detect one failure (or, similarly, to inform a 0.995 reliability requirement) [18]. While the raw data trend and model predictions for the worst-case temperature and loading conditions show significant margin (~ 3.25 V) with minimal uncertainty (~ 0.14 V), when the worst case aging impact is considering, the margin becomes small (~ 0.25 V). Here margin is defined as the distance from the model's mean estimate of the 99.5th percentile and uncertainty is distance from the mean 99.5th percentile estimate to the lower 95% confidence interval bound. With such a small margin, the results have an increased sensitivity to the assumptions used to extrapolate with the model. Where the uncertainty in the margin prediction was insignificant when age effects were neglected, it becomes potentially significant once that effect is considered. In a standard QMU analysis, the potential impact of an unquantified variable like age would likely not be presented.

2.5 Summary

Following the recent revamping of the QMU process at Sandia and current emphasis on prediction credibility, guidance for assessing the credibility of QMU analyses is needed. Direction for how to communicate credibility of CompSim and experimental gathering campaigns (designed to support CompSim analysis) is already being developed. The future QMU paradigm will likely look more like experimentally supported CompSim than the historic model that was largely experimental based. With this change in QMU paradigm comes the need to provide credibility evidence with any QMU result. Five elements have been proposed as the basis for QMU credibility assessment framework: requirement definition and QoI selection, data quality, model uncertainty, calibration/parameter estimation, and validation. Through considering those elements and proposed subelements, documentation and communication of such information should be included in the communication of any QMU results. With this information the decision-maker receives a greater appreciation of the assumptions that went into generating the results as well understanding of the utility of the information provided. The application of this QMU credibility framework has been demonstrated on a molten-salt battery dataset.

Acknowledgements

Review We would like to thank John R. Lewis and Aubrey C. Eckert-Gallup for their helpful comments that allowed us to refine and improve this paper.

Funding This work was supported by a Sandia National Laboratories Laboratory Directed Research and Development (LDRD) grant. Sandia National Laboratories is a multimission laboratory managed and operated by National Technology and Engineering Solutions of Sandia, LLC., a wholly owned subsidiary of Honeywell International, Inc., for the U.S. Department of Energy's National Nuclear Security Administration under contract DE-NA0003525. SAND2018-11643 C.

References

1. Merriam-Webster Dictionary. <https://www.merriam-webster.com/dictionary/credibility>
2. National Research Council: Evaluation of Quantification of Margins and Uncertainties Methodology for Assessing and Certifying the Reliability of the Nuclear Stockpile Committee on the Evaluation of Quantification of Margins and Uncertainties Methodology for Assessing and Certifying the Reliability of the Nuclear Stockpile. National Academies Press, Washington (2008)
3. Kaplan, S., Garrick, B.J.: On the quantitative definition of risk. *Risk Anal.* **1**(1), 11–27 (1981)
4. Pilch, M., Trucano, T., Helton, J.: Ideas underlying quantification of margins and uncertainties (QMU): a white paper, Technical Report SAND2006-5001, Sandia National Laboratories (2006)
5. Newcomer, J.: A new approach to quantification of margins and uncertainties for physical simulation data, Technical Report SAND2012-7912, Sandia National Laboratories (2012)
6. Hund, L., Schroeder, B., Rumsey, K., Murchison, N.: Robust approaches to quantification of margin and uncertainty for sparse data, Technical Report SAND2017-9960, Sandia National Laboratories (2017)
7. Roy Dholakia, R., Sternthal, B.: Highly credible sources: persuasive facilitators or persuasive liabilities? *J. Consum. Res.* **3**(4), 223–232 (1977)
8. Gass, R.H., Seiter, J.S.: Persuasion: Social Influence and Compliance Gaining. Routledge, Abingdon (2015)
9. Lev-Ari, S., Keysar, B.: Why don't we believe non-native speakers? The influence of accent on credibility. *J. Exp. Soc. Psychol.* **46**(6), 1093–1096 (2010)
10. Chaiken, S., Maheswaran, D.: Heuristic processing can bias systematic processing: effects of source credibility, argument ambiguity, and task importance on attitude judgment. *J. Pers. Soc. Psychol.* **66**(3), 460 (1994)
11. Heesacker, M., Petty, R.E., Cacioppo, J.T.: Field dependence and attitude change: source credibility can alter persuasion by affecting message-relevant thinking. *J. Personal.* **51**(4), 653–666 (1983)
12. Mehta, U., Romero, V., Eklund, D., Pearce, J., Keim, N.: The JANNAF simulation credibility guide on verification, uncertainty propagation and quantification, and validation. In: 53rd AIAA Aerospace Sciences Meeting, AIAA SciTech Forum (2015)
13. Oberkampf, W.L., Pilch, M., Trucano, T.G.: Predictive capability maturity model for computational modeling and simulation, Technical Report SAND2007-5948, Sandia National Laboratories (2007)
14. Beghini, L., Hough, P.: Sandia verification and validation challenge problem: a PCMM-based approach to assessing prediction credibility. *J. Verif. Valid. Uncertain. Quantif.* **1**, 011002 (2016)
15. Schroeder, B., Silva, H., Smith, K.: Separability of mesh bias and parametric uncertainty for a full system thermal analysis. In: ASME 2018 Verification and Validation Symposium, pp. V001T04A003–V001T04A003. American Society of Mechanical Engineers, May 16, 2018
16. Oberkampf, W.L., Smith, B.: Assessment criteria for computational fluid dynamics model validation experiments. *J. Verif. Valid. Uncertain. Quantif.* **2**, 031002 (2017)
17. Kieweg, S.L., Witkowski, W.R.: Experimental credibility and its role in model validation and decision making. In: Model Validation and Uncertainty Quantification, vol. 3, pp. 31–36. Springer, Cham (2019)
18. Hund, L., Schroeder, B., Rumsey, K., Huerta, G.: Distinguishing between model- and data-driven inferences for high reliability statistical predictions. *Reliab. Eng. Syst. Saf.* **180**, 201–210 (2018)

19. Hemez, F., Atamturktur, H.S., Unal, C.: Defining predictive maturity for validated numerical simulations. *Comput. Struct.* **88**(7–8), 497–505 (2010)
20. Pearl, J., Glymour, M., Jewell, N.P.: *Causal Inference in Statistics: A Primer*. Wiley, Hoboken (2016)
21. Bareinboim, E., Pearl, J.: Causal inference and the data-fusion problem. *Proc. Natl. Acad. Sci.* **113**(27), 7345–7352 (2016)
22. Oberkampf, W., Barone, M.: Measures of agreement between computation and experiment: validation metrics. *J. Comput. Phys.* **217**(1), 5–36 (2006)
23. Liu, Y., Arendt, P., Huang, H.: Toward a better understanding of model validation metrics. *J. Mech. Des.* **133**(7), 071005 (2011)
24. Stone, M.: Cross-validatory choice and assessment of statistical predictions. *J. R. Stat. Soc. Ser. B Methodol.* **36**, 111–147 (1974)
25. Efron, B.: Estimating the error rate of a prediction rule: improvement on cross-validation. *J. Am. Stat. Assoc.* **78**(382), 316–331 (1983)
26. Hastie, T., Tibshirani, R., Friedman, J.: *The Elements of Statistical Learning: Data Mining, Inference, and Prediction*, 2nd edn. Springer Series in Statistics. Springer, New York (2009)
27. Zeng, Z., Di Maio, F., Zio, E., Kang, R.: A hierarchical decision-making framework for the assessment of the prediction capability of prognostic methods. *Proc. Inst. Mech. Eng. O: J. Risk Reliab.* **231**(1), 36–52 (2017)
28. EricksonKirk, M., et al.: Sensitivity studies of the probabilistic fracture mechanics model used in FAVOR version 03.1. In: NUREG-1808, US Nuclear Regulatory Commission, ADAMS ML, vol. 61580349 (2004)
29. Coles, S., Bawa, J., Trenner, L., Dorazio, P.: *An Introduction to Statistical Modeling of Extreme Values*, vol. 208. Springer, London (2001)



Chapter 3

Failure Behaviour of Composites Under Both Vibration Loading and Environmental Conditions

Georgios Voudouris, Dario Di Maio, and Ibrahim Sever

Abstract The study focuses on the understanding of failure behaviour of composites which are subjected to vibration fatigue under environmental temperature conditions. The study of vibration fatigue failure in composites can be challenging because of the coupling between mechanical and thermal properties. In fact, stiffness distribution and self-heating are typically occurring under vibration conditions. As the problem stands, the sole use of either testing or simulation would not be adequate to understand the failure behaviour fully. This paper will present both an experimental and numerical work, based on a component designed with a ply-drop feature to enhance and localise the damage occurrence. The vibration testing experiments were carried while an environmental chamber was used to control the exposure temperature. Similar experimental conditions are simulated in a finite element multi-physics environment, where the crack opening is modelled by VCCT method. The simulation environment is very challenging because both mechanical (dynamics) and thermal behaviours need to be incorporated to study the failure of a given vibration loading. Both experimental and numerical results will be qualitatively compared.

Keywords High cycle vibration fatigue · Environmental temperatures conditions · Carbon fibre reinforced polymers · Finite element · Virtual crack closure technique

3.1 Introduction

The accurate prediction of fatigue failure, of polymer-based composites, depends on the effects of various factors, such as the environmental conditions as well as the material properties. It is understood that changes in the temperature and moisture conditions, can lead to an acceleration in the fatigue damage accumulation of composite components. Therefore, it is of greater significance to consider the role of the ambient temperature when studying the fatigue failure of composites.

There are only a few references in the literature relating the surrounding temperature and the fatigue characteristics of composite materials. A typical feature of most studies is to investigate the behaviour of composites at pure mode I or II while the excitation frequency is not greater than 10 Hz [1–4]. In a recent study, Coronado et al. [1] asses the Interlaminar Fracture Toughness (IFT) of Uni-Directional carbon fibre composite (AS4/3501). Static and fatigue tests were carried out in a temperature range between –60 °C and 90 °C. The authors reported that under cyclic loading, the initiation Energy Release Rate is increased with temperature while less energy is required for the crack propagation. Overall, elevated temperatures seem to lead to higher ductility while sub-zero temperature can result in a more brittle behaviour of the material. It was also observed that the Fatigue Delamination Growth Rate (FDGR), at –30 °C and –60 °C, progressively dropped as the delamination length increased. Sjögren and Asp [2], continued the work of Asp [3], and studied the delamination characteristics of a carbon fibre system (HTA/6376), at 20 °C and 100 °C. The tests were performed for three different loading scenarios: Pure Mode I and II and for a 50% mode-mixity. It was noticed that the FDGR is accelerated at higher exposure temperatures. Furthermore, it seems that mode II can affect greatly the delamination growth. In addition to these,

G. Voudouris
Bristol Composites Institute (ACCIS), University of Bristol, Bristol, UK
e-mail: G.Voudouris@bristol.ac.uk

D. Di Maio (✉)
Department of Mechanical Engineering, University of Bristol, Bristol, UK
e-mail: Dario.DiMaio@bristol.ac.uk

I. Sever
Rolls-Royce plc, Derby, UK
e-mail: Ibrahim.Sever@rolls-royce.com

Charalambous et al. [4], performed a fatigue delamination characterisation study on Carbon Fibre Reinforced Polymers (CFRP), namely IM7/8552, at an ambient temperature range between 50 °C and 80 °C. A mode-mixity of 43% was investigated at a frequency of 5 Hz. The authors concluded that delamination crack propagates two orders of magnitude faster at 80 °C in comparison to Room Temperature.

Most studies seem to prefer low cycle, mechanical three-point bending tests, over high cycle vibration fatigue ones. This strategy can be explained since the viscoelastic properties of composite components can introduce added challenges in the fatigue testing. So, researchers would prefer low cycle testing in an effort to eliminate this phenomenon. More specifically, during high cycle fatigue testing of composite components, the internal temperature of the specimens is increased [5]. This phenomenon is commonly known as the self-heating temperature. It has been reported that the self—the heating temperature has the potential to alter the fatigue strength of specimens [2, 6].

However, certain attends have been made in the past for high cycle vibration fatigue testing. Only recently, Just-Agosto [7] introduced a vibration fatigue testing method which he then used for testing a foam material. In a continuation of this study, Gu et al. [8] applied this tree point bending technique to analyse the fatigue behaviour of a Glass Fibre material system. Di Maio [9] develop a testing technique which dictates that a specimen be excited at resonance until fatigue damage is developed. Magi et al. [10] utilised this method for the investigation of CFRP. They correlated the change of dynamic properties of a specimen, during endurance testing, with its stiffness degradation.

It is therefore apparent that various factors, such as the ambient and the shelf-heating temperatures, can affect the fatigue life of composite components. For this reason, one might never be able to isolate the mechanical and thermal properties of carbon fibre composites, fully. For this reason, the primary purpose of this paper is to show that the integration of experimental and analytical results aids the in-depth analysis of the fatigue failure characteristics of CFRP while taking into account the ambient temperature levels.

3.2 Experimental and Numerical Methods

3.2.1 Experimental Procedure

A customised fixture was developed to accommodate the endurance testing of specimens in an environmental chamber which can maintain and control the temperature condition during the test. The environmental chamber was insulated; apart from a small opening on the top which permits a Thermal Camera and a Scanning Laser Vibrometer to take a reading during testing. Thermocouples were installed at critical positions in the chamber to ensure that the temperature level is similar for different tests. Before each test, a stabilisation period of 90 min was required for the specimens to reach thermal equilibrium. In addition to this, an appropriate heat input value was selected in the chamber which maintains the inside temperature within a range of ± 0.5 °C for 10^7 cycles. The fixture was attached to an Electromagnetic Shaker which excites the specimens close to resonance frequency (Fig. 3.1). Strain gauges were installed to correlate the vibration amplitude at the measurement point of the laser beam and the strain level. Fatigue tests were carried out at 25 °C, 50 °C, 65 °C and 75 °C; keeping strain levels of the tests the same for the different temperature levels. This approach permits the comparison of the results. Furthermore, this technique promotes the separation between the mechanical and the ambient temperature effects since the applied strain level is the same at different temperature levels. As a result, the exposure temperature has the dominant effect in the fatigue failure of specimens.

The component is a rectangular specimen 185 mm × 50 mm, made with 20 prepreg plies of IM7/8552, four of which are interrupted plies 110 mm × 50 mm (Fig. 3.2). The stacking sequence is [0, 0drop, 90drop, (0, 90)3, 0]s. The ply-drop section acts as stress raiser and allocates the damage initiation region. Specimens were cut into shape with great accuracy (≤ 1 mm) since uneven dimensions, among specimens, can lead to undesired behaviours, such as the rotation of the sample during vibration, which was experienced on some experiments.

3.2.2 Experimental Results

Di Maio's experimental method was adopted for this study [9]. The technique dictates that the specimens should be excited near the resonance frequency (≈ 400 Hz) and at the first bending mode. The testing coupons are excited at a constant amplitude which translates to a constant strain level for the duration of the experiment. A key feature of the method is that the typical Phase Lock Loop (PLL) is replaced by a Frequency Lock Loop (FLL) to trace the response phase rather than



Fig. 3.1 Experimental set up

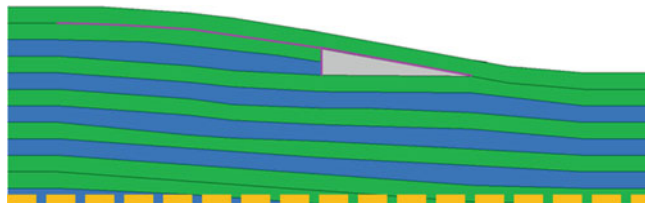


Fig. 3.2 Specimen layup and ply drop (green: 0° plies/blue: 90° plies/grey: resin pocket/purple: crack propagation)

the resonance frequency. In fact, by fixing the excitation frequency, one can observe more accurately how a change of the internal stiffness distribution affects the component dynamics. After a sudden change at the beginning of the test, which is assumed to be transverse crack development, the response phase traces a constant slope decay which is believed to be initial delamination opening. A sudden change in the response phase is measured when the delamination size becomes critical (critical event) The High Cycle Fatigue (HCF) tests are interrupted if either the Critical Delamination Size (CDS) or the 10^7 cycles are met first.

Further testing revealed that the self-heating temperature of a specimen, follows almost a reversed behaviour (Fig. 3.3). This behaviour is better presented in Fig. 3.4, where the response phase is plotted against the temperature profile. This is repeated for three environmental temperatures and the plots clearly show linearity with different slopes. Since the specimen's self-heating temperature is the result of an applied strain the plot in Fig. 3.4 includes the three parameters, such as phase, temperature and strain.

By analysing the Fig. 3.3 further, one can notice that the graphs are separated into three quasi-linear regions. Region A corresponds to the achievement of a hysteretic equilibrium between the forced vibrations and the heat dissipation. The self-heating temperature would stabilise if the strain energy in the sample would not allow any crack propagation. The rapid change of the response phase in this region implies that the transverse crack is being developed.

As soon as the hysteretic thermo-mechanical equilibrium is reached the phase and the specimen's temperature experience linear increase and decrease, respectively (Region B). This condition is being understood because of the modelling of the

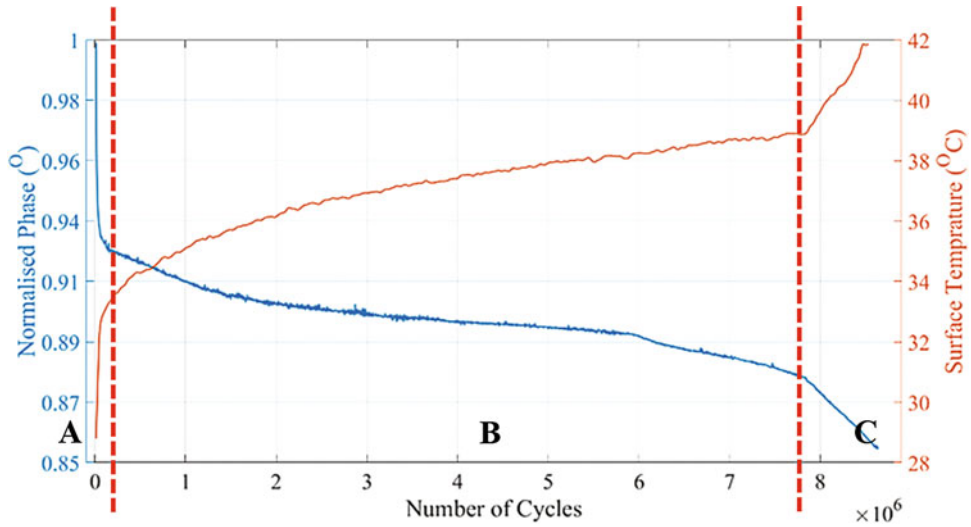


Fig. 3.3 Phase/specimen's surface temperature change during endurance testing

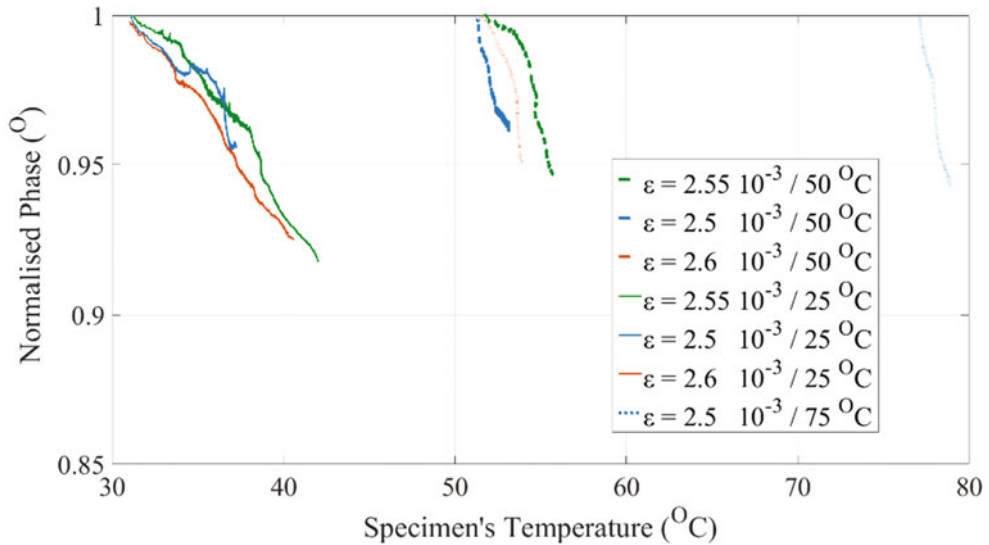


Fig. 3.4 Quasi-linear curves describing the phase vs. the specimen's temperature profile at different environmental temperatures

crack propagation by Virtual Crack Closure Technique. In fact, the model (described in the following section) shows how the crack opens and develops because of the mechanical dynamic stress.

Eventually, the crack reaches a critical size which, for the given vibration energy, will open up to a certain length. As a result of the delamination opening, the surface temperature of a specimen increases rapidly due to the ply by ply rubbing. The newly formed delamination leads to a rapid deterioration of the specimen's stiffness.

Figure 3.5 presents the typical Response Phase evolution of specimens that are subjected to vibration fatigue and different strain levels. It can be seen that with increasing strain, the fatigue life of specimens decreases. This implies that the stiffness of specimens deteriorates faster.

Figure 3.6 presents the Phase Evolution of testing coupons that are excited at the same strain level (2.55×10^{-3}) but they are exposed at different surrounding temperatures. One can observe that the critical event occurs faster at elevated temperatures. Therefore, the fatigue life of CFRP is shorter at higher ambient temperature levels. It is also important to notice that the effect of environmental temperature seems to be more severe than the strain effects on the fatigue life of CFRP.

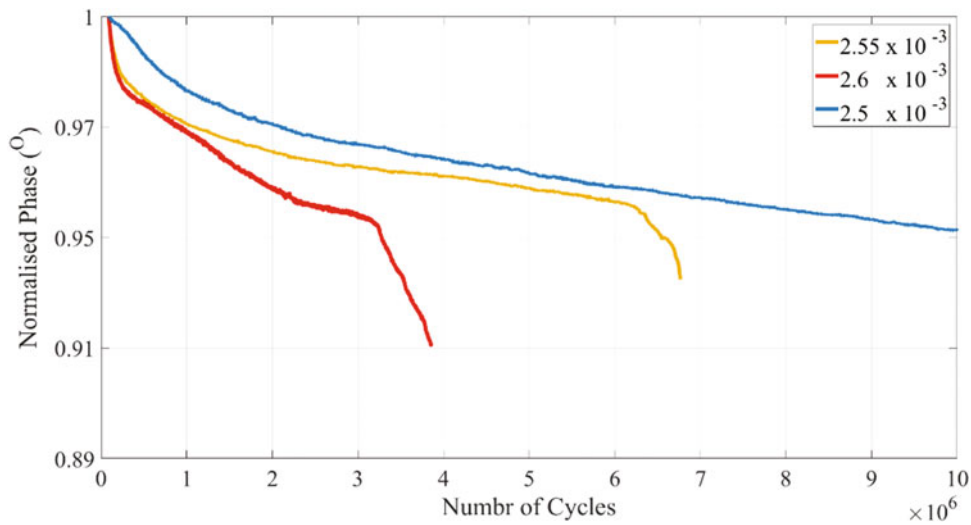


Fig. 3.5 Phase evolution at different strain levels

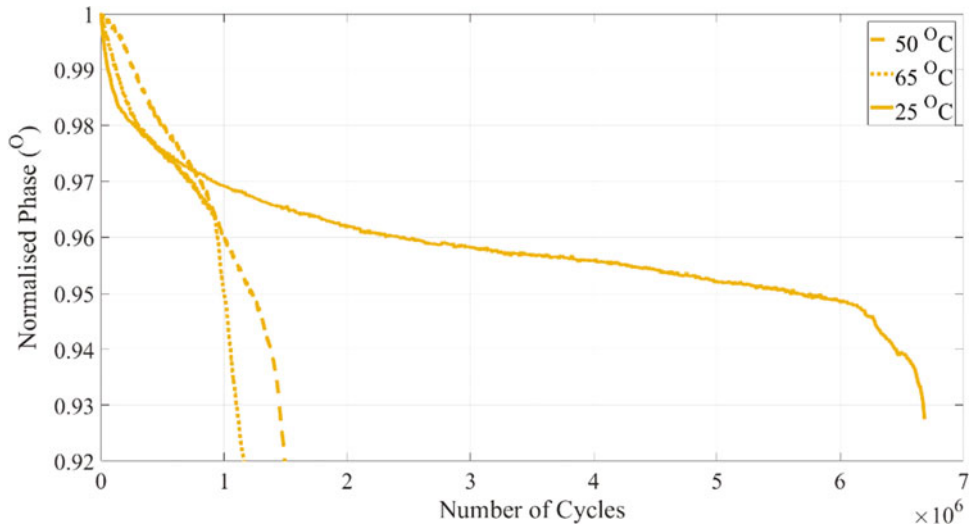


Fig. 3.6 Phase evolution at different ambient temperature levels ($\varepsilon = 2.55 \times 10^{-3}$)

3.2.3 Numerical Approach

Magi [11] applied the Virtual Crack Closure Technique (VCCT) to verify that the experimental results were sensible. In fact, there were other experimental methods to measure the crack opening during the vibration fatigue and to verify that the change in the response phase was associated with an almost abrupt crack opening. The numerical experiment proved that delamination opens earlier than the change observed in the response phase, but the delamination size becomes critical when the phase suddenly drops. However, he did not take into account the self-heating and environmental temperature. This section aims at repeating the work of Magi for the VCCT and also include the ambient temperature as an additional parameter affecting the formation of a crack.

A 2D model was employed for the VCCT. The model was built to resemble the testing coupons (Fig. 3.2) closely. It is important to build the correct geometry of the specimens in order to capture the correct vibration mode. For this reason, the shape of the ply-drop was traced from the micrographs of the specimens. CT scans also showed that crack initiates from the resin pocket and then develops into delamination (Fig. 3.2). As a result, a similar pattern was used in the Finite Element Model. However, multiple iterations are required to study each step of the crack propagation with high accuracy. The model was implemented on Abaqus using the Steady-State Dynamics Analysis.

Table 3.1 Physical and mechanical properties of HTA/6376

E_1 (GPa)	$E_2 = E_3$ (GPa)	$v_{12} = v_{13}$ (GPa)	v_{23} (GPa)	ρ (kg/m ³)
164	10	0.3	0.45	1571

Table 3.2 Fracture mechanics properties of HTA/6376 [12]

	20 °C			100 °C		
	G_{Ic} (J/m ²)	C_m	n_m	G_{Ic} (J/m ²)	C_m	n_m
Mode I	260	1.2×10^7	5.5	249	4.2×10^6	4.2
Mode II	1002	7.5×10^7	4.4	701	9.1×10^6	4.6

As it was discussed in [11], a Paris Law has to be used to investigate the Crack Growth Propagation Rate. Therefore, the Paris Law can be described as follows:

$$\frac{da}{dN} = C_m \times \left(\frac{G_{I_{max}}}{G_{Ic}} + \frac{4G_{II_{max}}}{G_{IIc}} \right)^{n_m} \quad (3.1)$$

Where da is the crack length, dN is the Number of Cycles and $G_{I_{max}}$, $G_{II_{max}}$ are the fracture toughness of the material for the opening and sliding modes, respectively. C_m , n_m , G_{Ic} and G_{IIc} are constants. These constants are significantly affected by the testing temperature and their respective values for CFRP systems can be found in the literature (Tables 3.1 and 3.2). Therefore, one can investigate the behaviour of the material at different ambient temperatures by employing the appropriate material properties.

Finally, it is essential that the analytical model follow the experimental method. Hence, the vibration response was kept constant at each iteration in order to trace the Response Phase, correctly. In order to achieve this requirement, the excitation force was altered in every iteration, to reflect the deterioration in stiffness of the specimen at given vibration frequency. The stiffness deteriorates as the crack propagates.

3.2.4 Analytical Results

Figure 3.7 shows the analytical results acquired from the VCCT simulation. It can be observed that this technique managed to replicate the Response Phase evolution, closely. More specifically, the phase follows similar quasi-linear trends, and it can be separated into three regions. Hence, the critical event can be easily identified. Figure 3.7 displays the numerical data from simulations of different excitation amplitudes but at the same ambient temperature level. It can be seen that the critical event occurs earlier at higher severity levels; similar to the experimental trends. This implies a shorter fatigue life that emerges from an accelerated stiffness deterioration.

The effects of environmental temperature are presented in Fig. 3.8. For this scenario, the simulations were implemented using the appropriate material properties, given by literature, to reflect the changes in ambient temperature. Despite that, the vibration amplitude was kept the same to accommodate the comparison of the results. It can be observed that the analytical results follow the experimental trends in this case, too. Fatigue life decreases with increasing temperature since the critical event develops faster. Moreover, as it was discussed for the experimental data, the effects of the surrounding temperature levels seem to be harsher on the fatigue strength of the material than strain levels.

3.3 Conclusion

The VCCT for simulating the crack opening caused by vibration fatigue, at different ambient temperature levels, was introduced and the data were analysed. Data analysis revealed that the simulated response phase evolution follows the experimental data closely. However, the model was not able to capture the exact amount of time required to failure. This phenomenon can be explained since multiple factors affect the final results; as a result, the model is currently unable to integrate all of them. Despite that, the VCCT analysis showed by a qualitative solution how much the environmental temperature could affect the crack opening for a given vibration loading.

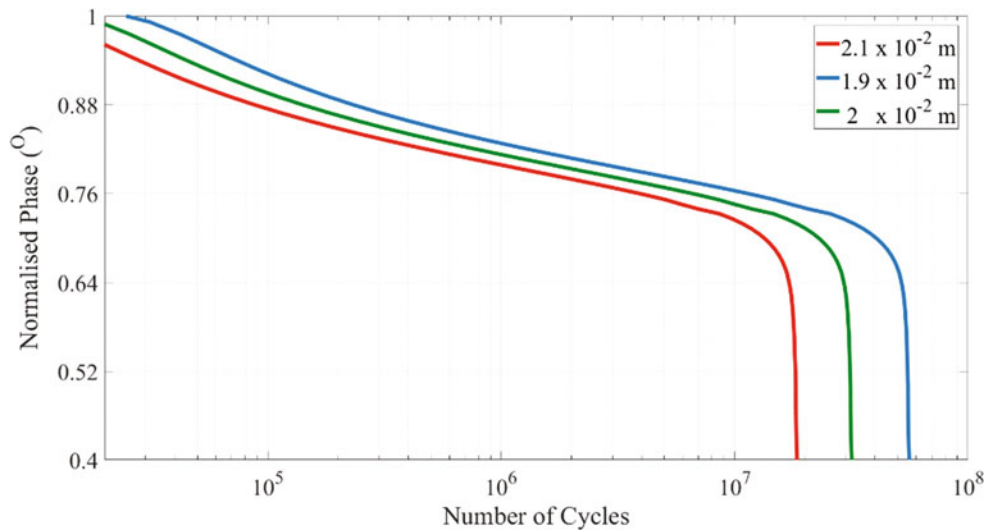


Fig. 3.7 Simulated phase evolution at different amplitudes (m)

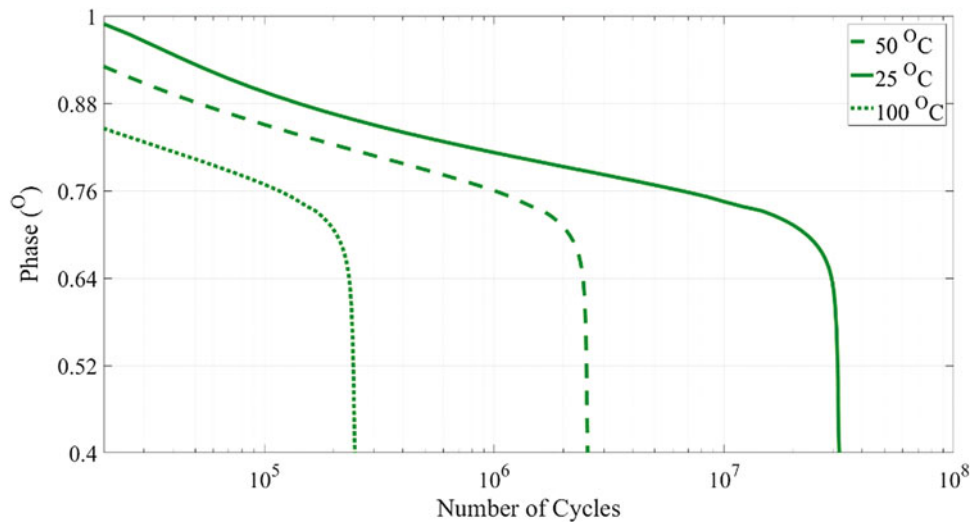


Fig. 3.8 Simulated phase evolution at different ambient temperature levels (at 2×10^{-3} m)

Furthermore, the simulated data were verified against the experimental results, confirming once again how important the use of a numerical aid. It will be essential to understand what parameters should be integrated to perform a comprehensive model validation. Furthermore, interrupted HCF tests were executed and the samples analysed by CT scans. The NDT measurements confirmed that delamination opens before becoming critical as the model simulated it. Finally, the fusion of test and analysis is seen as fundamental to navigate towards the best understanding possible.

Acknowledgements The authors would like to acknowledge the support of Rolls-Royce plc for this research through the Composites University Technology Centre (UTC) at the University of Bristol, UK.

References

1. Coronado, P., Argüelles, A., Viña, J., Mollón, V., Viña, I.: Influence of temperature on a carbon-fibre epoxy composite subjected to static and fatigue loading under mode-I delamination. *Int. J. Solids Struct.* **49**, 2934–2940 (2012)
2. Sjögren, A., Asp, L.E.: Effects of temperature on delamination growth in a carbon/epoxy composite under fatigue loading. *Int. J. Fatigue.* **24**, 179–184 (2002)

3. Asp, L.E.: The effects of moisture and temperature on the interlaminar delamination toughness of a carbon/epoxy composite. *Compos. Sci. Technol.* **58**, 967–977 (1998)
4. Charalambous, G., Allegri, G., Hallett, S.R.: Temperature effects on mixed mode I/II delamination under quasi-static and fatigue loading of a carbon/epoxy composite. *Compos. Part A* **77**, 75–86 (2015)
5. Katunin, A., Fidali, M.: Self-heating of polymeric laminated composite plates under the resonant vibrations: Theoretical and experimental study. *Polym. Compos.* **33**, 138–146 (2012)
6. Varvani-Farahani, H., Mivehchi, A.: Temperature dependence of stress fatigue life data of FRP composites. *Mech. Compos. Mater.* **47**(3), 185–192 (2011)
7. Just-Agosto, F., Peralta, A., Shaq, B., Serrano, D.: A vibration technique to obtain fatigue. In: ICCM17 Proceedings, Edinburgh, UK, 2009
8. Gu, J., Sol, H., Van Paepengem, W.: The study of resonance fatigue testing of test beams made of composite material. In: Proceedings of PACAM XI (2009)
9. Di Maio, D., Magi, F.: Development of testing methods for endurance trials of composites components. *J. Compos. Mater.* **49**, 2977–2991 (2014)
10. Magi, F., Di Maio, D., Sever, I.: Damage initiation and structural degradation through resonance vibration: Application to composite laminates in fatigue. *Compos. Sci. Technol.* **132**, 47–56 (2016)
11. Magi, F., Di Maio, D., Sever, I.: Validation of initial crack propagation under vibration fatigue by Finite Element analysis. *Int. J. Fatigue.* **104**, 183–194 (2017)
12. Sjögren, A., Asp, L.E., Greenhalgh, E.S., Hiley, M.J.: Interlaminar Crack Propagation in CFRP: Effects of Temperature and Loading Conditions on Fracture Morphology and Toughness, Composite Materials: Testing, Design, and Acceptance Criteria, ASTM STP 1416, 2002



Chapter 4

Verification and Validation for a Finite Element Model of a Hyperloop Pod Space Frame

Vignesh Jayakumar, T. S. Indraneel, Rohan Chawla, Sudeshna Mohanty, Shishir Shetty, Dhaval Shiyani, and Shabaan Abdallah

Abstract This paper discusses the verification and validation of a finite element (FE) model of the space frame built by the Hyperloop University of Cincinnati (HUC) team for the first student design competition organized by SpaceX. For the purpose of studying the frame performance in various dynamic scenarios, development of a reliable FE model was crucial. A verification and validation (V&V) strategy utilizing physical modal tests and torsional stiffness tests was adopted to ensure that the FE model was capable of accurately capturing the dynamic characteristics of the constructed space frame. This work aims to present the details of the V&V activities as performed on the main frame.

Keywords Hyperloop · Verification · Validation · Calibration · Modal testing · Torsional stiffness testing

4.1 Introduction

The Hyperloop concept was proposed by Elon Musk in a white paper released in 2013 [1]. To accelerate the research and development of the technology, SpaceX had announced a design competition in 2015. As a part of the competition, teams were required to design reduced scale pods that were to be propelled down a mile-long test track by an electric vehicle pusher. One of the main ideas behind the concept was to maximize the speed of transport by minimizing the friction at the tires through levitation mechanisms and minimizing the air drag by maintaining the test track at sub atmospheric pressures. The pods were also required to brake and come to a halt within the limits of the test track. Modular subsystems on the pod were designed to enable levitation, braking and stability. The main frame was designed to withstand all the loads from these subsystems.

Apart from ensuring that frame satisfies the static load cases and packaging requirements of different subsystems, performance in different dynamic scenarios was required to be studied. In the absence of any existing benchmark data and information on the track loads and due to different cases that needed to be considered, it was decided to rely on a computational approach to study the frame response. Model verification and validation is an activity that carried much importance in achieving this. A verified and validated model helps to improve the confidence in the results from multibody dynamics (MBD) models or any other dynamic studies carried out using the model. The aim of this work is to highlight the verification and validation efforts for the main frame of the pod structure. The results from modal impact testing and torsional stiffness testing were used to calibrate and validate the FE model respectively. A brief description of the pod design is presented first to provide some context. This is followed by an overview of the verification and validation activities as defined in literature and finally the details of the tests and results carried out as a part of this study.

4.2 Frame Design

Figure 4.1 provides a general overview of the HUC pod design and the individual subassemblies that attach to the frame. The main frame weighed 70 lb. and was designed for a safety factor of 2. Hollow aluminum tubes of OD 2" × ID 1.87" and OD 1" × ID 0.93" were welded together to construct the main frame. The overall pod dimensions were 3.42' in height, 3' in width and 15.6' in length. The tubes on the topside of the frame were primarily aimed at providing a bolting and supporting

V. Jayakumar (✉) · T. S. Indraneel · R. Chawla · S. Mohanty · S. Shetty · D. Shiyani · S. Abdallah
Hyperloop UC, University of Cincinnati, Cincinnati, OH, USA
e-mail: jayakuvh@mail.uc.edu

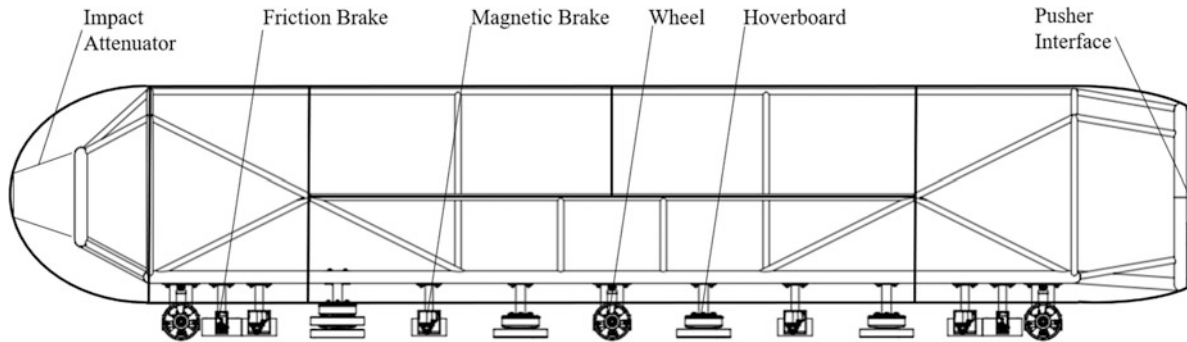


Fig. 4.1 HUC pod design overview

surface for the carbon fiber skin panels used to cover the pod. The pod rested on six wheels and also housed eight levitation hoverboards. The six wheels were provided to help with the takeoff and landing phases of the pod motion. Commercial hoverboards were used as levitation skids, and magnetic arrays (activated by linear actuators) were selected for braking. The initial propulsion for the pod was provided with help of a large electric vehicle (pusher) attached to the back of the pod via a semi-hemispherical pusher interface. The pod structure housed magnetic brake mechanisms and friction brake mechanisms which aimed to bring the pod to rest safely within the mile-long test track.

4.3 Verification and Validation

Verification and validation is a well-documented procedure and there are several guides available in literature that sheds light on how to implement the process [2, 3]. The guides define the two parts of this process as follows:

1. Verification: The process of determining if a computational model accurately represents the underlying mathematical model and its solution.
2. Validation: The process of determining the degree to which a model is an accurate representation of the real world from the perspective of the intended uses of the model.

Verification can be divided into two parts—code verification and calculation verification. Code verification refers to the verification of the FE code that is used in the study and checking for errors in its implementation. This was not deemed necessary for this project as a commercial software was being utilized to implement the FE model in this project. Calculation verification involves checking for the level of discretization errors in the mathematical model. This is usually carried out as a mesh verification study by comparing the results of the mathematical model to that obtained from analytical models for the same system. Additionally, mesh convergence studies can also be utilized to ensure that the discretization errors are minimal, and this approach is handy especially in cases where analytical models are not available. The validation activity is carried out in two stages. The first stage involves calibration which is defined by the ASME guide as the process of adjusting the physical modeling parameters in the computational model to improve agreement with experimental data [4–6]. In the second stage the calibrated model is used to check the model's ability to predict accurately by comparing results from computational model to that of experimental data for different load cases.

4.4 Mesh Verification

For the purposes of this study, since the main components in the frame construction were aluminum tubes, the FE mesh was verified by comparing the modal frequencies with analytical results for a simple tube model. The mesh for the weld regions were not included in this phase of the study. The main aim of the study was to develop a model capable of replicating the dynamic responses of the structure. Hence the mesh at the weld regions were addressed in the model calibration stage with the goal of capturing the stiffness characteristics accurately. Table 4.1 below highlights the mesh verification study results for a tube of length 125 mm, nominal radius 25 mm and thickness 1.25 mm. Shell elements were utilized in the construction of the mesh. The results indicate that the discretization error is very small in the 20–5 mm range for mesh size and not much

Table 4.1 Mesh verification for the model

Element size (mm)	Number of elements	Analytical frequency (Hz) [7]	FEA modal frequency (Hz)—from ANSYS	Percentage difference (%)
20	120	12,076.16	12,135	0.48
10	208		12,117	0.34
5	775		12,087	0.09

improvement is expected by further refining the mesh. For the purposes of the frame model construction a mesh size of around 10 mm was utilized observation [9] of this study.

4.5 Modal Testing and Model Calibration

The verified model was validated in two stages. The first stage involved updating and calibrating the model. A modal test case was to be utilized to update and calibrate the FE model's stiffness properties. Modal frequency estimates and the mode shapes were used to compare the FE model and the real structure during the model updating and calibration phase. This activity ensures confidence in the accuracy of the computational model. This is of importance in a structure having several welded joints.

4.5.1 Test Setup

The modal test was performed in a free-free condition by resting the space frame on top of soft foam materials placed on sawhorse tables. The sawhorse tables were located 10 ft. apart and a traditional impact hammer approach was used for the modal test. A 10×20 measurement (20 input points and 10 output points) was carried out. A Poly-reference Time Domain (PTD) algorithm was used for the modal parameter and mode shape estimation [8].

4.5.2 Results

Following the tests, the FE model was calibrated by updating the stiffness properties to better correlate modal frequencies and mode shapes with those of the real structure. The material Young's modulus of the tubes and Young's modulus and size of the welds at the joints were the parameters that were calibration in this phase. Figures 4.2 and 4.3 highlights the mode shapes and modal frequencies obtained from testing and the updated FE model. Modal Assurance Criterion (MAC) plots were used to further confirm this observation [9]. Figure 4.4 presents a MAC plot comparing the first four modes from testing and simulation and the high values along the diagonals indicate a good match. Table 4.2 provides a comparison of the modal frequencies from the updated FE model and the test activity.

4.5.3 Discussion of Errors

The first mode was the most sensitive to the boundary conditions and hence shows a higher error percentage. This can be attributed to the fact that it's possible to define truly free-free condition in a FE model, however, the free-free condition that the test structure was subjected was not ideal. The sawhorses on which the structure was rested provided some degree of vertical restraint. The other modes were observed to show much better correlation. The range of 5–6% error was a good correlation considering the number of welds in the structure that are difficult to model accurately.

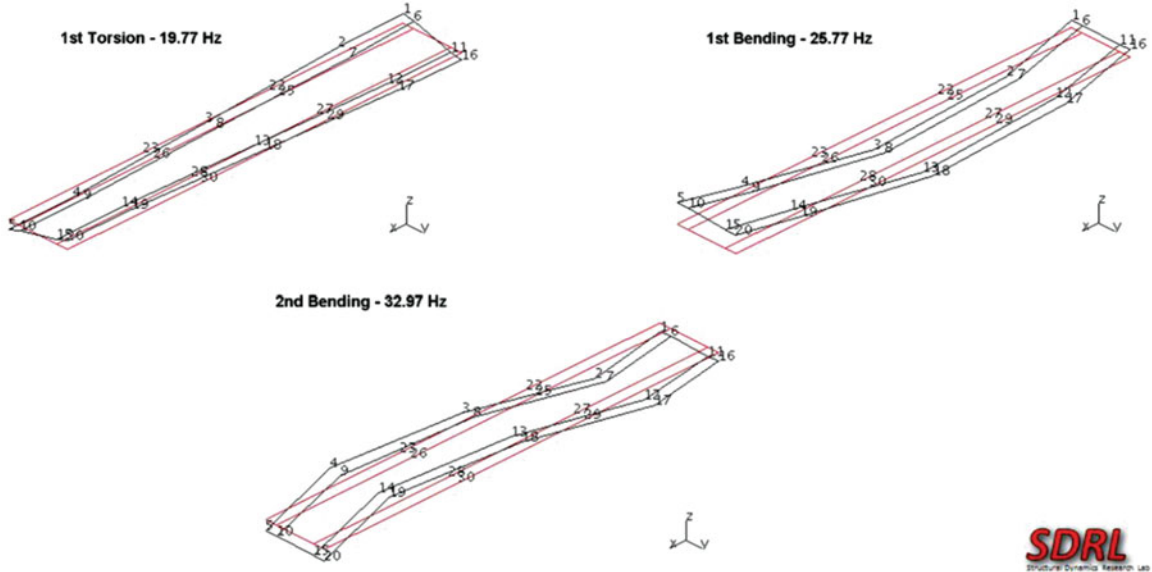


Fig. 4.2 Mode shape (Test results for the base of the frame structure)

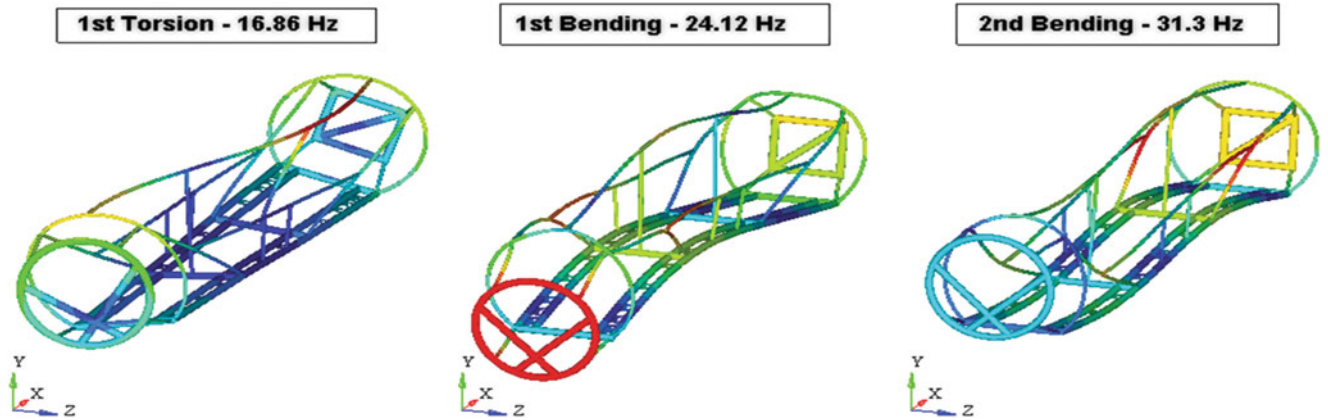


Fig. 4.3 Mode shape (FE Results for the base of the frame structure) [9]

4.6 Torsional Testing and Model Validation

The calibrated frame model was used to validate the frame by comparing the results from the FE model for a torsional stiffness test to the results from experimental data obtained from a hydraulic four poster setup

4.6.1 Test Setup

UC-FSAE torsional stiffness measurement machine (TSMM) was used to carry out the static torsional stiffness measurements [10, 11]. The setup (Fig. 4.5) consisted of a hydraulic four poster (a MTS[®] 320 Tire-Coupled Road Simulator) to provide the input loads, linear variable differential transformers (LVDTs) internal to the posts to measure the deflection, two 60' steel I-beams, and PCB model 1380-03A load cells to measure the forces were included in the setup. The space frame was attached to the top flange of the I-beam using C-clamps. The torsional stiffness of the space frame was measured in three sections of 4 ft. length: front, middle and back. The frame was clamped at points 1, 2, 7 and 8 for front section case; points 1, 2, 3 and 4 for middle section case and 3, 4, 5 and 6 for the back section case (Fig. 4.5). In each of these cases, the torsional stiffness was estimated by two methods, i.e. front twist and back twist. In the front twist, the two hydraulic inputs on the rear side

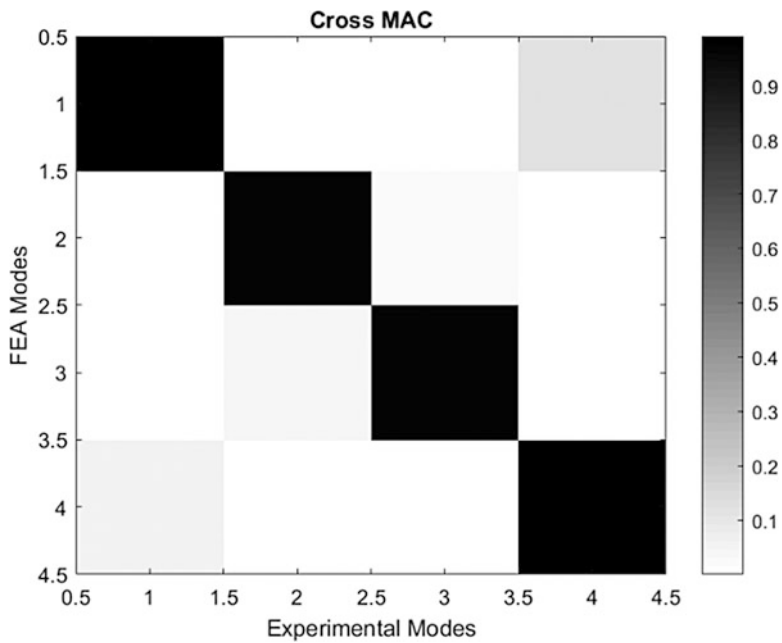


Fig. 4.4 Cross MAC plot

Table 4.2 Modal frequency comparison and error percentages

Mode	Testing (Hz)	FEM (Hz)	Percentage difference (%)
1st torsion	19.77	16.9	-14.5
1st bending (transverse)	25.77	24.1	-6.5
1st bending (sideways)	28.81	29.8	3.4
2nd bending (transverse)	32.77	31.3	-4.5

of the space frame were held fixed, and the front two input points were given an equal and opposite displacement, thereby twisting the space frame, and vice versa in the back twist. In both the front and back twist cases, a complete hysteresis loop was recorded.

4.6.2 Results

Figure 4.6 highlights the comparison of the results from the torsional testing and the simulation from the updated and verified model. The x-axis shows the angle of twist and the y-axis shows the reaction torque experienced by the hydraulic four posters.

4.6.3 Discussion of Errors

The experimental data is seen to match well with the simulation data for smaller angles of twist for all three sections that were tested. As the angle of twist was increased, local displacements were observed at the c-clamps junctions. This was observed to adversely affect the zero error in the load cells during the test. As a consequence a greater difference is observed between the measured and the simulated results for higher angles of twist. The TSMM setup was originally developed for FSAE frame testing and so there were some features of the setup that were not ideal for the frame structure of the pod. The forces generated during the torsional stiffness measurements were very low compared to the maximum range of the load cells incorporated in the TSMM. The displacements and forces applicable on the aluminum frame were limited to ensure that the frame was not subjected to any yield or damage. Hence, the range and sensitivity of the load cells was not ideal and contributed a source of uncertainty to the measurements. Figure 4.7 highlights the standard deviations for each

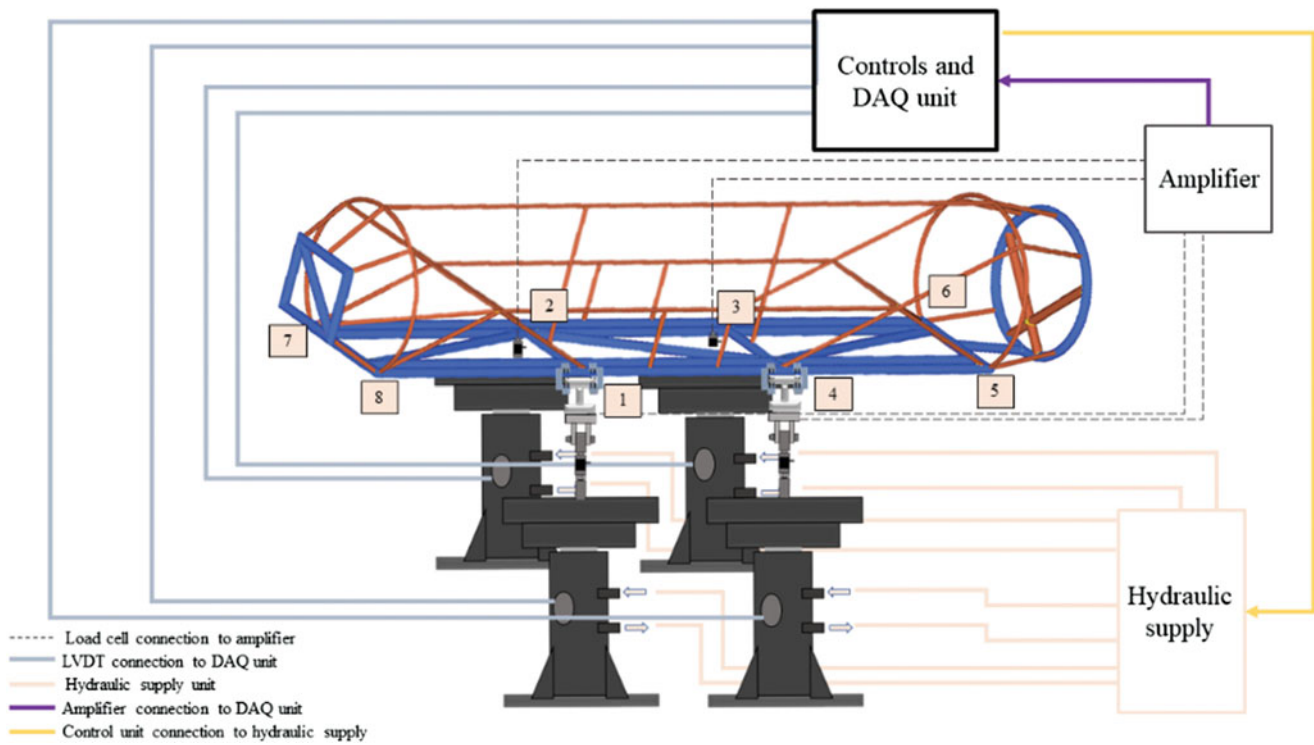


Fig. 4.5 TSMM setup

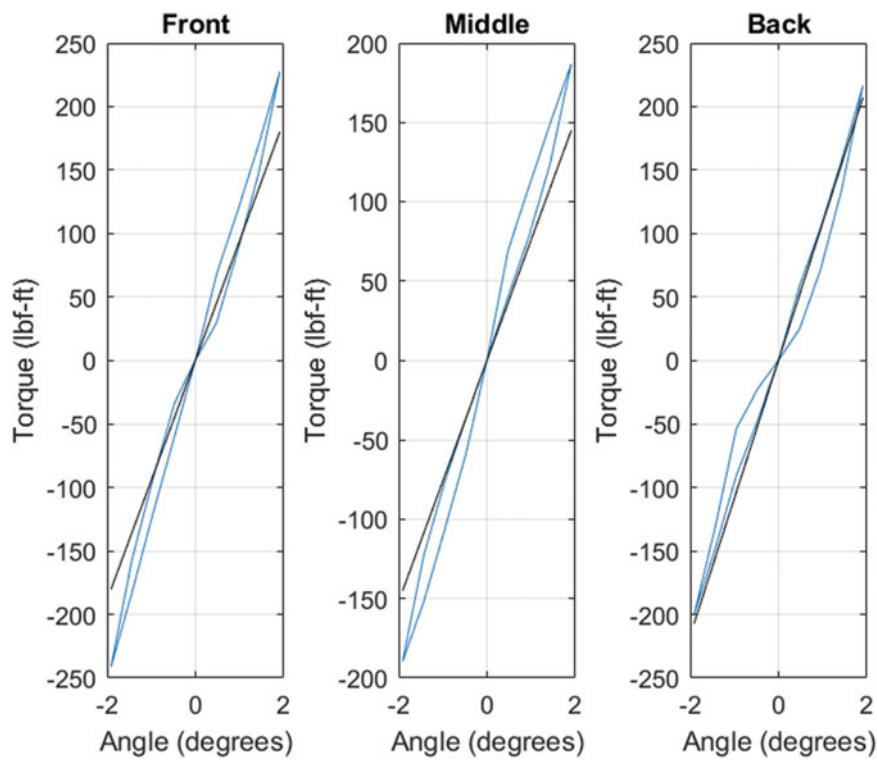


Fig. 4.6 Torsional test result comparison (test vs. simulation)

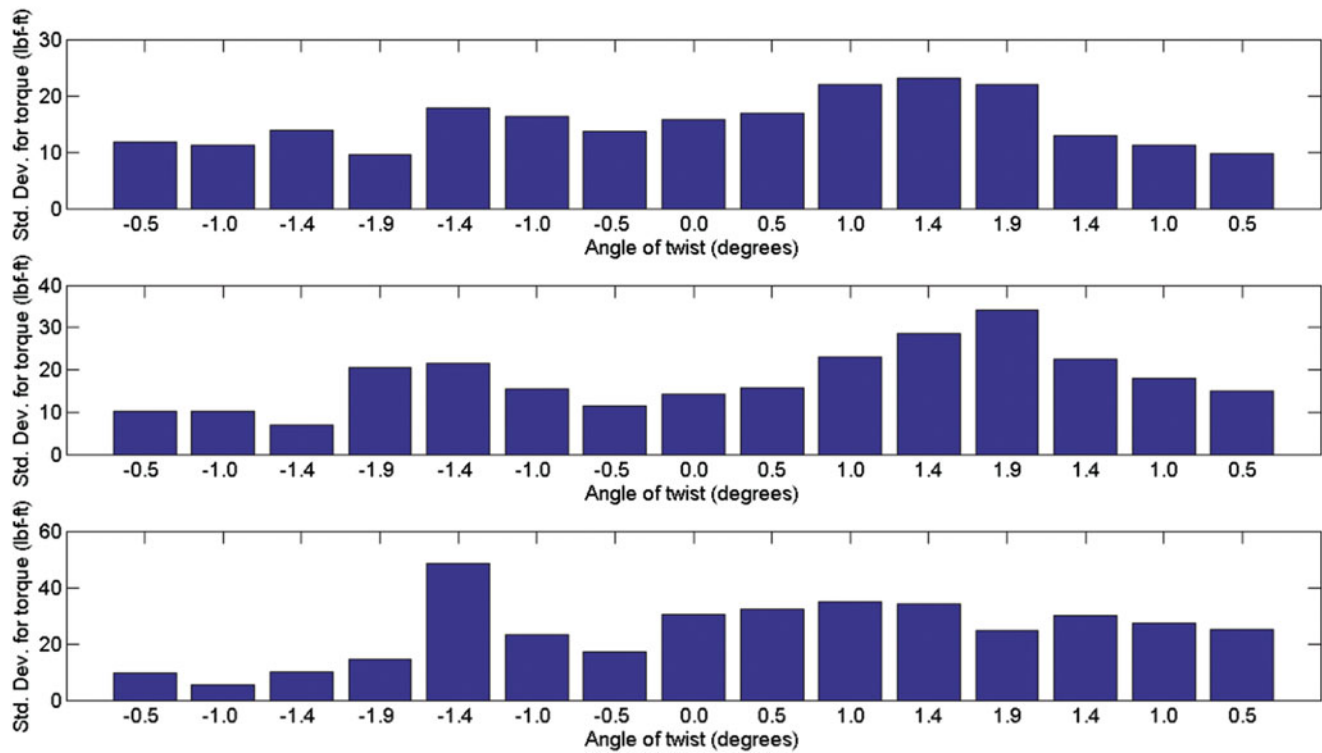


Fig. 4.7 Standard deviation from the measurements over a measurement cycle **(a)** (Top) Front portion test. **(b)** (Middle) Middle portion test. **(c)** (Bottom) Back portion test

measurement observed because of the above factors. These errors in measurement explain some of the variations in torsional stiffness comparison presented in Fig. 4.6. Even though these errors were deemed to be within acceptable limits for the validation activity, the results from testing can be improved addressing these sources of errors. Modifying the TSMM setup with load cells that are more sensitive in the load range the space frame is being subjected to can help reduce the error in the experimental setup. Additionally, use of node blocks on the frame or any other provision to improve the join of the frame to the I-beam would help improve the experimental data and help overcome some of the random and biased errors creeping into the measurement as well.

4.7 Conclusion

The back-portion testing exhibited consistent measurement data while also correlating well with simulations. Considering the difficulties in measurement, it is possible to conclude that the FE model is able to predict the stiffness of the frame quite well. Thereby a validated and reliable FE model was developed and is available for use in further studies of dynamics of the pod.

Acknowledgement The Hyperloop pod design venture was a massive team effort of over 50 student volunteers across Mechanical Engineering, Aerospace Engineering, Electrical Engineering and Computer Science departments as well as Lindner Business College and College of Design, Architecture and Art Planning of which the presented material forms a small component and could not have been completed without their contribution to the project. The authors would like to acknowledge the entire Hyperloop UC team for their efforts as a collective group in the design of the pod and accompanying test setups.

Hyperloop UC was fortunate to have sponsors who provided technical advice and manufacturing help particularly Justin Atkins (Cincinnati Incorporated), Tri-State Fabricators and Jack Malluege (ANSYS), their support is highly appreciated. The authors would also like to acknowledge the contributions of Ronald Hudepohl for his manufacturing guidance and Dr. Randall Allemand for his valuable technical guidance and for the use of SDRL lab space and resources for testing activities. Additionally, we would like to thank SpaceX for organizing this competition.

References

1. Musk, E.: Hyperloop alpha. SpaceX, 2013
2. AIAA: Guide for the Verification and Validation of Computational Fluid Dynamics Simulations, AIAA G-077-1998, 1998
3. American Society of Mechanical Engineers (ASME): Guide for Verification and Validation in Computational Solid Mechanics, ASME V&V. American Society of Mechanical Engineers, New York (2006)
4. Friswell, M.I., Mottershead, J.E.: Finite Element Model Updating in Structural Dynamics. Kluwer Academic Publishers, Dordrecht (1995)
5. Pasha, H.G., Kohli, K., Allemand, R.J., Phillips, A.W., Brown, D.L.: Structural dynamics model calibration and validation of a rectangular steel plate structure. In: Conference Proceedings of the Society for Experimental Mechanics Series, Vol. 3, pp. 351–362, 2015
6. Jayakumar, V., Kim, J.: A Two-Step Approach to Build a FEM Model of a Built-Up Structure with Special Attention to Description of Boundary Conditions and System Damping. INTER-NOISE and NOISE-CON Congress and Conference Proceedings, NoiseCon17, Grand Rapids, MI, pp. 1–1004, 786-797(12)
7. Chung, H.: Free vibration analysis of circular cylindrical shells. *J. Sound Vib.* **74**(3), 331–350 (1981)
8. Vold, H., Kundrat, J., Rocklin, T., Russell, R.: A multi-input modal estimation algorithm for mini-computers. *SAE Transact.* **91**, 815–821 (1982)
9. Allemand, R.J., Brown, D.L.: A correlation coefficient for modal vector analysis. In: Proceedings, International Modal Analysis Conference. pp. 110–116 (1982)
10. Steed, Thomas. Torsional Stiffness Measuring Machine (TSMM) & Automated Frame Design Tools (Master's Thesis), University of Cincinnati, 2009
11. Young, Alexander: Validating Automotive Frame Torsion Stiffness Measurement Techniques (Master's Thesis), University of Cincinnati, 2016



Chapter 5

Investigating Nonlinearities in a Demo Aircraft Structure Under Sine Excitation

S. B. Cooper, S. Manzato, A. Borzacchiello, L. Bregant, and B. Peeters

Abstract Developing on the basic idea behind parametric and non-parametric identification of nonlinear systems, another case study on integrating system identification and finite element modelling of nonlinear structures is presented. The first step, which is the focus of this paper, involves using acquired input and output data to derive an experimental model for both the underlying linear model and nonlinear model of the proposed structure, no information about the system is required and only the applied excitations and corresponding accelerations are implemented in the nonlinear identification step. The proposed case study is demonstrated on a nonlinear simple metallic plane assembly with localized stiffness and damping nonlinearities; in this case, an updated linear finite element model of the structure is derived and the nonlinearities experimentally characterised.

Keywords Nonlinear identification · Experimental data · Finite element model · Numerical simulation and system integration

5.1 Introduction

Nonlinearities often originate from different sources in engineering structures most especially in an industrial application, a large majority of these nonlinearities are narrowed down to the design of the structure, nature of the joints, material and geometric properties. Research on bolted joints and other types of nonlinear features have been proven to introduce large uncertainties in the stiffness and damping properties of a structure which can often render the response of the structure nonlinear, identifying and predicting the effect of these nonlinearities at operational conditions is of current challenge to present structural engineers dealing with complex nonlinear structures. In this context the integration of experimental nonlinear identification and finite element modelling of engineering structures would be of great advantage to the present structural dynamics society. Experimental nonlinear identification is important in many structural dynamic applications, for example in complex aerospace and mechanical structures [1], micromechanical systems with magnetic or friction forces [2], machineries with rubber isolation mounts and assembled structures with bolted interfaces [3]. In most engineering design, the base line structure is often linear, but the vibration testing and operational performance of some of these structures exhibit a level of nonlinear phenomena which can no longer be ignored or assumed as linear [4]. Hence, the accurate representation of these nonlinear behavior in the finite element model of the structure or built up assembly would be of extreme benefit in obtaining better response prediction at the forcing range of interest.

Examples on the real life application of some of these developed nonlinear identification methods are also available in the literature where the identification of weak nonlinearities was studied on a more complex aerospace structure in [5] where a strategy for non-linear modal identification of weak nonlinear effects on a large aircraft was presented. An aluminum plate

S. B. Cooper
Test Division, Siemens Industry Software NV, Leuven, Belgium

Department of Mechanical Engineering, University of Bristol, Bristol, UK

S. Manzato (✉) · B. Peeters
Test Division, Siemens Industry Software NV, Leuven, Belgium

A. Borzacchiello
Test Division, Siemens Industry Software NV, Leuven, Belgium

Department of Engineering and Architecture, Università degli Studi di Trieste, Trieste, Italy

L. Bregant
Department of Engineering and Architecture, Università degli Studi di Trieste, Trieste, Italy

attached with two stores used to illustrate the behavior of a wing and an engine suspended by a means of nonlinear pylon also displayed the presence of weak nonlinearities during a vibration test, the results obtained illustrated some hardening characteristics as shown in [6]. Similar study was also carried out on a large helicopter with the identification of weak nonlinear softening behavior on one of the vibration modes as shown in [7]. Other examples of case studies where nonlinearity have been noticed in aerospace structures can be found in [8] where nonlinearity was also detected at the elastomeric mounts supporting the four turboprop engines of the aircraft during the Ground Vibration Test (GVT) of the Airbus A400M aircraft designed for military purpose. The F-16 fighter aircraft also showed a nonlinear behavior at wing-to-payload mounting interface of the aircraft when a similar GVT was conducted [9]. Nonlinearities were also detected on the Cassini spacecraft due to the presence of gaps in the support of the Huygens probe [10]. More case studies on the presences of nonlinearities in engineering structures can be found in the literature, it is therefore possible to conclude that the development of identification techniques which are capable of producing satisfactory results when linear identification techniques fail is an active area of study in today's structural dynamics society. In the real-world application nonlinearity is ever-present and as engineers push to design lighter, more flexible and more efficient structures, the design are shifting towards non-linear regime which also shows that there is a need for developing strategies for understanding the nonlinear response of these structures. Hence this paper addresses the nonlinear experimental identification, and the force controlled experimental test conducted on a demo aircraft model. This involves the use of established and robust identification techniques to identify the type of nonlinearity present in the assembled missile, the complete identification process i.e. (Detection, Characterization and initial Parameter estimation) was achieved based on experimental data. Measured time series and frequency data driven by sine-sweep test and random excitation were exploited to gain an initial insight to the dynamic behavior and properties of the assembly. The structure of the paper is as follows: Sect. 5.3 describes the first case experimental study conducted on the demo aircraft followed by the linear identification based on measured data from low level random excitation and a correlation and model updating step. Section 5.4 includes the pylon elements in the physical and numerical model, and correlate the former using again a low level random excitation. In Sect. 5.5, the nonlinear identification is initiated based on measured data and the use of the first two stages of the white-box identification process. (Detection, Characterization and Parameter Estimation), where random multisines, sine sweeps and force-controlled stepped sine data were used for most of the analyses. The conclusion of the study, an outline on future works and the collective use of different analysis techniques in this research are finally summarized in Sect. 5.6.

5.2 Description of the Test Item

The baseline test item analyzed in this paper is a demo aircraft model, used extensively for demonstration and training purposes in the context of modal analysis and GVT. The plane, entirely built in aluminum, consists of a beam with square cross-section (the fuselage), connected to a bigger (wings) and smaller (horizontal stabilizer or tail plane)-plates. An additional vertical plate, representing the fin or vertical stabilizer, is connected to the tail plane by means of L-shaped beam. All components are connected by mean of bolts. At the front and rear of the fuselage, two eye bolts easily allow suspending the demo aircraft and obtain the desired boundary conditions for modal testing. A CAD representation of the whole aircraft model is shown in Fig. 5.1. To introduce a local nonlinearity, the pylon models previously analyzed in [6, 11] are also here used: in these elements, the geometric nonlinearity of the thin plates supporting the lumped masses is combined with the cubic profiles of the blocks which connect the “engine” to the wing. As the engine deflection increases, a bigger portion of the pylon comes into contact with the blocks' surface, thus introducing a stiffening effect. The position of the pylons on the wings and the length and thickness of it were designed and optimized to observe modal interactions when the nonlinearity is excited.

By connecting the pylon to the slender wings, it is expected that some nonlinearities on the aircraft might also be triggered. First of all, the connection between the pylon and the wings relies on two M3 bolts, which might cause the connection to open when the system is excited at resonance. Secondly, all plates are connected with bolts which, at high response levels, might induce a local softening behaviour. Finally, as the wings are relatively slender, it might be expected that, similarly to the pylon, they might also experience a geometric nonlinear response for high wing tip displacements. It will be also an objective of this paper to detect and quantify the nonlinear response at these locations, but the identification will mostly focus on the pylon behavior.

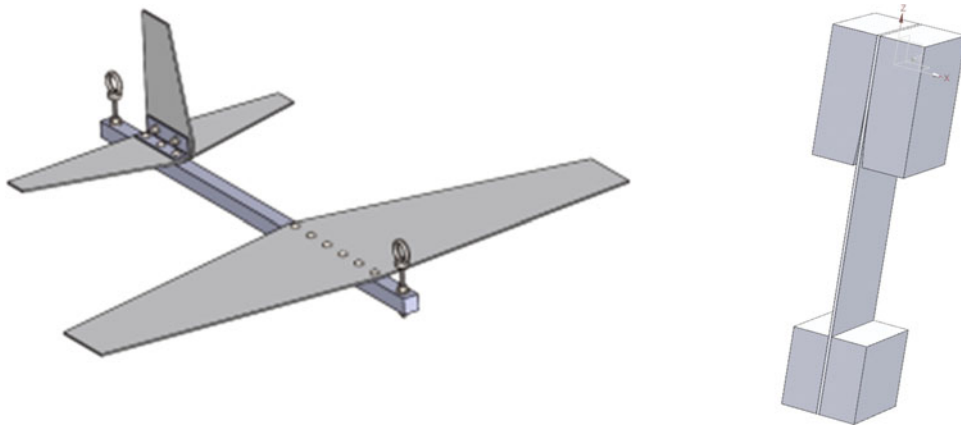


Fig. 5.1 CAD models of (left) the full aircraft and (right) the pylon subassembly

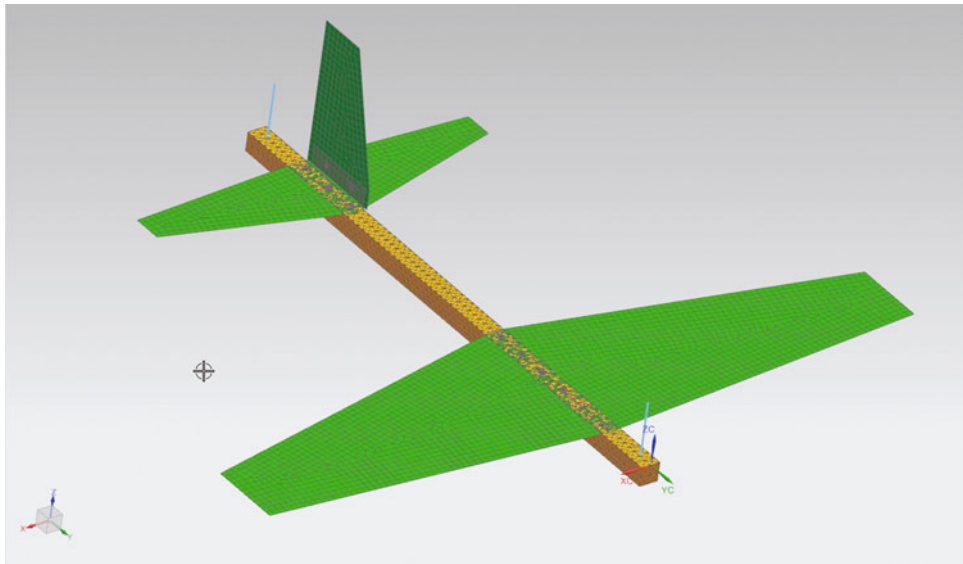


Fig. 5.2 Preliminary FE model

5.3 Experimental and Numerical Analysis of the Aircraft

The main objective of the paper is, as mentioned, to present a step-by-step procedure that allows in the end to obtain a validated non-linear Finite Element of the test object, which in this case is the aircraft model with the pylons. Obviously, the first step is to deal with what we know (or can know) fairly accurately, which in this case is the aircraft without the pylons. Consequently, this section will present the preliminary and simplified aircraft model built starting from the CAD, the Experimental Modal Analysis campaign and the model upgrading and updating phases to increase the accuracy of the FE model.

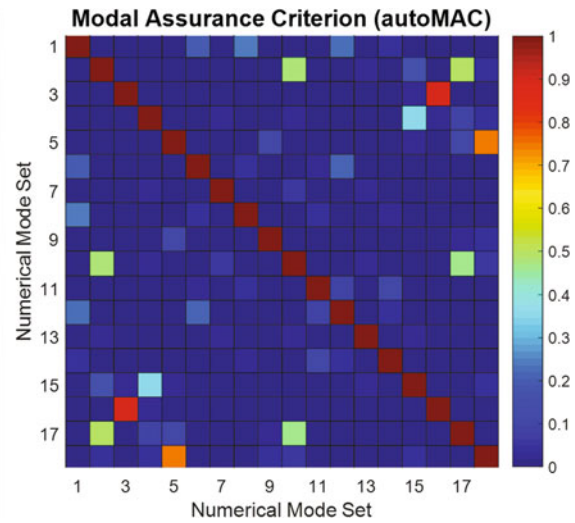
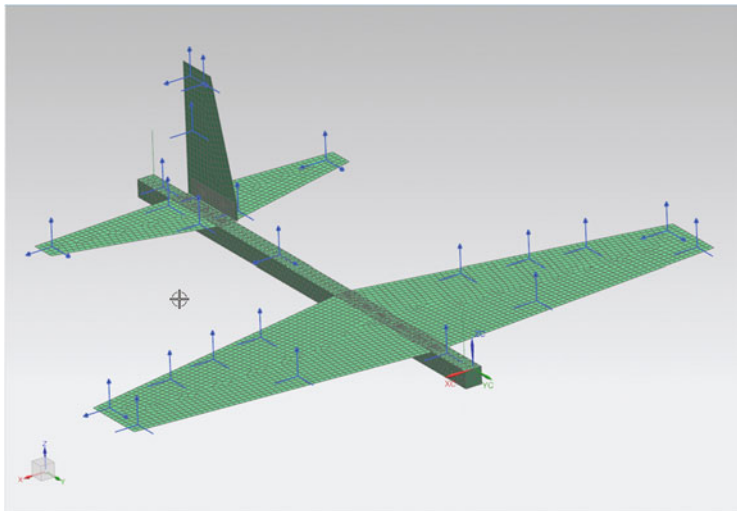
5.3.1 Preliminary FE Model

Based on the nominal dimensions of the aircraft components, a preliminary FE model was built, with the objective of getting a first idea of the global modes and plan the experimental campaign accordingly, in particular with respect to the number and positions of the sensors.

The model is shown in Fig. 5.2. Each main element (Fuselage, Wings and Tail) is modelled using nominal dimensions and material properties as illustrated in Table 5.1. Solid elements are used for the fuselage bar (to allow taking into account

Table 5.1 Elements properties and material used in the model in Fig. 5.2

Component	Element type	Element properties
Fuselage	CTETRA10	Aluminium
Wings—Tail Plane—Fin	CQUAD8	Thickness: 3 mm Aluminium
Eye bolts	CBAR	Diameter: 8 mm Steel
Bolt heads	CQUAD8	Thickness: 5 mm Steel

**Fig. 5.3** Pre-test analysis results: (left) candidate sensor locations and (right) autoMAC using the candidate sensor set

in more advanced models the contact surface with the other structural elements), while all the plates are modelled using standard 2D elements. The connection elements, which are made of steel, are here mostly included to account for their mass contribution; indeed, the actual connections have been modeled using node-to-node rigid connection elements and more accurate representation will be introduced after the reference experimental results are available.

The total mass of the physical plane was measured to 3.17 kg, while the one computed from the model amount to 3.10 kg. At this stage, this is considered to be reasonably good to determine the main modes and the frequency range of interest. The results of this FE are then used to define a test setup. When the objective of a modal test is the validation of the FE model, it is important that the identified modes are as much as possible unique, that is their cross-correlation should be as small as possible. Besides, it is also important to ensure that the experimental mode shapes can be easily interpreted and the test geometry gives a clear idea of the motion of the structure. Consequently, based on the availability of sensors, a preliminary test setup was assessed, the mode shapes reduced to the “measured” DOFs and the autoMAC computed. The results are summarized in Fig. 5.3, where it is confirmed that the selected sensor locations will allow a good and unique description of the modes up to 400 Hz.

5.3.2 Experimental Modal Analysis

Based on the observation from the preliminary analysis of the Finite Element model, a preliminary Experimental Modal Analysis campaign is then performed, under the assumption that the aircraft model behaves linearly and with the objective of identifying its modal parameters with which the model could be updated. In total, 24 sensors were used (6 triaxial and 18 single axis accelerometers), for a total of 36 degrees of freedom. Although they are supposedly the ideal locations to excite the structures, wing tips were avoided because of the very high response for such a lowly damped structure, as this could generate issues when trying to control the excitation (e.g. with stepped sine tests). Consequently, the two shakers were connected approximately half way through the trailing edge of the wings, ensuring a good excitation of all modes (including the torsional ones) while limiting the shaker stroke required to follow the structural response at resonance. Figure 5.4 shows the instrumented plane, as well as the test geometry with the two red arrows indicating the excitation locations and directions.

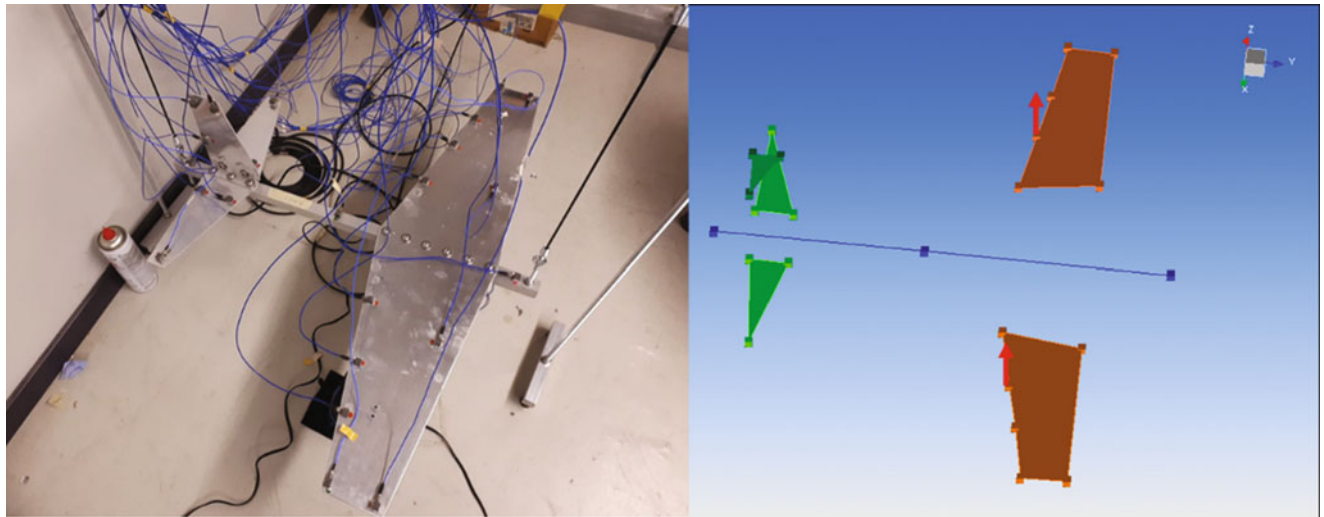


Fig. 5.4 Experimental modal analysis setup (left) and test geometry (right) for the identification of the linear modal model of the plane

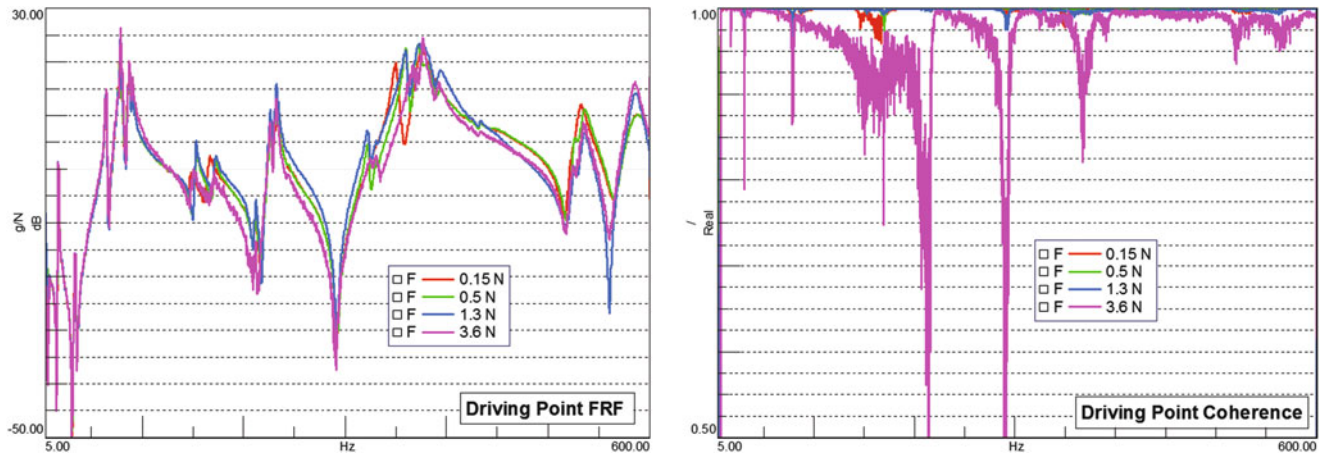


Fig. 5.5 Linearity check for Driving Point FRF (left) and Coherence (right) for four different pseudo random excitation levels. Force level are expressed as RMS values

To excite the structure, a Pseudo Random excitation with random phase randomization was selected. In view of the low damping expected on such a structure, two delay blocks were specified to give the system enough time to reach steady state conditions after each new realization. To achieve the prescribed number of averages (40), a combination of 4 repetitions and 10 realizations are specified.

The airplane was excited between 5 and 600 Hz, while the bandwidth has been set to 800 Hz, with a frequency resolution of 0.195 Hz. To verify for the system linearity, 4 different excitation levels are defined, and the results are compared in Fig. 5.5. If the system is linear, the FRFs acquired for different excitation levels should perfectly overlay, which is not exactly the case here. Also the coherence can help assessing the linearity of the system, but more in general a low coherence can be due to noise, nonlinearities or even leakage. By looking at both representations, it can be concluded that, for the lower level, the excitation might still be not high enough to consistently excite the structure, and the measurements are affected by noise. The two intermediate levels, except at higher frequencies, are very consistent and show the highest coherence across the frequency range. For the higher level, it is clear from the coherence plot that the system has a clear nonlinear behavior across the frequency range. Based on this, it can be concluded that in general, if the level is sufficiently high, the plane model will show some nonlinear behavior, possibly due to the bolted connections and geometric nonlinearities on the plate.

Finally, linearity of the system was also verified by checking for reciprocity between excitation and response locations. The results in Fig. 5.6 show a very good reciprocity between the measured FRFs up to 400 Hz, giving confidence in the system linearity at the considered level.

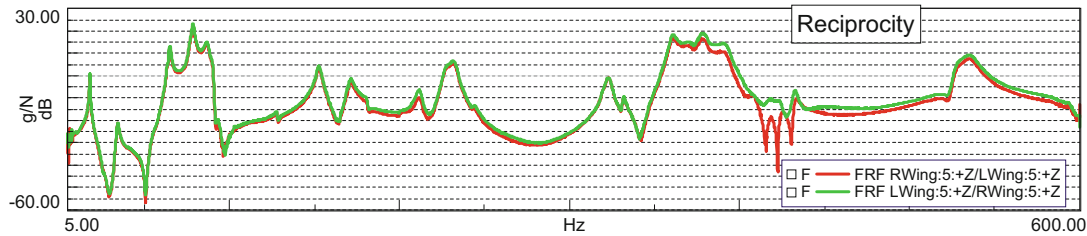


Fig. 5.6 Reciprocity check for 0.5 N RMS excitation level

Table 5.2 Summary of natural frequency errors for mode pairs showing a MAC higher than 0.5

Test mode #	Test frequency	FE mode #	FEM frequency	Freq. % error
1	17.69	1	19.42	9.8
2	34.06	2	38.36	12.6
3	63.21	3	71.39	12.9
4	64.53	4	73.89	14.5
5	76.08	5	87.60	15.1
6	78.33	6	92.20	17.7
7	86.91	7	101.44	16.7
8	90.17	8	102.07	13.2
9	103.57	9	114.33	10.4
10	152.70	10	176.65	15.7
12	181.14	11	193.41	6.8
13	211.70	12	235.74	11.4
14	226.94	13	260.92	15.0
15	232.40	14	267.30	15.0
16	243.73	15	271.57	11.4
17	318.62	16	349.00	9.5
18	322.99	17	373.27	15.6
19	348.06	18	389.74	12.0
22	377.82	20	438.07	15.9
23	381.10	19	433.02	13.6
24	391.85	23	461.93	17.9

To further check for the system linearity, modal analysis was performed on the FRF derived for all 4 load levels and the results compared. In general, estimated modal parameters are quite consistent, with the bigger scatter observed, as expected for the lower and higher levels. Based on these observation, the results observed at 0.5 N RMS (Table 5.2) excitation will be those used for the model validation and assumed as reference.

5.3.3 Plane Model Validation and Updating

One key elements for being able to accurately predict the nonlinear response with a numerical model is to make sure that the linear behavior matches as closely as possible the experimental data. Obviously, structural dynamics provides the ideal framework to objectively assess the degree of correlation between the model and the experiments as it allows to compare the natural frequencies and mode shapes. Figure 5.7 shows the MAC between the numerical and experimental mode shapes: the model is able to predict the first 18 experimental modes very accurately, with a match to the experimental ones above 85%. Above these, the MAC still has a diagonal trend but the actual correlation values are lower and some of the modes appear in different order. It is then also possible to use the MAC matrix to identify mode pairs and compare the values of the natural frequencies, as shown in Table 5.2. The results clearly shows that the model is consistently stiffer (or inversely lighter) than the physical structure, which make sense considering the already mention difference in mass and the fact that the local mass introduced by the sensors is not added to the model. This comparison gives a clear indication on where the model updating should focus, which is on the overall mass and stiffness of the model, probably due to material properties

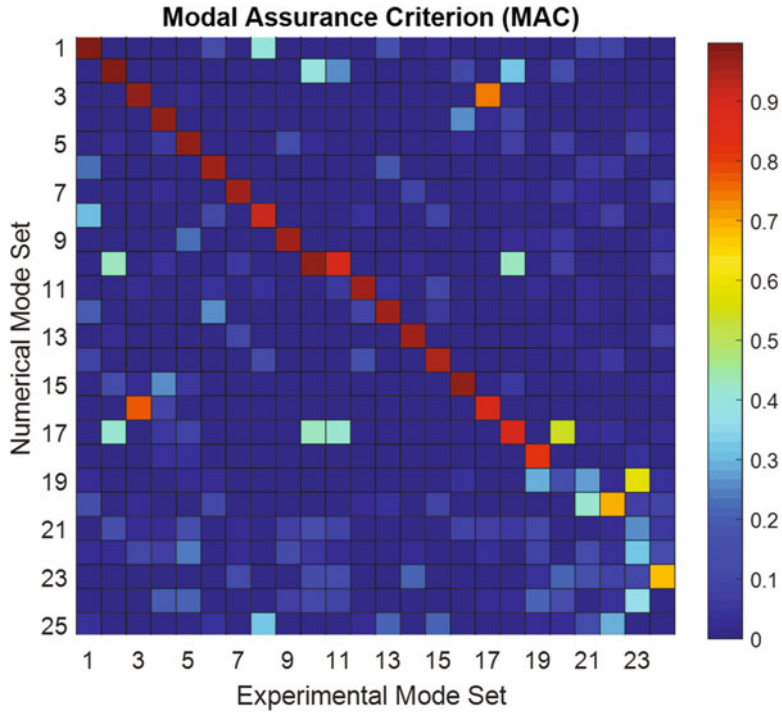


Fig. 5.7 MAC matrix for the experimental mode shape from the linear plane analysis and the numerical one from the preliminary model

not exactly matching the nominal ones. Such a good initial correlation between the experimental and numerical mode shapes indicates that the model assumptions (in terms of mass and stiffness distribution) are generally correct up to approximately 400 Hz; the upgrading will thus only focus on the material properties and overall mass to improve the frequency correlation. The first step is to include the local masses of the sensors: here, lumped masses are added to the model in correspondence of the nodes where a sensor is placed, with the value equal to that reported by PCB on the sensor types used (5 g for the triax and 4 g for the single axis accelerometers). Additionally, the properties of the aluminium used to model the plates was modified, with the density increased to match the total measured mass and the Young Modulus slightly decreased. With these very limited modification, the results in Figs. 5.8 and 5.9 could be achieved: the error between the natural frequencies is now consistently below 10%, and for the majority of the modes even below 5%, from which we can conclude that the model is valid up to 400 Hz.

5.4 Modal Identification of the Aircraft with the Pylons

Now that the desired level of correlation between the linear baseline aircraft model and the experimental results is reached, the two pylons are added to the aircraft. Firstly, a linear test is performed to identify an experimental modal model to validate and, if necessary, further update, the finite element model. As the focus is now on the wings and pylons, and the way they interact with each other, some of the sensors from the tail substructures are moved to these elements, as shown in Fig. 5.10. Different levels of Pseudo Random excitations are applied verify the linearity of the system, and the FRF are displayed in Fig. 5.11. We can clearly observe how the FRFs change from low to high level, with a general softening trend. The FRFs from the lower level are used for modal analysis.

Compared to the analysis in Sect. 5.3, FRFs are measured only up to 200 Hz, where approx. 20 modes could be expected. It should also be stressed that some manufacturing differences can be expected in the pylons, which might propagate to the airframe breaking its symmetry and consequently making a direct comparison to the FE model more challenging than in the previous case. Despite this, the correlation between the experimental and simulated modes looks very good, as shown in Fig. 5.12. The majority of the identify modes have a MAC above 70%, with two clusters were the correlation is lower. A more focused analysis shows that these modes correspond to the sets of first torsion and second bending of the pylon (Fig. 5.13). While in the model they appear as pair of symmetric modes, in the experimental mode sets it is more difficult to clearly

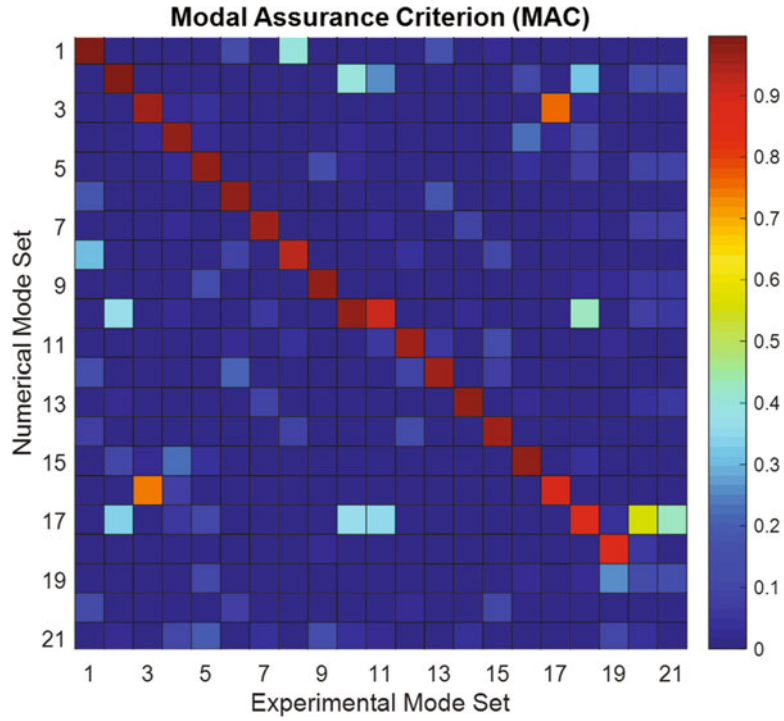


Fig. 5.8 MAC matrix between experimental and numerical mode shapes after updating

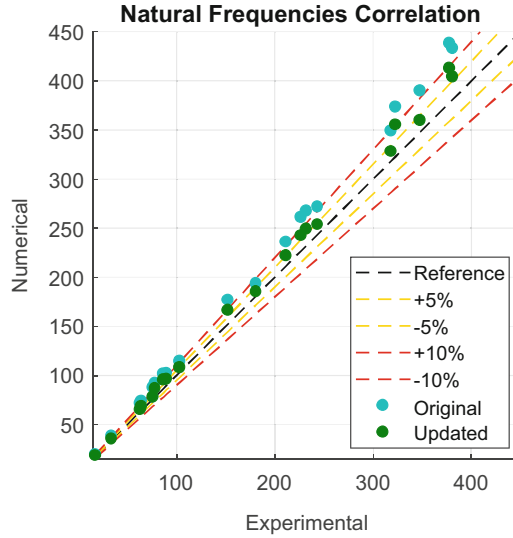


Fig. 5.9 Correlation between experimental and numerical natural frequencies before and after updating

identify them. For the pair of torsional modes, the symmetric one is coupled with a mode of the wing which is almost at the same frequency and in the second only one of the two pylons moves. For the second bending mode, the problem is related to the fact that the mode is difficult to identify since no sensors were placed on the thin plate to limit mass loading. With these consideration in mind, it can be concluded that the model nicely represent the experimental data, as also in these case the natural frequencies are in general within 10% of those measured experimentally.

Since currently the majority of the methods for characterization of nonlinearities relies on SIMO measurements, a final linear experimental modal analysis is performed, by only considering the shaker under the left wing. By using only one shaker, it is expected that the symmetry of the structure is broken and some of the modes might not be identified as clearly as before. The measured data and estimated modal parameters for the same excitation profile and level, but using one or two shakers simultaneously, are compared in Figs. 5.14 and 5.15. The peaks in the two FRFs match nicely, but some differences

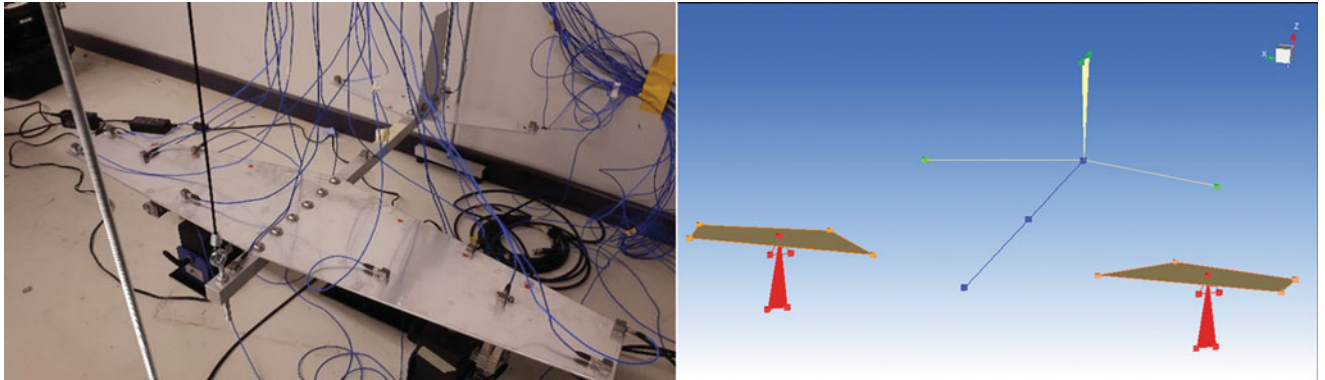


Fig. 5.10 Test setup for the linear identification of the aircraft with pylons. Left: physical structure. Right: Test Geometry

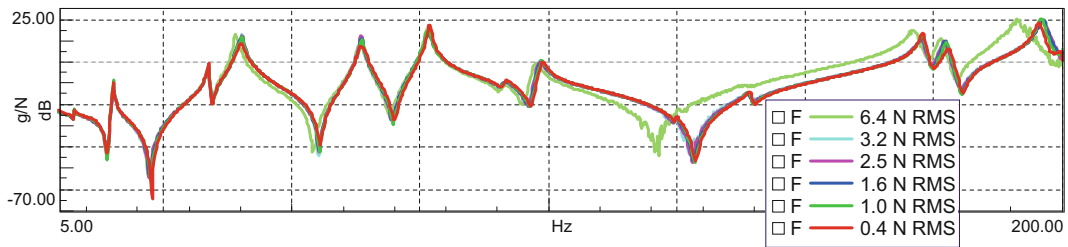


Fig. 5.11 Aircraft with pylons: FRF linearity check with Pseudo Random excitation

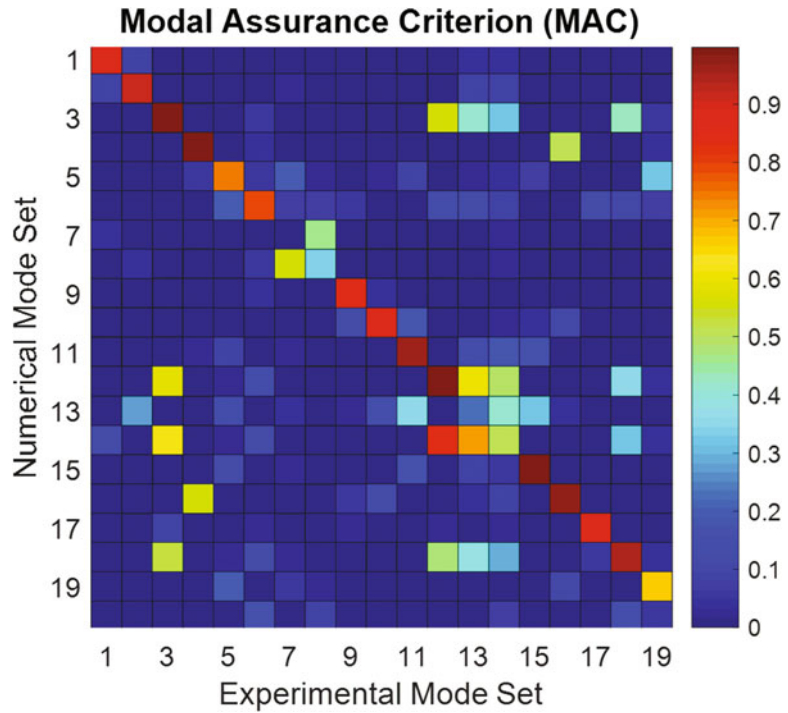


Fig. 5.12 MAC matrix between experimental and numerical modes for the aircraft with pylons case

are clearly visible, in particular for the mode around 35 Hz. In terms of mode shapes, generally the majority of the modes is well captured, except those where mode pairs appear at very close frequency: there, using multiple exciters surely helps in separating the contributions of these modes and obtain a better estimation.

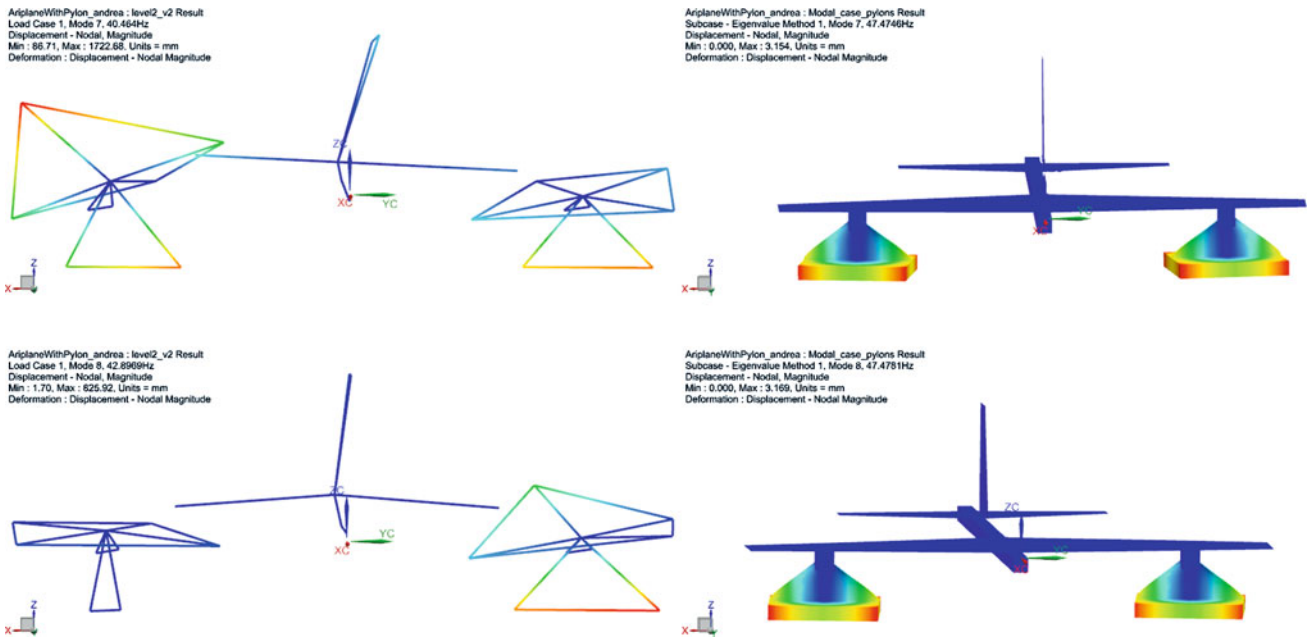


Fig. 5.13 Comparison between experimental (left) and numerical (right) symmetric (top) and asymmetric (bottom) torsion modes

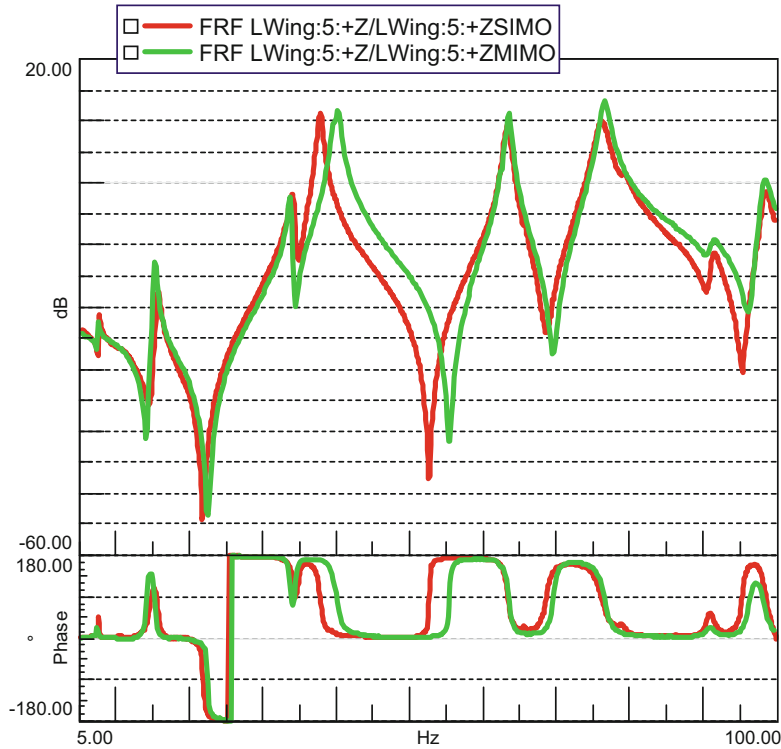


Fig. 5.14 MIMO vs. SIMO FRF for the same excitation level and profile

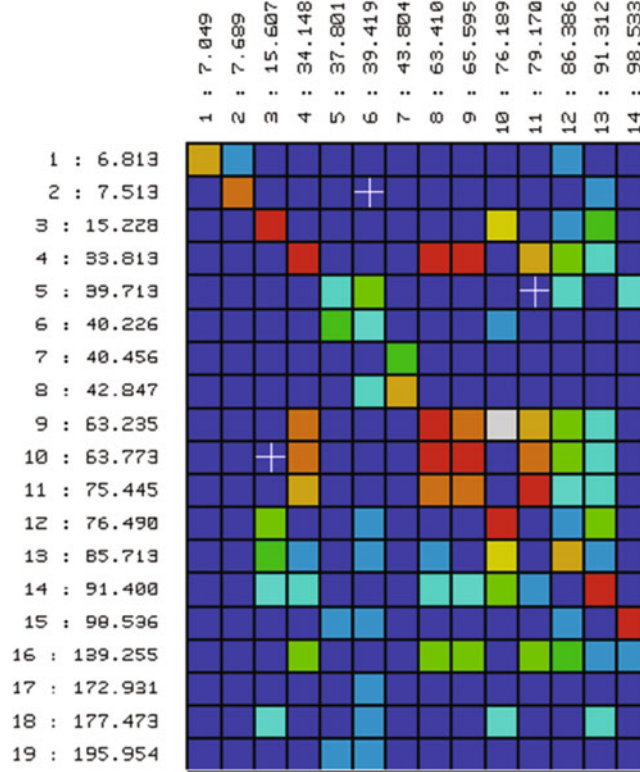


Fig. 5.15 MIMO vs. SIMO estimated mode shapes and natural frequencies

5.5 Nonlinear Identification

5.5.1 Nonlinear Detection Based on Time Series and FRF Inspection

Nonlinear detection is the first step in a nonlinear identification process to consider if the structure exhibits some level of nonlinear behavior under different excitation conditions. To check for symptoms of nonlinear behavior on the demo plane, several tests are conducted on the entire plane assembly using different types of excitation signals. In this paper, stepped and swept-sine excitations are predominantly used for investigating the nonlinear effects observed in the measured response of the assembly from low to higher excitation levels. Stepped and swept sine excitation signals were selected based on their deterministic nature. For a linear system or structure, the output response would produce a pure sine wave and for a nonlinear case, distortions are easily detected by visualizing the output response of the sine wave.

These stepped-sine FRFs only consider the first harmonic and neglect all other higher-order harmonic components in both input and output. Figure 5.16 shows the lack of homogeneity in the measured FRFs over different excitation levels, this is a clear breakdown of the superposition principle coming from linear theory. Evidence of nonlinearity is observed based on the shift in frequency and maximum amplitude for the measured frequency bandwidth. In addition to the observed frequency and amplitude shifts, the resonant peaks also lean to the left as shown in Fig. 5.16, causing a sudden transition (jump) down to a lower energy state when increasing in frequency, and a smaller transition (jump) up to a higher energy state when decreasing in frequency. This is most evident in the FRFs reporting the responses between 6.5 and 8.20 Hz.

Sine-sweep test was also conducted on the plane assembly at multiple excitation levels to gain some insight into the time series data, covering a frequency bandwidth of 5.5–100 Hz. Accelerations at selected locations of the plane were measured at 0.6 N, 0.8 N, 1 N and 1.2 N excitation levels. Figure 5.17 shows selected plots of the measured acceleration against sweep frequency for the modes of the plane in that bandwidth. Symptoms of nonlinearity are visible in the plots presented in Fig. 5.17 where both frequency and amplitude shift are observed for all modes when the excitation is increased. The lack of symmetry feature is also observed around the resonance peak of 39.6 Hz for high amplitude of vibration, skewness of the signal envelop is also observed around the resonance peaks at high excitation level.

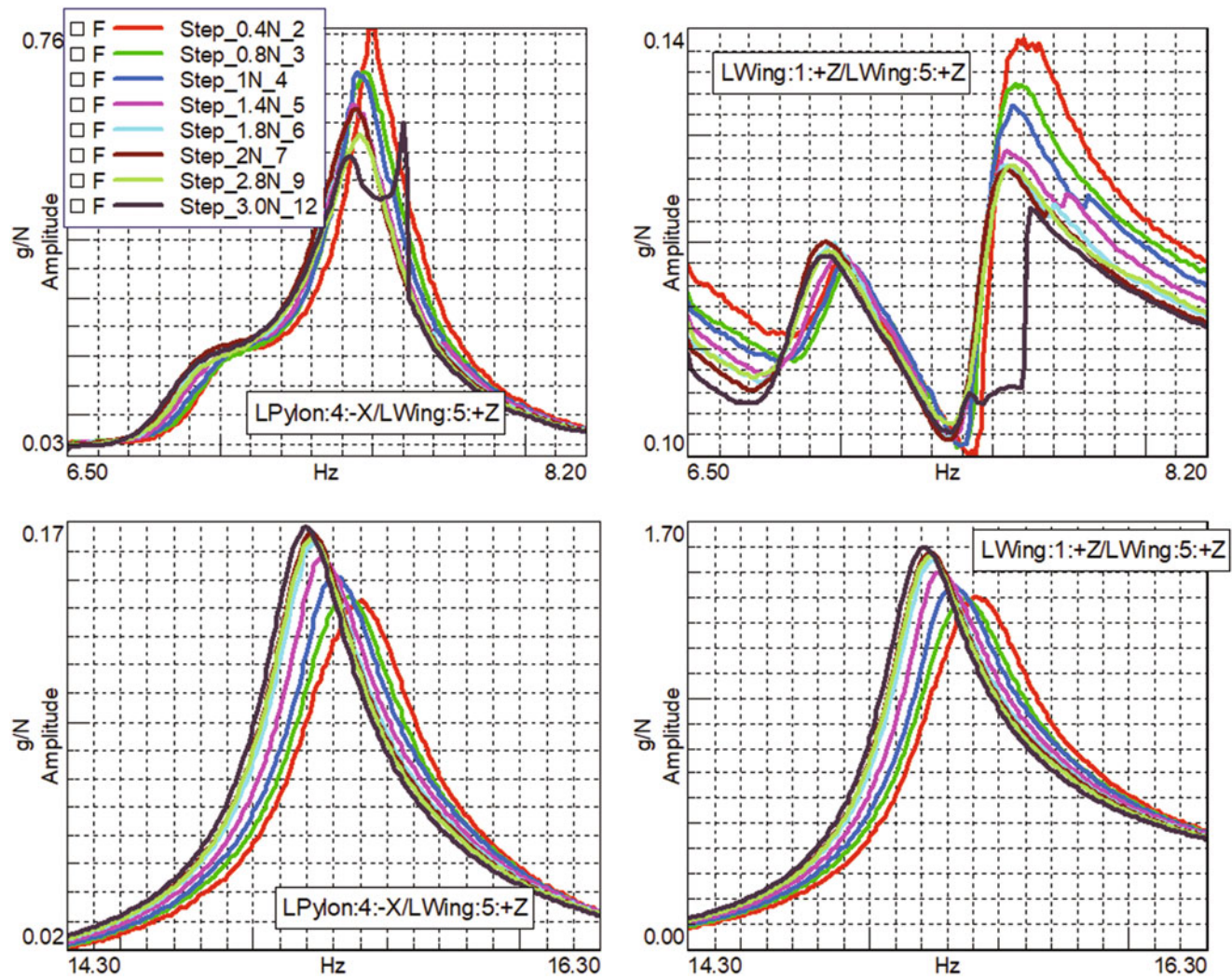


Fig. 5.16 Comparison of force controlled stepped sine frequency response measured at the left wing and left pylon for frequency range 6.5–8.2 Hz and 14.30–16.30 Hz

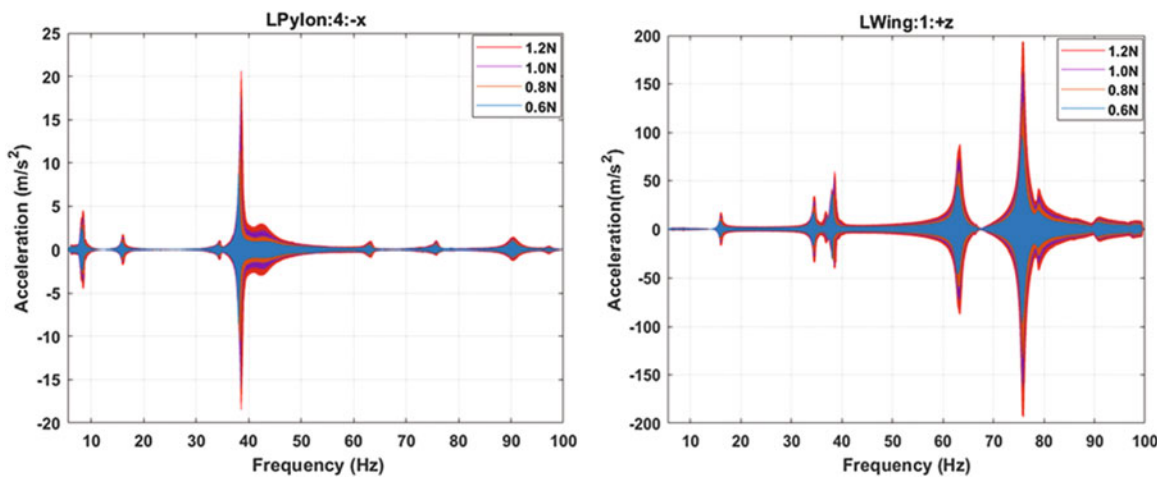


Fig. 5.17 Comparison sine-sweep acceleration response measured at the left wing and left pylon for frequency range 5.5–100 Hz

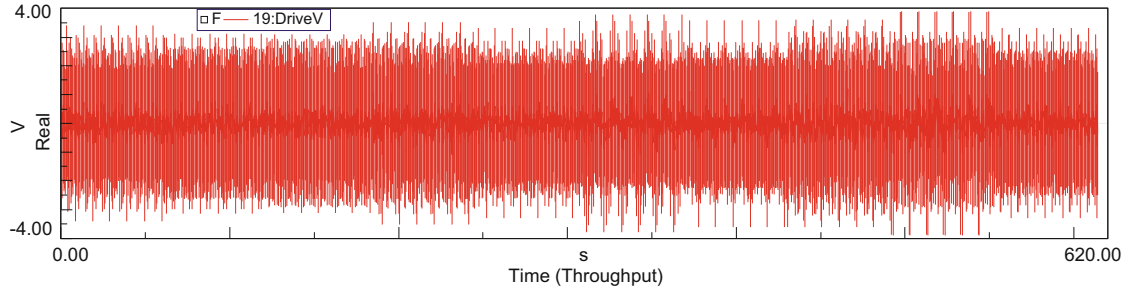


Fig. 5.18 Oddmultisine drive signal with bandwidth from 5 to 100 Hz and consisting of 10 realizations with 2 delay blocks and 4 repetitions

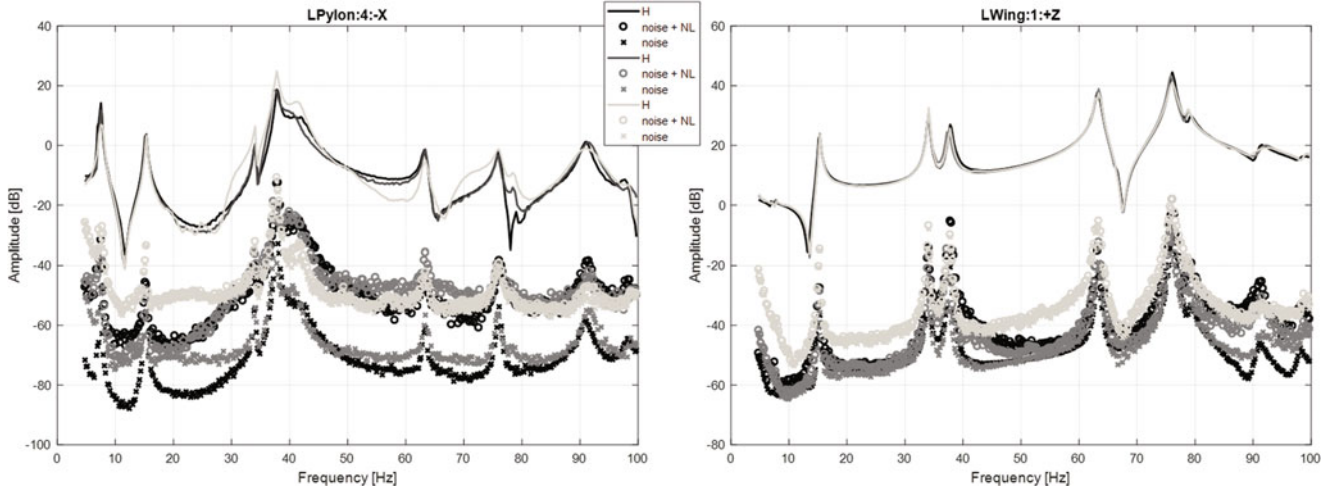


Fig. 5.19 Results of BLAs estimation with oddmultisine excitation on a sensor on the pylon (left) and on the wing tip (right). Black: 3 N; Dark Grey: 0.3 N; Light Grey: 0.03 N

5.5.2 Best Linear Approximation Estimation with Oddmultisines Excitation

Amongst the several techniques available to estimate the Best Linear Approximation of a nonlinear system, the one based on the multisine excitation is surely, from an industrial point of view, one of the most interesting and easier to use. The key reason for this is that it relies on excitation signals and averaging scheme very close to those of the classical Pseudo Random excitation. More details on the odd-multisines, their properties and how the BLA is estimated can be found in [12]. The main difference with a regular FRF estimation is that instead of using the averaged input and output data, a partial BLA estimate is calculated for each period of the excitation. A BLA FRF estimate, for a given signal, is then calculated via the average of the different BLAs: this allows to derive the noise and standard deviation of the estimates at each frequency line. The difference between the total variance of the BLA and the noise variance is an estimate of the variance of the stochastic nonlinear contribution.

The excitation signal was generated to be equivalent to the pseudo random one used in the previous sections to identify the linear model, with the difference that in each realization a number of randomly selected odd harmonics are not excited. The reference drive signal is shown in Fig. 5.18. The same drive signal was scaled to 3 excitation levels, respectively at 0.03, 0.3 and 3 N RMS. The estimated BLAs, noise and nonlinear contributions are displayed in Fig. 5.19. First, by comparing the BLAs on the two displayed measured locations, it is immediately evident (as expected) that nonlinearities are much stronger on the pylon than at the wing, as the BLAs are significantly different across the three levels. The actual nonlinear response can be quantified by the difference between the “noise” and the “noise + NL” estimates at each level. At the lower level, the SNR is very low, and thus the estimate noise variance is extremely high; moreover, as expected, the nonlinear distortion is marginal. This is in line with what was shown in Fig. 5.5. From the other two levels, more information can be derived. First of all, it is confirmed that the wing response is relatively linear at lower frequencies, and starts to become significant only above 80 Hz. On the contrary, the pylon shows a significant nonlinear behavior, which increases with the load level and appears constant throughout the considered frequency band.

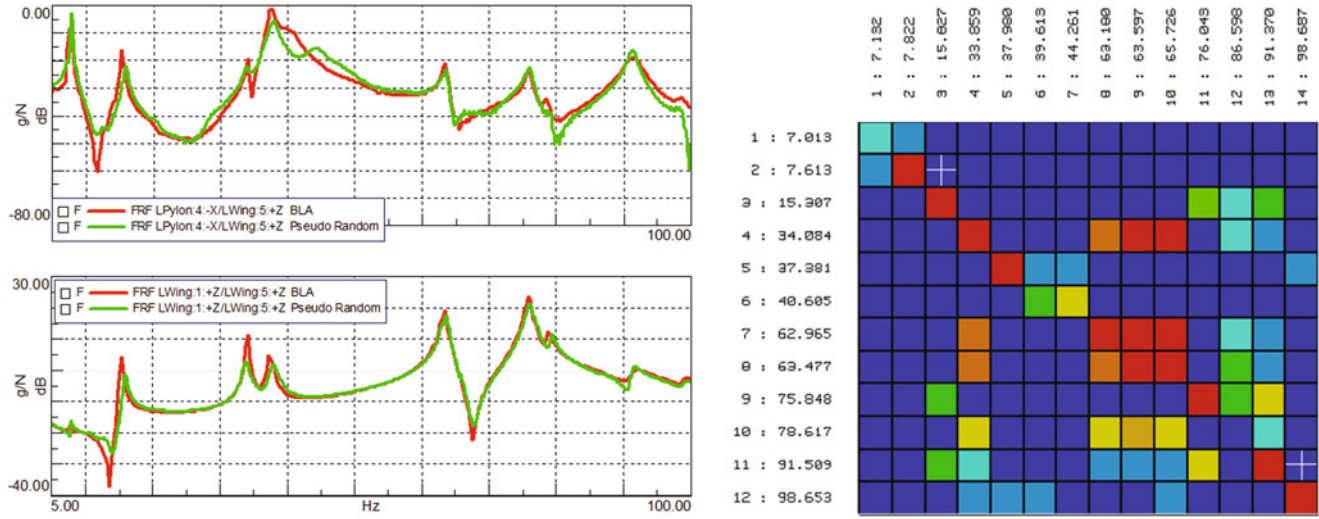


Fig. 5.20 (Left) Comparison of BLA and regular FRF estimates from a Pseudo Random Excitation. (Right) MAC matrix of BLA and FRF mode shapes

The estimated BLAs can now be used to identify a modal model, which will represent the best linear approximation of the underlying linear model at that specific excitation level, for which the nonlinearities can be clearly quantified. This gives more confidence in the results than just using regular pseudo random, where the nonlinear contribution is just averaged out instead of being estimated as is the case here. This is shown in Fig. 5.20, where on the left the BLAs derived with the intermediate levels are compared with those derived, for the same excitation level, with those from a regular pseudo random excitation. In terms of end results, the modal parameters, the two analysis yield similar results.

5.5.3 Best Linear Approximation Estimation with Sine-Sweep Excitation

As alternative approach to the one described in the previous paragraph, sine-sweep input and output data acquired at different excitation levels can also be used. Although a sine-sweep is a deterministic signal instead of a random one, the initial linear state space and the FRF of the BLA can still be obtained using the expression given by:

$$G_{BLA}(k) = \frac{Y(k)}{U(k)} \quad (5.1)$$

at the excited frequency lines k . The fact that the spectrum $U(k)$ of a sine-sweep is not rough at all frequencies could pose a challenge in the calculation 15, however the LPM (Local Polynomial Model) can still be applied based on calculating the difference between the input at two consecutive frequencies i.e., $(U(k) - U(k - 1))$. Figure 5.20 shows the corresponding estimated FRFs and total distortions for the parametric and nonparametric BLA for the two main frequency bandwidths of interest (6–100 Hz) the selected FRFs and total distortion (=noise + nonlinear) levels are based on excitation levels ranging 0.6–1 N.

Figure 5.21 shows an illustration of the estimated amplitudes and total distortion levels across the different excitation levels and frequency bandwidths of interest. Slight shift in the resonance peaks and reduction in amplitude is observed across the FRFs obtained from the multiple forcing level BLA estimation as shown in Fig. 5.21 as the excitation level increases. Similarly, it is evident that the total distortion (noise + nonlinear distortions) also affects the response of the structure.

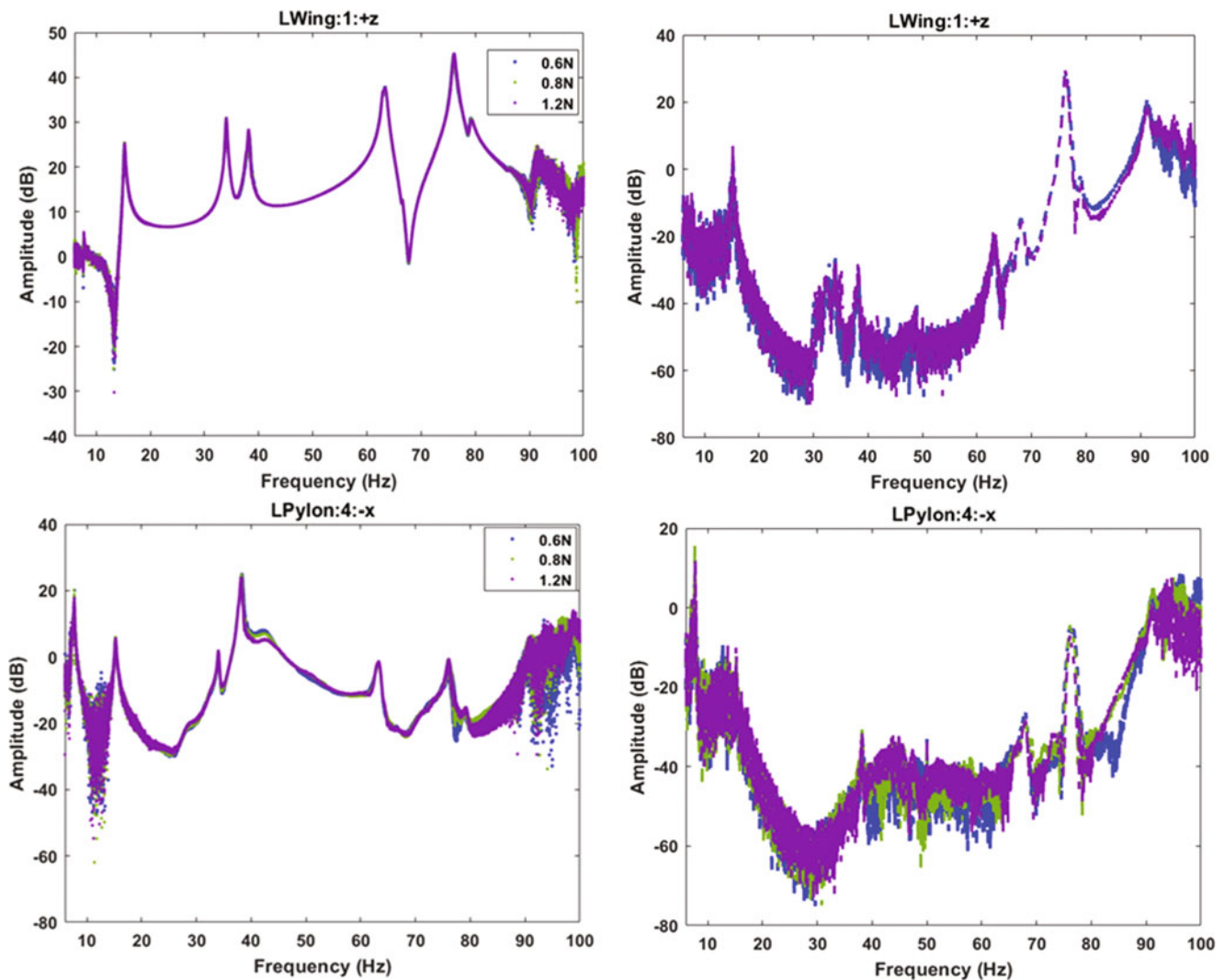


Fig. 5.21 Nonparametric FRFs and total distortions for two different output sensors on the assembly based on measured sine-sweep data for frequency range 6–100 Hz

5.5.4 Nonlinear Characterisation

Nonlinear characterisation helps in determining the type of nonlinearity in the structure and in addition seeks to provide answers to some major questions that arise when dealing with nonlinear system. Some of the typical questions that arises are listed below:

- (a) What is the strength of the nonlinearity? i.e. is it weak or strong nonlinearity
- (b) What is the source of the nonlinearity? i.e. is it stiffness or damping nonlinearity or both
- (c) What is the nonlinear stiffness characteristic? i.e. is it hardening or softening
- (d) What is the characteristic of the restoring force? i.e. is it symmetric or asymmetric

Of all the characterization methods available in the literature, the Acceleration Surface Method has proven its ability to characterize the stiffness and damping properties of a nonlinear structure due to its in-built characterization competences. By presenting the restoring force surface results for a nonlinear structure as a function of the displacement, velocity and acceleration in a three-dimensional plot, it is possible to visualize the type of nonlinearity in the system. The stiffness and damping properties of the nonlinearity can also be visualized by taking a slice of the three-dimensional plot at zero values of the corresponding velocity and displacements.

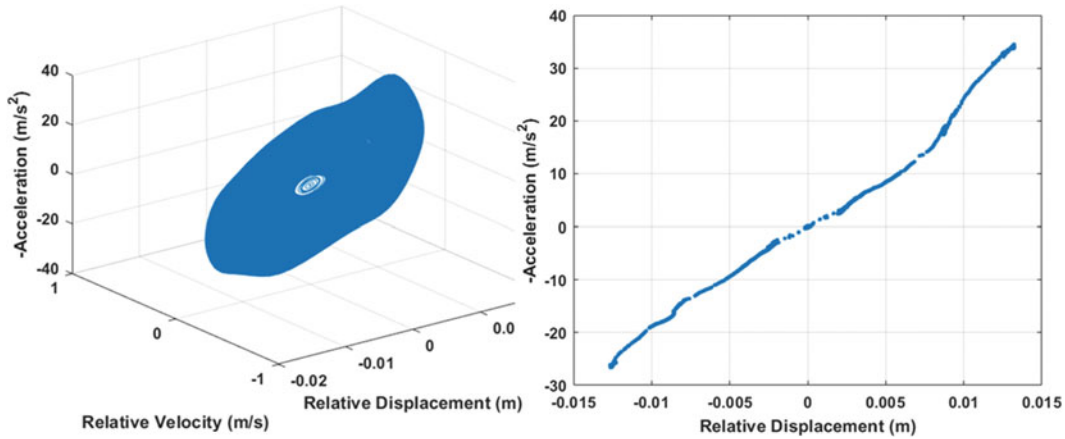


Fig. 5.22 3D and 2D Acceleration Surface Method results between 6.5 and 8.2 Hz at the pylon connection

In this case, narrow band sine-sweep test was conducted around the first of mode (6.5–8.2 Hz) of the plane assembly at high level of excitation this mode was observed as the mode that activates the connection between the left pylon and the left wing of the plane. The acceleration surface was computed using acceleration data measured at the bottom surface of the wing and the pylon for the selected mode, the velocity and displacement vectors were obtained by integrating the acceleration vectors of the selected points. These measured points were selected to visualize the nonlinear behaviour caused by the connection. To visualise the form of elastic nonlinearities in this connection, a cross section along the axis of the zero velocity value of the acceleration surface plot in was plotted and presented on the second plot of Fig. 5.22.

5.6 Conclusion

This paper has presented a case study on investigating the nonlinearities observed during the experimental campaign of a demo aircraft structure designed to understand the side effects of nonlinearities caused by bolted joints and multibody assemblies. The overall aim of the paper was to demonstrate the application of a selected number of techniques for experimental identification of the demo aircraft structure with nonlinear features incorporated in the design. The aim was achieved by three different types of experimental test, the type of test included Random excitation test which was used for the linear identification. The second test was based on sine-sweep and stepped sine excitation test, results obtained from this test were used to detect and ascertain the existence of nonlinearity in the measured time response envelop. The overall results obtained from this investigation has demonstrated the presence of a bilinear type of nonlinearity in the structure and it is therefore important to include such nonlinear phenomena in the finite element model of the structure. Starting from the validated linear Finite Element model, future activities will aim at finding simplified yet accurate ways of introducing the experimentally characterized nonlinear behavior in the aircraft and pylon models.

References

1. Noël, J.P., Renson, L., Kerschen, G.: Complex dynamics of a nonlinear aerospace structure: experimental identification and modal interactions. *J. Sound Vib.* **333**(12), 2588–2607 (2014)
2. Czaplewski, D.A., et al.: A soft landing waveform for actuation of a single pole single throw ohmic RF MEMs switch. *J. Micromech. Sys.* **15**, 1586–1594 (2006)
3. Segalman, D.J., et al.: Handbook on dynamics of jointed structures, pp. 1–532. Sandia National Laboratories National Technical Information Service, Albuquerque, NM (2009)
4. T. Dossogne, et al.: Nonlinear ground vibration identification of an F-16 Aircraft—Part II understanding nonlinear behaviour in aerospace structures using sine-sweep testing. In: International Forum on Aeroelasticity and Structural Dynamics, Bristol (2015)
5. Fuellekrug, U., Goege, D.: Identification of weak non-linearities within complex aerospace structures. *Aerosp. Sci. Technol.* **23**(1), 53–62 (2012)
6. Platten, M.F., Wright, J.R., Cooper, J.E., Dimitriadis, G.: Identification of a nonlinear wing structure using an extended modal model. *J. Aircr.* **46**(5), 1614–1626 (2009)

7. Carrella, A., Ewins, D.J.: Identifying and quantifying structural nonlinearities in engineering applications from measured frequency response functions. *Mech. Syst. Signal Proce.* **25**(3), 1011–1027 (2011)
8. Croufer,C., Santangelo, A.: Modern solutions for ground vibration and modal survey testing_LMS. In: LMS Ground Vibration Test Workshop, Spain (2010)
9. Noel, J.P., et al.: Nonlinear dynamic analysis of an F-16 aircraft using GVT data. In: Proceedings of the International Forum on Aeroelasticity and Structural Dynamics (IFASD), Bristol (2013)
10. Carney, K., et al.: Nonlinear-dynamic-behavior-cassini-spacecraft-modal-survey. In: Proceedings of the 15th International Modal Analysis Conference (IMAC), Orlando, FL (1997)
11. Dossogne, T.: Detection and characterization of nonlinearities in aircraft structures. Master's Thesis Dissertation, University of Liège (2014)
12. Pintelon, R., Schoukens, J.: System identification: a frequency domain approach. John Wiley & Sons, New Jersey (2012)



Chapter 6

Sensor Placement for Multi-Fidelity Dynamics Model Calibration

G. N. Absi and S. Mahadevan

Abstract This paper studies a multi-fidelity resource optimization methodology for sensor location in the calibration of dynamics model parameters. Effective calibration can only be achieved if the information collection in the experiments is successful. This requires a thoughtful study of the sensor configuration to maximize information gain in the calibration of system parameters. This paper proposes a framework for optimizing the sensor number and locations to maximize information gain in the calibration of damping parameters for non-linear dynamics problems. Further, we extend the basic framework to the case of multi-fidelity modeling. In the presence of models of multiple fidelity, runs from the high-fidelity model can be used to correct the low-fidelity surrogate and result in stronger physics-informed priors for calibration with experimental data. This multi-fidelity calibration allows the fusion of information from low and high-fidelity models in inverse problems. The proposed sensor optimization methodology is illustrated for a curved panel subjected to acoustic and non-uniform thermal loading. Two models of different fidelity (a time history analysis and a frequency domain analysis) are employed to calibrate the structure's damping parameters and model errors. The optimization methodology considers two complicating factors: (1) the damping behavior is input-dependent, and (2) the sensor uncertainty is affected by temperature.

Keywords Bayesian calibration · Multi-fidelity · Optimization · Sensor location · Structural dynamics

6.1 Introduction

Inferring unknown system parameters in dynamics problems is a critical initial task in understanding the behavior of a structure. The success of a calibration exercise depends on the quality of the information extracted from an experimental setup and is directly related to the sensor configuration. This paper proposes a framework that optimizes the number and location of strain gages in test structures with non-linear dynamics such that the information gain in calibration of the unknown system parameters is maximized.

Several different metrics for information gain have been investigated in the literature. Some studies have used the Fisher information matrix to optimize sensor location. Shah and Udwadia [1] define a method of finding the optimal location for a single sensor in a building structure to calibrate the shear stiffness. Kammer [2] maximizes the trace of the Fisher information matrix to find a sensor configuration set from a larger candidate set that maintains independence of the finite element model target modes partitions. Kirkegaard and Brincker [3] investigate the influence of the increasing number of sensors on the noise-to-signal ratio at the optimal sensor locations. Heredia-Zavoni et al. [4, 5] have focused on minimizing the Bayesian loss function in the trace of the inverse Fisher information matrix to find the optimal sensor location to calibrate lateral stiffness and base flexibility in multiple degrees of freedom shear systems.

In the presence of large data sets, the determinant of the Fisher information influences the information entropy [6]. Studies have used different entropy measures to quantify information gain. Papadimitriou et al. [7] minimize the uncertainty in the model parameter estimates by minimizing the information entropy measure, also known as Shannon's entropy. Papadopoulou et al. [8] use the joint entropy measure to select optimal sensor locations for the purpose of improving predictions of wind flow around buildings. Hu et al. [9] use the relative entropy measure, i.e., the Kullback Leibler divergence, in optimizing experimental input settings in order to maximize information gain for calibration of thermal conductivity and volumetric heat capacity in heated concrete slabs.

Work in structural health monitoring (SHM) has also focused on strain gage location optimization. Abdullah et al. [10] studied the optimization of sensors (or controllers) in discrete locations for control of civil engineering structures. Raich and

G. N. Absi (✉) · S. Mahadevan
Department of Civil and Environmental Engineering, Vanderbilt University, Nashville, TN, USA
e-mail: gina.nakad@vanderbilt.edu

Liszka [11] optimize the location and number of sensors to maximize the quality of the information collected in addition to the location of the excitation in a multi-objective optimization approach. Guratzsch and Mahadevan [12] optimize sensor location to detect damage in structures under transient mechanical and thermal loading.

When model parameters are constant and/or deterministic, it has been shown that optimizing the location of one sensor may be enough for calibration [13]. However, when the system parameters and/or the model errors are spatially variant, optimization becomes more challenging [14].

This work aims to optimize the number and location of sensors in the calibration of unknown system parameters that are dependent on multiple inputs in non-linear structural dynamics by maximizing the information gain in the parameters' joint posteriors. We also consider the effect of the input on the sensors by including an input-dependent degradation function in the sensor uncertainty measure. We further extend the optimization framework to model calibration problems where models of multiple fidelity are used. The proposed sensor optimization methodology is illustrated for a curved panel subjected to acoustic and non-uniform thermal loading.

6.2 Background

The sensor location optimization developed in this paper can be applied to single fidelity models as well models with multiple fidelity. In this paper, the emphasis is on calibration of input (temperature) dependent damping parameters, spatially varying errors, and input-depending experimental errors in the presence of models of multiple fidelity.

6.2.1 Damping Calibration

Structural dynamics models are typically formulated as:

$$[\mathbf{M}] \{ \ddot{x}(t) \} + [\mathbf{C}] \{ \dot{x}(t) \} + [\mathbf{K}] \{ x(t) \} = \{ f(t) \} \quad (6.1)$$

where the mass matrix $[\mathbf{M}]$ and the stiffness matrix $[\mathbf{K}]$ can be calculated based on measurements, and the damping matrix $[\mathbf{C}]$ inferred from results in an experimental setup of the structure under dynamic excitation.

Damping is associated with the dissipation of energy in a vibrating structure. Different types of damping can be present, and the structural configuration of an experimental setup dictates which type of damping dominates [15]. A broadening of the resonant peak of the frequency response curve under amplified acoustic loading in some experiments [16] motivated studying the effect of input on damping values in non-linear applications.

6.2.2 Bayesian Calibration

Calibration of model parameters may be performed using Bayes' theorem as

$$\pi_{\Theta}(\Theta | \mathbf{Y}_{\text{obs}}) \propto \pi_{\Theta}(\Theta) \cdot L(\Theta) \quad (6.2)$$

where $\pi_{\Theta}(\Theta | \mathbf{Y}_{\text{obs}})$ is the posterior distribution of the parameter Θ after calibration with the data \mathbf{Y}_{obs} , $\pi_{\Theta}(\Theta)$ is the prior distribution of Θ , and $L(\Theta)$ is the likelihood function or the probability of observing \mathbf{Y}_{obs} for a specific value of the calibration parameter. Markov Chain Monte Carlo (MCMC) sampling can be used to draw samples from the posterior distributions. Several algorithms are available for MCMC sampling: Metropolis-Hastings [17], Gibbs sampling [18], slice sampling [19], etc. In this paper, and for illustration purposes, we use slice sampling to evaluate Eq. 6.2. Using MCMC sampling methods is usually very expensive: thousands of samples are needed to correctly estimate the posterior distributions. Expensive simulation models need to be replaced by cheaper surrogates. Many surrogate modeling techniques can be used for that purpose such as polynomial-based response surfaces [20], artificial neural networks [21], polynomial chaos expansion [22], and Gaussian process (GP) interpolation (or Kriging) [23]. Here, we illustrate our approach using a polynomial chaos expansion (PCE) regression model.

6.2.3 Kullback–Leibler Divergence

It is well established that a significant posterior distribution change compared to a prior distribution in a calibration exercise implies significant information gain in the calibration process. In order to optimize the sensor location to include the most relevant information into the calibration, we pick the sensor number and locations that yield the largest posterior changes in calibration. The changes can be reflected in a shift of the posteriors (bias change), a reduction in the uncertainty, or both. In order to account for both the bias and uncertainty changes, we use the Kullback–Leibler (KL) [24] divergence calculation.

KL divergence is a non-symmetric measure of the relative entropy between two probability distributions. It has been used as a measure of information lost when a new distribution is trying to approximate an old one or as a measure of information gain when the gain is reflected by a large divergence of the posterior distribution compared to the prior in calibration. The latter measure is of interest in the context of calibration.

Assume $p(x)$ and $q(x)$ are two probability distributions of a random variable x . The KL divergence KLD of $q(x)$ compared to $p(x)$ is defined as:

$$KLD(p(x) \parallel q(x)) = \int_{-\infty}^{\infty} p(x) \ln \frac{p(x)}{q(x)} dx \quad (6.3)$$

Note that KL divergence is not a distance measure: $KLD(p(x) \parallel q(x)) \neq KLD(q(x) \parallel p(x))$. In addition, $KLD(p(x) \parallel q(x)) \geq 0$ and $KLD(p(x) \parallel q(x)) = 0$ if and only if $p(x) = q(x)$ for all x .

In this paper, we compute the KL divergence for the joint posterior distribution compared to the joint prior distribution within the optimization algorithm.

6.3 Sensor Location Optimization

The optimized selection of sensor locations in the experiments can be applied in the general case where only one model is available (single fidelity example) or in the case of multi-fidelity simulations. We consider a grid of candidate sensor locations in the experimental setup and find the optimal number and location of the sensors to retain the most information in the calibration of system parameters. The optimization objective is to select the sensor locations that maximize the KL divergence between the joint prior distribution of the calibration parameters and the model errors and their joint posterior distribution.

Since we cannot run experiments with actual sensors in all candidate locations, we replace the experimental observations with synthetic observed data. In the case of multi-fidelity modeling, the synthetic experimental data can be sampled using the multi-fidelity model (i.e., a low-fidelity surrogate corrected with high-fidelity simulations at all possible candidate sensor locations), with an added noise term.

We start by selecting a low number of sensors from the candidate locations. We then calibrate the system parameters for different location combinations of the sensors and calculate the KL divergence of the posterior distributions with regards to the priors for each location combination. The optimal location consists of the location at which the calculated KL divergence is maximized. Since the candidate locations are discrete, we employ a discrete optimization algorithm such as simulated annealing for this purpose. We repeat the optimization methodology for an increasing number of sensors. Convergence is reached when adding more sensors does not yield higher KL divergence values from the previous case.

6.4 Numerical Example

6.4.1 Problem Description

The application is a simplified representation of an aircraft fuselage panel subjected to dynamic acoustic loading (P) and high temperature loads (T). The panel is curved (Fig. 6.1) and modeled using the FEA software ANSYS.

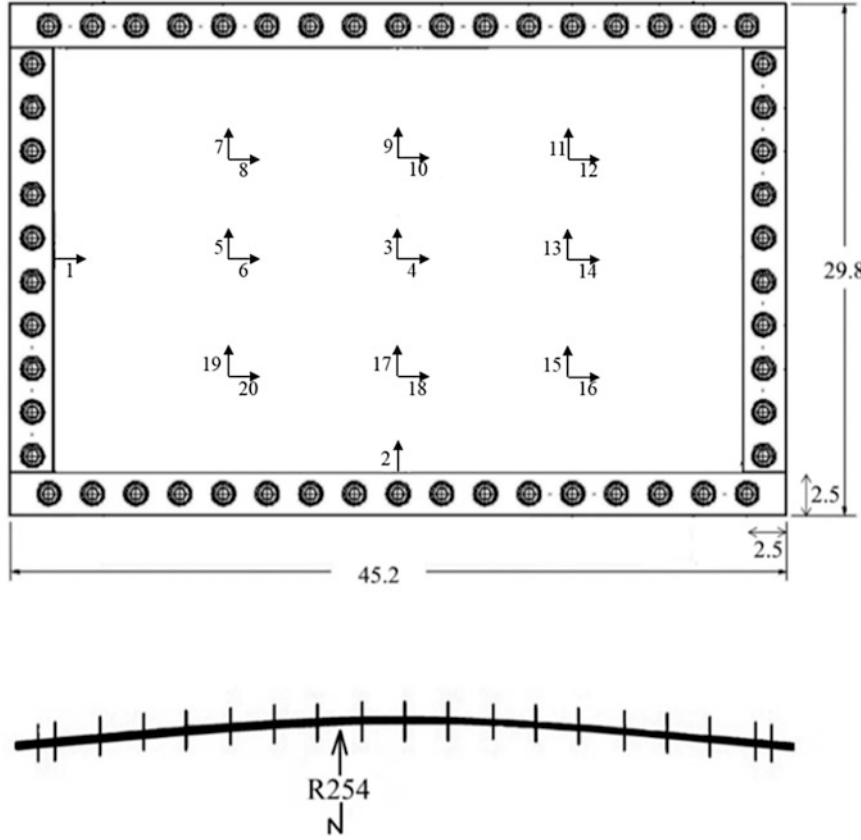


Fig. 6.1 Curved panel dimensions and strain gage locations (units: cm)

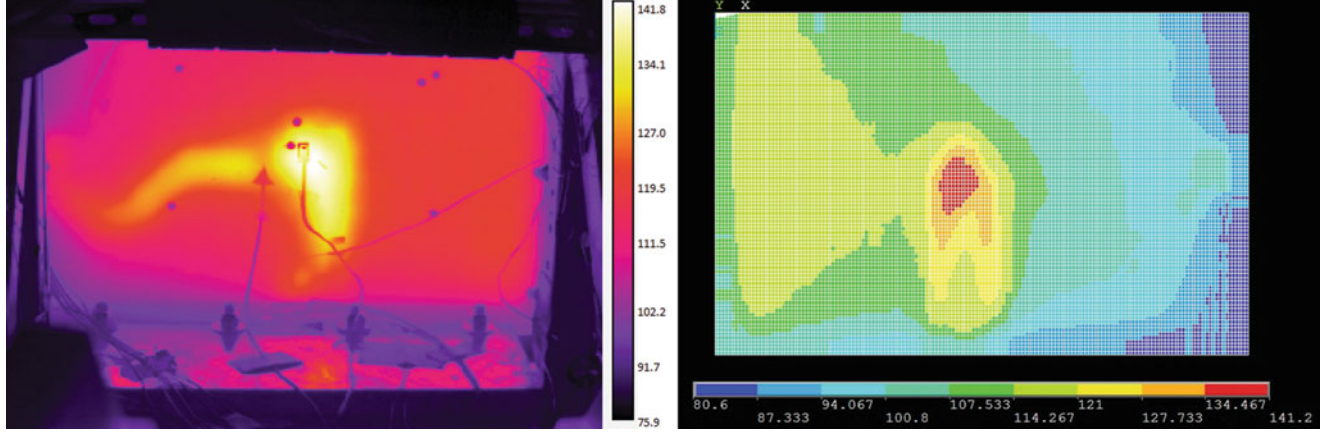


Fig. 6.2 Temperature distribution in experimental setup (left) and ANSYS model (right)

The acoustic load is assumed to be a uniform pressure on the plate surface, with testing magnitudes of 160, 166, 172 and 178 dB. The temperature load follows the experimental setup distribution as seen in Fig. 6.2. A laser beam centered at the center of the panel heats it for temperatures of 120 and 180 °F.

The experimental setup is simulated using two different models: a high-fidelity time-history analysis, and a low-fidelity power spectral density analysis. Both models have the same mesh size and consider a non-linear stress-strain relationship (material non-linearity). For more details on the models physics, and for discussion regarding the non-linearity of the analysis, please refer to [25]. Two types of damping need to be calibrated: Frictional damping (FD), a type of Coulomb damping resulting from the friction on the boundary of the panel with the experimental setup, and material damping (MD) or Raleigh damping throughout the remainder of the plate. FD and MD are assumed linear functions of the temperature gradient

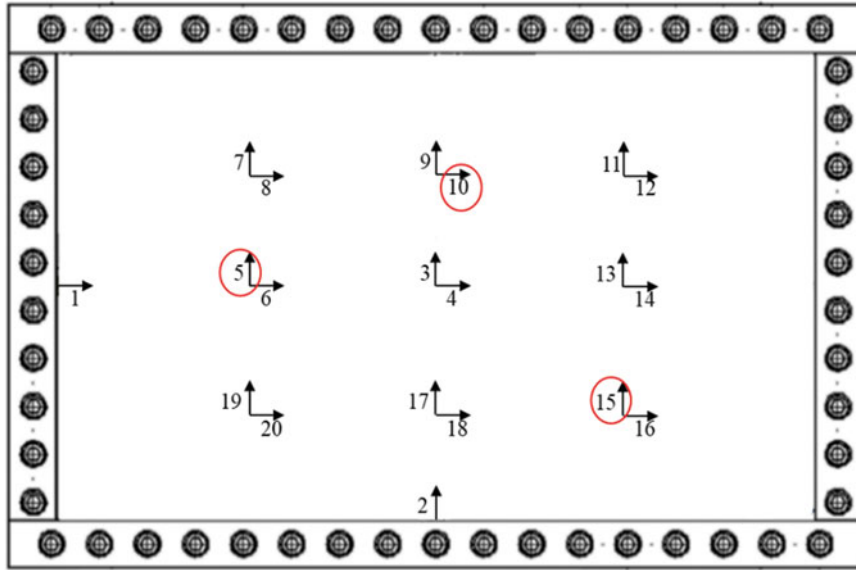


Fig. 6.3 Optimized location for three strain gages

$\Delta T = T - T_{Room} = T - 70$. We also calibrate the fixity ratio, which is the length of fixed plate boundary divided by the total boundary length, to account for the uncertainty with respect to the boundary conditions. Lastly, knowing that the recorded strain doesn't start at the initial time of the experiment, we include an initial stress (IC) on the plate in the form of a uniform pressure on the panel in the calibration variables. The model form errors are considered input dependent too. We also assume that high temperature affects the strain recordings, and we account for that in the form of an exponential degradation function of the variance of the experimental error. The aim is to find the optimal number and location of the experimental strain gages to efficiently calibrate the damping coefficients.

6.4.2 Sensor Location Optimization Results

Calibration of the damping parameters as well as the fixity ration, initial conditions, and model errors was done for three sensors. The calibration strain gages with the maximum KL divergence were found to be at (5,10,15). Figure 6.3 shows these locations on the curved panel:

Subsequent optimizations for increasing numbers of strain gages can be done until convergence is reached, i.e., when adding more strain gages does not increase the gain in information in the joint posterior distributions (no increase in subsequent KL divergence values).

6.5 Conclusion

This work provides a framework for selecting the optimal number and locations of strain gages in non-linear dynamics experiments for the purpose of model calibration, in the presence of multiple inputs. It takes into consideration the strain gage uncertainty as an increasing function of the input temperature and selects the optimal number and location of the strain gages that maximizes the information gain in calibration. Future work needs to address the computational challenges associated with a large number of candidate sensor locations.

References

1. Shah, P.C., Udwadia, F.: Methodology for optimum sensor locations for parameter identification in dynamic systems. *J. Eng. Mech.* **120**(2), 188–196 (1994)
2. Kammer, D.C.: Sensor placement for on-orbit modal identification and correlation of large space structures. *J. Guid. Control. Dyn.* **14**, 251–259 (1991)
3. Kirkegaard, P.H., Brincker, R.: On the optimal location of sensors for parametric identification of linear structural systems. *Mech. Syst. Signal Process.* **8**, 639–647 (1994)
4. Heredia-Zavoni, E., Esteva, L.: Optimal instrumentation of uncertain structural systems subject to earthquake ground motions. *Earthquake Eng. Struct. Dyn.* **27**, 343–362 (1998)
5. Heredia-Zavoni, E., Montes-Iturriaga, R., Esteva, L.: Optimal instrumentation of structures on flexible base for system identification. *Earthquake Eng. Struct. Dyn.* **28**, 1471–1482 (1999)
6. Papadimitriou, C.: Pareto optimal sensor locations for structural identification. *Comput. Methods Appl. Mech. Eng.* **194**, 1655–1673 (2005)
7. Papadimitriou, C., Beck, J.L., Au, S.-K.: Entropy-based optimal sensor location for structural model updating. *J. Vib. Control.* **6**, 781–800 (2000)
8. Papadopoulou, M., Raphael, B., Smith, I., Sekhar, C.: Hierarchical sensor placement using joint entropy and the effect of modeling error. *Entropy* **16**, 5078 (2014)
9. Hu, Z., Ao, D., Mahadevan, S.: Calibration experimental design considering field response and model uncertainty. *Comput. Methods Appl. Mech. Eng.* **318**, 92–119 (2017)
10. Abdulla, M.M., Richardson, A., Hanif, J.: Placement of sensors/actuators on civil structures using genetic algorithms. *Earthquake Eng. Struct. Dyn.* **30**, 1167–1184 (2001)
11. Raich, A.M., Liszkai, T.R.: Multi-objective optimization of sensor and excitation layouts for frequency response function-based structural damage identification. *Comput. Aided Civ. Inf. Eng.* **27**, 95–117 (2012)
12. Guratzsch, R.F., Mahadevan, S.: Structural health monitoring sensor placement optimization under uncertainty. *AIAA J.* **48**, 1281–1289 (2010)
13. Huan, X., Marzouk, Y.: Gradient-based stochastic optimization methods in Bayesian experimental design. *Int. J. Uncertainty Quantification.* **4**, 479–510 (2014)
14. Nath, P., Hu, Z., Mahadevan, S.: Sensor placement for calibration of spatially varying model parameters. *J. Comput. Phys.* **343**, 150–169 (2017)
15. Adhikari, S.: Damping Models for Structural Vibration, Trinity College, University of Cambridge, Cambridge, England (2000)
16. Gordon, R.W., Hollkamp, J.J.: Reduced-order models for acoustic response prediction, DTIC Document (2011)
17. Hastings, W.K.: Monte Carlo sampling methods using Markov chains and their applications. *Biometrika* **57**, 97–109 (1970)
18. Casella, G., George, E.I.: Explaining the Gibbs sampler. *Am. Stat.* **46**, 167–174 (1992)
19. Neal, R.M.: Slice sampling. *Ann. Statist.* **31**, 705–767 (2003)
20. Zhang, Z., Jiang, C., Han, X., Hu, D., Yu, S.: A response surface approach for structural reliability analysis using evidence theory. *Adv. Eng. Softw.* **69**, 37–45 (2014)
21. Hurtado, J.E., Alvarez, D.A.: Neural-network-based reliability analysis: a comparative study. *Comput. Methods Appl. Mech. Eng.* **191**, 113–132 (2001)
22. Ghanem, R.G., Spanos, P.: Stochastic Finite Elements: A Spectral Approach. Springer, Berlin (1991)
23. Romero, V.J., Swiler, L.P., Giunta, A.A.: Construction of response surfaces based on progressive-lattice-sampling experimental designs with application to uncertainty propagation. *Struct. Saf.* **26**, 201–219 (2004)
24. Kullback, S., Leibler, R.A.: On information and sufficiency. *Ann. Math. Statist.* **22**, 79–86 (1951)
25. Absi, G.N., Mahadevan, S.: Input-dependence effects in dynamics model calibration. *Mech. Syst. Signal Process.* **109**, 285–304 (2018)



Chapter 7

Application of Cumulative Prospect Theory to Optimal Inspection Decision-Making for Ship Structures

Changqing Gong, Dan M. Frangopol, and Minghui Cheng

Abstract The selection of optimal maintenance solutions under uncertainty is affected by the risk perception of decision-makers. The solution predicted by the minimum expected cost criterion may not conform to the preferences of decision-makers. The aim of this paper is to develop a risk-informed maintenance decision-making framework for corroding ship structures considering risk perceptions. Cumulative prospect theory is employed to model the choice preferences under uncertainty. The optimal ship maintenance strategy is developed as a single goal to maximize the expected prospect value. The uniform inspection interval is assumed to be the only design variable and a condition-based repair policy is considered. Monte Carlo simulations are employed to obtain the distribution of the maintenance and failure costs within the considered service life. The application of the developed framework is demonstrated on a ship hull girder structure.

Keywords Risk perception · Cumulative prospect theory · Ship risk · Inspection optimization

7.1 Introduction

Corrosion is one of the most common threats to the safety of ship structures [1]. Under chloride marine environment, corrosion on the surface of plates and stiffeners can grow over time. Without proper inspection and repairing to arrest or eliminates corrosion, plastic collapse of the hull girder may eventually occur as the result of cross-section reduction. Significant uncertainties are inherent to corrosion propagation, external wave loading, and hull girder resistance, among others. Maintenance decisions are usually made in the presence of uncertain ship structural performance. Ship maintenance involves expensive labor and material cost. There is a need for an optimal planning framework that can comprehensively consider optimum maintenance budget allocation, corroding structural performance uncertainties, and perceptions of risk of decision-makers.

The minimum expected cost criterion is widely used to select optimal design and maintenance solutions for structures and infrastructure systems [2–4]. This criterion is sufficient if decision-makers are risk-neutral to the high-order magnitude of cost uncertainties, e.g., variance [5]. However, because of the subjective perceptions of uncertainty, the “optimal” implied by the minimum expected cost may not be the most desirable to the decision-maker. For example, among the choices with the same expected cost, a risk-prone decision-maker prefers the one with greater uncertainty to obtain potential small cost returns. Utility theory transforms solution outcomes into utility values based on the risk attitude of decision-makers. Risk neutrality, aversion, and propensity are characterized using linear, concave, and convex functions, respectively [6]. Most preferred is a solution with the maximum sum of utility values of possible outcomes weighted by their respective probabilities. Utility theory has been incorporated in the civil and marine maintenance framework to capture the impact of decision-makers’ risk attitudes [7–10]. These studies reveal that utility theory can act as a simple practical tool in guiding the selection among competing maintenance solutions. Nevertheless, empirical observations show that actual decision-making under uncertainty deviates from the prediction by utility theory [11]. People are observed to evaluate choices based on losses and gains relative to a reference point. People are found to be risk-averse over gains, risk-prone over losses, and more sensitive to losses than gains. In addition, people do not weight the probabilities linearly and tend to subjectively distort the physical probabilities by overemphasizing small probabilities and underemphasizing large probabilities [11]. To accommodate the observed cognitive behavior, cumulative prospect theory (CPT) is developed and considered to be a dominant alternative to utility theory. The optimal seismic design of civil structures based on CPT has been presented in [5, 12]. The advantage and flexibility of CPT in modeling risk decision-making are demonstrated in these studies.

C. Gong (✉) · D. M. Frangopol · M. Cheng

Department of Civil and Environmental Engineering, ATLSS Engineering Research Center, Lehigh University, Bethlehem, PA, USA

e-mail: chg218@lehigh.edu

In this paper, an attempt is made to incorporate CPT in the corroding ship hull structure maintenance planning to explore the optimal solution to decision-makers' choices from the perspective of risk perception. To this end, the optimal maintenance is investigated by maximizing the preference characterized by CPT. The design variable selected is the inspection time. It is assumed that ship components are repaired after inspection if their corrosion depth reaches the allowance of the Classification Societies Rules [13]. The uncertainties associated with material strength, geometry, corrosion growth rate, bending resistance model, and external loadings are considered. The distributions of ship life-cycle maintenance and failure costs are computed using Monte Carlo simulation, and CPT preference is evaluated on this basis.

7.2 Cumulative Prospect Theory

CPT consists of a value function and a probability weighting function. The value function describes the desirability of the solution outcome (e.g. cost). Contrary to the utility function considering the consistent risk attitude for all outcomes, the value function is convex for losses and concave for gains, in agreement with the observed people's risk-prone and risk-averse behaviors for losses and gains, respectively. Losses and gains are classified according to a reference point, which represents decision-makers' expectation of future outcomes [14]. The weighting function is inverse S-shaped, reflecting the fact that people subjectively overweight small probabilities and underweight moderate and high probabilities in the decision-making process [11].

Consider a set of possible monetary outcomes relative to the reference point in ascending order $G = (x_1, p_1; \dots, x_n, p_n)$, where p_i denotes the probability of the i -th monetary outcome x_i ($i = 1, 2, \dots, n$) with $\sum_{i=1}^n p_i = 1$. According to CPT, decision-makers choose an alternative that maximizes the expected prospect value [11]:

$$E[V] = \sum_{j=1}^m \pi_j^- v(x_j) + \sum_{k=m+1}^n \pi_k^+ v(x_k) \quad (7.1)$$

where x_j ($j = 1, \dots, m$) ≤ 0 ; x_k ($k = m + 1, \dots, n$) ≥ 0 ; $v(\bullet)$ is the prospect function; π_j^- ($j = 1, \dots, m$) and π_k^+ ($j = m + 1, \dots, n$) are decision weights for losses and gains, respectively. The decision weights are [11]

$$\pi_1^- = w^-(p_1), \pi_n^+ = w^+(p_n) \quad (7.2a)$$

$$\pi_j^- = w^-(p_1 + \dots + p_j) - w^-(p_1 + \dots + p_{j-1}), \text{ if } 1 < j \leq m \quad (7.2b)$$

$$\pi_k^+ = w^+(p_k + \dots + p_n) - w^+(p_{k+1} + \dots + p_n), \text{ if } m < k < n \quad (7.2c)$$

where $w^+(\cdot)$ and $w^-(\cdot)$ are the weighting functions for gains and losses, respectively. Tversky and Kahneman [11] suggests probabilities weighting functions $w^+: [0, 1] \rightarrow [0, 1]$ for gains and $w^-: [0, 1] \rightarrow [0, 1]$ for losses, respectively, as

$$w^+(\cdot) = \frac{(\cdot)^{b^+}}{\left((\cdot)^{b^+} + (1 - (\cdot))^{b^+}\right)^{1/b^+}} \quad (7.3a)$$

$$w^-(\cdot) = \frac{(\cdot)^{b^-}}{\left((\cdot)^{b^-} + (1 - (\cdot))^{b^-}\right)^{1/b^-}} \quad (7.3b)$$

with b^- and $b^+ \in (0, 1)$. The value function is defined as

$$v(x) = \begin{cases} x^\alpha, & \text{if } x \geq 0 \\ -\lambda(-x)^\beta, & \text{if } x < 0 \end{cases} \quad (7.4)$$

where λ specifies loss aversion degree with $\lambda \geq 1$; $\alpha, \beta \in (0, 1)$ are the exponential parameters. λ is introduced to reflect more sensitivity to losses than gains. Tversky and Kahneman [11] found that $\alpha = \beta = 0.88$, $\lambda = 2.25$, $b^- = 0.69$, and $b^+ = 0.61$.

7.3 Reliability Assessment

7.3.1 Limit State Function

Subjected to global still waver and wave-induced vertical bending moment, the most critical ship failure mode is the ultimate collapse of the hull girder cross-section at mid-span [15]. This failure mode can result in the loss of the ship and its cargo, causing significant economic and environmental consequences. The limit state function associated with the hull girder at mid-span is [15]

$$G = \xi_u M_u - \xi_{sw} M_{sw} - \xi_w \xi_{w,n} M_{we} \quad (7.5)$$

where M_u is the ultimate vertical bending capacity of the hull girder; M_{sw} is the maximum still water induced moment at mid-span during one voyage; M_{we} is the annual maximum wave-induced bending moment; ξ_u and ξ_{sw} are the model errors for predicting the ultimate bending capacity and still water moment, respectively; ξ_w and $\xi_{w,n}$ are the model error of wave-induced moment predictions, respectively. Note that ξ_w specifically accounts for the uncertainty of linear response prediction, and $\xi_{w,n}$ is a correction factor considering the nonlinearity of responses due to hull flare and large ship motion amplitude [15].

7.3.2 Ultimate Bending Capacity

The vertical bending strength is predicted using simple analytical expressions by Paik and Mansour [16]. This method assumes that the hull girder cross-section fails by overall plastic collapse when the tensile flange yields and compression flange reaches the ultimate buckling strength. With the assumed longitudinal stress distribution over the cross-section, the ultimate bending strength of the hull girder in sagging (M_{us}) and hogging (M_{uh}) conditions are [16]

$$\begin{aligned} M_{us} = & -A_D(D-g)\sigma_{uD} - \frac{A_s}{D}(D-H)(D+H-2g)\sigma_{uS} - A_B g \sigma_{yB} + \frac{A'_B}{H}(g-D_B)[D_B\sigma_{uS} - (H-D_B)\sigma_{yS}] \\ & - \frac{A_s H}{3D}[(2H-3g)\sigma_{uS} - (H-3g)\sigma_{yS}] \end{aligned} \quad (7.6)$$

$$\begin{aligned} M_{uh} = & A_D g \sigma_{yD} + A_B(D-g)\sigma_{uB} + A'_B(D-g-D_B)\sigma'_{uB} + \frac{A_s H}{3D}[(2H-3g)\sigma_{uS} - (H-3g)\sigma_{yS}] \\ & + \frac{A_s}{D}(D-H)(D+H-2g)\sigma_{uS} \end{aligned} \quad (7.7)$$

where D is the hull girder depth; D_B is the double bottom height; A_B , A'_B , A_D , and A_S are the total sectional area of the outer bottom, inner bottom, deck, and half-sectional area of the side, respectively; g denotes the neutral axis position; H is the depth of hull section in linear elastic state; σ_{yB} , σ_{yS} , and σ_{yD} are the yield strength of the bottom, side, and deck, respectively; σ_{uD} , σ'_{uB} , σ_{uD} , and σ_{uS} are the ultimate compression strength of the bottom, inner bottom, deck, and side, respectively. For the detailed calculation of g and H , readers are referred to Paik and Mansour [16]. The flange and side of the ship hull girder are stiffened panels with spaced flat, angle or T-bars. A stiffened panel consists of stiffened plate elements with stiffeners of various sizes. The strength of stiffeners is typically higher than that of plates. The ultimate strength of the flange and side is approximated as the equivalent value strength of stiffened plate elements. Similarly, the yield strength of a stiffened plate element equals the equivalent yield strength of the plate and its stiffener. The ultimate compression strength, σ_u , of a stiffened plate is evaluated using the following formulations [17]:

$$\sigma_u/\sigma_{ye} = \left(0.995 + 0.936\lambda^2 + 0.107\beta^2 + 0.188\lambda^2\beta^2 - 0.067\lambda^4\right)^{-0.5} \quad (7.8a)$$

$$\lambda = \frac{l}{\pi r} \sqrt{\frac{\sigma_{ye}}{E}} \quad (7.8b)$$

$$\beta = \frac{b}{wt} \sqrt{\frac{\sigma_{yp}}{E}} \quad (8.8c)$$

where σ_{ye} is the equivalent yielding strength of the stiffened plate; l is the longitudinal stiffened plate length between transverse webs; r is the gyration radius of the stiffened plate; E is Young's modulus; b is the breadth of the plate between longitudinal stiffeners; and wt is the wall thickness of the plate.

7.3.3 Still Water Bending Moment

Still water bending moment is caused by the difference in distribution between weight and the buoyancy force along the ship longitudinal direction. In the ship loading manual [13], it is recommended that maximum bending moment is calculated as

- (a) for sagging condition

$$M_{sw,max} = -0.05185 C_{wv} L^2 B (C_b + 0.7) \text{ KNm} \quad (7.9a)$$

- (b) for hogging condition

$$M_{sw,max} = 0.01 C_{wv} L^2 B (11.97 - 1.9 C_b) \text{ KNm} \quad (7.9b)$$

where B is the ship breadth; C_b is the ship block coefficient; L is the ship length; C_{wv} is the wave coefficient given as [13]

$$C_{wv} = \begin{cases} 10.75 - [(300 - L) / 100]^{1.5} & \text{for } 90 \text{ m} \leq L \leq 300 \text{ m} \\ 10.75 & \text{for } 300 \text{ m} \leq L \leq 350 \text{ m} \\ 10.75 - [(L - 350) / 100]^{1.5} & \text{for } 350 \text{ m} \leq L \leq 500 \text{ m} \end{cases} \quad (7.10)$$

In addition to the ship size, still water moment is also dependent on the ship type and load condition. During one voyage, the maximum still water moment can be different because of the fuel consumption and load redistribution. There exist uncertainties associated with the maximum still water moment. Statistical analysis of various types of ships on a number of voyages found that the maximum bending moment during one voyage can be described using a normal distribution with the mean and standard deviation given, respectively, as $\mu_{sw} = \gamma_1 M_{sw,max}$ and $\sigma_{sw} = \gamma_2 M_{sw,max}$, where $\gamma_1 = 0.70$; $\gamma_2 = 0.20$ [18].

7.3.4 Wave-Induced Bending Moment

The wave-induced moment is the result of hull girder hydrodynamic response under the dynamic distribution of buoyancy forces. By assuming the wave in the short period as a stationary Gaussian process, the response can be predicted using the stochastic spectrum analysis with the peak moment response at a random time point approximated as a Rayleigh distribution [15]. In a long time duration, the ship experiences a variety of different sea states. To account for this, the Rayleigh distribution is weighted proportional to the time the ship spent in different sea states. Statistical analysis based on the sea wave condition given in the IACS North Atlantic scatter diagram shows that the weighted Rayleigh distribution can be approximated by the Weibull distribution [15]:

$$F_{M_e}(m_e) = 1 - \exp \left[-\left(\frac{m_e}{w} \right)^k \right] \quad (7.11)$$

where $k = 1$; $w = -M_{w,max}/\ln 10^{-8}$; $M_{w,max}$ is the maximum wave-induced bending moment in the ship loading manual [13], which is given as:

- (a) for sagging condition

$$M_{w,max} = -0.11 C_{wv} L^2 B (C_b + 0.7) \text{ KNm} \quad (7.12)$$

(b) for hogging condition

$$M_{w,\max} = 0.19C_{wv}L^2BC_b \text{ KNm} \quad (7.13)$$

For a period of one year, in-service ships experience many peak cycles. It follows that the annual maximum wave-induced bending moment is described by Gumbel distribution

$$F_{M_{we}}(m_{we}) = \exp\left[-\exp\left(-\frac{m_{we} - \lambda_0}{\theta_0}\right)^k\right] \quad (7.14)$$

where λ_0 and θ_0 are the characteristic value and scale parameter of Gumbel distribution, respectively. The parameters of Gumbel distribution are [18]

$$\lambda_0 = w \left[\ln\left(\frac{a_c T_r}{T_w}\right) \right]^k \text{ and } \theta_0 = \frac{w}{k} \left(\ln\left(\frac{a_c T_r}{T_w}\right) \right)^{\frac{1-k}{k}} \quad (7.15)$$

where T_r is the considered reference time, i.e., $T_r = 1$ year; T_w is the average wave period, i.e., $T_w = 8.0$ s; a_c is a factor accounting for the time fraction of a load condition, e.g., $a_c = 0.35$ for a full load condition.

7.4 Ship Life-Cycle Cost

Within the considered service life, the life-cycle cost of ship hull girder is

$$C_0 = \sum_{l=1}^{n_{in}} \frac{C_{in}}{(1+v_0)^{T_{in,l}}} + \sum_{l=1}^{n_{rep}} \frac{C_{rep}}{(1+v_0)^{T_{rep,l}}} + \sum_{l=1}^{n_f} \frac{C_f}{(1+v_0)^{T_{f,l}}} \quad (7.16)$$

where v_0 denotes the discount rate; n_{in} , n_{rep} , and n_f are the number of inspections, repair, and failure events, respectively; $T_{in,l}$, $T_{rep,l}$, and $T_{f,l}$ are the time of the l th inspection, repair, and failure, respectively; C_{in} , C_{rep} , and C_f are the costs of inspection, repair, and ship failure, respectively. In the CPT assessment, the overall monetary cost is expressed as $C_R = R - C_0$, where R denotes the reference cost. The cost of repairing a ship structural element includes material, welding, labor, and electricity costs, while the failure cost includes the direct cost of the ship structure and cargo loss, as well as indirect costs of environment pollution and spillage clean-up, and loss of human life. A detailed repair cost estimate is presented in [19].

7.5 Optimization Framework

7.5.1 Repair Policy

The detailed inspection of the ship hull girder is periodically conducted on an empirical basis of five years [20]. For inspection, the ship is transported to a dry dock and the net thickness of the ship's steel plates are measured by ultrasound equipment. Classification Societies specifies that corroded structural elements are replaced with new ones if the renewal criterion is satisfied [13]: $t_m < t_{as-built} - t_{was}$, where $t_{as-built}$ is the as-built thickness; t_m is the measured thickness; t_{was} is the double side waste allowance, rounded up the nearest 0.5 mm. The as-built thickness is the sum of the structural design thickness plus corrosion addition. Corrosion addition adds a safety margin against corrosion. Since distinct environment exists across the mid-ship section, the corrosion growth rates of structural elements of the deck, sides, and bottom plating are different. To account for this, corrosion wastage allowance given by Classification Societies is specific to the location of the mid-ship section [13].

7.5.2 Inspection Optimization

The empirical ship inspection interval does not necessarily imply the optimal. As mentioned previously, the optimal solution under uncertainty is often selected by minimizing the expected life-cycle cost, $E[C_0]$. CPT is better in predicting the preferences among choices. The optimal inspection interval, t_{in} , in this paper is therefore investigated by maximizing the CPT prospect value corresponding to the distribution of life-cycle cost. The optimization formulation is as follows

$$\text{Find } t_{in} \quad (7.17a)$$

$$\text{Minimize } E [V] \quad (7.17b)$$

The distribution of the life-cycle cost is calculated using the Monte Carlo simulation. It is assumed that throughout the considered time, the repair of ship structural elements is only applied after inspection. This assumption is in agreement with repair policy specified in IACS [13].

7.6 Case Study

A double hull tanker adapted from Hu et al. [21] is utilized to illustrate the application of the developed decision-making methodology. The ship has a length of $L = 168$ m and a breadth of $B = 28$ m. The length of the longitudinal stiffeners between transverse webs is $l = 3925$ mm. It is assumed in this study that the ship has a block coefficient of $C_b = 0.48$ and a hull girder depth of $D = 16$ m. The mid-ship section of the double hull girder is shown in Fig. 7.1 with a close-up view of a structural member. The structure members are labeled with a number (1–81). Table 7.1 lists the nominal values of the geometry dimension and material properties of structural members. In the simulation analysis used for obtaining the life-cycle cost, b_p , h_w , and b_f are assumed to be deterministic, while t_p and t_f are normally distributed with the mean equal to the nominal value given in Table 7.1 and the coefficient of variation (COV) of 0.1. It is further assumed that for each structural member, Young's modulus, E , follows a normal distribution with the mean of 205,800 MPa and COV of 0.03. A linear corrosion model is adopted to predict the time-variant uniform corrosion depth on the surface of the plating and stiffeners. Table 7.2 summarizes the probabilistic characteristics of corrosion parameters. All the random variables representing the same physical parameters associated with different structural members are assumed partially dependent with the correlation coefficient of 0.5. The variables representing the same parameters are assumed to be independent.

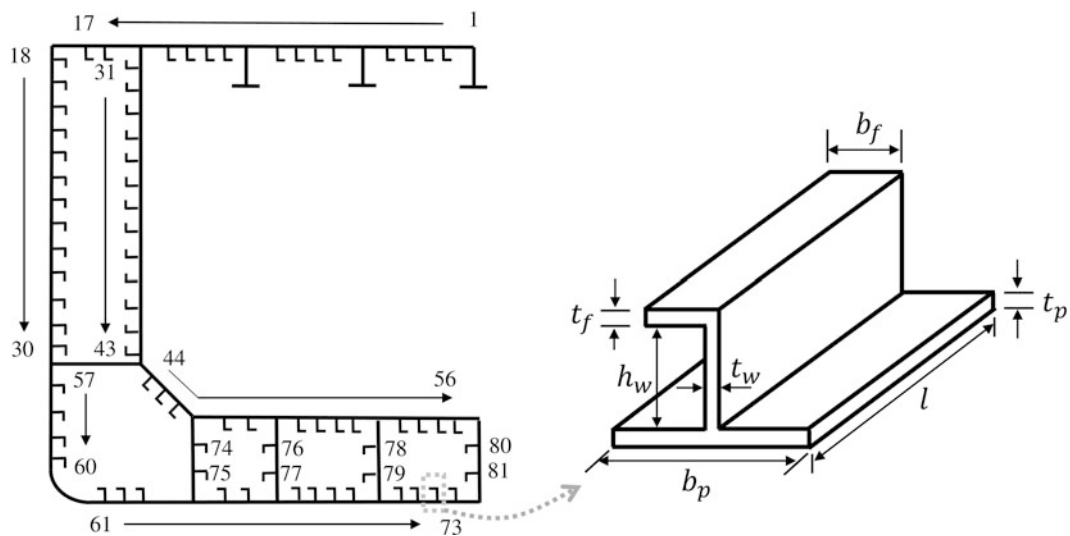


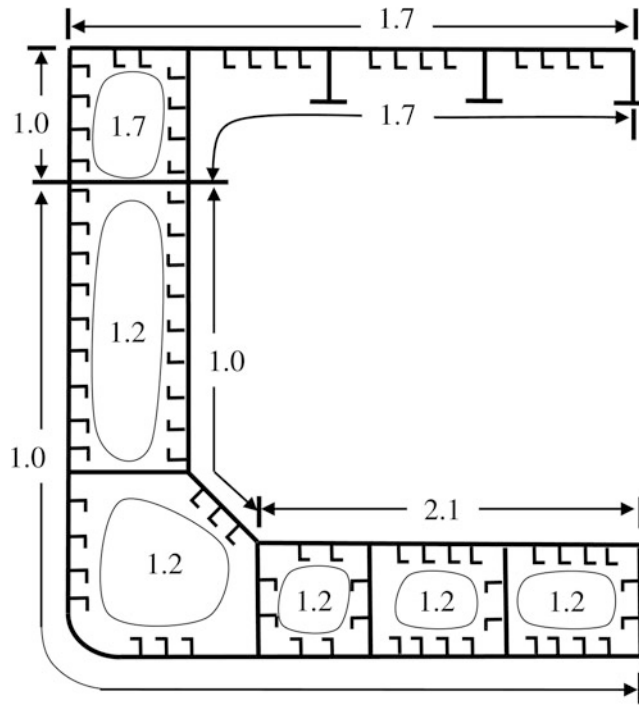
Fig. 7.1 Mid-ship cross-section of the tanker (adapted from Hu et al. [21])

Table 7.1 Geometry and material property of structure elements in Fig. 7.1 (adapted from Hu et al. [21])

Member number	Plating			Stiffener				
	b_p (mm)	t_p (mm)	σ_{yp} (MPa)	h_w (mm)	t_w (mm)	b_f (mm)	t_f (mm)	σ_{yp} (MPa)
1,6,11	800	15	235	1050	10.5	300	15	235
2–5, 7–10	800	12.5	235	350	9	90	13	353
12–15	800	14	235	300	10.5	100	15	353
16–17	800	14	235	200	9	90	12	353
18–43	750	12.5	235	300	10.5	120	16	235
44–56	750	13.5	235	350	10.5	120	18	235
57–60	750	12.5	235	350	10.5	120	16	235
61–73	750	14	235	350	10.5	120	16	235
74–81	1100	14	235	350	10.5	120	18	235

Table 7.2 Probabilistic characteristics of corrosion growth parameters

Variable	Distribution	Mean	COV
Coating life (years) [2]	Deterministic	3	—
Deck plating corrosion rate (mm/year) [22]	Weibull	0.065	0.5
Side plating corrosion rate (mm/year) [22]	Weibull	0.03	0.1
Inner and outer bottom plating rate (mm/year) [22]	Weibull	0.17	0.5

**Fig. 7.2** Wastage allowance, t_{was} , at different ship locations (mm) (according to IACS [13])

The wastage allowance for structural member renewal according to IACS [13] is described in Fig. 7.2. The ship inspection cost is assumed to be \$200,000. Using the repair cost estimation method developed by Rigterink et al. [19], the average member repair cost of the plate for the considered hull girder is \$461 per m^2 . It is further assumed that the length of repaired structural members is equal to the longitudinal length between transverse webs.

The failure cost is estimated at \$298 million, calculated based on the empirical equation provided by Guia et al. [23], assuming the ship deadweight of 166,300 ton and ignoring the ship scrapping value loss. The money discount rate is assumed to be 5%. The total number of simulation samples is 10^5 . The reference point in CPT is dependent on the expectations of decision-makers. To avoid introducing subjectivity by assuming an arbitrary value, parametric studies are conducted considering a set of reference cost values $R = \{\$0, \$10^4, \$10^6, \$10^8\}$.

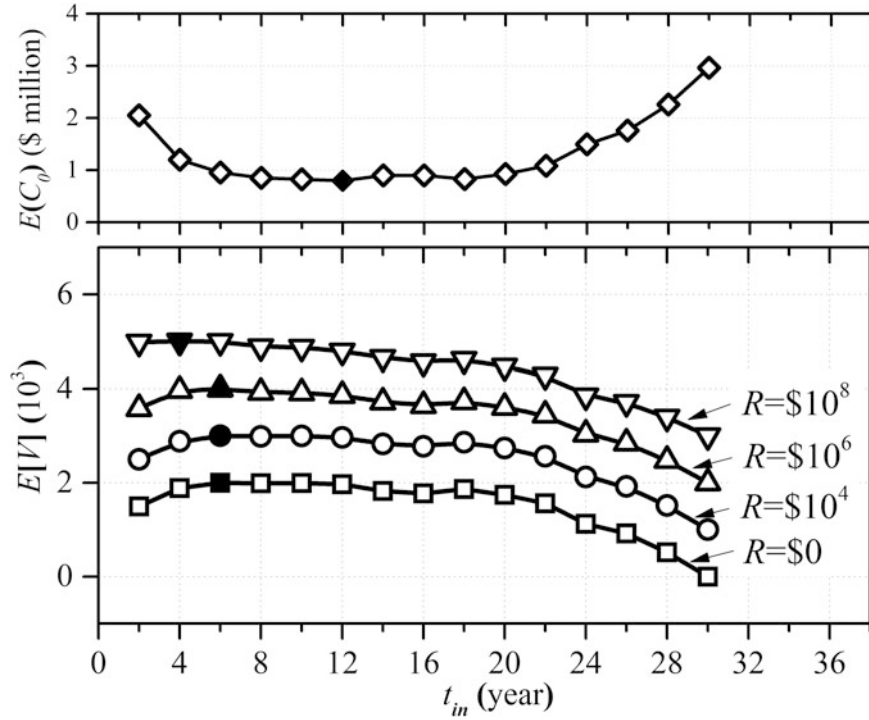


Fig. 7.3 Expected life-cycle cost and expected prospect value with a varied inspection time interval from 2 to 30 years

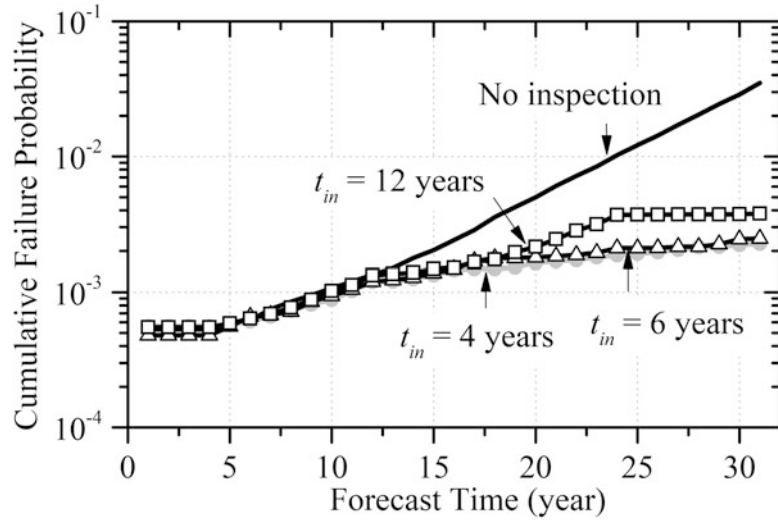


Fig. 7.4 Cumulative failure probability for different inspection time intervals

Figure 7.3 shows the expected prospect value as the inspection interval increases from 2 to 30 years, together with the expected cost. Note that the magnitude of prospect values with different reference point is distinct. Direct comparison of absolute values obtained assuming different reference points is meaningless [5]. In Fig. 7.3, the prospect values are scaled such that the preference trends can be easily compared. The shaded markers imply the optimal solutions for different criteria. It is showed in Fig. 7.3 that the inspection interval for minimizing the expected life-cycle cost is 12 years. The optimal inspection time suggested by CPT is 6 years when $R = \$0$, $\$10^4$, and $\$10^6$, while the optimal solution is 4 years when the reference cost is $R = \$10^8$. This indicates that the expectation of the life-cycle cost of decision-makers can affect the preferred inspection interval but not in a significant manner. The life-cycle costs with $t_{in} = 4$ and 6 years are \$1.20 million and \$0.96 million, respectively, both of which are larger than the minimum life-cycle cost of \$0.78 million. This suggests that CPT results in optimal inspection intervals that are different from the optimal based on the minimum expected cost criterion. The time-variant cumulative probabilities corresponding to the four selected optimal solutions are plotted as a function of forecast time in Fig. 7.4. It is seen that in this case the inspections with repair action based on the corrosion wastage

allowance reduce the cumulative failure probability at year 31 from 2.31% to 0.23% ($t_{in} = 4$ years), 0.25% ($t_{in} = 6$ years), and 0.38% ($t_{in} = 12$ years), respectively. The cumulative failure probabilities associated with $t_{in} = 4$ and 6 years throughout the considered time are similar, whereas that with $t_{in} = 12$ years are higher. $t_{in} = 12$ years leads to the minimum life-cycle cost. In this case, the expected maintenance cost dominates the expected failure cost because of the small failure probabilities.

7.7 Conclusions

In the presence of uncertainty, ship operators need to determine the optimal inspection and repair schedules that consider not only the cost-effectiveness of maintenance investment but also people's inherent risk perceptions. This paper uses CPT to investigate the optimal inspection interval of corroded ship hull girders subjected to collapse failure. To this end, Monte Carlo simulation is employed to compute the distribution of life-cycle costs, in which a condition-based industry repair policy is implemented, namely, structural members are replaced when corrosion penetration exceeds the wastage allowance given in IACS [13]. The optimal solution is explored by maximizing the expected prospect value of CPT with the uniform inspection time interval selected as the design variable. The methodology is demonstrated on a hypothetical ship hull girder. The optimal solutions dictated by the minimum $E[C_0]$ and $E[V]$ are compared. The analysis results show that, for the considered example, considering risk perception using CPT leads to inspection plans that have a higher expected life-cycle cost than the minimum $E[C_0]$; the impact of the reference point in CPT has no impact on the preferred inspection interval unless a significantly large cost is assigned as reference cost.

Acknowledgments The support by grants from (a) the U.S. Office of Naval Research (ONR) Awards N00014-08-1-0188, N00014-12-1-0023, and N00014-16-1-2299, (b) the National Science Foundation (NSF) Award CMMI-1537926, and (c) the Commonwealth of Pennsylvania, Department of Community and Economic Development, through the Pennsylvania Infrastructure Technology Alliance (PITA) Awards, is gratefully acknowledged. Opinions presented in this paper are those of the authors and do not necessarily reflect the views of the sponsoring organizations.

References

- Hess, P., Aksu, S., Vaz, M., Feng, G., Li, L., Jurisic, P., Andersen, M.R., Cardis, P., Boote, D., Murayama, H., Amila, N., Leira, B., Tammer, M., Blake, J., Chen, N., Egorov A. Structural longevity. In: Proceedings of the 20th International Ship and Offshore Structures Congress (ISSC 2018), Belgium and Amsterdam, Vol. 2, pp. 391–460 (2018).
- Kong, J.S., Frangopol, D.M.: Evaluation of expected life-cycle maintenance cost of deteriorating structures. *J. Struct. Eng.* **129**(5), 682–691 (2003)
- Zhou, W., Nessim, M.A.: Optimal design of onshore natural gas pipelines. *J. Press. Vessel. Technol.* **133**(3), 1–11 (2011)
- Gomes, W.J., Beck, A.T., Haukaas, T.: Optimal inspection planning for onshore pipelines subject to external corrosion. *Reliab. Eng. Syst. Saf.* **118**, 18–27 (2013)
- Goda, K., Hong, H.P.: Optimal seismic design considering risk attitude, societal tolerable risk level, and life quality criterion. *J. Struct. Eng.* **132**(12), 2027–2035 (2006)
- Ang, H.S., Tang, W.H.: Probability Concepts in Engineering Planning and Design, Vol. 2—Decision, Risk, and Reliability. Wiley, New York (1984)
- Dong, Y., Frangopol, D.M.: Risk-informed life-cycle optimum inspection and maintenance of ship structures considering corrosion and fatigue. *Ocean Eng.* **101**, 161–171 (2015)
- Sabatino, S., Frangopol, D.M.: Decision making framework for optimal SHM planning of ship structures considering availability and utility. *Ocean Eng.* **135**, 194–206 (2017)
- Sabatino, S., Frangopol, D.M., Dong, Y.: Life cycle utility-informed maintenance planning based on lifetime functions: optimum balancing of cost, failure consequences and performance benefit. *Struct. Infrastruct. Eng.* **12**(7), 830–847 (2016)
- Liu, Y., Frangopol, D.M.: Probabilistic risk, sustainability, and utility associated with ship grounding hazard. *Ocean Eng.* **154**, 311–321 (2018)
- Tversky, A., Kahneman, D.: Advances in prospect theory: cumulative representation of uncertainty. *J. Risk Uncertain.* **5**(4), 297–323 (1992)
- Cha, E.J., Ellingwood, B.R.: Risk-averse decision-making for civil infrastructure exposed to low-probability, high-consequence events. *Reliab. Eng. Syst. Saf.* **104**, 27–35 (2012)
- IACS: Common Structural Rules for Bulk Carriers and Oil Tankers. International Association of Classification Societies, London (2014)
- Kőszegi, B., Rabin, M.: A model of reference-dependent preferences. *Q. J. Econ.* **121**(4), 1133–1165 (2006)
- Gaspar, B., Teixeira, A.P., Soares, C.G.: Effect of the nonlinear vertical wave-induced bending moments on the ship hull girder reliability. *Ocean Eng.* **119**, 193–207 (2016)
- Paik, J.K., Mansour, A.E.: A simple formulation for predicting the ultimate strength of ships. *J. Mar. Sci. Technol.* **1**(1), 52–62 (1995)
- Paik JK, Thayamballi AK. An empirical formulation for predicting the ultimate compressive strength of stiffened panels. In: Proceedings of the Seventh International Offshore and Polar Engineering Conference, Honolulu, May. The International Society of Offshore and Polar Engineers, pp. 328–338 (1997)
- Soares, C.G.: On the definition of rule requirements for wave induced vertical bending moments. *Mar. Struct.* **9**(3-4), 409–425 (1996)

19. Rigterink, D., Collette, M., Singer, D.J.: A method for comparing panel complexity to traditional material and production cost estimating techniques. *Ocean Eng.* **70**, 61–71 (2013)
20. Paik, J.K., Melchers, R.E.: Condition assessment of aged Structures. CRC Press, New York (2008)
21. Hu, Y., Cui, W., Pedersen, P.T.: Maintained ship hull ultimate strength reliability considering corrosion and fatigue. *Mar. Struct.* **17**(2), 91–123 (2004)
22. Akpan, U.O., Koko, T.S., Ayyub, B., Dunbar, T.E.: Risk assessment of aging ship hull structures in the presence of corrosion and fatigue. *Mar. Struct.* **15**(3), 211–231 (2002)
23. Guia, J., Teixeira, A.P., Soares, C.G.: Probabilistic modelling of the hull girder target safety level of tankers. *Mar. Struct.* **61**, 119–141 (2018)



Chapter 8

Establishing an RMS von Mises Stress Error Bound for Random Vibration Analysis

David Day, Moheimin Khan, Michael Ross, and Brian Stevens

Abstract The root mean square (RMS) von Mises stress is a criterion used for assessing the reliability of structures subject to stationary random loading. This work investigates error in RMS von Mises stress and its relationship to the error in acceleration for random vibration analysis. First, a theoretical development of stress-acceleration error is introduced for a simplified problem based on modal stress analysis. Using results from the example as a basis, a similar error relationship is determined for random vibration problems. Finite element analyses of test structures subject to an input acceleration auto-spectral density are performed and results from parametric studies are used to determine error. For a given error in acceleration, a relationship to the error in RMS von Mises stress is established. The resulting relation is used to calculate a bound on the RMS von Mises stress based on the computed accelerations. This error bound is useful in vibration analysis, especially where uncertainty and variability must be thoroughly considered.

Keywords Acceleration · Error bound · Random vibration · RMS von Mises stress · Uncertainty quantification

8.1 Introduction

Finite element models are used to analyze physical systems of interest and they contain errors that arise due to discrepancies between the approximate model and actual system. The source of error in finite element simulations can be generally attributed to three major factors: data input, physics model, and numerical solution accuracy [1]. When the finite element formulation adequately represents the physics of the problem with sufficient numerical accuracy, data input becomes the main source of error. These input errors are often due to uncertainties in loads, geometry, material properties, or boundary conditions.

In structural analysis, a typical use for finite element analysis (FEA) is to evaluate the response of a system under a loading condition and to make predictions, such as determining a margin using some specific criteria. Oftentimes, the quantity of interest is stress, so any source of data input error will cause an uncertainty in stress and the resulting margin. To accurately assess the failure of the system under consideration, it is important to be able to quantify this error relation.

For a random vibration analysis, loading is in the form of an auto-spectral density, or ASD, which is often determined from test results. The quantities of interest are the root mean square von Mises (VRMS) stress and response acceleration ASD. The VRMS is used to predict the failure of structures subject to probabilistic loads and accounts for the complete frequency response of the structure [2]. Data input error arising from uncertainty in material and system properties affects the resulting stresses and accelerations. The acceleration is an important quantity, since most random vibration tests collect acceleration measurements at several locations in a system. Accelerometer data is often readily available, but the stress state at a specific point in a structure may not be. Thus, it is important to quantitatively bound uncertainty and error in stress through the acceleration.

Sandia National Laboratories is a multimission laboratory managed and operated by National Technology and Engineering Solutions of Sandia, LLC, a wholly owned subsidiary of Honeywell International, Inc., for the U.S. Department of Energy's National Nuclear Security Administration under contract DE-NA0003525.

D. Day · M. Khan · M. Ross (✉) · B. Stevens
Sandia National Laboratories, Albuquerque, NM, USA
e-mail: mross@sandia.gov

In this work, data input errors are used as perturbations to introduce acceleration error and evaluate the limits of the error in stress. Three different example cases are analyzed. The first case uses the magnitude of the error in acceleration to determine a bound on the modal von Mises stress for a free-free beam. In the second and third cases, two different beams are studied in a random vibration setting. For these problems, the sources of error are perturbations in the modulus, density, damping, and length. The random vibration solution uses the method presented in [2], where the VRMS stress is calculated using modal stress and displacement amplitudes. An in-depth theoretical development is discussed and the stress-acceleration error relation for the example problem is studied first, followed by results from the other two cases in a random vibration context.

8.2 Theory

The equation of motion for a damped, multi-degree of freedom (MDOF) system under load $\underline{F}(t)$ can be expressed as

$$[m]\ddot{\underline{u}}(t) + [c]\dot{\underline{u}}(t) + [k]\underline{u}(t) = \underline{F}(t) \quad (8.1)$$

where $[m]$, $[c]$, $[k]$ are the system mass, damping, and stiffness matrices, respectively. In a direct solution, the displacements, $\underline{u}(t)$, are computed by numerically solving the coupled partial differential equations of motion. Modal superposition, used in modal-based methods such as random vibration, takes advantage of the modal degrees of freedom, or modal coordinates, $q_n(t)$, to uncouple the equations using the system mode shapes, ϕ_n , as given in [3]:

$$u_n(t) = \phi_n q_n(t) \quad (8.2)$$

$$[M]\ddot{\underline{q}}(t) + [\Phi]^T [c] [\Phi] \dot{\underline{q}}(t) + [K]\underline{q}(t) = \underline{Q}(t) \quad (8.3)$$

Here, $[M] = [\Phi]^T [m] [\Phi]$ is the modal mass matrix, $[K] = [\Phi]^T [k] [\Phi]$ is the modal stiffness matrix, and $\underline{Q}(t) = [\Phi]^T \underline{F}(t)$ is the modal force vector. The displacements are calculated by solving the n uncoupled equations for each $q_n(t)$, which are used to determine the strains and stresses at a given time.

In random vibration problems, the quantities of interest are statistical in nature, so a metric such as the VRMS is used to assess failure. For random vibration of MDOF systems in the time domain, the mean square von Mises stress can be calculated using the modal coordinates and the stress mode shapes of the structure [2],

$$\sigma_{VRMS}^2 = E[p^2(t)] = \sum_{i,j} \Gamma_{ij} T_{ij} = \sum_{i,j} E[q_i(t)q_j(t)] \Psi_i^{\sigma T} A \Psi_j^{\sigma} \quad (8.4)$$

Here, $E[p^2(t)]$ is the expected value, or mean, of the square of the von Mises stress, $p(t) = \sigma(t)^T A \sigma(t)$, where $\sigma(t)^T = [\sigma_{xx} \sigma_{yy} \sigma_{zz} \sigma_{yz} \sigma_{xz} \sigma_{xy}]$. The VRMS is calculated using the modal covariance, $\Gamma_{ij} = E[q_i(t)q_j(t)]$, the stress modes $\Psi_i^{\sigma T}$, Ψ_j^{σ} , and matrix A , defined in [2].

In the frequency domain, the modal coordinate, $q_i(\omega)$, is related to the input loads, $f_j(\omega)$, by the transfer function, $H_{ij}(\omega)$ [2].

$$q_i(\omega) = H_{ij}(\omega) f_j(\omega) \quad (8.5)$$

From [4], the spectral density matrix of the response, $[S_X(\omega)]$, is calculated from the transfer function and the given spectral density matrix, $[S_F(\omega)]$,

$$[S_X(\omega)] = [H(\omega)] [S_F(\omega)] [H(\omega)]^\dagger \quad (8.6)$$

This reduces in the case of a single input to

$$[S_X(\omega)] = |H(\omega)|^2 [S_F(\omega)] \quad (8.7)$$

In the frequency domain, the mean square von Mises stress is given as

$$E [p^2(t)] = \sum_m \sum_n \frac{1}{2\pi} \int_{-\infty}^{\infty} [(H^\sigma(\omega))^\dagger A H^\sigma(\omega)]_{mn} S_{ff}(\omega)_{mn} d\omega \quad (8.8)$$

Additional steps in determining the above equation for VRMS are given in [2].

8.2.1 Theoretical Development of Acceleration Error

This section details the theory used in relating the modal stress error and acceleration error.

A model is used to attempt to predict measurements. One assumption is that the model converges to the actual measurements under mesh refinement, so predictions can be made regarding the model errors. These predictions are initially made on a coarse mesh. A fine mesh is also used, which is fine enough that the error is approximately the difference between the coarse and the fine values. The purpose of this section is to describe the calculation of an error bound for the maximum possible modal von Mises stress on the fine mesh. The input to the algorithm is:

1. A coarse mesh and a fine mesh
2. Mode shapes on both meshes
3. Stress mode shapes on the fine mesh
4. A linear interpolation operator called the prolongation (coarse to fine)
5. Fine mesh mass matrix
6. Normal acceleration on the coarse mesh, at some time
7. Bound on the L_2 error in the acceleration at that time

The displacements $u(x, t)$ are approximated by their value on some fine mesh, $u_h(x, t)$. A sufficiently fine mesh is chosen such that $u - u_h$ is much smaller than $u_H - u_h$, where $u_H(x, t)$ is the displacement on the coarse mesh. Similar conditions are required for accelerations and von Mises stress. The next assumption is that the trajectory, $u(x, t)$, accelerations and von Mises stress can be well approximated by the low frequency modal approximation, meaning that the modes appropriately describe the system within a valid frequency range of interest.

Reduction to Linear Algebra

In this section, some intermediate steps are omitted, so further details are given in Appendix 1.

On the fine mesh, the modes are the columns of the mode shape vector, $\Phi^h = [\phi_1^h, \dots]$, defined on the mesh nodes. The displacement, u_h , has modal expansion $u_h(x, t) = \Phi_i^h(x)q(t)$, where $q = [q_1, \dots]$. Similarly, the coarse mesh has $u_H = \Phi_i^H(x)b(t)$, with $\Phi^H = [\phi_1^H, \dots]$, and $b = [b_1, \dots]$. Using the corresponding stress modes, $\Psi^h = [\psi_1^h, \dots]$, defined at element centroids, a stress state associated with the corresponding stress mode can be obtained as

$$\sigma_h(x, t) = \Psi^h(x)q(t) \quad (8.9)$$

The von Mises stress, σ^v , can be calculated from the deviatoric stress tensor, σ^{dev} , as $\sigma^v = \sqrt{\frac{3}{2} (\sigma^{dev} : \sigma^{dev})}$, where “:” denotes the double dot product. Thus, using the deviatoric stress modes, $\sigma_h^{dev}(x, t) = \Psi^{dev}(x)q(t)$, the von Mises stress can be expressed in modal terms as

$$\sigma_h^v(x, t) = \sqrt{\frac{3}{2}} \|\Psi^{dev}(x)q(t)\|_F$$

The goal is to relate to the (squared) maximum von Mises stress, $\max(\sigma_h^v)^2$, to acceleration error and obtain a bound, δ^2 , such that

$$\|\ddot{u}_h - P\ddot{u}_H\|_{L^2}^2 < \delta^2 \quad (8.10)$$

Here, the error is calculated from the Euclidean or L_2 norm of $\ddot{u}_h - P\ddot{u}_H$, and P is a fine to coarse mesh transfer linear operator called the prolongation.

The solution of the optimization problem is the maximum of the solutions over each element. Eigenvalues connect accelerations and displacements, $\ddot{q} = -\Omega_h^2 q$ and $\ddot{b} = -\Omega_H^2 b$ and rigid body modes can be ignored. Due to $q = -\Omega_h^{-2}\ddot{q}$, there holds $(\sigma_h^v)^2 = \ddot{q}^T X \ddot{q}$ for

$$X = [\chi_{ij}], \quad \chi_{ij} = \frac{3}{2} \frac{\psi^{dev}}{\omega^2} : \frac{\psi^{dev}}{\omega^2} \quad (8.11)$$

Here, X is a symmetric matrix with a positive diagonal, composed of the deviatoric stress modes and eigenvalues. The bound on the stress is determined by solving the nonlinear Eq. (8.10). Some assumptions are made which explain how, for the purposes of this study, solving the nonlinear equation is relatively easy because several complications do not arise. Details are given in Appendix 1.

The basic problem is as follows: for given \ddot{b} on the coarse mesh, to maximize $(\sigma_h^v)^2 = \ddot{q}^T X \ddot{q}$ over all \ddot{q} such that the error in acceleration, $\|\ddot{u}_h - P\ddot{u}_H\|_{L_2}^2 < \delta^2$. This provides an understanding of the relationship between the accuracy in acceleration to the accuracy in stress, and how this bound varies with the state of acceleration on the coarse mesh, \ddot{u}_H .

8.3 Analysis Examples

FEA was performed for three different example problems and a stress-acceleration error relationship was determined for each case. The error is defined as the percent difference in stress or acceleration from a base model that ideally represents the system. Using the theory presented in the previous section, the first case examines the error bound for an unsupported, or free-free, beam. An acceleration error is imposed and the relation to the maximum modal von Mises stress error is found. The second and third cases involve more practical examples, in which random vibration of a cantilever beam and two-material, joint rectangular beam is considered. Material properties and beam geometry are varied (perturbed) to obtain an error in acceleration that is related to the VRMS error. All analysis was performed using Sandia's in-house finite element code Sierra/SD, along with MATLAB and Python scripts.

8.3.1 Case 1: Free-Free Beam

Analysis for this problem follows the steps outlined in Sect. 8.2.1, with further details provided in Appendix 1. An acceleration is initially applied to all nodes in the coarse mesh and the resulting L_2 error in acceleration is linearly varied from an initial δ_{min} , to $\delta_{min} + 2\|c\|$, which is twice the norm of the initial fine mesh acceleration. For the free-free beam, the maximum modal von Mises stress was calculated on the fine mesh for different values of this L_2 acceleration error. Stress and displacement mode shapes from 16 calculated modes were used.

The beam material is steel and it is 1 in. (25.4 mm) in diameter and 10 in. (254 mm) in length. The beam was meshed with a total of 1920 8-node, linear hexahedral elements (Hex8) as shown in Fig. 8.1. All stress calculations were done on the fine mesh, with a coarse mesh of 240 elements used to apply the acceleration, as mentioned in Sect. 8.2.1.

The resulting plot in Fig. 8.2 shows a linear relationship between the maximum stress error in the model and the acceleration error. The modal von Mises stress distributions¹ for the initial and final stress states are also presented. The acceleration error reached a maximum of 393%, and the error in the von Mises stress was 154%, giving the maximum stress error to acceleration error ratio of 0.392. This error ratio, defined as the maximum percent VRMS error divided by the maximum acceleration percent error relationship provides a measure of the sensitivity of stress error change relative to the acceleration error. It also describes how the errors are bound and is the slope of the percent error plot for a linear relation.

This relation between the maximum modal stress in the model and the acceleration error is a first step to obtaining a practical error bound. The example case is theoretical, since the accelerations are ideally applied and the resulting modal stresses cannot be used to directly evaluate failure. We are typically interested in more realistic boundary conditions and

¹Like the mode shape amplitudes, the mode shape stresses can be arbitrarily scaled, so only the relative values are important here.

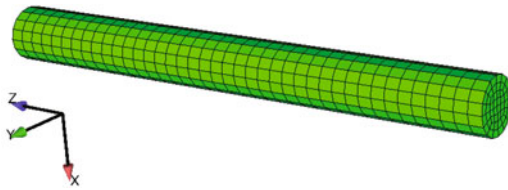


Fig. 8.1 Free-free beam model: fine mesh

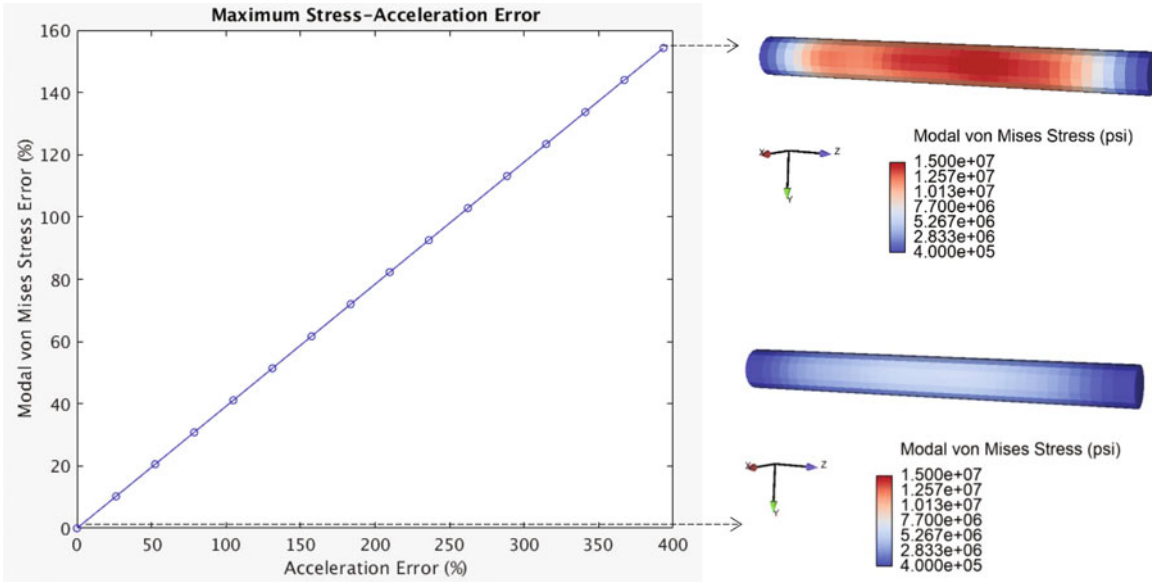


Fig. 8.2 Stress-acceleration error relationship and stress contours for lowest and highest error values

loading scenarios. Thus, the following sections describe a similar stress-acceleration relationship for beams subject to random vibration loading.

8.3.2 Case 2: Cantilever Beam Random Vibration

In this example, a cantilever beam is subjected to a $1 \text{ g}^2/\text{Hz}$ flat random vibration input from 20 to 2000 Hz. The frequency resolution used in the simulations is 0.1 Hz and the input ASD is shown in Fig. 8.3. The loading is applied in the positive Z direction using a concentrated, seismic mass attached with rigid bar elements to the end of the beam. The mass is constrained in all directions except the input to ensure uniform loading.

To obtain an error in acceleration, the data input values perturbed in the FE simulations were the material and geometric properties, or model parameters. The modulus of elasticity, density, damping ratio (percent of critical), and length were the selected parameters, and each was independently increased by 1% per simulation with a total of 20 simulations per parameter. As one parameter is varied, the others are fixed to a nominal value. The output RMS acceleration in the Z-direction (AZRMS) was studied at two different nodes (points) on the mesh and the average VRMS of the Hex8 elements sharing the point was obtained. For this problem, the locations of the points were the same for each simulation except for the length perturbation, where the distance from the beam end and distance between points was held constant.

The resulting absolute value in VRMS error was plotted versus the absolute value of the AZRMS error. The error for each simulation was calculated using the following Eq. (8.12).

$$\%Error_{a_{rms}}^n = \frac{100|a_{rms}^n - a_{rms}^0|}{a_{rms}^0} \quad (8.12)$$

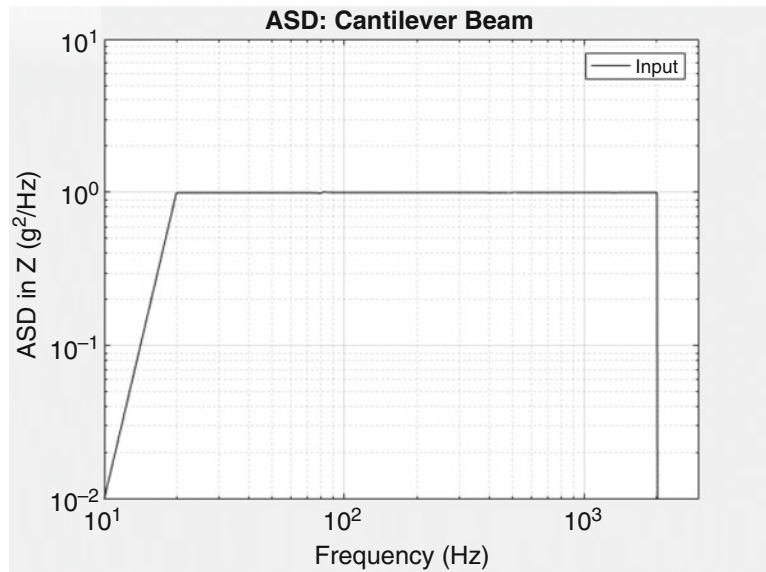


Fig. 8.3 Random vibration input ($1 \text{ g}^2/\text{Hz}$ over 20–2000 Hz; $0.01 \text{ g}^2/\text{Hz}$ at 10 Hz and 2010 Hz)

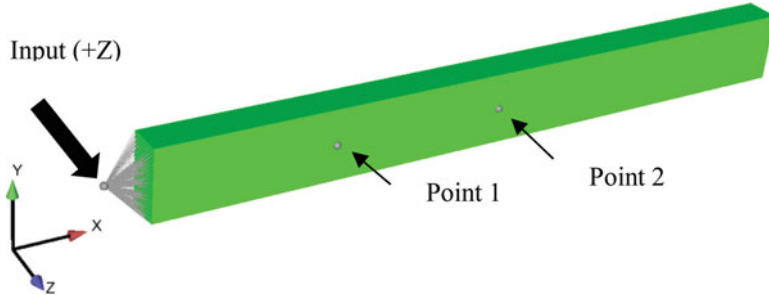


Fig. 8.4 Cantilever beam model with coordinate system, input, and point location

Here, a_{rms}^0 is the RMS value at a selected point for the initial, unperturbed model and a_{rms}^n is the RMS value at the same point for the n^{th} perturbed model, where n ranges from 1 to 20 and each subsequent n is a 1% increase in one of the parameters. The same calculation was also done using the maximum values of VRMS and AZRMS over the entire model.

The cantilever beam dimensions are 1 in. (25.4 mm) by 2 in. (50.8 mm) by 20 in. (508 mm) and the material is aluminum. A stress refinement study was initially performed and the final model consists of approximately 160,000 Hex8 elements. Fig. 8.4 shows the beam model.

The response ASD at the two points of interest and the relevant mode shapes for the unperturbed, base model are shown in Fig. 8.5. The three bending modes about the Y axis are exaggerated for visualization purposes.

Plots of the error in VRMS and AZRMS are presented for each of the parameter perturbation studies: modulus of elasticity, damping, density, and length. In addition, the maximum VRMS stress error for each model was plotted against the maximum AZRMS error to obtain an error bound similar to Fig. 8.2 in the previous section. A table summarizing the range of maximum values is also given at the end of the section.

For the change in modulus, a one-to-one linear relationship was observed at both points and for the maximum values, as presented in Fig. 8.6. A perturbation in damping also resulted in a direct linear relationship; this was expected for uniform modal damping, so the plots are not shown here and are given in Appendix 2. The density relationship in Fig. 8.7 was also linear, while the length perturbation exhibited some nonlinearity,² which is especially prevalent in the Point 2 plot in Fig. 8.8. After the 16th simulation, there is a turning point in the relation at which the acceleration error decreases while the stress

²All results are for a linear elastic constitutive model and no frictional effects are considered, so the term “nonlinear” is used in the context of describing the relationship between the errors.

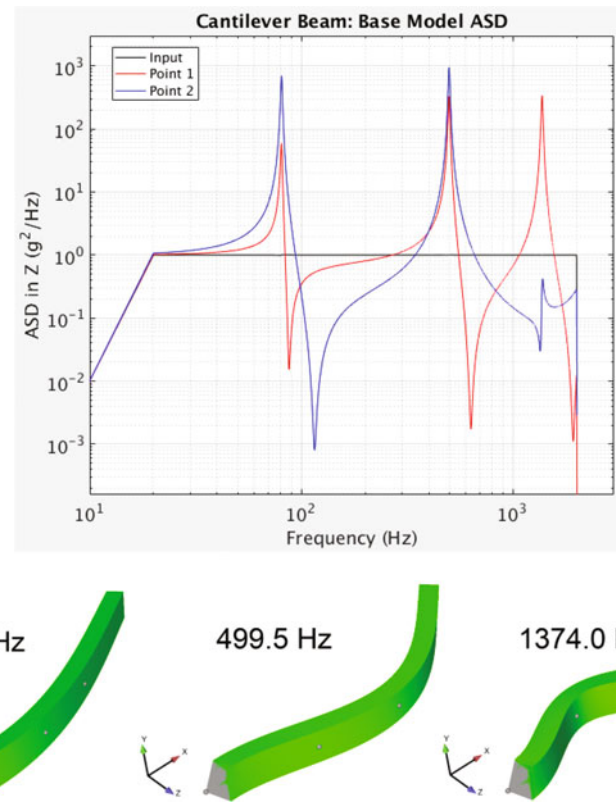


Fig. 8.5 Cantilever beam: base model response ASD and contributing modes

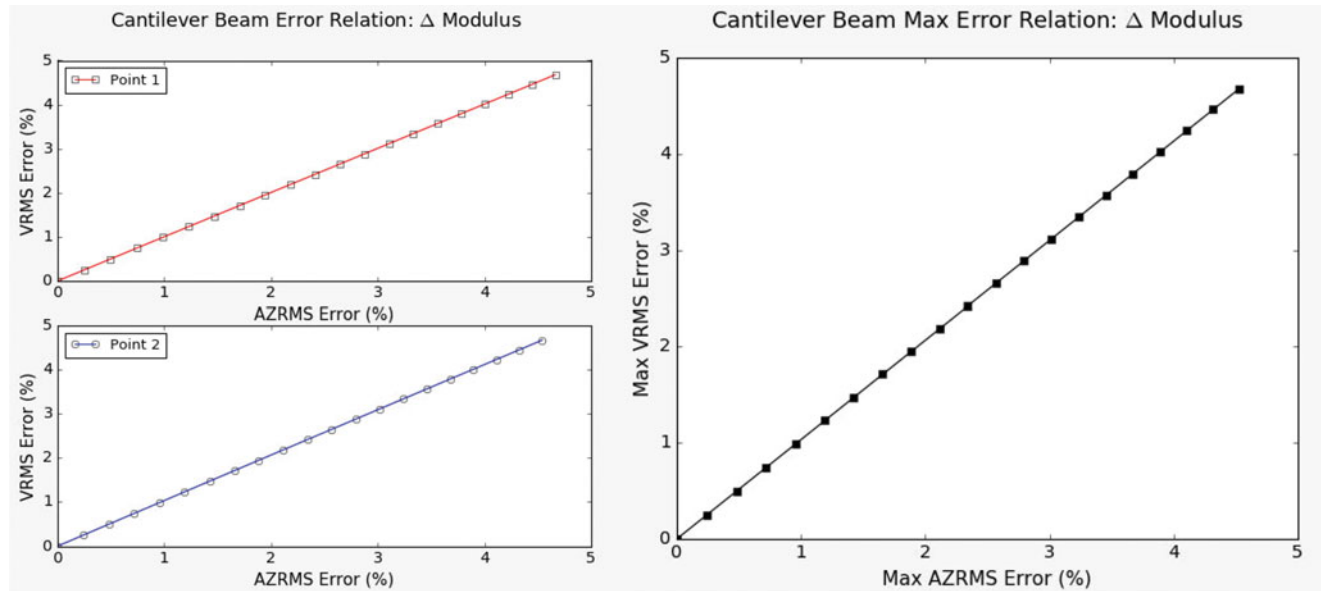


Fig. 8.6 Cantilever beam: effect of modulus change on stress-acceleration error relation, selected points and maximum

error continues to increase. In addition, the other two length plots look linear initially, but start behaving nonlinearly as the acceleration error increases.

To further investigate possible sources of this nonlinear error relationship, the ASD at Point 2 was plotted for each of the 20 length perturbation simulations. The first plot in Fig. 8.9 indicates that a fourth mode starts entering the 20–2000 Hz frequency range once the beam length is increased past a certain point. In addition, the response due to the mode initially

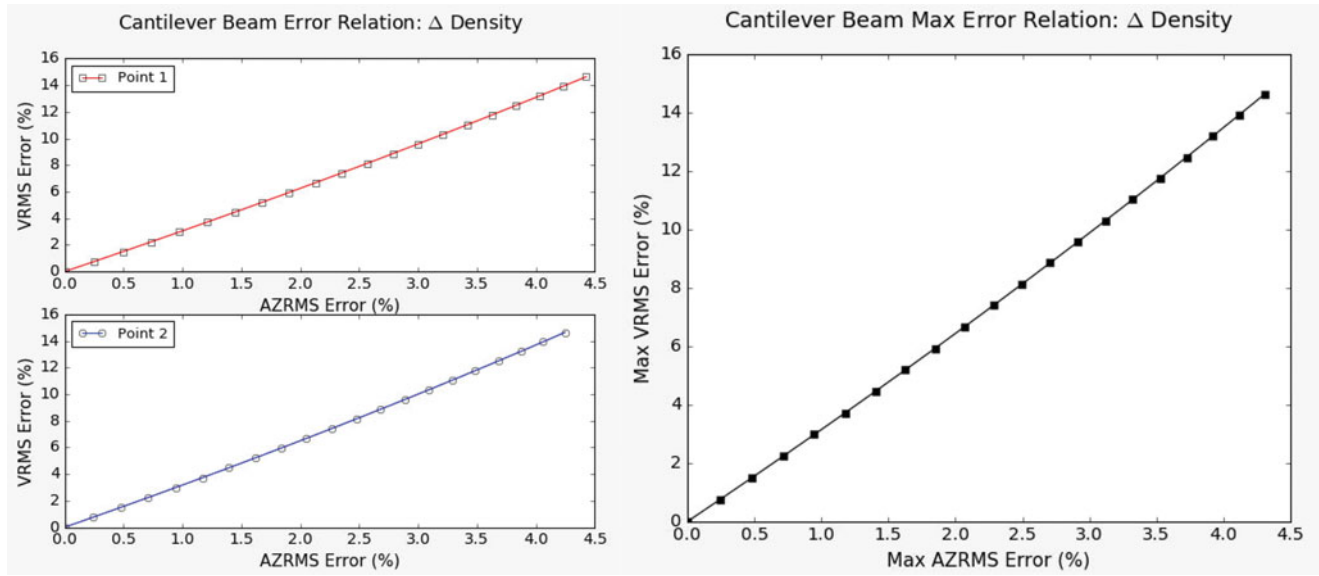


Fig. 8.7 Cantilever beam: effect of density change on stress-acceleration error relation, selected points and maximum

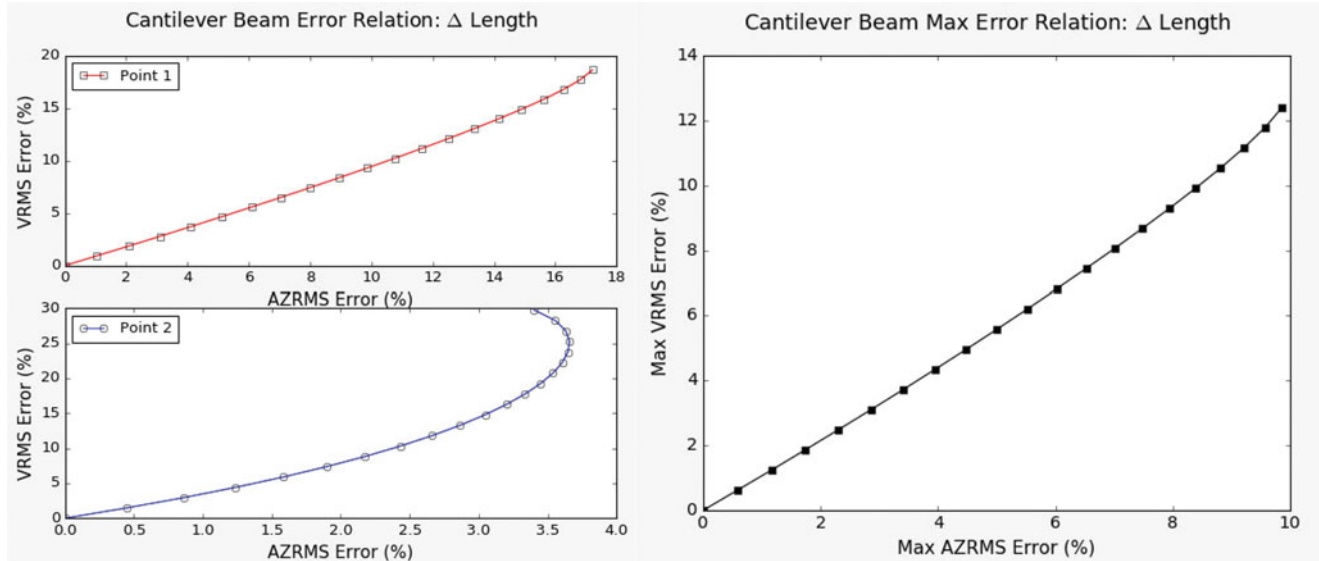


Fig. 8.8 Cantilever beam: effect of length change on stress-acceleration error relation, selected points and maximum

at 1374 Hz starts to increase well beyond the input level. These two factors suggest that the changing error relationship in the Point 2 plot of Fig. 8.8 is caused by the influence of the new mode and the increased response of an existing mode. This significant change in modes and frequencies disrupts the initially linear error relation. On the other hand, the response ASD for the modulus perturbations shown in the second plot of Fig. 8.9 demonstrates consistency in the modes and small changes across all 20 simulations, leading to the error relation shown previously in Fig. 8.6.

A summary of the range of stress-acceleration error and the error ratios is given in Table 8.1. The range of stress values is also listed for reference. The data presented in the table is for the error in the maximum value at any point in the model. This is distinct from the maximum error for a single point in model, but similar values can also be found at the individual points.

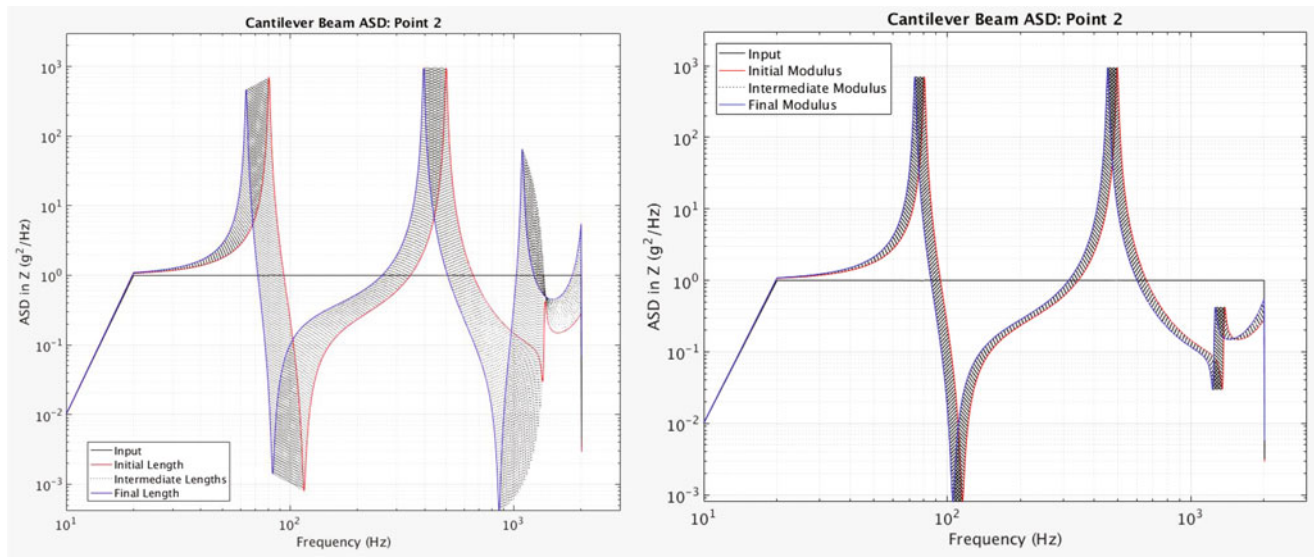


Fig. 8.9 Cantilever beam: complete range of response ASD for length (left) and modulus (right) perturbations

Table 8.1 Cantilever beam: maximum value error summary

Perturbation	VRMS range (psi/MPa)	Maximum VRMS % error	Maximum AZRMS % error	Error ratio
Modulus	390/2.7	4.7	4.5	1.03
Damping	729/5.0	8.7	8.7	1.00
Density	1220/8.4	14.6	4.3	3.40
Length	1034/7.1	12.4	9.9	1.26

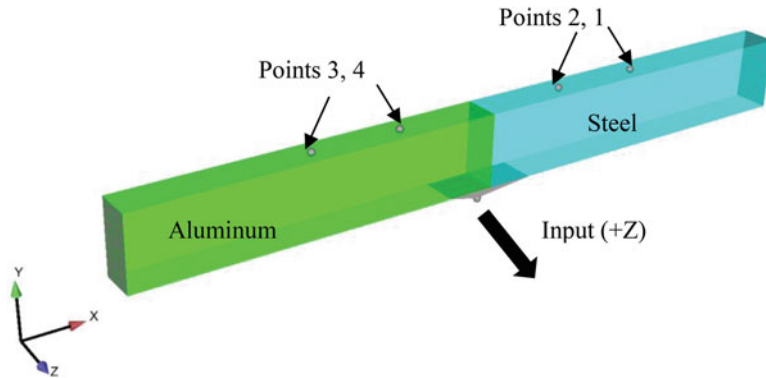


Fig. 8.10 Combined beam model with coordinate system, input, and point location for the two sections

8.3.3 Case 3: Combined Beam Random Vibration

Analysis on a two-material, combined beam was performed in the same manner as the cantilever beam, with a few modifications. For the input loading, the ASD frequency range is changed to 100–3000 Hz and the input location is moved to the bottom of the beam, in between the two joined sections (blocks), as shown in Fig. 8.10. The loading direction is kept the same- in the positive Z direction. Also, two points are used to probe the acceleration and stress for each block, for a total of four points in the combined beam model. These points are placed at the top of the blocks to study results in a different location than Case 2.

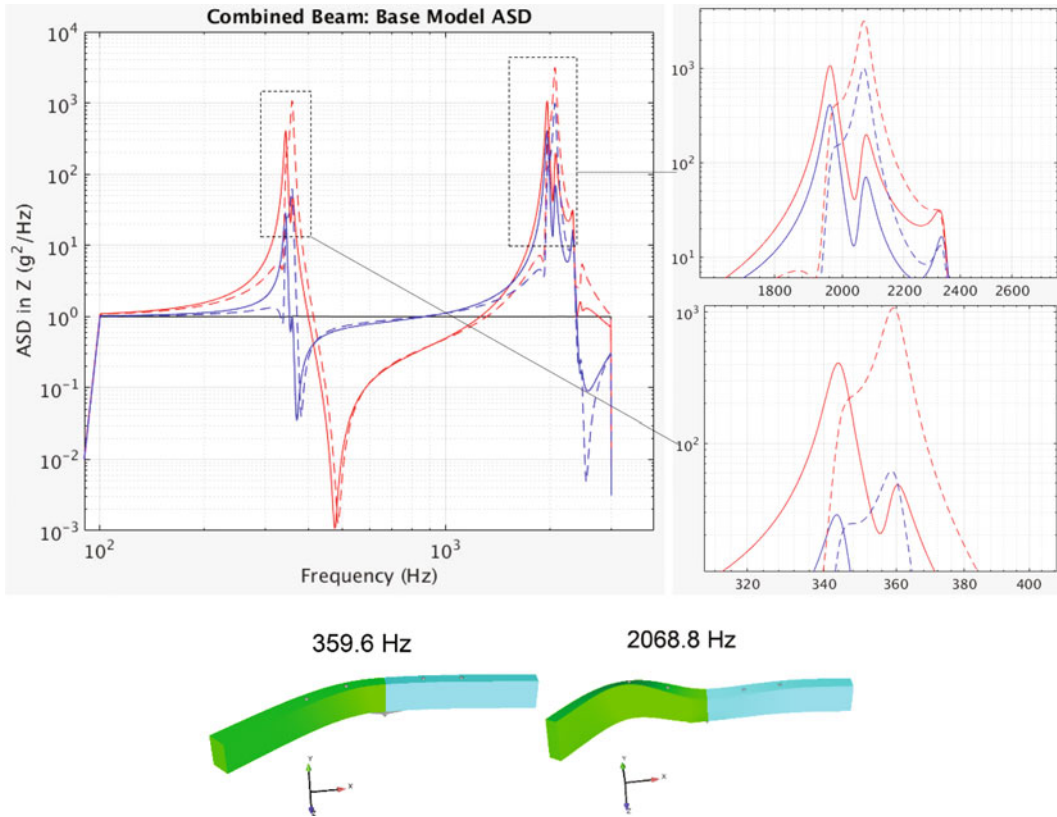


Fig. 8.11 Combined beam: base model ASD and modes with highest response

The combined beam model is the same overall length and mesh size as the cantilever beam, and the two blocks are joined together, with the material properties defined independently. The model is half steel, half aluminum, with equivalenced nodes at the interface to provide an ideal joint. The perturbation is performed similarly to the previous problem, except that the modulus, density, and length are only changed for the aluminum beam. For the perturbed length model, the length of the aluminum beam was increased by 0.125 in. (3.2 mm) for each simulation and the point coordinates were unchanged.

The response ASD for the base model is shown in Fig. 8.11. There are several modes across the frequency range, many of which are close in frequency. Two of the modes that produce the highest response are also shown in Fig. 8.11.

Examining the results for the modulus perturbation in Fig. 8.12, the general trends are like those from the cantilever beam problem. However, the error relation is clearly nonlinear. For the change in damping, a linear relationship similar to the cantilever beam was observed, although it was not one-to-one for the maximum; the plots are given in Appendix 2. For the density and length perturbations, the results were much more unpredictable than the previous example. The error plots for the density change in Fig. 8.13 are nonlinear and inconsistent, with several turning points, although some sections appear uniform. The error results for the length perturbation shown in Fig. 8.14 are also erratic.

As in the previous example, the response ASD is studied to determine the source of the inconsistency between stress error and acceleration error. Fig. 8.15 shows the ASD at Point 1 for each simulation in the modulus perturbation study. The modes change gradually as the modulus changes and no new modes enter the input frequency range, but the large variation in response could contribute to the nonlinearity of the plots in Fig. 8.12.

Next, we examine possible reasons for the unpredictable error relation presented earlier. In Fig. 8.14, there is a large AZRMS error caused by a 1% perturbation in length. From the second to the third perturbed model, an increase in length of 0.125 in. (3.2 mm) resulted in a 15% change in acceleration error and almost a 10% change in maximum stress error. These changes are apparent in the ASD, in Fig. 8.16. The peak acceleration response nearly doubled at 2 kHz for Point 3. Additionally, two modes near 350 Hz are nearly indistinguishable before the small change in length, yet clearly distinct after the small increase in length. These abrupt changes had a substantial impact on the resulting error relationship.

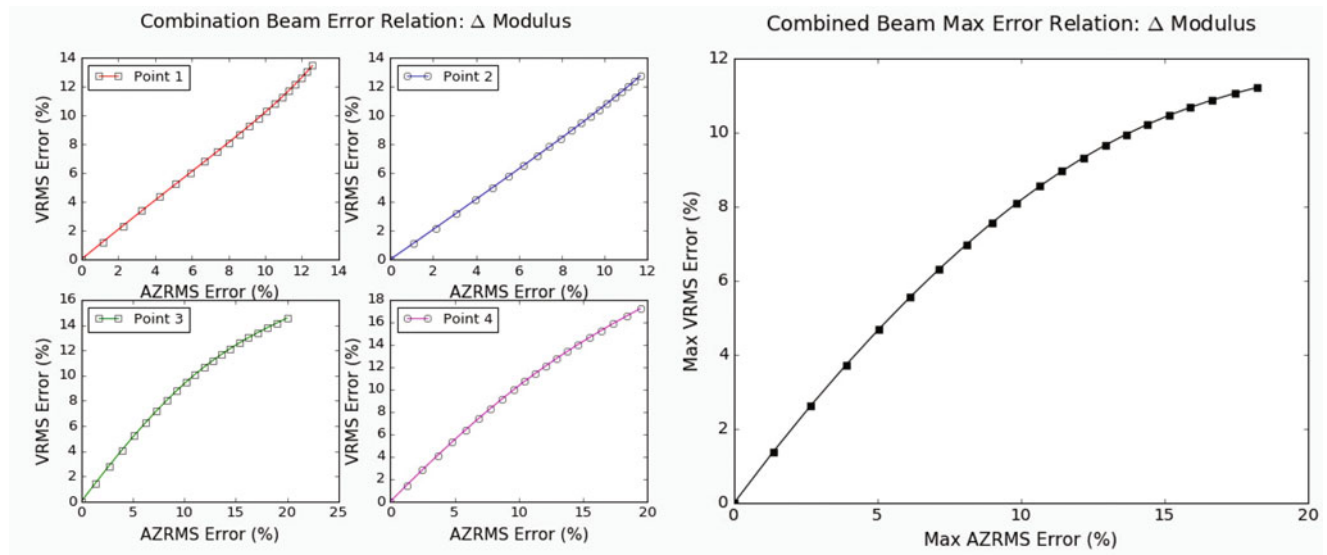


Fig. 8.12 Combined beam: effect of modulus change on stress-acceleration error relation, selected points and maximum

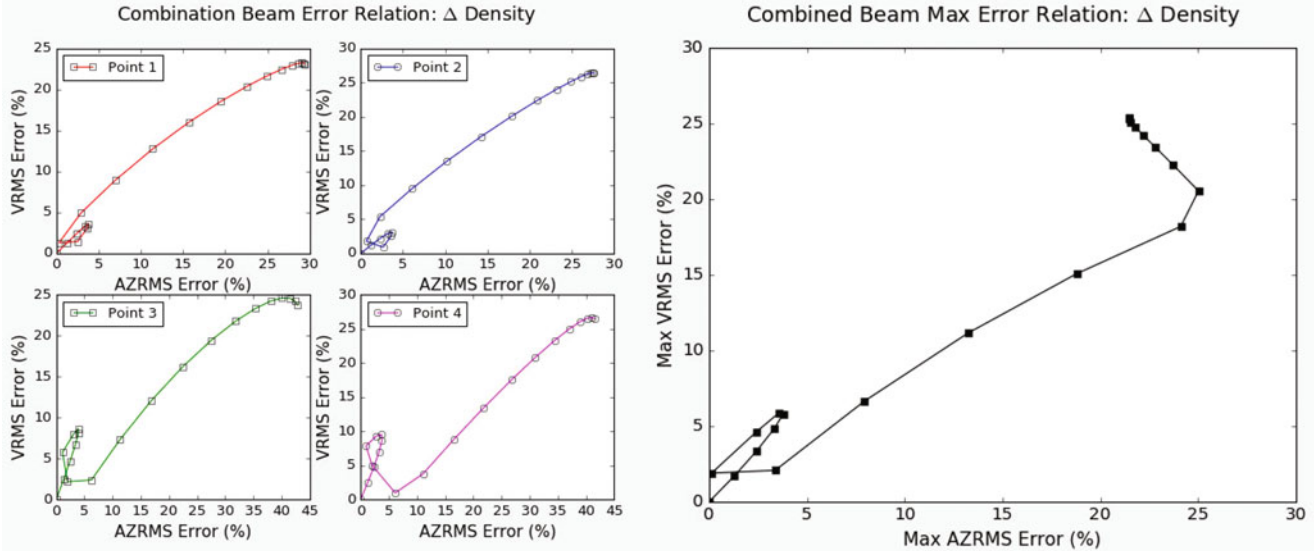


Fig. 8.13 Combined beam: effect of density change on stress-acceleration error relation, selected points and maximum

Furthermore, some parts of the error relationship were consistent, such as models 9 through 12 of the length perturbation study, shown in Fig. 8.17. This can be attributed to the lack of new modes introduced to the input load frequency range, illustrated in the Fig. 8.18 ASD. The response over models 9 through 12 is relatively stable, which is contrasted by the drastic change in the response over the entire perturbation range.

Although many of the results obtained from this combined beam example were not as straightforward as the previous two cases, the error ratio still gives an idea of the observed limits of stress and acceleration error. For the density and length studies, the error ratio is omitted since the inconsistent trends make it an inadequate measure of the error bound. A summary of the maximum value results is given in Table 8.2.

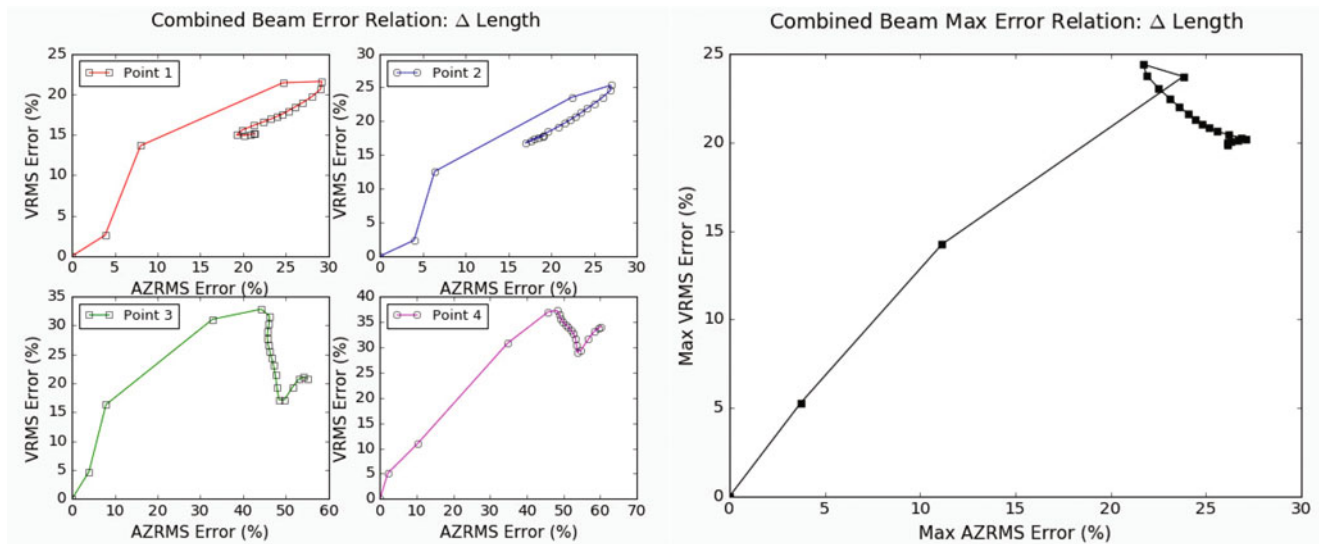


Fig. 8.14 Combined beam: effect of length change on stress-acceleration error relation, selected points and maximum

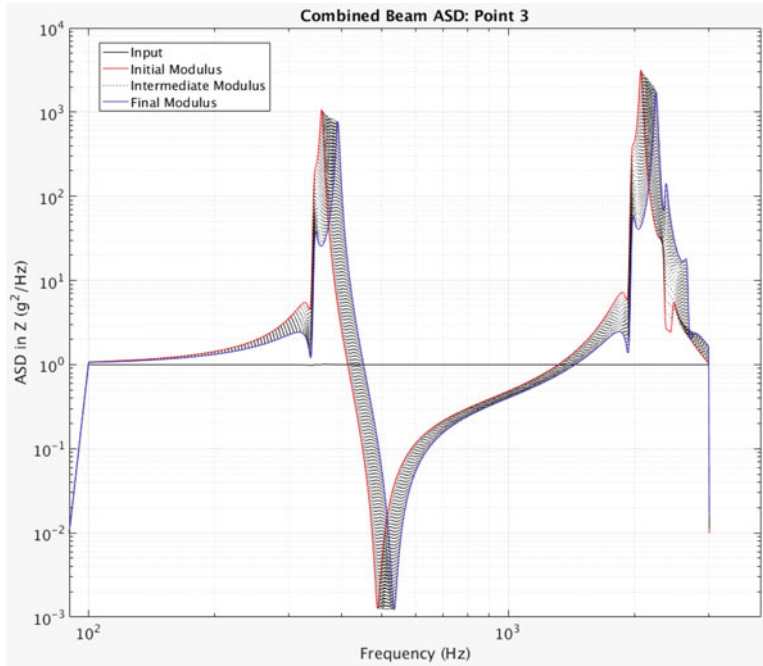


Fig. 8.15 Combined beam: complete range of response ASD for modulus perturbations

8.4 Evaluation

The data suggests that in an ideal case, a linear relationship between the stress error and acceleration error should be expected. However, as uncertainties in model parameters cause the system modes to change significantly, the results can vary greatly and it becomes difficult to quantify the error relationship.

Case 1 presents a theoretical linear relationship between the error in maximum modal von Mises stress and acceleration. As a practical extension of this initial study, Case 2 and 3 demonstrate a similar relationship for random vibration simulations. Results show that there can be large changes in the stress error and acceleration error if the mode shapes are significantly affected by a relatively small change in properties. These perturbations can have a pronounced effect if modes are close in frequency, and the error relation can become unpredictable.

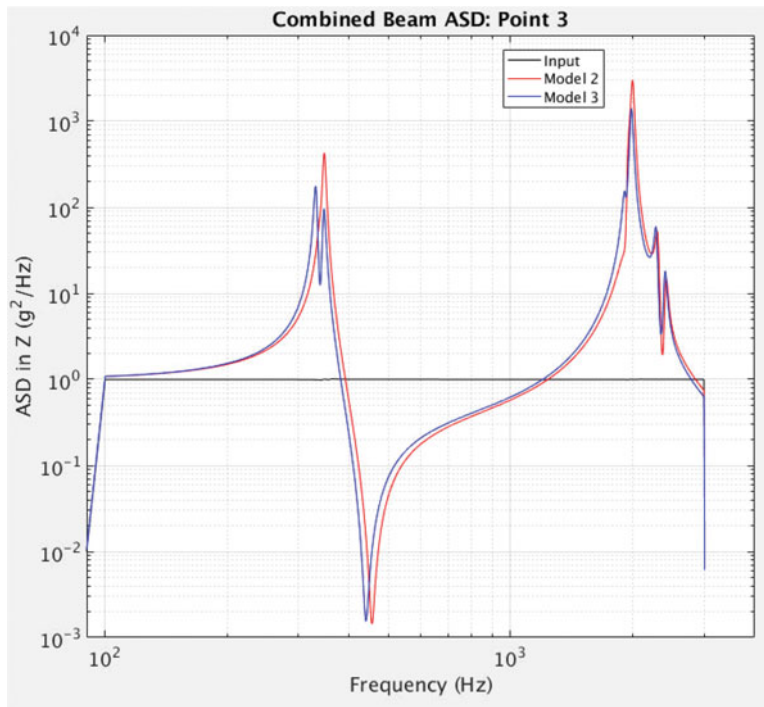


Fig. 8.16 Combined beam: model 1 and 2 response ASD for length perturbations

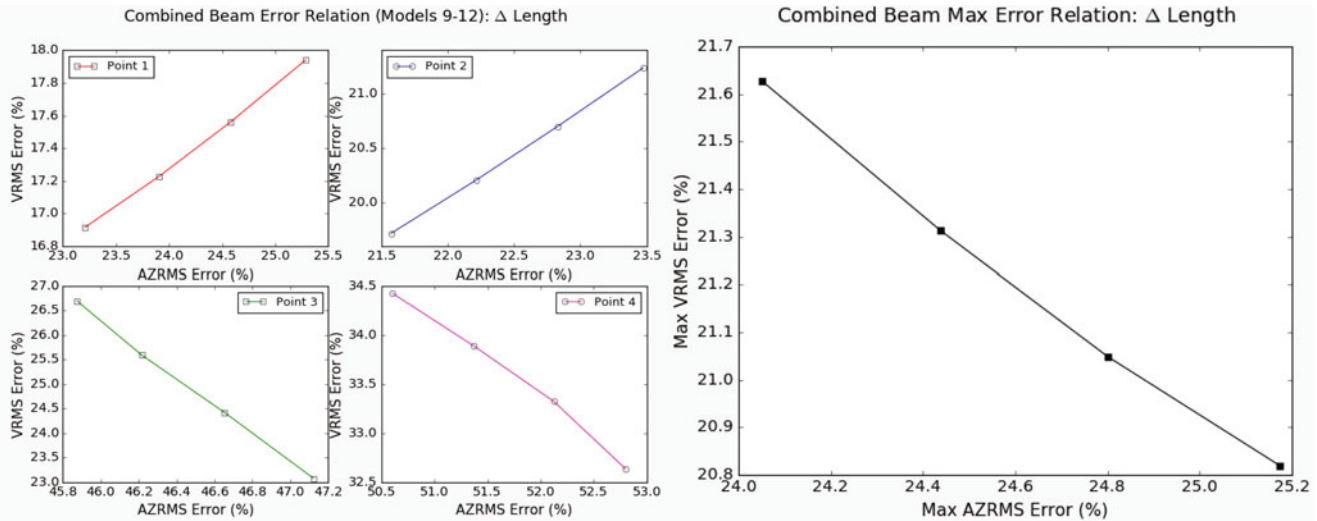


Fig. 8.17 Combined beam: effect of length change on stress-acceleration error relation (models 9 through 12)

For the random vibration examples, a change in damping exhibited the only consistently linear error relationship, with a direct relationship between VRMS and AZRMS error at each point, although the error ratio was not necessarily 1 over the model maximum. Still, this direct relationship is to be expected since uniform modal damping was specified. As for the range of errors, over the 20% perturbation in each model parameter, the highest stress error was 25.4% for the density and length perturbation in Case 3. In addition, the highest error ratio observed was 3.4, for the cantilever beam density perturbation. The error ratio is a useful measure for the cantilever beam, but it is specific to the system and model parameter. It may have limitations if the model increases in complexity, or if measurements are made at stress concentrations or near boundary conditions. Additionally, a low error in acceleration does not necessarily correspond to a low error in stress, since it depends on the modes of the system being predictable and stable, or having a low sensitivity to the uncertainty in model parameters.

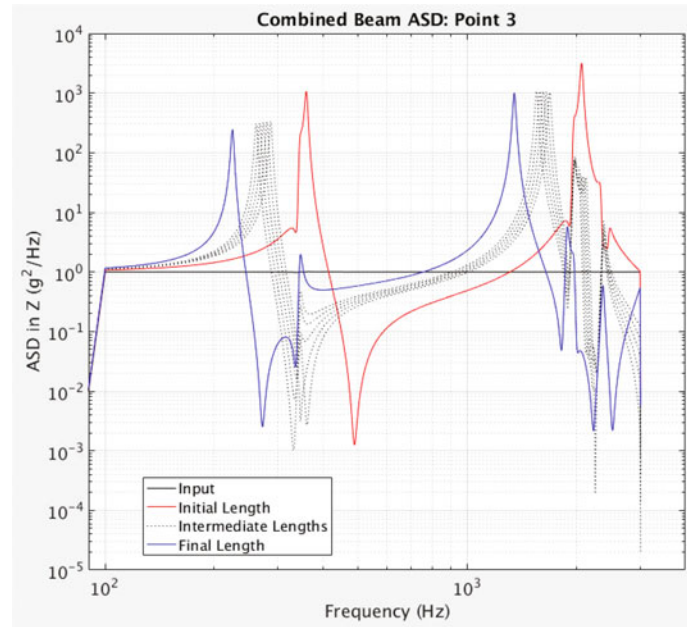


Fig. 8.18 Combined beam: models 9 through 12 and range of response ASD for length perturbations

Table 8.2 Combined beam: maximum value error summary

Perturbation	VRMS range (psi/MPa)	Maximum VRMS % error	Maximum AZRMS % error	Error ratio
Modulus	1767/12.2	8.2	18.2	0.45
Damping	2304/15.9	7.8	9.9	0.79
Density	13,960/96.3	25.4	25.0	—
Length	13,250/91.4	24.4	27.1	—

More data is needed to see how results hold for more complex systems, and future work could include multiaxial inputs, input load uncertainty, and coupled parametric effects. It would also be interesting to study results from other modal-based analyses, such as a modal transient solution to see if a bound could be determined even if the modal stress is not directly used.

8.5 Conclusion

A relationship between the error in stress and acceleration was calculated for three example problems. For the first case, a linear relation and theoretical bound for the maximum modal von Mises stress error and acceleration error was determined. The results were extended to a random vibration solution that utilized the modal stress and two example cases were considered. An error in acceleration due to changes in modulus of elasticity, damping ratio, density, and length for each example beam was related to the error in VRMS stress. An error ratio was defined to describe and bound the relationship and results were found to be linear if the system mode shapes do not change significantly with perturbation in model parameters. Irregular behavior was observed when new modes were introduced into the input load frequency range, influencing the response between perturbed models. The results of this work support that, given the stability of system modes across uncertainty in model parameters, the error in stress could be related to and bound through the errors in acceleration for a random vibration analysis. These error trends are useful for providing a quantitative measure of accuracy in stress and acceleration predictions.

Appendix 1

This section includes further explanation of the theory discussed in Sect. 8.2.1. Additional details on the nonlinear equation to be solved, $\|\ddot{u}_h - P\ddot{u}_H\|_{L^2}^2$, are also presented. If the approximations are accurate, the solution is not difficult. As the acceleration grows however, larger bounds on the stress must be computed carefully.

At some time, t , the error is given as

$$\|\ddot{u}_h - P\ddot{u}_H\|_{L^2}^2 = \langle \Phi^h \ddot{q} - P \Phi^H \ddot{b}, \Phi^h \ddot{q} - P \Phi^H \ddot{b} \rangle_M \quad (8.13)$$

Introducing the matrices

$$T = \phi^T P^T M P \phi, \quad B = \phi^T P^T M P \phi^h \quad (8.14)$$

There holds

$$\|\ddot{u}_h - P\ddot{u}_H\|_{L^2}^2 = \ddot{q}^T \ddot{q} - 2\ddot{b}^T B \ddot{q} + \ddot{b}^T T \ddot{b} \quad (8.15)$$

Note that B and T are identity matrices if the modes are exact. An alternative to the acceleration problem is the displacement problem, involving

$$\|u_h - P u_H\|_{L^2}^2 = q^T q - 2b^T B q + b^T T b \quad (8.16)$$

For the displacement problem, Ω^h is omitted from the definition of X . For the acceleration problem, q, b, c are replaced by \ddot{q}, \ddot{b} and \ddot{c} respectively. Setting c as

$$c = B^T b \quad (8.17)$$

The goal is to establish sufficient conditions for $q^T X q \approx c^T X c$. And setting

$$\beta = \sqrt{b^T T b} \quad (8.18)$$

Next comes the second assumption about how typically the nonlinear equations are easy to solve. We can expect $\beta \geq \|c\|$, but for clarity we assume $\beta \geq \|c\|$.

$$q^T q - 2b^T B q + b^T T b = q^T q - 2c^T q + \beta^2 = \|q - c\|^2 + \beta^2 - \|c\|^2 \quad (8.19)$$

The case of interest is the case in which q cannot have rotated around from c all the way to the eigenvectors of X with large eigenvalues.

A Lagrangian for this problem is $L(q, \lambda) = \frac{1}{2}q^T X q - \frac{1}{2}\lambda(q^T q - 2q^T c + c^T c)$, the critical points satisfy $Xq = (q - c)\lambda$.

Two definitions are included for clarification. First let $\delta_{min} = (\beta^2 - \|c\|^2)^{1/2}$. And second, let $\bar{\delta} = \sqrt{\delta^2 - \delta_{min}^2}$.

To determine the Lagrange multiplier, first solve for q , and then eliminate q from the constraint equations,

$$q = (\lambda - X)^{-1} c \lambda, \quad \|(\lambda - X)^{-1} X c\| = \bar{\delta} \quad (8.20)$$

Equation 8.20 must be solved for λ . The value of the Lagrange multiplier is not unique. The equation $Xq = (q - c)\lambda$ implies that $\|Xq\| = \bar{\delta} |\lambda|$. So, in practice the maximum corresponds to the largest positive Lagrange multiplier, $\lambda > \|X\|$. However, in general this would have to be another assumption. We assume that $\lambda_{max}(X) = \|X\|$.

There is a case in which an approximate solution is obvious. Suppose that $\tau = \|Xc\|/\delta \gg \|X\|$. In this case $(\tau - X)^{-1} \sim \tau^{-1}$ and $\lambda \sim \tau$. For sufficiently small δ , $\lambda \sim \|Xc\|/\delta$ and $\lambda > \|X\|$. A more precise statement involves $\gamma \geq 1$ defined by $\|Xc\| = \|X\| \|c\| \gamma$.

It turns out that if $\delta < \gamma \|c\|$, then $\lambda \sim \|Xc\|/\delta$. This is seen by manipulating the equation $\tau = \|Xc\|/\delta \geq \|X\|$. First using the definition of γ , $\|Xc\| \gamma / \delta > \|X\|$. Next, $\|X\|$ is cancelled, leaving $\|c\| \gamma / \delta > 1$ or $\|c\| \gamma > \delta$.

This means that the estimated value of λ can be used instead of the exact value and that $q \sim c$, which is the benign case. This is to be expected, since usually the approximation is quite accurate and the nonlinear equation is trivial to solve.

Typically, $\gamma \ll 1$. On the other hand, if $\delta > \|c\|\gamma$, then it is worthwhile to carefully solve the nonlinear equation that determines λ ; we expect that $\|a\| \sim \bar{\delta}$.

Appendix 2

This section includes the stress-acceleration error plots omitted from the main text (Figs. 8.19 and 8.20).

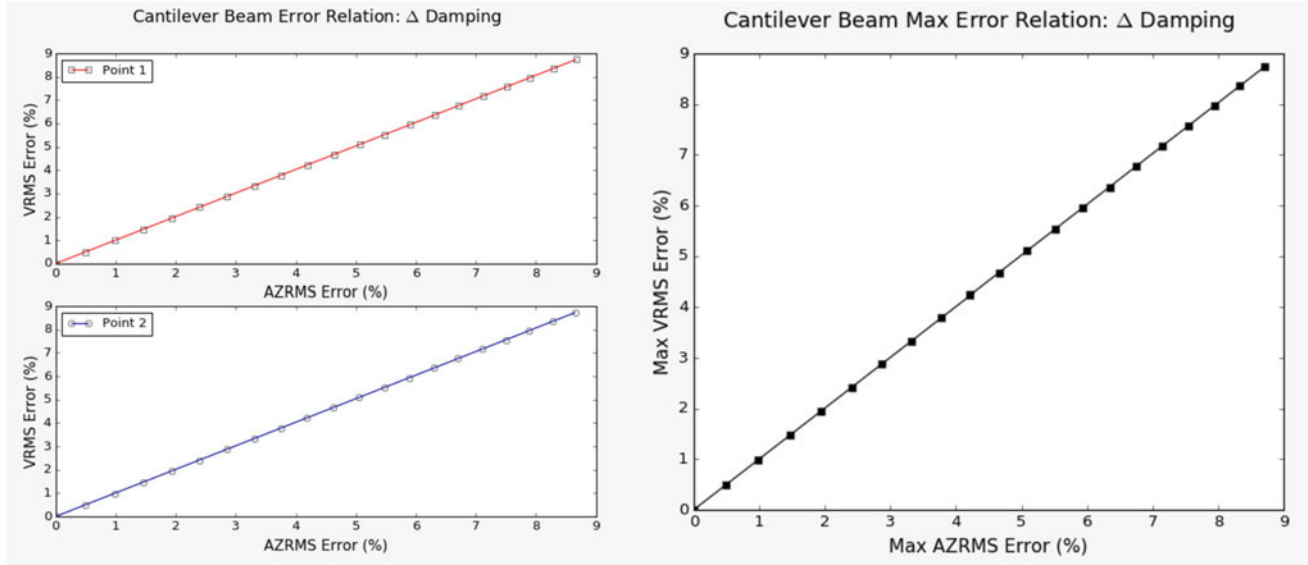


Fig. 8.19 Cantilever beam: effect of damping change on stress-acceleration error relation, selected points and maximum

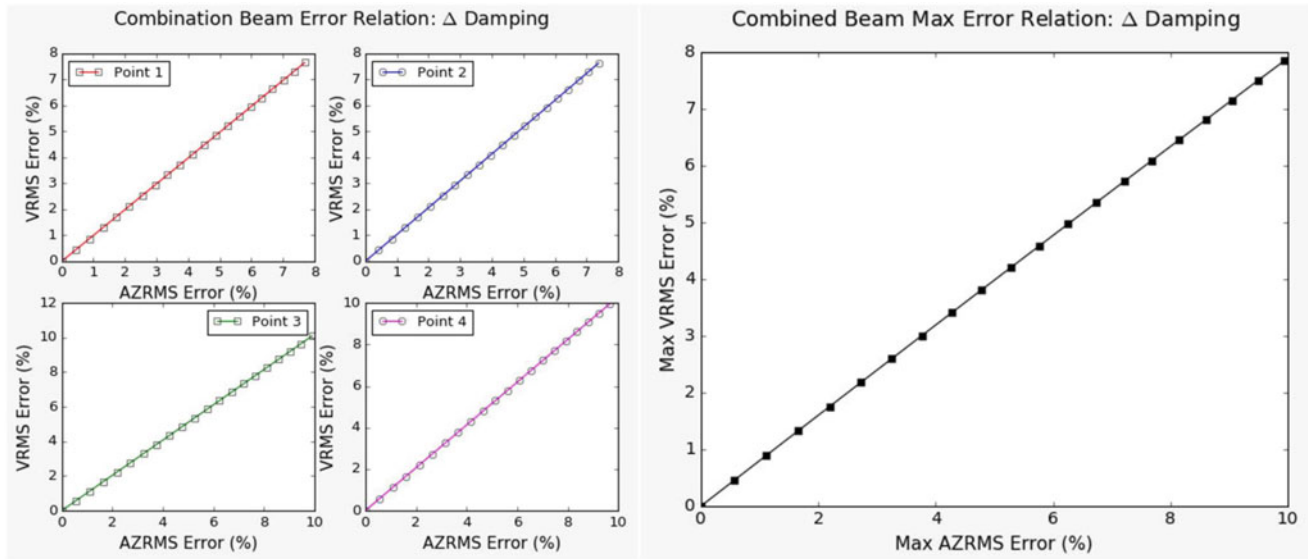


Fig. 8.20 Combined beam: effect of damping change on stress-acceleration error relation, selected points and maximum

References

1. Christie, M.A., Glimm, J., Grove, J.W., Higdon, D.M., Sharp, D.H., Wood-Schultz, M.M.: Error analysis and simulations of complex phenomena. *Los Alamos Sci.* **29**, 6–25 (2005)
2. Segalman, D.J., Fulcher, C.W.G., Reese, G.M., Field Jr., R.V.: An efficient method for calculating RMS. von Mises stress in a random vibration environment. *J. Sound Vib.* **230**(2), 393–410 (2000)
3. Clough, R., Penzien, J.: *Dynamics of Structures*, 2nd edn. Computers and Structures, Inc, Berkeley, CA (2010)
4. Wirsching, P.H., Paez, T.L., Ortiz, K.: *Random Vibrations: Theory and Practice*. Dover Publications, Inc., Mineola, NY (2006)



Chapter 9

A Neural Network Surrogate Model for Structural Health Monitoring of Miter Gates in Navigation Locks

Manuel Vega, Ramin Madarshahian, and Michael D. Todd

Abstract Structural health monitoring (SHM) of miter gates of navigation locks is crucial for facilitating cargo ship navigation. Closure of these inland waterway structures causes considerable economical loss to the marine cargo and associated industries. In practice, strain gauges are often mounted in many of these miter gates for data collection, and various inverse finite element techniques are used to convert the strain gauges data to damage-sensitive features. Arguably, these models are computationally expensive and sometimes they are not suitable for real-time health monitoring or for monitoring confounding environmental effects. In this work, a Multi-Layer Artificial Neural Network (MANN) is designed to serve as a “run time” surrogate model that links data (from the strain gages) to damage classification (gaps in the miter gate contact). Three cases of complexity, combining hydrostatic and thermal loading scenarios with varying gap scenarios, are considered to design the MANN. A confusion matrix is used to evaluate the performance of the networks and derive probabilities. Results show the potential of MANNs as a reliable surrogate model for computationally expensive inverse finite element modeling in damage classification for this application.

Keywords Miter gates · Artificial neural networks · Surrogate model · Finite element · Inverse model

9.1 Introduction

In the United States, the U.S. Army Corps of Engineers (USACE) owns and operates 236 locks at 191 sites [1]. According to a report published by USACE in 2017, more than half of these assets are older than their economic design life, 50 years, and need a prudent structural health monitoring solution to ensure their safe and reliable operation [2].

Damage to the locks may lead to closures of the lock chamber, which impose economic losses on the commercial shippers. Two types of closures (i.e. scheduled and unscheduled) apply to miter locks. Scheduled lock closures allow commercial shippers to adjust their activities to be coordinated to optimize their benefit. However, unexpected events such as accidents, weather, or emergency maintenance needs can result to unscheduled closures, which can negatively impact commercial activities [3]. Therefore, there is a need to identify the current state of lock gates to see how reliable they are when unforeseen events are present. Knowing the condition of a lock gate and its components can allow to take preventive measures to avoid or minimize the loss in unscheduled closures. Miter gates are the most common type in the United States with other types of lock gates being sector and vertical lift [4].

For miter gates, some experienced engineers and lock operators from USACE [2] agree that one of the primary concerns for inspection, maintenance and repair are the condition of the quoin and gaps between the lock wall and the quoin block. A “gap” is referred to as the loss of bearing contact between the quoin attached to the gate and the lock wall. A “gap” in the quoin block changes the load path in the miter gate, leading to higher stresses on some places in the lock gate (e.g., the pintle) and leading to operational and/or structural failure. Therefore, monitoring the condition of the “gap” can be used to extend the life of the gate and/or suggest repairs and maintenance in a timely manner. Some other concerns related to miter gates are corrosion and fatigue deterioration [5].

Most of the miter gates owned by USACE are strategically instrumented with strain gauges for data acquisition [6]. The strain topography in the structure changes as the boundary conditions change, in other words, as the size of a gap changes for a gate. Therefore, finite element (FE) models could be used to map the strain gauges data to a specific “gap” in an inverse analysis. However, these models are computationally expensive and sometimes they are not feasible for real-time health

M. Vega · R. Madarshahian · M. D. Todd (✉)

Department of Structural Engineering, Jacobs School of Engineering, University of California, San Diego, La Jolla, CA, USA

e-mail: madarshahian@ucsd.edu; mdtodd@engr.ucsd.edu

monitoring or for monitoring fluctuating environmental effects. Consequently, a surrogate model with fast predictions of the target damage (e.g., the “gap”) can be used.

Artificial neural network (ANN) modeling, which are lately used extensively in many areas of science and engineering, could be a powerful way to predict the contact “gap” at the quoin block. Some researchers have used ANNs as surrogate models, using validated FE models to generate data to train the network [7–8].

In this paper, a Multi-Layer Artificial Neural Network (MANN) is designed to serve as a computational inexpensive surrogate model that links the strain gages data to the “gap” in the quoin block. An ABAQUS FE model of a miter gate is used to obtain synthetic strain data to design such MANN.

The paper first explains the finite element model and then describes the architecture of the MANN. In the result section, the efficiency of MANN is examined by considering three cases of different complexity. A confusion matrix is used to evaluate the performance of the networks under these realistic cases. Results show the potential of MANNs as an inexpensive reliable alternative for computationally expensive inverse finite element modeling in the classification of the “gap” size in miter gates. Other analysis would have to be performed to see which “gap” size is critical in redistributing the load in such a way that some failure in the gate or in one of its component may happen rapidly.

9.2 Finite Element Modeling

Instrumentation on miter gates have started recently. Additionally, tracking the “gap” size has not been monitored constantly. Therefore, due to the lack of actual experimental data, FE simulations are needed to understand the effect of different “gap” size on the strain gage readings and the redistribution of loads along the miter gate. The FE model has been previously validated with the available strain gage readings from the Greenup miter gate. The Greenup gate is a brand-new gate where a very small or nonexistent “gap” can be assumed for validation purposes.

Consequently, simulated data was used for training and testing, which are generated by integrating ABAQUS and Python. In this paper, a single gap scenario is used as shown in Fig. 9.1 to generate the training and testing data.

Gap length is a random number between 0 and 180 in. under random loading scenarios defined by two normal distributions for upstream and downstream hydrostatic pressure [9]. For simplification purposes, the gate and the quoin block attached to the gate are modeled as a single part (denoted in gray). All the elements in the domain are 3D linear shells elements to reduce the computational cost of such a large model.

A hard-contact condition is used between the lock wall (denoted in yellow) and the gate (denoted in gray), making this a nonlinear problem. The opposite side of the lock wall uses fixed boundary conditions. Symmetry boundary conditions are used at the right end (i.e., miter) of the gate to simulate the right leaf. The miter gate is subjected to upstream and downstream hydrostatic loading as shown in Fig. 9.2.

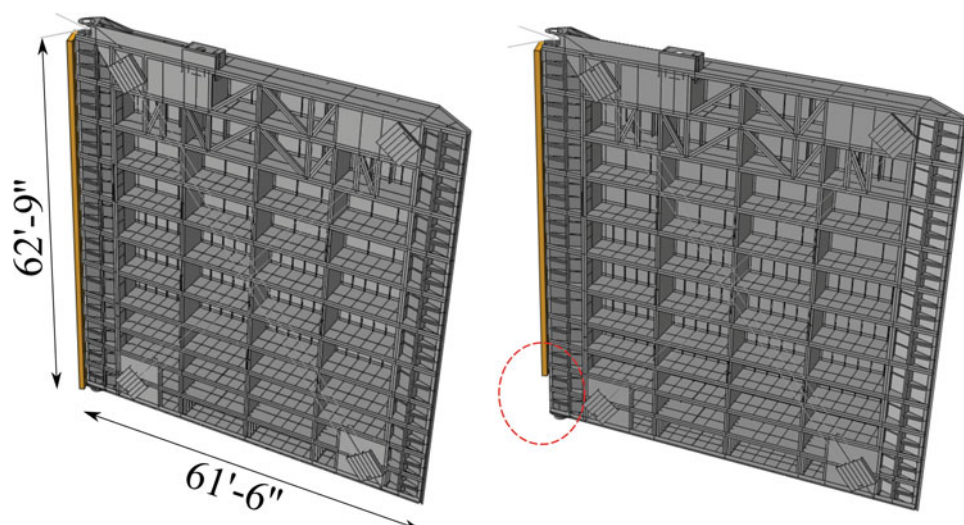


Fig. 9.1 Gap modeling (Left: No gap, Right: Schematic gap)

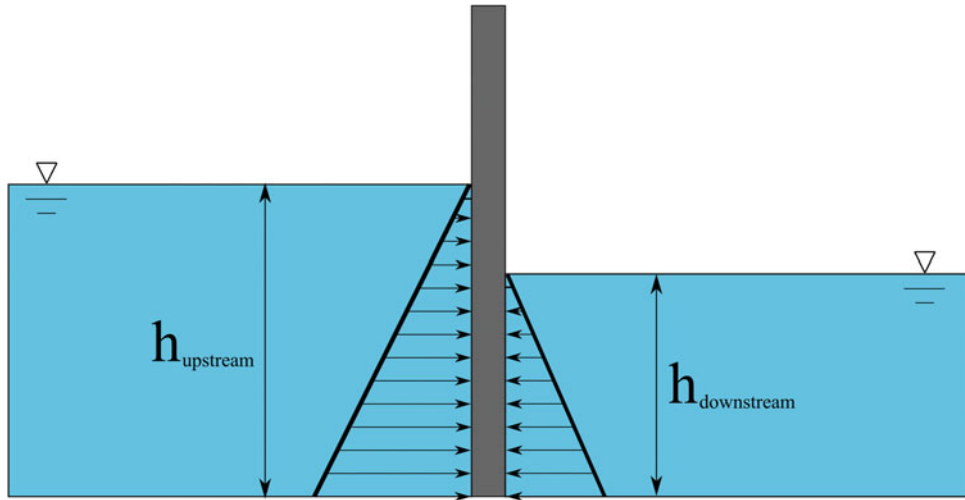


Fig. 9.2 Hydrostatic loading on miter gates

The ABAQUS Greenup model was run with python to obtain 3000 realizations, 2000 for training and 1000 for testing data. Generating this data took almost one week using a 4-cpu desktop.

9.3 Multi-Layer Artificial Neural Network

9.3.1 Preliminary Design

The MANN was designed using the open-source platform TensorFlow, which has been used for several real-world applications [10, 11]. In the first demonstration, only three damage levels were defined (i.e., low, moderate, and high) based on the gap length (i.e. 0–60 in., 60–120 in. and 120–180 in.). In this MANN, shown in Fig. 9.3, a 99% accuracy was reached. Two thousand data sets are used to create 300,000 mini-batches, which are small random sets of the original data sets. Then, Mini-batch Gradient Descent algorithm uses the mini-batches sets used for training and validation to minimize the loss function by changing the weights and biases. After, the MANN finishes its training and validation stage, 1000 new data sets not seen in training are used for testing the MANN.

9.3.2 Extended Design

Subsequent to the first demonstration, the MANN was extended to consider 18 cases based on the gap length (i.e. increments of 10 in. within a range of 0–180 in.). The new MANN was designed with 6 hidden layers (228 neurons) with a decreasing learning rate to improve the final accuracy. The Softmax function is used for the last layer as an activation function to reach a value between zero and one for each class, allowing indication of the damage case. Three cases of complexity, combining hydrostatic and thermal loading scenarios with varying gap scenarios, are considered to design the MANN.

Case 1: Consider “gap” length to be a random number between 0 and 180 in. with a constant (known) hydrostatic loading, and neglect thermal environmental load effects.

Figure 9.4 shows a confusion matrix, sometimes called matching matrix, for the testing data, which reveals the MANN performance on classifying the gap length when only raw strain gauge data are used as an input. The obtained confusion matrix for the MANN is a heavily-banded matrix with a few gap lengths misclassified to an adjacent class. This happens because sometimes a gap length, which in fact is a continuous parameter, lays in the boundary of two discretely-divided classes. Overall, the confusion matrix shows an accuracy of 98.8%.

Case 2: Consider “gap” length to be a random number between 0 and 180 in. with a random loading scenario defined by two normal distributions for upstream and downstream hydrostatic pressure, and neglecting thermal environmental load effects.

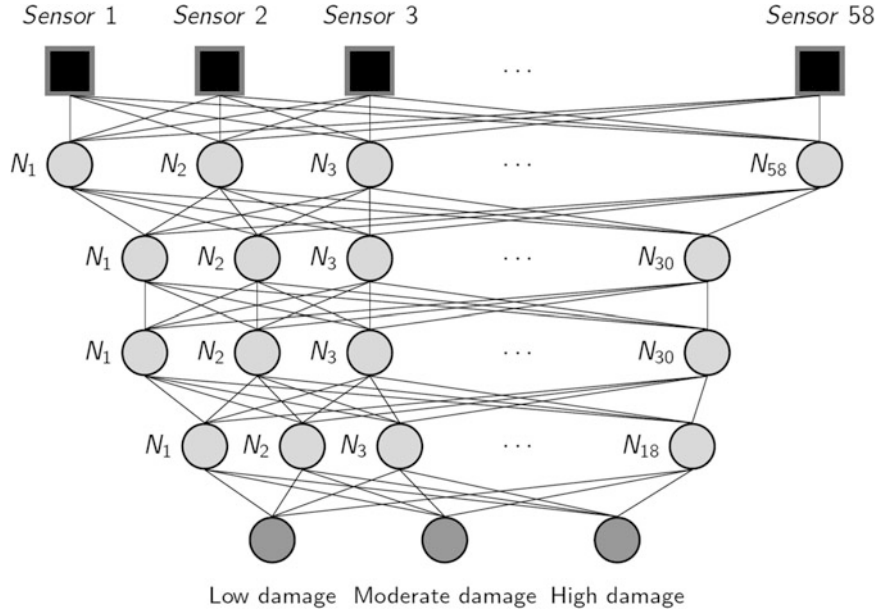


Fig. 9.3 MANN to classify three different gap length ranges (levels)

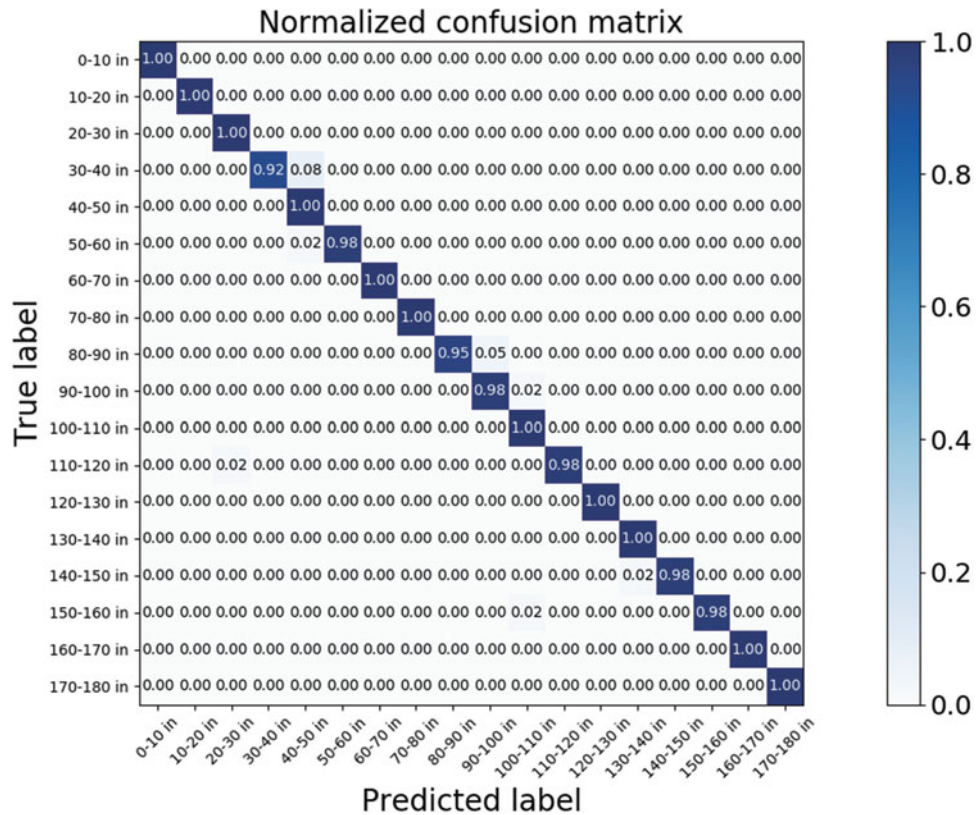


Fig. 9.4 Confusion (Matching) Matrix using NN to classify 18 scenarios (Case 1)

Case 3: The same as Case 2 except that the environmental temperature, which will add thermal strain effects, is defined as a random number based on the lowest and highest temperature value recorded by thermometers in the actual Greenup gate data.

Again, the ABAQUS Greenup model was run with Python to obtain 3000 realizations, 2000 for training and 1000 for testing data for every case.

Table 9.1 Testing accuracy of MANN designs

Case	Testing accuracy
1	0.988
2	0.961
3	0.958

Table 9.2 MANN verification (testing accuracy)

Cross verification	Test Case 1	Test Case 2	Test Case 3
Train Case 1	0.988	0.459	0.097
Train Case 2	0.887	0.961	0.213
Train Case 3	0.798	0.911	0.958

Table 9.1 summarizes the accuracy obtained for Cases 1 through 3. Interestingly, a very high accuracy is reached for all cases. It is important to note that the number of layers and neurons were manually modified to allow Case 1 reach a very high accuracy. Alternatively, a higher accuracy may be reached by optimizing the number of layers along with a dropout function to prevent overfitting. For Cases 2 and 3, the same numbers of layers and neurons as Case 1 were used. Therefore, an individual optimization of the number of layers can also be performed to improve the case by case testing accuracy.

9.3.3 Cross Verification

In general, it could be expected that the MANN trained for Case 3 be used to predict Case 1 and 2, since Case 3 includes all Case 1 and Case 2 effects. Conversely, the MANN trained for Case 1 should have very poor results when predicting Case 2 and 3. Therefore, to verify the results shown in Table 9.1, the following was observed using different data of each case for training and testing of the MANN:

As expected, the MANN trained with the data of Case 3 achieves a good testing accuracy when using data of Case 1, 2 and 3 as shown in Table 9.2. Similarly, the MANN trained with the data of Case 2 performs good for Cases 1 and 2. On the other hand, a very poor accuracy is obtained when a MANN is trained with Case 1 but tested with Case 2 or 3 and when is trained with Case 2 but tested with Case 3. Based on the table above, it can be concluded that variability in the loading and temperature are both very critical to consider in the training because inevitable the data in a real SHM setup would be affected by such effects. Again, note that 2000 data points were used for training and 1000 were used for testing for every value shown in Table 9.2.

9.4 Conclusion and Further Work

A MANN can successfully predict the condition of a “gap” in the quoin blocks when enough data is available. For this paper, the FE model was used as a source of generating synthetic training and testing data. Cross Verification can be useful to identify what effects are important to consider in the training phase of a MANN. Finally, a MANN with three sources of variability was designed that can accurately predict a “gap” between 79.8 and 95.8% of the times. And when not, it can predict the value to a very close class (i.e. a banded confusion matrix). In the real world, testing data should be obtained directly from physical strain gages. As demonstrated, a MANN can have a very high testing accuracy up to 95.8% if trained with all the sources of variability that a real strain gauge is subjected. Contrarily, a MANN can have a very poor testing accuracy as low as 9.7% if trained with data obtained from an oversimplified FEM model. Additionally, strain gauges are installed in specific places and record the strain in a specific direction. Any additional information can be used to build a more sophisticated network.

Acknowledgements Funding for this work was provided by the United States Army Corps of Engineers through the U.S. Army Engineer Research and Development Center Research Cooperative Agreement W912HZ-17-2-0024.

References

1. U.S. Army Corps of Engineers Headquarters: Navigation. <http://www.usace.army.mil/Missions/CivilWorks/Navigation.aspx> (2018). Accessed 1 August 2018
2. Foltz, S.D.: Investigation of Mechanical Breakdowns Leading to Lock Closures. Technical Report. Champaign, IL (2017)
3. Kress, M.M., et al.: ERDC/CHL TR-16-8 Marine Transportation System Performance Measures Research Coastal and Hydraulics Laboratory. Vicksburg, MS (2016)
4. Alexander, Q., Netchaev, A., Smith, M., Thurmer, C., Klein, J. D.: Telemetry techniques for continuous monitoring of partially submerged large civil infrastructure. In Sensors and Smart Structures Technologies for Civil, Mechanical, and Aerospace Systems 2018, 2018, vol. 1059823, no. March, p. 76
5. Estes, A.C., Frangopol, D.M., Foltz, S.D.: Updating reliability of steel miter gates on locks and dams using visual inspection results. Eng. Struct. **26**(3), 319–333 (2004)
6. U.S. Army Corps of Engineers Headquarters: SMART GATE. <https://www.erdc.usace.army.mil/Media/Fact-Sheets/Fact-Sheet-Article-View/Article/476668/smart-gate/>. Accessed 1 August 2018
7. Artero-Guerrero, J.A., Pernas-Sánchez, J., Martín-Montal, J., Varas, D., López-Puente, J.: The influence of laminate stacking sequence on ballistic limit using a combined Experimental/FEM/Artificial Neural Networks (ANN) methodology. Compos. Struct. **183**(1), 299–308 (2018)
8. Koeppe, A., Hernandez Padilla, C.A., Voshage, M., Schleifenbaum, J.H., Markert, B.: Efficient numerical modeling of 3D-printed lattice-cell structures using neural networks. Manuf. Lett. **15**, 147–150 (2018)
9. Eick, B.A., et al.: Automated damage detection in miter gates of navigation locks. Struct. Control Heal. Monit. **25**(1), 1–18 (2018)
10. Abadi, M., et al.: TensorFlow: a system for large-scale machine learning. 12th USENIX Symp. Oper. Syst. Des. Implement. **16**(4), 486–492 (2016)
11. Madarshahian, R., Caicedo, J.M., Haerens, N.: Human Activity Benchmark Classification Using Multilayer Artificial Neural Network, pp. 207–210. Springer, Cham (2019)



Chapter 10

Model Validation Strategy and Estimation of Response Uncertainty for a Bolted Structure with Model-Form Errors

Huijie Li, Qintao Guo, Ming Zhan, and Yanhe Tao

Abstract The model-form uncertainty and the connection parameter uncertainty are difficult to separate in structural dynamics. In this paper, we study a model-form uncertainty substructure identification method. Through the precision evaluation of the hyper-model of the substructure, and the experimental modal analysis of the substructure, the method of identifying the model-form uncertainty in the overall structure is given. Through the experimental modal analysis of the connection substructure, the uncertainty quantification is conducted and the joints parameters of the structure are identified. Finally, the response error estimation of the overall structure is given by combining the uncertainty of model form and of parameters. By comparing with the response errors estimated of the overall experiment, the proposed method is validated. In this paper, using modal parameters and frequency response as the response feature. A general definition of validation metrics was conducted which related to frequency response function. By using a bolted frame the framework of model validation is illustrated and the validation of the method in this paper is proved.

Keywords Structural dynamics · Model validation · Model-form uncertainty · Uncertainty quantification

10.1 Introduction

It is becoming more and more common to use numerical models to predict the behavior of physical systems in engineering and complex environments, especially when experiments are hampered by money or security. However, some assumptions and simplifications will inevitably be introduced in the establishment of numerical models, so that the model prediction can only be an approximation of reality. For this reason, the uncertainty of numerical simulation prediction must be validate so that simulation prediction can effectively replace or supplement full-scale experiments [1–3].

Typical numerical prediction uncertainties come from parametric numerical, and model-form uncertainties. Uncertainties in parameters represent variability or unknown values of coefficients of constitutive models, energy recovery coefficients, or coefficients of contact conditions between two surfaces. Because of the uncertainties of the size of the contact surface, the friction coefficient and the installation preload, this paper proposes to treat the contact stiffness of the connection structure as a random distributed parameter, and uses the model updating method based on the response surface method and the distributed algebra method to quantified it [4]. The method is feasible and convenient for practical engineering application. For the model-form uncertainties and numerical uncertainties, their error sources are input error ϵ_{in} (model size parameters), discrete error ϵ_h and surrogate model prediction error ϵ_{SU} [5, 6]. Ideally, the input parameters of the computational model should be the same as those of the real physical system, but the input errors of the computational model will be caused by the variability of the experiment and the influence of the measurement errors. In simulation, we will discretize the model into finite nodes or grids or decompose the time into finite time steps, which will cause discrete errors. The total uncertainty is written as the sum of all components [7]:

$$\epsilon_{num} = \epsilon_{in} + \epsilon_h + \epsilon_{SU} \quad (10.1)$$

Because the physical model studied in this paper is a benchmark structure and pay much attention on its modal parameters, so ϵ_{in} and ϵ_{SU} can be ignored. Therefore, the quantification of uncertainty in numerical calculation can be approximated by discrete error quantification. The uncertainty of model form is fuzzy compared with parameter and numerical uncertainties.

H. Li · Q. Guo (✉) · M. Zhan · Y. Tao
College of Mechanical and Electrical Engineering, Nanjing University of Aeronautics & Astronautics, Nanjing, China
e-mail: guo_qintao@nuaa.edu.cn

It comes from known or unknown assumptions and simplifications, such as small deformation and large deformation model, linear elastic and elastic-plastic model, or Euler-Navier-Stokes equation [8]. By evaluating the accuracy of the supermodel of substructure, or by experimental modal analysis of substructure, the identification method of model form uncertainty for the overall structure is given.

10.2 Numerical Error Quantification

Quantization discretization error is to quantify the difference between theoretical solution and numerical solution. This paper is concerned with the modal frequency of the model, which gradually tends to a limit value as the discrete scale decreases. A posteriori estimation mixed order extrapolation based on Richardson extrapolation can be used to quantify the discrete error [9]. This method can satisfy the definite condition only if the results of three groups of different scales can be satisfied. The mixed order extrapolation formula is.

$$f = \frac{r^3 f_1 - r(r+1) f_2 + f_3}{(r+1)(r-1)^2} \quad (10.2)$$

Among them, f is the limit value when the discrete scale tends to zero, which is also the theoretical solution, f_1 represents discrete solutions of fine grids, f_2 represents discrete solutions of medium grids, f_3 represents discrete solutions of rough grids. The discrete characteristic relations of the three grids are:

$$h_3 = rh_2 = r^2 h_1, h_1 = h \quad (10.3)$$

Among them, h is the discrete characteristic quantity, that is the length of the grid, $r = 2$ represents mesh encryption factor. According to the analysis of Richardson's mixed order extrapolation formula, it is shown that f must be less than f_1 , and there is a relationship:

$$f - f_1 < f_1 - f_2 < f_2 - f_3 \quad (10.4)$$

The difference between theoretical value f_{exact} and f should satisfy the following relations:

$$|f - f_{exact}| < |f - f_1| \quad (10.5)$$

The absolute value symbol indicates that f_{exact} may be between f_1 and f , or less than f . This uncertainty is due to the lack of sufficient understanding of the theoretical solution, so it is necessary to take this uncertainty into account when quantifying the uncertainty. Therefore, the discrete error can be transformed into the uncertainty of physical quantities after the range of the difference between the theoretical solution and the limit value of the convergent solution is obtained. The scope of its uncertainty is:

$$-|f - f_1| < f - f_{exact} < |f - f_1| \quad (10.6)$$

Uncertainty U_1 is:

$$U_1 = 2|f - f_1| \quad (10.7)$$

10.3 Model Form Error Estimation (ϵ_{model})

Suppose the real response of the physical system is y_{true} , the measured response value is y_{obs} , the experimental measurement error is ϵ_{om} , the predicted value of the model is y_{pred} , the response value calculated by simulation is y_c . Then there should be the following relationships [7]:

$$y_{true} = y_{pred} + \epsilon_{num} + \epsilon_{model} \quad (10.8)$$

$$y_{true} = y_{obs} + \epsilon_{om} \quad (10.9)$$

$$y_{pred} + \epsilon_{num} + \epsilon_{model} = y_{obs} + \epsilon_{om} \quad (10.10)$$

$$y_c = y_{pred} + \epsilon_{num} \quad (10.11)$$

$$\epsilon_{model} = y_{obs} + \epsilon_{om} - y_c \quad (10.12)$$

But most of the time we need to quantify ϵ_{model} to predict y_{obs} . Here we first quantify model uncertainty ϵ_{model} of the substructures by using a parameterization equivalent analysis method which modulus E of the substructure can be taken as a virtual parameter. By statistics sampling the sample of the substructure modal parameters can obtain a mean E_0 and its standard deviation. Variance of E_0 is used to describe the model form error to a certain degree of perturbation (random distribution). Our goal, of course, is not just precisely reproduce the experimental measurements by studying and calibrating the parameters. Instead, our goal is to build numerical models that allow predictive responses to encompass uncertain experimental measurements.

10.4 Analysis

The research object of this paper is an aluminum frame consisting of a bottom plate, a top beam, two columns and four angles, as shown in the Fig. 10.1. The width of the beam and the side columns is 50.8 mm and the width of the floor is 152.4 mm. The beam and column, the column and the floor are connected by L-shaped angle steel. The angles and beams and columns are connected by bolts with a diameter of 12.7 mm and a length of 25.4 mm. The connection to the base plate is four 10–24 socket cap screws with a length of 12.7 mm.

The simulation model of the aluminum frame is shown in the Fig. 10.2, and the bolt connection is modeled by the bush elements as depicted in Fig. 10.3.

In this paper, we only study the modal response of the frame and each substructure. By quantifying the numerical error and model form error of each substructure, the prediction response of the whole frame structure can envelop the experimental measurement with uncertainty.

The numerical error of frame structure is quantified based on Richardson extrapolation method. The Initial mesh size of each structure size is 1 mm, and three grids with grid sizes of 1.25 mm, 2.5 mm, and 5 mm are sequentially created. The same mesh density is used for each seed structure, that is, the beam, the side column, and the bottom plate. The variation of the modal frequency difference for each structure as the mesh density increases is shown in the Fig. 10.4 [10].

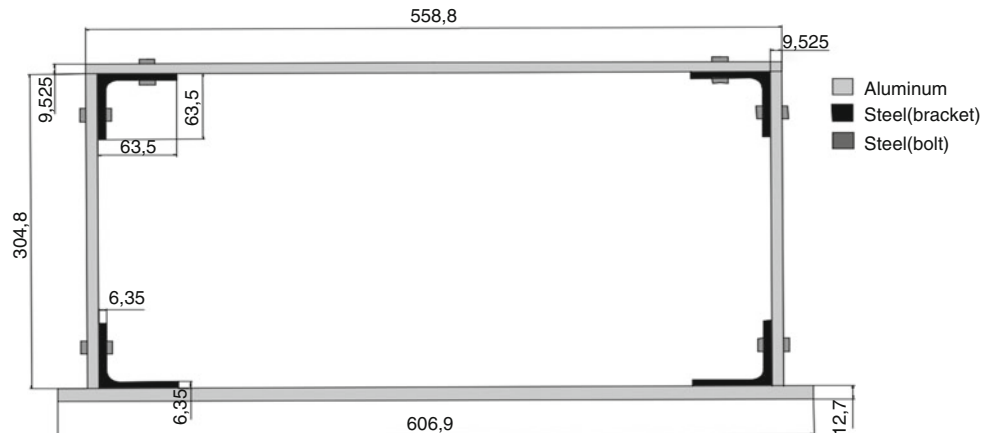


Fig. 10.1 The schematics of the portal frame structure with dimension in millimeter

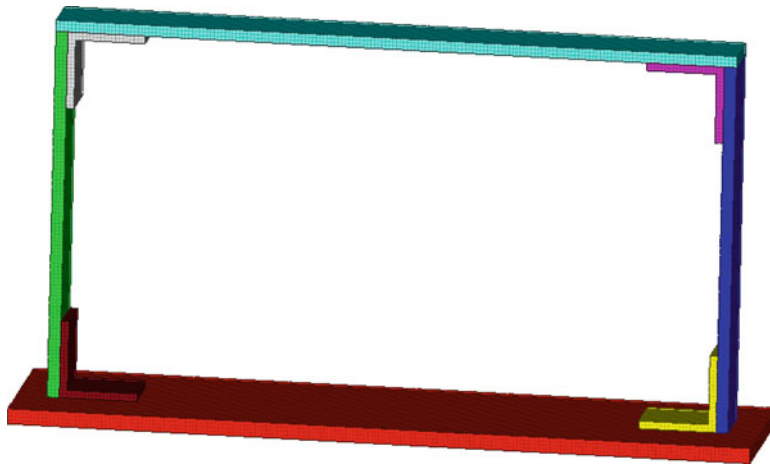


Fig. 10.2 The FEM of the portal frame structure

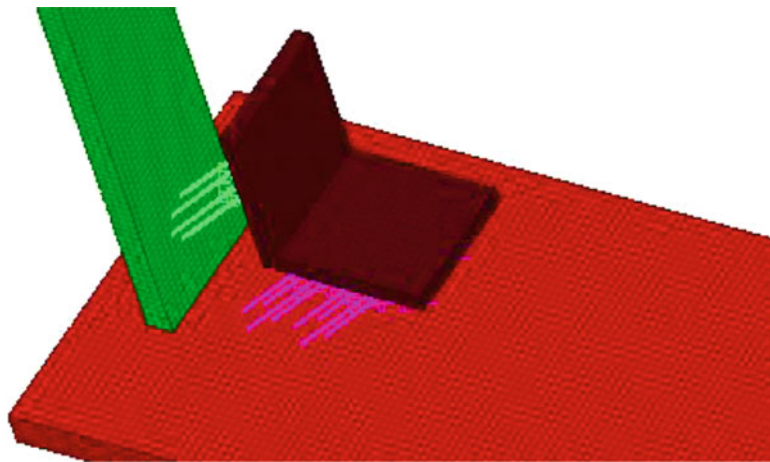


Fig. 10.3 The bolted connections of FEM are expressed by Bush elements

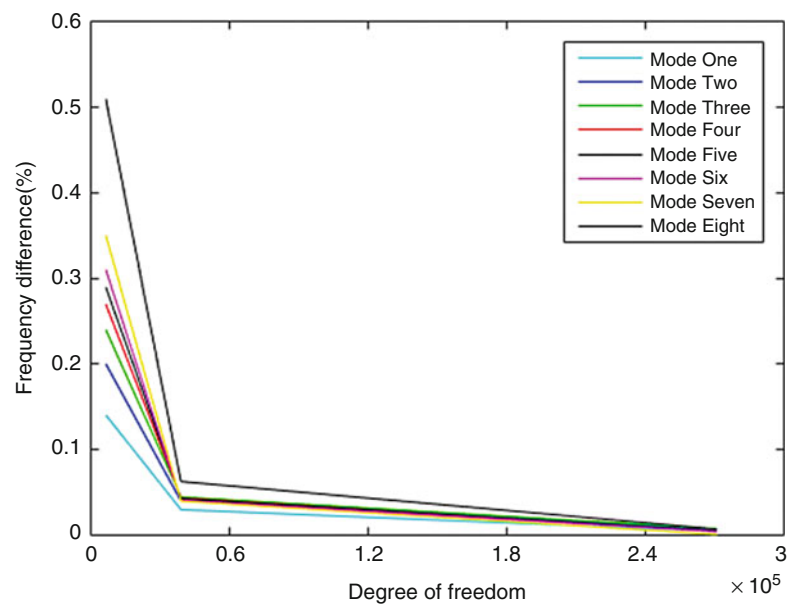


Fig. 10.4 The frequency difference of the structure varies with the degree of freedom of the model

Considering the size of the model and the number of degrees of freedom of the model, the substructures in the frame structure are selected from the grid density of 2.5 mm as the prediction model. The numerical error of this mesh density is also the uncertainty of the discrete error quantized by Richardson extrapolation as shown in the Table 10.1.

The samples of each substructure were calculated, and the same mesh density was used for each sample. The mean and standard deviation of the elastic modulus per substructure are shown in the following Table 10.2.

Studies have shown that in the overall experiment of the frame, the torque of the bolt will affect the stiffness of the overall frame order, thus changing the resonant frequency. The bolt tightening sequence and the tightening method also have an effect on the experimental results, but the impact is small and can be ignored. The measurement results of the overall experiment under different torques are displayed in Table 10.3 [11], the modes are depicted in Figs. 10.5, 10.6, 10.7, and 10.8.

For the connecting part of the frame bolts model were built with a bush element, which has six parameters, three translational stiffness parameters, and three rotational stiffness parameters. The rotational stiffness parameter has little effect on the response of the frame. The axial stiffness k_z in the translational stiffness parameter is the main parameter affecting its mode, and the shear stiffness k_s has some effect on the mode. According to the change of bolt torque in the experiment and identification results, the axial stiffness $k_z \in [110, 1 \times 10^7]$ and the shear stiffness $k_s \in [600, 1 \times 10^7]$ are also used to describe the experiment in the model and the variance in the torque of the bolt. In the model prediction of the overall

Table 10.1 Numerical error of each mode of substructure (modal frequency %)

Substructure	First order	Second order	Third order	Fourth order	Fifth order	Sixth order
Bottom plate	0.02	0.42	0.14	0.78	0.28	1.2
Side column	0.34	1	1.8	2.8	2.4	1.4
Beam	0.02	0.04	0.06	1.3	0	2.6

Table 10.2 The quantification of model form error for substructure (virtual modulus Mpa)

Substructure	Mean	Standard deviation	Relative uncertainty (%)
Bottom plate	65,000	2080	3.2
Side column	65,360	1844.885	3.2
Beam	69,167.5	1394.742	1.7

Table 10.3 Overall ranges of resonant frequency variability (from measurement)

Torque level(Nm)	Shearing		Torsion		Out-bending		In-bending	
	Low	High	Low	High	Low	High	Low	High
4.52	58.8	63.0	97.5	99.0	102	104	170	178
9.04	62.8	66.6	99.8	101	104	105	180	178
18.08	66.3	71.6	102.0	103	105	106	183	193

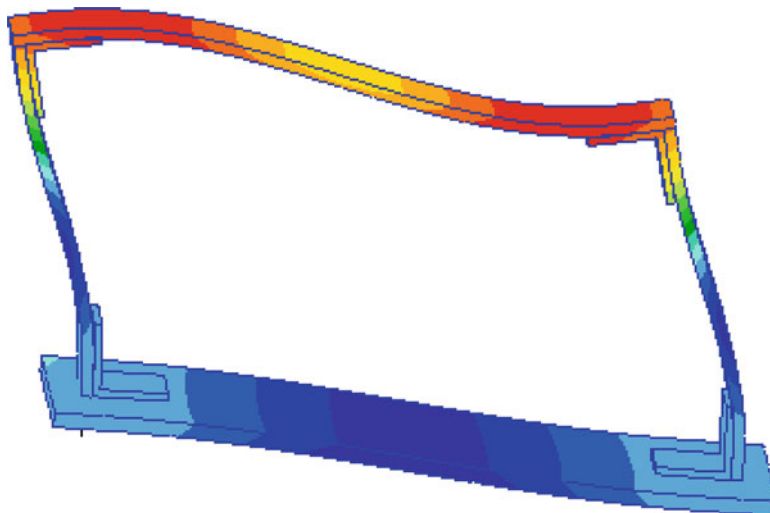


Fig. 10.5 The first mode frequency of the portal frame structure is 67.217 Hz

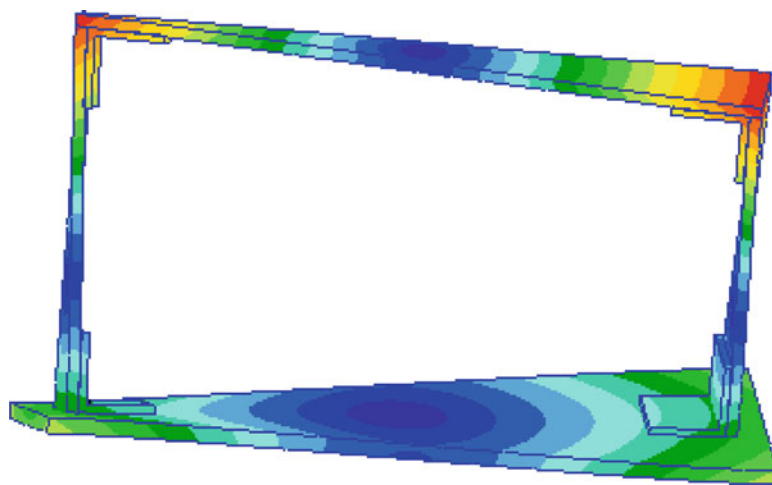


Fig. 10.6 The second mode frequency of the portal frame structure is 97.254 HZ

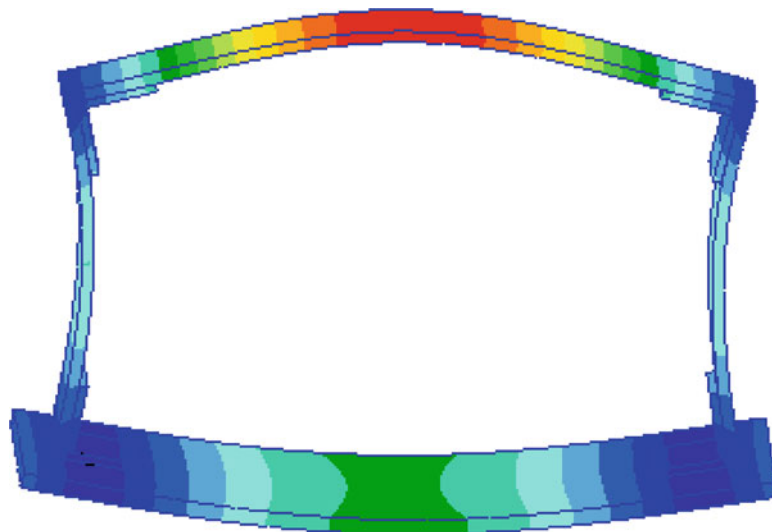


Fig. 10.7 The third mode frequency of the portal frame structure is 105.88 HZ

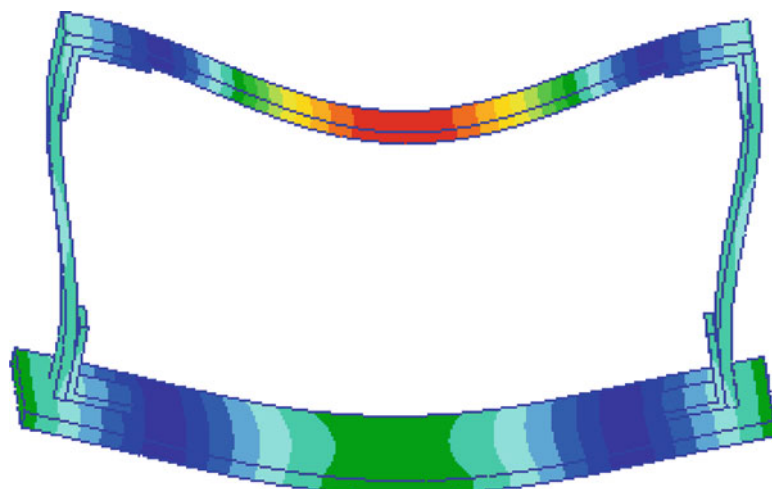


Fig. 10.8 The fourth mode frequency of the portal frame structure is 185.01 HZ

Table 10.4 Ranges of measured and predicted resonant frequencies of the first four modes

Mode	Measurements		Prediction	
	Bounds	Range	Bounds	Range
1	58.8–71.6	12.8	55.9–72.1	16.2
2	97.5–103.0	5.5	91.6–103.1	11.5
3	102.0–106.0	4.0	98.2–110.9	12.7
4	170.0–193.0	23.0	160.5–196.5	36

frame, the parameters of the angle steel are fixed. When the elastic modulus of the substructure and the translational stiffness of the bolt change in the above quantitative range, the prediction range of the first four-order model is compared with the experimental variation range as shown in Table 10.4.

10.5 Conclusion

The numerical analysis of the first four order modes of frame structures is validated in this paper. The numerical uncertainties of substructures, the model form uncertainties and the parameter uncertainties of bolted joints are quantified respectively. The quantification of the numerical uncertainty was given directly by Richardson extrapolation; The uncertainty measurement of the model form is conducted by the parameterization of the elastic modulus of the substructure, and were shown as the mean and standard deviation of the modulus; the parameters of bolted connection structure was given by the difference of the modal parameter. Finally, the modal range predicted by the model envelops the experimental value of uncertainty. This quantitative method makes the prediction of the model more reliable and accurate.

Acknowledgements The study in this paper was supported by National Key Laboratory of Science and Technology on Helicopter Transmission in NUAA. And this study also was supported by NSAF (Grant No. U1530122).

References

1. Sankararaman, S., Mahadevan, S.: Integration of model verification, validation, and calibration for uncertainty quantification in engineering systems. *Reliab. Eng. Syst. Safe.* **138**(7), 194–209 (2015)
2. Urbina, A., Mahadevan, S., Paez, T.L.: Quantification of margins and uncertainties of complex systems in the presence of aleatoric and epistemic uncertainty. *Reliab. Eng. Syst. Safe.* **96**(9), 1114–1125 (2011)
3. Sankararaman, S., Ling, Y., Mahadevan, S.: Uncertainty quantification and model validation of fatigue crack growth prediction. *Eng. Fract. Mech.* **78**(7), 1487–1504 (2011)
4. Guo, Q.T., Zhang, L.M.: Identification of the mechanical joint parameters with model uncertainty. *Chin. J. Aeronaut.* **18**(1), 47–52 (2005)
5. Ma, Z., Ying, Y., Zhu, J.: QMU authentication method and its implementation path. *Nucl. Sci. Eng.* **29**(1), 1–9 (2009)
6. Ma, Z., Zheng, W., Yin, J., et al.: Quantitative method for detonation simulation uncertainty. *Chin. J. Comput. Phys.* **28**(1), 66–74 (2011)
7. Liang, B.: Title page for ETD etd-08162010-154212. *Int. J. Uncertain. Quantif.* **1**(2), 149–150 (2011)
8. Nannapaneni, S., Hu, Z., Mahadevan, S.: Uncertainty quantification in reliability estimation with limit state surrogates. *Struct. Multidiscip. Optim.* **54**(6), 1509–1526 (2016)
9. Yin, J., Ma, Z., Sun, Y.: A Posteriori Estimation of Discrete Errors in Numerical Simulation. China Mechanics Conference 2011 and Qian Xuesen's 100th Anniversary Commemorative Meeting, 2011
10. Liu, Z.: Dynamics Modeling and Characterization of an Aeroengine Coupling. Nanjing University of Aeronautics and Astronautics, Nanjing (2017)
11. Gonzales, L.M., Hall, T.M., Buren, K.L.V., et al.: Quantification of prediction bounds caused by model form uncertainty. *Model Validation and Uncertainty Quantification*, Volume 3. Springer International Publishing, 2014, pp. 53–66



Chapter 11

Characteristic Analysis of Modified Dolly Test: A Sensitivity Study of Initial Conditions on Rollover Outcomes

Mohammad Reza Seyedi, Sungmoon Jung, and Jerzy Wekezer

Abstract Rollover crashes are known as the most dangerous type of accidents throughout the world. They are associated with multi-directional velocities and accelerations which creates a complex dynamic behavior of the vehicle. Several experimental and numerical methods have been used to gain a better understanding of kinematics of the vehicle and occupants during the rollover crashes. Due to the complex nature of the rollover, any change in the initial conditions may significantly influence the rollover outcomes. The main goal of this study is to assess the effects of initial conditions on dynamic responses of the bus using a modified dolly rollover test procedure. Since the experimental rollover test is very expensive and to decrease the computational costs, the numerical model of cutaway bus was developed using lumped mass-spring-damper in PC-Crash software. First, the model was validated using the experimental data. Then, a series of simulations have been conducted with considering various initial conditions (inputs) such as initial velocity, friction of rollover surface, height of bus's CG, and initial roll angle. The range of initial variables were selected based on Latin Hypercube Sampling (LHS) with uniform distribution. The simulation results were used to build the surrogate model using Kriging model for each rollover outcomes (outputs) including number of quarter turns, roll distance, deceleration rate, and maximum impact force. The sensitivity of the model to 400 set of input data was computed in MATLAB. The results of the sensitivity analysis indicate that the number of quarter turns and roll distance was highly affected by the initial velocity of the bus. Furthermore, the deceleration rate controlled mainly by friction and initial velocity and a negative correlation with the initial roll rate. No strong correlation between maximum impact force and any input parameters was observed. This led us to perform further research on exploring the effects of dynamic characteristics of the bus on maximum impact force.

Keywords Modified dolly rollover test · PC-Crash · Sensitivity analysis · Kriging model

11.1 Introduction

Rollover accidents are reported as the most dangerous crash mode among road traffic accidents in terms of the fatality rate [1]. Rollover crashes have a complex kinematics because they are usually multidirectional and associated with multiple impacts. The development of hardware and software helped researchers to conduct the more accurate experimental and computer simulation of rollover crashes. Therefore, various methods have been developed to replicate the actual kinematics of the vehicle and occupants during the rollover in laboratory conditions [2]. Among available test procedures, dolly rollover test is one of the most widely used test procedures for the safety assessment of the vehicle. In a typical dolly test procedure, the vehicle placed in the tilted cart (23°) and moved laterally to reach the desired velocity (part c in Fig. 11.1). Then the cart suddenly stopped and the vehicle started to roll over a flat surface (test bed can be a soil, concrete or asphalt). Also, depends on the cart geometry, a vehicle can be released with different initial slope, height from the ground, and initial roll rates (Fig. 11.1). Find the effects of test's parameter on the kinematics of the vehicle is a very pivotal step to improve the reliability and accuracy of results in rollover safety assessment.

Despite increasing the computational capabilities, it is fairly costly to conduct sensitivity studies using finite element analysis (FEA) for rollover crash simulation. For instance, with our current hardware, simulating the FE model of dolly rollover for only 3 s takes more than 72 h to finish. Therefore, the kinematics of the vehicle was simulated using lumped-mass-spring-damper model in PC-Crash. The objective of this study is to compute the sensitivity of the rollover outcomes to the initial conditions of the test. First, the dynamic characteristics of the actual cutaway bus such as suspension and

M. R. Seyedi (✉) · S. Jung · J. Wekezer

Department of Civil and Environmental Engineering, Florida A&M University—Florida State University College of Engineering, Tallahassee, FL, USA

e-mail: reza.seyedi@fsu.edu

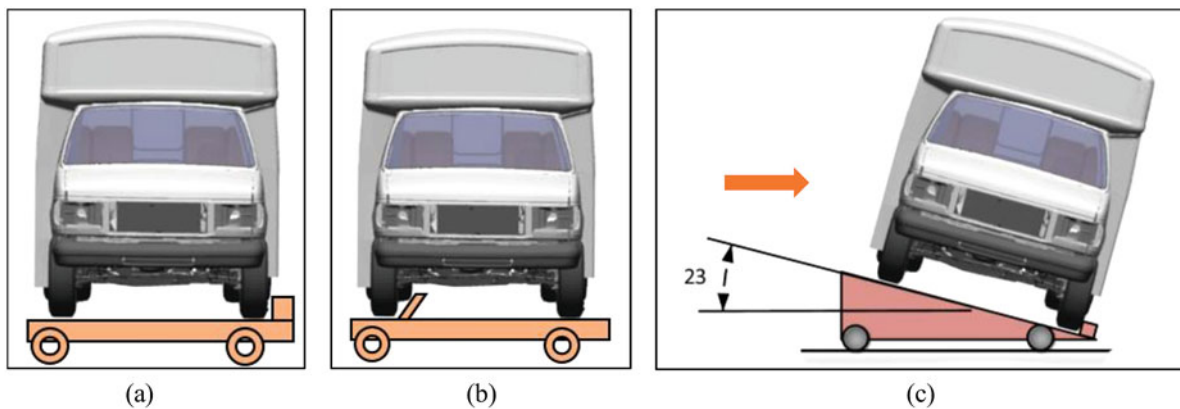


Fig. 11.1 Different platforms to conduct the rollover accident: (a) rollover sled test [3]; (b) Modified dolly rollover for heavy vehicles [4]; (c) Standard dolly test

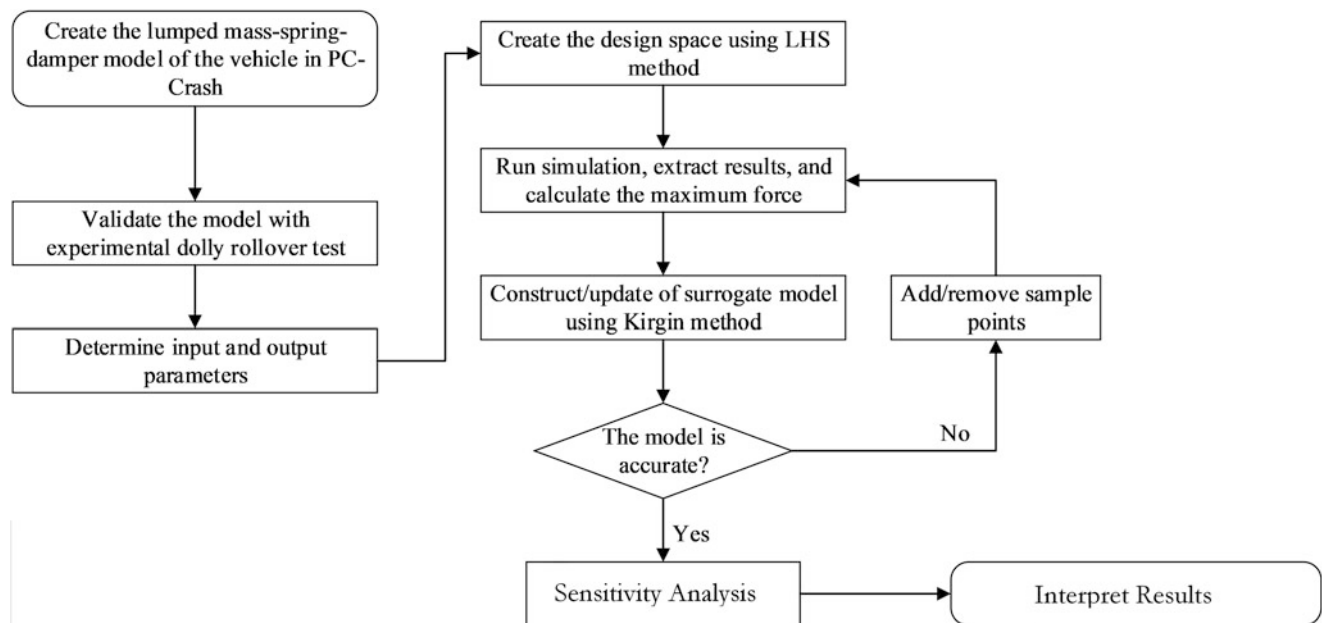


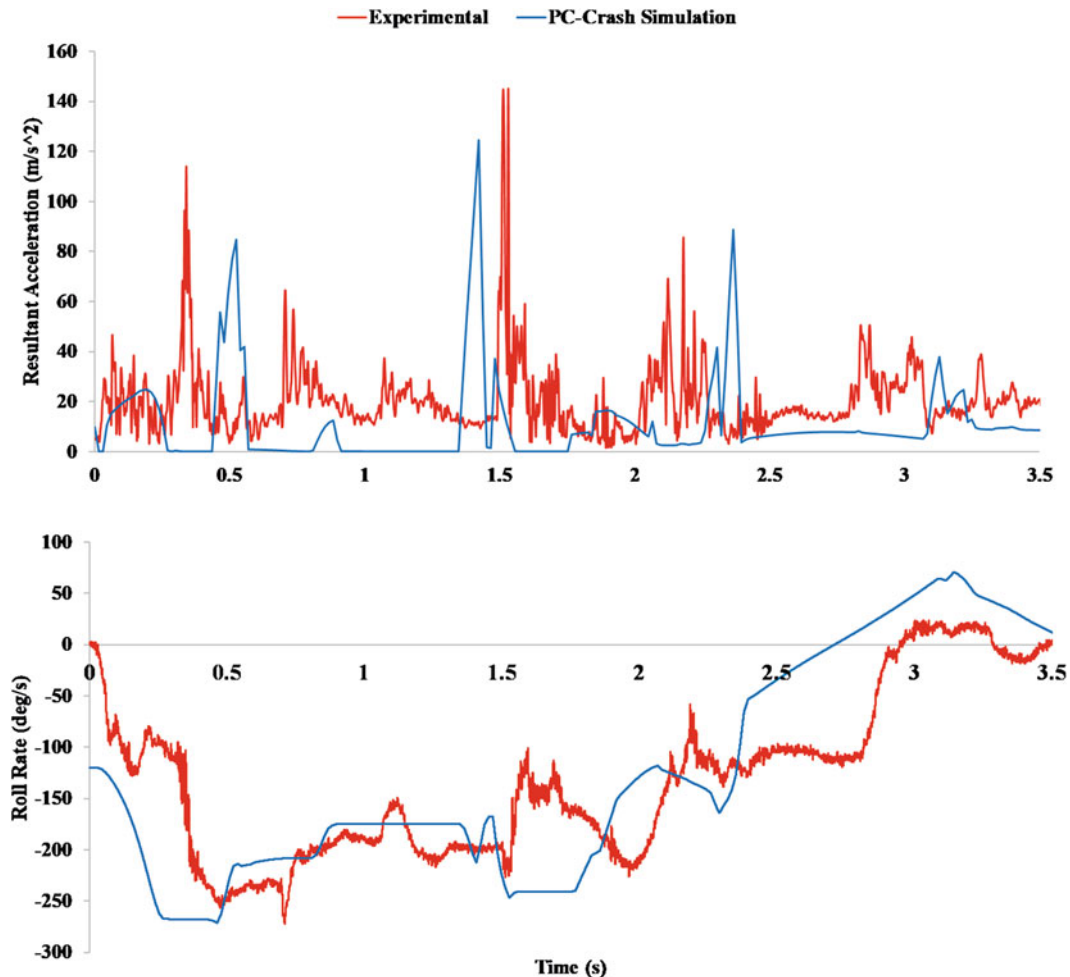
Fig. 11.2 The sensitivity analysis process

inertial properties, the center of the gravity (COG), and overall dimensions were extracted. Then, the data were used to build the dynamic model of the bus in PC-Crash software. The details about the theory of dynamic model and its accuracy and reliability can be found in several studies [5–10]. Next, to validate the model, the results from PC-Crash included overall motion, a number of quarter turns (N_q), roll distance (R_d), and angular rates were compared with similar experimental results. Figure 11.2 shows the steps that have been followed to perform the sensitivity analysis using the simulation results.

The input parameters with proper range and uniform distribution were selected to create the design space using Latin Hypercube Sampling (LHS). Among various available surrogate models [11–13], Kriging method was used to build the response surfaces for all outputs. Finally, after checking the accuracy of the model the sensitivity of selected rollover outcomes to the input parameters was evaluated by computing the standardized regression correlation (SRC). By comparing the results of SA given by these methods, this study provides an insight into the relationship between initial conditions of dolly rollover test and rollover outcomes.

Table 11.1 Vehicle specifications

Item	Value
Total weight (loaded) (kg)	4788
Wheelbase (m)	3.51
Overall dimensions (m)	H=2.7, L=6.1, W=2.2
Inertial properties (kg. m ²)	I _{roll} =3897, I _{yaw} =12992, I _{pitch} =12992

**Fig. 11.3** Comparison of experimental and PC-Crash results

11.2 Dynamic Model of the Bus

The details of the vehicle specifications are shown in Table 11.1. The dynamic components of the bus were modeled in PC-Crash and the similar body was assigned to the model only for a visual purpose. This software calculates the rigid body motion of the vehicle based on the 3D kinetic vehicle model. The data from the library was also used to simulate the tires using TM-Easy model.

An experimental dolly rollover test was performed using specific initial conditions is shown in Table 11.3 in Appendix. The data were then used to validate the model. The dominant movement of the bus in a dolly rollover test is usually rotational movement around the longitudinal axis (roll) and translational movement in a lateral direction. Therefore, the roll rate and resultant acceleration resulted from the numerical model were compared with corresponded experimental data (Fig. 11.3).

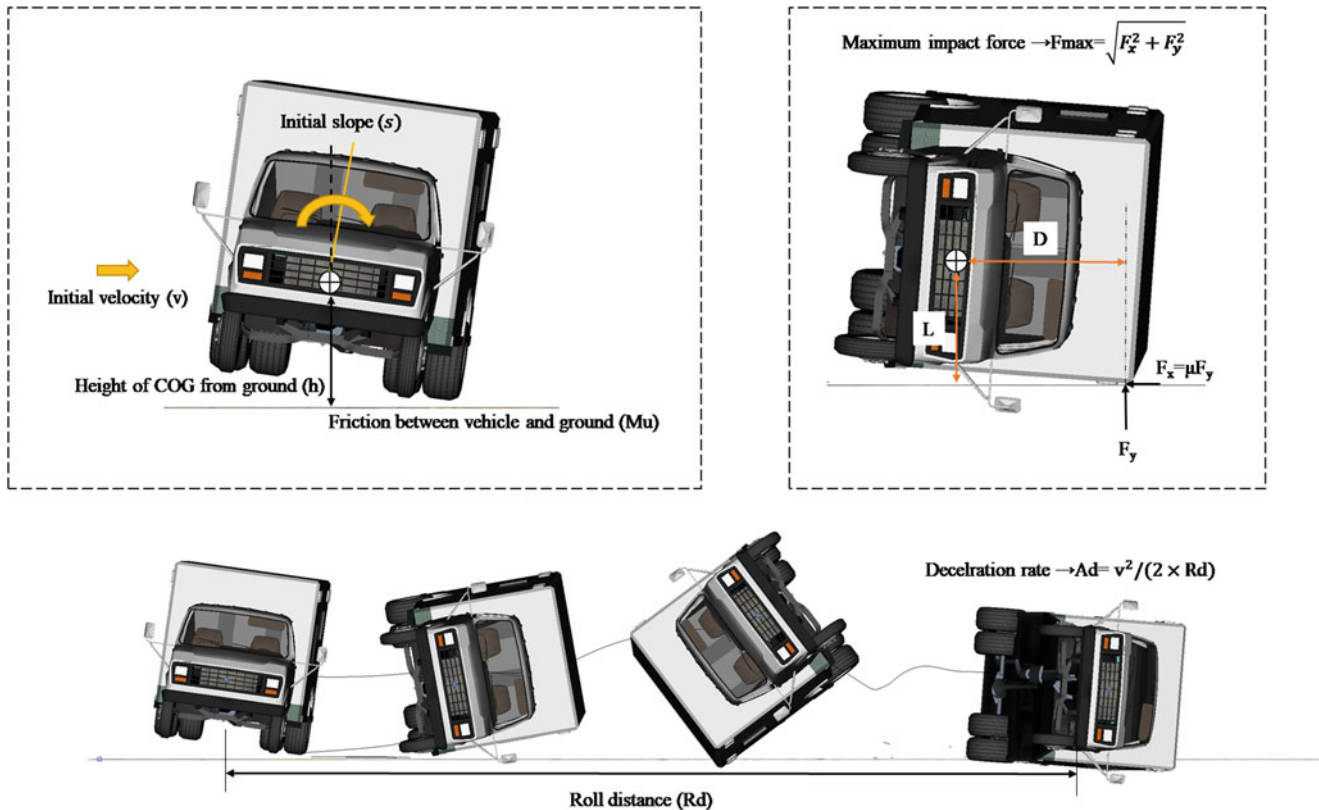


Fig. 11.4 Details of input and output parameters selected in a modified dolly rollover test

Different factors contributed to the discrepancies between the numerical and experimental results. First, it can be explained by the rigid behavior of the bus in the simulation analysis. In the experimental test, the deformation of the bus can significantly affect the overall kinematics of the bus while in the numerical model the bus was rigid. Also, the friction is not constant during the rollover, because contacts happened between different parts of the bus and ground. Furthermore, because the cart was not modeled in this simulation, the initial roll rate 120 deg/s at $t = 0.25$ s was used to create actual rollover condition [14]. The overall motion of the bus from both experimental and numerical analysis was compared in Appendix Fig. 11.6. The total rotation of the bus was the same as the experimental data (5 quarter turns–450°). This quantitative and qualitative comparison of the numerical results in PC-Crash and experimental dolly indicate that the model is sufficiently reliable and accurate enough to build the surrogate model.

11.3 Sensitivity Analysis Using a Surrogate Model

In this study, since we were not able to perform a direct coupling between PC-Crash and mathematical model (written in MATLAB), the surrogate model was used to perform the sensitivity analysis. The initial position and orientation of the bus, friction, and initial rotational and translational velocities were selected as input parameters. The selected input and output parameters are shown in Fig. 11.4. The approximate maximum impact force and deceleration rate were also found to be significant parameters in rollover outcomes [15]. To extract the maximum force, some assumptions were made. First, the impact was assumed to occur in a single plane. Second, the impact force applied at a single point where we can use Newton's second law equation to extract forces. Then we assume that the friction force is the only horizontal force that applied to the vehicle [16]:

$$\sum M_G = I_G \times \alpha \rightarrow F_y \cdot D - \mu \cdot F_y \cdot L = I \times \alpha \rightarrow F_y = I \times \alpha / (D - \mu \cdot L) \quad (11.1)$$

M: The net torque

I: Moments of inertia in roll direction around COG

A: Angular acceleration

To define time and orientation of the bus at maximum impact force, the position of the bus at the maximum angular acceleration was determined. As a result, depending on the orientation of the bus, the maximum impact force applied to either roof or tires. Based on Eq. (11.1), in some cases, the value of the denominator reaches zero which can significantly influence the final value of the calculated force. This is because friction value assumed to be coulomb friction with no relative velocity between vehicle's body and ground whereas in some cases it would be less than coulomb friction. To prevent this situation, these cases were removed from sample points.

The LHS method was used to generate optimal sample points. This sampling method creates a uniform distribution of optimal points which can minimize the bias part of the mean square error. In the present study, a uniform distribution for five input parameters was selected with a certain range (Table 11.2).

The range of each input parameter was chosen based on different experimental values that were used in rollover tests. For example, the lowest value for friction represents the flat wet concrete where the upper bound represent the raked concrete surface [17]. The maximum 23° are currently used for the initial slope of the passenger cars and 0° for the rollover sled test. For heavy vehicles, due to the high amount of crash energy that dolly test produced, usually the vehicle placed on the flat cart without tilting. The maximum height 0.8 m was chosen from the tilt table test procedure to show the effects of height on output parameters. For each set of input parameters, the output parameters from PC-Crash simulation was extracted and considered as "training" points for Kriging model formation. We used R Squared to evaluate the accuracies of the metamodels (see [11]). The results of the accuracy evaluation are shown in Fig. 11.7. It should be noted that for certain initial conditions, the number of quarter turns was equal to zero which indicates that the rollover did not happen (see Fig. 11.7).

Here, the global sensitivity analysis was performed using the constructed surrogate model for each output parameters in MATLAB. The sensitivity analysis investigated in this study include Standardized Regression Coefficient (SRC). SRC gives the strength of the correlation between output and input variables [18]. In Fig. 11.8, the output parameters for 400 sample points were plotted with respect to all variables. The results were then used to compute the SRC and reveal the correlation between initial conditions and corresponded rollover outcomes (Fig. 11.5).

Table 11.2 Selected input parameters to build the Kriging model

Item	Range	Distribution
Initial velocity (m/s)	[0–30]	Uniform
Height (m)	[0–0.8]	Uniform
Orientation (degree)	[0–23]	Uniform
Initial roll rate (deg/s)	[0–200]	Uniform
Friction	[0.2–0.9]	Uniform

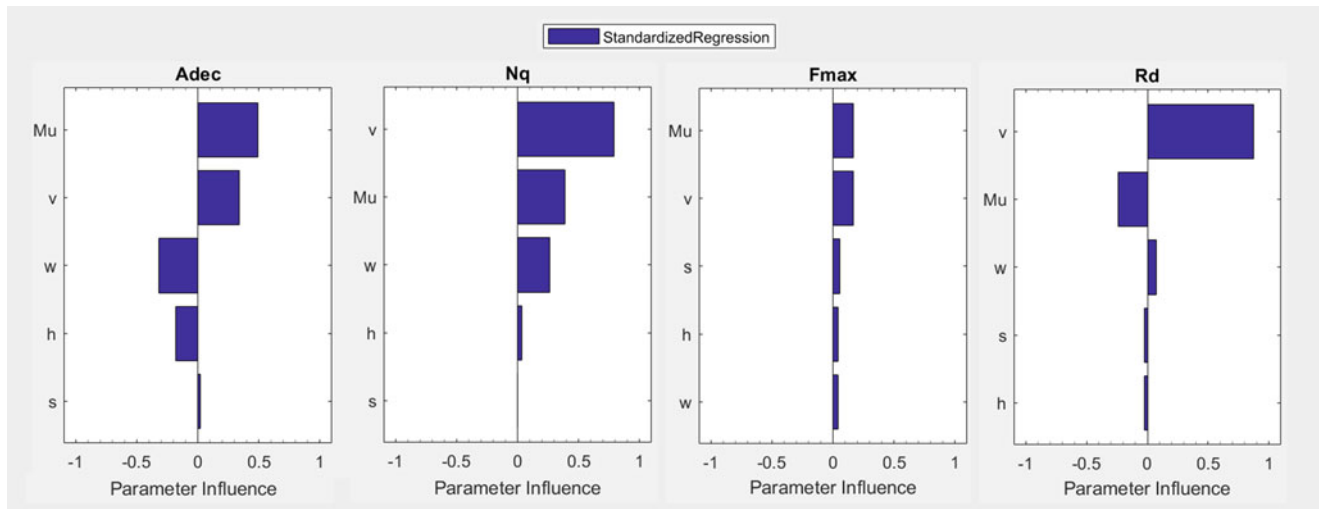


Fig. 11.5 The SRC results for each output parameter

11.4 Summary and Conclusion

Initial conditions of the vehicle can have significant effects on rollover outcomes. To quantify the sensitivity of the rollover outcomes to test parameters, using high fidelity models (i.e. FE model) is computationally expensive. For instance, a rollover crash event takes a longer time (seconds) than other crash modes (millisecond) which has a profound effect on computational costs. Therefore, the lumped-mass-spring-damper method was used to characterize the kinematics of the vehicle in a dolly rollover test. Then, based on the LHS method, a set of parameters for initial conditions have been selected to create different rollover scenarios. Several simulations have been conducted and their results were used to construct the surrogate model. Finally, the sensitivity of the rollover outcomes to their initial condition was computed.

The results indicate that the number of quarter turns and roll distance are highly affected by the initial velocity such that as the initial velocity increased both N_q and R_d went up. The deceleration rate (A_d) was mainly controlled by friction and velocity. Also, the initial roll rate has a negative correlation coefficient on A_d which means that the A_d will decrease when the initial roll rate goes up. The maximum impact force (F_{max}) was not significantly affected by input parameters. It should be noted that uncertainties of the assumptions that we made to calculate the maximum force and the rigidity of the body in simulations might influence the outcome. However, the results may indicate the possibility that the F_{max} was mainly affected by vehicle characteristics rather than the test parameters. The total weight, moment of inertia, and suspension properties can be considered as important factors in maximum impact force.

Appendix

Table 11.3 The initial condition of the experimental dolly rollover test

Item	Value
Initial velocity (m/s)	11.2
Initial slop (deg)	5
Initial roll rate (deg/s) ^a	120
Friction (racked concrete)	0.85
Initial height (m)	0.3

^aExtracted from Fig. 11.3

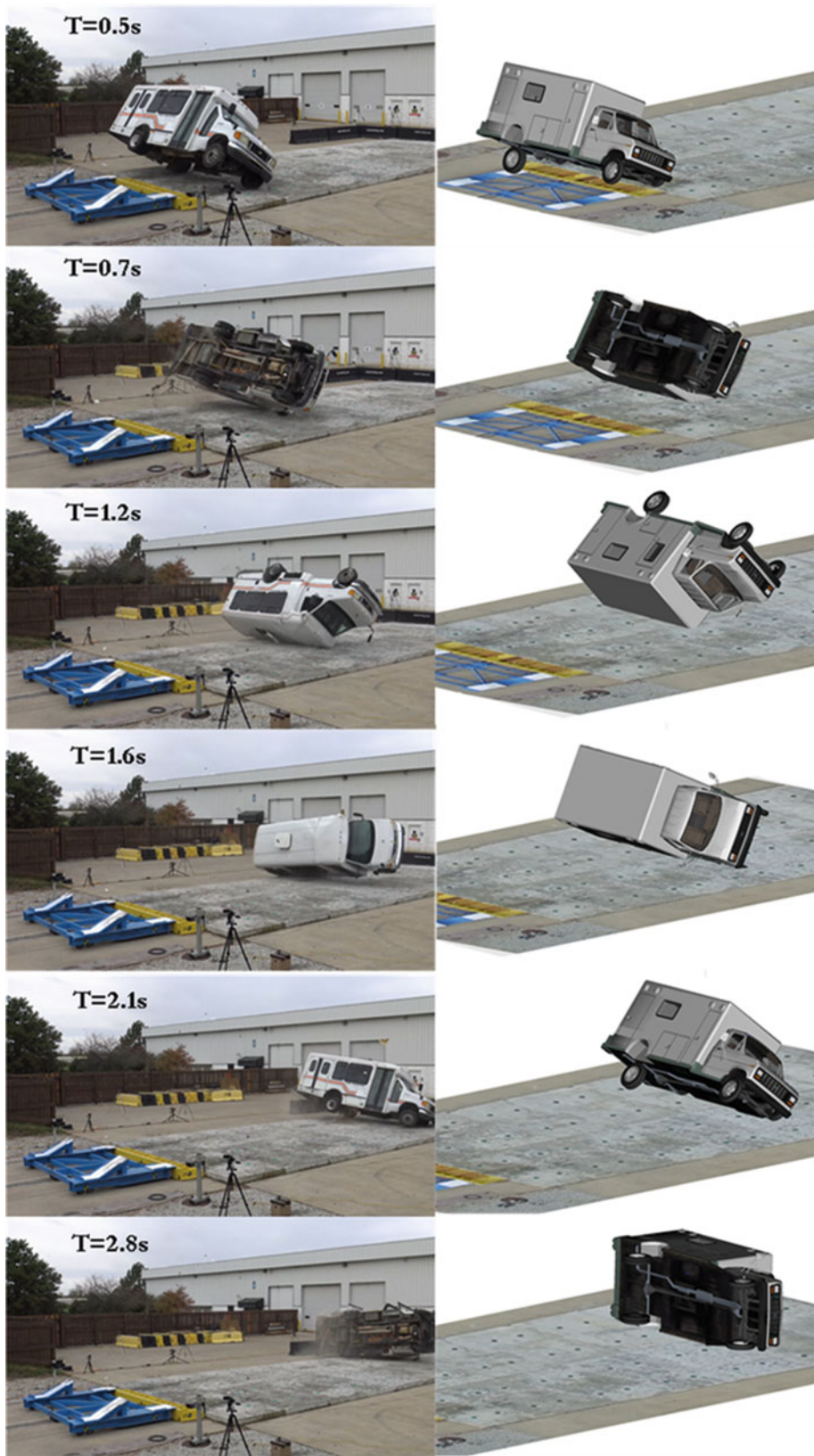


Fig. 11.6 Comparison of vehicle's motion resulted from PC-Crash and experimental rollover test

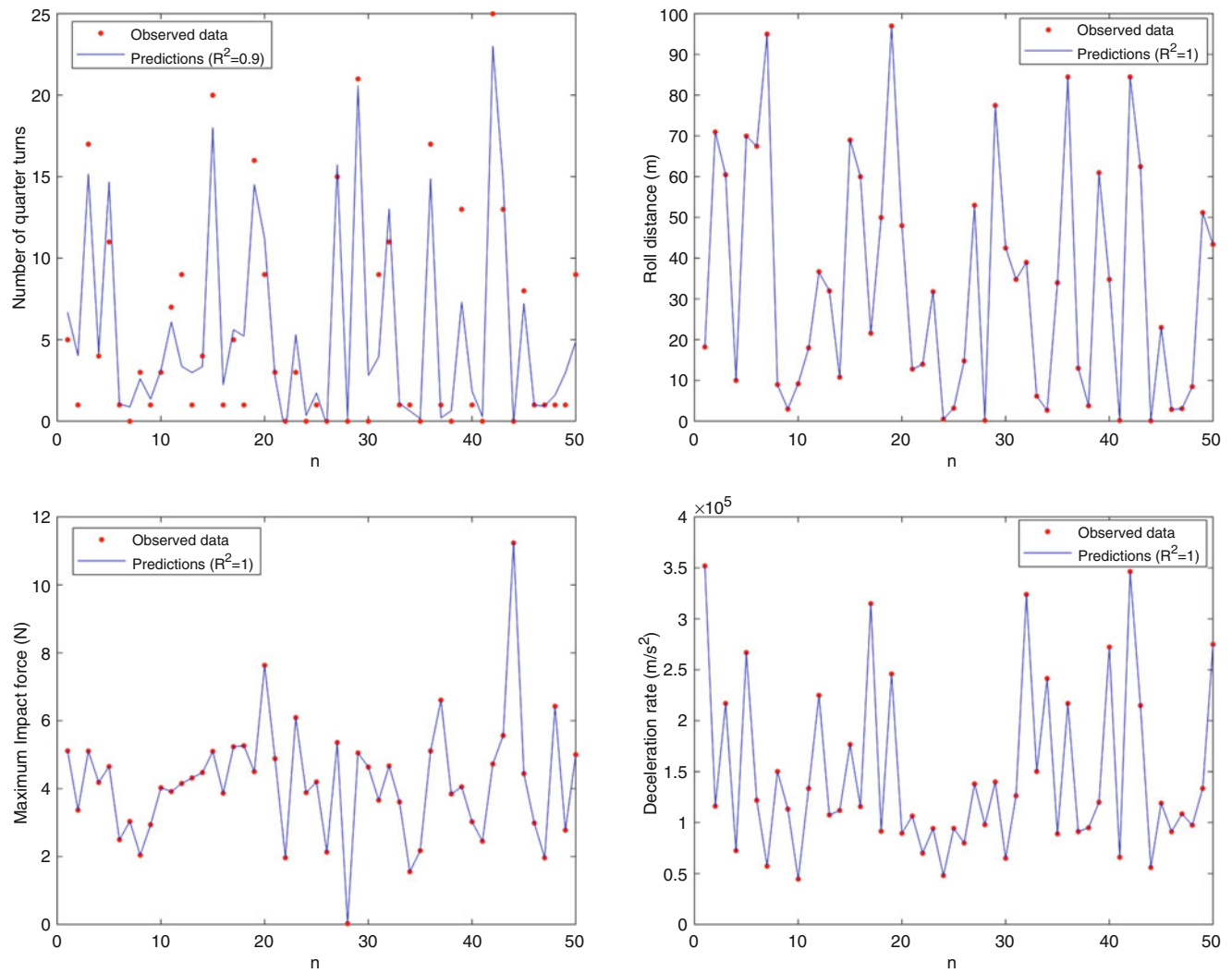


Fig. 11.7 Kriging model for predicting the output parameters and its Accuracy

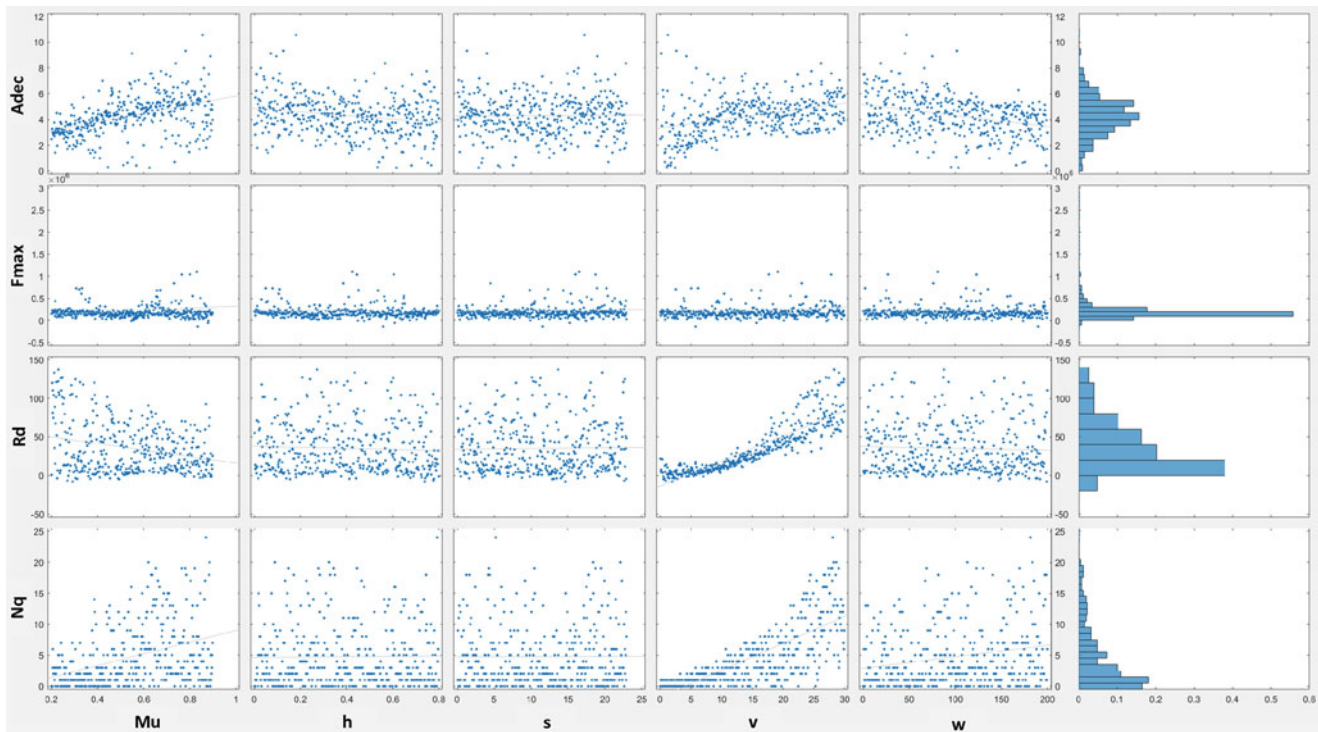


Fig. 11.8 The scatter plot of the output parameters (decoration (A_{dec}), maximum impact force (F_{max}), roll distance (R_d), number of quarter turns (N_q) with units of m/s^2 , N , m respectively) for 400 set of input parameters

References

1. NHTSA, "Traffic safety facts 2012: A compilation of motor vehicle crash data from the fatality analysis reporting system and the general estimates system. In: Report No. DOT HS, 2012, vol. 812
2. Chou, C.C., McCoy, R.W., Le, J.: A literature review of rollover test methodologies. *Int. J. Veh. Saf.* **1**(1–3), 200–237 (2005)
3. Stein, D.J., Rossey, M.P., Jarvis, A.U., Davis, M.G., BÖrgman, J.: Rollover sled test device and method, ed: Google Patents (2003)
4. Hu, J. et al.: Development of A New Dynamic Rollover Test Methodology for Heavy Vehicles. SAE Technical Paper 0148-7191 (2017)
5. Steffan, H., Moser, A.: The Collision and Trajectory Models of PC-CRASH. SAE Technical Paper 0148-7191 (1996)
6. Steffan, H., Moser, A., Geigl, B.C., Motomiya, Y.: Validation of the Coupled PC-CRASH-MADYMO Occupant Simulation Model. SAE Technical Paper 0148-7191 (2000)
7. Schran, R.: Accident Analysis and Evaluation of PC-Crash. Technical Report, Chalmers University of Technology, Department Machine and Vehicle Systems, Sweden (2005)
8. Han, I., Rho, K.: Characteristic analysis of vehicle rollover accidents: rollover scenarios and prediction/warning. *Int. J. Automot. Technol.* **18**(3), 451–461 (2017)
9. Rose, N.A., Kineticorp, L.L.C., Beauchamp, G.: Reconstruction and Analysis of Rollover Crashes of Light Vehicles. Report No. 377, Society of Automotive Engineers Course C1502- (2017). <http://kineticorp.com/rose-reconstruction-of-rollovers-chapter-3.pdf>
10. Rose, N.A., Carter, N.: An Analytical Review and Extension of Two Decades of Research Related to PC-Crash Simulation Software. SAE Technical Paper, no. 2018-01, p. 0523 (2018)
11. Jin, R., Chen, W., Simpson, T.W.: Comparative studies of metamodelling techniques under multiple modelling criteria. *Struct. Multidiscip. Optim.* **23**(1), 1–13 (2001)
12. Yang, R., Wang, N., Tho, C., Bobineau, J., Wang, B.: Metamodelling development for vehicle frontal impact simulation. *J. Mech. Des.* **127**(5), 1014–1020 (2005)
13. Fang, J., Sun, G., Qiu, N., Kim, N.H., Li, Q.: On design optimization for structural crashworthiness and its state of the art. *Struct. Multidiscip. Optim.* **55**(3), 1091–1119 (2017)
14. Rose, N.A., Beauchamp, G.: Analysis of a Dolly Rollover with PC-Crash. SAE Technical Paper 0148-7191 (2009)
15. Carter, J.W., Luepke, P., Henry, K.C., Germane, G.J., Smith, J.W.: Rollover dynamics: an exploration of the fundamentals. *SAE Int. J. Passeng. Cars Mech. Syst.* **1**(2008-01-0172), 80–104 (2008)
16. Rose, N.A., Beauchamp, G.: Development of a variable deceleration rate approach to rollover crash reconstruction. *SAE Int. J. Passeng. Cars Mech. Syst.* **2**(2009-01-0093), 308–332 (2009)
17. Warner, C.Y., Smith, G.C., James, M.B., Germane, G.J.: Friction applications in accident reconstruction. SAE Technical Paper 0148-7191 (1983)
18. Nguyen, A.-T., Reiter, S.: A performance comparison of sensitivity analysis methods for building energy models. *Build. Simul.* **8**(6), 651–664 (2015)



Chapter 12

Input Estimation of a Full-Scale Concrete Frame Structure with Experimental Measurements

Xi Liu and Yang Wang

Abstract This paper studies input estimation of a full-scale concrete frame structure, which is modeled with over a thousand degrees-of-freedom (DOFs). With acceleration response measured from dynamic testing, the natural frequencies and mode shapes of the concrete frame are first identified. The experimentally identified modal properties are compared with those obtained from a finite element (FE) model using nominal material properties. The FE model is then used to construct state-space system matrices for input estimation. With only acceleration measurements, an unbiased minimum-variance estimator combined with an online drift filter is used to estimate the dynamic input generated by a shaker. The estimation results show acceptable performance of the proposed algorithms for application on the full-scale two-story two-bay concrete frame with both simulated and experimental measurements. The effect of sensor locations on input estimation performance is also discussed.

Keywords Input estimation · Minimum-mean-square-error estimation · Linear stochastic system · Modal analysis · Sensor instrumentation

12.1 Introduction

In civil engineering, structures are often subject to unknown dynamic excitations, such as wind or traffic loads, which are generally difficult or expensive to measure directly. In such scenarios, numerical techniques can be developed to estimate the unknown input using structural response measurements. Among early studies in input estimation, Kitanidis [1] proposed a recursive state estimator that minimizes the trace of the state estimation error covariance, while subject to an unbiasedness constraint to account for the unknown input. This approach provided an optimal state estimation in the minimum mean square error (MMSE) sense, but without an explicit estimation of the unknown input. Gillijns and De Moor [2] extended the work and proposed a joint input-state estimation algorithm by combining a minimum-mean-square-error (MMSE) estimator and a weighted least squares (WLS) objective. Lourens et al. and Maes et al. applied the estimation algorithm to a reduced-order model of a footbridge for hammer force identification using field measurement [3, 4]. Maes et al. also studied the identifiability, stability and uniqueness conditions of the estimation approach for modally reduced-order models [4]. It was observed that a low-frequency drift occurs in the estimated input if using only acceleration measurements. To improve the estimator performance, Azam et al. proposed a dual Kalman filter by estimating the input and state in two different stages [5], which assumes the unknown input and state are uncorrelated. Azam et al. further compared the dual estimator with the one proposed by Gillijns et al. using a small-scale laboratory structure excited at the base [6]. The approach could reduce the input estimation drift but needs a proper choice of estimator covariance.

This paper investigates simultaneous input-state estimation for a full-scale concrete structure. When using only acceleration measurements, a high-pass drift filter is added to the input estimator at each time step. The drift filter is pre-tuned using simulated measurements and can be used for online estimation without the need of an offline filter as in [7]. The proposed input estimation approach is validated on a two-story two-bay concrete frame with dense sensor instrumentation. The rest of the paper is organized as follows. The input estimation problem and the corresponding algorithm are introduced

X. Liu

School of Civil and Environmental Engineering, Georgia Institute of Technology, Atlanta, GA, USA

Y. Wang (✉)

School of Civil and Environmental Engineering, Georgia Institute of Technology, Atlanta, GA, USA

School of Electrical and Computer Engineering, Georgia Institute of Technology, Atlanta, GA, USA

e-mail: yang.wang@ce.gatech.edu

in Sect. 12.2. Section 12.3 describes the full-scale structure and experimental modal analysis results. Section 12.4 describes input estimation results with both simulated and experimental acceleration measurements. Finally, the paper is summarized with conclusions and future work.

12.2 Input Estimation Algorithm

Consider a discrete-time stochastic linear state-space system as shown in Eqs. (12.1) and (12.2),

$$x_{k+1} = Ax_k + Bu_k + v_k \quad (12.1)$$

$$y_k = Cx_k + Du_k + w_k \quad (12.2)$$

where $x_k \in \mathbb{R}^n$ is the state at time step k , $u_k \in \mathbb{R}^{n_u}$ is the unknown input, $v_k \in \mathbb{R}^n$ is the process noise or disturbance, $y_k \in \mathbb{R}^m$ is the measurement output, and $w_k \in \mathbb{R}^m$ is the measurement noise. It is assumed: (1) the system is observable, i.e. the observability matrix $\mathcal{O} \triangleq [C^T \ (CA)^T \ \dots \ (CA^{n-1})^T]^T$ has full rank; (2) $v_k \sim \mathcal{N}(0, \Sigma_v)$ and $w_k \sim \mathcal{N}(0, \Sigma_w)$ are white Gaussian noise; (3) w_k and v_l are independent for all k and l ; (4) initial state is random $x_0 \sim \mathcal{N}(\mu_0, \Sigma_0)$ and independent from w_k and v_l for all k and l ; (5) the number of unknown inputs is smaller than the number of measurements, $n_u \leq m$, and $\text{rank}(D) = n_u$. The following notations are used: the minimum-mean-square-error (MMSE) estimate of x_k given cumulative sequential measurements $y_l^{\text{seq}} = [y_0^T \ y_1^T \ \dots \ y_l^T]^T$ is denoted as $\hat{x}_{k|l} \triangleq \mathbb{E}(x_k | y_l^{\text{seq}})$. The conditional covariance of x_k given y_l^{seq} is $\Sigma_{x_k|l} \triangleq \text{cov}(x_k | y_l^{\text{seq}})$. The weighted least squares (WLS) estimate of u_k is $\hat{u}_k \triangleq h(y_k)$, i.e. a function $h(\bullet)$ of measurement y_k at time step k only. The cross-covariance between the input and state given y_l^{seq} is $\Sigma_{x_k u_k|l} \triangleq \text{cov}(x_k, u_k | y_l^{\text{seq}})$.

Overall, the estimation algorithm is divided into the following stages shown in Fig. 12.1, including input estimation, input drift filtering, measurement update of state and time update of state. In the first stage, the unknown input u_k is estimated using the new measurement y_k at time step k . The input estimation gain L_{u_k} (Eq. 12.5) is obtained by solving a WLS optimization

Initialization:	$\hat{x}_{0 -1} = \mu_{x_0}, \Sigma_{x_{0 -1}} = \Sigma_{x_0}, \tilde{u}_0 = 0$
Input estimation:	$\Sigma_{y_{k k-1}} = C\Sigma_{x_{k k-1}}C^T + \Sigma_w \quad (12.3)$ $\Sigma_{u_k} = (D^T\Sigma_{y_{k k-1}}^{-1}D)^{-1} \quad (12.4)$ $L_{u_k} = \Sigma_{u_k} D^T \Sigma_{y_{k k-1}}^{-1} \quad (12.5)$ $\hat{u}_k = L_{u_k} (y_k - C\hat{x}_{k k-1}) \quad (12.6)$ $\Sigma_{x_k u_k k} = \Sigma_{u_k x_k k}^T = -\Sigma_{x_{k k-1}} C^T \Sigma_{y_{k k-1}}^{-1} D \Sigma_{u_k} \quad (12.7)$
Input drift filtering:	$\hat{u}_k^f = G_f \tilde{u}_k + D_f \hat{u}_k \quad (12.8)$ $\tilde{u}_{k+1} = A_f \tilde{u}_k + B_f \hat{u}_k \quad (12.9)$
Measurement update of state:	$L_{x_k} = \Sigma_{x_{k k-1}} C^T \Sigma_{y_{k k-1}}^{-1} \quad (12.10)$ $\hat{x}_{k k} = \hat{x}_{k k-1} + L_{x_k} (y_k - C\hat{x}_{k k-1} - D\hat{u}_k^f) \quad (12.11)$ $\Sigma_{x_{k k}} = \Sigma_{x_{k k-1}} - L_{x_k} (\Sigma_{y_{k k-1}} - D \Sigma_{u_k} D^T) (L_{x_k})^T \quad (12.12)$
Time update of state:	$\hat{x}_{k+1 k} = A \hat{x}_{k k} + B \hat{u}_k^f \quad (12.13)$ $\Sigma_{x_{k+1 k}} = [A \ B] \begin{bmatrix} \Sigma_{x_{k k}} & \Sigma_{x_k u_k k} \\ \Sigma_{u_k x_k k} & \Sigma_{u_k} \end{bmatrix} \begin{bmatrix} A^T \\ B^T \end{bmatrix} + \Sigma_v \quad (12.14)$
	end

Fig. 12.1 Simultaneous input-state estimation

problem. The state measurement update gain L_{x_k} (Eq. 12.10) is obtained by minimizing the trace of the state estimation covariance $\Sigma_{x_{k|k}}$ subject to an unbiasedness constraint of the state [1, 2]. The drift filter is represented in state-space form by A_f , B_f , C_f and D_f , which can be pre-tuned using a nominal FE model of the structure of interest. The state of the drift filter at time step k is denoted as \tilde{u}_k . The filtered input estimate \hat{u}_k^f is then used to update the state using the new measurement y_k (Eq. 12.11). Finally, time update of the state can be derived using the known state-space system in Eq. (12.1). Without the input drift filtering stage, the estimation of state is optimal in the sense of MMSE and the estimation of input is optimal in the sense of WLS [2]. Figure 12.1 summarizes the estimation procedures from time step k to $k + 1$.

12.3 Test Structure

Figure 12.2 shows the two-story two-bay concrete test frame. In order to prevent excessive out-of-plane movement of the test frame, a collapse prevention frame was built next to the test frame. When testing the frame, a hydraulic linear inertia shaker provided by NEES@UCLA was installed at the middle beam-column joint on the roof (i.e. the second elevated slab). The inertia force of the moving mass on the shaker is used to dynamically excite the structure [8, 9]. Accelerometers, strain gages, and linear variable displacement transducers (LVDTs) were instrumented on the concrete frame to measure structural responses during the shaker tests. Specifically, nine tri-axial accelerometers (Kinematics EpiSensor ES-T) were installed at beam-column joints, and 33 uniaxial accelerometers (Kinematics EpiSensor ES-U) were installed at mid-length and quarter length locations of columns and longitudinal beams of both the first and second elevated slabs. This study uses 26 longitudinal (shown in blue) and 16 vertical (shown in red) acceleration channels (see details in Fig. 12.3 and [9]). In addition, an accelerometer was installed on the moving mass of the shaker for calculating the excitation force.

The first test on the frame was a scaled El Centro input, when the maximum displacement of the shaker mass was scaled to 1 in. The low-magnitude input caused little to no damage to the frame, and the frame can be treated as a linear structure in this case. The acceleration responses were sampled at 200 Hz and a 30 Hz low-pass filter is applied during post-processing. Using the filtered acceleration response, the first four modes are identified through the Numerical Algorithms for Subspace State Space System Identification (N4SID) [10]. Figure 12.4 shows the experimentally identified resonance frequencies, mode shapes and damping ratios of the concrete frame.

An FE model with 2482 DOFs is built in SAP2000, where the nominal material properties are obtained from concrete cylinder tests during each concrete pour, ranging from 22.1 to 26.9 GPa (3200–3900 ksi). Modal assurance criterion (MAC) is used to evaluate the similarities between each pair of experimental and simulated mode shapes at measured DOFs, defined as

$$\text{MAC}_i = \frac{\left((\Psi_i^{\text{EXP},m})^T \Psi_i^{\text{FE},m}(\alpha) \right)^2}{\|\Psi_i^{\text{EXP},m}\|_2^2 \|\Psi_i^{\text{FE},m}(\alpha)\|_2^2} \text{ for the } i\text{-th mode. The closer the MAC value gets to 1, the better the two mode shapes match.}$$

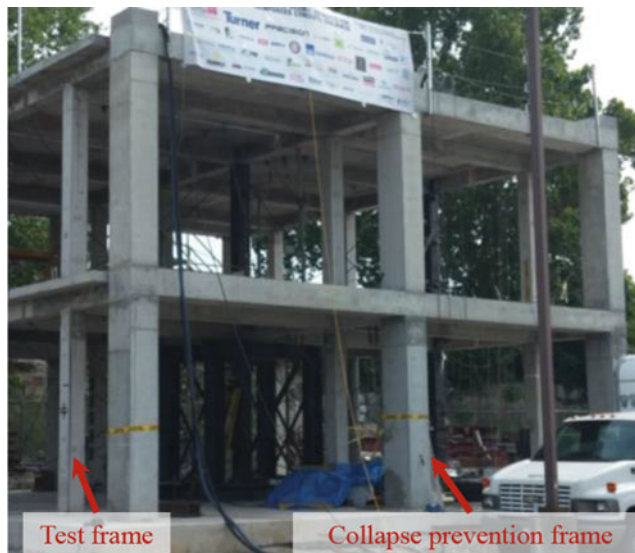


Fig. 12.2 Full-scale test frame

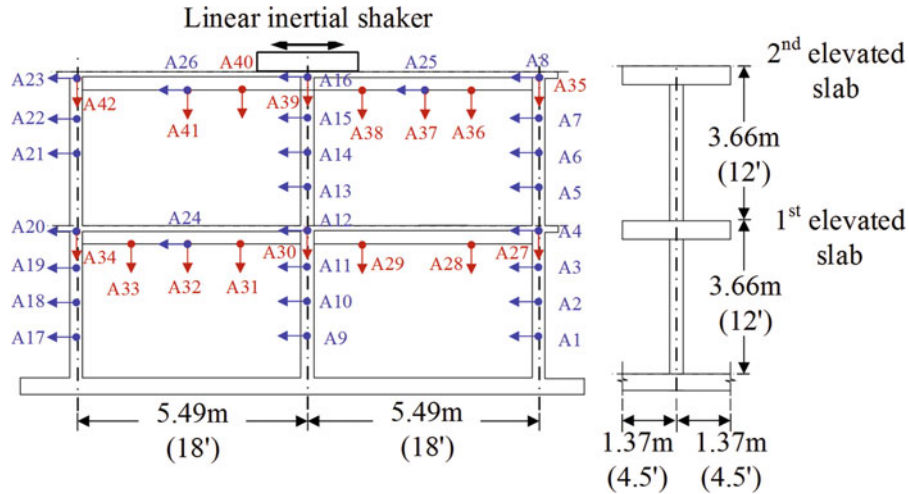
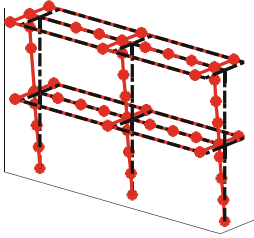
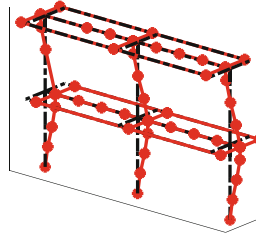


Fig. 12.3 Acceleration measurements

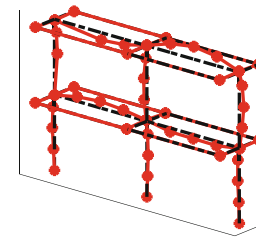
Mode1: $f = 2.00\text{Hz}$ $\zeta = 4.9\%$



Mode2: $f = 5.41\text{Hz}$ $\zeta = 5.42\%$



Mode3: $f = 13.92\text{Hz}$ $\zeta = 2.61\%$



Mode4: $f = 19.82\text{Hz}$ $\zeta = 2.27\%$

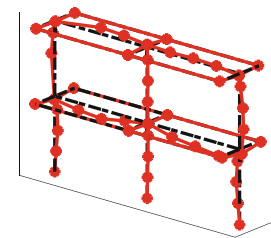


Fig. 12.4 Experimentally identified modes of the test frame

Table 12.1 Modal property comparison between experiment and FE model

Mode	1st	2nd	3rd	4th
Experiment f_i^{EXP} (Hz)	2.00	5.41	13.92	19.82
FE model f_i^{FE} (Hz)	1.96	5.63	14.96	20.61
$(f_i^{\text{FE}} - f_i^{\text{EXP}}) / f_i^{\text{EXP}}$	-1.57%	4.16%	7.44%	4.00%
MAC values	0.999	0.988	0.935	0.887

Table 12.1 shows the comparison of modal properties between experimentally identified results and those of the FE model. It can be seen that the difference in natural frequencies is within 8%. The MAC values of the first three modes are larger than 0.9. The FE model is shown to be reasonably accurate in describing the contribution from the first two modes, which are more significant than higher modes for in-plane longitudinal response. To validate the input-state estimation framework presented in Fig. 12.1, the FE model is used to simulate structural responses under shaker excitation as well as providing the mass and stiffness matrices used to construct the state-space system for input estimation. Future work is under plan to perform detailed FE model updating using experimentally identified modes. Upon future model updating, the updated model can be used in combination with experimental responses for input-state estimation.

12.4 Validation of Input Estimation Algorithm

The state-space dynamical system as shown in Eqs. (12.1) and (12.2) can be constructed based on the following equations of motion with n_{DOF} degree-of-freedoms (DOFs):

$$M\ddot{q}(t) + C_{\text{damp}}\dot{q}(t) + Kq(t) = \Gamma_u u(t) \quad (12.15)$$

where $M, K \in \mathbb{R}^{n_{\text{DOF}} \times n_{\text{DOF}}}$ are the mass and stiffness matrices, which can be obtained from the FE model in Sect. 12.3; $C_{\text{damp}} \in \mathbb{R}^{n_{\text{DOF}} \times n_{\text{DOF}}}$ is the damping matrix, which can be constructed using a Rayleigh damping model based on the experimentally identified damping ratios of the first two modes (Fig. 12.4); $q(t), \dot{q}(t)$ and $\ddot{q}(t) \in \mathbb{R}^{n_{\text{DOF}}}$ are displacement, velocity and acceleration vectors; $\Gamma_u \in \mathbb{R}^{n_{\text{DOF}} \times n_u}$ is the input mapping matrix with ones at the input DOFs and zeros elsewhere; and $u(t) \in \mathbb{R}^{n_u}$ is the shaker force input, which is a scalar in this application ($n_u = 1$).

A possible choice to formulate a state-space model is to define the state vector $x(t)$ as the displacement and velocity of all DOFs. In this case, the dimension of the state-space system (Eq. 12.1) is two times the number of DOFs of the FE model. As a result, when the input estimation algorithm is applied to a full-scale structure, the dimension of the system could easily be over thousands or more, e.g. 4964 in this concrete frame example. Therefore, for computational feasibility, a model reduction approach is needed to improve the computational efficiency in such applications. The approach considered here is to use the structural modal properties to reduce the dimension of state-space systems. The displacement, velocity and acceleration vectors q, \dot{q}, \ddot{q} in Eq. (12.15) are converted to modal coordinates using $q = \Psi z, \dot{q} = \Psi \dot{z}, \ddot{q} = \Psi \ddot{z}$, where Ψ is the mass-normalized eigenvectors of the model. Left multiplying Ψ^T to both sides of Eq. (12.15) and replacing q, \dot{q}, \ddot{q} with z, \dot{z}, \ddot{z} gives:

$$(\Psi^T M \Psi) \ddot{z} + (\Psi^T C_{\text{damp}} \Psi) \dot{z} + (\Psi^T K \Psi) z = \Psi^T \Gamma_u u \quad (12.16)$$

Here $\Psi^T M \Psi = I$, $\Psi^T K \Psi = \Omega^2$, and Ω is a diagonal matrix with diagonal entries equal to the natural frequencies of the structure. As a result, a reduced-order continuous state-space system can be formulated in modal coordinates as follows.

$$\dot{x} = \begin{Bmatrix} \dot{z} \\ \ddot{z} \end{Bmatrix} = \begin{bmatrix} 0 & I \\ -\Omega^2 & -\Psi^T C_{\text{damp}} \Psi \end{bmatrix} \begin{Bmatrix} z \\ \dot{z} \end{Bmatrix} + \begin{bmatrix} 0 \\ \Psi^T \Gamma_u \end{bmatrix} u = A_c x + B_c u \quad (12.17)$$

Here A_c and B_c represent the system matrix and the input matrix of the continuous state-space model. When m acceleration measurements are available, i.e. $y(t) \in \mathbb{R}^m$, the corresponding measurement equation is

$$y = \Gamma_y \ddot{q} + w = \Gamma_y \Psi \left[-\Omega^2 - \Psi^T C_{\text{damp}} \Psi \right] \begin{Bmatrix} z \\ \dot{z} \end{Bmatrix} + \Gamma_y \Psi \Psi^T \Gamma_u u + w = C_c x + D_c u + w \quad (12.18)$$

Here $\Gamma_y \in \mathbb{R}^{m \times n_{\text{DOF}}}$ is the output mapping matrix; $w \in \mathbb{R}^m$ is the measurement noise; C_c is the output matrix and D_c is the feedthrough matrix of the continuous state-space model. To implement estimators in discrete time, a zero-order-hold discretization method is used to convert the continuous system to discrete state-space system. In addition, a fictitious process noise $v_k \sim \mathcal{N}(0, \Sigma_v)$ is added to the discrete system to tune the estimator, which can help improve the conditioning of $\Sigma_{y_{k|k-1}}$ in Eq. (12.3) by increasing $\Sigma_{x_{k|k-1}}$ during the time update stage as shown in Eq. (12.14). In this example, the diagonal entries of Σ_v are heuristically set to a small number of 10^{-10} . To assess the performance of the estimator, both simulated and experimental acceleration measurements are used to estimate the unknown shaker input, respectively. Note that process noise v_k is only added to the estimator and not used in generating simulated measurements.

12.4.1 Input Estimation with Simulated Measurement

First, the FE model is used to simulate acceleration response, including 26 longitudinal and 16 vertical channels as shown in Fig. 12.3, excited by the measured shaker input. The measurement noise level is set as $\sigma_w = 0.1$ mg. The initial values corresponding to the estimated state are set as $\mu_{x_0} = 0$ and $\Sigma_{x_0} = 10^{-10}$. To reduce the dimension of the system, the first two modes from the FE model are used to formulate the state-space system in Eqs. (12.17) and (12.18). To quantify the difference between the estimated \hat{u}_k and the actual input u_k , root mean square (RMS) error is calculated, defined as

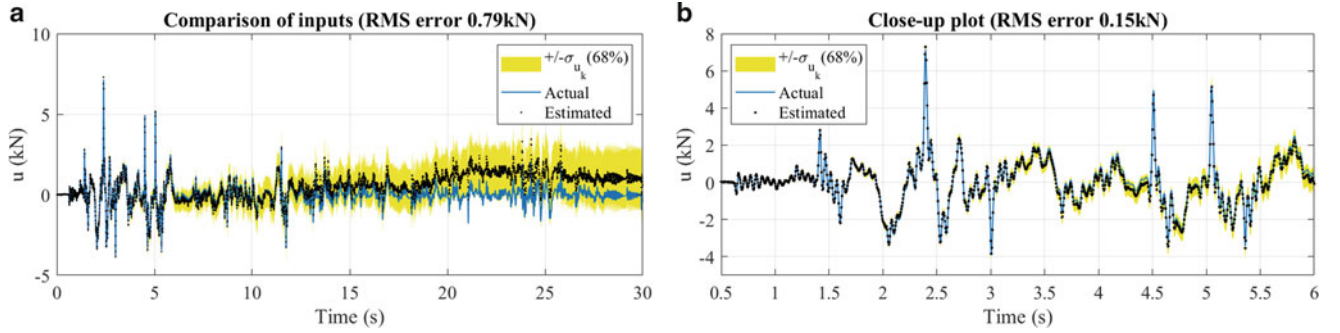


Fig. 12.5 Estimation of shaker input: simulated measurements without drift filter. (a) Comparison of inputs 0–30 s. (b) Comparison of inputs 0.5–6 s

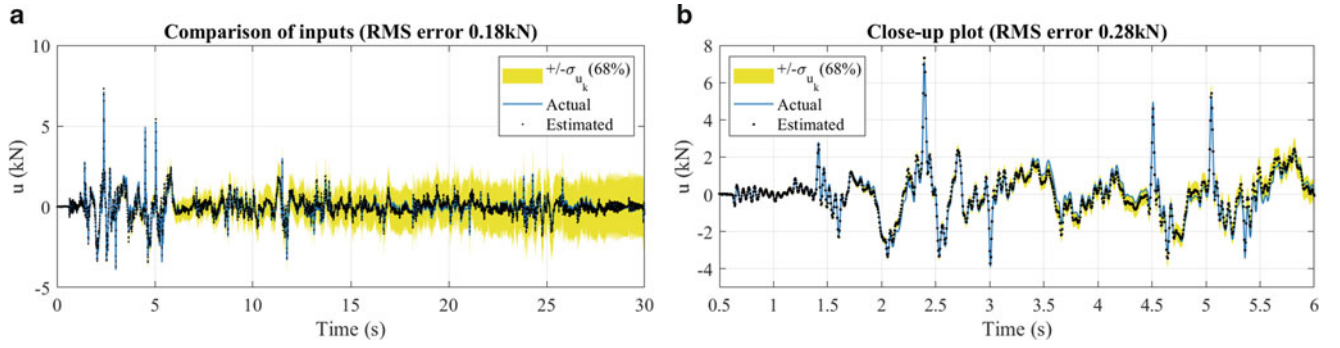


Fig. 12.6 Estimation of shaker input: simulated measurements with drift filter. (a) Comparison of inputs 0–30 s. (b) Comparison of inputs 0.5–6 s

$\sqrt{\frac{1}{\mathbb{K}} \sum_{k=1}^{\mathbb{K}} |u_k - \hat{u}_k|^2}$, where \mathbb{K} is the total number of data points. Figure 12.5a shows the comparison of inputs without using the drift filter. A 68% confidence interval of the input estimation trajectory, indicated by the standard deviation σ_{u_k} of the input estimation error, is also included. It can be seen that a low-frequency fictitious drift is visible after around 12 s, resulting in a RMS error of 0.79 kN. Figure 12.5b shows the close-up plot from 0.5 to 6 s with an RMS error of 0.15 kN. To improve the estimator performance, a fourth order high-pass Chebyshev Type I filter is tuned with cut-off frequency of 10^{-4} Hz and 0.05 dB of passband ripple to reduce drift error. Figure 12.6 shows the input comparison after combining the drift filter at each time step. The RMS error is reduced to 0.18 kN for the time period of 0–30 s with a slight increase to 0.28 kN during 0.5–6 s.

12.4.2 Input Estimation with Experimental Measurement

Next, input estimation is conducted using 42 experimental acceleration measurements from the same 1-in. El Centro shaker excitation as used in Sect. 12.4.1. The first two modes from the FE model are used to formulate the state-space model, and the measurement noise level is assumed to be $\sigma_w = 0.1$ mg. The initial values corresponding to the estimated state are kept the same as in Sect. 12.4.1, i.e. $\mu_{x_0} = 0$ and $\Sigma_{x_0} = 10^{-10}$. Figure 12.7a shows that the estimated input starts to drift from around 6 s, which resulting in a large RMS of 0.53 kN. Figure 12.7b shows the corresponding close-up plot of the input comparison. Figure 12.8 compares the input estimation results with the measured shaker input for both the 0.5–6 s duration and the entire 30 s when the drift filter is added. It can be seen that the estimated input could match better with the measured input after combining the drift filter, which reduces RMS error especially for the entire time history.

To further investigate the effect of sensor locations on input estimation, the magnitude of the feedthrough matrix D is examined. In general, according to Eq. (12.2), larger magnitude in D results in more contribution of input u to measurement y . On the contrary, if D is too small, input can be inundated by measurement noise w . When zero-order-hold discretization is used, the magnitude of the feedthrough matrix is given by $D = D_c = \Gamma_y \Psi \Psi^T \Gamma_u$. The mass normalized eigenvector can be expressed as $\Psi = [\psi_1 \psi_2 \dots \psi_{n_{\text{mode}}}]$, where ψ_i denotes the eigenvector of the i th mode with length equal to n_{DOF} , i.e.

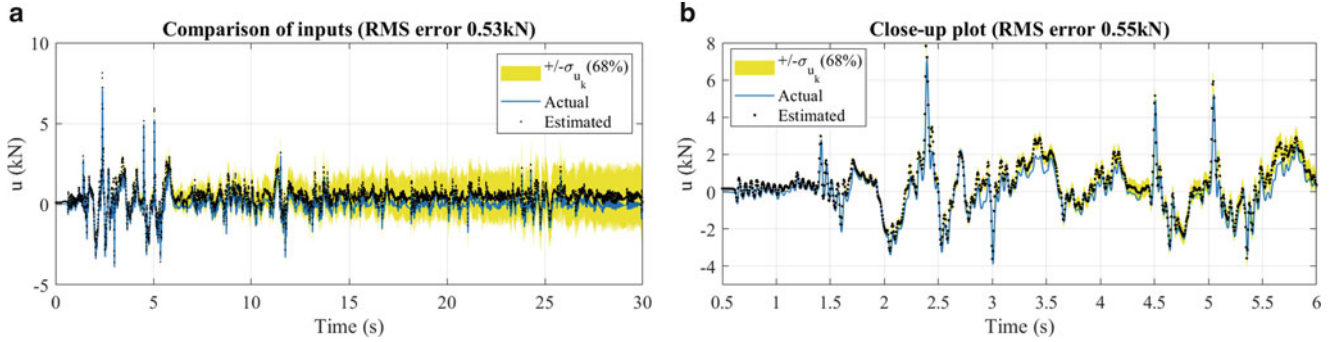


Fig. 12.7 Estimation of shaker input: experimental measurements without drift filter. (a) Comparison of inputs 0–30 s. (b) Close-up plot (RMS error 0.55kN)

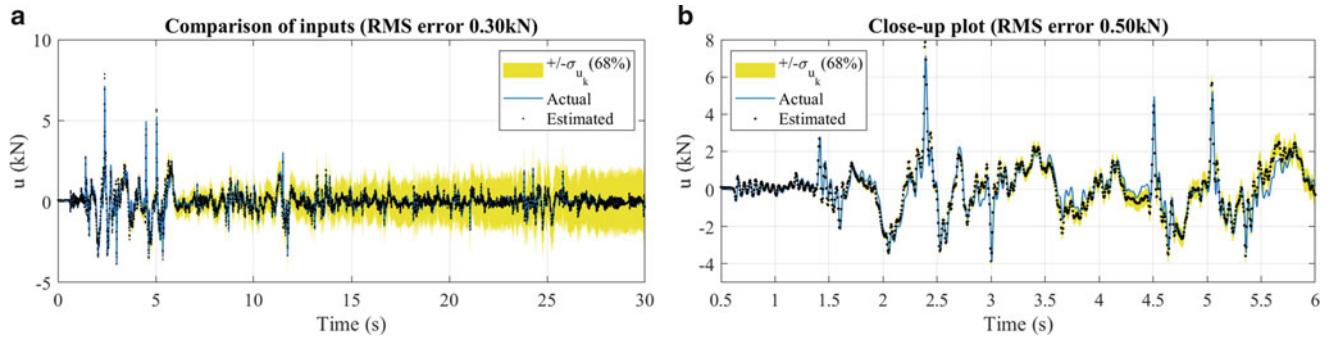


Fig. 12.8 Estimation of shaker input: experimental measurements with drift filter. (a) Comparison of inputs 0–30 s. (b) Close-up plot (RMS error 0.50kN)

$\psi_i = [\psi_{1,i} \ \psi_{2,i} \ \dots \ \psi_{n_{\text{DOF}},i}]^T$. Recall that the input mapping matrix Γ_u has value one at the input DOFs and zero elsewhere. In this example, the input vector dimension is $n_u = 1$; Γ_u is therefore a column vector with value one at the input DOF entry (denoted as the p -th DOF) and zero elsewhere. The rows of the output mapping matrix Γ_y have value one at the measured DOFs (denoted as the j_1, \dots, j_m -th DOFs) and zero elsewhere. Finally, since Γ_u is a column vector in this example, the feedthrough matrix D also degenerates to a vector:

$$\begin{aligned}
 D = D_c &= \Gamma_y \Psi \Psi^T \{\Gamma_u\} = \Gamma_y \left(\sum_{i=1}^{n_{\text{mode}}} \psi_i \psi_i^T \right) \{\Gamma_u\} = \Gamma_y \sum_{i=1}^{n_{\text{mode}}} \begin{bmatrix} \psi_{1,i}^2 & \psi_{1,i}\psi_{2,i} & \dots & \psi_{1,i}\psi_{n_{\text{DOF}},i} \\ \psi_{2,i}\psi_{1,i} & \psi_{2,i}^2 & \dots & \psi_{2,i}\psi_{n_{\text{DOF}},i} \\ \vdots & \vdots & \ddots & \vdots \\ \psi_{n_{\text{DOF}},i}\psi_{1,i} & \psi_{n_{\text{DOF}},i}\psi_{2,i} & \dots & \psi_{n_{\text{DOF}},i}^2 \end{bmatrix} \{\Gamma_u\} \\
 &= \sum_{i=1}^{n_{\text{mode}}} \left\{ \begin{array}{l} \psi_{j_1,i}\psi_{p,i} \\ \psi_{j_2,i}\psi_{p,i} \\ \vdots \\ \psi_{j_m,i}\psi_{p,i} \end{array} \right\}
 \end{aligned} \tag{12.19}$$

where $\psi_{p,i}$ denotes the value of the i th mode eigenvector at the input DOF- p ; $\psi_{j_1,i}$ denotes the value of the i th mode eigenvector at the first measured DOF j_1 ; $\psi_{j_2,i}$ denotes the value of the i th mode eigenvector at the second measured DOF j_2 , etc. The equation indicates that D has larger magnitude when both mode shape values of $\psi_{j(\cdot),i}$ and $\psi_{p,i}$ are large.

In this example, recall the input DOF- p is along the longitudinal direction on the second elevated slab (roof). Mode shape values at this DOF from the first two modes, $\psi_{p,1}$ and $\psi_{p,2}$, are relatively large compared with many other DOFs. When an acceleration channel is instrumented longitudinally and close to the input DOF- p , the value of $\psi_{j(\cdot),i}$ will be close to $\psi_{p,i}$ and be relatively large. This provides a larger product between $\psi_{j(\cdot),i}$ and $\psi_{p,i}$, and a larger magnitude in the corresponding row-(•) of the feedthrough matrix (vector) D . In particular, measurements A6–8, A14–16, A21–23, A25 and A26 in Fig. 12.3 contribute most to the input estimation due to their corresponding relatively large mode shape entries $\psi_{j(\cdot),i}$ for the first two

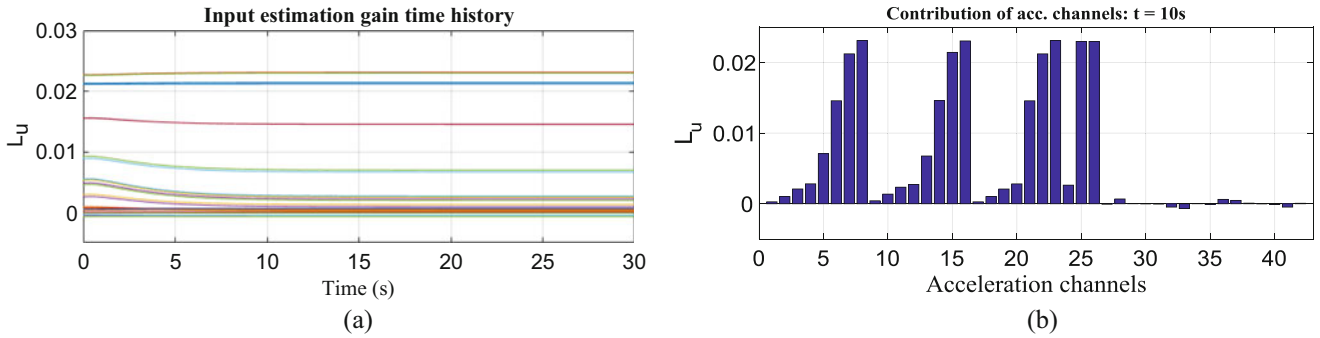


Fig. 12.9 Effect of measurement locations on input estimation. (a) Convergence of input estimation gain. (b) Input estimation gain of each measurements at 10 s

modes. For acceleration channels in vertical directions, or in longitudinal directions but at DOFs further away from the input DOF- p (particularly those on and below the first elevated slab), the corresponding mode shape entries of the first two modes are relatively small. These measurements can help reduce the input estimation error when used together with the longitudinal measurements close to the input location. However, these measurements alone are not suitable for estimating the shaker input, due to the relatively small feedthrough matrix (vector) D . In other words, the input signal-to-noise ratio is low if the magnitude of D is small. If only a limited number of sensors are available, it is suggested to place the sensors close to the input location, i.e. at and above the mid-height of the second-elevated-slab columns in this example. If the sensors could only be placed far from the input location, a modified input estimation algorithm without the direct feedthrough matrix (vector) D is needed.

The measurement allocation effect can also be observed in the estimation gain L_u . Figure 12.9a shows the time history of input estimation gain L_u of different acceleration channels. After around 7 s, during which the most significant input happens, the input estimation gain L_u converges to steady state value. Figure 12.9b compares the steady state estimation gains among different acceleration channels, which are numbered as A# in Fig. 12.3. In general, longitudinal measurements (channel A1–A26) have much more significant contribution to the input estimation compared to vertical measurements (channel A27–A42). Among the longitudinal measurements, sensors instrumented at and above the mid-height of the second-elevated-slab columns have larger estimation gains, which have more contribution to the input estimation compared to the measurements on and below the first elevated slab.

12.5 Conclusions

This paper presents the input estimation of a full-scale concrete frame using acceleration measurements. Modal properties of the test frame are first identified by N4SID using experimental measurements and compared with those of an FE model. Upon constructing system matrices based on the FE model, input estimation is then applied to estimate shaker force input with both simulated and experimental measurements. Because no displacement measurements are used, a recursive drift filter is adopted and tuned to reduce estimation error. The estimated input and experimentally measured shaker input are compared and acceptable performance is observed. In addition, the effect of sensor locations on the input estimator performance is also discussed. It is observed that when sensors are instrumented far away from the input location, the corresponding entries in the feedthrough matrix D is small and these measurements alone could not be used to estimate the input due to the presence of measurement noise. For practical applications, the performance of the algorithm also largely depends upon the accuracy of the state transition matrix A , which is constructed using the structural stiffness, damping and mass matrices. To achieve more accurate input estimation results, FE model updating with experimental measurements through non-convex optimization can be incorporated in future work.

References

1. Kitanidis, P.K.: Unbiased minimum-variance linear state estimation. *Automatica*. **23**(6), 775–778 (1987)
2. Gillijns, S., De Moor, B.: Unbiased minimum-variance input and state estimation for linear discrete-time systems with direct feedthrough. *Automatica*. **43**(5), 934–937 (2007)
3. Lourens, E., Papadimitriou, C., Gillijns, S., Reynders, E., De Roeck, G., Lombaert, G.: Joint input-response estimation for structural systems based on reduced-order models and vibration data from a limited number of sensors. *Mech. Syst. Signal Process.* **29**, 310–327 (2012)
4. Maes, K., Lourens, E., Van Nimmen, K., Reynders, E., De Roeck, G., Lombaert, G.: Design of sensor networks for instantaneous inversion of modally reduced order models in structural dynamics. *Mech. Syst. Signal Process.* **52**, 628–644 (2015)
5. Azam, S.E., Chatzi, E., Papadimitriou, C.: A dual Kalman filter approach for state estimation via output-only acceleration measurements. *Mech. Syst. Signal Process.* **60**, 866–886 (2015)
6. Azam, S.E., Chatzi, E., Papadimitriou, C., Smyth, A.: Experimental validation of the Kalman-type filters for online and real-time state and input estimation. *J. Vib. Control.* **23**(15), 2494–2519 (2017)
7. Maes, K., Nimmen, K.V., Lourens, E., Rezayat, A., Guillaume, P., Roeck, G.D., Lombaert, G.: Verification of joint input-state estimation for force identification by means of in situ measurements on a footbridge. *Mech. Syst. Signal Process.* **75**, 245–260 (2016)
8. Yu, E., Whang, D.H., Conte, J.P., Stewart, J.P., Wallace, J.W.: Forced vibration testing of buildings using the linear shaker seismic simulation (LSSS) testing method. *Earthquake Eng. Struct. Dyn.* **34**(7), 737–761 (2005)
9. Dong, X., Liu, X., Wright, T., Wang, Y., DesRoches, R.: Validation of wireless sensing technology densely instrumented on a full-scale concrete frame structure. In: Proceedings of International Conference on Smart Infrastructure and Construction (ICSIC), Cambridge, United Kingdom, 2016
10. Van Overschee, P., De Moor, B.: Subspace Identification for Linear Systems: Theory-Implementation-Applications. Springer Science & Business Media, Berlin (2012)



Chapter 13

Bayesian Estimation of Acoustic Emission Arrival Times for Source Localization

Ramin Madarshahian, Paul Ziehl, and Michael D. Todd

Abstract The onset time of an Acoustic Emission (AE) signal is an important feature for source localization. Due to the large volume of data, manually identifying the onset times of AE signals is not possible when AE sensors are used for health monitoring of a structure. Numerous algorithms have been proposed to autonomously obtain the onset time of an AE signal, with differing levels of accuracy. While some methods generally seem to outperform others (even compared to traditional visual inspection of the time signals), this is not true for all signals, even within the same experiment. In this paper, we propose the use of an inverse Bayesian source localization model to develop an autonomous framework to select the most accurate onset time among several competitors. Without loss of generality, three algorithms of Akaike Information Criterion (AIC), Floating Threshold, and Reciprocal-based picker are used to illustrate the capabilities of the proposed method.

Data collected from a concrete specimen are used as an input of the proposed technique. Results show that the proposed technique can select the best onset time candidates from the three mentioned algorithms, automatically. The picked onset time is comparable with manual selection, and accordingly has better accuracy for source localization when compared to any of the single methods.

Keywords Onset time · Acoustic emission · Bayesian inference · Automatic picker

13.1 Introduction

Assessment of microcrack network characteristics in cement-based materials is vital to determine the consequences of degradation on its physical behavior, e.g. mass transfer or tensile strength [1–3]. When a microcrack develops, the released energy propagates as stress waves to the surface of the structure. Sensors, usually of a piezoelectric type, are used to detect these acoustic emission (AE) signals generated by extension and coalescence of microcracks. AE activities are localized knowing the differences in arrival times (i.e. when P waves reach to sensors) of signals at different sensor locations. The technique is known as the time of arrival (TOA) method, which is highly sensitive to the accuracy of the measurement of the AE onset time [4].

AE activities are recorded in the presence of environmental and sensor noise. Detection of an actual AE signal in a noise-contaminated signal environment is critical for robust source localization. Visual inspection plausibly is the most precise way to determine the onset time, particularly for an experienced operator used to seeing AE signals. This method, however, has two main drawbacks: first, considering that the microsecond duration of an AE signal is minuscule compared to the monitoring life of a typical structure, it is not feasible to conduct visual inspections of AE signals for continuous health monitoring of a structure. Second, AE signals are sometimes embedded in the noise with a low signal-to-noise ratio (SNR), whether due to propagation distance, dissipation, or environmental noise.

Automatic pickers are intensively used to find the arrival time that best determines the onset of a signal from the noise. These methods work based on different features of signals such as amplitude, energy, and statistical properties. Fixed and Floating Threshold methods, Akaike's Information Criterion (AIC), Hinkley Criterion [5], cross-correlation based methods [6, 7], CWT based binary map [7] and Reciprocal-based Onset time selector [8] are a few examples of many algorithms developed for automatic onset time detection. The goal of this paper is not to evaluate these algorithms or to propose a new competing algorithm. Studies of these methods confirms that although some methods are in general more reliable than

R. Madarshahian (✉) · M. D. Todd
University of California at San Diego, La Jolla, CA, USA
e-mail: madarshahian@ucsd.edu

P. Ziehl
University of South Carolina, Columbia, SC, USA

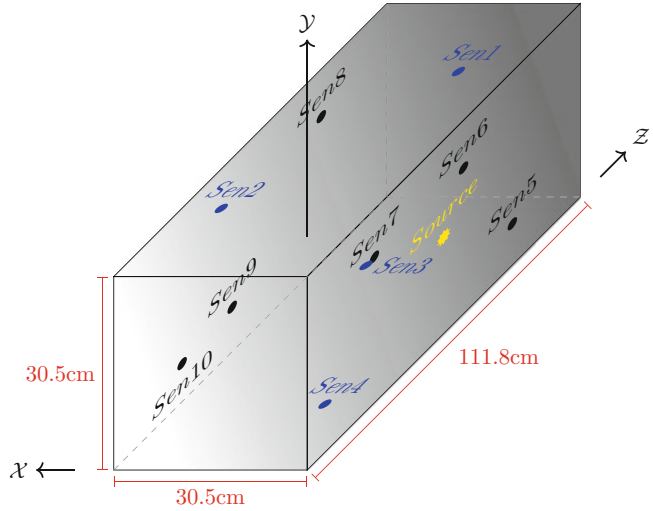


Fig. 13.1 Concrete block and sensors layout

others, there are always cases that other methods could have obtained the onset time more accurately [9]. Madarshahian et al., proposed that a Bernoulli parameter can be used to select an onset time, when two competing methods are available [10]. In this work, we show that several different methods can be used simultaneously to result in a more accurate estimate of source coordinates. To do this, we introduce a Bayesian approach to automatically select the most accurate onset time for source localization from the candidate algorithms' for onset time detection.

The proposed approach is explained by considering three onset time detectors. These methods, including a model for source localization and the proposed approach for onset time selection, are explained and discussed in Sect. 13.3 of this paper. Experimental data, generated by a pencil-lead breakage (PLB) test [12], is used to illustrate the method capability. Results are shown by illustrating an example of onset time detection methods on one of the signals, implementation of the proposed approach, and comparison of different sets of onset time on source localization.

13.2 Experimental Data

The data of this work is collected from a PLB test on a concrete block specimen shown in Fig. 13.1. The AE signals are recorded using ten sensors located on different faces of the concrete block. The source is located in the \mathcal{ZY} face of the concrete block as shown in Fig. 13.1.

The AE signals are recorded using ten sensors at different faces of the concrete block. Source is located in the \mathcal{ZY} face of the concrete block as shown in Fig. 13.1. The data can be found in the reference [11].

13.3 Methodology

This section is organized in to three parts. In the first part, three different methods to detect the onset time of AE signals are introduced. In the second part, the shortest path method which is used to obtain the \mathcal{P} wave travel time is explained. In the third part the proposed approach to select the best onset time among those onset times obtained by the three methods is introduced.

13.3.1 Automatic Onset Detection Algorithms

The three onset time selectors, or automatic pickers, are used in this paper are: (1) Floating Threshold picker, (2) AIC picker, and (3) The Reciprocal-based picker.

Floating Threshold

The Floating Threshold algorithm is one of the most common and simplest picking algorithms. Onset time is the moment when signal amplitude passes a threshold calculated as a factor of the root mean square amplitude for the first portion of each time series, known to be before the signal onset. In this work, we consider four times the noise standard deviation as the threshold. It is assumed that noise follows a zero-mean normal distribution, and it is therefore very unlikely that a sample of the noise distribution falls out of the interval specified by four standard deviations from zero. Therefore, the first point of a signal that passes this threshold is classified as an AE event, yielding the onset time. Although the Floating Threshold algorithm is used intensively due its simplicity, it is not very useful when SNR is low or sudden spikes exist in the signal. The Floating threshold can be expressed mathematically by Eq. 13.1.

$$t_{onset} = \operatorname{argmin}(t_i | \operatorname{abs}(X[t_i]) > X_{tre}), \quad (13.1)$$

where t_{onset} is the first arrival time, obtained by finding the smallest time (t_i) correspond to samples ($X[t_i]$) with absolute value greater than the threshold (X_{tre})

AIC Picker

Auto-regressive algorithms are another class of pickers which use statistical properties of a signal to find the onset time. These algorithms are threshold independent and insensitive to random spikes in time-series [13]. The Akaike's Information Criterion (AIC) is commonly used for onset determination of AE signals. The AIC function of an AE signal reaches its minimum at the onset time. The AIC algorithm has been compared to many other auto-pickers, and it is proven that it has a reliable onset determination [14, 15]. Equation 13.2 shows a fitness function which is used in the AIC method. The time corresponding to the minimum of this function is considered as the onset time of an AE signal.

$$\begin{aligned} AIC(t_i) &= t_i \ln(\sigma^2(X[1, t_i])) + (t_N - t_{i+1}) \ln(\sigma^2(X[t_{i+1}, t_N])) \\ t_{onset} &= \operatorname{argmin}(AIC(t_i)) \end{aligned} \quad (13.2)$$

In Eq. 13.2 t_i is the time corresponds to the i th sample and N is the total number of samples in signal X , $\sigma^2 s[p, q]$ is variance of the portion of signal X from sample p to q . The onset time is considered as the moment corresponding to the minimum of the fitness function shown in Eq. 13.2.

In an interesting study, the AIC and Floating Threshold methods are compared when onset times were obtained manually using visual inspection as the metric. It was shown that AIC outperformed the Floating Threshold method generally. However, in some cases the latter identified the onset time more accurately [9].

The Reciprocal-Based Picker

This method is conceptually similar with the AIC method, the point of difference is its fitness function which is shown in Eq. 13.3.

$$\begin{aligned} REC(t_i) &= -\frac{i}{\sigma^2(X[1, t_i])} - \frac{N - i}{\sigma^2(X[t_{i+1}, t_N])} \\ t_{onset} &= \operatorname{argmin}(REC(t_i)) \end{aligned} \quad (13.3)$$

In research by Babjak et al., the AIC and Reciprocal-based picker were compared, and it was shown that the Reciprocal-based picker could detect onset time more accurately than the AIC picker for their structural health monitoring problem [8].

13.3.2 The Shortest Path Model

The shortest path model is used to obtain the traveling time of a \mathcal{P} wave from source to sensors. This model is not the most accurate model for a heterogeneous material like concrete. The distance between the source and a sensor divided by the \mathcal{P} wave speed, models the time of arrival for each sensor. Equation 13.4 shows the mathematical expression of this model [16].

$$\Delta t_i = \frac{\sqrt{(X_0 - X_i)^2 + (Y_0 - Y_i)^2 + (Z_0 - Z_i)^2}}{V} - t_0 \quad (13.4)$$

Where $\Delta t_i + t_0$ is the time that an AE wave reaches to the i th sensor from the source. Source coordinates are shown by X_0 , Y_0 , and Z_0 and coordinates of the i th sensor are shown by X_i , Y_i , and Z_i . The last parameter of the model is V which is the \mathcal{P} wave speed.

13.3.3 The Proposed Bayesian Picker

Bayesian methods are intensively used for model updating inverse problems [17–19]. Equation 13.5 shows the mathematical expression of the Bayes theorem,

$$P(\theta|D) = \frac{P(D|\theta)P(\theta)}{P(D)}, \quad (13.5)$$

where our initial belief about parameters, i.e. prior $P(\theta)$, is updated by seeing new evidence, D , conditioned on the model parameters in the likelihood function $P(D|\theta)$. Here, the updated belief, known as the posterior, is shown by $P(\theta|D)$.

Obtained onset times from an automatic picker can be used as input data, but since the onset times obtained from different methods are not exactly the same, the posterior for source location shows different amount of uncertainty and bias. Our data may be structured as a matrix of $n \times m$, which n is numbers of sensors and m is numbers of candidates for an onset time. Here m is three since we used three methods to identify the onset times. Considering that we used ten sensors in our test, the data $D = [d_{ij}]_{n \times m}$ will be a 10 by 3 matrix.

Obviously, one of the suggested onset times for each signal is closer to the unknown *true* value of the onset time. Of course, we do not know which one is the most accurate without doing some kind of independent visual inspection. However, intuitively the most accurate onset times leads to the least amount of uncertainty in the inference of source coordinates. We propose to let the Bayesian model pick the onset times from the pool of data by introducing a new latent parameter, denoted by α . The new parameter is a categorical parameter consists of one outcome out of m possible outcomes. Here, since m is three, the possible outcomes of α would be 0, 1, or 2. Each of these numbers represents one of the automatic pickers, i.e. 0 for AIC picker (d_{i0}), 1 for the floating threshold (d_{i1}) and 2 for the reciprocal-based picker (d_{i2}). Then the data is fed to the model using Eq. 13.6:

$$d_i = 0.5 \times d_{i0}(1 - \alpha)(2 - \alpha) + d_{i1}(\alpha)(2 - \alpha) + 0.5 \times d_{i2}(\alpha - 1)(\alpha) \quad (13.6)$$

When we run MCMC algorithm, each time only one of the obtained onset times is selected for each sensor. For the prior of this parameter, we can assign the probability of $\frac{1}{3}$ to each method if our initial belief about them has no preference. However, based on the literature, generally in most of cases AIC picker gives us more accurate estimation of the onset time than floating threshold method [9]. Furthermore, in another work it was implied that the Reciprocal-based picker arguably gives better estimation of onset time than AIC picker in most of the cases [8]. The power of Bayesian inference is that we can consider this information in our priors before observing the data by assigning subjective probabilities to each automatic picker as we did in this work.

Priors for source coordinates are assigned uniformly distributed over the known block dimensions. Similarly, a range of variation is selected for the wave speed prior. Finally, using our prior about the \mathcal{P} wave speed and considering the dimensions of the block, a positive-valued distribution is assigned to t_{min} .

Categorical Gibbs Metropolis method is used for inference about α , and No U-Turn Sampler (NUTS) method is used for other parameters [20]. After implementing MCMC a chance of success is assigned to each picker for each sensor considering numbers of related α value in each chain (e.g., counts of the value “1” in the MCMC chain of α for the Floating Threshold method). Finally, the onset time with highest probability is selected for each sensor, and the model is run again by considering only the chosen onset time.

13.4 Results

Figure 13.2 shows an example of the implementation of the three methods. It illustrates that these methods may identify the onset time differently. From visual inspection it seems in this case that the Reciprocal-based picker detects the onset time more accurately than other two, and Floating Threshold method is more accurate than AIC picker. Implementing the proposed approach, the posterior for the categorical parameter, shown in Fig. 13.3, reflects a similar expectation. Even though in the prior, based on the literature, we assigned more chance of success to the AIC picker than Floating Threshold; our method for sensor 8 suggested a higher probability for the Floating Threshold onset time in comparison with AIC picker, and the highest probability is obtained for the Reciprocal-based picker as expected based on visual inspection shown in Fig. 13.2. The categorical parameter sometimes shows a very similar chance of success for two of pickers (e.g. AIC and reciprocal-based

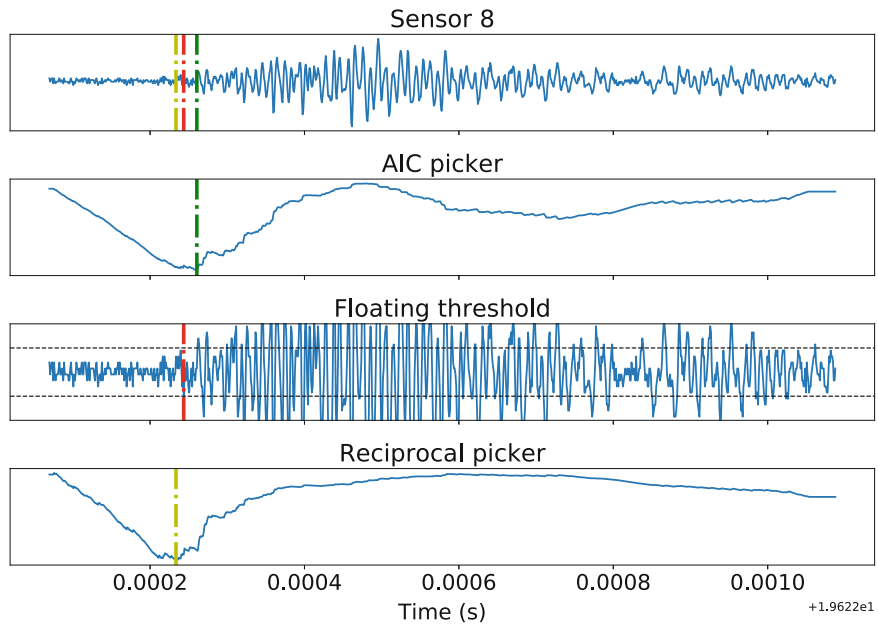


Fig. 13.2 Comparison of onset time detection using three methods for sensor 8

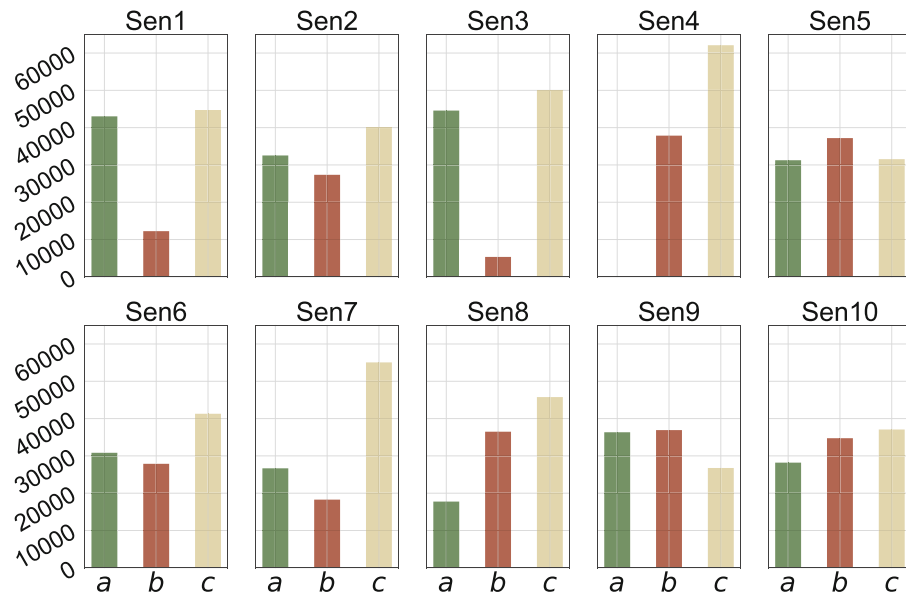


Fig. 13.3 Histogram for Bernoulli parameter indicating posterior probability of selection. (a) AIC picker, (b) floating threshold picker, (c) reciprocal-based picker

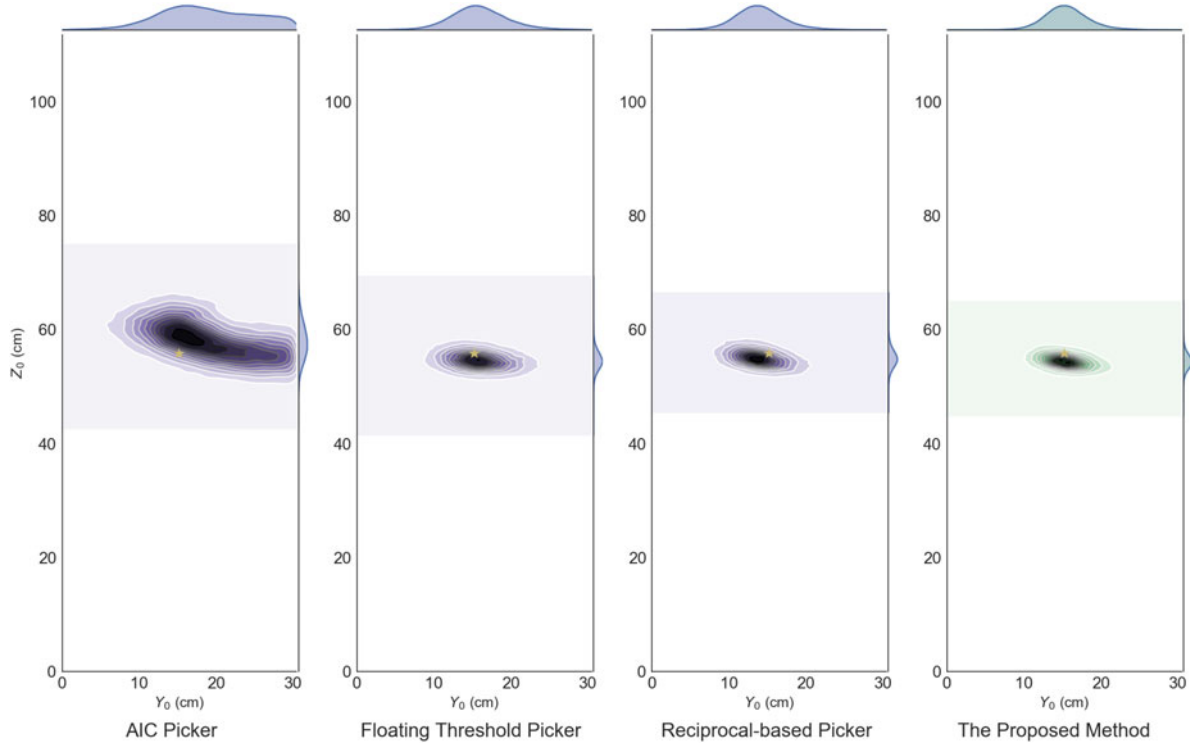


Fig. 13.4 Comparison of source

picker for sensor 1). Checking their corresponding onset times, we found that these values are almost the same, and then a similar posterior probability is expected intuitively.

To study the effect of onset times on source localization, each set of onset times is used for source localization using Bayesian inference and performing MCMC sampling. Then, results were compared with the selected onset times using the proposed method. The source obtained by those onset times which are selected by the proposed approach shows less amount of uncertainty compared to when only onset times from one of the other methods are used. Figure 13.4 shows the joint Bayesian inference for two coordinates of the source in comparison with that obtained using the chosen onset times by the proposed approach.

13.5 Concluding Remark

In this paper, a Bayesian model selection process was formulated for optimal AE signal onset time detection for the purpose of source localization. The selection process works by choosing the most accurate onset time from a population of onset times identified by using different established algorithms. Here, three methods of AIC Picker, Floating Threshold and Reciprocal-based method were used as a suite of well-known, mature, widely-used onset time detectors. The proposed method was implemented on a set of experimental data obtained from a PLB test. Results showed that the posterior probability obtained for each picker is in accordance with our expectation concluded from visual inspection. Moreover, onset times obtained from each method were used for source localization. Bayesian source localization using the selected onset times by the proposed method was less biased in comparison with the use of each set of onset times separately. The proposed approach implementation is straightforward and fast, showing strong potential to be used for continuous monitoring of structures using AE methods.

Acknowledgements This work was partially supported by the U.S. Department of Energy under Award Number DE-NE0008544 and also supported by the US Army Engineer Research and Development Center (ERDC) under cooperative agreement W912HZ-17-2-0024. The authors would like to thank Vafa Soltangharaei and Rafal Anay, Ph.D. candidates in the university of South Carolina, for providing technical support for data collection.

References

1. Attiogbe, E.K., Darwin, D.: Submicrocracking in cement paste and mortar. *Mater. J.* **84**(6), 491–500 (1987)
2. Liners, A.D.: Microcracking of concrete under compression and its influence on tensile strength. *Mater. Struct.* **20**(2), 111–116 (1987)
3. Landis, E.N., Shah, S.P.: The influence of microcracking on the mechanical behavior of cement based materials. *Adv. Cem. Based Mater.* **2**(3), 105–118 (1995)
4. Kurz, J.H., Köppel, S., Linzer, L.M., Schechinger, B., Grosse, C.U.: Source localization. In: *Acoustic Emission Testing*, pp. 101–147. Springer, Berlin (2008)
5. Hinkley, D.V.: Inference about the change-point from cumulative sum tests. *Biometrika* **58**(3), 509–523 (1971)
6. Ziola, S.M., Gorman, M.R.: Source location in thin plates using cross-correlation. *J. Acoust. Soc. Am.* **90**(5), 2551–2556 (1991)
7. Ciampa, F., Meo, M.: Acoustic emission source localization and velocity determination of the fundamental mode a_0 using wavelet analysis and a newton-based optimization technique. *Smart Mater. Struct.* **19**(4), 045027 (2010)
8. Babjak, B., Szilvási, S., Volgyesi, P., Yapar, O., Basu, P.K.: Analysis and efficient onset time detection of acoustic emission signals with power constrained sensor platforms. In: *SENSORS*, 2013, pp. 1–4. IEEE, Piscataway (2013)
9. Schechinger, B., Vogel, T.: Acoustic emission for monitoring a reinforced concrete beam subject to four-point-bending. *Constr. Build. Mater.* **21**(3), 483–490 (2007)
10. Madarshahian, R., Ziehl, P., Caicedo, J.M.: Acoustic emission Bayesian source location: onset time challenge. *Mech. Syst. Signal Process.* **123**, 483–495 (2019)
11. Madarshahian, R., Soltangharaei, V., Anay, R., Caicedo, J.M., Ziehl, P.: Hsu-Nielsen source acoustic emission data on a concrete block. *Data Brief.* 103813 (2019)
12. Sause, M.G.: Investigation of pencil-lead breaks as acoustic emission sources. *J. Acoust. Emiss.* **29**, 184–196 (2011)
13. Mborah, C., Ge, M., Wang, Z.: Exploring the use of a time-frequency domain technique for the filtering of acoustic emission/microseismic data. In: *Second International Conference on Information Systems Engineering (ICISE)*, 2017, pp. 59–63. IEEE, Piscataway (2017)
14. Kurz, J.H., Grosse, C.U., Reinhardt, H.-W.: Strategies for reliable automatic onset time picking of acoustic emissions and of ultrasound signals in concrete. *Ultrasonics* **43**(7), 538–546 (2005)
15. Liu, M., Yang, J., Cao, Y., Fu, W., Cao, Y.: A new method for arrival time determination of impact signal based on HHT and AIC. *Mech. Syst. Signal Process.* **86**, 177–187 (2017)
16. Gollob, S., Kocur, G.K., Schumacher, T., Mhamdi, L., Vogel, T.: A novel multi-segment path analysis based on a heterogeneous velocity model for the localization of acoustic emission sources in complex propagation media. *Ultrasonics* **74**, 48–61 (2017)
17. Beck, J.L., Katafygiotis, L.S.: Updating models and their uncertainties. I: Bayesian statistical framework. *J. Eng. Mech.* **124**(4), 455–461 (1998)
18. Aster, R.C., Borchers, B., Thurber, C.H.: *Parameter Estimation and Inverse Problems*, vol. 90. Academic, Cambridge (2011)
19. Vakilzadeh, M.K., Huang, Y., Beck, J.L., Abrahamsson, T.: Approximate Bayesian computation by subset simulation using hierarchical state-space models. *Mech. Syst. Signal Process.* **84**, 2–20 (2017)
20. Salvatier, J., Wiecki, T.V., Fonnesbeck, C.: Probabilistic programming in python using pymc3. *PeerJ Comput. Sci.* **2**, e55 (2016)



Chapter 14

Quantification and Evaluation of Parameter and Model Uncertainty for Passive and Active Vibration Isolation

Jonathan Lenz and Roland Platz

Abstract Vibration isolation is a common method used for minimizing the vibration of dynamic load-bearing structures in a region past the resonance frequency, when excited by disturbances. The vibration reduction mainly results from the tuning of stiffness and damping during the early design stage. High vibration reduction over a broad bandwidth can be achieved with additional and controlled forces, the active vibration isolation. In this context, “active” does not mean the common understanding that the surroundings are isolated against the machine vibrations. Also in this context, “passive” means that no additional and controlled force is present, other than the common understanding that the machine is isolated against the surroundings. For active vibration isolation, a signal processing chain and an actuator are included in the system. Typically, a controller is designed to enable a force of an actuator that reduces the system’s excitation response. In both passive and active vibration isolation, uncertainty is an issue for adequate tuning of stiffness and damping in early design stage. The two types of uncertainty investigated in this contribution are parametric uncertainty, i.e. the variation of model parameters resulting in the variation of the systems output, and model uncertainty, the uncertainty from discrepancies between model output and experimentally measured output. For this investigation, a simple one mass oscillator under displacement excitation is used to quantify the parameter and model uncertainty in passive and active vibration isolation. A linear mathematical model of the one mass oscillator is used to numerically simulate the transfer behavior for both passive and active vibration isolation, thus predicting the behavior of an experimental test rig of the one mass oscillator under displacement excitation. The models’ parameters that are assumed to be uncertain are mass and stiffness as well as damping for the passive vibration isolation and an additional gain factor for the velocity feedback control in case of active vibration isolation. Stochastic uncertainty is assumed for the parameter uncertainty when conducting a Monte Carlo Simulation to investigate the variation of the numerically simulated transfer functions. The experimental test rig enables purposefully adjustable insertion of parameter uncertainty in the assumed value range of the model parameters in order to validate the model. The discrepancy between model and system output results from model uncertainty and is quantified by the Area Validation Metric and an Bayesian model validation approach. The novelty of this contribution is the application of the Area Validation Metric and Bayes’ approach to evaluate and to compare the two different passive and active approaches for vibration isolation numerically and experimentally. Furthermore, both model validation approaches are compared.

Keywords Vibration isolation · Velocity feedback control · Monte Carlo simulation · Model uncertainty · Area validation metric

14.1 Introduction

The consideration and quantification of uncertainty in mechanical structures is becoming more significant in early design stages for decision making. For example, the final product’s design properties vary within today’s increasing solution space of passive, semi-active and active solutions. Over the last years, active solutions have been increasingly investigated in the scientific community because of their variability and the establishment and popularity of smart materials and structures that are often used in active systems. However, the increased possibilities may lead to neglect the advantages of passive solutions that may be less expensive, more reliable and investigated thoroughly, e.g. vibration reduction with absorbing material or compensators [1]. While active systems may reduce the vibrations more effectively than passive systems, the active system is

J. Lenz (✉)

Technische Universität Darmstadt, System Reliability, Adaptive Structures and Machine Acoustics SAM, Darmstadt, Germany
e-mail: lenz@sam.tu-darmstadt.de

R. Platz

Fraunhofer Institute for Structural Durability and System Reliability LBF, Darmstadt, Germany

more complex because of the necessary inclusion of sensors, actuators, interfaces, a signal processing chain and a controller [2]. They lead to additional uncertainty in the system that should be taken into account when deciding about the favorite technology in early design stages.

Platz et al. showed analytically in [3] the principle deviation of amplitude and phase responses of a one mass oscillator with passive and active vibration isolation when the corresponding system's parameters mass, stiffness, damping coefficient and gain vary. This first but only rough investigation lead to the conclusion that active vibration isolation may result in less uncertainty of the model's output over the frequency range of interest when using a direct MONTE CARLO simulation. A more precise analysis is presented in [4], where Platz et al. utilized the χ^2 -Test to validate the assumption of normal distribution of the model's input parameters when using 100 and 10,000 samples for a MONTE CARLO simulation. The variations of the system's properties were investigated for six different characteristic points of the amplitude and phase response like resonance and isolation frequency for both passive and active vibration isolation. The standard deviation of that characteristic properties was not considerably affected by using 100 or 10,000 samples, but the higher sampling rate resulted in the acceptance of normal distribution assumption for all input parameters. It was shown that active vibration isolation analysis in early design stages does not necessarily result in less uncertainty of the system's output throughout the whole frequency range of interest. In a third contribution, Platz and Melzer [5] compared the probabilistic approaches from [3] and [4] with non-probabilistic approaches in early design stages, like the direct interval analysis, the direct fuzzy analysis and the simplified worst case analysis. The non-probabilistic approaches require less computational cost but overestimate the uncertainty in amplitude and phase response for passive and active vibration isolation in comparison to the MONTE CARLO simulation. However, when the interrelation between the standard deviation of the MONTE CARLO simulation and the membership function of the fuzzy approach are known beforehand, the latter is an effective alternative to predict uncertainty in early design stage with less computational cost than with the MONTE CARLO simulation.

Now, in this contribution the authors not only investigate the parametric uncertainty for numerical simulations they also validate the mathematical models for passive and active vibration isolation of a one mass oscillator. The model uncertainty is quantified with the Area Validation Metric (AVM) proposed by Roy and Oberkampf in [6] and a Bayesian approach with hypothesis testing based on [7] and [8]. Any further differentiation between a systematic discrepancy bias and a random experimental error as introduced in [9] is not taken into account. As in [3], the model uncertainty was quantified for the five evaluation criteria that are taken into consideration again:

1. the varying maximum vibration amplitude V_{\max} ,
2. the varying resonance frequency ω_{res} at maximum vibration amplitude $|V(\Omega = \omega_{\text{res}})| = V_{\max}$,
3. the varying isolation frequency ω_{iso} at $|V(\Omega = \omega_{\text{iso}})| = 0 \text{ dB}$,
4. the varying amplitude $|V(\Omega = 100 \text{ 1/s})| = V_{100}$ at the excitation frequency $\Omega = 100 \text{ 1/s} > \omega_{\text{iso}}$,
5. and the varying excitation frequency ω_{15} for -15 dB isolation attenuation.

These five evaluation criteria cover relevant points of interest in amplitude and phase response of passive and active vibration isolation for the frequency range of interest. The advantages and disadvantages between the two model validation methods are discussed and the model uncertainty in passive and active vibration isolation is compared.

14.2 System Description

14.2.1 Linear Mathematical Dynamic Model of the One Mass Oscillator for Passive and Active Vibration Isolation

The simple one degree of freedom model of a suspension leg supporting a vehicle's chassis, Fig. 14.1a, is used in this contribution to compare passive and active vibration isolation with respect to parametric and model uncertainty, [3, 4] and [5]. In the mechanical model in Fig. 14.1b (left), the mass m represents usually one fourth of a chassis while the suspension leg's mechanical properties result from the stiffness k and the damping coefficient b for passive vibration isolation and the velocity feedback gain g for active vibration isolation. The suspension leg is assumed to be free of mass. Since the simple linear mathematical model is derived and discussed thoroughly in [3] and [4], here the authors only present the basic principle and the final dynamic transfer relation used to calculate the evaluation criteria in order to quantify parametric and model uncertainty.

When excited by harmonic base point stroke

$$w(t) = \hat{w} \cos(\Omega t + \delta) \quad (14.1)$$

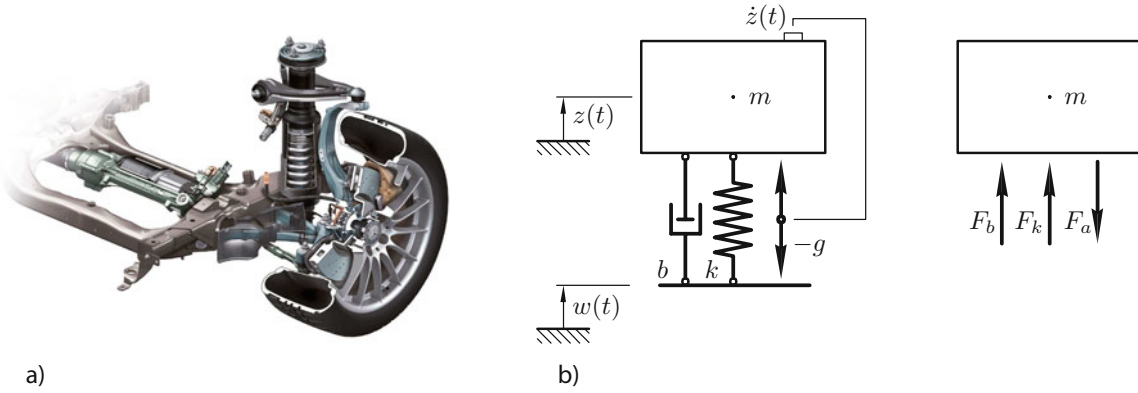


Fig. 14.1 One mass oscillator, (a) suspension leg (DAIMLERBENZ), (b) simple mechanical model (left) and cut free forces (right), [3]

with the angular excitation frequency Ω , excitation amplitude \hat{w} , time t and phase shift $\delta = 0$, the mass oscillates in z -direction. With linearity assumed, the damping and stiffness forces in Fig. 14.1b are

$$F_b = b(\dot{z}(t) - \dot{w}(t)), \quad F_a = -g\dot{z}(t) \quad \text{and} \quad F_k = k(z(t) - w(t)). \quad (14.2)$$

Using the forces in (14.2) as well as the angular eigenfrequency $\omega_0 = \sqrt{k/m}$ and the damping ratio $D = b/(2\omega_0 m)$, the complex amplification function

$$\underline{V}(\eta) = \frac{\widehat{z}_p}{\widehat{w}} = \frac{1 + i 2 D \eta}{(1 - \eta^2) + i(2 D \eta + g \zeta)} \quad (14.3)$$

is derived [4], with $\eta = \Omega/\omega_0$ and $\zeta = \Omega/(m \omega_0^2)$. Its corresponding real amplitude is

$$|V(\eta)| = \sqrt{\frac{1 + (2 D \eta)^2}{(1 - \eta^2)^2 + (2 D \eta + g \zeta)^2}} \quad (14.4)$$

and its real phase is

$$\varphi(\eta) = \arctan \frac{-2 D \eta^3 - g \zeta}{1 - \eta^2 + (2 D \eta)^2 + 2 D \eta g \zeta}. \quad (14.5)$$

14.2.2 Realization of the Test Rig

The test rig is shown in Fig. 14.2a with its schematic sketch in Fig. 14.2b. It is used to experimentally validate the linear mathematical model introduced in Sect. 14.2.1. The mass A is attached to four rectangular leaf springs B that bend laterally in z -direction and one voice coil actuator C. The leaf spring and the voice coil actuator are fixed to a frame D, an electrodynamic shaker harmonically excites the frame at the point E in z -direction. The stiffness k of the mechanical model in Fig. 14.1a is realized through the four leaf springs while the passive and active damping is realized through the voice coil actuator that is controlled by a DSP/SPACE system and MATLAB/SIMULINK. The damping forces in (14.2) are calculated using the signal from two accelerometers attached to the mass and frame of the test rig. These realizations of the stiffness and damping forces enable precise adjustment and variation of the stiffness k , damping coefficient b and gain g , thus allowing to cover a wide range of parameter values for the investigation and quantification of uncertainty. Additionally, the mass can be varied by attaching magnets G to the oscillating mass.

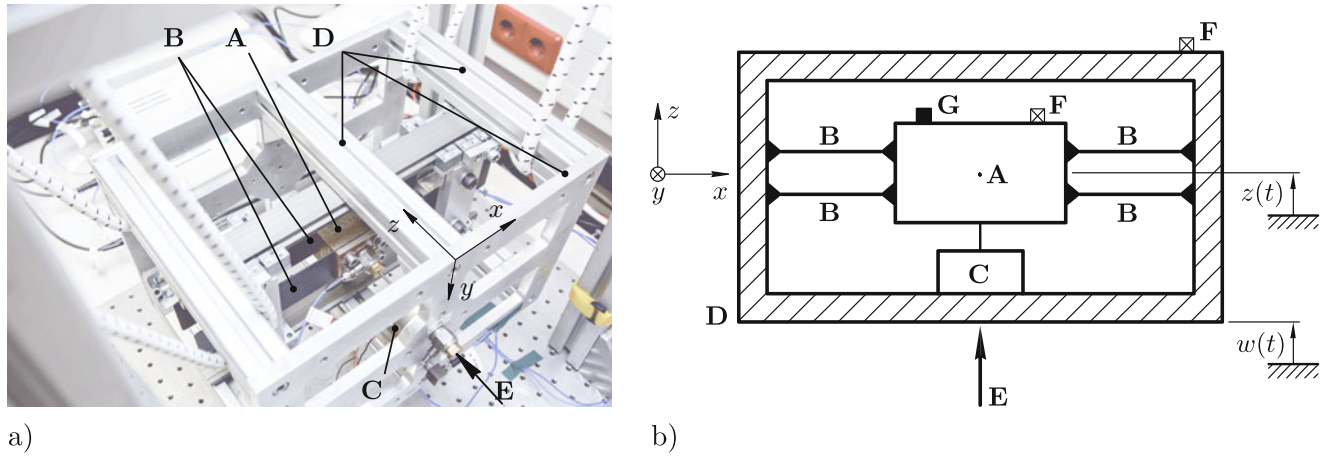


Fig. 14.2 Experimental test setup for passive and active vibration isolation (a) photo of the test rig with sloped top view, (b) schematic sketch of test rig with straight top view in y-direction

Table 14.1 Constant and varied parameters of the leaf springs and voice coil actuator

Element	Property	Variable	Value	Unit
Leaf spring parameter	Young's modulus	E_s	6200	N/m ²
	Width	t_s	0.04	m
	Height	h_s	0.01	m
Voice coil parameter	Resistance	R_e	4.8	Ω
	Inductance	L_e	0.003	H
	Force constant	Ψ_e	17.5	N/A
	Factor passive	$g_p, -$	1.68	As/m
		\bar{g}_p	2.4	As/m
		$g_p, +$	3.12	As/m
	Factor active	$g_a, -$	1.68	As/m
		\bar{g}_a	2.4	As/m
		$g_a, +$	3.12	As/m

The stiffness of one rectangular leaf spring is

$$k_s = \frac{E_s t_s h_s^3}{l_s^3}, \quad (14.6)$$

with the Young's modulus E_s , the width t_s , the height h_s and the length l_s of the leaf spring. The first three parameters are constant with their corresponding values displayed in Table 14.1, while the length of the leaf spring can be varied to set the stiffness to the desired value. The mass is attached to four leaf springs in parallel, hence (14.6) is multiplied with the factor 4 to calculate the total stiffness

$$k = 4 k_s = 4 \frac{(E_s t_s h_s^3)}{l_s^3} \quad (14.7)$$

of the system in Fig. 14.1b. The passive and active damping forces from (14.2) are realized with the voice coil actuator's force

$$F_v(t) = \Psi_e I_v(t) \quad (14.8)$$

with the actuator's force constant Ψ_e and the current $I_v(t)$ of the electrical network, a series connection of the constant inductance L_e and resistance R_e [10]. The differential equation of the electrical network is

$$I_v(t) R_e + \frac{dI_v(t)}{dt} L_e + U_{\text{ind}}(t) = U_v(t) \quad (14.9)$$

with the control voltage $U_v(t)$ as input parameter and the induced voltage $U_{\text{ind}}(t) = \Psi(\dot{z}(t) - \dot{w}(t))$ resulting from the relative velocity between the base excitation point and the oscillating mass in Fig. 14.1b. With the relation

$$\frac{dI_v(t)}{dt} \equiv i\omega I_v(t) \quad (14.10)$$

and substituting $I_v(t)$ from (14.9) in (14.8) follows

$$\underline{F}_v(\omega) = \Psi_e \frac{\underline{U}_v(\omega) + i\omega \Psi_e (z(\omega) - w(\omega))}{\underline{Z}_e(\omega)} \quad (14.11)$$

with the electrical impedance

$$\underline{Z}_e(\omega) = i\omega L_e + R_e. \quad (14.12)$$

Thus, through variations of the control voltage $U_v(t)$, the actuator's force in (14.11) can be varied only with limited precision due to the frequency dependency of the electrical impedance (14.12) and the dependency of the induced voltage $U_{\text{ind}}(t)$ on the relative velocity [10]. Therefore, in [10] Perfetto et al. proposed a method that compensates those effects by calculating the control voltage

$$\underline{U}_v(\omega) = g_{\text{amp}} (g_C + i\omega g_p \underline{Z}_e(\omega)) (z(\omega) - w(\omega)) + i\omega g_{\text{amp}} g_a \underline{Z}_e(\omega) z(\omega) \quad (14.13)$$

with the compensator gain $g_C = -\Psi_e/g_{\text{amp}}$, with is the constant gain g_{amp} of a voltage amplifier in the signal processing chain. The factor g_p is used to adjust the passive damping coefficient b in (14.2) and the factor g_a to adjust the feedback gain g in (14.2). Substituting (14.13) for $\underline{U}_v(\omega)$ in (14.11) and considering the relation (14.13) leads to the actuator force

$$F_v(t) = g_{\text{amp}} \Psi_e g_p (\dot{z}(t) - \dot{w}(t)) + g_{\text{amp}} \Psi_e g_a \dot{z}(t) \quad (14.14)$$

that can freely be adjusted by g_p and g_a . From the comparison of $F_v(t)$ with the passive damping force, F_b , and the active damping force, F_a from (14.2) follows the equations

$$b = g_{\text{amp}} \Psi_e g_p + b_0 = b_p + b_0 \quad \text{and} \quad g = g_{\text{amp}} \Psi_e g_a, \quad (14.15)$$

where b_p is the passive damping coefficient resulting set by the voice coil actuator. The damping coefficient $b_0 = 2 D_0 \omega_0 m$ is the inherent damping of the test rig with the open circuited voice coil actuator e. g. $F_v(t) = 0 \text{ N}$. Then, only the stiffness force F_k from (14.2) and the damping force $F_b(t) = b_0 (\dot{z}(t) - \dot{w}(t))$ act on the mass. From experimental measurements, the value of the constant damping ratio $D_0 = 0.0039\%$ is determined. The variation of the passive g_p and active factor g_a are discussed in the following section.

14.2.3 Variation of the Input Parameters

The parameter uncertainty results in the variation of the model's output, the numerically simulated amplitude and the phase, (14.4) and (14.5), and in the variation of the experimentally measured output data from the test rig due to the varying parameters mass m , stiffness k , damping coefficient b and gain g according to Table 14.2. Furthermore, the model's output and measured output data deviate from each other due to the model uncertainty. The model uncertainty results from the simplifications of the mathematical model compared to the real test rig such as assuming linearity or the use of discrete homogeneous stiffness and damping behavior. The effects of parameter and model uncertainty are briefly presented in the following based on the example of passive vibration isolation with a varying damping coefficient b .

Table 14.2 Varying input parameter values

Property	Variable	Value	Unit	Variation
Mass	m_-	0.64	kg	-15.88%
	\bar{m}	0.757	kg	0%
	m_+	0.875	kg	+16.01%
Stiffness	k_-	23,090	N/m	-19.42%
	\bar{k}	32,980	N/m	0%
	k_+	39,673	N/m	+20.28%
Damping coefficient	b_-	43.88	Ns/m	-30%
	\bar{b}	62.69	Ns/m	0%
	b_+	81.49	Ns/m	+30%
Gain	g_-	43.88	Ns/m	-30%
	\bar{g}	62.69	Ns/m	0%
	g_+	81.49	Ns/m	+30%

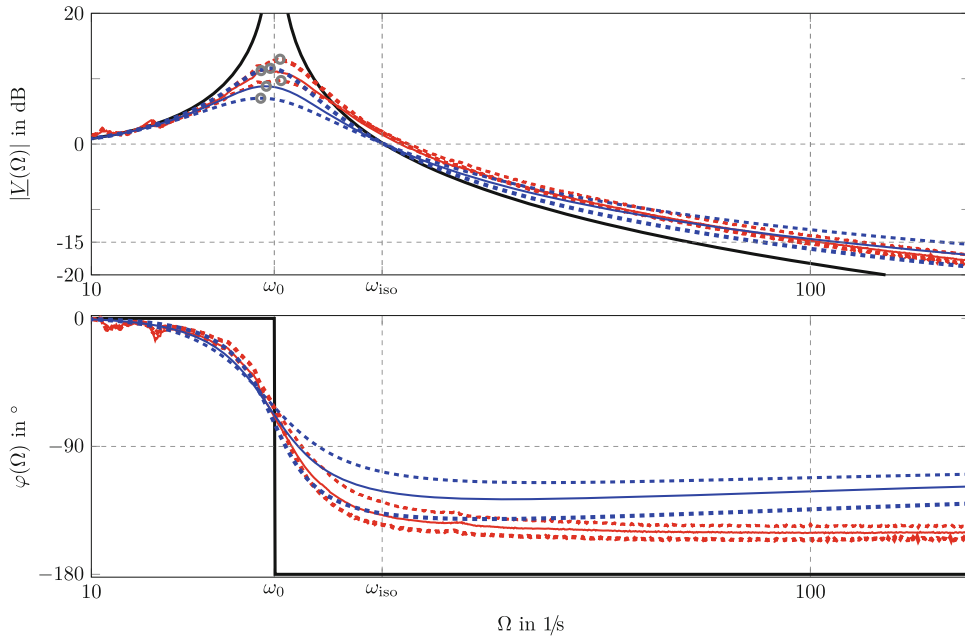


Fig. 14.3 Numerically simulated and measured amplitude $|V(\Omega)|$ and phase $\varphi(\Omega)$ for passive vibration isolation with $g = 0$, constant $m = \bar{m}$, constant $k = \bar{k}$ and varying b as shown in Table 14.2 for the simulated data (black solid line) $b_{1,\text{sim}} = 0$ Ns/m, (blue dashed dotted line) $b_{1,\text{sim}}$, (blue solid line) $b_{2,\text{sim}}$, (blue dashed line) $b_{3,\text{sim}}$ and the measured data (red dashed dotted line) $b_{1,\text{exp}}$, (red solid line) $b_{2,\text{exp}}$, (red dashed line) $b_{3,\text{exp}}$. The maximum amplitude V_{\max} for each case is marked with the grey circle o

Figure 14.3 shows the amplitude $|V(\Omega)|$ and phase $\varphi(\Omega)$ for passive vibration isolation of the analytical model, (14.4) and (14.5), and of the measured output data after transforming back $\Omega = \eta \omega_0$ within the frequency range $10 \leq \Omega \leq 120$ 1/s. The parameters $m = \bar{m}$ and $k = \bar{k}$ are the mean values chosen from Table 14.2 and the gain for active vibration isolation is $g = 0$ Ns/m while the damping coefficient varies with $b_1 < b_2 < b_3$.

Figure 14.3 shows amplitudes and phases for three different damping coefficients, $b_{1,\text{sim}} < b_{2,\text{sim}} < b_{3,\text{sim}}$ and $b_{1,\text{exp}} < b_{2,\text{exp}} < b_{3,\text{exp}}$, for numerical simulations and experiments. For both simulated and measured amplitude and phase responses in Fig. 14.3, a higher damping leads to a lower amplitude at their resonance frequency ω_{res} , but to a less decrease of amplitudes beyond the isolation frequency $\Omega > \omega_{\text{iso}}$, which is well known. For all three damping coefficients, b_- , \bar{b} and b_+ , the measured maximum amplitudes V_{\max} are higher than the simulated amplitudes. Furthermore, the simulated amplitude responses intersect at the model's isolation frequency ω_{iso} while the measured amplitude responses do not. Typical for passive vibration, the theoretical phase shift $\varphi(\Omega \gg \omega_0) = -90^\circ$ does not occur at undamped resonance frequency ω_0 for the three damping coefficients. The simulated phases tend towards $\varphi(\Omega \gg \omega_0) = -90^\circ$ for higher excitation frequencies but, the higher the damping coefficient, the lower the frequency at which the phase reaches close to -90° . For the measured phase, the tendency of the phase reaching -90° for frequencies $\Omega > \omega_0$ is not observed within the frequency range $10 \leq \Omega \leq 120$ 1/s.

Additionally, the deviation in the measured phase is lower than in the simulated phase for the three different damping coefficients.

In Fig. 14.3 only the damping coefficient b was varied in three different cases to demonstrate the differences between the numerical simulation and the experiments. For a thorough investigation of parameter and model uncertainty, first the interval of variation of each input parameter is set and presented in Table 14.2. The intervals are chosen in reference to previous work in [5] but have been adjusted due to geometrical restrictions of the test rig. The mass may vary about $\pm 16\%$ and the stiffness about $\pm 20\%$, which are higher values than previously used in [5]. The damping coefficient for passive vibration isolation and the gain for active vibration isolation vary with $\pm 30\%$ around their means, Table 14.2. The variations are assumed to be normally distributed with standard deviation σ for the simulation and the upper and lower values resulting from the variation range represent $\pm \sigma$ with 99.7% probability. That is an accepted approach for the standard deviation when assuming normal distribution [11]. The complex amplification function from (14.3) was calculated $N = 1000$ times via MONTE CARLO simulation for N independently varying, normally distributed samples of the mass, the stiffness and the damping coefficient for passive vibration isolations as well as the gain for active vibration isolation via MATLAB. Conducting the χ^2 -test according to [4] shows that the Null-hypothesis for assumed normal distribution is accepted for 1000 samples.

The experimental measurements are conducted for every combination of the three parameters mass, stiffness and damping coefficient or gain at their three different values from Table 14.2, according to a full factorial design of experiments. This allows to capture the effect of every input parameter on the measured output [12] leading to the number of $27 = 3^3$ combinations of the three different parameters for each, passive and active vibration isolation. In order to minimize deviations due to measurement errors or environmental changes, i.e. different temperatures, five repetitions for each of the 27 combination are conducted, leading to a total of $K = 5 \cdot 27 = 135$ measurements. The χ^2 -test is again used to prove that the measured outputs are normally distributed, thus validating the assumption of normal distribution of parameters for the MONTE CARLO simulation.

14.3 Quantification of Model Uncertainty

The mathematical models of the one mass oscillator introduced in Sect. 14.2.1 predict the amplitude and phase responses in case of passive and active vibration isolation according to the parameter variation in Table 14.2 via a MONTE CARLO simulation with $N = 1000$ samples. The model uncertainty for the five evaluation criteria introduced in Sect. 14.1, V_{\max} , V_{100} , ω_{res} , ω_{iso} and ω_{100} , is quantified and compared. The authors validate the models with the experimental data via the Area Validation Metric [6] and a Bayesian probabilistic approach using Bayes factors [7, 8].

14.3.1 Quantification of Uncertainty with the Area Validation Metric

The Area Validation Metric (AVM)

$$d(x) = \int_{-\infty}^{\infty} |F_{\text{sim}}(x) - F_{\text{exp}}(x)| dx \quad (14.16)$$

was presented by Roy and Oberkampf in [6] as a method to quantify model uncertainty. In (14.16), the absolute value of the difference between the cumulative density functions (CDF) of the numerical simulated data $F_{\text{sim}}(x)$ from the MONTE CARLO simulation and the experimental measurements $F_{\text{exp}}(x)$ is calculated by integration. The variable x is a simulated or measured evaluation criterion, in our case V_{\max} , V_{100} , ω_{res} , ω_{iso} or ω_{15} . The CDF of normally distributed data is

$$F(x) = \frac{1}{2} \left[1 + \frac{2}{\sqrt{\pi}} \int_0^{x_{\max}} e^{-(x - \bar{x})^2 / (2\sigma_x^2)} dx \right] \quad (14.17)$$

with the mean \bar{x} and standard deviation σ_x of the simulated evaluation criteria and represents the probability that the evaluation criteria is equal to or smaller than x .

Passive Vibration Isolation

In Fig. 14.4 the CDF from the MONTE CARLO simulation and the measured evaluation criteria, V_{\max} , V_{100} , ω_{res} , ω_{iso} and ω_{15} for passive vibration isolation are presented, with the AVM as the gray area between the CDF. Three different characteristics exist to evaluate parameter and model uncertainty of the evaluation criteria: the slope of the CDF, possible intersection of the CDFs and the area between the CDF. First, the higher the slope, the smaller the parameter uncertainty, because the range of possible values of the evaluation criteria is smaller. Thus, the observation of the slope of simulated and measured output enables a comparison between parameter uncertainty of the simulated and measured outputs. Second, if both curves intersect at some point, then the evaluation criteria has identical or similar values in the area around the intersection, thus the model uncertainty is smaller than without any overlapping but only at the point of intersection. Finally the smaller the AVM, the smaller the model uncertainty.

The slopes of all simulated CDF for the five evaluation criteria in Fig. 14.4 are similar to the slopes of the measured output data, but the difference between the slopes varies for the evaluation criteria. For passive vibration isolation, the size of the AVM of the maximum amplitude V_{\max} is higher than for the other four evaluation criteria, showing that a systematic bias exists between mathematical model and the test rig. The CDF of V_{\max} are the only ones that do not intersect. The AVM are normalized to the mean values of the simulated output data and are listed in Table 14.3. For passive vibration isolation, the highest normalized AVM results for the maximum amplitude with $d_{p,n,V_{\max}} = 0.208$, while the lowest normalized AVMs are $d_{p,n,\omega_{\text{res}}} = d_{p,n,\omega_{\text{iso}}} = 0.034$.

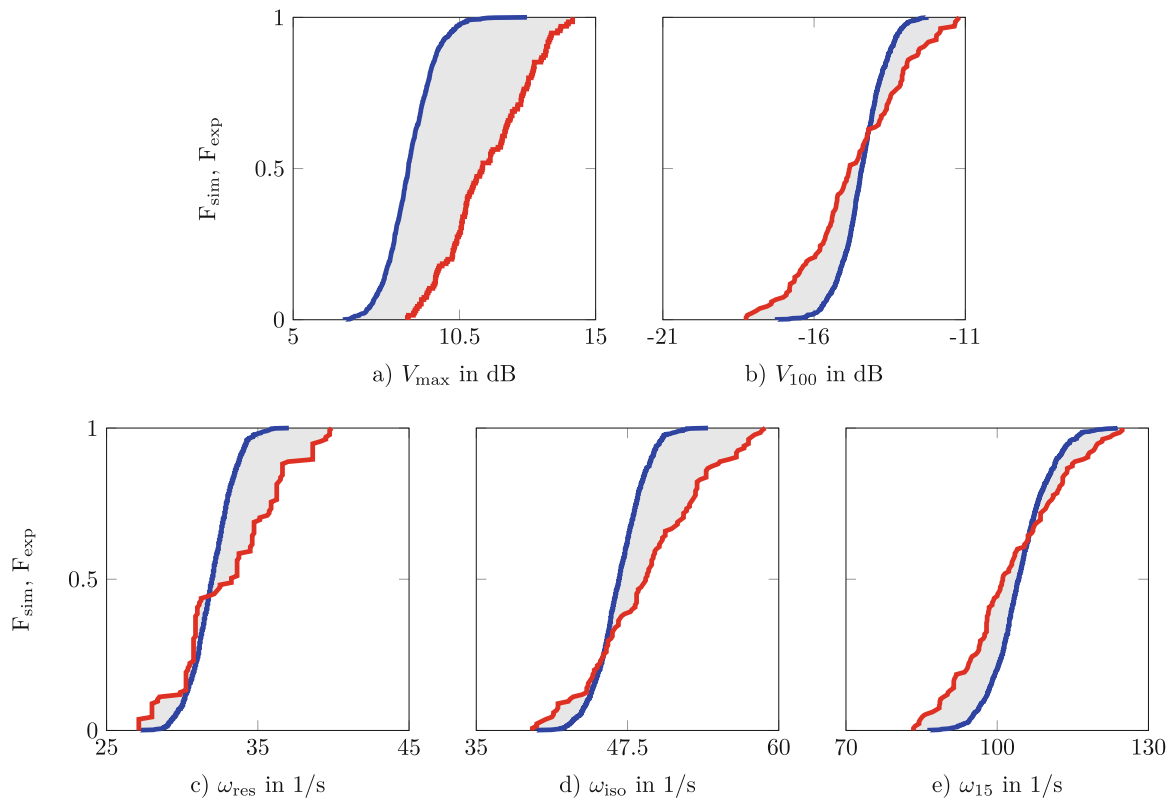


Fig. 14.4 Area Validation Metric for passive vibration isolation is the grey area between the CDF for the simulated F_{sim} (blue solid line) and the measured output data F_{exp} (red solid line) for the evaluation criteria (a) the maximum amplitude V_{\max} , (b) the amplitude V_{100} at $\Omega = 100 \text{ l/s}$ (c) the resonance frequency ω_{res} , (d) the isolation frequency ω_{iso} and (e) the frequency ω_{15} at $|V(\Omega)| = -15 \text{ dB}$

Table 14.3 Area validation metric of the evaluation criteria

Vibration isolation	AVM	V_{\max}	V_{100}	ω_{res}	ω_{iso}	ω_{15}
Passive	$d_{p,\text{abs}}$	2.079	1.038	1.182	1.644	5.730
	$d_{p,n}$	0.207	0.072	0.034	0.034	0.055
Active	$d_{a,\text{abs}}$	2.071	1.119	1.038	1.449	5.198
	$d_{a,n}$	0.207	0.077	0.032	0.029	0.041

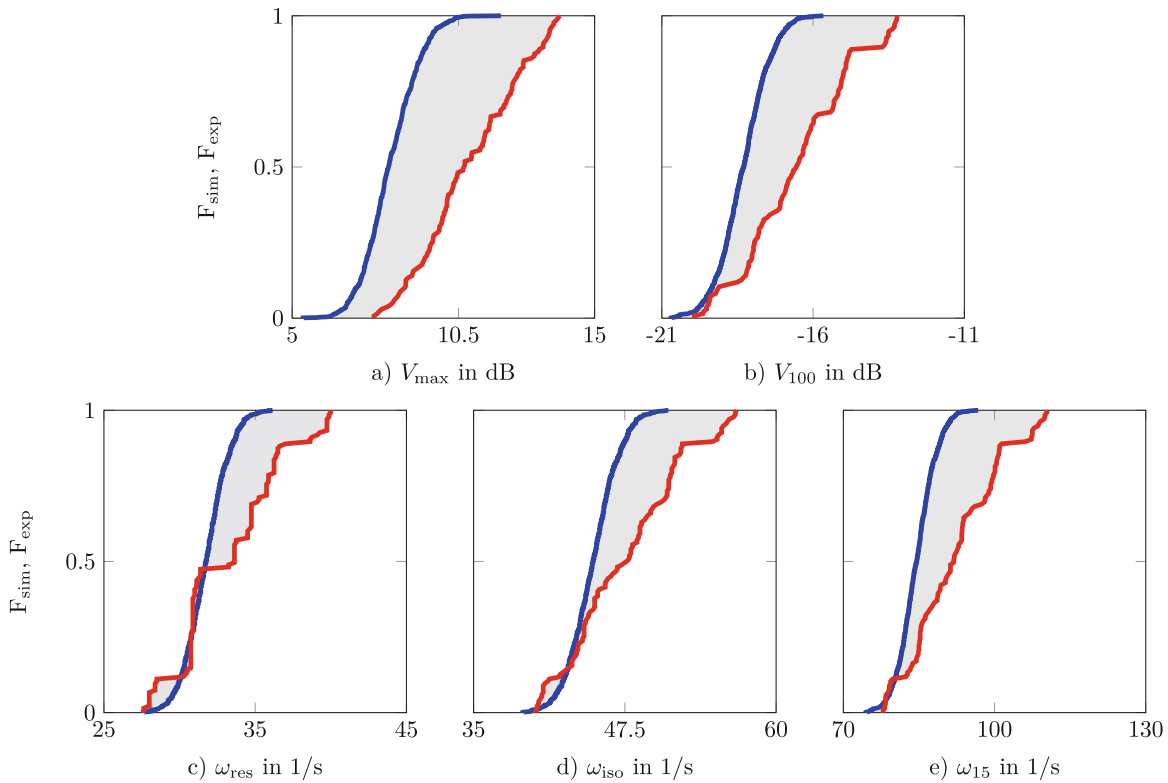


Fig. 14.5 Area Validation Metric for active vibration isolation is the grey area between the CDF for the simulated F_{sim} (blue solid line) and the measured output data F_{exp} (red solid line) for the five evaluation criteria (a) the maximum amplitude V_{max} , (b) the amplitude V_{100} at $\Omega = 100 \text{ l/s}$, (c) the resonance frequency ω_{res} , (d) the isolation frequency ω_{iso} and (e) the frequency ω_{15} at $|\underline{V}(\Omega)| = -15 \text{ dB}$

Active Vibration Isolation

The CDF from the MONTE CARLO simulation and the measured evaluation criteria for active vibration isolation are presented in Fig. 14.5. As was observed for passive vibration isolation in Fig. 14.4, the slopes of all simulated curves are similar to the slopes of the measured output data. The AVM of the maximum amplitude V_{max} is the highest, meaning it has the highest bias between simulated and measured output data. In difference to passive vibration isolation, there is no intersection between the CDF of V_{max} and V_{100} . The normalized AVM of the five evaluation criteria are listed in Table 14.3. The highest model uncertainty exists for V_{max} with $d_{a,n,V_{\text{max}}} = 0.204$ and the model uncertainty for ω_{iso} is the lowest with $d_{a,n,\omega_{\text{iso}}} = 0.029$, which differs with a value of 0.003 from $d_{a,n,\omega_{\text{res}}} = 0.032$.

Comparison of the Model Uncertainty for Passive and Active Vibration Isolation

The normalized AVM in Table 14.3 show that the model output deviates from the real system's output of the test rig in Fig. 14.2 for both passive and active vibration isolation for all five evaluation criteria due to model uncertainty. The highest model uncertainty occurs at the maximum amplitude V_{max} with $d_{a,n,V_{\text{max}}} = 0.207$ for passive and $d_{a,n,V_{\text{max}}} = 0.204$ for active vibration isolation. It is followed by the model uncertainty at the amplitude V_{100} with $d_{a,n,V_{100}} = 0.072$ and $d_{a,n,V_{100}} = 0.08$.

The model prediction at the three frequency points is more accurate than at the two amplitudes, with the lowest model uncertainty occurring for the resonance and isolation frequencies, $d_{p,n,\omega_{\text{res}}} = 0.034$ and $d_{p,n,\omega_{\text{iso}}} = 0.034$ for passive and $d_{a,n,\omega_{\text{res}}} = 0.032$ and $d_{a,n,\omega_{\text{iso}}} = 0.029$ for active vibration isolation. Summing up, the model uncertainty for the active system model is lower than for the passive system model for all evaluation criteria except for V_{100} , but the difference only varies slightly.

14.3.2 Quantification of Model Uncertainty with a Bayesian Approach

The Bayesian approach introduced in Sect. 14.2.1 uses the single n -th posterior probability

$$p(H_{n,x}|A_x) = \frac{p(A_x|H_{n,x}) p(H_{n,x})}{\sum_{n=1}^N p(A_x|H_{n,x}) p(H_{n,x})} \quad (14.18)$$

that represents the probability of the numerically simulated events $H_{n,x}$ for $n = 1, 2, 3, \dots, N = 1000$ samples of an evaluation criteria x under the condition of the observed event A_x , here the experimentally measured evaluation criteria at the test rig [7, 8, 13]. Thereby $p(A_x|H_{n,x})$ is the likelihood, $p(H_{n,x})$ is the prior probability and $\sum_{n=1}^N p(A_x|H_{n,x}) p(H_{n,x})$ is the total probability, a normalizing factor to ensure that the integral of the posterior probability is equal to one. The single n -th prior probability

$$p(H_{n,x}) = \frac{1}{\sigma_H \sqrt{2\pi}} e^{-\frac{1}{2} \left(\frac{H_{n,x} - \bar{H}}{\sigma_H} \right)^2} \quad (14.19)$$

is the normal density function of the numerical simulated events $H_{n,x}$, with mean \bar{H} and standard deviation σ_H , and gives the range and probability of the evaluation criteria x expected to predict the experimental data. The assumption of normal distribution of the numerical simulated events is based on the accepted χ^2 -test of the experimental data in Sect. 14.2.3. However, the prior is a hypothesis rather than a probability. The likelihood

$$p(A_x|H_{n,x}) = \prod_{k=1}^K \frac{1}{\sigma_H \sqrt{2\pi}} e^{-\frac{1}{2} \left(\frac{A_{x,k} - H_{n,x}}{\sigma_H} \right)^2} \quad (14.20)$$

represents the similarity between the observed events A_x of an evaluation criteria x and the hypothesis events $H_{n,x}$ from the mathematical models [8], when $A_{x,k}$ is the k -th observed event for the number $k = 1, 2, 3, \dots, K = 135$ of experimental measurements set in Sect. 14.2.3 for each evaluation criterion. The posterior (14.18) and prior probabilities (14.19) are used to calculate the Bayes factor

$$B = \frac{p(\bar{H}_x|A_x)}{p(\bar{H}_x)} \quad (14.21)$$

that is defined as the ratio of the posterior probability and prior probability of the mean \bar{H}_x of the numerical simulated events $H_{n,x}$. The Bayes factor provides a threshold value $B = 1$. If $B > 1$, the mathematical model is deemed adequate to predict the experimental or, if $B < 1$, the mathematical model is inadequate [8].

Passive Vibration Isolation

Figure 14.6 shows the prior (14.18) and posterior probabilities (14.19) for each evaluation criteria V_{\max} , V_{100} , ω_{res} , ω_{iso} or ω_{15} , introduced in Sect. 14.1. The vertical, dashed line illustrates the mean \bar{H}_x . For V_{\max} , the prior and posterior density functions do not overlap, indicating that the predicted model output differs from the experimental data, Fig. 14.6. For the other four evaluation criteria, the prior and posterior probabilities overlap in various degrees. The most central overlapping occurs for V_{100} in Fig. 14.6, which means that the model uncertainty is lower than for the other four evaluation criteria. Those assumptions are confirmed by the calculated Bayes factors in Table 14.4, with $B_{p,V_{100}}=0,038$ and $B_{p,\omega_{15}}=0,006$ being the only factors with values $B_p > 0$. However, the Bayes factors for all evaluation criteria are smaller than one, which means that the mathematical model for passive vibration isolation is deemed inadequate to predict any of the five evaluation criteria.

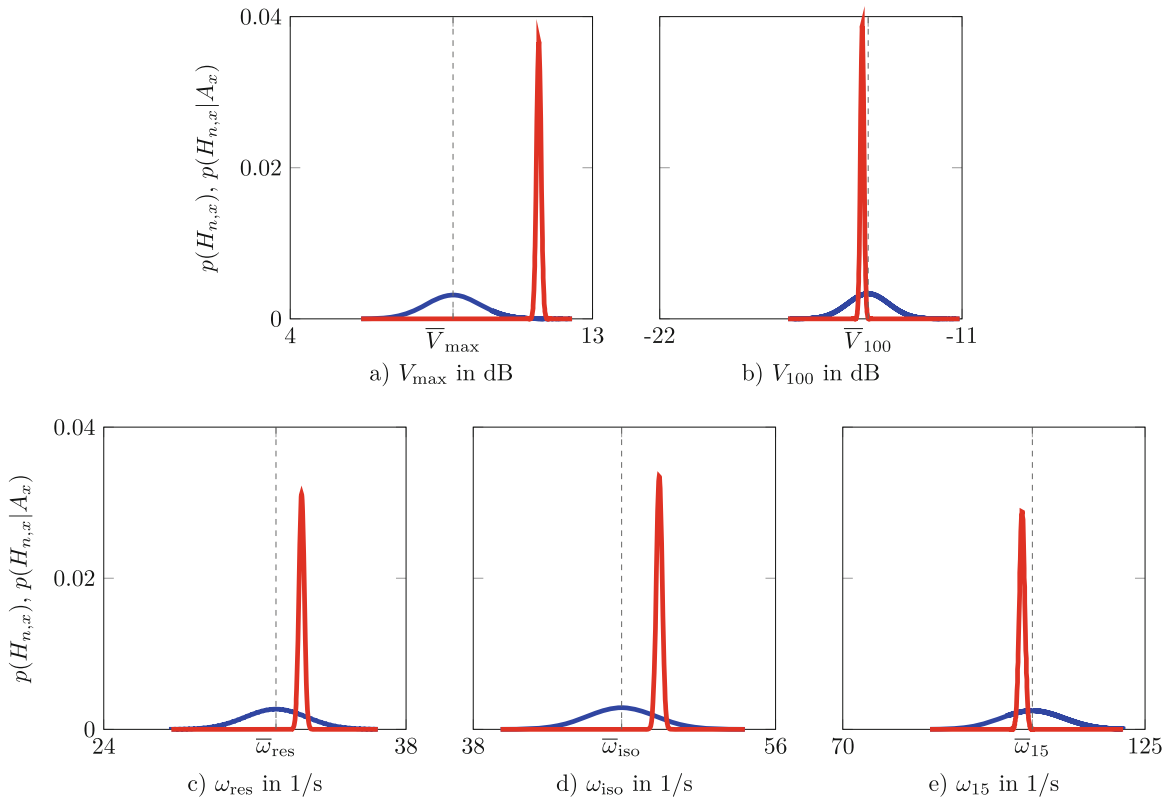


Fig. 14.6 Bayes approach with prior $p(H_{n,x})$ (blue solid line) and posterior probability $p(H_{n,x}|A_x)$ (red solid line) for passive vibration isolation for the evaluation criteria (a) the maximum amplitude V_{\max} , (b) the amplitude V_{100} at $\Omega = 100$ 1/s, (c) the resonance frequency ω_{res} , (d) the isolation frequency ω_{iso} and (e) the frequency ω_{15} at $|\underline{V}(\Omega)| = -15$ dB

Table 14.4 Bayes factors B for passive and active vibration isolation

Bayes factor B	V_{\max}	V_{100}	ω_{res}	ω_{iso}	ω_{100}
B_p	0.000	0.038	0.000	0.000	0.006
B_a	0.000	0.000	0.000	0.000	0.000

Active Vibration Isolation

Figure 14.7 shows the prior (14.18) and posterior probabilities (14.19) of the five evaluation criteria, V_{\max} , V_{100} , ω_{res} , ω_{iso} and ω_{15} for active vibration isolation. The prior and posterior density functions overlap noticeably only for ω_{res} and ω_{iso} . Most overlapping occurs at the resonance and isolation frequencies ω_{res} and ω_{iso} , indicating the lowest model uncertainty. According to the Bayes factors in Table 14.4, the mathematical model for active vibration isolation is inadequate to predict the system's output because $B_a < 1$ for all five evaluation criteria.

Comparison of the Model Uncertainty for Passive and Active Vibration Isolation

The use of the Bayes approach including the Bayes factor shows the difference between the model uncertainty of the passive and active system model. The overlapping of the prior and posterior density functions is more noticeably in case of passive vibration isolation, however, the mathematical models of the passive and active systems are both inadequate to predict the system's output when $B < 1$ occurs.

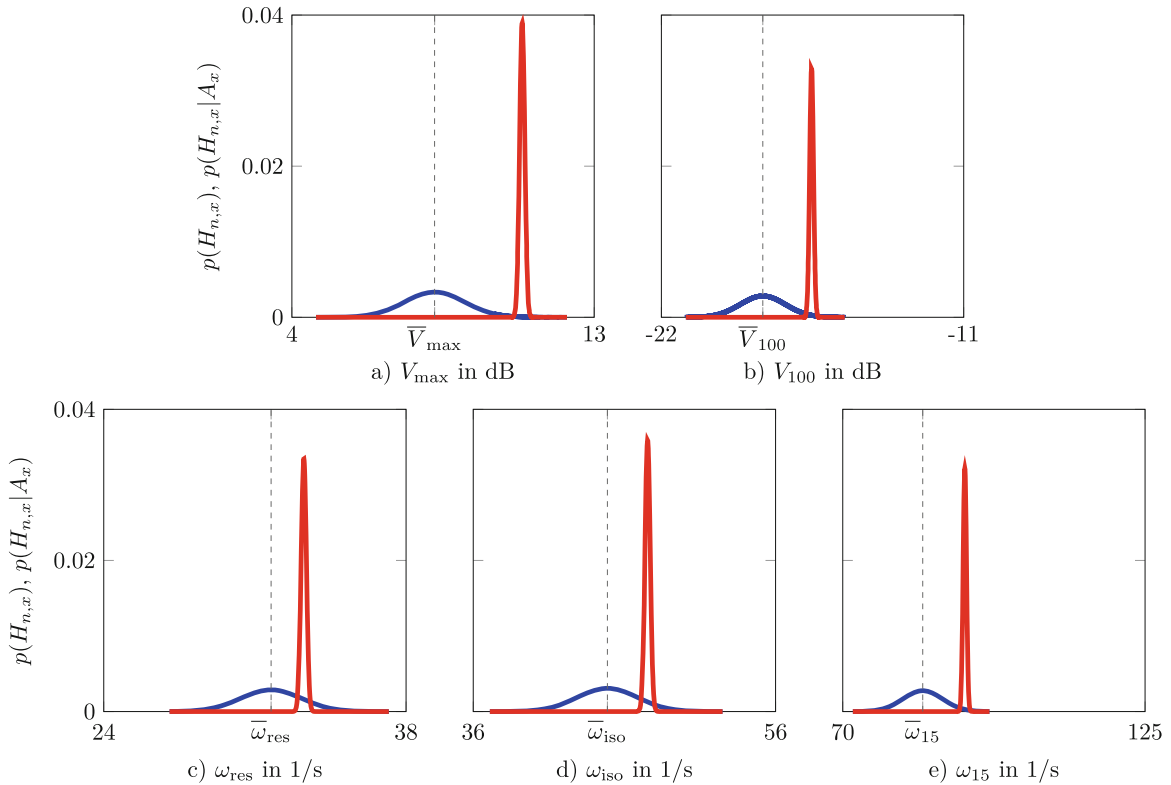


Fig. 14.7 Bayes approach with prior $p(H_{n,x})$ (blue solid line) and posterior probability $p(H_{n,x}|A_x)$ (red solid line) for active vibration isolation for the evaluation criteria (a) the maximum amplitude V_{\max} , (b) the amplitude V_{100} at $\Omega = 100 \text{ l/s}$, (c) the resonance frequency ω_{res} , (d) the isolation frequency ω_{iso} and (e) the frequency ω_{15} at $|\underline{V}(\Omega)| = -15 \text{ dB}$

14.4 Conclusion

In this contribution, model uncertainty of passive and active vibration isolation models of a one mass oscillator is quantified with respect to major characteristic points in amplitude and frequency, such as maximum amplitude at resonance frequency, the isolation frequency and amplitudes beyond the isolation frequency. For active vibration isolation, a simple constant velocity feedback controller is used. The uncertainty is quantified with two different methods, the Area Validation Metric and a Bayesian approach using the Bayes factor. For both methods, numerically simulated model output from a MONTE-CARLO simulation and experimentally measured data of a test rig according to a full factorial design of experiment are utilized to quantify uncertainty. It is shown that the discrepancy between model and test rig of the observed maximum amplitudes at resonance frequency is higher than of the frequencies beyond the isolation frequency. Furthermore, both validation methods show that no significant difference between the uncertainty in modeling the passive and active vibration isolation exist. However, when using the Bayes factor's threshold value of one, the linear mathematical model's are deemed to be inadequate to predict the test rig's output. In future work, the authors will quantify and compare the uncertainty for passive vibration isolation with more complex methods of active vibration isolation than the constant velocity feedback control, such as adaptive feedforward controller and robust controller.

Acknowledgements The authors like to thank the German Research Foundation DFG for funding this research within the SFB 805.

References

1. VDI 2062: Vibration Insulation – Insulation Elements, Part 2. Verein Deutscher Ingenieure, Beuth Verlag, Berlin (2007)
2. VDI 2064: Aktive Schwingungsisolierung – Active Vibration Isolation. Verein Deutscher Ingenieure, Beuth Verlag, Berlin (2010)
3. Platz, R., Ondoua, S., Enss, G.C., Melz, T.: Approach to evaluate uncertainty in passive and active vibration reduction. In: SEM Society for Experimental Mechanics, 2014, Proceedings of the 32nd IMAC, pp. 345–352. Springer, Cham (2014)

4. Platz, R., Enss, G.C.: Comparison of uncertainty in passive and active vibration isolation. In: SEM Society for Experimental Mechanics, 2015, Proceedings of the 33rd IMAC, pp. 15–25 (2015)
5. Platz, R., Melzer, C.: Uncertainty quantification for decision making in early design phase for passive and active vibration isolation. In: Proceedings of ISMA 2016 Including ISMA Advance Conference Programme, pp. 4501–4513 (2016)
6. Roy, C.J., Oberkampf, W.L.: A complete framework for verification, validation, and uncertainty quantification in scientific computing (invited). In: 48th AIAA Aerospace Sciences Meeting Including the New Horizons Forum and Aerospace Exposition, p. 124 (2010)
7. Mallapur, S., Platz, R.: Quantification and evaluation of uncertainty in the mathematical modelling of a suspension strut using Bayesian model validation approach. In: SEM Society for Experimental Mechanics, 2017, Proceedings of the 35rd IMAC, pp. 113–124 (2017)
8. Sankararaman, S., Mahadevan, S.: Model validation under epistemic uncertainty. Reliab. Eng. Syst. Saf. **96**, 1232–1241 (2011)
9. Kennedy, M., O'Hagan, A.: Predicting the output from a complex computer code when fast approximations are available. Biometrika **2000**, 1–13 (2000)
10. Perfetto, S., Rohlfing, J., Infante, F., Mayer, D., Herold, S.: Test rig with active damping control for the simultaneous evaluation of vibration control and energy harvesting via piezoelectric transducers. J. Phys. Conf. Ser. **744**, 012010 (2016)
11. Schuëller, G.I.: On the treatment of uncertainties in structural mechanics and analysis. Comput. Struct. **85**, 235–243 (2007)
12. Siebertz, K., van Bebber, D., Hochkirchen, T.: Statistische Versuchsplanung: Design of Experiments (DoE). Springer, Berlin (2010)
13. Mallapur, S., Platz, R.: Uncertainty quantification in the mathematical modelling of a suspension strut using Bayesian inference. Mech. Syst. Signal Process. **118**, 158–170 (2019)



Chapter 15

Bayesian Model Updating of a Five-Story Building Using Zero-Variance Sampling Method

Mehdi M. Akhlaghi, Supratik Bose, Peter L. Green, Babak Moaveni, and Andreas Stavridis

Abstract This study presents the Bayesian model updating and stochastic seismic response prediction of a reinforced concrete frame building with masonry infill panels. After the 2015 Gorkha earthquake, some of the authors visited the building and recorded ambient vibration data using a set of accelerometers. The seismic response of the building was also recorded during one of the moderate aftershocks, using a set of sensors at the basement and the roof. In this study, the ambient vibration data is used to calibrate a model and the earthquake data is used to validate it. Natural frequencies and mode shapes of the building are extracted through an output-only system identification process. An initial finite element model of the building is developed using a recently proposed modeling framework for masonry-infilled RC frames. Bayesian model updating is then performed to update the stiffness of selected structural elements and evaluate their respective uncertainties, given the available data. A novel sampling approach, namely Zero-Variance MCMC, is implemented to address the computational challenges of stochastic simulation when estimating the joint posterior probability distribution of the model's parameters. This sampling approach has been shown to drastically improve computational efficiency while preserving adequate accuracy. The calibrated model is used for the probabilistic prediction of the seismic response of the building to a moderate earthquake. This predicted response is shown to be in good agreement with the available recorded response of the building at the roof.

Keywords Bayesian Model Updating · Zero-Variance Markov Chain Monte Carlo · System Identification · Response Prediction

15.1 Introduction

Following the development of fast computers, numerically intensive sampling methods for statistical inference have gained a lot of attention. These methods are generally easy to implement and result in a point cloud of sample points that can help us understand the uncertainties involved in the process much better. Markov chain Monte-Carlo (MCMC) method is one of these methods that has been used extensively in many research studies.

For more complicated problems involving large number of updating parameters, these sampling algorithms can become inefficient or computationally expensive. This has resulted in a series of efforts to improve the efficiency of this method leading to algorithms like adaptive MCMC [1] and transitional MCMC [2], each of which has tried to address part of the problem with this sampling technique. The Zero-Variance method which is used in this research study has been shown to significantly reduce the sample variance of the structural parameters estimated using Monte Carlo methods and also increase the efficiency of the algorithm [3].

M. M. Akhlaghi (✉) · B. Moaveni
Department of Civil and Environmental Engineering, Tufts University, Medford, MA, USA
e-mail: mehdi.akhlaghi@tufts.edu

S. Bose · A. Stavridis
Department of Civil, Structural and Environmental Engineering, University at Buffalo, Buffalo, NY, USA

P. L. Green
Department of Civil Engineering and Industrial Design, University of Liverpool, Liverpool, UK

15.2 Analysis

The 5-story masonry infilled reinforced concrete building of the National Society of Earthquake Technology (NSET), is chosen for this research study. Ambient vibration data has been collected following the 2015 Gorkha earthquake using a set of 16 accelerometers. The structure is also equipped with a continuous monitoring system which has recorded the acceleration data at the 4th floor and ground level during the earthquake [4]. Figure 15.1 shows the street view and the plan view of the building, depicting the location of the masonry and shear walls in the plan view.

System identification had been conducted using an output only method and eigenfrequency and mode shapes of the building are calculated. A 3D model of the building is built following a recently proposed methodology [5, 6] based on the

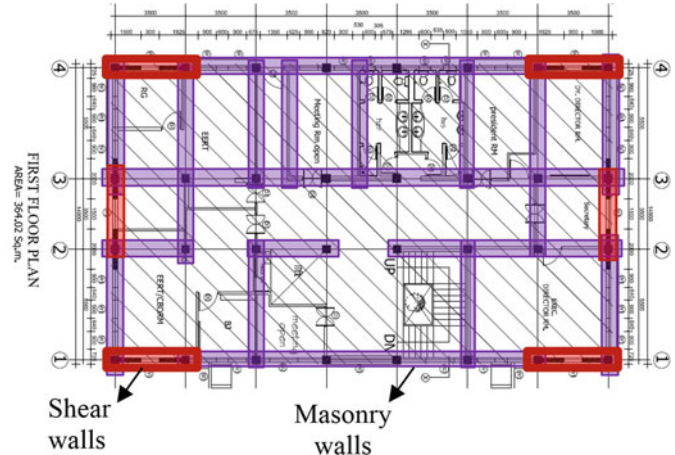


Fig. 15.1 NSET building from the street view and the plan

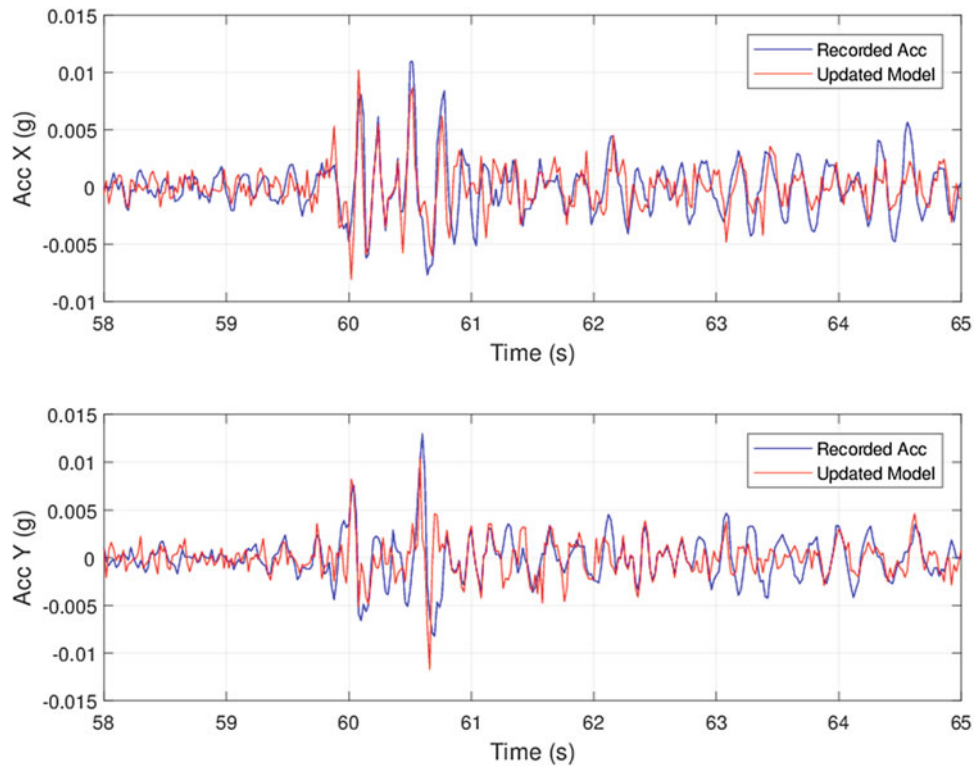


Fig. 15.2 Response prediction of the 4th floor based on the deterministic model updating results

available data and is then calibrated using both deterministic and probabilistic model updating. For the probabilistic part, Bayesian model updating is conducted using both basic and zero variance MCMC algorithms. Results from these two sets of analyses are compared along with the results from the deterministic model updating. The seismic response of the building is then predicted using this calibrated model and the results are compared to the actual acceleration data available at the fourth floor of the building during the earthquake. Figure 15.2 demonstrates an initial response prediction based on only the deterministic model updating results.

Acknowledgements Partial support of this study by the National Science Foundation Grants 1254338, 1430180 and 1545595 is gratefully acknowledged. The opinions, findings, and conclusions expressed in this paper are those of the authors and do not necessarily represent the views of the sponsors and organizations involved in this project.

References

1. Gilks, W.R., Roberts, G.O., Sahu, S.K.: Adaptive Markov Chain Monte Carlo. *J. Am. Stat. Assoc.* **93**, 1045–1054 (1998)
2. Ching, J., Chen, Y.C.: Transitional Markov chain Monte Carlo method for Bayesian model updating, model class selection, and model averaging. *J. Eng. Mech.* **133**(7), 816–832 (2007)
3. Green, P.L., Maskell, S.: Parameter estimation from big data using a sequential Monte Carlo sampler, 27th ISMA Conference on Noise and Vibration Engineering, Leuven, Belgium, September 19–21, 2016
4. Akhlaghi, M.M., Bose, S., Moaveni, B., Stavridis, A.: Structural Identification of a Five-Story Reinforced Concrete Office Building in Nepal, 36th IMAC Conference, Orlando, FL, February 2018
5. Bose, S., Martin, J., Stavridis, A.: Framework for the non-linear dynamic simulation of the seismic response of infilled RC frames. In: Proceedings of the 11th National Conference on Earthquake Engineering, Los Angeles, CA, June 2018
6. Stavridis, A., Martin J., Bose S.: Updating the ASCE 41 provisions for infilled RC frames. In: Proceedings of the 2017 SEAOC Convention, San Diego, CA, September 2017



Chapter 16

Input Estimation and Dimension Reduction for Material Models

Sam Myren, Emilio Herrera, Andrew Shoats, Earl Lawrence, Emily Casleton, D. J. Luscher, and Saryu Fensin

Abstract Computer models for applications such as climate or materials have become increasingly complex. In particular, the input and output dimensions for these types of models has grown steadily larger, which has increased the computational burden of comparing these models with experimental data. This has spurred the development of statistical techniques for estimating outputs and reducing the dimension. This paper will show an example of these approaches applied to modeling and experiments for Tantalum, a material of interest for the Departments of Defense and Energy. We obtain results from a number of small-scale tests of Tantalum single crystals and use these results in a Bayesian statistical procedure to constrain the range and dimensionality of a Tantalum model.

Keywords Dimension reduction · Material modeling · Model calibration · Emulation · Tantalum

16.1 Introduction

Many materials are used in engineering applications under conditions that are considerably more extreme than those we can test in a laboratory. We need well-calibrated, physics-based materials models in order to extrapolate from laboratory experiments to actual use cases. Ideally, these models are calibrated in a way that provides quantified uncertainty along with predictions so that we can properly assesses risk under the true operating conditions. This paper presents one solution to this problem that uses Bayesian statistics to estimate input parameters of a strength model for tantalum based on laboratory experiments.

Tantalum is a rare earth refractory metal that is most commonly used in the electronics industry on capacitors. It is particularly useful because of its high melting point and corrosion resistance. These properties are desirable for defense applications where tantalum may be used for material containment under extreme temperatures or on missiles/spacecraft. Therefore, it is important to understand how tantalum will respond to a variety of external stimuli. Unfortunately, due to the expense of the material and the extreme conditions under which it will be used, it is costly or impossible to run even small-scale experiments. Computer model simulations of tantalum provide a mechanism to learn more about the material under different scenarios.

We consider a simulation model for compressive tantalum. The model predicts experimental stress-strain curves as a function of the experimental conditions (e.g., the temperature and strain rate) and materials properties of the tantalum (e.g., Boltzmann constant and Burger's Vector). Sometimes, material properties are relatively well-accepted within the field. This work focuses on those parameters that are more difficult to characterize. Among these are χ , C_1 , and C_A which represent the percent of work converted to heat under high strain rate tests, the material's hardening response to stress, and the reduction of dislocation density through annihilation due to stress, respectively.

However, the computational cost of running such computer simulations can also be time and resource expensive. In addition, a given computer simulation does not perfectly describe nature. This paper employs sensitivity analysis and

S. Myren
Department of Physics and Optical Engineering, Rose-Hulman Institute of Technology, Terre Haute, IN, USA

E. Herrera
Department of Mechanical Engineering, New Mexico Institute of Mining and Technology, Socorro, NM, USA

A. Shoats
Department of Mechanical Engineering, Stanford University, Stanford, CA, USA

E. Lawrence · E. Casleton (✉) · D. J. Luscher · S. Fensin
Los Alamos National Laboratory, Los Alamos, NM, USA
e-mail: ecasleton@lanl.gov

emulation of the model, along with a Markov chain Monte Carlo approach, to attempt to estimate the values of 14 unknown parameters that produce outputs that match corresponding experimental data. Through the process presented here, we can estimate parameter values with corresponding uncertainty, which could then inform other models. We do so by applying the framework presented in [1, 2].

16.2 Physical Measurements

We use two types of experiments on two experimental devices in order to learn how tantalum responds to low and high strain rates.

For the low strain rate (ASTM standard of 10^{-3} – 10^{-1} s $^{-1}$) tests, a Materials Testing System (MTS) was utilized. MTS testing entails slow loading the specimen from above at a controlled rate while measuring the strain of the sample as a function of applied stress. Strain is measured by displacement sensors placed at the base and top of the samples. As the operator of the MTS increases the known pressure from above, the sample bears the added pressure and compresses, and the strain of the specimen is tracked as the displacement sensors get closer together. Figure 16.1 displays a Tantalum specimen resting on the platform within the MTS machine. In total, seven experiments were performed using this experimental setup; each at a different strain rate and temperature. Two tests at 21 °C were performed for strain rates of $1\text{e}-1$ s $^{-1}$ and $1\text{e}-3$ s $^{-1}$, two tests at –80 °C were performed at $1\text{e}-1$ s $^{-1}$ and $1\text{e}-3$ s $^{-1}$, one test at 200 °C was performed at $1\text{e}-3$ s $^{-1}$, and two tests at 400 °C were performed at $1\text{e}-1$ s $^{-1}$ and $1\text{e}-3$ s $^{-1}$.

For the high strain rate (4×10^3 – 5×10^3 s $^{-1}$) tests, a split Hopkinson Bar was utilized. In the split Hopkinson Bar test, tantalum samples are placed between two metal bars: the incident bar and the transmission bar. A gas gun accelerates the incident bar toward the sample. The sample is struck by the incident bar and compresses between the incident bar and the transmission bar. During compression, strain gauges record the displacement of the sample. Three experiments were performed using this experimental setup; each at a different strain rate and temperature. The first test was performed at a strain rate of 4400 s $^{-1}$ at 200 °C, the second test at 5000 s $^{-1}$ at 400 °C, and the third test at 5300 s $^{-1}$ at 600 °C.

In all experiments, the tantalum specimens were single crystals and compressed in the [100] direction. The specimens were cylinders with a height and diameter of about 1.0 cm. The testing generated stress/strain relationship plots. Our experimental data are shown in Fig. 16.2.

16.3 Computer Model Simulation

The compressive tantalum model subject to optimization in this investigation is based on the single-crystal constitutive theory from [3, 4] applied here to computing uniaxial stress response during dynamic loading of single crystal BCC tantalum, for example under split Hopkinson pressure bar loading. Under these conditions and for crystallographic orientations (e.g. loading along [100]) in which the response exhibits symmetric slip on a subset of all available slip systems, an assumption of small strains enables a simple evaluation of the stress, $\bar{\sigma}$, versus strain, $\bar{\epsilon}$, curve given a prescribed strain rate, $\dot{\bar{\epsilon}}$, or strain versus time history, $\bar{\epsilon}(t)$. The shear stress on each of the N_A active slip systems can be expressed as $\tau = f_\tau \bar{\sigma}$ where

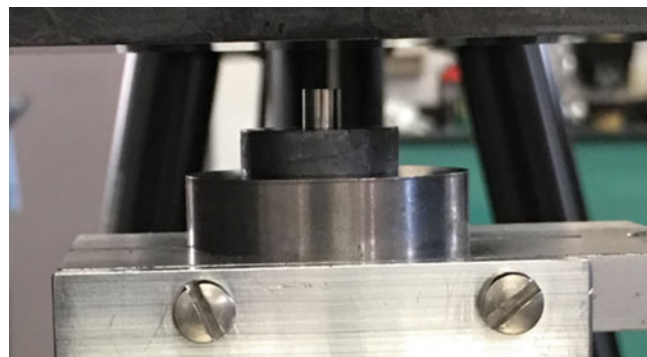


Fig. 16.1 Tantalum specimen prepared for compression in the MTS machine

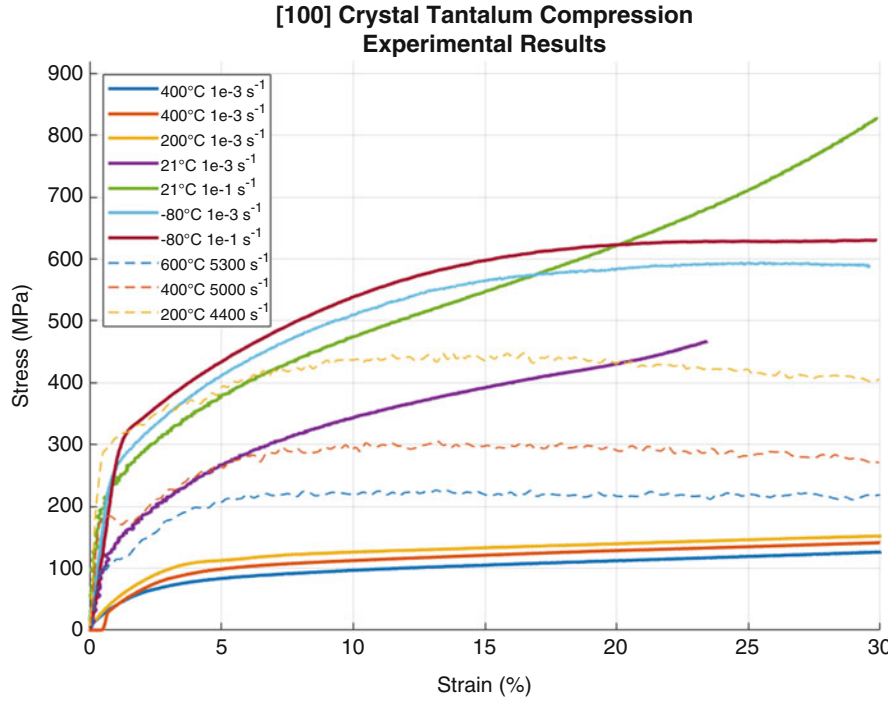


Fig. 16.2 Stress-strain curves from the experiments performed on the MTS machine and Hopkinson Bar

the coefficient $f_\tau = n_1 s_1$ is computed from the slip system normal and slip direction vectors, \mathbf{n} and \mathbf{s} , respectively, for the symmetrically identical active slip systems. Similarly, the effective plastic strain rate is computed by $\dot{\epsilon}_p = f_\gamma \dot{\gamma}$ where the coefficient $f_\gamma = N_A f_\tau$ and $\dot{\gamma}$ is the slip rate on each of the active slip systems.

For our particular choice of constitutive model, the slip rate is related to the density of mobile dislocations, ϱ_M , the velocity of mobile dislocations, v , and the magnitude of a unit of slip, i.e. the Burgers vector magnitude, b , according to Orowan's relation $\dot{\gamma} = \varrho_M v b$. Under conditions of uniaxial stress, it is convenient to neglect the small elastic strains and deal with a purely viscoplastic response such that the prescribed effective strain (or strain rate) history is considered to be purely plastic, i.e. $\dot{\epsilon}_p = \dot{\bar{\epsilon}}$. This leads to an expression that can be solved for the shear stress at each increment of the strain history

$$\tau = \tau^* \text{ s.t. } \widehat{v}(\tau^*, \varrho_M, \varrho_1, T; \{\theta\}) - \frac{\dot{\bar{\epsilon}}}{\varrho_m b f_\gamma} = 0 \quad (16.1)$$

where ϱ_1 and T are the immobile dislocation density and the material temperature, respectively, and $\{\theta\}$ represents the material model parameters. We hold the state variables, ϱ_M , ϱ_1 , and T , fixed at each increment to solve for the shear stress. The temperature is subsequently updated using an explicit forward Euler integration of

$$\dot{T} = \frac{(1 - \chi) \bar{\sigma} \dot{\bar{\epsilon}}}{\rho C_v} \quad (16.2)$$

where χ is the complement to the Taylor-Quinney factor, ρ and C_v are the mass density and specific heat of tantalum, respectively, and we neglect any thermoelastic contributions to the free energy (cf. [5]). Similarly, the dislocation density on all slip systems is updated via forward Euler integration of their respective evolution rates

$$\dot{\varrho}_{1,M} = \widehat{\dot{\varrho}}_{1,M}(v, T, \varrho_M, \varrho_1; \{\theta\}) \quad (16.3)$$

The constitutive equations $\widehat{v}(\tau^*, \varrho_M, \varrho_1, T; \{\theta\})$ and $\widehat{\dot{\varrho}}_{1,M}(v, T, \varrho_M, \varrho_1; \{\theta\})$ are those given in [4]. We focus our attention on estimating the 14 input parameters listed in Table 16.1. Any input values not included in the table, but that were input variables to the materials model can be found in [5].

Table 16.1 Parameters and ranges considered in the compressive tantalum model

Parameter	Units	Description	Min.	Max.
C_1	—	Taylor hardening coefficient	0.3	1
B_0	MBar- μs	Reference phonon drag viscosity	2e-11	1e-9
g_0	—	Dislocation barrier energy coefficient	0.01	1
ω_0	MHz	Dislocation attempt frequency	0.04375	8.75
p	—	Energy barrier shape coefficient	0.1	2
q	—	Energy barrier shape coefficient	0.1	2
τ_0	stress-MBar	Intrinsic lattice resistance	1e-06	1e-2
Varrhom0 (ϱ_{M0})	cm ⁻²	Initial mobile dislocation density	1e8	1e12
Varrhoi0 (ϱ_{i0})	cm ⁻²	Initial immobile dislocation density	1e1	1e12
L	cm	Mean spacing between barriers	1e-5	1e-4
C_M	—	Dislocation multiplication coefficient	0.01	10
C_A	—	Dislocation annihilation coefficient	0.1	1000
C_T	—	Dislocation trapping coefficient	0.1*C _M	1*C _M
Rhosati (ϱ_i^{SAT})	cm ⁻²	Saturation density of immobile dislocations	Varrhoi0	Varrhoi0 + 1e15

16.4 Methodology

16.4.1 Bayesian Statistics and Estimation

We adopt a Bayesian approach to the problem of estimating the best fitting input parameters for the computational materials model. A Bayesian statistical model has two parts, a likelihood and a prior distribution. The likelihood describes the probability distribution of the data given the unknown materials parameters. The prior distribution describes our best guess at a probability distribution for the unknown parameters before considering the current data.

To build our likelihood, we assume that the experimental data are a noisy version of the materials model run at the best fitting parameters. The materials model at a given parameter setting returns a stress-strain curve. Our experiments also produce such a curve. We will assume that the experimental curve should be a materials model curve with Gaussian error at each point. Denote our experimental curve by y , our unknown best fitting materials parameters by θ , the materials model by $\eta(\cdot)$, and our Gaussian error variance as σ^2 . We can write

$$y \sim N \{ \eta(\theta), \sigma^2 I \} \quad (16.4)$$

which says that the vector y is multivariate normal with mean vector given by $\eta(\theta)$ and independent noise at each location with variance σ^2 . Our prior distribution for the unknown parameter vector θ is just uniform over a fixed range for each parameter independently. The ranges are given in Table 16.1 and are chosen based on expert knowledge about the materials properties and model, derived in [3, 4].

The posterior distribution is the probability distribution of the unknown parameters given the observed experimental data. It is proportional to the product of the prior and the likelihood

$$p(\theta|y) = f(y|\theta) I\{\theta \in H\} / K \quad (16.5)$$

where $f(y|\theta)$ is the Gaussian likelihood described above and $I\{\theta \in H\}$ is the uniform prior distribution. The value K is a normalizing constant that typically cannot be computed because it involves the solution to a difficult integral. This means it is hard to compute things like the mean and variance directly. It is also difficult to sample from this distribution using straightforward approaches. Instead, we use an approach called Markov chain Monte Carlo (MCMC).

MCMC is a sequential sampling procedure that produces a correlated sample from a specified distribution. The algorithm is described in Fig. 16.3. Because the unknown normalizing constant appears in both the numerator and denominator of the acceptance probability of Step 2, it cancels out and we do not ever need to compute it. This approach only requires forward evaluations of the posterior; we do not need to invert it or compute derivatives. Thus, we can use this approach with the compressive tantalum materials model simply by computing the output at any candidate input from Step 1.

One disadvantage of this algorithm is that it may require tens of thousands of correlated samples in order to produce good estimates. This can be intractably slow when used with a materials model, even if the simulation requires only a few

Assume θ follows some distribution with density p and that we have θ_k with $p(\theta_k) > 0$.

1. Draw a candidate θ' from $q(\theta'|\theta_k)$.
2. Compute $\alpha = \frac{p(\theta')q(\theta_k|\theta')}{p(\theta_k)q(\theta'|\theta_k)}$
3. Draw $u \sim \text{Unif}(0, 1)$.
4. If $u \leq \alpha$, set $\theta_{k+1} = \theta'$, else set $\theta_{k+1} = \theta_k$.

Fig. 16.3 MCMC Algorithm

seconds to evaluate. Thus, we need to alter the approach to require just a few hundreds of material model evaluations. We do this through the construction of an emulator, a fast, statistical approximation to the materials model, described next.

16.4.2 Emulation

In order to perform the parameter estimation and sensitivity analysis, we will need to run the computer model simulation many thousands of times at various input parameter settings. To speed up the computation time, we built an emulator of the computer model. An emulator is a statistical approximation to the computer model output that predicts the output that would have been produced by the computer model simulation at new values of the input parameters. Where the computer model may take minutes to produce a stress/strain relationship curve, a trained emulator can produce one in fractions of a second.

Our emulator is based on Gaussian process regression. Gaussian process regression is a flexible approach to regression that can capture a wide variety of flexible behavior and can be made to interpolate the training set. Training the model can be slow, but afterwards, it produces very fast predictions. Details can be found in [6] and its references. We produced our emulator using the Emulator Generating Gadget (EGG) [7] which takes a training set of input-output pairs from the materials model and returns C code that can be compiled into the fast predictor. The inputs were selected using a Latin Hypercube Sampling design [8] so as to avoid any large gaps in parameter space. This approach guarantees that the inputs fill the space uniformly without any large gaps. Once built, we can use the fast emulator in place of the computationally expensive model in the MCMC scheme described above.

16.4.3 Sensitivity Analysis

We also consider methodology to determine whether some of the parameters can be fixed. Sensitivity analysis is a broad term for such a practice. We use the active subspace approach [9]. The general idea is that some parameters have a negligible effect on the output, they can be fixed and effectively removed from study. The active subspace approach does this through a study of the model's gradients. A gradient matrix is produced and decomposed using a singular value decomposition. The singular vectors indicate the directions in parameter space that capture most of the changes in the model. If certain parameters do not contribute significantly to any of the singular vectors with large singular values, they can be removed from study.

16.5 Results

To begin, we obtained a Latin Hypercube design of 500 runs and obtained simulation results for each set of inputs. The design is shown in Fig. 16.4 and the simulations with a strain rate of 10^{-3} s⁻¹ and temperature of 400 K are shown in Fig. 16.5.

The 500 input and output pairs discussed above were used to build the emulator. To test the accuracy of the emulator, seven “testing” sets of input parameters not used to train the emulator were produced. Stress-strain curves were generated from both the emulator and the original materials model. The emulator error is estimated as the difference between the two curves produced from the same input parameter set, with results shown in Fig. 16.6. The scale of the emulator error is typically less than 5% of the total variation in the outputs, confirming that the emulator could reasonably be substituted for the materials model in the parameter estimation process. Note that to test the trained emulator, parameter sets not used to

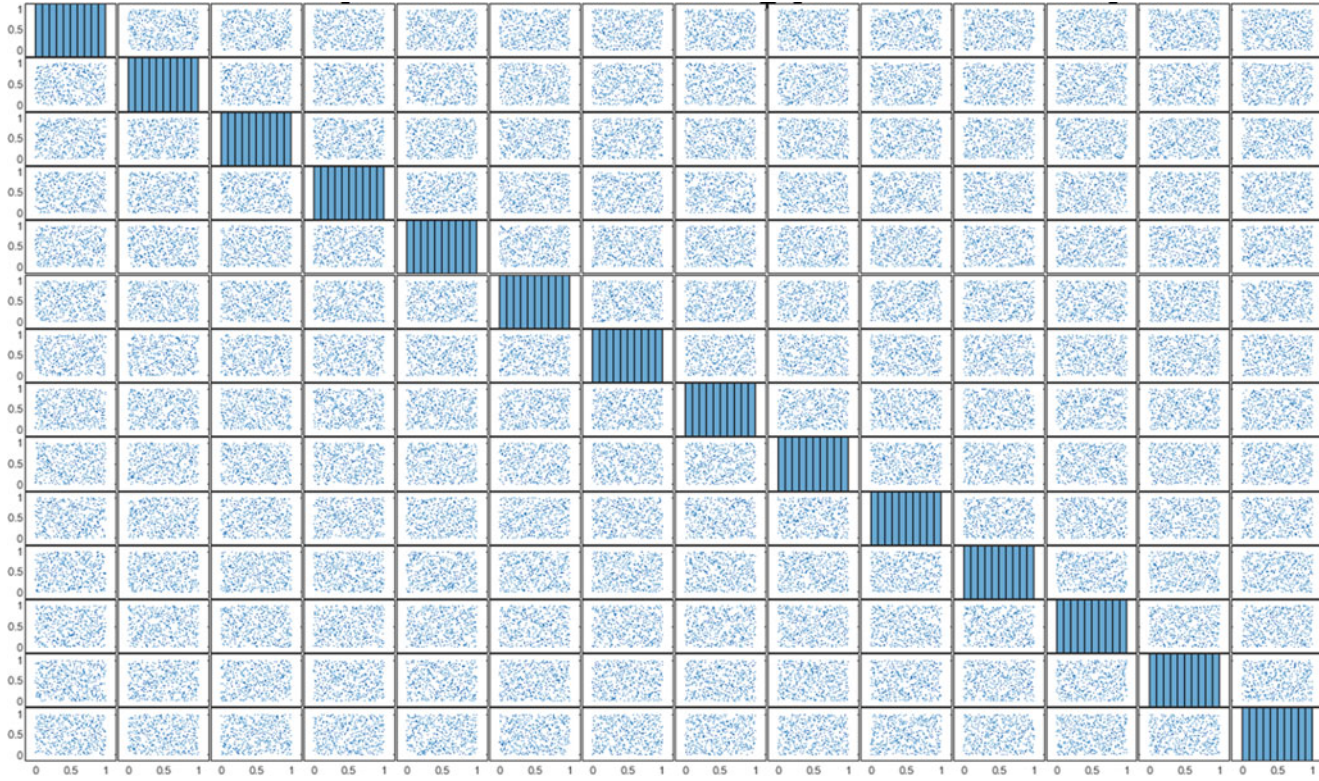


Fig. 16.4 Each parameter is uniformly distributed, with respect to the others, across the parameter space by using a Latin Hypercube experimental design

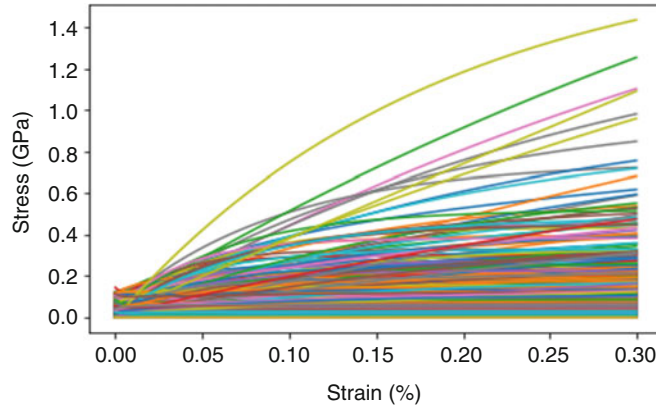


Fig. 16.5 Stress-strain curves for tantalum materials model generated from Latin-Hypercube design of parameter space, at a strain rate of 10^{-3} s^{-1} and temperature of 400 K

the train the model must be used. Because the emulator building process assumes the materials model is deterministic, i.e., identical inputs produce identical outputs, the emulator is a perfect interpolator, i.e., training input parameter sets will return identical output from the materials model.

Figure 16.7 summarizes the results of the sensitivity analysis. In lieu of a formal active subspace analysis, we focus on an examination the gradient matrix directly. Each line in the figure corresponds to one of the 500 training points. The values indicate a standardized gradient for each parameter for a single location on the stress-strain curve (shown in the inset). These are the raw values that feed into the formal active subspace approach. The results seem to indicate that a few of the parameters play only a small role in the output. In particular, B_0 and ω_0 have gradients that are small over the entire parameter space relative to the other parameters. The results at other points on the stress-strain curve tend to have smaller overall gradients, but tell a broadly similar story. Some direct experimentation indicates that these parameters have only a few percent effect on the output. We do not remove these parameters in the rest of our analysis, but it may make sense to fix them in the future.

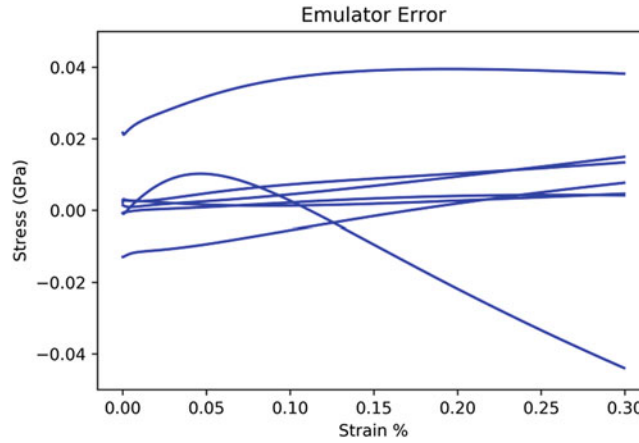


Fig. 16.6 Emulator error as defined by the difference between the emulator and the materials model an identical set of input parameters

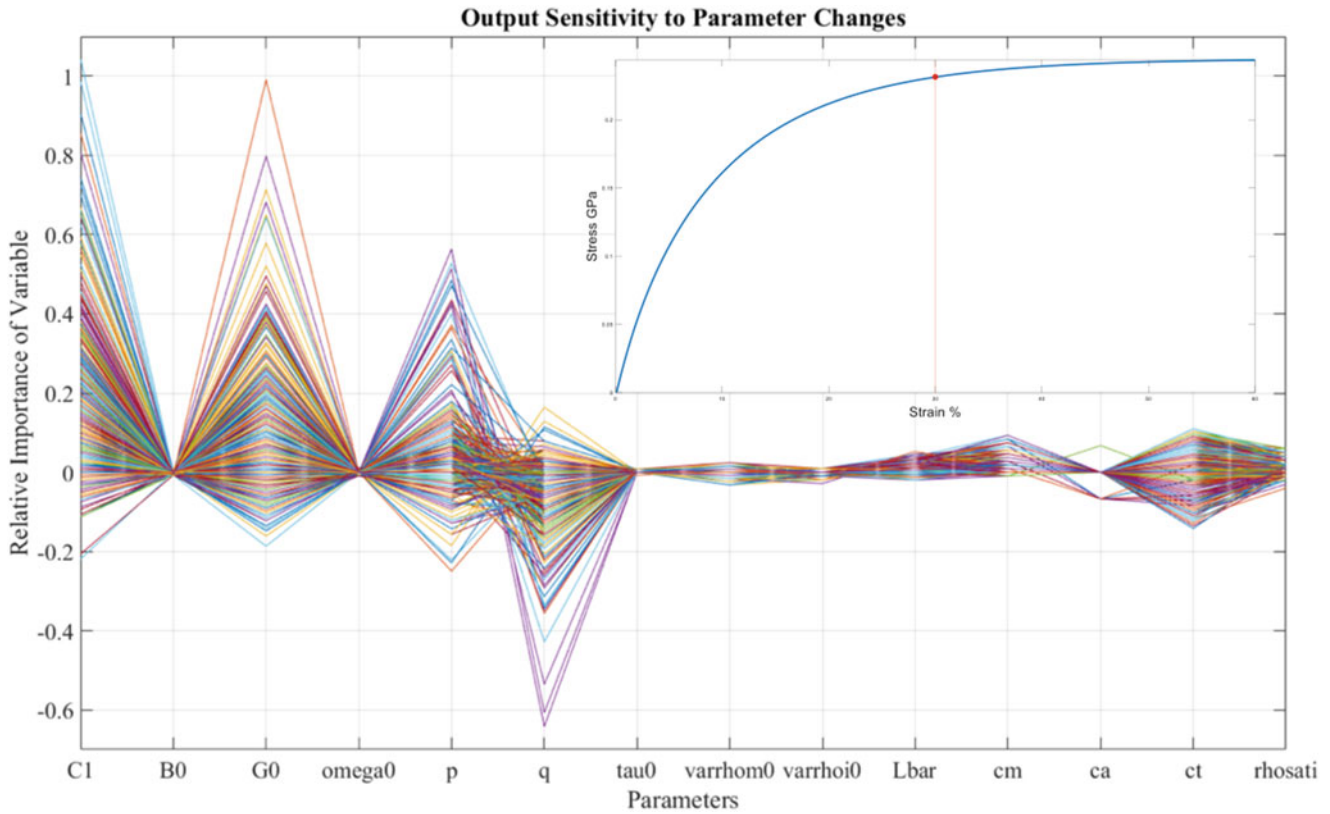


Fig. 16.7 Sensitivity Analysis results a measured by the value of the gradient at the point depicted in the insert for 500 input parameter sets

Before analyzing the experimental data, we test the procedure using a simulation result in place of the experimental data. In this case, we know the true parameters at which the simulation was run, so we can evaluate the quality of the estimation procedure. Figure 16.8 shows the posterior distribution for two of the parameters. The posterior means lie very close to the true values and are good estimates of the true values in this case. Further, we can use the entire distribution to summarize the uncertainty in the result and propagate this uncertainty into future predictions of material performance.

We now turn to analysis of the experimental data. Unfortunately, we are not able to obtain trustworthy results. The parameter estimation gives results that are near the boundaries of the ranges considered for many of the parameters. Figure 16.9 demonstrates the problem of a mismatch between the materials model and experiment. The red curve in this figure is the result of one experiment from the MTS machine at 21 °C with strain rate of $1\text{e}-1 \text{ s}^{-1}$; the black curves show the results from the 500 training curves used to build the emulator. The materials model over the range of input parameters, and

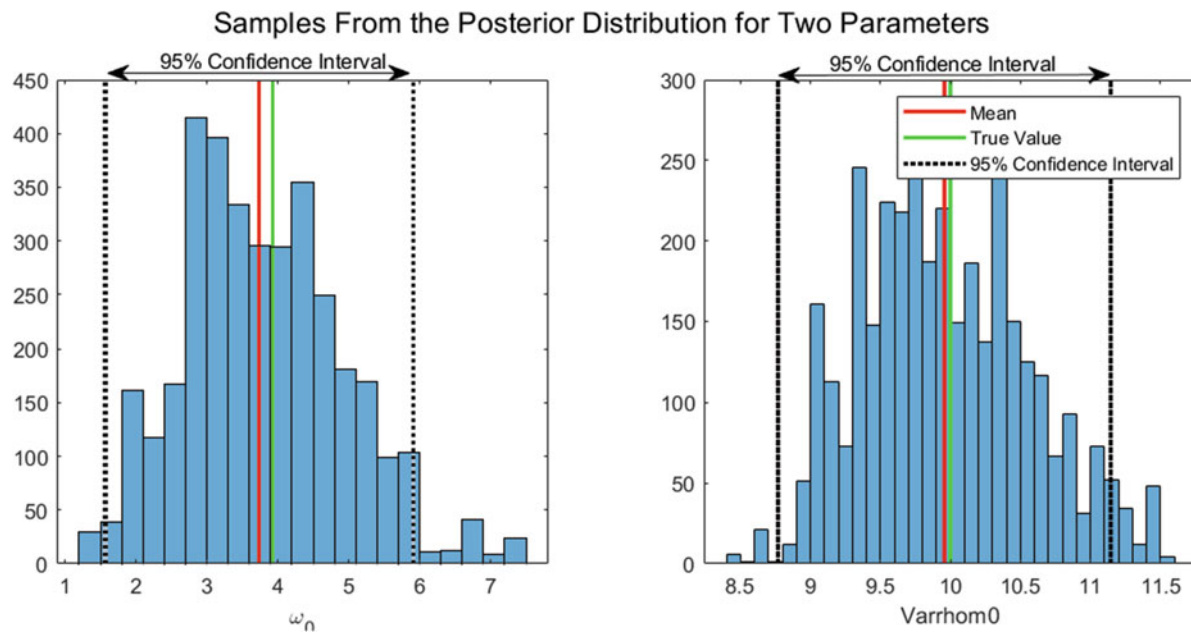


Fig. 16.8 Posterior distribution for two parameters from the test analysis

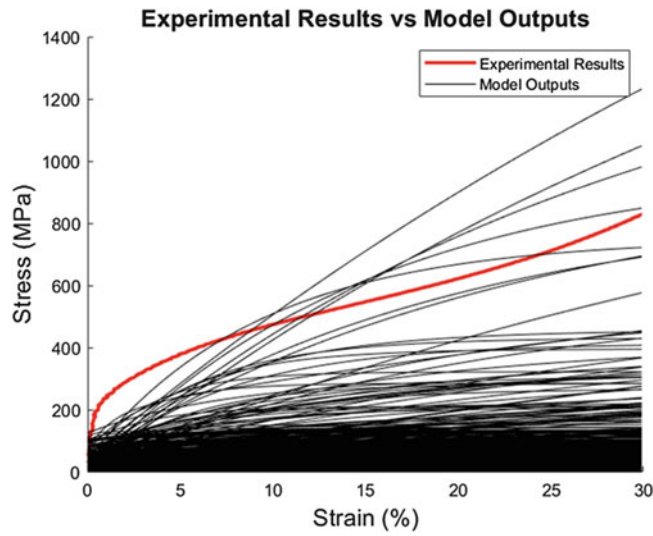


Fig. 16.9 Stress-strain curves for the training set used to build the emulator and the experimental data for which we attempted to perform calibration

therefore the emulator, do not produce any results that look like the experiment. The experimental curve has a faster initial rise than anything we see in from the materials model.

16.6 Conclusions and Future Work

We have demonstrated the application of a statistical technique for comparing experiments and computationally intensive materials models. The procedure is based on the use of a Bayesian statistical model estimated through a Markov chain Monte Carlo algorithm and an emulator, a fast, statistical surrogate for the materials model. The procedure works well in a test case. In addition, a sensitivity analysis was performed on the 14 input parameters under consideration. Parameters that were found to have a small effect on the output could be fixed when estimating the remaining input parameters, leading to decreased computation time and less uncertainty.

Unfortunately, we were not able to successfully calibrate our materials model to actual experimental data because of significant discrepancies between the two. Additional study will be required to determine the source of these differences. It is possible that the materials model may lack important physics or there may be greater dependency between the strain rate and stress-strain curves than is captured in the materials model. There may also be systematic errors in the experiment that account for these differences. The strain rate and temperature have a big effect on the output both from simulation and experiment, so the next step may be comparing theory and experiment at ideal, well-behaved experimental conditions and then increasing the complexity once the discrepancies are better understood.

Acknowledgements We would like to thank James Valdez, Michael Torrez, and Carl Trujillo for their expertise and guidance in running the experiments. We would also like to thank Los Alamos National Laboratory for supporting our group and this project as part of the Los Alamos Dynamics Summer School program.

References

1. Higdon, D., Gattiker, J., Williams, B., Rightley, M.: Computer model calibration using high-dimensional output. *J. Am. Stat. Assoc.* **103**(482), 570–583 (2008)
2. Brynjarsdóttir, J., O'Hagan, A.: Learning about physical parameters: the importance of model discrepancy. *Inverse Probl.* **30**(11), 114007 (2004)
3. Luscher, D.J., Mayeur, J.R., Mourad, H.M., Hunter, A., Kenamond, M.A.: Coupling continuum dislocation transport with crystal plasticity for application to shock loading conditions. *Int. J. Plast.* **76**, 111–129 (2016)
4. Luscher, D.J., Addessio, F.L., Cawkwell, M.J., Ramos, K.J.: A dislocation density-based continuum model of the anisotropic shock response of single crystal α -cyclotrimethylene trinitramine. *J. Mech. Phys. Solids.* **98**, 63–86 (2017)
5. Luscher, D.J., Buechler, M.A., Walters, D.J., Bolme, C.A., Ramos, K.J.: On computing the evolution of temperature for materials under dynamic loading. *Int. J. Plast.* **111**, 188–210 (2018)
6. Lawrence, E., Heitmann, K., White, M., Higdon, D., Wagner, C., Habib, S., Williams, B.: The coyote universe. III. Simulation suite and precision emulator for the nonlinear matter power spectrum. *Astrophys. J.* **713**(2), 1322 (2010)
7. Lawrence, E.: The emulator generating gadget (EGG). [Online]. Available: <https://github.com/lanl/egg> (2018)
8. McKay, M.D., Beckman, R.J., Conover, W.J.: Comparison of three methods for selecting values of input variables in the analysis of output from a computer code. *Technometrics.* **21**(2), 239–245 (1979)
9. Constantine, P.G., Dow, E., Wang, Q.: Active subspace methods in theory and practice: applications to kriging surfaces. *SIAM J. Sci. Comput.* **36**(4), A1500–A1524 (2014)



Chapter 17

Augmented Sequential Bayesian Filtering for Parameter and Modeling Error Estimation of Linear Dynamic Systems

Mingming Song, Hamed Ebrahimian, and Babak Moaveni

Abstract In this paper an augmented sequential Bayesian filtering approach is proposed for parameter and modeling error estimation of linear dynamic systems of civil structures using time domain input-output data through a sequential maximum a posteriori (MAP) estimation approach, which is similar to Kalman filtering method. However, in the application of existing Kalman filters, the estimation of modeling errors is rarely considered. Unlike traditional Kalman filter which provides state estimation at every time step, the proposed filtering approach estimates the parameter and modeling error on a windowing basis, i.e., the input and output data are divided into windows for estimation which would save computation burden. The analytical derivation of the proposed augmented sequential Bayesian filtering method is first presented, and then the method is verified through a numerical case study of a 3-story building model. An earthquake excitation is used as the input and the acceleration time history response of the building model is simulated. The simulated response is then polluted with different levels of Gaussian white noise to account for the measurement noise. The simulated response is used as the measured data for calibrating another 3-story shear building model which is different from the original model for simulation. Modeling errors are introduced in this shear building model including the shear building assumption, grouping strategy and boundary conditions. The augmented sequential Bayesian filtering approach is applied to estimate the model parameters and modeling error. The performance of the proposed method is studied with respect to modeling errors, the number of sensors and the level of noise.

Keywords Sequential Bayesian filtering · Model parameter estimation · Modeling error estimation · Uncertainty quantification

17.1 Introduction

Kalman filter is one of the most common methods for state estimation given a series of input-output data. Considering its efficiency and application simplicity, a class of different Kalman filter methods has been developed and applied for different purposes, e.g., state estimation, model parameter estimation, input estimation, modeling uncertainty estimation, or joint estimations. Extended Kalman filter (EKF) and unscented Kalman filter (UKF) have been the most popular Kalman filter methods for model parameter estimations of civil engineering structures. Numerical applications of UKF for model parameter estimation are presented in these two studies [1, 2]. Azam et al. proposed a dual-Kalman filter for joint state-input estimation given output-only acceleration measurements [3]. Astroza et al. applied a dual adaptive filtering approach for nonlinear finite element (FE) calibration accounting for modeling uncertainty [4]. In this study, a new filtering approach is proposed for model parameter and modeling error estimation.

M. Song (✉) · B. Moaveni

Department of Civil and Environmental Engineering, Tufts University, Medford, MA, USA
e-mail: mingming.song@tufts.edu

H. Ebrahimian

SC Solutions Inc., Sunnyvale, CA, USA

17.2 Methodology

The proposed augmented sequential Bayesian filtering method estimates the model parameters and modeling errors through a maximum a posteriori (MAP) estimation approach. It can be seen as an extension of the existing Bayesian filtering method [5, 6] which allows model parameters estimation. The FE model of the considered structure is assumed to depend on a set of regular parameters, θ_1 , and another set of model parameters which are functions of additional parameters θ_h (referred to as high-level parameters), i.e., $\theta_2 = \mathbf{f}(\theta_h)$. The model-predicted response is denoted by $\hat{\mathbf{y}} = \tilde{\mathbf{h}}(\theta_1, \theta_2) = \tilde{\mathbf{h}}(\theta_1, \mathbf{f}(\theta_h))$, in which the function $\tilde{\mathbf{h}}(\dots)$ evaluates the response from the FE model. The model-predicted response can be denoted as $\hat{\mathbf{y}} = \mathbf{h}(\theta_1, \theta_h)$ without loss of generality. The measured structural response \mathbf{y} is assumed to be equal to the sum of model-predictions and a prediction error, i.e., $\mathbf{y} = \mathbf{h}(\theta_1, \theta_h) + \mathbf{e}$, in which \mathbf{e} refers to the prediction error and follows a normal distribution $\mathbf{e} \sim N(\mu_e, \Sigma_e)$. The mean vector and variance matrix of \mathbf{e} approximately quantify the modeling errors through a normal distribution. The unknown parameters to be estimated include θ_1 , θ_h , μ_e and Σ_e . For brevity, a new parameter θ is defined to combine all model parameters (regular and high-level parameters), i.e., $\theta = [\theta_1^T, \theta_h^T]^T$, and a new vector Ψ is defined to include all unknown parameters to be estimated, i.e., $\Psi = [\theta^T, \alpha^T]^T$, in which $\alpha = [\mu_e^T, \mathbf{r}^T]^T$ and $\mathbf{r} = (\text{diag}(\Sigma_e))$ which denotes the diagonal terms of Σ_e . In this study, Σ_e is assumed to be a diagonal matrix which ignores the correlation between different prediction error components. The objective of the proposed filtering method is to find the MAP estimation of Ψ at each time window.

Based on Bayes' theorem, the posterior probability density function is proportional to the product of likelihood function and prior distribution:

$$p(\Psi | \mathbf{y}) \propto p(\mathbf{y} | \Psi) p(\Psi) \quad (17.1)$$

In the framework of Bayesian filtering, the prior distribution of the current time window is chosen as the posterior distribution of previous window, i.e., $\Psi \sim N(\widehat{\Psi}^-, \widehat{\mathbf{P}}_\Psi^-)$. Therefore, the natural logarithm of the posterior distribution is derived below:

$$\begin{aligned} \log(p(\Psi | \mathbf{y})) &= c - \frac{1}{2} \log(|\Sigma_e|) - \frac{1}{2} (\mathbf{y} - \mathbf{h}(\theta) - \mu_e)^T (\Sigma_e)^{-1} (\mathbf{y} - \mathbf{h}(\theta) - \mu_e) \\ &\quad - \frac{1}{2} (\Psi - \widehat{\Psi}^-)^T (\widehat{\mathbf{P}}_\Psi^-)^{-1} (\Psi - \widehat{\Psi}^-) \end{aligned} \quad (17.2)$$

Then by setting the derivative $\log(p(\Psi | \mathbf{y}))$ of Ψ over equal to zero, the MAP estimation of Ψ can be obtained:

$$\partial \log(p(\Psi | \mathbf{y})) / \partial \Psi = \left[\frac{\partial \log(p(\Psi | \mathbf{y}))}{\partial \theta} \quad \frac{\partial \log(p(\Psi | \mathbf{y}))}{\partial \mu_e} \quad \frac{\partial \log(p(\Psi | \mathbf{y}))}{\partial \mathbf{r}} \right] = \mathbf{0} \quad (17.3)$$

The three partial derivatives are derived separately:

$$\widehat{\theta}^+ = \widehat{\theta}^- + \left[\mathbf{C}_\theta^T (\Sigma_e)^{-1} \mathbf{C}_\theta |_{\widehat{\theta}^-} + \mathbf{P}_{\theta\theta} \right]^{-1} \left[\left(\mathbf{C}_\theta^T (\Sigma_e)^{-1} (\mathbf{y} - \mathbf{h}(\widehat{\theta}^-) - \mu_e) \right) - \mathbf{P}_{\theta\alpha} (\alpha - \widehat{\alpha}^-) \right] \quad (17.4)$$

where $\mathbf{C}_\theta = \frac{\partial \mathbf{h}(\theta)}{\partial \theta}$, which can be evaluated using analytical (e.g., direct differentiation method) or numerical (e.g., finite difference method) methods, and $(\widehat{\mathbf{P}}_\Psi^-)^{-1} = \begin{bmatrix} \mathbf{P}_{\theta\theta} & \mathbf{P}_{\theta\alpha} \\ \mathbf{P}_{\alpha\theta} & \mathbf{P}_{\alpha\alpha} \end{bmatrix}$.

$$\mu_e = \mathbf{y} - \mathbf{h}(\theta) - \Sigma_e \left(\frac{\partial \Psi}{\partial \mu_e} \right)^T (\widehat{\mathbf{P}}_\Psi^-)^{-1} (\Psi - \widehat{\Psi}^-) \quad (17.5)$$

$$-\frac{1}{2} (\Sigma_e)^{-1} \mathbf{I}_{n_y \times 1} + \frac{1}{2} (\Sigma_e)^{-2} (\mathbf{y} - \mathbf{h}(\theta) - \mu_e)^2 - \left(\frac{\partial \Psi}{\partial \mathbf{r}} \right)^T (\widehat{\mathbf{P}}_\Psi^-)^{-1} (\Psi - \widehat{\Psi}^-) = \mathbf{0} \quad (17.6)$$

in which $(\mathbf{y} - \mathbf{h}(\theta) - \mu_e)^2 = [(y_i - h_i(\theta) - \mu_{e_i})^2]$ is a $n_y \times 1$ vector.

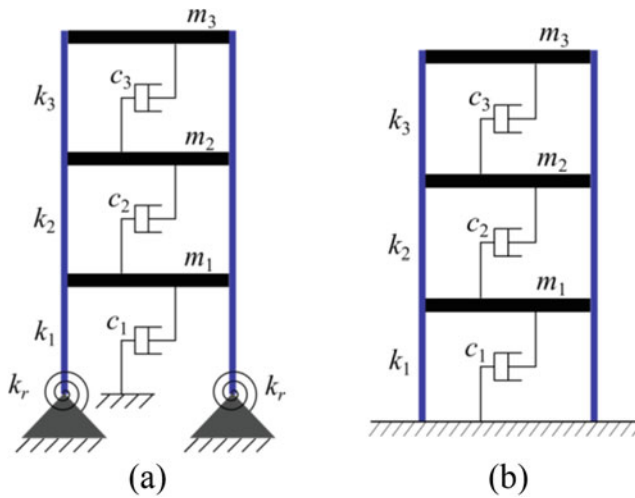


Fig. 17.1 (a) 3-story frame model (true structure); (b) 3-story shear building model (with modeling errors)

The three partial derivative equations, Eqs. (17.4)–(17.6), should be solved simultaneously; however, it is mathematically difficult to obtain an analytical closed form solution which satisfies all three equations. Therefore, an iterative numerical solution is proposed here:

For window k :

1. Update $\widehat{\theta}^+$ using previous estimated $\widehat{\theta}^-$ while keeping μ_e and $r = (\text{diag}(\Sigma_e))$ the same as last iteration.
2. Update μ_e with $\widehat{\theta}^+$.
3. Update $r = (\text{diag}(\Sigma_e))$ with $\widehat{\theta}^+$ and μ_e .
4. Go to step 1 until the convergence criteria is reached.

Then move to next window $k + 1$.

The proposed augmented Bayesian filtering method is verified through a numerical case study of a 3-story building model. The response of the building is first simulated using a 3-story frame model which represents the true structure as shown in Fig. 17.1a. An earthquake ground excitation is used as the input of the structure and its acceleration response is simulated and polluted with white noise. Then a 3-story shear building model with significant modeling errors, as shown in Fig. 17.1b, is created for model parameter and modeling error estimation using the proposed filtering approach. The performance of the proposed method is studied with respect to modeling errors, the number of sensors and the level of noise.

References

1. Wu, M., Smyth, A.W.: Application of the unscented Kalman filter for real-time nonlinear structural system identification. *Struct. Control Health Monit.* **14**, 971–990 (2007)
2. Chatzi, E.N., Smyth, A.W.: The unscented Kalman filter and particle filter methods for nonlinear structural system identification with non-collocated heterogeneous sensing. *Struct. Control Health Monit.* **16**, 99–123 (2009)
3. Azam, S.E., Chatzi, E., Papadimitriou, C.: A dual Kalman filter approach for state estimation via output-only acceleration measurements. *Mech. Syst. Signal Process.* **60**, 866–886 (2015)
4. Astroza, R., Alessandri, A., Conte, J.P.: A dual adaptive filtering approach for nonlinear finite element model updating accounting for modeling uncertainty. *Mech. Syst. Signal Process.* **115**, 782–800 (2019)
5. Ebrahimian, H., Kohler, M., Massari, A., et al.: Parametric estimation of dispersive viscoelastic layered media with application to structural health monitoring. *Soil Dyn. Earthq. Eng.* **105**, 204–223 (2018)
6. Ebrahimian, H., Astroza, R., Conte, J.P.: Extended Kalman filter for material parameter estimation in nonlinear structural finite element models using direct differentiation method. *Earthq. Eng. Struct. Dyn.* **44**, 1495–1522 (2015)



Chapter 18

On-Board Monitoring of Rail Roughness via Axle Box Accelerations of Revenue Trains with Uncertain Dynamics

V. K. Dertimanis, M. Zimmermann, F. Corman, and E. N. Chatzi

Abstract In addressing recent demands for increasing loads and speed of Railways, as well as increasing railway network usage, inexpensive and frequent monitoring of the infrastructure may be adopted to ensure safe and reliable operation. Presently, inspection of railway infrastructure is carried out visually or with dedicated Track Recording Vehicles (TRV), which are equipped with a number of optical and inert sensors and periodically collect geometric data. However, such inspection is costly, may only be carried out at periodic, and thereby infrequent intervals, and may disrupt other services and regular operation. As an alternative, relatively low-cost on-board monitoring data collected from revenue-making trains, could offer a cost-effective and more robust approach to monitor railway tracks. This approach relies on accelerometers mounted either on the axle box or on the car body, with the potential of almost continuous monitoring, earlier fault detection and thereby serving as a natural fit for predictive maintenance. However, the dynamics collected from revenue service trains, via low-cost sensors, are inevitably described by uncertainties (speed, weight, rolling stock condition). To this end, we propose an approach relying on model-based system identification for increasing the estimation capacity. A vehicle–rail interaction model is coupled with a dual Kalman filter (KF) on measured axle box vibration data from in-service trains, in order to estimate the input excitation (e.g. rail roughness). Via estimation of the input, we may distinguish between isolated defects (e.g. squats, turnout frogs, welded joints) and effects distributed over a certain track length (e.g. concrete sleeper, wood sleeper, ballast, slab track).

Keywords Rail roughness · Substructuring · Dual Kalman filter · On-board monitoring · Uncertainty

18.1 Introduction

The traditional approach to life-cycle assessment (LCA) and maintenance planning of infrastructure almost exclusively relies on inspections that are either carried out in regularly spaced intervals, or are triggered due to manifestation of irregular or potentially unsafe behavior. The drawbacks of such an approach with respect to ensuring resilience (i.e., prompt reaction to condition degradation) are self-evident. A more informative alternative has long been in place, namely the practice of Structural Health Monitoring (SHM), i.e., the utilization of sensors for extracting continual information on system behavior [1]. Many railway Bodies in Europe already investigate the turn to such a data-driven LCA scheme for the management of both rail infrastructure and the vehicle fleet, with high quality data collected by means of diagnostic service vehicles.

In a time where competition between rail and road transport is intensifying and overall system costs are expected to rise, an efficient approach to maintenance planning could prove key in enhancing the competitiveness of railway transportation against other transport modes. The inexpensive and frequent monitoring of the complete infrastructure network via “smart” on-board monitoring schemes [2–4] can enable a shift from the current costly scheduled maintenance regimes toward data-driven predictive maintenance. This reduces downtime and emergency maintenance actions, with positive implications on rail traffic reliability and maintenance costs.

Thus far, inspection of railway infrastructure has been carried out visually or with dedicated Track Recording Vehicles (TRV), which are equipped with a number of optical and inertial sensors and periodically collect geometric data. However, such inspection is costly, may only be carried out at periodic, and thereby not so frequent, intervals, and may disrupt other

V. K. Dertimanis (✉) · E. N. Chatzi
Institute of Structural Engineering, ETH Zürich, Zürich, Switzerland
e-mail: v.derti@ibk.baug.ethz.ch

M. Zimmermann · F. Corman
Institute for Transport Planning and Systems, ETH Zürich, Zürich, Switzerland

services and regular operation. As an alternative, relatively low-cost continuous monitoring, based on on-board vibration data, collected from revenue-making trains, could be a cost-effective approach to monitor railway tracks [5–9]. It is worth mentioning that on-board monitoring systems using diverse sensor technologies are also investigated in road vehicles [10, 11].

In this work we explore this second option through the adoption of a minimum intervention strategy. This pertains to the use of a single sensor for tracking the train vibration, and the implementation of a dual KF (KF) [12] for the estimation of the unmeasured input force that is developed as the result of train-track interaction [13]. Via estimation of the latter, identification of isolated defects (e.g. squats, turnout frogs, welded joints, etc.), as well as of effects distributed over a certain track length (e.g. superstructure type, ballast condition, soil properties, etc.) can be accomplished.

18.2 Description of the Method

Figure 18.1 displays a simplified model for the description of the vertical dynamics of a train vehicle. The chassis is modelled as a lumped mass with two degrees of freedom (DOFs) that correspond to bounce and pitch, while each bogie and wheelset are modelled as lumped masses with a single DOF (e.g. bounce). All vehicle parts are connected through the primary and secondary suspensions and the wheel-rail interaction is modelled with a linear Hertzian spring.

A limitation hindering implementation of the proposed method to the state-space model of the original vector structural equation pertains to the input delay that is associated to the rear wheelset. To this end, the dual KF estimation is succeeded by (1) establishing the transfer function that connects the induced wheel-rail interaction force to the acceleration of a measured DOF, which herein assumed to be the bounce of the front wheelset; (2) transforming the latter into a state-space model ; (3) discretizing the state-space model using an appropriate sampling rate; and (4) setting up the dual KF, by adopting a fictitious equation for the unknown forces.

In more detail, the differential equation that describes the bounce motion of the front wheelset is

$$m_{wf} \ddot{x}_{wf}(t) + c_{pf} \dot{x}_{wf}(t) + k_{wf} x_{wf}(t) = f_{wf}(t) + f_{pf}(t) \quad (18.1)$$

in which $f_{wf}(t) = k_{wf} r_f(t)$ is the wheel contact force and $f_{pf}(t)$ is the interaction force between the wheelset substructure and the rest of the vehicle, given by

$$f_{pf}(t) = c_{pf} (\dot{x}_{bf}(t) - \dot{x}_{wf}(t)) + k_{pf} (x_{bf}(t) - x_{wf}(t)) \quad (18.2)$$

This latter force carries all uncertainties associated with the parameters of the vehicle (excluding the ones of the wheelset substructure) and especially the mass M_c and inertia I_c of the chassis, which correspond to the varying amount of passengers during operation. The effects of this force to the vibration acceleration of the wheelset mass are expected to be considerably lower, compared to the ones of the wheel contact force, allowing thus a relative accurate estimation of the latter.

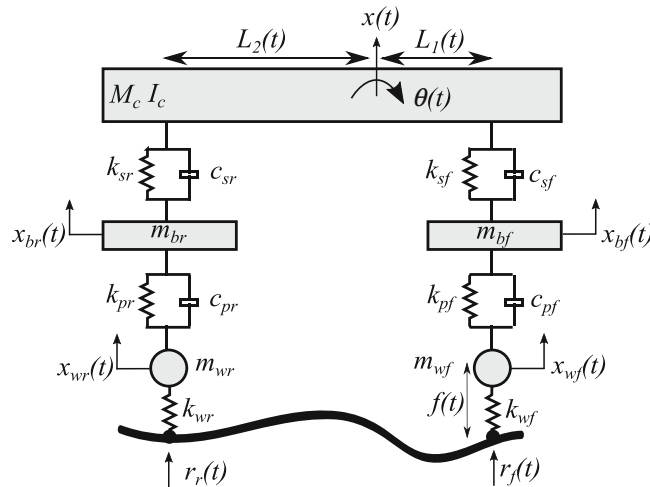


Fig. 18.1 Pitch-bounce model of a railway vehicle

Under the availability of vibration acceleration measurements, Eq. 18.1 admits a state-space representation of the form

$$\dot{\xi}(t) = \mathbf{A}\xi(t) + \mathbf{B}u(t) \quad (18.3a)$$

$$y(t) = \mathbf{H}\xi(t) + \mathbf{D}u(t) \quad (18.3b)$$

where $\xi(t) = [x_{wf}(t) \ \dot{x}_{wf}(t)]^T$, $u(t) = f_{wf}(t) + f_{pf}(t)^T$ and

$$\mathbf{A} = \begin{bmatrix} 0 & 1 \\ -\frac{k_{wf}}{m_{wf}} & -\frac{c_{pf}}{m_{wf}} \end{bmatrix}, \quad \mathbf{B} = \begin{bmatrix} 0 & 0 \\ \frac{1}{m_{wf}} & \frac{1}{m_{wf}} \end{bmatrix} \quad (18.4a)$$

$$\mathbf{H} = \begin{bmatrix} -\frac{k_{wf}}{m_{wf}} & -\frac{c_{pf}}{m_{wf}} \end{bmatrix}, \quad \mathbf{D} = \begin{bmatrix} \frac{1}{m_{wf}} & \frac{1}{m_{wf}} \end{bmatrix} \quad (18.4b)$$

Under the assumption of constant intersample behaviour of the input forces (e.g. the zero-order hold principle), the discrete-time counterpart of Eq. 18.3 reads

$$\dot{\xi}[k+1] = \mathbf{A}_d\xi[k] + \mathbf{B}_du[k] \quad (18.5a)$$

$$y[k] = \mathbf{H}_d\xi[k] + \mathbf{D}_du[k] \quad (18.5b)$$

for $\mathbf{A}_d = e^{\mathbf{A}T_s}$, $\mathbf{B}_d \approx T_s\mathbf{B}$, $\mathbf{H}_d = \mathbf{H}$ and $\mathbf{D}_d = \mathbf{D}$, where T_s denotes the sampling period.

The realization of the dual KF [12] initiates by adopting a random walk model for the temporal evolution of the unknown input

$$u[k+1] = u[k] + w_u[k] \quad (18.6)$$

where $w_u[k]$ is a zero-mean Gaussian white noise process of variance σ_{uu}^2 . Accordingly, by adopting the procedure described in Eftekhar Azam et al. [12], Eqs. 18.5 and 18.6 can be transformed into the following dual set of KFs:

Input Estimation

$$u[k+1] = u[k] + w_u[k] \quad (18.7a)$$

$$y[k] = \mathbf{H}_d\xi[k] + \mathbf{D}_du[k] + w_y[k] \quad (18.7b)$$

State Estimation

$$\dot{\xi}[k+1] = \mathbf{A}_d\xi[k] + \mathbf{B}_du[k] + \mathbf{w}_{\xi}[k] \quad (18.8a)$$

$$y[k] = \mathbf{H}_d\xi[k] + \mathbf{D}_du[k] + w_y[k] \quad (18.8b)$$

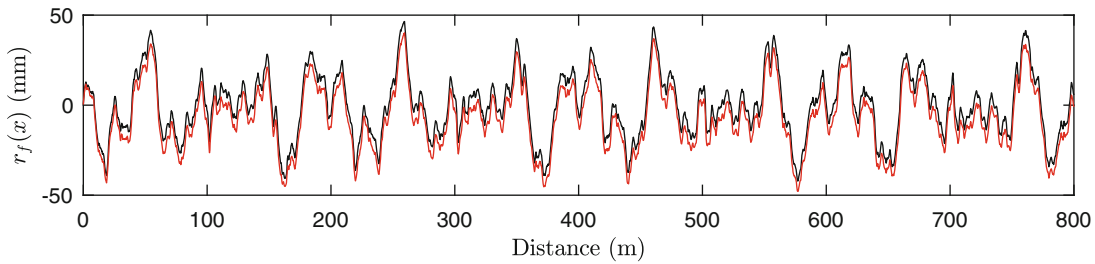
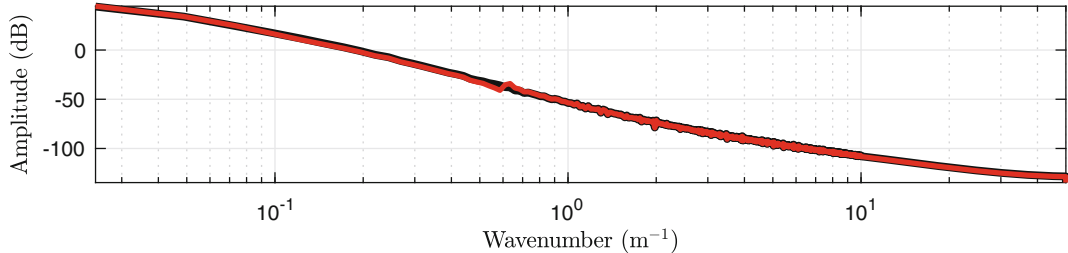
In Eqs. 18.7b and 18.8, process and measurement noise has been added to the state and the output equations of the original discrete-time state-space representation of the wheelset, modelled also as zero-mean white noise processes of covariance matrix $\Sigma_{\xi\xi}$ and variance σ_{yy}^2 , respectively.

18.3 Numerical Implementation

The proposed method is evaluated by simulating the pitch-bounce model of Fig. 18.1, using the structural parameters given in Table 18.1. Excitation is realized by adopting the American Railway Standard, developed by the US Federal Railroad Administration, to generate an artificial rail profile of average quality (e.g. grade 4, [14]). A range of wavelengths between 0.10 and 70 m is assumed, for a distance of 800 m and a travelling velocity of 150 km/h. The selected values for the input, process and measurement noise second-order statistics are $\sigma_{uu}^2 = 10^{-2}$, $\Sigma_{\xi\xi} = 10^{-12}\mathbf{I}_2$, and $\sigma_{yy}^2 = 10^{-10}$, respectively, while the initial variance/covariance matrix of the unknown input and state vector are $P_{uu}^2[0] = 10^{-1}$ and $\mathbf{P}_{\xi\xi}[0] = 10^{-5}\mathbf{I}_2$, respectively.

Table 18.1 Numerical values for the structural parameters of the pitch-bounce model

Parameter	Symbol	Value	Unit
Front wheelset mass	m_{wf}	1220	kg
Rear wheelset mass	m_{wr}	1200	kg
Front/rear bogie mass	m_{bf}, m_{br}	850	kg
Chassis mass	M_c	4125	kg
Chassis inertia	I_c	1.25×10^5	kg m^2
Front/rear wheelset Hertzian contact spring	k_{wf}, k_{wr}	3.00×10^7	N/m
Front/rear primary suspension stiffness	k_{pf}, k_{pr}	3.00×10^6	N/m
Front/rear secondary suspension stiffness	k_{sf}, k_{sr}	6.00×10^6	N/m
Front/rear primary suspension damping	c_{pf}, c_{pr}	0.60×10^4	N s/m
Front/rear secondary suspension damping	c_{sf}, c_{sr}	1.80×10^4	N s/m
Distance of the chassis centre of gravity from the front/rear suspensions	L_1, L_2	8.53	m

**Fig. 18.2** True (black) and estimated (red) rail profile**Fig. 18.3** True (black) and estimated (red) one-sided power spectral density for the profiles of Fig. 18.2

The results are expanded over Figs. 18.2 and 18.3 and indicate very good performance of the dual observer. The estimated profile resembles in good accuracy its true counterpart, with the minor discrepancies attributed to the effects of the force $f_{pf}(t)$ that is also “hidden” in the estimate. These effects are more obvious in the wavenumber domain, where a small peak appears in the spectral amplitude of the estimated profile: this corresponds to a frequency band around 25–26 Hz, in which the pitch-bounce model has two closely-spaced modes (25.35 and 25.56 Hz).

18.4 Conclusions

The encouraging results suggest further investigation of the method, especially with respect to a number of aspects that render its actual implementation successful. These include, among others, a more systematic investigation of the effects of vehicle uncertainties, by integrating them into the estimation process [15]. Of primary importance is the extension of the method to cover the direct prediction of ballast condition and soil properties, towards its integration into an actual monitoring alternative of railway infrastructure.

References

1. Farrar, C.R., Worden, K.: An introduction to structural health monitoring. *Philos. Trans. R. Soc. A Math. Phys. Eng. Sci.* **365**(1851), 303–315 (2007)
2. Barke, D., Chiu, W.K.: Structural health monitoring in the railway industry: a review. *Struct. Health Monit.* **4**(1), 81–93 (2005)
3. Edwards, M., Donelson III, J., Zavis, W., Prabhakaran, A., Brabb, D., Jackson, A.: Improving freight rail safety with on-board monitoring and control systems. In: Proceedings of the 2005 ASME/IEEE Joint Rail Conference, vol. 29, pp. 117–122 (2005)
4. Chatzi, E.N., Dertimanis, V.K.: On the monitoring-driven assessment of engineered systems. In: Barthorpe, R. (ed.) *Model Validation and Uncertainty Quantification*, vol. 3, pp. 309–312. Springer, Cham (2019)
5. Lederman, G., Chen, S., Garrett, J.H., Kovačević, J., Noh, H.Y., Bielak, J.: A data fusion approach for track monitoring from multiple in-service trains. *Mech. Syst. Signal Process.* **95**, 363–379 (2017)
6. Molodova, M., Li, Z., Nunez, A., Dollevoet, R.: Automatic detection of squats in railway infrastructure. *IEEE Trans. Intell. Transp. Syst.* **15**(5), 1980–1990 (2014)
7. Real, J., Salvador, P., Montalbán, L., Bueno, M.: Determination of rail vertical profile through inertial methods. *Proc. Inst. Mech. Eng. F: J. Rail Rapid Transit* **225**(1), 14–23 (2011)
8. Molodova, M., Li, Z., Dollevoet, R.: Axle box acceleration: measurement and simulation for detection of short track defects. *Wear* **271**(1–2), 349–356 (2011)
9. Boccilone, M., Caprioli, A., Cigada, A., Collina, A.: A measurement system for quick rail inspection and effective track maintenance strategy. *Mech. Syst. Signal Process.* **21**(3), 1242–1254 (2007)
10. Matarazzo, T.J., Pakzad, S.N.: Structural identification for mobile sensing with missing observations. *J. Eng. Mech.* **142**(5), 04016021 (2016)
11. AlOrabi, W.A., Rahman, S.A., Barachi, M.E., Mourad, A.: Towards on demand road condition monitoring using mobile phone sensing as a service. *Prog. Comput. Sci.* **83**, 345–352 (2016). The 7th International Conference on Ambient Systems, Networks and Technologies (ANT 2016)/The 6th International Conference on Sustainable Energy Information Technology (SEIT-2016)/Affiliated Workshops
12. Eftekhar Azam, S., Chatzi, E., Papadimitriou, C.: A dual Kalman filter approach for state estimation via output-only acceleration measurements. *Mech. Syst. Signal Process.* **60**, 866–886 (2015)
13. Zimmermann, M., Dertimanis, V.K., Chatzi, E.N., Corman, F.: Estimating track condition based on axle box accelerations of revenue trains. In: Fourth International Conference on Railway Technology: Research, Development and Maintenance (RAILWAYS 2018), Barcelona (2018)
14. Podworna, M.: Modelling of random vertical irregularities of railway tracks. *Int. J. Appl. Mech. Eng.* **20**(3), 647–655 (2015)
15. Dertimanis, V., Chatzi, E., Eftekhar Azam, S., Papadimitriou, C.: Output-only fatigue prediction of uncertain steel structures. In: 8th European Workshop on Structural Health Monitoring (EWSHM 2016), Bilbao (2016)



Chapter 19

Bayesian Identification of a Nonlinear Energy Sink Device: Method Comparison

Alana Lund, Shirley J. Dyke, Wei Song, and Ilias Bilionis

Abstract Nonlinear energy sink (NES) devices have recently been introduced in civil engineering for structural control. Because of the essential geometric nonlinearities governing these devices, identification must be performed in the time domain. Such methods can be challenging due to processing requirements, sensitivity to noise, and the presence of nonlinearity. Bayesian analysis methods have been shown to overcome these challenges, providing robust identification of nonlinear models. In this study we compare the unscented Kalman filter and the particle filter for the identification of a prototype NES device. Simulated responses developed using a device model and a sample set of parameters are used here to demonstrate and evaluate the identification process. Analysis of the identification results is conducted by varying the identification technique used and the selection of the prior distributions on the parameters. These preliminary numerical results will inform a later implementation on experimental response data.

Keywords Nonlinear Energy Sink · Bayesian Analysis · Model Identification · Unscented Kalman Filter · Particle Filter

19.1 Introduction

The nonlinear energy sink (NES) is of interest to the structural engineering community for its ability to passively dissipate structural vibration over a wide range of frequencies. This property encourages its long-term use in structures whose dynamic behavior is subject to change due to the effects of aging, repurposing, and rehabilitation. The NES device concept was first explored in a series of studies by Gendelman et al. [1] and Vakakis and Gendelman [2] in 2001. The dynamic analysis of these devices and their performance when coupled with linear systems is a topic of ongoing research [3–8]. Recent studies attempt device identification, using static testing for specific parameters [5] and the restoring force method for global identification [7].

Bayesian system identification techniques provide a promising alternative to these methods. Of these techniques, Kalman filters [9] and particle filters (PF) [10] are commonly used for recursive estimation. In the Kalman filter class, the unscented Kalman filter (UKF) [11] and its variants have been shown to be the most applicable for the robust identification of nonlinear systems with additive Gaussian noise [12–14]. The PF has likewise been shown to be reliable for identifying generalized nonlinear systems, though it does suffer from increased computation time [15–17]. In this study we compare the ability of these techniques to accurately identify the parameters of a prototype NES device from its simulated responses. The results of the identification process for each method are also analyzed in terms of the selection of the prior distributions on the parameters.

A. Lund (✉)

Lyles School of Civil Engineering, College of Engineering at Purdue University, West Lafayette, IN, USA
e-mail: alund15@purdue.edu

S. J. Dyke

Lyles School of Civil Engineering, College of Engineering at Purdue University, West Lafayette, IN, USA
School of Mechanical Engineering, College of Engineering at Purdue University, West Lafayette, IN, USA

W. Song

Department of Civil, Construction, and Environmental Engineering, College of Engineering at University of Alabama, Tuscaloosa, AL, USA

I. Bilionis

School of Mechanical Engineering, College of Engineering at Purdue University, West Lafayette, IN, USA

19.2 Background

The NES device investigated in this study, shown in Fig. 19.1, is similar to the small-scale Type 1 NES device designed by Wierschem [7]. An additional Coulomb damping term is incorporated in the governing equation in anticipation of frictional effects in the experimental implementation of the device. The complete model is given by

$$m\ddot{x} + c_v\dot{x} + c_f \tanh(200\dot{x}) + kx + zx^3 = -m\ddot{x}_g, \quad (19.1)$$

where m is the mass of the device (0.664 kg), c_v is the viscous damping coefficient (0.419 Ns/m), c_f is the Coulomb damping coefficient (0.054 N), k is the linear stiffness coefficient (21.8 N/m), z is the nonlinear stiffness coefficient ($696,295$ N/m 3), x is the displacement of the mass, and \ddot{x}_g is the acceleration of the base. The term $\tanh(200\dot{x})$ is a continuous approximation of the idealized discontinuous Coulomb damping force. The excitation used in this study corresponds to an acceleration resulting from a 5 mm sine sweep displacement at the base, varying linearly in frequency from 0 to 5 Hz over 30 s. This excitation was selected because it demonstrates a clear variation in the behavior of the device over a frequency range of interest. The response, shown in Fig. 19.2, is calculated using 4th order Runge-Kutta integration at a sampling frequency of 2048 Hz.

The UKF and PF algorithms are implemented to identify the parameters $\theta = [c_v \ c_f \ k \ z]$ using displacement and acceleration response signals with 10% process and measurement noise. The parameters are logarithmically transformed during algorithm operation to allow unconstrained optimization over the parameter space, which is known to be positive. The UKF approach used in this study is described in detail in [11, 12]. State augmentation is used to facilitate the joint estimation of the states and parameters. The PF approach used in this study is described in [10, 16] and implemented with the python library pyParticleEst [18]. Expectation-maximization (EM) is used with the PF to facilitate joint estimation [19].

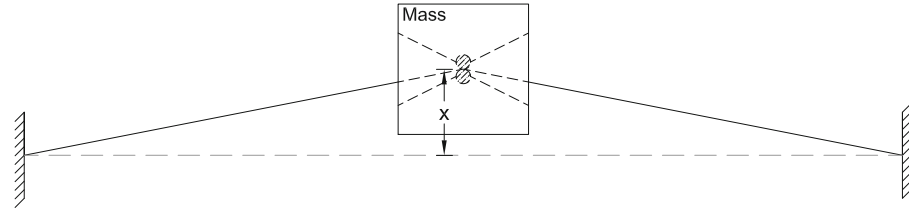


Fig. 19.1 Schematic diagram of the NES device

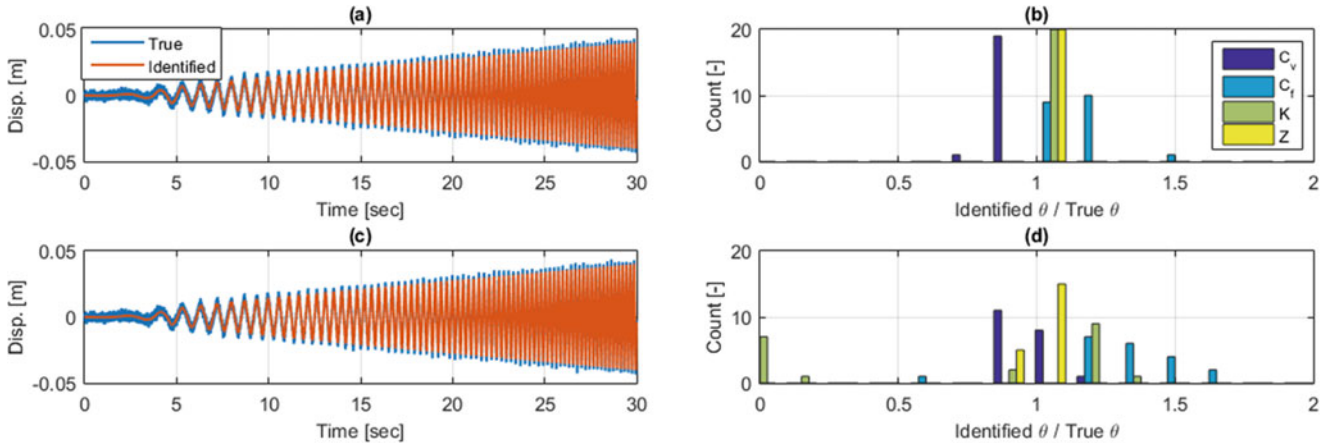


Fig. 19.2 Displacement response of true and identified model using UKF (a) and PF (c) and distribution of candidate parameter sets estimated by UKF (b) and PF (d)

19.3 Analysis

Parameter identification results from this preliminary analysis are given in Fig. 19.2, with results from the UKF method shown in Fig. 19.2a, b and results from the PF method shown in Fig. 19.2c, d. Each method is evaluated with 20 sets of initial parameters. The final parameters are determined from the resulting candidate solutions as those minimizing the RMS error on the displacement response. The final parameter sets are $\theta_{\text{UKF}} = [0.376, 0.058, 22.65, 697, 397]$ and $\theta_{\text{PF}} = [0.416, 0.064, 20.87, 699, 874]$. With the exception of the Coulomb damping parameter identified by the PF, all identified parameters are within 10% of the true values. The UKF and PF generate similar results and similarly good representations of the response, as shown in Fig. 19.2a, c. The consistency with which they attained these solutions differs, as shown in Fig. 19.2b, d. The UKF generates a far narrower set of solutions using the same set of initial parameters.

19.4 Conclusion

These preliminary results suggest that a state augmentation approach to the UKF has the potential to generate a more consistent set of identified parameters for the NES device than an EM approach with the PF. Further investigations will be performed to systematically compare the methods, particularly with respect to the experimental response of the NES.

Acknowledgements This work is partially supported by the National Science Foundation (NSF) under Grant No. DGE-1333468. Any opinions, findings, and conclusions or recommendations expressed in this material are those of the authors and do not necessarily reflect the views of the NSF. The authors also acknowledge Christian Silva, who designed and constructed this NES device.

References

1. Gendelman, O., Manevitch, L.I., Vakakis, A.F., M'Closkey, R.: Energy pumping in nonlinear mechanical oscillators: Part I—dynamics of the underlying Hamiltonian systems. *J. Appl. Mech.* **68**(1), 34 (2001)
2. Vakakis, A.F., Gendelman, O.: Energy pumping in nonlinear mechanical oscillators: Part II—resonance capture. *J. Appl. Mech.* **68**(1), 42 (2001)
3. Vakakis, A.F., Manevitch, L.I., Gendelman, O., Bergman, L.: Dynamics of linear discrete systems connected to local, essentially non-linear attachments. *J. Sound Vib.* **264**(3), 559 (2003)
4. Sapsis, T.P., Quinn, D.D., Vakakis, A.F., Bergman, L.A.: Effective stiffening and damping enhancement of structures with strongly nonlinear local attachments. *J. Vib. Acoust.* **134**(1), 011016 (2012)
5. McFarland, D.M., Bergman, L.A., Vakakis, A.F.: Experimental study of non-linear energy pumping occurring at a single fast frequency. *Int. J. Nonlinear Mech.* **40**(6), 891 (2005)
6. Wierschem, N.E., Quinn, D.D., Hubbard, S.A., Al-Shudeifat, M.A., McFarland, D.M., Luo, J., Fahnestock, L.A., Spencer, B.F., Vakakis, A.F., Bergman, L.A.: Passive damping enhancement of a two-degree-of-freedom system through a strongly nonlinear two-degree-of-freedom attachment. *J. Sound Vib.* **331**, 5393 (2012)
7. Wierschem, N.E.: Targeted energy transfer using nonlinear energy sinks for the attenuation of transient loads on building structures, PhD Dissertation, University of Illinois at Urbana-Champaign (2014)
8. Nucera, F., Lo Iacono, F., Mcfarland, D.M., Bergman, L.A., Vakakis, A.F.: Application of broadband nonlinear targeted energy transfers for seismic mitigation of a shear frame: Experimental results. *J. Sound Vib.* **313**, 57 (2008)
9. Kalman, R.E.: A new approach to linear filtering and prediction problems. *J. Fluids Eng.* **82**, 35 (1960)
10. Gordon, N.J., Salmond, D.J., Smith, A.F.M.: Novel approach to nonlinear/non-Gaussian Bayesian state estimation. *IEE Proc. F (Radar Signal Process.).* **140**(2), 107 (1993)
11. Wan, E.A., Van Der Merwe, R.: The unscented Kalman filter for nonlinear estimation. *IEEE Adapt. Syst. Signal Process. Commun. Control Symp.*, p. 153 (2000)
12. Wu, M., Smyth, A.W.: Application of the unscented Kalman filter for real-time nonlinear structural system identificatio. *Struct. Control Health Monit.* **14**(1), 971 (2007)
13. Mariani, S., Ghisi, A.: Unscented Kalman filtering for nonlinear structural dynamics. *Nonlinear Dyn.* **49**, 131 (2007)
14. Song, W., Dyke, S.: Real-time dynamic model updating of a hysteretic structural system. *J. Struct. Eng.* **140**(3), 1 (2013)
15. Chatzi, E., Smyth, A.: Particle filter scheme with mutation for the estimation of time-invariant parameters in structural health monitoring applications. *Struct. Control Health Monit.* **20**(1), 1081 (2013)
16. Chatzi, E., Smyth, A.: The unscented Kalman filter and particle filter methods for nonlinear structural system identification with non-collocated heterogeneous sensing. *Struct. Control Health Monit.* **19**(1), 88 (2009)
17. Olivier, A., Smyth, A.W.: Particle filtering and marginalization for parameter identification in structural systems. *Struct. Control Health Monit.* **24**(3), 1 (2017)
18. Nordh, J.: pyParticleEst: a python framework for particle based estimation methods. *J. Stat. Softw.* **78**(3), 1–25 (2017)
19. Bishop, C.M.: Pattern Recognition and Machine Learning. Michael J., Jon K., Bernhard S. (eds.), Springer Science+Business Media, New York, NY (2006)



Chapter 20

Calibration of a Large Nonlinear Finite Element Model of a Highway Bridge with Many Uncertain Parameters

Rodrigo Astroza, Nicolás Barrientos, Yong Li, and Erick Saavedra Flores

Abstract Finite element (FE) model updating has emerged as a powerful technique for structural health monitoring (SHM) and damage identification (DID) of civil structures. Updating mechanics-based nonlinear FE models allows for a complete and comprehensive damage diagnosis of large and complex structures. Recursive Bayesian estimation methods, such as the Unscented Kalman filter (UKF), have been used to update nonlinear FE models of civil structures; however, their use have been limited to models with a relatively low number of degrees of freedom and with a limited number of unknown model parameters, because it is otherwise impractical for computationally demanding models with many uncertain parameters. In this paper, a FE model of the Marga-Marga bridge, an eight-span seismically-isolated bridge located in Viña del Mar-Chile, is updated based on numerically simulated response data. Initially, 95 model parameters are considered unknown, and then, based on a simplified sensitivity analysis, a total of 27 model parameters are considered in the estimation. Different measurement sets, including absolute accelerations, relative displacements, strains, and shear deformations of the isolators, are analyzed to investigate the effects of considering heterogeneous responses on the estimation results. In addition, a non-recursive estimation procedure is presented and its effectiveness in reducing the computational cost, while maintaining accuracy and robustness in the estimation, is demonstrated.

Keywords Model updating · Nonlinear finite element model · Parameter estimation · High-dimensional parameter space

20.1 Introduction

Finite element (FE) model updating aims to determine a set of parameters, defined in deterministic or probabilistic terms, of a model such that the misfit between the FE-predicted and measured responses, or quantities derived therefrom, is minimized [1]. In structural engineering, an important application of FE model updating is damage identification. In his area, linear FE model updating has attracted significant attention from the community, by proposing methodologies and verifying and validating them with simulated and experimental data (e.g., [2]). However, linear FE models need to be employed with data recorded from excitations of low amplitude (e.g., ambient vibrations), and therefore, damage is described as a reduction of the effective stiffness of the structure being analyzed. As an alternative, updating of nonlinear FE models allows a more comprehensive characterization of the damage, including strength deterioration and ductility capacity, by using the data recorded during damage inducing events.

In recent years, some research efforts have been devoted to update mechanics-based nonlinear FE models, mainly using a Bayesian estimation framework (e.g., [3–5]). In particular, Astroza et al. [6–8] and Ebrahimian et al. [9] proposed using the unscented Kalman filter (UKF) and the extended Kalman filter (EKF) to estimate parameters defining mechanics-based nonlinear FE models. These studies have provided promising results, however, all of them have tackled the estimation of nonlinear models with a limited number of degrees of freedom and/or with a low number of parameters to be identified. In real world, it is anticipated that nonlinear FE models to be solved correspond to large and complex models involving a large number of parameters to be estimated. Therefore, it is required to validate the performance of the previously proposed

R. Astroza (✉) · N. Barrientos
Facultad de Ingeniería y Ciencias Aplicadas, Universidad de los Andes, Santiago, Chile
e-mail: rastroza@miuandes.cl

Y. Li
Department of Civil and Environmental Engineering, University of Alberta, Edmonton, AB, Canada

E. Saavedra Flores
Departamento de Ingeniería en Obras Civiles, Universidad de Santiago de Chile, Santiago, Chile

methods and also their feasibility in terms of the computational resources required. In this paper, the performance of the UKF when dealing with the updating of a FE model of a seismically isolated highway bridge including many degrees of freedom and material nonlinearities, and requiring the estimation of a large number of parameters is investigated. The effects of considering heterogeneous response measurements is also studied and a batch-recursive approach is presented to reduce the computational cost involved in the estimation process.

20.2 FE Model Updating

The nonlinear differential equation describing the response of a nonlinear FE model of a structural systems subjected to uniform seismic excitation can be written as

$$\mathbf{M}(\boldsymbol{\theta}) \ddot{\mathbf{q}}_{k+1}(\boldsymbol{\theta}) + \mathbf{C}(\boldsymbol{\theta}) \dot{\mathbf{q}}_{k+1}(\boldsymbol{\theta}) + \mathbf{r}_{k+1}(\mathbf{q}_{1:k+1}(\boldsymbol{\theta}), \boldsymbol{\theta}) = -\mathbf{M} \mathbf{L} \ddot{\mathbf{u}}_{k+1}^g \quad (20.1)$$

where $\mathbf{q}_{k+1}, \dot{\mathbf{q}}_{k+1}, \ddot{\mathbf{q}}_{k+1} \in \mathbb{R}^{n \times 1}$ = displacement, velocity, and acceleration response vectors, $\mathbf{M}, \mathbf{C} \in \mathbb{R}^{n \times n}$ = mass and damping matrices, $\mathbf{r}_{k+1}(\mathbf{q}_{1:k+1}(\boldsymbol{\theta}), \boldsymbol{\theta}) \in \mathbb{R}^{n \times 1}$ = nonlinear resisting force vector, n = number of degrees of freedom, $\boldsymbol{\theta} \in \mathbb{R}^{n_\theta \times 1}$ = vector of model parameters, n_θ = number of model parameters, $\mathbf{L} \in \mathbb{R}^{n \times r}$ = influence matrix and $\ddot{\mathbf{u}}_{k+1}^g \in \mathbb{R}^{r \times 1}$ = seismic base acceleration vector, r = number of components of base excitation, $k = 0, 1, \dots, N-1$ denotes the time step, and N is the number of data samples of the input acceleration vector. At discrete time t_{k+1} , different types of responses can be extracted from the FE model ($\widehat{\mathbf{y}}_{k+1}(\boldsymbol{\theta}) \in \mathbb{R}^{n_y \times 1}$, with n_y = number of measured responses) and related with their measured counterparts ($\mathbf{y}_{k+1} \in \mathbb{R}^{n_y \times 1}$):

$$\mathbf{y}_{k+1} = \widehat{\mathbf{y}}_{k+1}(\boldsymbol{\theta}, \ddot{\mathbf{u}}_{1:k+1}^g) + \mathbf{v}_{k+1} \quad (20.2)$$

where the $\widehat{\mathbf{y}}_{k+1}(\boldsymbol{\theta}, \ddot{\mathbf{u}}_{1:k+1}^g)$ is an implicit nonlinear response function (i.e., the FE model), $\ddot{\mathbf{u}}_{1:k+1}^g$ includes the ground accelerations from time t_1 to t_{k+1} , and \mathbf{v}_{k+1} is the prediction error vector, which is assumed here to be described by a white Gaussian process with zero mean and covariance matrix \mathbf{R} .

The vector of model parameters to be estimated ($\boldsymbol{\theta}$) is modeled as a random walk, defining together with Eq. (20.2), the following nonlinear state-space model:

$$\begin{aligned} \boldsymbol{\theta}_{k+1} &= \boldsymbol{\theta}_k + \mathbf{w}_k \\ \mathbf{y}_{k+1} &= \mathbf{h}_{k+1}(\boldsymbol{\theta}_{k+1}, \ddot{\mathbf{u}}_{1:k+1}^g) + \mathbf{v}_{k+1} \end{aligned} \quad (20.3)$$

where $\mathbf{h}_{k+1}(\boldsymbol{\theta}_{k+1}, \ddot{\mathbf{u}}_{1:k+1}^g) = \widehat{\mathbf{y}}_{k+1}(\boldsymbol{\theta}, \ddot{\mathbf{u}}_{1:k+1}^g)$, \mathbf{w}_k is the process noise assumed white Gaussian with zero-mean and diagonal covariance matrices \mathbf{Q} and statistically uncorrelated with \mathbf{v}_k . Instead of updating the FE model at every time step as proposed in [6], a batch-recursive approach is employed. This aims to reduce the computational cost involved in the estimation process and therefore allow calibrating nonlinear FE models with a large number of degrees of freedom and requiring the estimation of a high number of parameters. A single forward analysis of these types of models may require a significant amount of time, and consequently, the inverse problem involving many parameters to be estimated may be prohibitive using existing methods. In the batch-recursive approach the FE model is updated every $D > 1$ time steps, where D corresponds to the updating step. Then, the model parameters are estimated at t_{k+1} , $k = D-1, 2D-1, \dots$, instead of at every time step. When the model is updated at time t_{k+1} , the innovation vector is extended to include the responses from times t_{k-D+2} to t_{k+1} , then, no measured information is discarded in the estimation process. A summary of the batch-recursive approach used in this paper is shown in Fig. 20.1.

20.3 Application Example: Marga-Marga Bridge

20.3.1 Description of the Structure, FE Model, and Input Motion

The Marga-Marga bridge is an eight-span highway bridge located in Chile (Fig. 20.2). The bridge reinforced concrete deck is supported on four steel girders which are connected to the piers and abutments by high-damping rubber bearings. Reinforcing

Initialization: $\hat{\theta}_{0 0}$ and $\hat{P}_{0 0}^{00}$ $k = D-1$ while $k \leq N$	Initial estimates of parameter vector and parameter covariance matrix Initialization of counter Loop over time steps
Prediction: (i) $\hat{\theta}_{k+1 k-D+1} = \hat{\theta}_{k-D+1 k-D+1}$ (ii) $\hat{P}_{k+1 k-D+1}^{00} = \hat{P}_{k-D+1 k-D+1}^{00} + Q_{k-D+1}$ (iii) Generate SP $\mathbf{g}_{k+1}^{(i)}$ ($i=1, \dots, 2n_0 + 1$) based on $\hat{\theta}_{k+1 k-D+1}$ and $\hat{P}_{k+1 k-D+1}^{00}$ (iv) $\hat{\mathbf{y}}_{k+1}^{(i)} = \mathbf{h}_{k+1}(\mathbf{g}_{k+1}^{(i)}, \hat{\mathbf{u}}_{1:k+1}^g)$ (v) $\hat{\mathbf{y}}_{k+1} = \sum_{i=1}^{2n_0+1} W_m^{(i)} \hat{\mathbf{y}}_{k+1}^{(i)}$ where $\hat{\mathbf{y}}_{k+1}^{(i)} = [\mathbf{g}_{k+1}^{(i)T}, \mathbf{y}_{k+1}^{(i)T}, \mathbf{y}_{k+1}^{(i)T}]^T$ (vi) $\hat{P}_{k+1}^{\bar{y}\bar{y}} = \sum_{i=1}^{2n_0+1} W_c^{(i)} [\hat{\mathbf{y}}_{k+1}^{(i)} - \hat{\mathbf{y}}_{k+1}] [\hat{\mathbf{y}}_{k+1}^{(i)} - \hat{\mathbf{y}}_{k+1}]^T + \tilde{R}_{k+1}$ where $\tilde{R}_{k+1} = \text{diag}[\mathbf{R}_{k-D+2}, \dots, \mathbf{R}_k, \mathbf{R}_{k+1}]$ (vii) $\hat{P}_{k+1}^{0\bar{y}} = \sum_{i=1}^{2n_0+1} W_c^{(i)} [\mathbf{g}_{k+1}^{(i)} - \hat{\theta}_{k+1 k-D+1}] [\hat{\mathbf{y}}_{k+1}^{(i)} - \hat{\mathbf{y}}_{k+1}]^T$	<i>A priori</i> estimate of parameter vector <i>A priori</i> estimate of parameter covariance matrix Generate SPs Output vector for each SP Augmented predicted response vector Augmented measurement covariance matrix Augmented measurement noise covariance matrix Augmented cross-covariance matrix
Correction: output measurement \mathbf{y}_{k+1} is recorded	
(viii) $\tilde{K}_{k+1} = \hat{P}_{k+1}^{0\bar{y}} (\hat{P}_{k+1}^{\bar{y}\bar{y}})^{-1}$	Kalman gain
(ix) $\hat{\theta}_{k+1 k+1} = \hat{\theta}_{k+1 k-D+1} + \tilde{K}_{k+1} (\bar{\mathbf{y}}_{k+1} - \hat{\mathbf{y}}_{k+1})$	<i>A posteriori</i> estimate of parameter vector
(x) $\hat{P}_{k+1 k+1}^{00} = \hat{P}_{k+1 k-D+1}^{00} - \tilde{K}_{k+1} \hat{P}_{k+1}^{\bar{y}\bar{y}} \tilde{K}_{k+1}^T$	<i>A posteriori</i> estimate of parameter covariance matrix
$k = k + D$ <i>end for</i>	

Fig. 20.1 Batch-recursive estimation procedure for large FE models with high-dimensional parameter space

steel and concrete of the structural components have nominal yield strength of 420 MPa and maximum compressive strength of 25 MPa, respectively. More information about the bridge is available in [10].

The open-source software platform *OpenSees* [11] was used to model the bridge. The superstructure, which includes the girders and the deck, was modeled with an equivalent cross-section. The rigid offsets of the structure were modeled with rigid linear beam-column elements (Fig. 20.3). The piers were modeled using nonlinear distributed plasticity beam-column elements and the concrete and steel fibers considered the constitutive laws *concrete04* and *steel02* as available in *OpenSees*.

The reinforcing steel model is defined by four primary parameters: elastic Young's modulus (E_0), initial yield stress (f_{ys}), strain hardening ratio (b_s), and a parameter describing the curvature of the transition curve between the asymptotes of the elastic and plastic branches during the first loading (R_0). The concrete model is defined by four parameters, modulus of elasticity (E_c), maximum compressive strength (f'_c), strain at the maximum compressive strength (ϵ_c), and strain at the crushing strength (ϵ_{cu}). The seismic isolators were modeled employing the Elastomeric Bearing element available in *OpenSees*, which is defined by five parameters, the initial elastic stiffness (K_e), yield strength (f_y), post-yield stiffness ratio of linear hardening component (b), post-yield stiffness ratio of nonlinear hardening component (α_2), and an exponent of non-linear hardening component (μ).

The mass properties of the bridge were computed based on the volume of the components and their material densities and were lumped at the nodes of the FE model. Rayleigh damping model with critical damping ratio of 2% for the first longitudinal and transverse modes was assumed. No contribution of the isolators was considered in the Rayleigh damping model. Uniform base excitation was considered at both bridge ends and at the bottom of the piers. The 90°, 0°, and UD (vertical) ground motion components recorded at the Los Gatos station during the 1989 Loma Prieta earthquake (Fig. 20.4) were considered in the longitudinal, transverse, and vertical directions of the bridge. More details about the FE model can be found in [12].



Fig. 20.2 Marga-Marga bridge. Top: photo, Bottom: elevation view

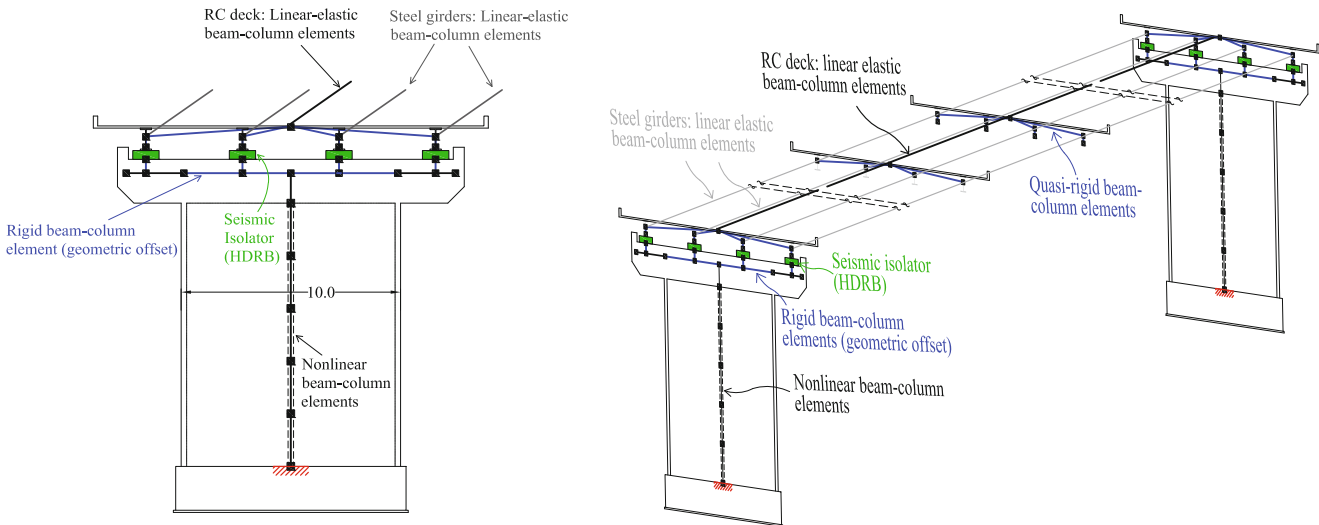


Fig. 20.3 FE model of the Marga-Marga bridge. Left: pier, Right: typical span

20.3.2 Response Simulation

The parameters of the reinforcing steel and concrete constitutive models, the parameters of the seismic isolator elements, the elastic modulus of the deck and steel girders (E_D and E_G , respectively), and the coefficients defining the Rayleigh damping matrix (α and β) are considered as model parameters. It is assumed that the seven piers and isolators are governed by different model parameters, then a total of 95 parameters are initially considered to be estimated. A set of true model parameter values are selected to simulate the response of the bridge. Their values were randomly selected assuming a Gaussian distribution for each parameter with nominal mean values of $E_0^{Ci} = 210$ GPa, $f_{sy}^{Ci} = 420$ GPa, $b_S^{Ci} = 0.005$, $R_0^{Ci} = 18$, $f_c'^{Ci} = 25$ MPa,

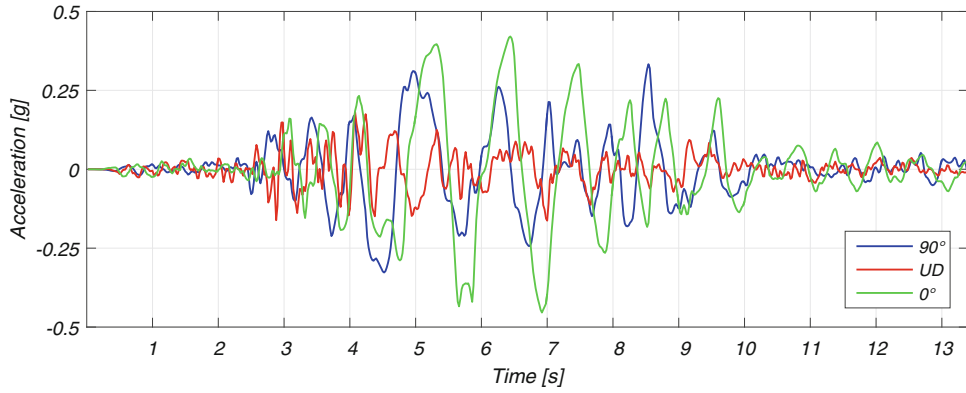


Fig. 20.4 Ground accelerations recorded at the Los Gatos station during the 1989 Loma Prieta earthquake

Table 20.1 True value of model parameters of the Marga-Marga bridge

Parameter	ID	Value
K_e^{C1}	1	13944 N/mm
f_y^{C1}	2	69894 N
b^{C1}	3	0.205
α_2^{C1}	4	0.158
μ^{C1}	5	1.493
K_e^{C2}	6	15941 N/mm
f_y^{C2}	7	74765 N
b^{C2}	8	0.213
α_2^{C2}	9	0.141
μ^{C2}	10	1.39
K_e^{C3}	11	14936 N/mm
f_y^{C3}	12	69265 N
b^{C3}	13	0.206
α_2^{C3}	14	0.165
μ^{C3}	15	1.451
K_e^{C4}	16	15501 N/mm
f_y^{C4}	17	70324 N
b^{C4}	18	0.202
α_2^{C4}	19	0.137
μ^{C4}	20	1.377
K_e^{C5}	21	15686 N/mm
f_y^{C5}	22	69197 N
b^{C5}	23	0.183
α_2^{C5}	24	0.145
μ^{C5}	25	1.46
K_e^{C6}	26	13175 N/mm
f_y^{C6}	27	67209 N
b^{C6}	28	0.182
α_2^{C6}	29	0.155
μ^{C6}	30	1.36
K_e^{C7}	31	14263 N/mm
f_y^{C7}	32	72408 N

Parameter	ID	Value
b^{C7}	33	0.216
α_2^{C7}	34	0.145
μ^{C7}	35	1.379
f_c^{C1}	36	23.44 MPa
E_c^{C1}	37	21.92 GPa
ε_c^{C1}	38	0.0022
ε_{cu}^{C1}	39	0.0066
f_c^{C2}	40	22.96 MPa
E_c^{C2}	41	22.38 GPa
ε_c^{C2}	42	0.0019
ε_{cu}^{C2}	43	0.0063
f_c^{C3}	44	23.46 MPa
E_c^{C3}	45	21.22 MPa
ε_c^{C3}	46	0.0019
ε_{cu}^{C3}	47	0.0065
f_c^{C4}	48	25.57 MPa
E_c^{C4}	49	21.60 GPa
ε_c^{C4}	50	0.0019
ε_{cu}^{C4}	51	0.0054
f_c^{C5}	52	24.82 MPa
E_c^{C5}	53	21.48 GPa
ε_c^{C5}	54	0.0022
ε_{cu}^{C5}	55	0.0057
f_c^{C6}	56	25.41 MPa
E_c^{C6}	57	25.36 GPa
ε_c^{C6}	58	0.0019
ε_{cu}^{C6}	59	0.0064
f_c^{C7}	60	24.51 MPa
E_c^{C7}	61	22.24 GPa
ε_c^{C7}	62	0.0018
ε_{cu}^{C7}	63	0.0058
f_{ys}^{C1}	64	439.1 MPa

Parameter	ID	Value
E_0^{C1}	65	189.9 MPa
b_s^{C1}	66	0.0048
R_0^{C1}	67	17.22
f_{ys}^{C2}	68	447.0 MPa
E_0^{C2}	69	212.4 MPa
b_s^{C2}	70	0.0055
R_0^{C2}	71	17.27
f_{ys}^{C3}	72	406.3 MPa
E_0^{C3}	73	201.2 MPa
b_s^{C3}	74	0.0048
R_0^{C3}	75	19.67
f_{ys}^{C4}	76	416.1 MPa
E_0^{C4}	77	191.4 MPa
b_s^{C4}	78	0.0047
R_0^{C4}	79	18.3
f_{ys}^{C5}	80	396.5 MPa
E_0^{C5}	81	222.0 MPa
b_s^{C5}	82	0.0048
R_0^{C5}	83	18.79
f_{ys}^{C6}	84	380.8 MPa
E_0^{C6}	85	202.6 MPa
b_s^{C6}	86	0.0047
R_0^{C6}	87	19.77
f_{ys}^{C7}	88	441.3 MPa
E_0^{C7}	89	205.5 MPa
b_s^{C7}	90	0.0047
R_0^{C7}	91	19.38
E_G	92	210 GPa
E_D	93	23.5 GPa
α	94	0.0562624
β	95	0.0017419

$\varepsilon_c^{Ci} = 0.002$, $\varepsilon_{cu}^{Ci} = 0.006$, $K_e^{Ci} = 14,600$ N/mm, $f_y^{Ci} = 6800$ N, $b_e^{Ci} = 0.2$, $\alpha_2^{Ci} = 0.15$, $\mu^{Ci} = 1.5$, $E_G = 210$ GPa, $E_D = 23.5$ GPa, $\alpha = 0.0563$, and $\beta = 0.0017$, where the superscript Ci denote the pier/column i (see Fig. 20.2), and a coefficient of variation of 10%. The true parameter values are shown in Table 20.1.

20.3.3 Sensitivity Analysis

A simplified one-at-a-time sensitivity analysis is conducted for the Marga-Marga bridge and the results are shown in tornado diagrams [13]. Local sensitivities of 36 different responses with respect to the 95 parameters described above are analyzed. The considered responses include: longitudinal and transverse absolute acceleration responses at the top of piers #2, #4, and #6 and at the deck above the same piers (i.e., 12 absolute acceleration responses, y_1 to y_{12}), relative displacements collocated with the acceleration responses (i.e., 12 relative displacement responses, y_{13} to y_{24}), strain responses on one steel and one concrete fiber at the bottom section of the same piers (i.e., 6 strain responses, y_{25} to y_{30}), and longitudinal and transverse shear strains on isolators located above piers #2, #4, and #6 (i.e., 6 isolators' shear strain responses, y_{31} to y_{36}). A perturbation of $\pm 5\%$ around the true value of each model parameter (Table 20.1) is considered. Then, the relative root mean square error (*RRMSE*) between the true responses (i.e., computed using the true parameter values) and those obtained with the perturbed parameter values is computed and plotted in tornado diagrams. Figure 20.5 shows the sensitivity results of one global response, the absolute acceleration response on top of pier #2 in the longitudinal direction (y_1), and one local response, the shear deformation of the isolator on top of pier #6 in the longitudinal direction (y_{35}). The parameter ID in Fig. 20.5 refers to the model parameters presented in Table 20.1. From Fig. 20.5 it is observed that response y_1 and y_{35} are mostly sensitive to parameters defining the response of the isolators in the interior piers (#2 to #6), elastic modulus of steel girders and deck (E_G and E_D), the stiffness-proportional parameter of the Rayleigh damping (β), and some concrete parameters (chiefly E_c, f'_c , and ε_c) of the interior piers (#2 to #6). As expected, the predominant effect of the isolation layer in the overall structural response is clearly captured by the simple sensitivity analysis conducted. Moreover, it is observed that global acceleration and displacement responses are more sensitive to concrete model parameters than shear deformation response of the isolators. This shows the importance of considering heterogeneous response quantities when calibrating large and complex nonlinear FE models. By comparing the magnitude of the *RRMSEs* related to the different responses analyzed, it is observed that shear deformation of the isolators experienced the highest variations (y_{31} to y_{36}), followed by global acceleration (y_1 to y_{12}) and displacement (y_{13} to y_{24}) responses, while fiber level responses (y_{25} to y_{30}) show the lowest variations. Then, the model parameters to be estimated are selected as those having a *RRMSE* equal or higher than 20% of the *RRMSE* for the most sensitive parameter, considering all the measured responses. A threshold value of 20% is chosen in this application because of the abrupt change in the swings of the tornado diagram. The twenty-seven (27) parameters satisfying this criterion are highlighted in grey in Table 20.1 and are chosen for the estimation and model updating phase.

20.3.4 Estimation of Model Parameters

The twenty-seven model parameters defined above define the vector $\boldsymbol{\theta}$. The true responses (\mathbf{y}^{true}) obtained using the true model parameters (Table 20.1) are polluted by white Gaussian noise to define the measured response (\mathbf{y}) employed for the estimation. For acceleration and displacement-related responses, levels of noise of $0.7\%g$ and 2.0 mm RMS , are respectively considered. Note that displacement-related responses includes relative displacement responses of the pier and deck, and also shear strain responses of the isolators. For the fiber strain responses, an absolute noise level of 0.005% is assumed. Then, the updating process employs the three components of seismic base acceleration ($\ddot{\mathbf{u}}^g$) and the measured response (\mathbf{y}) to estimate the twenty-seven FE model parameters. To investigate the effects of the number and type of the measured responses and of the updating step (D) considered in the estimation process, different instrumentation setups are considered to update the FE model. The twelve cases analyzed are summarized in Table 20.2 and include values of $D = 5, 10$, and 20 and measured responses considering only accelerations (cases B01 to B03), accelerations + displacements (cases B04 to B06), accelerations + displacements + strain in fibers (cases B07 to B09), and accelerations + displacements + strain in fibers + shear strain in isolators (cases B10 to B12).

\mathbf{w}_k is assumed zero-mean with diagonal covariance matrix \mathbf{Q} , whose diagonal entries are computed as $(q \times \widehat{\theta}_{0|0}^i)^2$, $i = 1, \dots, 27$ and $q = 1 \times 10^{-5}$. Matrix \mathbf{R} was constructed assuming standard deviations of 0.5% for acceleration responses, 1.3 mm for global displacement responses, 1.5 mm for shear deformation of isolator responses, and 0.003% for strain in steel and concrete fiber responses. Initial estimates of the parameters are randomly chosen from the ranges $[-20\%, -10\%]$ and $[10\%, 20\%]$ of the true parameter values. $\widehat{\mathbf{P}}_{0|0}^{\boldsymbol{\theta}\boldsymbol{\theta}}$ is taken as diagonal with entries equal to $(p \times \widehat{\theta}_{0|0}^i)^2$, with $i = 1, \dots, 27$ and $p = 5\%$. Figure 20.6 shows the time history of the mean estimate of the 27 parameters normalized with respect to the corresponding true values for cases B01 and B12. In cases B01, all the isolator model parameters, the elastic modulus of steel girders and deck (E_G and E_D), and most of the elastic modulus of concrete of the piers converge to the true values, while

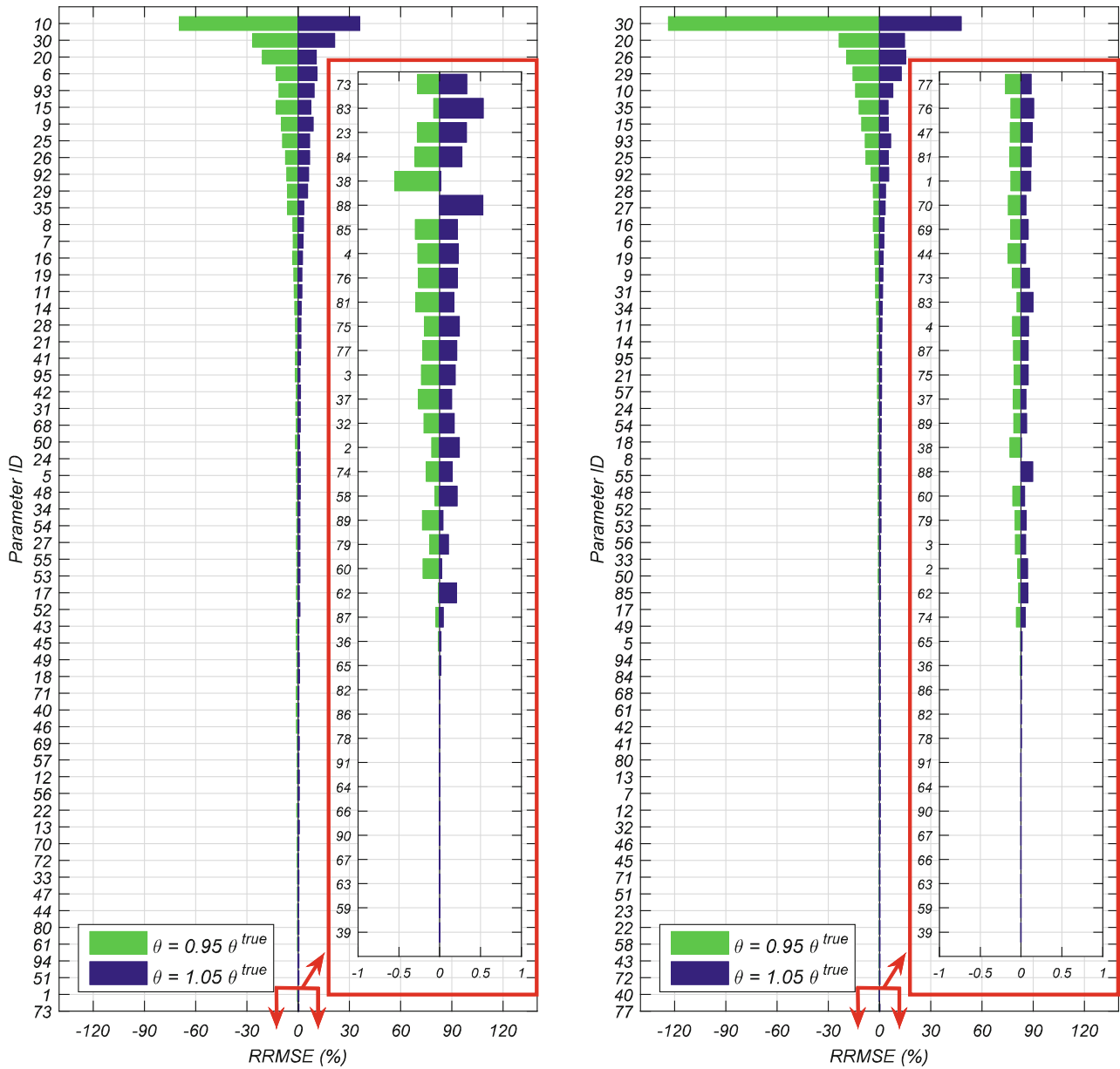


Fig. 20.5 Tornado diagrams for the model parameters of the Marga-Marga bridge. Left: y_1 = absolute acceleration response on top of pier #2 in the longitudinal direction. Right: y_{35} = shear deformation of isolator on top of pier #6 in the longitudinal direction

estimation errors for other model parameters vary from less than 10% (e.g., β , ε_c^{C2} , ε_c^{C3} , $\varepsilon_c^{C4^2}$) to larger than 15% (e.g., f_c^{C2} , f_c^{C5} , f_{ys}^{C2}). In case B12, all the model parameters are accurately estimated and all of them converge to their true values at about 6 s.

All the estimation results are summarized in Table 20.3, where the final estimates of the twenty-seven model parameters corresponding to the twelve cases analyzed are shown. Final estimates with relative errors lower than or equal to 5% are highlighted in grey. It can be clearly observed that most of the model parameters are accurately estimated. In particular, the isolator model parameters are very well estimated in all cases, even when the instrumentation is spatially sparse, include only acceleration responses, and a value of $D = 20$ is considered. Parameters β , E_G , E_D , and E_c^{Ci} with $i = 2, 3, 4, 5$ are also accurately estimated in most cases. The only parameters that show more values with errors larger than 5% are ε_c^{C3} , ε_c^{C5} , ε_{cu}^{C5} , and f_{ys}^{C2} , which is expected because the measured responses contain less information about these parameters compared to the other selected parameters. Overall, the estimation performance is excellent for all values of D analyzed,

Table 20.2 Response measurements considered for the Marga-Marga bridge

Case ID	D	$\mathbf{y}_1(\mathbf{a}_1) \rightarrow \mathbf{y}_{12}(\mathbf{a}_{12})$	$\mathbf{y}_{13}(\mathbf{d}_1) \rightarrow \mathbf{y}_{24}(\mathbf{d}_{12})$	$\mathbf{y}_{25}(\boldsymbol{\varepsilon}_1) \rightarrow \mathbf{y}_{30}(\boldsymbol{\varepsilon}_6)$	$\mathbf{y}_{31}(\Delta_1) \rightarrow \mathbf{y}_{36}(\Delta_6)$
B01	20	✓		—	—
B02	10	✓		—	—
B03	5	✓		—	—
B04	20	✓	✓	—	—
B05	10	✓	✓	—	—
B06	5	✓	✓	—	—
B07	20	✓	✓	✓	—
B08	10	✓	✓	✓	—
B09	5	✓	✓	✓	—
B10	20	✓	✓	✓	✓
B11	10	✓	✓	✓	✓
B12	5	✓	✓	✓	✓

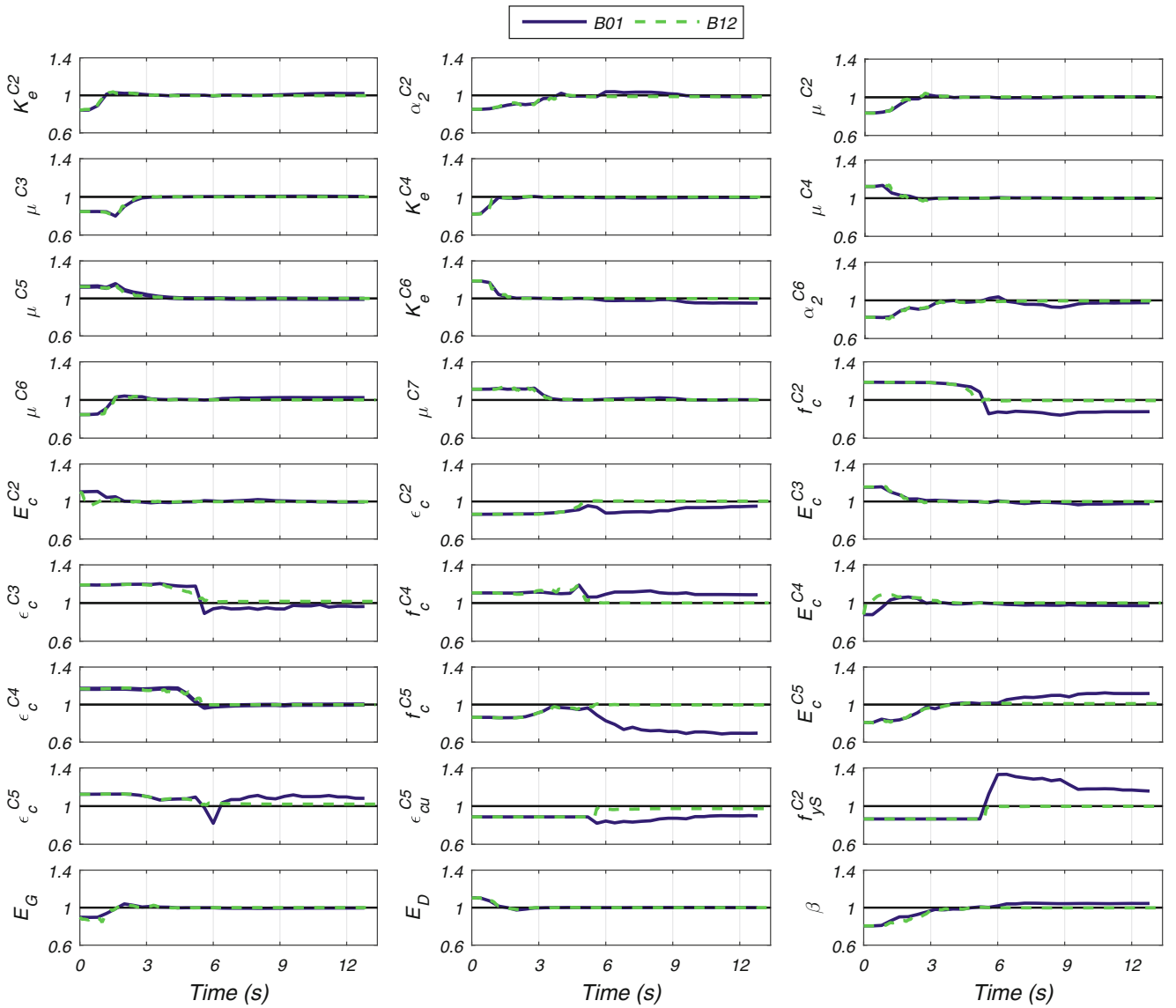
**Fig. 20.6** Updating history of the normalized parameter estimates for cases B01 and B12

Table 20.3 Final normalized parameter estimates for the Marga-Marga bridge

Parameter	ID	Case ID											
		B01	B02	B03	B04	B05	B06	B07	B08	B09	B10	B11	B12
K_e^{C2}	6	1.02	1.00	1.01	1.00	1.02	0.99	1.01	1.00	1.01	0.99	1.01	1.00
α_2^{C2}	9	0.99	1.00	0.98	1.00	0.97	1.02	1.06	1.02	0.98	1.03	0.97	0.99
μ^{C2}	10	1.00	1.00	1.00	1.00	1.00	1.00	0.98	1.00	1.00	1.00	1.00	1.00
μ^{C3}	15	1.01	1.00	1.00	1.00	1.00	1.00	1.00	1.00	1.00	1.00	1.00	1.00
K_e^{C4}	16	0.99	1.00	1.01	0.99	1.00	1.00	0.98	1.00	1.00	1.01	1.00	1.00
μ^{C4}	20	1.00	1.00	1.00	1.00	1.00	1.00	1.00	1.00	1.00	0.99	1.00	1.00
μ^{C5}	25	1.00	1.00	1.00	1.00	1.00	1.00	0.98	1.00	1.00	0.99	1.00	1.00
K_e^{C6}	26	0.95	1.00	1.01	0.98	1.01	1.00	0.98	1.00	1.01	1.02	0.99	1.00
α_2^{C6}	29	0.98	1.02	0.97	1.03	1.00	0.99	1.03	0.99	0.97	0.96	1.01	0.99
μ^{C6}	30	1.02	1.00	1.00	1.00	1.00	1.00	0.99	1.00	1.00	1.00	1.00	1.00
μ^{C7}	35	1.00	1.00	1.00	1.00	1.00	1.01	1.04	1.00	1.00	1.02	1.00	1.00
f_c^{C2}	40	0.88	1.03	0.94	0.88	0.98	0.96	0.87	0.99	0.99	1.02	0.99	0.99
E_c^{C2}	41	1.00	1.03	1.00	0.99	1.00	1.00	1.06	1.00	0.99	1.01	1.01	1.00
ε_c^{C2}	42	0.95	1.01	0.97	0.94	0.92	0.92	0.93	1.01	1.01	0.99	0.97	1.00
E_c^{C3}	45	0.98	1.01	1.01	0.98	1.00	1.03	1.07	0.98	0.99	1.01	1.00	1.00
ε_c^{C3}	46	0.96	1.06	0.99	0.91	0.94	0.90	1.12	0.98	1.04	0.99	1.01	1.02
f_c^{C4}	48	1.09	0.97	1.00	1.01	0.98	1.02	1.03	1.00	0.99	1.01	1.01	1.00
E_c^{C4}	49	0.97	0.99	1.01	1.00	1.00	0.99	0.97	0.99	1.01	1.01	1.00	1.00
ε_c^{C4}	50	1.00	0.98	0.99	0.98	0.98	1.00	1.07	0.99	1.00	0.96	0.98	1.00
f_c^{C5}	52	0.70	1.04	0.98	1.06	1.01	1.05	0.90	1.04	0.97	1.03	1.02	1.00
E_c^{C5}	53	1.12	1.02	1.00	1.01	0.98	0.99	0.85	1.02	1.01	0.97	1.01	1.01
ε_c^{C5}	54	1.08	0.96	0.98	0.90	0.95	1.06	0.94	0.92	0.97	0.98	0.94	1.02
ε_{cu}^{C5}	55	0.90	1.00	1.06	1.21	1.10	0.88	1.40	1.09	1.06	1.04	1.04	0.97
f_{ys}^{C2}	68	1.16	0.96	1.22	1.13	1.01	1.15	1.17	0.98	0.98	0.97	0.93	1.00
E_G	92	1.00	1.00	1.00	1.00	1.00	1.00	1.02	1.00	1.00	1.00	1.00	1.00
E_D	93	1.00	1.00	1.00	1.00	1.00	1.00	1.00	1.00	1.00	1.00	1.00	1.00
β	95	1.04	1.00	1.00	1.02	1.02	1.02	1.14	1.02	1.00	1.02	1.02	1.00

considering the large number of parameters to be estimated, the complexity of the nonlinear FE model, and the reduced number of measured responses.

20.3.5 Response Prediction Errors

Figure 20.7 shows the *RRMSEs* between the true and updated FE models corresponding to the measured response quantities (see Table 20.2) for the twelve cases analyzed (cases B01 to B12). In addition, the *RRMSEs* between the true and initial FE models are depicted in parenthesis and denoted by E_{ini} , which range between 7% (y_{23}) and 152% (y_{31}). After the updating process, the largest *RRMSEs* is about 28% (y_4 for case B05) and most of the errors are lower than 10%, confirming an excellent agreement between the true responses and the corresponding FE-predicted responses based on the updated model. Analyzing the effect of the updating step for each instrumentation setup, it is observed that as D decreases the *RRMSEs* also decreases. In this application example, the effect of the heterogeneous sensors is also evidenced, chiefly when displacement-related responses are added (i.e., global displacements and shear strain in isolators).

20.3.6 Computational Cost

All the analyses for the bridge model were conducted using three threads of an Intel Xeon E3-1230 processor and 32-GB random-access memory. Table 20.4 summarizes the wall-clock time (t_{wc}) for the 12 cases of analysis and also normalized times, with respect to the longest run (B06) and with respect to the time required for a single run of the FE model ($t_{run} = 6.5$ min). The time to conduct the updating processes depends on the value of the updating step (D) but is practically

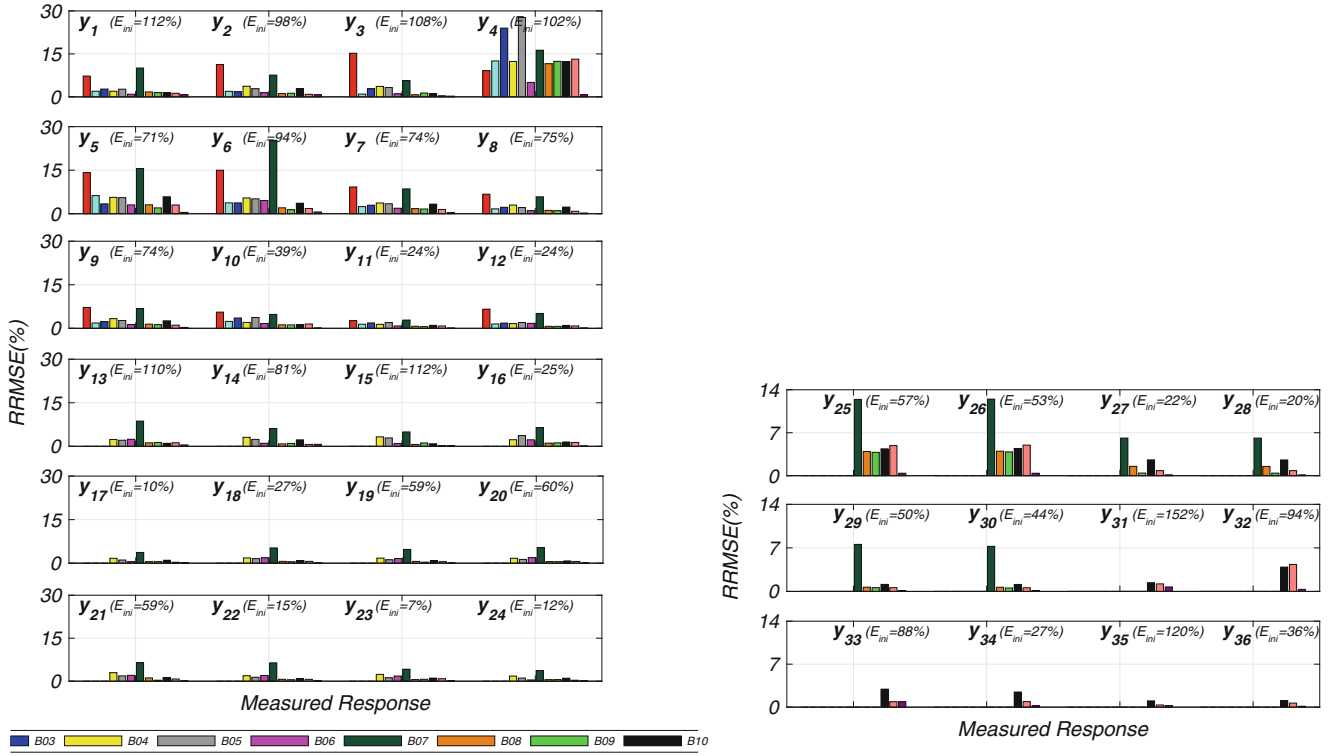


Fig. 20.7 Estimation errors in measured responses for the Marga-Marga bridge. Left: global responses, Right: local responses

Table 20.4 Wall-clock times of the estimation process for the Marga-Marga bridge

Case ID	D	Wall-clock time		
		h	%	t_{wc}/t_{run}
B01	20	45.3	26.8	418
B02	10	75.7	44.7	699
B03	5	160.3	94.7	1480
B04	20	42.8	25.3	395
B05	10	78.7	46.5	726
B06	5	169.2	100.0	1562
B07	20	43.7	25.8	403
B08	10	84.5	49.9	780
B09	5	161.5	95.4	1491
B10	20	44.1	26.1	407
B11	10	81.5	48.2	752
B12	5	158.4	93.6	1462

independent of the number of measured responses. Considerable reductions of the wall-clock time are achieved as D increases, without compromising the accuracy of the estimation results. The wall-clock time for $D = 20$ is about 25% of that for $D = 5$. It is noteworthy that the updating of the Marga-Marga bridge model was not conducted for $D = 1$, because excessively high running time was anticipated (about 14 days). Note that the wall-clock time can be further reduced if the estimation process is conducted in a more powerful computer. For example, if the updating process of the bridge model for case B04 ($D = 20$) is conducted using ten threads of a desktop workstation with an Intel Xeon E5-2650 processor and 64-GB random-access memory, the wall-clock time decreases to 13.5 h ($t_{wc}/t_{run} \approx 135$) (i.e., about 1/3 of the wall-clock time reported in Table 20.4).

20.4 Conclusions

This paper investigated the performance of the unscented Kalman filter (UKF) to update large and complex mechanics-based nonlinear finite element (FE) models with a large number of degrees of freedom and with a high number of unknown model parameters (i.e., a high dimensional parameter space). Because the use of recursive Bayesian estimation on these types of models is computationally demanding, it may be prohibitive for FE models of real-world civil structures. Then, this paper presents a practical approach comprising two steps: (1) one-at-a-time (OAT) sensitivity analysis based on tornado diagrams to select the most influential parameters and (2) a batch-recursive approach to reduce the computational cost of the updating process. The performance of the proposed approach was investigated for different updating step values (i.e., updating the model every few time steps) and instrumentation setups, including heterogeneous responses. The application example consisted of a three-dimensional isolated highway bridge model with 95 unknown model parameters. Heterogeneous responses, including global (acceleration and displacement) and local (shear deformation of isolators and strain of materials), were used and their effects on the estimation results were analyzed. For all the values of the updating step considered (5, 10, and 20) excellent estimation and prediction results were obtained, including parameter estimates and measured responses of the structure. The approach and results shown in this paper confirm that updating of large and complex nonlinear mechanics-based FE models with many degrees of freedom and involving a high number of parameters to be estimated is feasible and therefore, is an attractive alternative for damage identification of civil structures.

Acknowledgements R. Astroza acknowledges the financial support from the Chilean National Commission for Scientific and Technological Research (CONICYT), through FONDECYT research grant No. 11160009.

References

1. Friswell, M.I., Mottershead, J.E.: Finite element model updating in structural dynamics. Kluwer Academic Publishers, Dordrecht (1995)
2. Teugels, A., De Roeck, G.: Damage detection and parameter identification by FE model updating. *Arch. Comput. Methods Eng.* **12**(2), 123–164 (2005)
3. Wu, A.-L., Yang, J.N., Loh, C.-H.: A finite-element based damage detection technique for nonlinear reinforced concrete structures. *Struct. Control. Health Monit.* **22**, 1223–1239 (2015)
4. Astroza, R., Nguyen, L.T., Nestorović, T.: Finite element model updating using simulated annealing hybridized with unscented Kalman filter. *Comput. Struct.* **177**, 176–191 (2016)
5. Olivier, A., Smyth, A.W.: A marginalized unscented Kalman filter for efficient parameter estimation with applications to finite element models. *Comput. Methods Appl. Mech. Eng.* **339**, 615–643 (2018)
6. Astroza, R., Ebrahimiān, H., Conte, J.P.: Material parameter identification in distributed plasticity FE models of frame-type structures using nonlinear stochastic filtering. *J. Eng. Mech. ASCE* **141**(5), 04014149 (2015)
7. Astroza, R., Ebrahimiān, H., Li, Y., Conte, J.P.: Bayesian nonlinear structural FE model and seismic input identification for damage assessment of civil structures. *Mech. Syst. Signal Process.* **93**, 661–687 (2017)
8. Astroza, R., Ebrahimiān, H., Conte, J.P.: Performance comparison of Kalman–based filters for nonlinear structural finite element model updating. *J. Sound Vib.* **438**, 520–542 (2019)
9. Ebrahimiān, H., Astroza, R., Conte, J.P.: Extended Kalman filter for material parameter estimation in nonlinear structural finite element models using direct differentiation method. *Earthq. Eng. Struct. Dyn.* **44**(10), 1495–1522 (2015)
10. Sarrazin, M., Moroni, M.O., Neira, C., Venegas, B.: Performance of bridges with seismic isolation bearings during the Maule earthquake, Chile. *Soil Dyn. Earthq. Eng.* **47**, 117–131 (2013)
11. McKenna, F., Fenves, G.L., Scott, M.H.: Open System for Earthquake Engineering Simulation. Pacific Earthquake Engineering Research Center, University of California, Berkeley, CA (2000)
12. Li, Y., Astroza, R., Conte, J.P.: Nonlinear FE model updating and reconstruction of the response of an instrumented seismic isolated bridge to the 2010 Maule Chile earthquake. *Earthq. Eng. Struct. Dyn.* **46**(15), 2699–2716 (2017)
13. Porter, K.A., Beck, J.L., Shaikhutdinov, R.V.: Sensitivity of building loss estimates to major uncertain variables. *Earthq. Spectra* **18**(4), 719–743 (2002)



Chapter 21

Deep Unsupervised Learning for Condition Monitoring and Prediction of High Dimensional Data with Application on Windfarm SCADA Data

C. Mylonas, I. Abdallah, and E. N. Chatzi

Abstract In this work we are addressing the problem of statistical modeling of the joint distribution of data collected from wind turbines interacting due to collective effect of their placement in a wind-farm, the wind characteristics (speed/orientation) and the turbine control. Operating wind turbines extract energy from the wind and at the same time produce wakes on the down-wind turbines in a park, causing reduced power production and increased vibrations, potentially contributing in a detrimental manner to fatigue life. This work presents a Variational Auto-Encoder (VAE) Neural Network architecture capable of mapping the high dimensional correlated stochastic variables over the wind-farm, such as power production and wind speed, to a parametric probability distribution of much lower dimensionality. We demonstrate how a trained VAE can be used in order to quantify levels of statistical deviation on condition monitoring data. Moreover, we demonstrate how the VAE can be used for pre-training an inference model, capable of predicting the power production of the farm together with bounds on the uncertainty of the predictions.

Examples employing simulated wind-farm Supervisory Control And Data Acquisition (SCADA) data are presented. The simulated farm data are acquired from a Dynamic Wake Meandering (DWM) simulation of a small wind farm comprised of nine 5 MW turbines in close spacing using OpenFAST.

The contribution of this work lies in the introduction of state-of-the-art machine learning techniques in the general context of condition monitoring and uncertainty quantification. We show how the high dimensional joint probability distribution of condition monitoring parameters can be analyzed by exploiting the underlying lower dimensional structure of the data imposed by the physics of the problem. The process of making use of the trained joint distribution for the purposes of inference under uncertainty and condition monitoring is clearly exposed.

Keywords Uncertainty quantification · Deep learning · Variational autoencoder · Windfarm SCADA · DWM

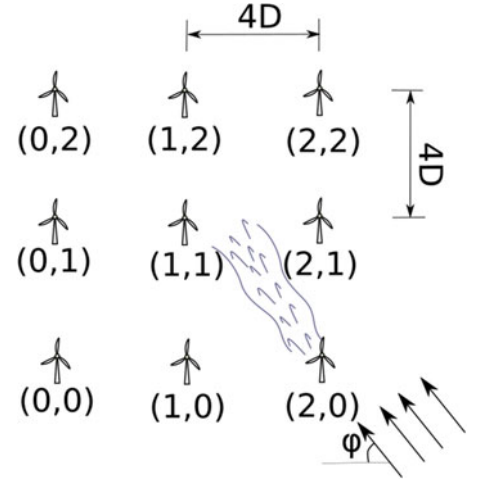
21.1 Introduction

Wind turbines are subjected to stochastic loadings throughout their lifetime. Many wind turbines are reaching their end of design life which is 20–25 years. It is of interest to estimate the level of structural damage they have been subjected throughout their lifetime. The turbines can either be refurbished or decommissioned depending on the estimated level of structural deterioration. Due to the requirements for control in the level of electrical grid integration, but also for optimal power production, utility-scale wind turbines contain a supervisory control and data acquisition platform (SCADA) which typically registers 10 min mean and standard deviation of several quantities of interest. The SCADA stream may contain useful information not only for estimating the current state of the structure based on past measurements, but also for detecting malfunctioning components based on instantaneous SCADA measurements. Both tasks rely on the statistical modelling of the SCADA stream, while at the same time modelling the environmental conditions. That is due to the fact that wind, together with pitch and yaw control, are the primary causes of mechanical straining for wind turbines.

Moreover, for the case of turbines positioned in a park, it is of importance to consider the potential interactions of them through wakes. Wakes in the context of this work, are the result of vortices produced on the tip of horizontal axis wind turbines (HAWT). In this work we have performed a medium-fidelity wake simulation for a windfarm containing 9 turbines with rated capacity of 5 MW in a three-by-three arrangement. We used the so-called Dynamic Wake Meandering (**DWM**)

C. Mylonas (✉) · I. Abdallah · E. N. Chatzi
Institute of Structural Engineering, ETH Zürich, Zürich, Switzerland
e-mail: mylonas@ibk.baug.ethz.ch

Fig. 21.1 The layout of the studied simulated farm



simulation model [1] for the effect of wakes as it is implemented in the NTWC simulation suite [2]. The two main parameters characterizing wind statistics in this work are the 10 min mean windspeed, and turbulence intensity. The mean windspeed distribution typically changes with height, however for the simulations that this work considers we have not statistically modelled this effect (typically referred to as *wind shear*).

21.2 Description of the Method

21.2.1 Simulated SCADA Dataset

Figure 21.1 displays a sketch of the turbine layout on the considered windfarm. In total, 600 aero-servo-elastic simulations were run for randomly sampled windseed and turbulence intensity, according to their joint distribution, as defined in IEC 64100 design standard [3] for a class C turbine. The raw simulated dataset consists of dynamic and operational measurements, such as time-domain tower and blade root moments and power production for the 9 wind turbines for 2000 s. The first 400 s in the time domain results are ignored in order for the farm to reach approximately stationary operational conditions. Consequently, two 600 s intervals are considered from each simulation, amounting to 1200 stochastic inputs.

The aero-servo-elastic simulations were performed with NREL-OpenFAST using the simplified ElastoDyn module and the AeroDyn14 module for aerodynamics and the simulations of the downstream wakes, using the DWM simulator. The windfields used for the simulations are created with TurbSim, with the Kaimal turbulence model and using a different random seed for every simulation. Therefore the response of each turbine and the farm as a whole is fully stochastic. The DWM model can capture the meandering and expanding of wakes.

21.2.2 Variational Autoencoder

Relatively recently, in the concurrent works of [4] and [5], an efficient method for building probabilistic latent variable models was proposed. The model form of the so-called *Variational Autoencoder* (VAE) is shown in Fig. 21.2.

The Variational Autoencoder (VAE) is a re-formulation of the autoencoder [6] where the encoder, referred to also as the *recognition model*, parametrizes a known probability distribution $q_\phi(\mathbf{x}|\mathbf{z})$ over latent variables \mathbf{z} which is an approximation to the true posterior distribution $p_\phi(\mathbf{x}|\mathbf{z})$. The encoder and the decoder, are both implemented as deep neural networks.

The likelihood of the datapoints reads

$$\log p_\theta(\mathbf{x}^{(1)}, \dots, \mathbf{x}^{(N)}) = \sum_{i=1}^N \log p_\theta(\mathbf{x}^{(i)}) \quad (21.1)$$

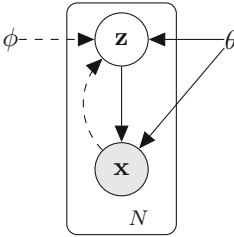


Fig. 21.2 The variational autoencoder as a probabilistic graphical model. Solid lines denote the generative model (decoder) $p_\theta(\mathbf{z}) p_\theta(\mathbf{x}|\mathbf{z})$, dashed lines denote the variational approximation $q_\phi(\mathbf{z}|\mathbf{x})$ to the posterior $p_\theta(\mathbf{z}|\mathbf{x})$. The variational parameters ϕ to be learned jointly with the generative model parameters θ

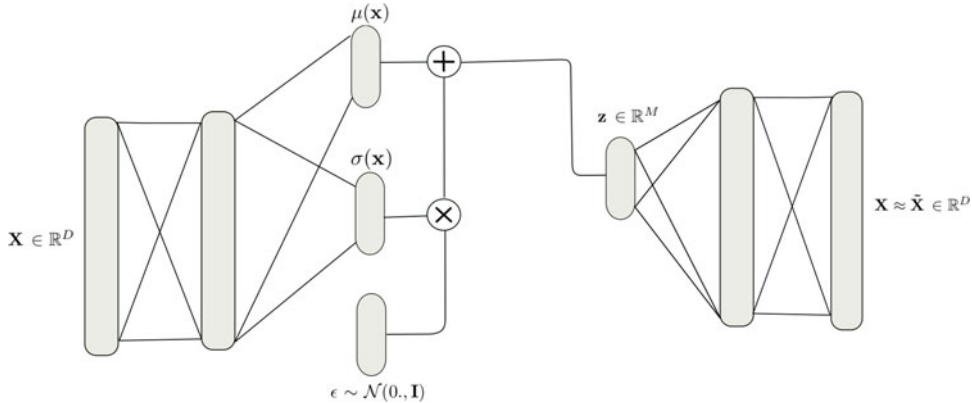


Fig. 21.3 The computational graph of a VAE with a Gaussian stochastic layer. In essence, we *compress* the raw high dimensional SCADA data $\mathbf{X} \in \mathbb{R}^D$ dimensional SCADA stochastic vectors, to a $\mathbf{z} \in \mathbb{R}^M$ dimensional stochastic vector ($M << D$)

For training the VAE, we optimize a lower bound on the likelihood of each datapoint that is given in Eq. (21.2).

$$\mathcal{L}(\phi, \theta; \mathbf{x}^{(i)}) = -D_{KL}(q_\phi(\mathbf{z}|\mathbf{x}^{(i)}) || p_\theta(\mathbf{z})) + \mathbb{E}_{q_\theta(\mathbf{z}|\mathbf{x}^{(i)})} \left[\log p_\theta(\mathbf{x}^{(i)}|\mathbf{z}) \right] \quad (21.2)$$

The first term of the right-hand-side is the *Kulback-Leibler* divergence between a prior over the latent variable \mathbf{z} and the variational posterior $q_\phi(\mathbf{z}|\mathbf{x})$. The second term in the RHS is the expected likelihood of the data given a set of samples from the latent space. The quantity in Eq. (21.2) is referred to as the *Evidence Lower Bound* (ELBO). We can chose $q_\phi(\mathbf{z}|\mathbf{x})$ to be from a parametric family. In this work, we chose a diagonal Gaussian $q_\phi(\mathbf{z}|\mathbf{x}) = \mathcal{N}(\mu(\mathbf{x}), \sigma(\mathbf{x}))$. We can re-parametrize samples from a Gaussian distribution, as scaled and shifted samples from a standard Gaussian auxiliary variable $\epsilon \sim \mathcal{N}(0, \mathbf{I})$, and consequently we can train on the scaling and shifting of the distribution, in practice, deterministically. Note, however, that during the evaluation of the network sampling is performed. The computational graph with this re-parametrization is shown in Fig. 21.3. This re-parametrization trick was proposed independently by Kingma and Welling [4] and Rezende et al. [5]. Without this re-parametrization, alternative sampling based estimators for the gradient could have been used for optimization of the hyper parameters. These sampling based estimates are far less efficient and are expected to have much higher variance, especially for cases of large and diverse datasets. This is the main trick that makes training of VAEs efficient and scalable to large datasets.

21.2.3 Sampling from the Trained Model

In the context of a VAE, the problem of approximating the high dimensional joint distribution of the 45 dimensional raw data vector, is cast as a problem of discovering a distribution over a lower dimensional random vector, that we have assumed is distributed according to a known prior distribution $q(\mathbf{z})$. For the simulated farm studied in this work, a stochastic latent vector of size 3 was found to be adequate to capture most of the variations in the data. The encoder is expected to exploit the correlations between the raw input variables, allowing for a lower dimensional representation. Samples from the training

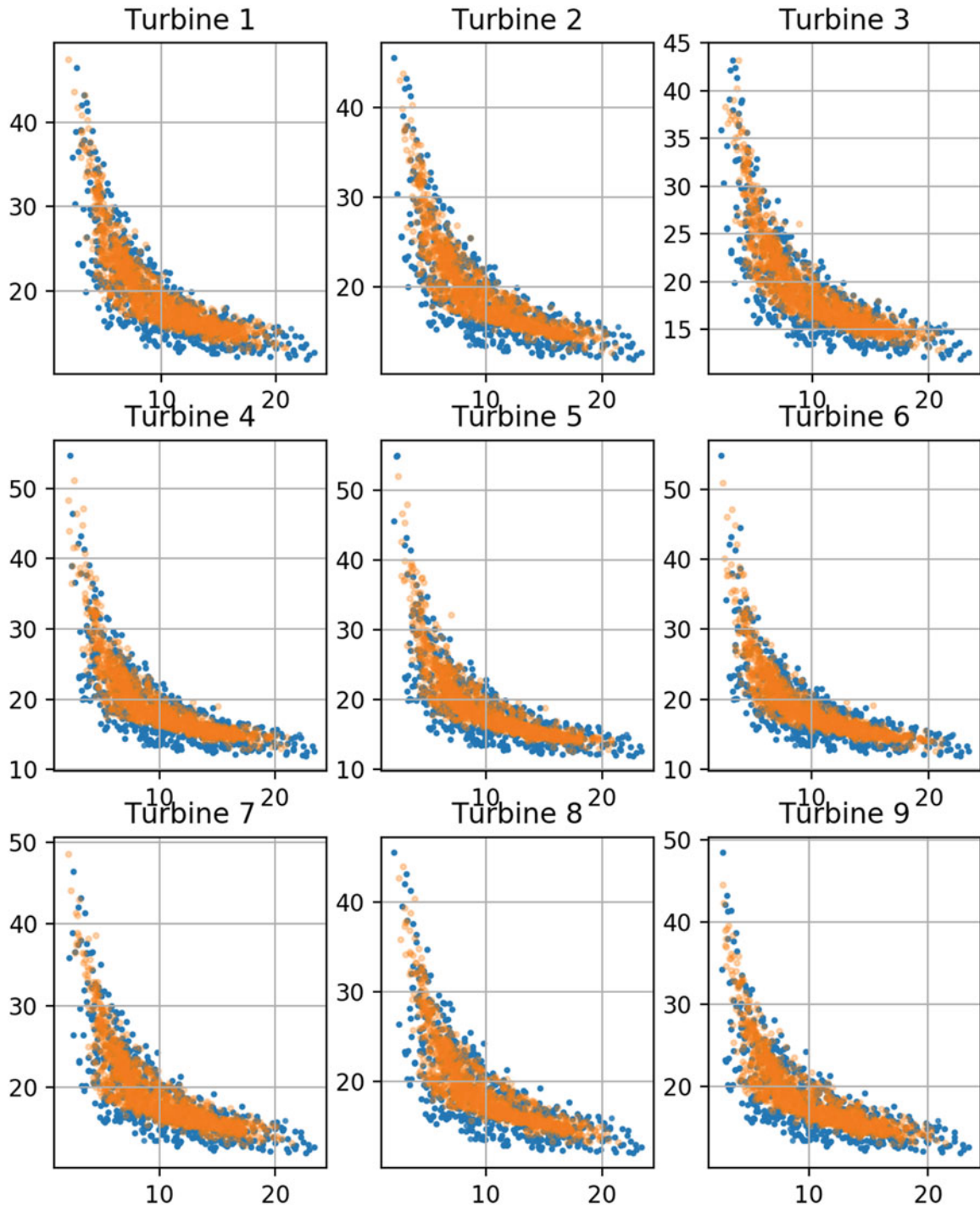


Fig. 21.4 The samples from the simulation are denoted with blue dots. With orange dots are the samples from the VAE. The autoencoder seems to perform well in capturing the windspeed and turbulence distribution of all the turbines

dataset, together with samples from a variational autoencoder trained on the simulated farm data are shown in Figs. 21.4 and 21.5. It is observed that the approximation is not as good in regions of lower probability mass. Nevertheless, for our purposes the VAE gives a good enough approximation. For clarity, the windspeed and turbulence intensity are shown separately for each turbine, whereas the autoencoder learns them jointly. Moreover, the angle-dependent effect of wakes makes the turbulence intensity higher on waked turbines and this cannot be seen in this figure.

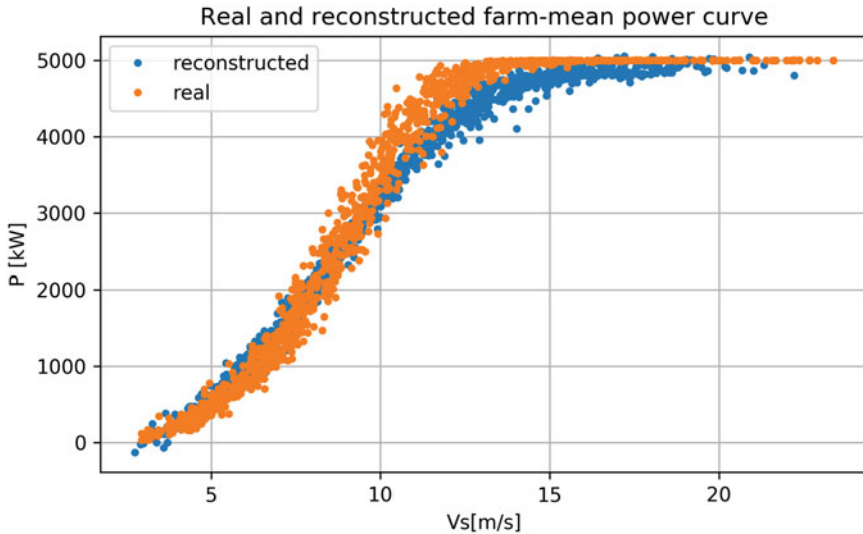


Fig. 21.5 Reconstruction of mean power curve for 3×3 farm

For more intuition on the representation that the autoencoder learns, the latent space is presented in Fig. 21.6. The first two columns are the sinus and cosinus of the mean angle of the wind in the farm. It is interesting to note, that the latent factor in column 4 seems to be directly correlated with mean windspeed. The mean inflow angle was kept as a deterministic variable in the latent space. We can easily control the mean angle and make predictions from the VAE with bounds on the uncertainty, while sampling from the prior distribution $p(\mathbf{z})$.

21.2.4 Using the Joint Distribution for Predictions

In Fig. 21.7, samples from the autoencoder are drawn, conditioned on a windspeed range from the middle of the power curve up to the rated power ([10 m/s, 12 m/s]). This region of the power curve is expected to have the most pronounced wake effects, in terms of power production. That is mostly due to the fact that we are in the below rated regime, and the windspeed is high enough for the effect to propagate in a large distance. Note, that the dots are 5000 samples from the autoencoder for varying wind orientation, and unseen examples. It is observed that the deficits on windspeed present extrema at multiples of 45° as it was expected from the configuration of the windfarm. Moreover, at multiples of 90° from zero, the farm presents the highest wake deficits, whereas on multiples of 90° from 45° the peaks of wake deficit are lower. This is expected due to the geometry of the farm. However, the autoencoder has not learned a representation that corresponds to the symmetries we would expect, since there is no effect captured in angles $\pm 26.56^\circ$ around every 45° spaced point. This is a subtle effect due to the alignment of the center turbine of one side of the farm, with the turbines on the edges of the opposing side. It is believed that this is mostly due to the relatively small number of simulations available for the problem at hand. Finally in Fig. 21.8 the ratio of power production of turbine $T^{(2,2)}$ to the maximum power produced in the farm is given. The correct angles are identified as the peaks of wake deficit, and bounds on the uncertainty of the estimation can be obtained by the samples of the autoencoder. There are some outliers which can be treated either with more training or more input data.

21.2.5 Using the VAE for Probabilistic Condition Monitoring

For a well trained variational autoencoder, where the latent variables have indeed converged to the assumed prior $p(\mathbf{z})$, given a raw SCADA measurement the encoder will produce a point in the latent space \mathbf{z} . Since we have endowed the latent space with a known probability distribution, we can compute the likelihood of the raw datapoint as the likelihood of the latent space. It has to be stressed, that this will be a good estimate only if the D_{KL} term in Eq. (21.2) is very low. In our examples we didn't have any simulated *faults* and therefore no results are presented for that application. This may be a complementary approach to fault detection as proposed in [7].

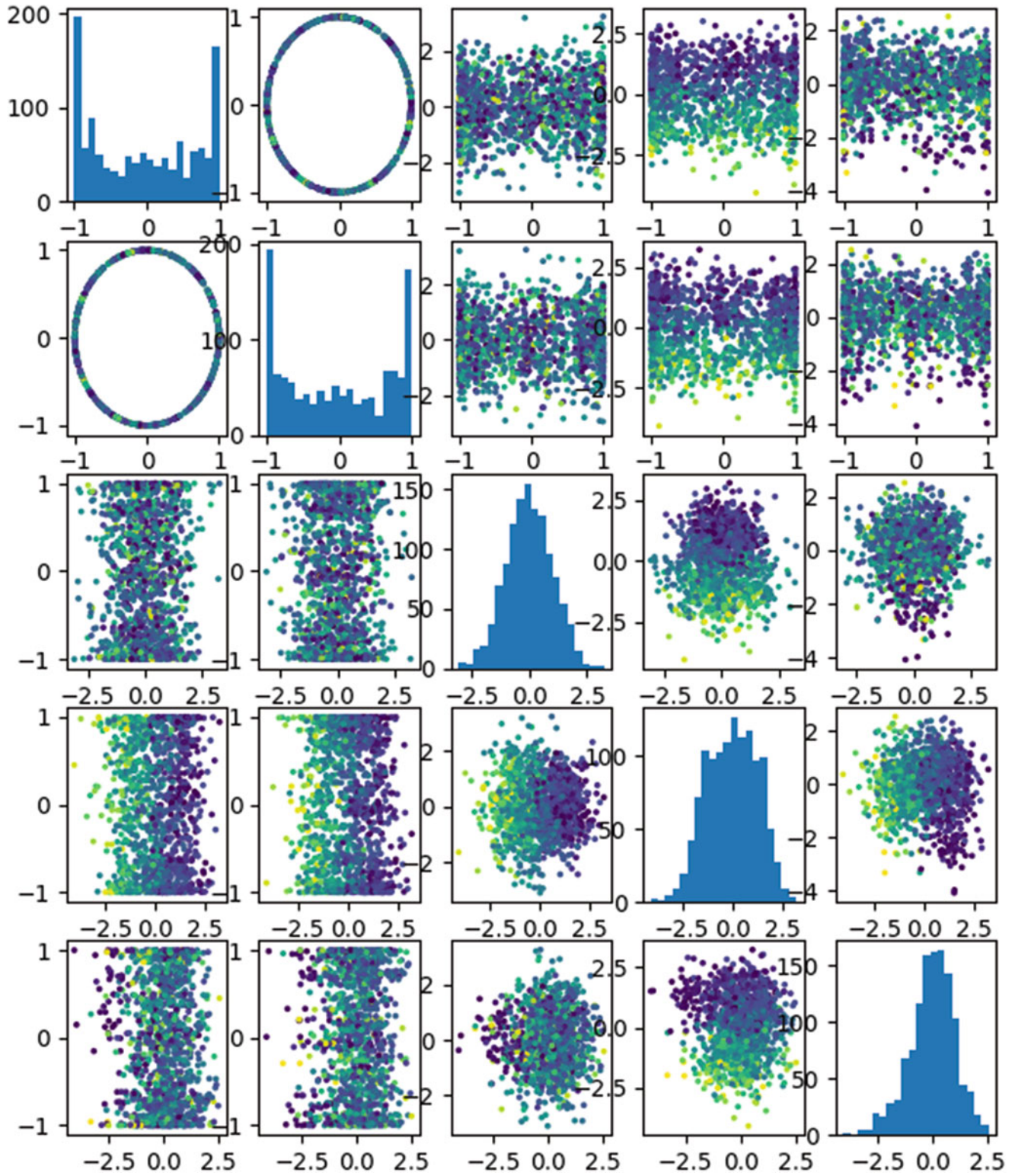


Fig. 21.6 The latent space variables, colored according to mean farm windspeed. Rows and columns 3–5 are the probabilistic latent factors, whereas the mean angle is kept deterministic for easier estimation of predictions w.r.t. angle

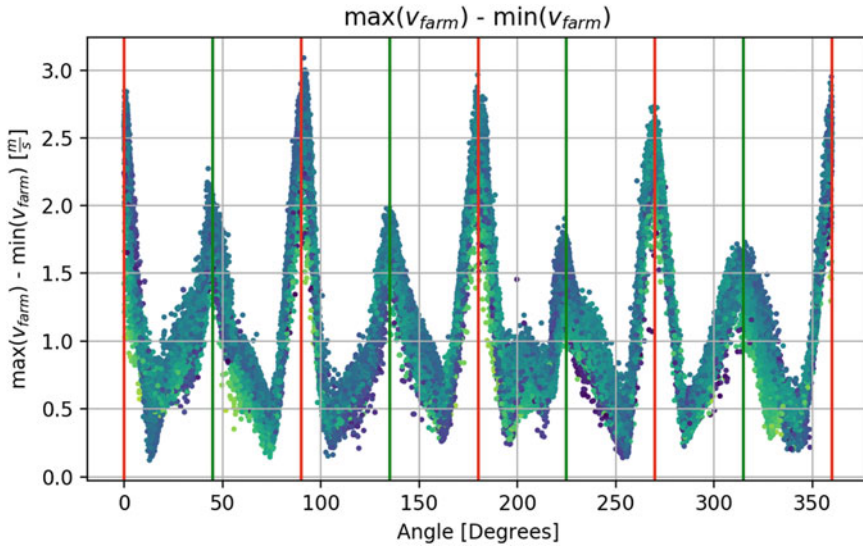


Fig. 21.7 Estimates of the maximum wake deficit estimated by the autoencoder. Red lines correspond to multiples of 90° for the angle of windspeed and green lines correspond to multiples of 90° but with a 45° shift

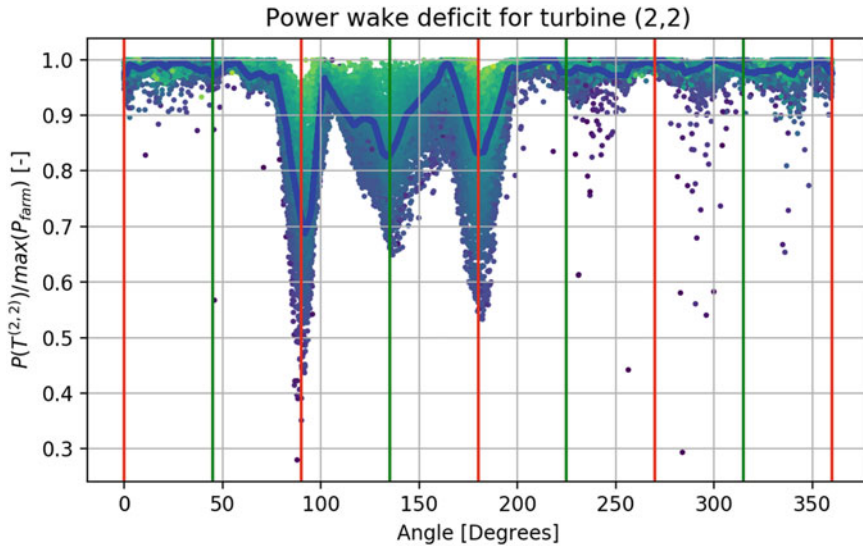


Fig. 21.8 VAE samples for the wake deficits for turbine (2,2) (see Fig. 21.1 for numbering). The power deficit is defined as the ratio of the power of the turbine, to the maximum power produced from the farm for a given sample. The estimated mean power deficit is shown with the blue curve

21.3 Conclusions

In this work we have demonstrated how a deep variational autoencoder neural network can be used in order to yield interpretable insights on high dimensional monitoring data. In works to follow, investigations on the architecture of the network are going to be presented, as well as results from the application of the technique on real farm SCADA data.

Acknowledgements The authors would like to gratefully acknowledge the support of the European Research Council via the ERC Starting Grant WINDMIL (ERC-2015-StG #679843) on the topic of Smart Monitoring, Inspection and Life-Cycle Assessment of Wind Turbines.

References

1. Larsen, G.C., Madsen, H.A., Bingöl, F., Mann, J., Ott, S., Sørensen, J.N., Okulov, V., Troldborg, N., Nielsen, M., Thomsen, K., et al.: Dynamic wake meandering modeling. Risø National Laboratory, Technical University of Denmark, Roskilde, Denmark, Risø (2007)
2. Hao, Y., Lackner, M.A., Keck, R.-E., Lee, S., Churchfield, M.J., Moriarty, P.J.: Implementing the dynamic wake meandering model in the NWTC design codes. In: 32nd ASME Wind Energy Symposium, p. 1089 (2014)
3. Turbines, W.: Part 1: design requirements. International Standard IEC 61400-1 (2005)
4. Kingma, D.P., Welling, M.: Auto-encoding variational Bayes (2013, preprint). arXiv:1312.6114
5. Rezende, D.J., Mohamed, S., Wierstra, D.: Stochastic backpropagation and approximate inference in deep generative models (2014, preprint). arXiv:1401.4082
6. Hinton, G.E., Salakhutdinov, R.R.: Reducing the dimensionality of data with neural networks. *Science* **313**(5786), 504–507 (2006)
7. Abdallah, I., Dertimanis, V., Mylonas, H., Tatsis, K., Chatzi, E., Dervilis, N., Worden, K., Maguire, E.: Fault diagnosis of wind turbine structures using decision tree learning algorithms with big data. In: Safety and Reliability-Safe Societies in a Changing World, pp. 3053–3061. CRC Press, Boca Raton (2018)



Chapter 22

Influence of Furniture on the Modal Properties of Wooden Floors

Lars Vabbersgaard Andersen, Christian Frier, Lars Pedersen, and Peter Persson

Abstract Structure-borne vibration and low-frequency re-radiated noise from internal and external sources cause annoyance for inhabitants in dwellings. A key parameter in the prediction of vibration and noise levels is the modal parameters of the floors in a building, since vibration and sound levels increase when natural frequencies of the floor coincide with the excitation frequencies of a source, e.g. monoharmonic vibration of unbalanced rotating machinery and appliances or HVAC system—or traffic induced ground vibration propagating into the building. This paper has focus on wooden floors built as an assembly of particleboard and timber joists. Such floors constitute horizontal divisions in many dwellings—both older, traditional buildings and new lightweight buildings. The analysis concerns the impact of furniture placed on a floor with otherwise known properties. Given the small mass of a traditional wooden floor, the presence of furniture can be expected to change the modal properties of the floor significantly. The finite-element model, developed for the present analyses, accounts for uncertainty in the position of the furniture, and the analysis addresses the importance of the elevation of the mass above the floor regarding the natural frequencies and the related modes of vibration.

Keywords Floor · Vibration · Finite-element model · Non-structural mass · Uncertainty

22.1 Introduction

Lightweight timber floors are usually designed and constructed in accordance with existing codes. In spite of this, users often experience discomfort associated with the dynamic serviceability of such floors [1], and the nature and amount of discomfort may be difficult to assess [2]. The annoyance can be caused by poor dynamic performance of the floor related to walking on it, or the annoyance may stem from vibration and re-radiated noise from internal or external sources. Low inertia and stiffness of lightweight floors provide part of the explanation, but another key factor may be uncertainty related to the modal properties, which makes the design of timber floors difficult from a serviceability point-of-view.

Uncertainty can be related to the material properties of the construction elements, as reported by Foschi and Gupta [3] as well as Persson and Flodén [4]. Furthermore, uncertainty is related to the boundary conditions and to internal joint flexibility. The influence of joint rigidity between the floors and the main structure was discussed by Andersen and Kirkegaard [5], whereas Andersen and co-workers examined the propagation of uncertainty in the support conditions into uncertainty in the eigenfrequencies of a rectangular concrete floor slab [6, 7]. For a double-leaf wooden wall panel, Domadiya et al. [8] examined the variations in eigenfrequencies due to different assembly approaches, including screws or glue between plates and studs. Similar variations can be expected for floors and may be influenced by workmanship. Further, a floor panel may be different when tested in a controlled laboratory environment or in a real building [9]. Flodén et al. [10] found that the modal properties of an empty floor can be determined quite accurately by computational models, but that it requires extensive testing of individual construction elements and joints, which is not possible for real-life construction.

However, even after final installation of a floor, its modal properties may change. For example, Devin et al. [11] found that non-structural partitions placed on a floor have a significant impact on the modal properties, but that this impact can be difficult to quantify in the design stage. Thus, the modal properties of a floor have a strong effect on the comfort associated

L. V. Andersen (✉)
Department of Engineering, Aarhus University, Aarhus, Denmark
e-mail: lva@eng.au.dk

C. Frier · L. Pedersen
Department of Civil Engineering, Aalborg University, Aalborg, Denmark

P. Persson
Department of Construction Sciences, Lund University, Lund, Sweden

with its use, but the use of the floor also has a strong influence on the modal properties of the floor. In this context, Pedersen et al. [12] as well as Frier et al. [13, 14] examined the influence of non-structural mass on a concrete slab floor. The analyses concerned the amount of non-structural mass associated with furnishing or storage as well as the elevation of the mass above floor level. Even for a heavy concrete floor, the variations in non-structural mass that may be expected due to different use of the floor were found to be significant. Especially, elevation of the mass was found to reduce the higher eigenfrequencies much more than the lower eigenfrequencies, proving a strong increase of the modal density in the frequency range relevant to traffic-induced structure-borne vibration and low-frequency re-radiated noise. Given the much larger ratio between non-structural mass and structural mass for lightweight timber floors, even higher impact on the modal properties of such floors can be expected.

Hence, the present analyses concern non-structural mass placed on a lightweight wooden floor panel, treating the total mass as well as its distribution and elevation above floor level as stochastic variables. Uncertainty related to eigenfrequencies in the low-frequency range associated with whole-body vibration is assessed, based on Latin Hypercube sampling. Section 2 provides a description of the computational model, including the finite-element model used for the floor panel and the model of the random elevated non-structural mass, while Sect. 3 presents the results of two case studies in which the non-structural mass has been placed on top of the joists or on the plate between the joists. Finally, the conclusions are provided in Sect. 4.

22.2 Computational Model for Wooden Floor with Furniture

This section concerns the computational model for the wooden floor. The finite-element model of the wooden floor is shortly described. Next, the modelling approach for elevated non-structural mass, used to represent furniture, will be described. Finally, the stochastic model for added, non-structural mass, including its elevation above floor level, is considered.

22.2.1 Finite-Element Model of Rectangular Wooden Floor

The analyses concern a single-span, single-leaf, light-weight wooden floor panel composed of a particleboard (chipboard) plate glued on top of timber joists. The floor is 6.0 m long, 4.2 m wide. The plate is 22 mm thick and considered to be seamless. The joists all have a rectangular cross section with a height of 225 mm and a width of 42 mm. They span across the width direction of the plate, and the distance between the joists is 600 mm centre-to-centre. Hence, a total of eleven joists support the plate in the span direction. It is noted that the two joists on the edges of the floor are moved 21 mm inward from the edge such that the outer side of the joists are aligned with the edge of the plate. Hence, the first bay at either end of the floor is 579 mm instead of 600 mm. Further, in addition to the main joists, timber beams (“side beams”) with the same profile are placed along the two remaining edges, again moved inward from the edges to align the exterior sides of the beams with the edges of the plate. Consequently, beams frame the entire edge of the floor. Finally, a 13 mm thick gypsum board lies on top of the particleboard. This gypsum board is considered as a non-structural mass, thus only contributing by its mass and not by stiffness.

The floor is supported along the 6 m long sides. The supports are placed at the base of the two side beams, 21 mm from the edges of the floor at the centre of the beam base, i.e. the span is 4158 mm. All degrees of freedom are fixed at either end, which effectively provides clamped boundaries of the floor along the two supported edges.

The particleboard plate and timber joists are assumed to behave linear elastically, given the small deformation levels relevant to vibration induced by external sources such as road traffic outside the building or internal sources such as walking on the floor. Particleboard is assumed to have a Young’s modulus of 3.0 GPa, a Poisson’s ratio of 0.30, a mass density of 767 kg/m³. Timber with a Young’s modulus of 8.5 GPa, a Poisson’s ratio of 0.20 and a mass density of 432 kg/m³ has been used. Both materials are considered isotropic and homogeneous. For the particleboard, this is considered a fair assumption, though a real board has slightly higher stiffness near the top and bottom and smaller stiffness in its interior as a result of the production process, resulting in a small degree of inhomogeneity and orthotropy. Timber has a pronounced orthotropic behaviour. However, applying beam theory, only the stiffness in the lengthwise direction is important. Finally, the gypsum board has a mass density of 692 kg/m³.

Mindlin theory (thick-plate theory) is applied for the particleboard, and the beams are treated by Timoshenko beam theory. Euler-Bernoulli theory would be inaccurate in the present analyses, already for low eigenmodes, given that the height of the beams is about 1/20 of the span, i.e. shear deformation is expected to contribute significantly to the response. Also, rotational inertia is accounted for in all parts of the model. Especially, to include the non-structural mass from the gypsum plate, the

thickness of the plate is artificially increased. A weighted average value of the mass density of particleboard and gypsum is then applied for the calculation of the inertia.

In the finite-element (FE) model, quadratic Lagrange interpolation is applied to the displacements and rotations of the cross sections in the plate as well as the beams. Thus, each shell element used to model the plate has nine nodes, and each beam element has three nodes. Selective integration is applied for all elements to avoid shear locking. The formulation does not account for drilling degrees of freedom in the shell elements. Instead, an infinitesimal artificial stiffness has been introduced to counteract ill-conditioning of the stiffness matrix. The mass matrix is obtained by full integration in all directions, including the thickness direction of the plate. For the beams, integration over the height and width directions are done analytically, i.e. with bending stiffnesses given in terms of the second moments of area. The shear factor for the beams as well as the plate have been set to 5/6 which is valid for rectangular cross sections, and the torsional constant for a rectangular solid profile has been used for the beams.

The FE models of the particleboard and the timber joists are first assembled separately. Hence, the plate is one sub-model and all beam elements constitute another sub-model. Lagrange multipliers are introduced to tie the two sub-models together, thus forming a system of auxiliary equations that establish rigid links between the nodes placed at the centrelines of the beams and at the neutral plane of the plate. In this way, the 123.5 mm offset between the beams and the plate are properly accounted for. Rigid connections between particleboards and joists have been proven to be a valid assumption if the boards are screwed as well as glued to the joists [10]. The FE model of the floor is illustrated in Fig. 22.1. The plate elements are shown in blue, whereas the beam elements are shown in red. Dashed red lines indicate the position of the neutral axis in each joist. The additional beams introduced at the 6 m long sides of the panel are visible. The mesh size is 0.60 m, corresponding to a distance of 0.30 m between the nodes. This mesh has been found to provide eigenfrequencies of adequate accuracy in the frequency range up to about 100 Hz. Finally, the first three eigenmodes of the empty floor are shown in Fig. 22.2.

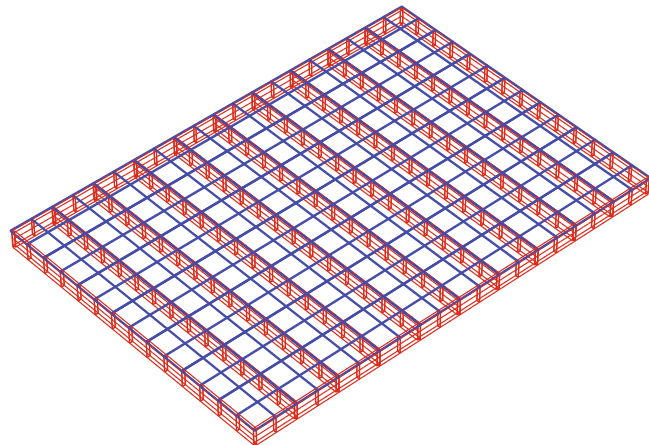


Fig. 22.1 Three-dimensional combined beam and plate finite-element model of the floor

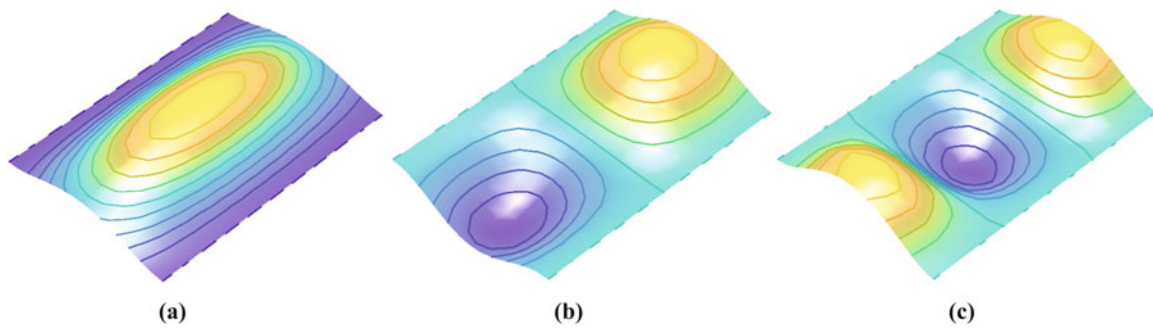


Fig. 22.2 The first three eigenmodes of the empty floor. (a) Mode 1 at 38.1 Hz, (b) Mode 2 at 39.0 Hz, and (c) Mode 3 at 40.9 Hz

22.2.2 Stochastic Model of Elevated Non-structural Mass

Whereas the material properties as well as the joint and support conditions are all considered deterministic, the present analyses concern random non-structural mass. The position of the individual masses will be considered deterministic (see Sect. 3), but the magnitudes of the masses as well as their elevations are modelled as random variables.

The total non-structural mass from usage of the floor, M_u , is assumed to be Gumbel distributed with a coefficient of variation of 0.2 and a 98% quantile value corresponding to a characteristic serviceability load of $0.2 \times 2.5 \text{ kN/m}^2$. This corresponds to 20% utilisation of a floor in an office or dwelling and provides a characteristic value of 1283 kg for the mass, which comes on top of the non-structural mass related to the gypsum board. For comparison, the structural mass is about 890 kg, i.e. about two thirds of the characteristic value of the non-structural mass from usage of the floor. For a concrete slab, the structural mass would be around 10–15 tonnes, i.e. higher than the non-structural mass, indicating the difference between a lightweight floor and a heavyweight floor.

To generate the individual masses in each realisation, uniformly distributed random numbers are first generated for all masses. Each of these uniformly distributed numbers is then divided by the sum of the uniformly distributed number and multiplied by M_u . Hence, the sum of the individual random masses will be equal to the Gumbel distributed total mass M_u . Each of the individual masses is elevated above the floor to model, for example, armchairs, sofas, low bookshelves, tables or other furniture. The elevation is considered uniformly distributed between 0 and 0.75 m. It is noted that all stochastic variables are assumed statistically independent. This may be unrealistic for a real floor, given that a user may place furniture or storage shelves in a less random configuration. However, a detailed analysis of correlations between individual masses, positions and elevations is beyond the scope of this analysis.

The elevated masses are assumed to be rigidly connected to the structure. Whereas constraints were introduced in terms of Lagrange multipliers to tie the beams to the plate, the elevated masses are modelled directly by introducing additional mass and rotational inertia into the nodes of the plate FE model at the relevant positions. Hence, no additional degrees of freedom or auxiliary equations are solved for the elevated masses.

22.3 Analysis of a Rectangular Wooden Floor with Furnishing

For the concrete slab analysed by Pedersen and co-workers [12–14], small changes in the positioning of furniture will lead to small changes in the modal properties of the system, since the floor is considered homogeneous. However, for the wooden floor considered in the present analyses, non-structural mass can be attached on top of the joists, or it can be placed on the particleboard between the joists. In order to study the importance of this relative placement, two extremes are analysed. Section 3.1 concerns Case 1, in which all non-structural mass is placed in a regular grid with nodes on top of the joists, and Sect. 3.2 concerns Case 2 with all non-structural mass placed in the midspan between the joists. It is noted that no masses are placed at the nodes on the edge of the plate in Case 1, and no masses are placed on the first lines of nodes 0.3 m from the edges of the floor in Case 2. Thus, only furniture placed “in the middle of the floor” is considered in the present analysis, whereas the effects of furniture placed “along the walls” will be a topic for future analysis (Fig. 22.3).

22.3.1 Case 1: Non-structural Mass Placed Over the Joists

Two situations are studied in Case 1 with the non-structural mass placed directly over the joists. Figure 22.4 shows the cumulative distribution functions (CDFs) for the first five undamped eigenfrequencies when the mass is placed at floor level, i.e. with no elevation. Similarly, Fig. 22.5 presents the CDFs for the first five undamped eigenfrequencies when the mass is elevated as described in Sect. 2.2. Latin Hypercube sampling with 20,000 realisations has been used, which provides smooth CDFs. The dashed vertical lines in the figures indicate the undamped eigenfrequencies of the empty floor, noting that Modes 4 and 5 follow the trend of Modes 1–3 (see Fig. 22.2), i.e. they have four and five local extremes along the width direction of the floor.

With reference to Fig. 22.4, the non-structural mass has a marked influence on the eigenfrequencies, even when placed directly on the floor with no elevation. On average, the first five eigenfrequencies are all reduced by about 14 Hz. Since the total mass is Gumbel distributed, the realisations of very low total non-structural mass occur with an extremely low probability. This explains the offset of the CDFs, even at cumulative probabilities near 1.0. A similar behaviour of the CDF curves can be seen at low cumulative probabilities. Very few realisations of extremely large total mass occur.

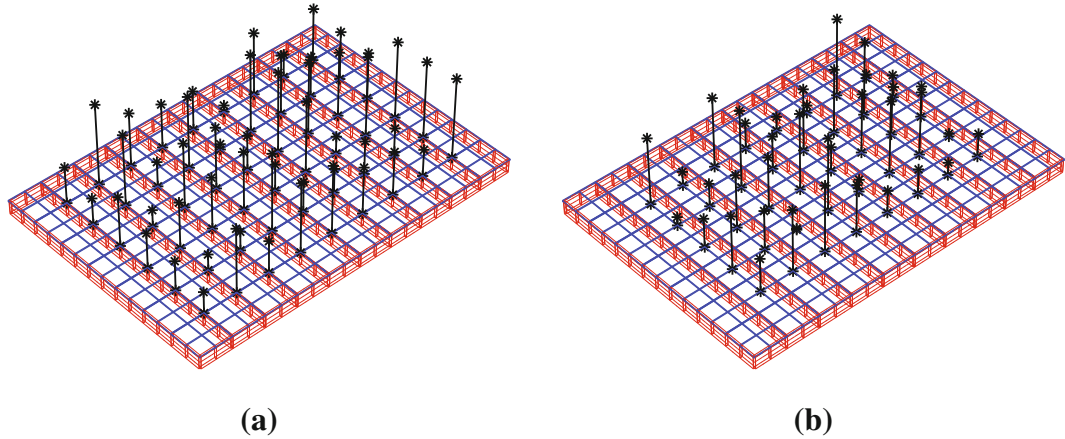


Fig. 22.3 Models with furniture placed (a) on top of the joists (Case 1), or (b) between the joists (Case 2)

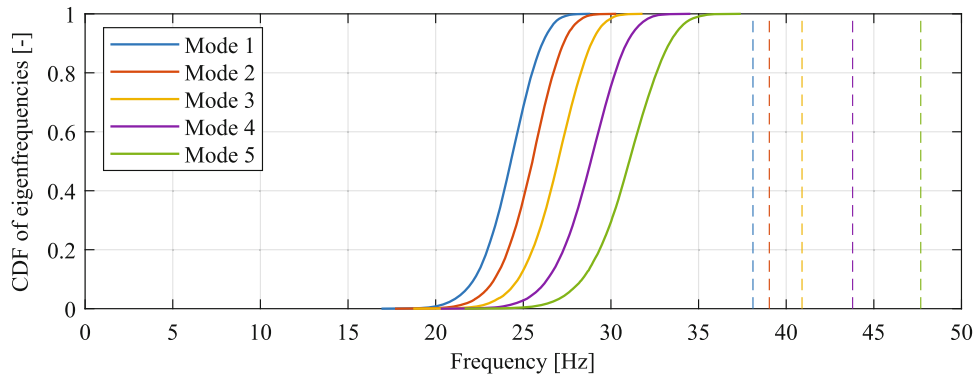


Fig. 22.4 Cumulative distribution functions for the first five eigenfrequencies—mass over joists *without* elevation

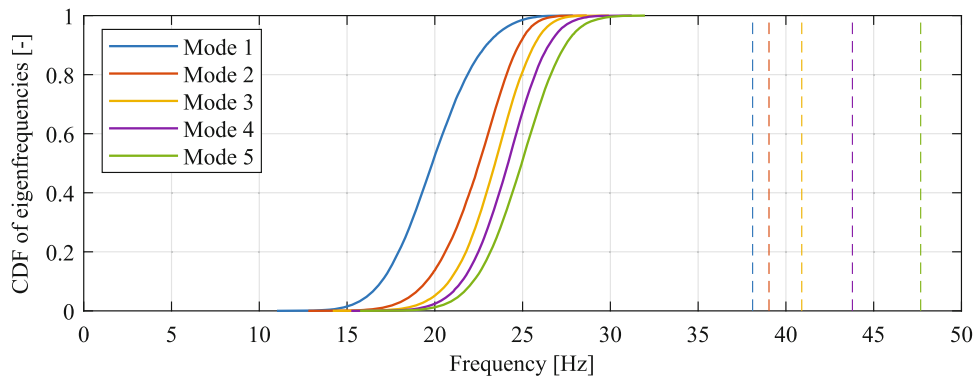


Fig. 22.5 Cumulative distribution functions for the first five eigenfrequencies—mass over joists *with* elevation

As expected, comparison of Figs. 22.4 and 22.5 shows that the eigenfrequencies are further reduced when the masses are elevated above the floor. As an interesting observation, the CDF for the eigenfrequency associated with Mode 1 has a slightly different shape than CDFs for the other eigenfrequencies. Also, the eigenfrequency of Mode 1 is reduced significantly more than that of Mode 2. A closer inspection of Mode 1 reveals that the nature of the mode differs between different realisations of the non-structural mass. Thus, in some realisations, the first mode (and in some cases other modes as well) are local and associated with rotational oscillation of a single elevated mass. The eigenfrequencies related to Modes 2–5 are reduced such that they lie closer when the mass is elevated compared to the situation with the mass placed directly on the floor. This can be attributed to the rotational inertia of the elevated masses that have stronger influence on higher modes compared to lower modes.

22.3.2 Case 2: Non-structural Mass Placed Between the Joists

Figure 22.6 shows the CDFs for the first five eigenfrequencies of the floor with non-structural mass placed right on the floor in the midspans between the joists. Again, Latin Hypercube sampling with 20,000 realisations has been performed to obtain smooth CDFs. Comparing these CDFs to those presented in Fig. 22.4, clearly the first two eigenfrequencies are lower when the masses are placed between the joists than when they are placed over the joists. However, the eigenfrequencies related to Modes 4 and 5 are higher in Case 2 compared to Case 1—for Mode 5 the difference is about 4 Hz in average. This indicates that the position of the mass relative to the joists is important, even when the mass has not been elevated. It is recalled that the total mass has the same Gumbel distribution in either case, so the difference in the CDFs is due to different relative positions of the individual masses and slightly larger individual masses in Case 2 compared to Case 1 (40 masses in Case 2 versus 54 masses in Case 1).

Next, Fig. 22.7 shows the CDFs for Case 2 with uncorrelated uniformly distributed elevation of the individual masses. Comparing these CDFs to those in Fig. 22.6, a distinct reduction in the eigenfrequencies can be observed as a result of elevating the masses. Thus, the first five eigenfrequencies drop by 10 Hz (Mode 1) to 18 Hz (Mode 5) for the 50% quantiles. This means that the eigenfrequencies are reduced to less than half their value in the situation with mass placed directly at floor level. The relatively marked differences in eigenfrequencies caused by elevating the mass in Case 2 can be explained by the low local bending and shear stiffnesses of the particleboard.

Furthermore, comparing Fig. 22.7 to Fig. 22.5, the first five eigenfrequencies for Case 2 with elevated masses are significantly lower than the equivalent eigenfrequencies in Case 1 with elevated masses. This difference has its origin in the character of the modes. Thus, in Case 1 it was observed that the first mode (and to some extent other modes) have a local character, as already mentioned in Sect. 3.1. This tendency becomes more pronounced in Case 2 with the masses placed between the joist. Here, the first five modes may in some realisations relate to oscillations of single elevated non-structural masses.

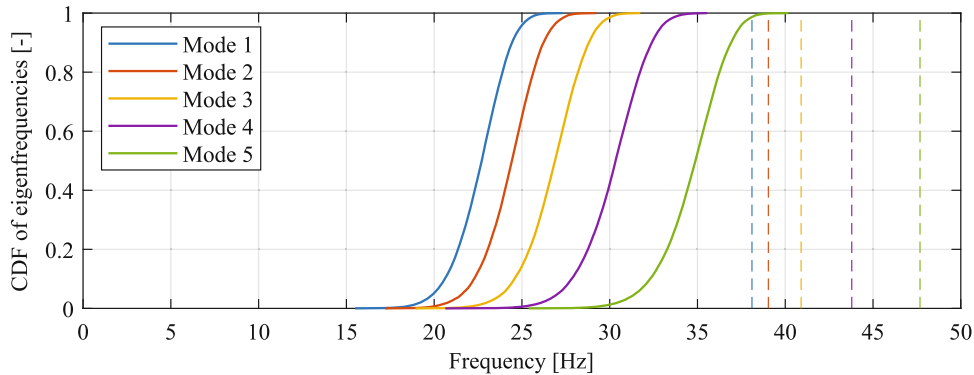


Fig. 22.6 Cumulative distribution functions for the first five eigenfrequencies—mass *between joists without elevation*

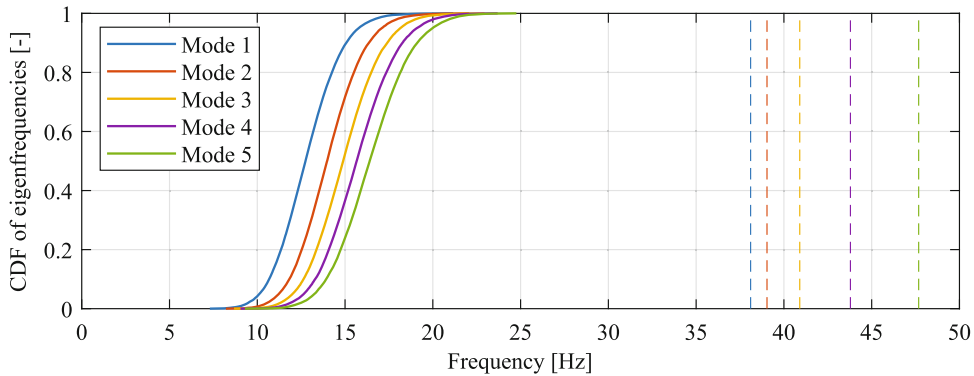


Fig. 22.7 Cumulative distribution functions for the first five eigenfrequencies—mass *between joists with elevation*

22.4 Discussion and Conclusion

A 6.0 m long, 4.2 m wide single-span, single-leaf floor panel made of particleboard on timber joists has been analysed using a finite-element model. Especially, the first five undamped eigenfrequencies have been determined and compared for two cases: Case 1 with non-structural mass placed over the joists and Case 2 with the mass placed between the joists. Situations with mass lying flat on the floor or elevated above the floor have been examined. In all analyses, Latin Hypercube sampling has been performed assuming the total mass to be Gumbel distributed, whereas the relative magnitudes of individual masses (and in two of the situations their elevation above the floor) have been assumed uniformly distributed.

The present analyses concerned a total non-structural mass with a characteristic value corresponding to 20% utilisation of a standard floor in an office or residential building. This non-structural mass is about twice the mass of the considered lightweight wooden floor panel. It corresponds to about 50 kg per square metre, which is judged to be reasonable for an office, a dining room, a living room, or similar, also accounting for people positioned on chairs. For such rooms, full utilisation up to a characteristic value of 2.5 kN/m^2 would be unrealistic.

However, the present study demonstrates that even the relatively small utilisation factor of 0.2 leads to significant drops in the eigenfrequencies compared to the empty floor—especially when the additional non-structural mass is placed between the joists and elevated above the floor, taking rotational inertia into consideration by assuming the mass to be rigidly connected to the floor. Whereas the first five eigenfrequencies of the empty floor lie in the range 38–48 Hz, reduction of all these eigenfrequencies down to about 10–20 Hz occur when placing elevated masses between the joists. Here, some or all of the first five eigenmodes can be characterised as local modes associated with oscillation of individual elevated masses, made possible by the relatively flexible plate spanning between the beams.

It can be argued that real furniture, such as tables or chairs placed in the middle of a floor, may have more (usually four) points of contact to the floor, and that uncorrelated masses with single points of contact do not provide a realistic model. Also, the assumption of rigid links to the elevated masses may be considered inaccurate. While the simplified model of furniture may provide results of fair accuracy for heavy floors made of, for example, concrete, a better model may be necessary for lightweight wooden floors, given the more delicate nature of the dynamic problem caused by strong inhomogeneity of stiffness. This will be a topic for future research.

In this context, it can be noted that larger non-structural mass on the considered wooden floor amplifies the behaviour observed already with the utilisation factor of 0.2. If full utilisation, i.e. non-structural mass providing a load of 2.5 kN/m^2 , is assumed, one would expect a first undamped eigenfrequency of about 12 Hz, since the non-structural mass would in this case be about 9.3 times larger than the structural mass, reducing the eigenfrequency by a factor of 3.2, approximately. However, when increasing the total mass, the individual masses also increase, given that the number of non-structural masses is unchanged. As a result of this, the dynamic response of the floor model will be dominated by the local modes associated with oscillation of individual masses—in particular when the masses are placed in the midspans between the joists. In this case, all the first five eigenfrequencies are reduced to values in the range 3–5 Hz, i.e. much lower than expected for a case in which the non-structural mass has been smeared out over the structure.

In any case, the present study indicates that the placement of furniture (and people) on a lightweight wooden floor has a significant impact on its modal properties. The present analyses assumed a Gumbel distribution for the total non-structural mass, which provides relatively narrow probability density functions for the eigenfrequencies compared to, for example, a uniformly distributed total mass. Still, differences of about 5 Hz can be observed between the 10 and 90% quantiles of the eigenfrequencies. This comes in addition to the differences of about 3–8 Hz caused by various placements of the mass relative to the joists.

Hence, it can be concluded that non-structural mass must be considered in the dynamic assessment of a wooden floor. The eigenfrequencies of the empty floor are highly unrealistic for a floor in service. Furthermore, the placement of furniture should be considered, since furniture placed between joists leads to different eigenfrequencies (and eigenmodes) than furniture placed directly over the joists. While this may be expected, it may be surprising that the differences in placement of the mass can lead to a halving of the eigenfrequencies.

Acknowledgement The research was carried out in the framework of the project “Urban Tranquility” under the Interreg V programme with participation of Aarhus University and Aalborg University as well as Lund University. The authors of this work gratefully acknowledge the European Regional Development Fund for the financial support.

References

1. Bernard, E.S.: Dynamic serviceability in lightweight engineered timber floors. *J. Struct. Eng.* **134**(2), 258–268 (2008)
2. Negreira, J., Trollé, A., Jarnerö, K., Sjökvist, L.-G., Bard, D.: Psycho-vibratory evaluation of timber floors—towards the determination of design indicators of vibration acceptability and vibration annoyance. *J. Sound Vib.* **340**, 383–408 (2015)
3. Foschi, R.O., Gupta, A.: Reliability of floors under impact vibration. *Can. J. Civ. Eng.* **14**(5), 683–689 (1987)
4. Persson, P., Flodén, O.: Towards uncertainty quantification of vibrations in wood floors. In: Proceedings of 25th International Congress Sound and Vibration, Hiroshima, Japan, 1–8, 2018
5. Andersen, L.V., Kirkegaard, P.H.: Vibrations in a multi-storey lightweight building structure: influence of connections and nonstructural mass. In: Research and Applications in Structural Engineering, Mechanics and Computation—Proceedings of 5th International Conference on Structural Engineering, Mechanics and Computation, SEMC 2013, 2013
6. Andersen, L.V., Frier, C.: Impact of support uncertainties on the modal properties of flooring systems. In: Høgsberg, J., Pedersen, N.L. (eds.) Proceedings of NSCM 30 – 30th Nord. Semin. Comput. Mech. 25–27 Oct. 2017, pp. 35–38. Department of Mechanical Engineering, Technical University of Denmark, Lyngby (2017)
7. Andersen, L.V., Frier, C., Pedersen, L.: Probabilistic analysis of modal properties for floor systems with uncertain support conditions. In: Pakzad, S. (ed.) Dynamics of Civil Structures, Conference Proceedings of the Society for Experimental Mechanics Series, vol. 2, pp. 67–75. Springer, Cham (2019)
8. Domadiya, P.G., Dickow, K.A., Andersen, L.V., Sorokin, S.V.: Evaluation of various joints between studs and plates on flanking noise transmission within lightweight periodic structures. In: Topping, B.H.V. (ed.) Proceedings of Eleventh International Conference on Computational Structures Technology CST2012 ECT2012. Civil-Comp Press, Glasgow (2012)
9. Jarnerö, K., Brandt, A., Olsson, A.: Vibration properties of a timber floor assessed in laboratory and during construction. *Eng. Struct.* **82**, 44–54 (2015)
10. Flodén, O., Persson, K., Sandberg, G.: A multi-level model correlation approach for low-frequency vibration transmission in wood structures. *Eng. Struct.* **157**, 27–41 (2018)
11. Devin, A., Fanning, P.J., Pavic, A.: Modelling effect of non-structural partitions on floor modal properties. *Eng. Struct.* **91**, 58–69 (2015)
12. Pedersen, L., Frier, C., Andersen, L.: Flooring-systems and their interaction with usage of the floor. In: Caicedo, J., Pakzad, S. (eds.) Dynamics of Civil Structures, Proceedings of 35th IMAC, A Conference Exposition on Structural Dynamics, 2017, vol. 2, pp. 205–211. Springer, Cham (2017)
13. Frier, C., Pedersen, L., Andersen, L.V., Persson, P.: Flooring-systems and their interaction with furniture and humans. *Procedia Eng.* **199**, 146–151 (2017)
14. Frier, C., Pedersen, L., Andersen, L.V.: Non-structural masses and their influence on floor natural frequencies. In: Pakzad, S. (ed.) Dynamics of Civil Structures, Conference Proceedings of the Society for Experimental Mechanics Series, vol. 2, pp. 59–65. Springer, Cham (2019)



Chapter 23

Optimal Sensor Placement for Response Reconstruction in Structural Dynamics

Costas Papadimitriou

Abstract A framework for optimal sensor placement (OSP) for response reconstruction under uncertainty is presented based on information theory. The OSP is selected as the one that maximizes an expected utility function taken as the mutual information between data and response quantities of interest (QoI). The expected utility function is extended to make the OSP design robust to uncertainties in structural model parameter and modelling errors. The resulting utility function is a multidimensional integral of the information entropy for each possible value of the model parameters, weighted by the prior or posterior probability distribution of the model parameters. The formulation uses the Gaussian nature of the response QoI given the measurements to simplify the expected utility function in terms of the covariance matrix of the uncertainty in the response output QoI given the values of modeling parameters. Methods to compute the multidimensional integrals and to optimize the sensor placement are discussed. The implementation is presented for two cases used to predict response time histories from output-only measured data: modal expansion techniques and filter-based techniques.

Keywords Information gain · Kullback-Leibler divergence · Relative entropy · Bayesian inference · Response prediction

23.1 Introduction

Vibration measurements taken from various locations in a structure are used to improve models and model-based predictions of output quantities of interest (QoI) that are critical of structural reliability and safety. The problem of predicting responses at unmeasured locations (e.g. accelerations, velocities, displacements, strain, stresses) in the presence of modelling and loading errors and uncertainties is often formulated using modal expansions or Kalman-type filtering techniques. Formulations have been developed for state estimation given input and associated uncertainties, as well as input-state estimation given output-only vibration measurements [1–6]. For linear model of structures the response is obtained to be Gaussian with the uncertainty in the response estimates described by the covariance matrix that depends on the structural model and modeling errors used. The objective in optimal sensor placement (OSP) is to collect the most informative data that minimize the uncertainties in the predictions of important output QoI. In this way the most reliable responses can be obtained. Such responses can be used to reconstruct important response quantities of interest that can further be used to assess the reliability and safety of the structure based on actual vibration measurements. In particular, reconstructing the stress time histories is critical in estimating fatigue damage accumulation based on actual vibration measurements collected from a monitoring system [1, 7]. In this paper, the response reconstruction problem is investigated from the optimal experimental design point of view. The problem to be addressed is to find the optimal sensor locations for obtaining the most accurate response predictions. Existing works on the subject concentrate on minimizing a measure of the covariance matrix of the error estimate of the output response QoI [8, 9]. In this work we present a framework based on information theory and utility functions and we extend existing developments to estimate optimal sensor configurations that are robust to uncertainties in model and prediction error parameters. The proposed framework is applicable to complex linear systems.

C. Papadimitriou (✉)
Department of Mechanical Engineering, University of Thessaly, Volos, Greece
e-mail: costasp@uth.gr

23.2 Background

Consider a structural model used to predict the temporal variability of the response vector $\underline{z}(t; \underline{\varphi}, \underline{u}) \in R^{n_z}$ (e.g. accelerations, velocities, displacements, strains, stresses) at n_z degrees of freedom (DOF) of an underlining structure given the value of a structural model parameter set $\underline{\varphi}$ (e.g. stiffness, mass and damping related parameters) and the excitation vector $\underline{u}(t) \in R^{n_u}$. Let $\underline{y}(t) \in R^{n_y}$ be response time history data collected from sensors. These data depend on the sensor configuration vector $\underline{\delta}$ containing the location and measurement direction of sensors placed in a structure. The data may consist of either acceleration, displacement and strain measurements. In what follows, a linear model of the structure is assumed. Also it will be assumed that the excitation response time histories $\underline{u}(t)$ are not available. Given output-only data, there are a number of methods to reconstruct the response of the structure at unmeasured locations. Two such cases are next considered for reconstructing estimates of response at output QoI.

In the first case the response reconstruction is obtained using modal expansion techniques, while in the second case state estimation or input-state estimation is performed using available filtering techniques [1–6]. Due to system linearity, the estimate of the response $\underline{z}(t)$ at time t given the data is derived to be a multi-variable Gaussian vector with mean that depends on the measurement output time histories and covariance matrix that depends on the structure of the linear model, its parameters $\underline{\varphi}$, and state, output and input error covariance matrices. This Gaussian distribution of the output vector QoI $\underline{z}(t)$ is denoted herein as $N(z; \widehat{z}(t), P(t))$, where the mean estimate $\widehat{z}(t) \equiv \widehat{z}(t; \underline{\varphi}, D, \underline{\delta})$ depends on the measured data, the model parameter set and the sensor configuration, while the covariance $P(t) \equiv P(t; \underline{\delta}, \underline{\varphi})$ of the error in the estimate depends on the sensor configuration and the parameter set, but is independent of the measured data D . For practical convenience and without loss of generality, stationarity conditions are assumed, where the covariance matrix of the error in the output response estimate or the error in the input-output response estimate is independent of t . We next explore further the two cases for which the multi-variable Gaussian distribution for the response quantity arises.

Using modal expansion for linear systems, the measured time histories, restricted for demonstration purposes to displacements at N_0 DOF, are given with respect to the modal coordinates as

$$\underline{y}(t) = \Phi(\underline{\delta}, \underline{\varphi}) \underline{\xi}(t) + \underline{\varepsilon}(t) \quad (23.1)$$

where $\Phi(\underline{\delta}, \underline{\varphi}) \in R^{N_0 \times m}$ is the modeshape matrix corresponding to m contributing modes, $\underline{\xi} \in R^m$ is the vector of modal coordinates, and $\underline{\varepsilon}(t)$ is a zero-mean measurement error with covariance matrix Q_e . For estimation purposes the following condition should be met $N_0 \geq m$ in order for the system to be identifiable. Displacement and strain predictions at output locations or DOF are given by the prediction equation

$$\underline{z}(t) = \Psi(\underline{\varphi}) \underline{\xi}(t) + \underline{\varepsilon}(t) \quad (23.2)$$

where $\Psi(\underline{\varphi}) \in R^{n_z \times m}$ are the corresponding displacement or strain modeshapes that relate modal coordinates to predicted displacement or strain quantities, and $\underline{\varepsilon}(t)$ is a zero-mean prediction error with covariance matrix Q_ε . The modeshape matrices $\Phi(\underline{\delta}, \underline{\varphi})$ and $\Psi(\underline{\varphi})$ are available by analyzing the model (e.g. finite element model) of the structure. Assuming Gaussian prediction errors $\underline{\varepsilon}(t)$ and $\underline{\varepsilon}(t)$ and using Bayesian inference to estimate the parameters $\underline{\xi}(t)$ and propagate to output quantities $\underline{z}(t)$, it is straightforward to show that the output $\underline{z}(t)$ is Gaussian with mean that depends on the data and covariance matrix $P_z(\underline{\delta}, \underline{\varphi})$ given by

$$P_z(\underline{\delta}, \underline{\varphi}) = \Psi(\underline{\varphi}) \Phi^T(\underline{\delta}, \underline{\varphi}) Q_e(\underline{\delta}, \underline{\varphi}) \Phi(\underline{\delta}, \underline{\varphi}) \Psi^T(\underline{\varphi}) + Q_\varepsilon \quad (23.3)$$

which is independent of the data. Also, the covariance matrix does not depend on the time t provided that the error covariance matrices are assumed to be independent of time.

In the second case, introducing the state vector consisting of displacement and velocities at all DOF, the equation of motion is re-formulated in the state-space continuous form

$$\dot{\underline{x}}(t) = A(\underline{\varphi}) \underline{x}(t) + B(\underline{\varphi}) \underline{u}(t) + \underline{e}_s(t) \quad (23.4)$$

with observation and prediction equation

$$\underline{y}(t) = C(\underline{\delta}, \underline{\varphi}) \underline{x}(t) + D(\underline{\delta}, \underline{\varphi}) \underline{u}(t) + \underline{e}(t) \quad (23.5)$$

$$\underline{z}(t) = C_p(\underline{\varphi}) \underline{x}(t) + D_p(\underline{\varphi}) \underline{u}(t) + \underline{\varepsilon}(t) \quad (23.6)$$

where the state matrices A, B, C and D depend on the stiffness, mass and damping matrices of the structure, $\underline{e}_s(t), \underline{e}(t)$ and $\underline{\varepsilon}(t)$ are respectively the zero-mean state, measurement and prediction errors with covariance matrices Q_s, Q_e and Q_ε , respectively, while C_p and D_p are system matrices that connect the output QoI to the state and input vectors. Similar description in the discrete state space form is also available. Also, a description can also be obtained in the modal space to simplify the formulation for complex linear systems in the case where only a fraction of the modes contribute to the response. For known input characteristics that are given by a linear filtering technique (for example, Kanai-Tajimi filter for earthquake excitations), the state vector can be augmented to include the states of the input filter, while the parameter set $\underline{\varphi}$ is augmented to include the parameters defining the input.

Using Eq. (23.6), the uncertainty in the prediction of output QoI $\underline{z}(t)$ is given by

$$P_z(\underline{\delta}, \underline{\varphi}) = [C_p(\underline{\varphi}) \quad D_p(\underline{\varphi})] P(\underline{\delta}, \underline{\varphi}) [C_p(\underline{\varphi}) \quad D_p(\underline{\varphi})]^T + Q_\varepsilon \quad (23.7)$$

and depends on the covariance matrix $P(\underline{\delta}, \underline{\varphi})$ of the error in the state and input estimates.

Various techniques exist to estimate the covariance of the state and input in the case of output-only vibration measurements. For example, consider the case of white noise input. This case arises also for non-white excitations modelled by a set of stochastic differential equations with parameters that captures the characteristics of the excitation. The filter parameters are usually uncertain and are included in the parameter set $\underline{\varphi}$. The stationary error covariance of the state estimate for displacement and velocity measurements is provided by the steady-state Riccati equation in the form

$$A(\underline{\varphi}) P_x(\underline{\delta}, \underline{\varphi}) + P_x(\underline{\delta}, \underline{\varphi}) A(\underline{\varphi}) - P_x(\underline{\delta}, \underline{\varphi}) C^T(\underline{\delta}, \underline{\varphi}) Q_e^{-1} C(\underline{\delta}, \underline{\varphi}) P_x(\underline{\delta}, \underline{\varphi}) + B(\underline{\varphi}) Q_s B^T(\underline{\varphi}) = 0 \quad (23.8)$$

Substituting the covariance matrix $P_x(\underline{\delta}, \underline{\varphi})$ into Eq. (23.7), one obtains the covariance of the state and input vector as a function of the sensor configuration $\underline{\delta}$.

Similarly, for the case where the input is not white noise but unknown, one can use existing input-state estimation techniques to estimate the error covariance for the predictions of both the state and the input. In this case the Riccati Eq. (23.8) is replaced by similar equation(s) that can be solved to estimate the joint covariance for state and input. The resulting formulation depends on the method used. One can find such formulation in references [8, 9]. The end result is that the covariance matrix $P(\underline{\delta}, \underline{\varphi})$ depends on the characteristics of the system and the input contained in the parameter vector $\underline{\varphi}$.

It is clear that the covariance of the error estimate for the state and input is independent of the measurements and depends only on the structural model parameters, as well as the state and measurement error covariances. The parameters that define the state and measurement error covariances can be included in the parameter set $\underline{\varphi}$. The covariance matrix $P(\underline{\delta}, \underline{\varphi})$, described in terms of the parameters $\underline{\varphi}$ and the sensor locations $\underline{\delta}$, is the main quantity used in the next section to solve the optimal sensor location problem for response reconstruction. To account for uncertain model and input characteristics $\underline{\varphi}$, a prior probability distribution $p(\underline{\varphi})$ can be used to quantify such uncertainties in the values of the model parameters. The data can also be used to learn a partition of the model parameter set $\underline{\varphi}$, with the rest of the parameters to be nuisance parameters. Using Bayesian inference for the parameters that are learned using the data, the prior probability distribution of these parameters can be replaced by the posterior probability distribution. Herein we will denote such distribution by $p(\underline{\varphi})$, without making the distinction between prior and posterior.

23.3 Optimal Sensor Placement Formulation

Information theory and utility functions are used to formulate the optimal sensor placement problem so that the most reliable response reconstruction is achieved that is robust to modeling and input uncertainties. The objective is to select the sensor locations (and DOF) to maximize the information contained in the data for predicting the output response QoI. Using Lindley's work [10] and extending the expected utility to include the uncertainty in the model parameters, one maximizes the expected utility function

$$U(\underline{\delta}) = \int_{\Phi} \int_{\Upsilon} \int_{\Theta} u(\underline{\delta}; \underline{z}, \underline{\varphi}, \underline{y}) p(\underline{z}, \underline{y}, \underline{\varphi} | \underline{\delta}) d\underline{z} d\underline{y} d\underline{\varphi} \quad (23.9)$$

that quantifies the usefulness of learning from the data in predicting output QoI, where $u(\underline{\delta}; \underline{z}, \underline{\varphi}, \underline{y})$ is the utility function given a particular value of the model parameter set $\underline{\varphi}$ and the data \underline{y} , $p(\underline{z}, \underline{y}, \underline{\varphi} | \underline{\delta}) = p(\underline{z} | \underline{y}, \underline{\varphi}, \underline{\delta}) p(\underline{y} | \underline{\varphi}, \underline{\delta}) p(\underline{\varphi})$, $p(\underline{z} | \underline{y}, \underline{\varphi}, \underline{\delta})$ is the posterior uncertainty in the response prediction given the data \underline{y} and the model parameter set $\underline{\varphi}$, $p(\underline{y} | \underline{\varphi}, \underline{\delta})$ is the uncertainty in the outcome \underline{y} given the model parameters, and $p(\underline{\varphi})$ is the uncertainty in the model parameters. A rational choice of the utility function is the information gained by the data, quantified by the Kullback-Leibler divergence [11] between the prior and posterior probability distribution given an outcome \underline{y} , obtained from an experimental design $\underline{\delta}$ and the model parameters $\underline{\varphi}$. The expected utility function is an average of the utility function over all possible values of the response predictions as they are inferred from the data, and all the possible data outcomes. In Eq. (23.9), the expected utility function has been extended to a robust measure that takes into account the uncertainty in the model parameters $\underline{\varphi}$ that are usually uncertain.

It can be readily shown that the expected utility function can be formulated in terms of the change in the information entropy before and after the data are collected, given by

$$U(\underline{\delta}) = \int_{\Phi} H_z(\underline{\varphi}) p(\underline{\varphi}) d\underline{\varphi} - \int_{\Phi} \int_{\Upsilon} H_{z|D}(\underline{y}, \underline{\varphi}, \underline{\delta}) p(\underline{y} | \underline{\varphi}, \underline{\delta}) d\underline{y} p(\underline{\varphi}) d\underline{\varphi} \quad (23.10)$$

where $H_z(\underline{\varphi})$ is the prior information entropy given the model parameter set, and $H_{z|D}(\underline{y}, \underline{\varphi}, \underline{\delta})$ is the posterior information entropy given the data set and the model parameter set. For Gaussian probability distribution of the response vector $\underline{z}(t)$, the posterior information entropy given the values of the data set and the model parameter set $\underline{\varphi}$ is given by

$$H_{z|D}(\underline{y}, \underline{\varphi}, \underline{\delta}) = \frac{1}{2} n_z \ln(2\pi) - \frac{1}{2} \ln \det P_z(\underline{\delta}, \underline{\varphi}) \quad (23.11)$$

and thus it depends on the covariance $P(\underline{\delta}, \underline{\varphi})$ of the error of the state and input estimation, as well as the sensor locations, while it is independent of the data. Taking into account that the prior information entropy $H_z(\underline{\varphi})$ in Eq. (23.10) is constant, independent of the sensor configuration vector $\underline{\delta}$, and that the posterior information entropy $H_{z|D}(\underline{y}, \underline{\varphi}, \underline{\delta})$ does not depend on the data, the expected utility function finally takes the form

$$U(\underline{\delta}) = c + \frac{1}{2} \int_{\Theta} \ln \det \left\{ P(\underline{\delta}, \underline{\varphi}) \right\} p(\underline{\varphi}) d\underline{\varphi} \quad (23.12)$$

which is a probability integral over the space of uncertain parameters $\underline{\varphi}$. The integral Eq. (23.12) represents the robust information entropy over all possible values of the model parameters quantified by the PDF $p(\underline{\varphi})$. The multidimensional integral can be evaluated using Monte Carlo techniques or sparse grid methods [12].

The optimal sensor configuration $\underline{\delta}_{opt}$ is obtained by maximizing the $U(\underline{\delta})$ with respect to the design variables $\underline{\delta}$

$$\underline{\delta}_{opt} = \arg \max_{\underline{\delta}} U(\underline{\delta}) \quad (23.13)$$

The optimal number of sensors in the sensor configuration can be estimated by monitoring the gain in information as additional sensors are placed in the structure. Usually, after sufficiently number of sensors placed in the structure, the information gain using additional sensors is relatively small. The optimal number of sensors is a trade-off between information gain and cost of sensors. The optimization in Eq. (23.13) may result in multiple local/global solutions. The optimization problem is solved in the continuous physical domain of variation of the sensor locations. Stochastic optimization algorithms, such as CMA-ES [13], can be employed in order to avoid premature convergence to a local optimum. Alternative heuristic forward and backward sequential sensor placement algorithms [14, 15] are effective in solving the optimization problem. The heuristic algorithm bypasses the problem of multiple local/global optima manifested in optimal experimental designs, providing near optima solutions in a fraction of the computational effort required in expensive stochastic optimization algorithms.

23.4 Conclusion

Using information theory and utility function, the optimal sensor placement problem for response reconstruction is formulated as a problem of maximizing a multi-dimensional integral of the minus the information entropy in the parameter space. The framework provides optimal sensor configurations that are robust to uncertainties in the model parameters as well as uncertainties in the state and measurement errors. Such uncertainties are not known in the initial optimal experimental design phase and thus need to be postulated or partly learned from the data using Bayesian inference techniques. Monte Carlo or sparse grid techniques can be used to estimate the multidimensional integral. Computationally efficient heuristic sequential sensor placement strategies can be employed to estimate the near optimal sensor locations. The proposed framework is applicable to complex linear systems involving uncertainties in their parameters. It is appropriate to use for reliably reconstructing responses that are important for providing data-driven reliability and safety estimates of systems, as well as reconstruct stress responses that are needed in fatigue damage accumulation theories [1, 7]. The proposed framework can be implemented with response reconstruction techniques based on modal expansion methods, as well as filter-based methods for joint input-state estimation. Moreover, it can be used to explore the number and type of sensors that are needed to provide reliable estimates of output QoI.

Acknowledgements The author gratefully acknowledges the European Commission for its support of the Marie Skłodowska Curie program through the ETN DyVirt project (GA 764547).

References

1. Papadimitriou, C., Fritzen, C., Kraemer, P., Ntotsios, E.: Fatigue predictions in entire body of metallic structures from a limited number of vibration sensors using Kalman filtering. *Struct. Control. Health Monit.* **18**, 554–573 (2011)
2. Lourens, E., Reynders, E., De Roeck, G., Degrande, G., Lombaert, G.: An augmented Kalman filter for force identification in structural dynamics. *Mech. Syst. Signal Process.* **27**, 446–460 (2012)
3. Lourens, E., Papadimitriou, C., Gillijns, S., Reynders, E., De Roeck, G., Lombaert, G.: Joint input-response estimation for structural systems based on reduced-order models and vibration data from a limited number of sensors. *Mech. Syst. Signal Process.* **29**, 310–327 (2012)
4. Azam, S.E., Chatzi, E., Papadimitriou, C.: A dual Kalman filter approach for state estimation via output-only acceleration measurements. *Mech. Syst. Signal Process.* **60**, 866–886 (2015)
5. Lourens, E., Fallais, D.J.M.: Full-field response monitoring in structural systems driven by a set of identified equivalent forces. *Mech. Syst. Signal Process.* **114**, 106–119 (2019)
6. Maes, K., Smyth, A.W., De Roeck, G., Lombaert, G.: Joint input-state estimation in structural dynamics. *Mech. Syst. Signal Process.* **70–71**, 445–466 (2016)
7. Papadimitriou, C., Chatzi, E.N., Azam, S.E., Dertimanis, V.K.: Fatigue monitoring and remaining lifetime prognosis using operational vibration measurements. In: *Model Validation and Uncertainty Quantification*, vol. 3, pp. 133–136. Springer, Berlin (2019)
8. Maes, K., Lourens, E., Van Nimmen, K., Reynders, E., De Roeck, G., Lombaert, G.: Design of sensor networks for instantaneous inversion of modally reduced order models in structural dynamics. *Mech. Syst. Signal Process.* **52–53**, 628–644 (2015)
9. Zhang, C.D., Xu, Y.L.: Optimal multi-type sensor placement for response and excitation reconstruction. *J. Sound Vib.* **360**, 112–128 (2016)

10. Lindley, D.V.: On a measure of the information provided by an experiment. *Ann. Math. Stat.* **27**, 986–1005 (1956)
11. Huan, X., Marzouk, Y.M.: Simulation-based optimal Bayesian experimental design for nonlinear systems. *J. Comput. Phys.* **232**(1), 288–317 (2013)
12. Gerstner, T., Griebel, M.: Numerical integration using sparse grids. *Numer. Algorithms* **18**, 209–232 (1998)
13. Hansen, N., Muller, S.D., Koumoutsakos, P.: Reducing the time complexity of the derandomized evolution strategy with covariance matrix adaptation (CMA-ES). *Evol. Comput.* **11**(1), 1–18 (2003)
14. Papadimitriou, C.: Optimal sensor placement methodology for parametric identification of structural systems. *J. Sound Vib.* **278**(4), 923–947 (2004)
15. Papadimitriou, C., Lombaert, G.: The effect of prediction error correlation on optimal sensor placement in structural dynamics. *Mech. Syst. Signal Process.* **28**, 105–127 (2012)



Chapter 24

Finite Element Model Updating Accounting for Modeling Uncertainty

Rodrigo Astroza, Andres Alessandri, and Joel P. Conte

Abstract A novel approach to deal with modeling uncertainty when updating mechanics-based finite element (FE) models is presented. In this method, a dual adaptive filtering approach is adopted, where the Unscented Kalman filter (UKF) is used to estimate the unknown parameters of the nonlinear FE model and a linear Kalman filter (KF) is employed to estimate the diagonal terms of the covariance matrix of the simulation error vector based on a covariance-matching technique. Numerically simulated response data of a two-dimensional three-story three-bay steel frame structure with eight unknown material model parameters subjected to seismic base excitation is employed to illustrate and validate the proposed methodology. The results of the validation studies show that the proposed approach significantly outperforms the parameter-only estimation approach widely investigated and used in the literature.

Keywords Finite element model · Modeling uncertainty · Parameter estimation · Dual filtering

24.1 Introduction

Improving the predictive capabilities of models, providing a tool for damage identification, and verifying modeling techniques are some significant problems that are assisted by model calibration. Significant research has been focused on updating linear finite element (FE) models [1]; however, calibration of nonlinear FE models has attracted the attention in recent years. Although the first studies dealing with the updating of nonlinear models of structures were conducted in the 70's and 80's (e.g., [2–4]), mechanics-based nonlinear FE models have been the subject of research only the last years (e.g., [5–10]). When state-of-the-art nonlinear FE models are updated using measured response data, a parameter-only estimation approach is considered, because it is not feasible to estimate the response variables defining the state vector (e.g., displacements and velocities at every degree of freedom of the model). This implies that modeling uncertainty is not accounted for, which may have detrimental effects in the prediction capabilities of the updated FE model [11] because any FE model is only an approximate representation of the system to be modeled [12–14].

In this paper, a dual adaptive filtering approach is proposed to deal with modeling uncertainty when updating mechanics-based nonlinear FE models. The method presented addresses the different sources of uncertainty involved in FE model updating, including parameter, modeling, and noise uncertainties. The unscented Kalman filter (UKF) is employed for parameter estimation and a linear Kalman filter is used to estimate the diagonal entries of the covariance matrix of the simulation error vector (e.g., [15, 16]), which are considered time variant because modeling uncertainty may vary in time.

24.2 Problem Formulation

The discrete-time equation of motion of a mechanics-based nonlinear FE model under uniform earthquake base excitation can be written as

$$\mathbf{M}(\mathbf{p}) \ddot{\mathbf{q}}_{k+1}(\mathbf{p}) + \mathbf{C}(\mathbf{p}) \dot{\mathbf{q}}_{k+1}(\mathbf{p}) + \mathbf{r}_{k+1}(\mathbf{q}_{k+1}(\mathbf{p}), \mathbf{p}) = -\mathbf{M}(\mathbf{p}) \mathbf{L}(\mathbf{p}) \ddot{\mathbf{u}}_{k+1} \quad (24.1)$$

R. Astroza (✉) · A. Alessandri
Facultad de Ingeniería y Ciencias Aplicadas, Universidad de los Andes, Santiago, Chile
e-mail: rastroza@miandes.cl

J. P. Conte
Department of Structural Engineering, University of California, San Diego, CA, USA

where, $\mathbf{p} \in \mathbb{R}^{n_p \times 1}$ = vector of model parameters, n_p = number of model parameters, $\mathbf{M}, \mathbf{C} \in \mathbb{R}^{n \times n}$ = mass and damping matrices, $\mathbf{q}, \dot{\mathbf{q}}, \ddot{\mathbf{q}} \in \mathbb{R}^{n \times 1}$ = nodal displacement, velocity, and acceleration vectors, $\mathbf{r}(\mathbf{q}(\mathbf{p}), \mathbf{p}) \in \mathbb{R}^{n \times 1}$ = internal resisting force vector, $\mathbf{L} \in \mathbb{R}^{n \times n_u}$ = influence matrix of the base excitation, n = number of degrees of freedom of the FE model, $\ddot{\mathbf{u}} \in \mathbb{R}^{n_u \times 1}$ = input ground acceleration vector with n_u = number of acceleration components of the base excitation, and the subscript denotes the time step.

Aleatory and epistemic uncertainties are present when selecting the model parameters, because they are defined based on the information contained in material specifications, characterization of external loads, blueprints, etc., therefore, in real structures it is not possible to have a precise estimation of the model parameters. In this paper, the vector of model parameters is written as $\mathbf{p} = [\boldsymbol{\theta}^T \ \boldsymbol{\varphi}^T]^T$, with $\boldsymbol{\theta} \in \mathbb{R}^{n_\theta \times 1}$ = vector of unknown model parameters to be estimated, and $\boldsymbol{\varphi} \in \mathbb{R}^{n_\varphi \times 1}$ = vector of modeling uncertainty parameters. Then, Eq. (24.1) can be written as

$$\mathbf{M}(\boldsymbol{\theta}, \boldsymbol{\varphi}) \ \ddot{\mathbf{q}}_{k+1}(\boldsymbol{\theta}, \boldsymbol{\varphi}) + \mathbf{C}(\boldsymbol{\theta}, \boldsymbol{\varphi}) \ \dot{\mathbf{q}}_{k+1}(\boldsymbol{\theta}, \boldsymbol{\varphi}) + \mathbf{r}_{k+1}(\mathbf{q}_{k+1}(\boldsymbol{\theta}, \boldsymbol{\varphi}), \boldsymbol{\theta}, \boldsymbol{\varphi}) = -\mathbf{M}(\boldsymbol{\theta}, \boldsymbol{\varphi}) \ \mathbf{L}(\boldsymbol{\theta}, \boldsymbol{\varphi}) \ \ddot{\mathbf{u}}_{k+1} \quad (24.2)$$

From Eq. (24.2), the FE-predicted response, $\widehat{\mathbf{y}}_{k+1} \in \mathbb{R}^{n_y \times 1}$, can be expressed as a nonlinear function of $\boldsymbol{\theta}$ and $\boldsymbol{\varphi}$, the time-history of earthquake excitation ($\ddot{\mathbf{u}}_{1:k+1} = [\ddot{\mathbf{u}}_1^T, \dots, \ddot{\mathbf{u}}_{k+1}^T]^T$), and the initial conditions (\mathbf{q}_0 and $\dot{\mathbf{q}}_0$), i.e.,

$$\widehat{\mathbf{y}}_{k+1} = \mathbf{h}_{k+1}(\boldsymbol{\theta}, \boldsymbol{\varphi}, \ddot{\mathbf{u}}_{1:k+1}, \mathbf{q}_0, \dot{\mathbf{q}}_0) \quad (24.3)$$

where $\mathbf{h}_{k+1}(\cdot)$ = nonlinear response function of the FE model.

Measured response, $\mathbf{y}_{k+1} \in \mathbb{R}^{n_y \times 1}$, can be used to calibrate $\boldsymbol{\theta}$ since it is related to the FE-predicted response by means of:

$$\mathbf{v}_{k+1} = \mathbf{y}_{k+1} - \widehat{\mathbf{y}}_{k+1} \quad (24.4)$$

where $\mathbf{v}_{k+1} \in \mathbb{R}^{n_y \times 1}$ = simulation error vector assumed Gaussian white with zero mean and covariance matrix $\mathbf{R}_{k+1} \in \mathbb{R}^{n_y \times n_y}$, i.e., $\mathbf{v}_{k+1} \sim N(\mathbf{0}, \mathbf{R}_{k+1})$. Effects of measurement noise and modeling errors are included in the simulation error vector. In this paper, modeling uncertainty is considered by defining different model classes for response simulation (\mathcal{M}_0) and model updating (\mathcal{M}_j) phases [11], i.e., $\mathcal{M}_j \neq \mathcal{M}_0$. Measured response data (\mathbf{y}) is obtained by using a set of pre-defined model parameters denoted by $\boldsymbol{\theta}^{true}$ and polluting the associated response (\mathbf{y}^{true}) with additive noise. Unknown model parameters defining the FE-predicted response, $\widehat{\mathbf{y}}$, will be estimated based on a model class \mathcal{M}_j . Different cases and levels of modeling uncertainty are analyzed, then, different model classes \mathcal{M}_j ($j = 1, 2, \dots$) are investigated.

Since the unknown model parameters are time invariant, they can be estimated assuming a random walk model. Then, the following nonlinear state-space model is defined

$$\begin{aligned} \boldsymbol{\theta}_{k+1} &= \boldsymbol{\theta}_k + \mathbf{w}_k \\ \mathbf{y}_{k+1} &= \mathbf{h}_{k+1}(\boldsymbol{\theta}_{k+1}, \boldsymbol{\varphi}, \ddot{\mathbf{u}}_{1:k+1}) + \mathbf{v}_{k+1} \end{aligned} \quad (24.5)$$

where the initial conditions have been omitted for notational convenience and $\mathbf{w}_k \in \mathbb{R}^{n_\theta \times 1}$ denotes the process noise assumed to be uncorrelated with \mathbf{v}_{k+1} , and Gaussian white with zero mean and covariance matrix $\mathbf{Q}_k \in \mathbb{R}^{n_\theta \times n_\theta}$, i.e., $\mathbf{w}_k \sim N(\mathbf{0}, \mathbf{Q}_k)$.

24.2.1 Parameter-Only Estimation Based on the UKF

The UKF can be used to recursively estimate the mean vector and covariance matrix of the $\boldsymbol{\theta}$, denoted by $\widehat{\boldsymbol{\theta}}$ and $\widehat{\mathbf{P}}^{\boldsymbol{\theta}\boldsymbol{\theta}}$, respectively. This parameter-only estimation approach has been investigated in detail by Astroza et al. [9, 11, 17], proving its robustness to input and output measurement noises and also to minor modeling uncertainty. Figure 24.1 summarizes the parameter-only estimation approach for nonlinear FE model updating based on the UKF. More details about this approach can be found in [17, 18].

Initialize: $\hat{\theta}_{0 0}$ and $\hat{P}_{0 0}^{00}$ for $k = 0, 1, 2, \dots$	Initial estimates of the mean and covariance matrix of the unknown model parameter vector Loop over time steps
Prediction step: (i) $\hat{\theta}_{k+1 k} = \hat{\theta}_{k k}$ (ii) $\hat{P}_{k+1 k}^{00} = \hat{P}_{k k}^{00} + Q_k$ (iii) Generate SPs $\vartheta_{k+1 k}^{(i)}$ ($i=1, \dots, 2n_0 + 1$) based on $\hat{\theta}_{k+1 k}$ and $\hat{P}_{k+1 k}^{00}$ (iv) $\psi_{k+1}^{(i)} = h_{k+1}(\vartheta_{k+1 k}^{(i)}, \bar{u}_{k+1}^g)$ (v) $\hat{y}_{k+1 k} = \sum_{i=1}^{2n_0+1} W_m^{(i)} \psi_{k+1}^{(i)}$ (vi) $\hat{P}_{k+1 k}^{yy} = \sum_{i=1}^{2n_0+1} W_c^{(i)} [\psi_{k+1}^{(i)} - \hat{y}_{k+1 k}] [\psi_{k+1}^{(i)} - \hat{y}_{k+1 k}]^T + R_{k+1}$ (vii) $\hat{P}_{k+1 k}^{0y} = \sum_{i=1}^{2n_0+1} W_c^{(i)} [\vartheta_{k+1 k}^{(i)} - \hat{\theta}_{k+1 k}] [\psi_{k+1}^{(i)} - \hat{y}_{k+1 k}]^T$	Prior estimate of the mean of θ at t_{k+1} Prior estimate of the covariance matrix of θ at t_{k+1} Sigma points FE-predicted response for each sigma point Predicted response at t_{k+1} Predicted response covariance matrix at t_{k+1} Predicted cross-covariance matrix at t_{k+1}
Correction step: output measurement y_{k+1} is recorded (viii) $K_{k+1} = \hat{P}_{k+1 k}^{0y} (\hat{P}_{k+1 k}^{yy})^{-1}$ (ix) $\hat{\theta}_{k+1 k+1} = \hat{\theta}_{k+1 k} + K_{k+1} (y_{k+1} - \hat{y}_{k+1 k})$ (x) $\hat{P}_{k+1 k+1}^{00} = \hat{P}_{k+1 k}^{00} - K_{k+1} \hat{P}_{k+1 k}^{yy} K_{k+1}^T$	Kalman gain matrix Posterior estimate of the mean of θ at t_{k+1} Posterior estimate of the covariance matrix of θ at t_{k+1}
end for	

Fig. 24.1 Framework for parameter estimation of nonlinear FE models using the UKF

24.2.2 Dual Approach Accounting for Modeling Uncertainty

Compensation effects arise in the parameter-only estimation approach when moderate to high levels of modeling uncertainty exists, and biased estimates (reaching even unphysical values) of the unknown model parameters are obtained, implying large estimation errors for unobserved responses [11]. To alleviate this issue, a dual adaptive filtering approach is presented here. The aims is to estimate θ and at the same time estimate the diagonal entries of R_{k+1} , i.e., the variances of the prediction error vector. To this end, a covariance-matching technique is employed, which goal is to make the innovations ($v_{k+1|k}$) compatible with their expected covariance matrix [16].

Here, it is assumed that R_{k+1} is diagonal and expressed as $R_{k+1} = \text{diag } (r_{k+1})$, i.e., that the simulation errors of the different response measurements are uncorrelated. Then, an UKF is used as master filter (MF) to estimate θ and a linear KF is employed as slave filter to estimate r_{k+1} . Figure 24.2 shows the proposed dual filtering approach, where the highlighted portion corresponds to the additional calculations required to incorporate the estimation of r_{k+1} . T and U are the time-invariant covariance matrices of the process and measurement noises, respectively, of the state-space model corresponding to the SF, both assumed Gaussian white with zero mean. Further details about the dual adaptive filtering approach can be found in [19].

24.3 Validation Study

The exterior north-south frame of a three-story steel moment-resisting frame building known as SAC-LA3 [20] under seismic base excitation is used as validation example. Columns and beams are made of A572 and A36 steel, respectively. Geometry of the frame is shown in Fig. 24.3a. A FE model is developed in the software *OpenSees* [21] using nonlinear force-based fiber-section beam-column elements. Each column and beam member is modeled with a single element and seven and six integration points, respectively. Rayleigh damping with mass- and tangent stiffness-proportional coefficients based on a critical damping ratio of 2% for the first two initial modes ($T_1 = 1.06$ [s] and $T_2 = 0.35$ [s]) is assumed. Element cross-

Initialize:	
$\hat{\theta}_{0 0}$ and $\hat{P}_{0 0}^{00}$: Initial estimates of the mean vector and covariance matrix of the unknown model parameter vector
$\hat{r}_{0 0}$ and $\hat{P}_{0 0}^{rr}$: Initial estimates of the mean vector and covariance matrix of the simulation error variances
\mathbf{T} and \mathbf{U}	: Process and measurement noise covariance matrices of slave filter (SF)
<i>for</i> $k = 0, 1, 2, \dots$	<i>Loop over time steps</i>
MF Prediction step:	
(i) $\hat{\theta}_{k+1 k} = \hat{\theta}_{k k}$	Prior estimate of the mean of θ at t_{k+1}
(ii) $\hat{P}_{k+1 k}^{00} = \hat{P}_{k k}^{00} + \mathbf{Q}_k$	Prior estimate of the covariance matrix of θ at t_{k+1}
(iii) Generate SP $\mathfrak{s}_{k+1 k}^{(i)}$ ($i=1, \dots, 2n_0 + 1$) based on $\hat{\theta}_{k+1 k}$ and $\hat{P}_{k+1 k}^{00}$	Sigma points
(iv) $\mathfrak{q}_{k+1}^{(i)} = \mathbf{h}_{k+1}\left(\mathfrak{s}_{k+1 k}^{(i)}, \mathbf{u}_{k+1}^g\right)$	FE-predicted response for each SP
(v) $\hat{\mathbf{y}}_{k+1 k} = \sum_{i=1}^{2n_0+1} W_m^{(i)} \mathfrak{q}_{k+1}^{(i)}$	Predicted response at t_{k+1}
(vi) $\mathbf{v}_{k+1 k} = \mathbf{y}_{k+1} - \hat{\mathbf{y}}_{k+1 k}$	Simulation error vector
(vii) $\mathbf{z}_{k+1} = \text{diag}\left(E\left[\left\{\mathbf{v}_{k+1 k} \mathbf{v}_{k+1 k}^T\right\}\right]\right)$	Diagonal of the simulation error covariance matrix
SF Prediction step:	
(viii) $\hat{\mathbf{r}}_{k+1 k} = \hat{\mathbf{r}}_{k k} ; \hat{P}_{k+1 k}^{rr} = \hat{P}_{k k}^{rr} + \mathbf{T}$	Prior estimates of mean and covariance matrix of \mathbf{r} at t_{k+1}
(ix) $\hat{\mathbf{z}}_{k+1 k} = \hat{\mathbf{r}}_{k+1 k} + \text{diag}\left(\sum_{i=1}^{2n_0+1} W_c^{(i)} \left[\mathfrak{q}_{k+1}^{(i)} - \hat{\mathbf{y}}_{k+1 k} \right] \left[\mathfrak{q}_{k+1}^{(i)} - \hat{\mathbf{y}}_{k+1 k} \right]^T\right)$	Predicted diagonal of simulation error covariance matrix
SF Correction step:	
(x) $\hat{P}_{k+1 k}^{zz} = \hat{P}_{k+1 k}^{rr} + \mathbf{U} ; \hat{P}_{k+1 k}^{rz} = \hat{P}_{k+1 k}^{rr}$	Predicted auto- and cross-covariance matrices of SF
(xi) $\mathbf{K}_{k+1}^r = \hat{P}_{k+1 k}^{rz} \left(\hat{P}_{k+1 k}^{zz} \right)^{-1}$	Kalman gain matrix of SF
(xii) $\hat{\mathbf{r}}_{k+1 k+1} = \hat{\mathbf{r}}_{k+1 k} + \mathbf{K}_{k+1}^r \left(\mathbf{z}_{k+1} - \hat{\mathbf{z}}_{k+1 k} \right)$	Posterior estimate of the mean of \mathbf{r} at t_{k+1}
(xiii) $\hat{P}_{k+1 k+1}^{rr} = \hat{P}_{k+1 k}^{rr} - \mathbf{K}_{k+1}^r \hat{P}_{k+1 k}^{zz} \left(\mathbf{K}_{k+1}^r \right)^T$	Posterior estimate of the covariance matrix of \mathbf{r} at t_{k+1}
(xiv) $\hat{\mathbf{R}}_{k+1} = \text{diag}\left(\hat{\mathbf{r}}_{k+1 k+1}\right)$	Predicted covariance matrix of the simulation error at t_{k+1}
(xv) $\hat{P}_{k+1 k}^{yy} = \sum_{i=1}^{2n_0+1} W_c^{(i)} \left[\mathfrak{q}_{k+1}^{(i)} - \hat{\mathbf{y}}_{k+1 k} \right] \left[\mathfrak{q}_{k+1}^{(i)} - \hat{\mathbf{y}}_{k+1 k} \right]^T + \hat{\mathbf{R}}_{k+1}$	Predicted response covariance matrix at t_{k+1}
(xvi) $\hat{P}_{k+1 k}^{0y} = \sum_{i=1}^{2n_0+1} W_c^{(i)} \left[\mathfrak{s}_{k+1 k}^{(i)} - \hat{\theta}_{k+1 k} \right] \left[\mathfrak{q}_{k+1}^{(i)} - \hat{\mathbf{y}}_{k+1 k} \right]^T$	Predicted cross-covariance matrix of MF at t_{k+1}
MF Correction step:	
(xvii) $\mathbf{K}_{k+1} = \hat{P}_{k+1 k}^{0y} \left(\hat{P}_{k+1 k}^{yy} \right)^{-1}$	Kalman gain matrix of MF
(xviii) $\hat{\theta}_{k+1 k+1} = \hat{\theta}_{k+1 k} + \mathbf{K}_{k+1} \left(\hat{\mathbf{y}}_{k+1} - \hat{\mathbf{y}}_{k+1 k} \right)$	Posterior estimate of the mean of θ at t_{k+1}
(xix) $\hat{P}_{k+1 k+1}^{00} = \hat{P}_{k+1 k}^{00} - \mathbf{K}_{k+1} \hat{P}_{k+1 k}^{yy} \mathbf{K}_{k+1}^T$	Posterior estimate of the covariance matrix of θ at t_{k+1}
<i>end for</i>	

Fig. 24.2 Pseudo-code of the proposed dual adaptive filtering approach for FE model updating

sections are discretized into fibers. Columns' webs into 6×1 fibers across their length and width, respectively, and each column's flange in a single fiber. Beams' webs into 16×1 , 14×1 and 11×1 fibers across their length and width, at the second, third and roof level, respectively, and each beam's flange in a single fiber. Further details of the structure and nonlinear FE model can be found in [17].

The Giuffre-Menegotto-Pinto (MGMP) constitutive model [22] is employed to model the nonlinear uniaxial stress-strain behavior of the steel fibers. This material model is defined by four primary parameters (which will be considered unknown and estimated), corresponding to modulus of elasticity (E_s), initial yield stress (f_y), a parameter defining the curvature of the elastic to plastic transition during the first cycle (R_0) and strain-hardening ratio (b) (see Fig. 24.3b). Two different sets of

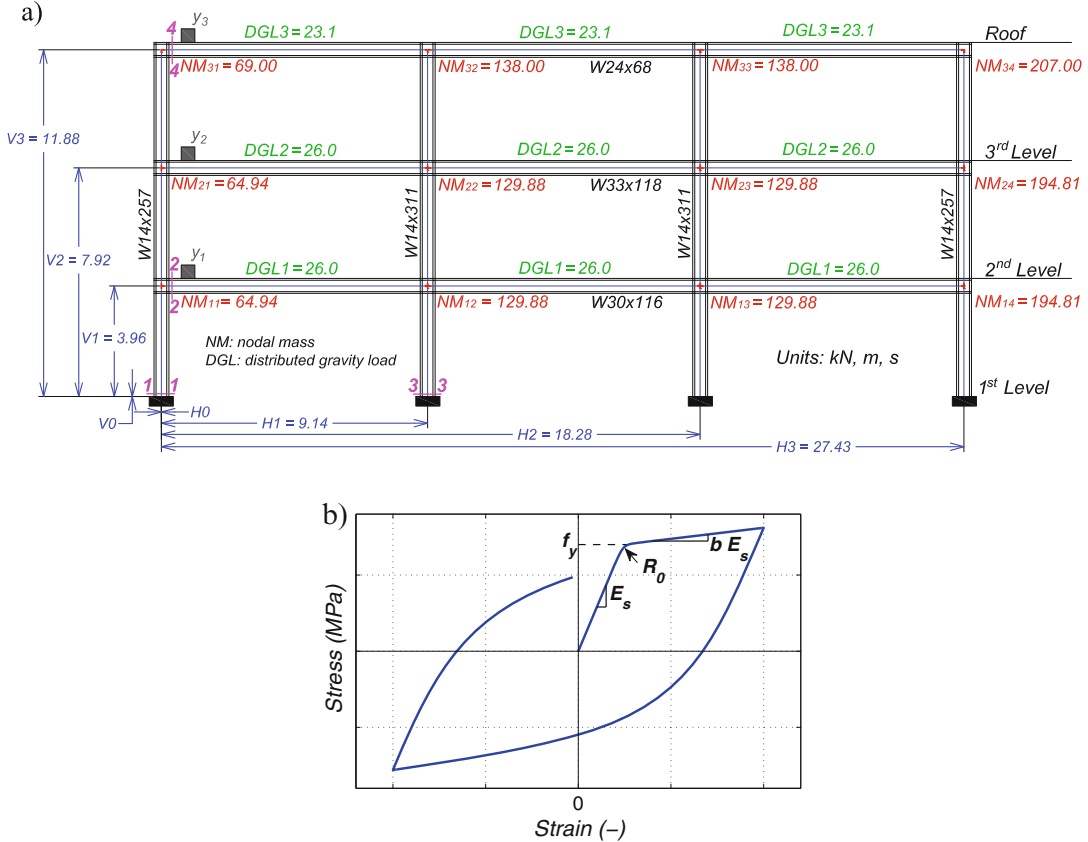


Fig. 24.3 (a) Model of the SAC-LA3 steel moment resisting frame building; (b) Modified Giuffre-Menegotto-Pinto steel constitutive model

model parameters are assumed for the MGMP of beams and columns, because these elements are made of different type of steel. Then, θ is defined by $\theta = [E_s^{col}, f_y^{col}, R_0^{col}, b^{col}, E_s^{beam}, f_y^{beam}, R_0^{beam}, b^{beam}] \in \mathbb{R}^{8 \times 1}$. φ incorporates different sources of modeling uncertainty, including gravity loads, geometry variables, damping properties, and mass properties (nodal masses). The response of the frame is simulated numerically considering defined values of modeling uncertainty parameter values and different sets of φ parameter values are considered to mimic diverse cases of modeling uncertainty.

24.3.1 Cases of Modeling Uncertainty

The cases of modeling uncertainty are taken from [11], and they were chosen to have large discrepancies between the measured and FE-predicted responses when a parameter-only estimation approach is used. Vector φ analyzed in this study is shown below and the levels (magnitudes) of modeling uncertainty are summarized in Table 24.1 (see Fig. 24.3 for notation). A total of 28 cases are studied (Table 24.2), then $j = 1, 2, \dots, 28$ for \mathcal{M}_j .

$$\varphi = \begin{bmatrix} [H_0 \ H_1 \ H_2 \ H_3 \ V_1 \ V_2 \ V_3]^T \\ [NM_{11} \ NM_{12} \ NM_{13} \ NM_{14} \ NM_{21} \ NM_{22} \ NM_{23} \ NM_{24} \ NM_{31} \ NM_{32} \ NM_{33} \ NM_{34}]^T \\ [DGL1 \ DGL2 \ DGL3]^T \\ [\alpha_M \ \beta_K]^T \end{bmatrix} \in \mathbb{R}^{24 \times 1}$$

Note that geometry parameters Ha ($a = 0, 1, 2, 3$) and Vb ($b = 1, 2, 3$) define the location of vertical and horizontal axes of the FE model; terms NM_{ik} denote the nodal mass at floor i and column k ($i = 1, 2, 3$ and $k = 1, 2, 3, 4$); DGL_c denotes

Table 24.1 Types and magnitudes of errors considered for the modeling uncertainty parameters

Parameter type	Parameters	Variation magnitude	Error
Geometry	H_0, H_1, H_2, H_3	Low	$\pm 3\%$ of bay-width (0.27 [m])
	V_1, V_2, V_3	Low	$\pm 3\%$ of story-height (0.12 [m])
Nodal Masses	NM_{ik}	Low	+5%
		High	+30%
Distributed Gravity Loads	DGL_1, DGL_2, DGL_3	Low	+5%
		High	+30%
Damping Coefficients	α_M, β_K	Low	+15%
		High	+50%

Table 24.2 Cases of modeling uncertainty considered for the frame (defined by coefficients applied to the modeling uncertainty parameters)

Case ID	H_0	H_1	H_2	H_3	V_1	V_2	V_3	NM_1	NM_2	NM_3	DGL_1	DGL_2	DGL_3	α_M	β_K
1	1.00	1.00	1.00	1.00	1.03	0.97	1.03	1.00	1.05	1.05	1.00	1.00	1.00	1.00	1.00
2	1.00	0.97	1.03	1.00	1.00	1.00	1.00	1.00	1.00	1.00	1.05	1.05	1.05	1.00	1.00
3	1.00	1.00	1.00	1.00	1.03	0.97	1.03	1.00	1.00	1.00	1.00	1.05	1.05	1.00	1.00
4	1.00	1.00	1.00	1.00	1.03	0.97	1.30	1.00	1.00	1.00	1.00	1.00	1.00	1.00	1.15
5	1.00	0.97	1.03	1.00	1.03	1.00	1.03	1.00	1.00	1.00	1.05	1.05	1.05	1.00	1.00
6	1.00	1.03	0.97	1.00	1.03	1.00	1.00	1.00	1.00	1.00	1.00	1.00	1.00	1.15	1.15
7	1.00	1.03	0.97	1.00	1.03	1.00	1.03	1.00	1.00	1.00	1.00	1.00	1.00	1.15	1.15
8	1.00	0.97	1.03	1.00	1.03	1.00	1.03	1.00	1.00	1.00	1.00	1.00	1.00	1.15	1.15
9	1.00	0.97	1.03	1.00	1.03	1.00	1.03	1.05	1.05	1.05	1.05	1.05	1.05	1.00	1.00
10	1.00	1.03	0.97	1.00	1.03	1.00	1.00	1.00	1.05	1.05	1.00	1.00	1.00	1.15	1.15
11	1.00	0.97	1.03	1.00	1.03	1.00	1.03	1.05	1.05	1.05	1.00	1.00	1.00	1.15	1.15
12	1.00	1.00	1.00	1.00	1.00	1.00	1.03	1.00	1.30	1.30	1.00	1.00	1.00	1.00	1.00
13	1.00	1.00	1.00	1.00	1.03	0.97	1.03	1.00	1.30	1.30	1.00	1.00	1.00	1.00	1.00
14	1.00	1.00	1.00	1.00	1.00	1.00	1.03	1.00	1.00	1.00	1.00	1.30	1.30	1.00	1.00
15	1.00	1.00	1.00	1.03	1.00	1.00	1.00	1.00	1.00	1.00	1.00	1.00	1.00	1.50	1.50
16	1.00	1.03	0.97	1.00	1.00	1.00	1.00	1.00	1.00	1.00	1.00	1.00	1.00	1.50	1.50
17	1.00	1.00	1.00	1.00	1.03	1.03	0.97	1.00	1.00	1.00	1.00	1.00	1.00	1.50	1.50
18	1.00	1.00	1.00	1.00	1.00	1.00	1.00	1.30	1.00	1.00	1.30	1.00	1.00	1.00	1.00
19	1.00	1.03	0.97	1.00	1.03	1.00	1.00	1.00	1.30	1.30	1.00	1.00	1.00	1.00	1.00
20	1.00	0.97	1.03	1.00	1.03	1.00	1.03	1.30	1.30	1.30	1.00	1.00	1.00	1.00	1.00
21	1.03	1.00	1.00	1.00	1.03	1.00	1.00	1.00	1.00	1.00	1.00	1.00	1.00	1.50	1.50
22	1.00	0.97	1.03	1.00	1.03	1.00	1.00	1.00	1.00	1.00	1.00	1.00	1.00	1.50	1.50
23	1.00	1.03	1.00	1.00	1.03	1.00	1.00	1.00	1.30	1.30	1.00	1.30	1.30	1.00	1.00
24	1.00	1.03	0.97	1.00	1.03	1.00	1.00	1.00	1.30	1.30	1.00	1.30	1.30	1.00	1.00
25	1.00	1.03	1.00	1.00	1.03	1.00	1.00	1.00	1.30	1.30	1.00	1.00	1.00	1.50	1.50
26	1.00	0.97	1.03	1.00	1.03	1.00	1.00	1.00	1.30	1.30	1.00	1.00	1.00	1.50	1.50
27	1.03	1.00	1.00	1.00	1.03	1.00	1.00	1.00	1.30	1.30	1.00	1.30	1.30	1.50	1.50
28	1.00	1.03	1.00	1.00	1.03	1.00	1.00	1.00	1.30	1.30	1.00	1.30	1.30	1.50	1.50

the gravity load acting on the beams at levels $c = 1, 2, 3$; and α_M and β_K are the mass and stiffness proportional coefficients defining the Rayleigh damping. The true structure does not consider any variation in φ .

Error related to geometry variables are defined as a percentage (%) of the bay-width and story-height. For example, a coefficient of 0.97 considered for V_3 means that roof coordinate is modified as $(V_3 - 0.03 \times \text{story height})$. Coefficients related to nodal masses are evenly modified for a given level.

Earthquake Input Motions

The 360° component of the ground motion recorded at Los Gatos station during the 1989 Loma Prieta earthquake (see Fig. 24.4) is used as base excitation. Model class M_0 of the frame is subjected to this record to numerically simulate the seismic response of the actual structure (y). Then, the estimation using this information and both estimation approaches

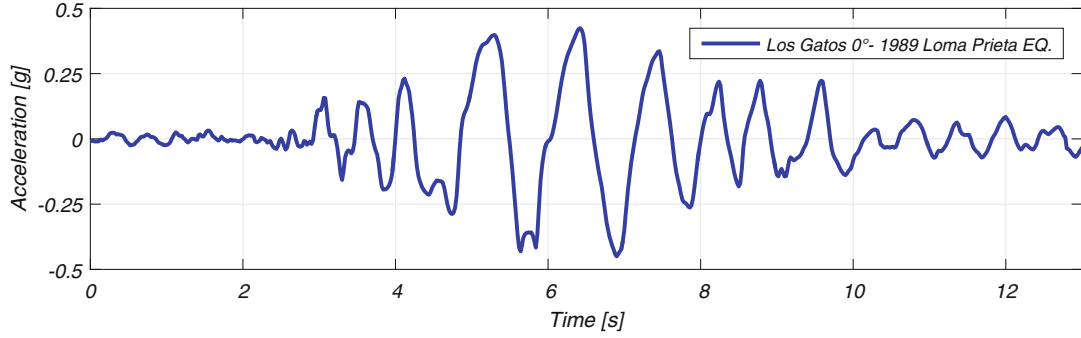


Fig. 24.4 Ground acceleration time history recorded at the Los Gatos station during the 1989 Loma Prieta earthquake

(parameter-only and dual) are employed to update different nonlinear FE models belonging to model classes \mathcal{M}_j ($j = 1, 2, \dots, 28$).

FE Model Updating Results

Dynamic Response Simulation

The horizontal absolute acceleration responses of the three levels of the frame are considered as measured responses and denoted by \mathbf{y}_1 , \mathbf{y}_2 , and \mathbf{y}_3 in Fig. 24.3a. The true response of the structure (\mathbf{y}^{true}) is numerically simulated using model class \mathcal{M}_0 with the following vector of true model parameters $\boldsymbol{\theta}^{true} = [200 \text{ GPa}, 345 \text{ MPa}, 20, 0.08, 200 \text{ GPa}, 250 \text{ MPa}, 18, 0.05]^T$

$$\text{and } \boldsymbol{\varphi}^{true} = \begin{bmatrix} [0.914 \ 18.28 \ 27.43 \ 3.96 \ 7.92 \ 11.88]^T \ [m] \\ [64.94 \ 129.88 \ 129.88 \ 194.81 \ 64.94 \ 129.88 \ 129.88 \ 194.81 \ 69 \ 138 \ 138 \ 207]^T \ \left[\frac{kN}{m} \cdot s^2\right] \\ [26.01 \ 25.99 \ 23.09]^T \ \left[\frac{kN}{m}\right] \\ [0.1782 \ 0.00167]^T \end{bmatrix}^T.$$

In the estimation phase, each component of the true response vector of the structure (\mathbf{y}^{true}) is polluted with an independent white Gaussian noise with zero-mean and $0.5\%g$ root-mean-square (RMS), to generate the measured response, \mathbf{y} . Thus, the measurement noise exact covariance matrix is $0.24 \times 10^{-2} \mathbf{I}_3 [(m/s^2)^2]$, where \mathbf{I}_i denotes the $i \times i$ identity matrix.

Estimation of Unknown Model Parameters

The model parameters characterizing the steel material constitutive model are considered unknown and to be estimated. Random initial values for the unknown model parameters are considered and then both estimation approaches are applied to calibrate the FE models (belonging to different model classes $\mathcal{M}_j, j = 1, \dots, 28$) using the measured response (\mathbf{y}).

The unknown model parameters are initially assumed statistically uncorrelated, and thus the initial estimate of their covariance matrix, $\widehat{\mathbf{P}}_{0|0}^{\theta\theta}$, is diagonal, with entries computed as $(p \times \widehat{\theta}_{0|0}^i)^2$, where $i = 1, \dots, n_\theta = 8$ and p denotes the initial coefficient of variation of the unknown model parameters. Then, the initial estimates of the mean vector and covariance matrix of the unknown model parameters are taken as

$$\begin{aligned} \widehat{\boldsymbol{\theta}}_{0|0} &= [1.3 E_s^{col}, 0.8 f_y^{col}, 0.7 R_0^{col}, 1.25 b^{col}, 0.8 E_s^{beam}, 0.75 f_y^{beam}, 1.3 R_0^{beam}, 1.4 b^{beam}]^T \\ &= [260 \text{ GPa}, 276 \text{ MPa}, 14, 0.1, 160 \text{ GPa}, 187.5 \text{ MPa}, 23.4, 0.07]^T \\ \widehat{\mathbf{P}}_{0|0}^{\theta\theta} &= \text{diag} \left[(0.2 \cdot \widehat{\boldsymbol{\theta}}_{0|0})^2 \right] \in \mathbb{R}^{8 \times 8} \end{aligned}$$

As proposed in [17, 18], a diagonal process noise covariance matrix $\mathbf{Q} = \text{diag} \left[(q \times \widehat{\boldsymbol{\theta}}_{0|0}^i)^2 \right]$ with $q = 1 \times 10^{-5}$ is assumed. In the parameter-only estimation approach, the simulation error covariance matrix is assumed fixed and equal to $\mathbf{R} = 0.87 \times 10^{-3} \mathbf{I}_3 [(m/s^2)^2]$. It is noteworthy that excellent estimation results were obtained in previous studies when using

the parameter-only approach with similar structures and levels of noise, when no model uncertainty is considered [17, 18]. In the dual approach, this covariance matrix is considered as the initial estimate for the simulation error covariance matrix, i.e., $\widehat{\mathbf{R}}_0 = \text{diag}(\widehat{\mathbf{r}}_{0|0}) = 0.87 \times 10^{-3} \mathbf{I}_3 \left[(m/s^2)^2 \right]$. In the SF, $\widehat{\mathbf{P}}_{0|0}^{\text{rr}}$ is assumed diagonal with entries computed according to $\widehat{\mathbf{P}}_{0|0}^{\text{rr}} = \text{diag}\left[\left(0.2 \times \widehat{\mathbf{r}}_{0|0}\right)^2\right]$. The time-invariant covariance matrices of the process and measurement noises used in the SF are taken as $\mathbf{T} = \mathbf{U} = 1 \times 10^{-20} \mathbf{I}_3$.

The final estimates of the unknown model parameters for all the modeling uncertainty cases (Table 24.2) obtained with both approaches (parameter-only and dual) are reported in Table 24.3. Here, the normalized parameter estimates (with respect to the true parameter values) and the associated final coefficient of variation (CV) are shown, and D and N denote the dual and parameter-only estimation approaches, respectively.

Results obtained with the dual approach (D) shows significant improvement with respect to the parameter-only approach in terms of parameter estimates, and also allows keeping higher level of uncertainty in those parameters for which the information contained in the measured responses is limited. When using the parameter-only approach, divergence and convergence to unphysical values of the unknown model parameters are observed, undesired effects that are controlled by the dual approach. Parameters E_s^{col} and E_s^{beam} are estimated by the parameter-only estimation approach in the range (85.91–205.84%) of their true values, and the estimation using the dual adaptive filtering approach narrows that range to (95.05–153.95%). Results for parameters f_y^{col} and f_y^{beam} are similar; using the parameter-only approach the estimates vary between 27.50% and 233.88% of the true values, and employing the dual adaptive filtering approach in the range (70.85–157.19%). Significant differences are also observed in the estimation of the post yield-related parameters, the less sensitive parameters for the acceleration response measurements considered [11]. For instance, the parameter-only approach estimates b^{col} in the range (10.01–400.51%), while with the dual adaptive filtering approach the estimates are in the range (30.56–155.09%) of the corresponding true parameter values, demonstrating a significant improvement. The final coefficient of variation estimates for b^{col} are between 0.51% and 5.74% for the parameter-only approach and between 1.54% and 15.72% for the dual adaptive filtering approach. Similar results are obtained for other post yield-related parameters (R_0^{col} , R_0^{beam} and b^{beam}).

Figure 24.5 shows the time histories of the normalized mean estimates of the unknown model parameters for case 11 (see Table 24.2). Results of the parameter-only and dual approaches are compared. At initial time steps, the amplitude of the response is low and the frame behaves in the linear-elastic range and therefore \mathbf{y} only contains information about E_s^{col} and E_s^{beam} . As the base excitation and the response increase (at about 3 s), the frame behaves nonlinearly and yielding of some fibers occurs and f_y^{beam} starts to be updated. At around 4 s, the measured response becomes sensitive to the other unknown model parameters (f_y^{col} , R_0^{beam} , R_0^{col} , b^{beam} , and b^{col}). When \mathbf{R} is also estimated (i.e., dual approach), the convergence of the unknown model parameters tends to be considerably more stable and smoother, not exhibiting abrupt changes. In Fig. 24.5, dashed lines show plus/minus two standard deviations ($\pm 2\sigma$). When the dual approach is used, unknown model parameter for which low information is contained in the measured response, the estimation uncertainty ($\pm 2\sigma$) remains high.

Errors in Observed Responses

For each case of modeling uncertainty, the final estimates of the unknown model parameters are used with the FE model belonging to the corresponding model class \mathcal{M}_j to predict the response of the structure when it is subjected to the seismic excitation. The responses of the calibrated models are compared to their true counterparts (defined by $\mathcal{M}_0(\boldsymbol{\theta}^{\text{true}}, \boldsymbol{\varphi}^{\text{true}})$) using the relative root-mean-square error (RRMSE), which is defined by $\text{RRMSE}(\mathbf{a}, \mathbf{b}) = \sqrt{\left[\frac{1}{N_s} \sum_{i=1}^{N_s} (a_i - b_i)^2 \right]} / \sqrt{\left[\frac{1}{N_s} \sum_{i=1}^{N_s} (a_i)^2 \right]} \times 100 \ (\%)$ for signals \mathbf{a} (reference) and \mathbf{b} , where N_s denotes the total number of data samples.

Figure 24.6 reports the RRMSEs between the true and FE-predicted measured (observed) acceleration responses for all cases studied (see Table 24.2) using the initial and final estimates of the unknown model parameters obtained from both approaches. The RRMSEs of the initial (non-updated) FE models range from 30.11% to 86.33%. The parameter-only approach reduces this misfit between the true and FE-predicted observed responses, with relative errors in the final FE-predicted responses ranging from 11.76% to 85.08%, but with none of the updated models achieving RRMSEs lower than 10% for the observed responses. On the contrary, when using the dual adaptive filtering approach, the RRMSEs decrease significantly, reaching values ranging between 0.68% and 25.02%, with 32% of the cases having relative errors below 10% for all measured responses, and 89% of the cases with relative errors below 20%, demonstrating an excellent performance in matching the observed responses.

Table 24.3 Normalized final estimates and coefficient of variation (%) (in parentheses) of the unknown model parameters obtained for the studied cases using parameter-only (*N*) and dual adaptive filtering (*D*) approaches

Case ID	$\frac{E_{col}^{est}}{E_{col}^{true}}$	$\frac{f_y^{est}_{col}}{f_y^{true}_{col}}$	$\frac{R_0^{est}_{col}}{R_0^{true}_{col}}$	$\frac{b_{col}^{est}}{b_{col}^{true}}$	$\frac{E_{beam}^{est}}{E_{beam}^{true}}$	$\frac{f_y^{est}_{beam}}{f_y^{true}_{beam}}$	$\frac{R_0^{est}_{beam}}{R_0^{true}_{beam}}$	$\frac{b_{beam}^{est}}{b_{beam}^{true}}$
1 (<i>N</i>)	1.03 (0.06)	1.31 (0.30)	0.42 (0.43)	1.87 (2.62)	1.27 (0.13)	0.98 (0.22)	0.75 (0.12)	0.58 (0.48)
1 (<i>D</i>)	1.10 (0.32)	1.17 (1.60)	0.54 (1.15)	0.55 (8.38)	1.14 (0.41)	0.92 (0.64)	1.07 (1.16)	1.32 (3.01)
2 (<i>N</i>)	0.95 (0.07)	2.18 (1.14)	0.16 (0.09)	1.37 (2.05)	1.06 (0.11)	1.02 (0.18)	0.88 (0.20)	0.49 (0.45)
2 (<i>D</i>)	1.00 (0.08)	0.99 (0.57)	1.02 (1.21)	1.01 (3.91)	1.00 (0.14)	0.99 (0.34)	1.01 (0.52)	1.03 (1.38)
3 (<i>N</i>)	1.11 (0.06)	1.18 (0.19)	0.58 (0.20)	0.10 (0.51)	1.05 (0.11)	0.99 (0.25)	0.82 (0.19)	0.85 (0.67)
3 (<i>D</i>)	1.13 (0.32)	1.02 (1.81)	0.72 (2.14)	1.17 (9.39)	1.01 (0.45)	0.89 (0.59)	1.08 (1.25)	1.17 (2.63)
4 (<i>N</i>)	1.11 (0.07)	0.77 (0.13)	0.92 (0.33)	1.00 (0.74)	1.10 (0.12)	1.02 (0.23)	0.67 (0.11)	0.73 (0.54)
4 (<i>D</i>)	1.15 (0.30)	1.19 (0.75)	0.57 (0.86)	0.31 (3.90)	0.99 (0.37)	0.89 (0.67)	1.09 (1.26)	1.43 (2.94)
5 (<i>N</i>)	1.05 (0.07)	1.11 (0.26)	0.70 (0.37)	0.54 (1.33)	1.02 (0.13)	1.23 (0.17)	0.56 (0.12)	0.10 (0.12)
5 (<i>D</i>)	1.06 (0.19)	1.13 (0.70)	0.63 (0.81)	0.38 (3.02)	1.04 (0.30)	0.95 (0.48)	1.09 (0.96)	1.09 (2.17)
6 (<i>N</i>)	1.03 (0.09)	0.98 (0.20)	0.96 (1.08)	1.44 (2.21)	0.96 (0.14)	1.16 (0.15)	0.56 (0.11)	0.10 (0.12)
6 (<i>D</i>)	1.02 (0.12)	0.95 (0.40)	1.08 (0.98)	1.36 (2.90)	1.00 (0.21)	0.94 (0.31)	1.04 (0.59)	1.18 (1.22)
7 (<i>N</i>)	0.99 (0.06)	1.41 (0.15)	0.54 (1.02)	0.16 (1.15)	1.16 (0.14)	1.11 (0.15)	0.58 (0.07)	0.10 (0.21)
7 (<i>D</i>)	1.06 (0.20)	1.09 (1.00)	0.74 (1.28)	0.59 (6.24)	1.03 (0.33)	0.93 (0.50)	1.04 (0.84)	1.25 (2.10)
8 (<i>N</i>)	0.99 (0.07)	2.34 (2.26)	0.19 (0.21)	0.63 (5.74)	1.11 (0.14)	0.97 (0.23)	0.88 (0.21)	0.78 (0.60)
8 (<i>D</i>)	1.06 (0.19)	1.08 (0.87)	0.65 (0.97)	0.41 (2.03)	1.03 (0.31)	0.94 (0.43)	1.10 (0.92)	1.20 (1.92)
9 (<i>N</i>)	1.06 (0.08)	1.02 (0.32)	0.52 (0.26)	1.34 (2.78)	1.18 (0.15)	1.21 (0.20)	0.56 (0.10)	0.10 (0.21)
9 (<i>D</i>)	1.10 (0.16)	1.08 (0.88)	0.87 (1.22)	0.98 (5.07)	1.09 (0.28)	1.04 (0.47)	0.95 (0.61)	1.04 (1.79)
10 (<i>N</i>)	1.04 (0.11)	1.22 (0.32)	0.27 (0.15)	0.48 (1.16)	1.04 (0.21)	0.86 (0.18)	0.50 (0.10)	0.10 (0.22)
10 (<i>D</i>)	1.02 (0.11)	0.99 (0.40)	1.11 (1.08)	1.30 (2.92)	1.06 (0.21)	1.02 (0.28)	1.01 (0.45)	1.10 (1.13)
11 (<i>N</i>)	1.09 (0.07)	1.09 (0.33)	0.63 (0.27)	0.10 (1.94)	1.18 (0.15)	1.17 (0.30)	0.63 (0.12)	0.41 (0.59)
11 (<i>D</i>)	1.10 (0.21)	1.05 (1.66)	0.79 (1.53)	1.21 (8.16)	1.09 (0.35)	1.01 (0.70)	0.95 (0.83)	1.15 (2.48)
12 (<i>N</i>)	1.17 (0.07)	1.02 (0.26)	0.63 (0.25)	1.22 (1.83)	1.23 (0.18)	0.87 (0.22)	0.32 (0.03)	0.40 (0.32)
12 (<i>D</i>)	1.10 (0.13)	1.21 (1.22)	0.69 (1.35)	0.33 (4.02)	1.40 (0.35)	1.02 (0.44)	1.50 (1.50)	1.53 (1.93)
13 (<i>N</i>)	1.05 (0.07)	1.22 (0.19)	0.36 (0.11)	1.61 (1.59)	2.06 (0.20)	0.99 (0.23)	0.68 (0.11)	0.59 (0.34)
13 (<i>D</i>)	1.13 (0.35)	1.31 (2.27)	0.48 (1.22)	1.09 (13.54)	1.54 (0.77)	0.93 (0.76)	1.36 (2.15)	1.66 (3.62)
14 (<i>N</i>)	1.03 (0.09)	1.19 (0.29)	0.49 (0.30)	0.31 (2.26)	1.06 (0.17)	1.12 (0.18)	0.46 (0.08)	0.10 (0.12)
14 (<i>D</i>)	1.03 (0.18)	1.52 (2.23)	0.34 (1.77)	0.77 (15.30)	1.04 (0.29)	0.71 (0.46)	1.36 (1.72)	1.31 (2.32)
15 (<i>N</i>)	0.97 (0.08)	1.67 (0.54)	0.17 (0.08)	2.22 (2.00)	1.03 (0.12)	0.98 (0.19)	0.99 (0.27)	0.57 (0.56)
15 (<i>D</i>)	1.01 (0.14)	0.95 (0.22)	0.97 (0.82)	1.07 (1.61)	0.97 (0.20)	0.96 (0.24)	1.00 (0.41)	1.22 (0.94)
16 (<i>N</i>)	1.11 (0.11)	0.28 (0.05)	1.62 (0.69)	3.30 (0.69)	0.89 (0.11)	1.36 (0.14)	0.47 (0.05)	0.14 (0.16)
16 (<i>D</i>)	1.00 (0.15)	0.95 (0.62)	1.05 (1.26)	1.20 (3.77)	0.98 (0.24)	0.97 (0.49)	0.97 (0.62)	1.18 (1.65)
17 (<i>N</i>)	0.97 (0.09)	0.68 (0.13)	1.34 (0.70)	1.49 (1.00)	0.98 (0.13)	1.23 (0.20)	0.50 (0.07)	0.10 (0.26)
17 (<i>D</i>)	0.95 (0.22)	0.92 (0.86)	1.25 (2.52)	1.30 (5.70)	0.95 (0.34)	1.00 (0.63)	0.96 (0.83)	0.94 (2.19)
18 (<i>N</i>)	1.14 (0.11)	0.84 (0.14)	0.28 (0.06)	1.44 (0.83)	1.11 (0.13)	1.24 (0.18)	0.52 (0.09)	0.10 (0.11)
18 (<i>D</i>)	1.22 (0.19)	1.30 (0.57)	0.67 (0.79)	0.33 (1.54)	0.95 (0.21)	1.02 (0.42)	0.97 (0.65)	0.82 (1.54)
19 (<i>N</i>)	1.02 (0.07)	1.40 (0.22)	0.35 (0.08)	0.71 (1.22)	1.70 (0.20)	1.03 (0.19)	0.83 (0.14)	0.68 (0.31)
19 (<i>D</i>)	1.07 (0.19)	1.57 (1.88)	0.92 (9.96)	1.04 (15.72)	1.38 (0.46)	0.94 (0.61)	1.27 (1.32)	1.03 (1.94)
20 (<i>N</i>)	1.29 (0.08)	1.53 (0.25)	0.41 (0.07)	0.13 (0.77)	1.51 (0.16)	1.12 (0.24)	0.97 (0.24)	0.96 (0.55)
20 (<i>D</i>)	1.35 (0.31)	1.38 (2.08)	0.66 (2.09)	1.00 (11.01)	1.38 (0.53)	0.87 (0.62)	1.50 (2.74)	1.96 (3.47)
21 (<i>N</i>)	1.03 (0.10)	0.87 (0.12)	0.55 (0.12)	0.34 (0.53)	1.00 (0.13)	1.14 (0.17)	0.74 (0.19)	0.31 (0.26)
21 (<i>D</i>)	1.03 (0.17)	0.95 (0.66)	1.08 (1.72)	1.30 (3.84)	0.97 (0.28)	0.95 (0.59)	0.99 (0.87)	1.19 (2.17)
22 (<i>N</i>)	1.00 (0.12)	0.61 (0.16)	0.21 (0.06)	4.01 (1.04)	1.09 (0.12)	0.91 (0.11)	1.31 (0.60)	0.97 (0.48)
22 (<i>D</i>)	1.03 (0.21)	0.97 (1.00)	0.94 (1.56)	1.07 (5.25)	0.97 (0.32)	0.97 (0.65)	0.96 (0.83)	1.16 (2.48)
23 (<i>N</i>)	0.86 (0.08)	0.87 (0.27)	0.23 (0.10)	3.53 (2.55)	2.04 (0.27)	1.18 (0.17)	0.45 (0.04)	0.12 (0.16)
23 (<i>D</i>)	1.08 (0.17)	1.02 (1.26)	1.33 (2.92)	1.55 (7.96)	1.39 (0.39)	1.08 (0.53)	1.30 (1.19)	1.65 (1.90)
24 (<i>N</i>)	1.01 (0.06)	1.77 (0.23)	0.26 (0.17)	0.28 (2.51)	1.87 (0.23)	0.78 (0.17)	0.60 (0.07)	0.61 (0.29)
24 (<i>D</i>)	1.11 (0.17)	1.11 (1.34)	1.03 (2.17)	1.18 (6.55)	1.36 (0.37)	1.11 (0.43)	1.27 (1.01)	1.54 (1.65)
25 (<i>N</i>)	1.07 (0.10)	1.12 (0.32)	0.53 (0.23)	1.45 (2.17)	1.41 (0.24)	1.51 (0.26)	0.50 (0.09)	0.10 (0.19)
25 (<i>D</i>)	1.09 (0.27)	1.22 (0.84)	0.80 (1.19)	0.53 (3.79)	1.36 (0.47)	1.25 (0.58)	1.09 (0.94)	1.32 (2.41)
26 (<i>N</i>)	1.08 (0.11)	1.18 (0.35)	0.72 (0.67)	1.55 (2.41)	1.37 (0.27)	1.50 (0.28)	0.41 (0.07)	0.10 (0.12)
26 (<i>D</i>)	1.08 (0.36)	1.24 (1.14)	0.43 (0.71)	0.89 (5.53)	1.37 (0.66)	1.26 (0.70)	0.96 (1.06)	1.12 (2.75)
27 (<i>N</i>)	1.04 (0.09)	1.35 (0.28)	0.49 (0.15)	0.20 (1.44)	1.50 (0.23)	1.32 (0.31)	0.67 (0.12)	0.51 (0.59)
27 (<i>D</i>)	1.09 (0.23)	1.16 (0.69)	1.18 (2.37)	1.34 (5.57)	1.33 (0.47)	1.28 (0.60)	0.98 (0.76)	1.15 (1.88)
28 (<i>N</i>)	1.08 (0.10)	1.38 (0.27)	0.46 (0.18)	1.23 (1.76)	1.39 (0.22)	1.57 (0.20)	0.57 (0.11)	0.10 (0.14)
28 (<i>D</i>)	1.12 (0.22)	1.16 (0.91)	1.10 (1.86)	1.17 (4.98)	1.31 (0.44)	1.25 (0.74)	1.02 (0.90)	1.23 (2.24)

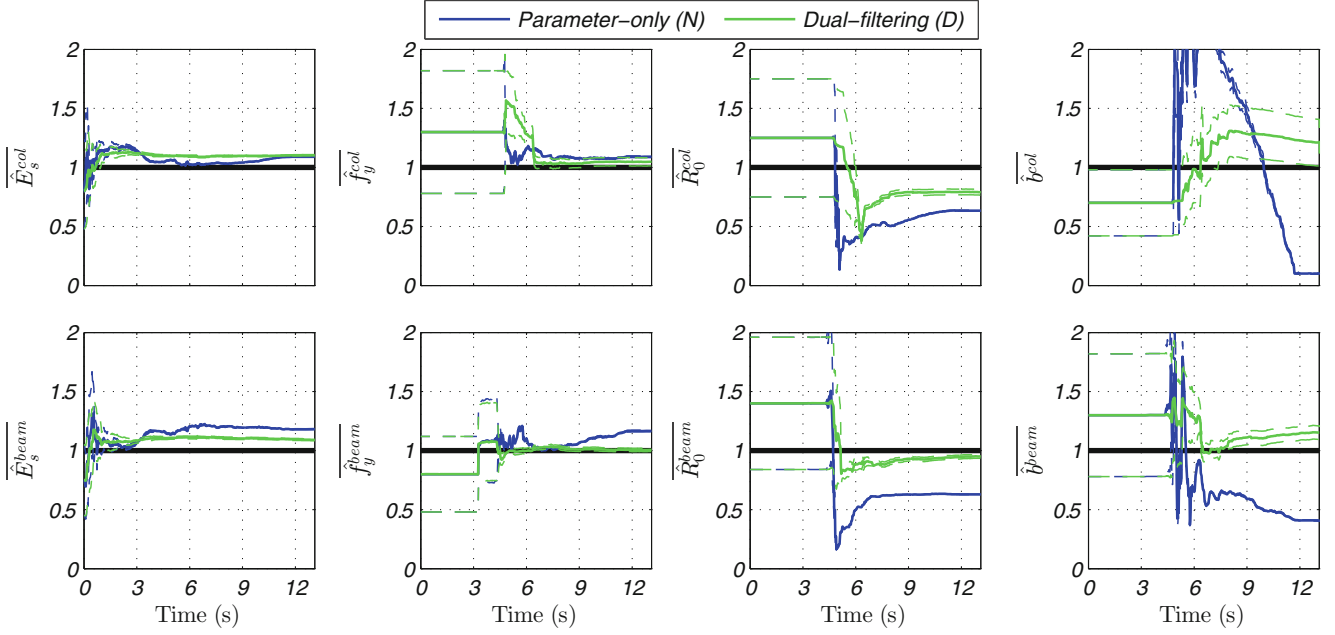


Fig. 24.5 Comparison of the parameter estimation time-histories for Case 11 (low-magnitude multi-parameter modeling uncertainty) obtained using the parameter-only and dual adaptive filtering estimation approaches

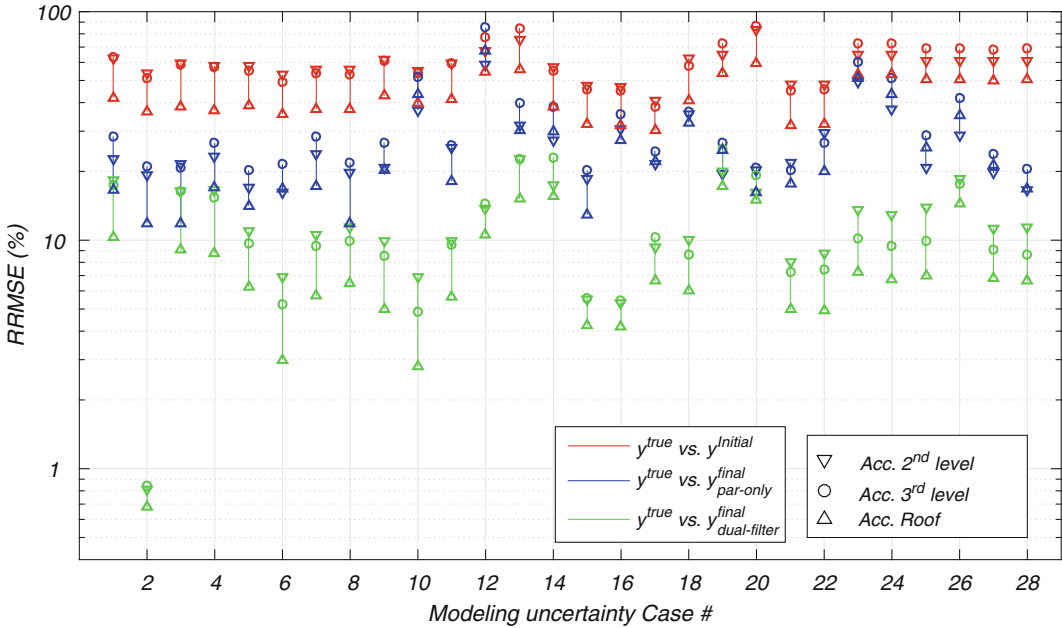


Fig. 24.6 RRMSEs between the true observed absolute acceleration responses and the corresponding initial and final FE-predicted responses for low- (1–11) and large-magnitude (12–28) modeling uncertainty cases for the frame subjected to the Los Gatos earthquake record

24.4 Conclusion

A dual filtering approach for updating mechanics-based nonlinear finite element (FE) models accounting for modeling uncertainty was presented. In this approach, the Unscented Kalman filter (UKF) was used to estimate the unknown FE model parameters and a linear Kalman filter (KF) to estimate the diagonal terms of the covariance matrix of the simulation error vector based on a covariance-matching technique. Estimation results, in terms of parameter and measured response, of the common parameter-only and the proposed dual approaches were compared and discussed considering as

application example a three-story three-bay 2D steel frame with nonlinear behavior subjected to seismic excitation. Different scenarios of modeling uncertainty were analyzed and eight unknown model parameters were estimated. It was shown that the proposed dual filtering approach outperforms the conventional parameter-only estimation approach, achieving better parameter estimates, avoiding divergence and estimation of unphysical parameter values, and attaining better match of the measured and unmeasured response quantities.

Acknowledgements R. Astroza acknowledges the financial support from the Chilean National Commission for Scientific and Technological Research (CONICYT), through FONDECYT research grant No. 11160009.

References

1. Friswell, M., Mottershead, J.: Finite Element Model Updating in Structural Dynamics. Kluwer Academic Publishers, Dordrecht (1995)
2. Distefano, N., Pena-Pardo, B.: System identification of frames under seismic loads. *J. Eng. Mech. Div.* **102**(EM2), 313–330 (1976)
3. Hoshiya, M., Sato, E.: Structural identification by extended Kalman filter. *ASCE J. Eng. Mech.* **110**(12), 1757–1770 (1984)
4. Bittanti, S., Maier, G., Nappi, A.: Inverse problems in structural elastoplasticity: a Kalman filter approach. In: Sawczuk, A., Bianchi, G. (eds.) *Plasticity Today: Modelling, Methods and Applications*, pp. 311–329. Elsevier, Amsterdam (1985)
5. Nasrellah, H.A., Manohar, C.S.: Finite element method based Monte Carlo filters for structural system identification. *Probab. Eng. Mech.* **26**(2), 294–307 (2011)
6. Song, W., Dyke, S., Harmon, T.: Application of nonlinear model updating for a reinforced concrete shear wall. *ASCE J. Eng. Mech.* **139**(5), 635–649 (2013)
7. Ebrahimian, H., Astroza, R., Conte, J.P.: Extended Kalman filter for material parameter estimation in nonlinear structural finite element models using direct differentiation method. *Earthq. Eng. Struct. Dynam.* **44**(10), 1495–1522 (2015)
8. Astroza, R., Nguyen, L.T., Nestorović, T.: Finite element model updating using simulated annealing hybridized with unscented Kalman filter. *Comput. Struct.* **177**, 176–191 (2016)
9. Astroza, R., Ebrahimian, H., Conte, J.P.: Bayesian nonlinear structural FE model and seismic input identification for damage assessment of civil structures. *Mech. Syst. Signal Process.* **93**, 661–687 (2017)
10. Ebrahimian, H., Astroza, R., Conte, J.P.: Nonlinear finite element model updating for damage identification of civil structures using batch Bayesian estimation. *Mech. Syst. Signal Process.* **84**, 194–222 (2015)
11. Astroza, R., Alessandri, A.: Effects of model uncertainty in nonlinear structural finite element model updating by numerical simulation of building structures. *Struct. Control. Health Monit.* **26**(3), e2297 (2019)
12. Sanaye, M., Wadia-Fascetti, S., Arya, B., Santini, E.M.: Significance of modeling error in structural parameter estimation. *Comput. Aided Civ. Inf. Eng.* **16**, 12–27 (2001)
13. Simoen, E., De Roeck, G., Lombaert, G.: Dealing with uncertainty in model updating for damage assessment: a review. *Mech. Syst. Signal Process.* **56–57**, 123–149 (2015)
14. Brynjarsdóttir, J., O'Hagan, A.: Learning about physical parameters: the importance of model discrepancy. *Inverse Probl.* **30**, 114007 (2014)
15. Mehra, R.K.: Approaches to adaptive filtering. *IEEE Trans. Autom. Control.* **17**(5), 693–698 (1972)
16. Brown, S.D., Rutan, S.C.: Adaptive Kalman filtering. *J. Res. Natl. Bur. Stand.* **90**(6), 403–407 (1985)
17. Astroza, R., Ebrahimian, H., Conte, J.P.: Material parameter identification in distributed plasticity FE models of frame-type structures using nonlinear stochastic filtering. *ASCE J. Eng. Mech.* **141**(5), 04014149 (2015)
18. Astroza, R., Ebrahimian, H., Conte, J.P.: Performance comparison of Kalman-based filters for nonlinear structural finite element model updating. *J. Sound Vib.* **438**, 782–800 (2019)
19. Astroza, R., Alessandri, A., Conte, J.P.: A dual filtering approach for nonlinear finite element model updating accounting for modeling uncertainties. *Mech. Syst. Signal Process.* **115**, 782–800 (2019)
20. Gupta, A., Krawinkler, H.: Behavior of ductile SMRFs at various seismic hazard levels. *ASCE J. Struct. Eng.* **126**(1), 98–107 (2000)
21. Mazzoni, S., McKenna, F., Fenves, G.L.: Opensees Command Language Manual. Pacific Earthquake Engineering Research, Berkeley (2005). <http://opensees.berkeley.edu/>
22. Filippou, F.C., Popov, E.P., Bertero, V.V.: Effects of bond deterioration on hysteretic behavior of reinforced concrete joints. In: Report EERC 83-19. Earthquake Engineering Research Center (EERC), University of California, Berkeley (1983)



Chapter 25

Model-Based Decision Support Methods Applied to the Conservation of Musical Instruments: Application to an Antique Cello

R. Viala, V. Placet, S. Le Conte, S. Vaiedelich, and S. Cogan

Abstract In musical instrument making and restoration domains, the variability of the materials and the irreversibility of the changes are issues for the experimental study of the impact of design changes and restorations on musical instruments. In addition, the analytical methods based on simplified geometries and models are not sufficiently detailed for the study of complex structures and phenomena. The virtual prototyping, and its different capabilities, can be a powerful method for instrument makers and museum curators as a decision support tool. Nevertheless, the accuracy of the model is an important matter to assess good predictions. In the case of antique and unique instruments, it is sometimes hard to obtain exhaustive geometrical properties. Similarly, it is also difficult to evaluate the material properties of full instruments, and this uncertainty may have a strong impact on the output features of the numerical models. In this study, a numerical model of cello is developed using finite element method. It is used to evaluate the impact of a modification of a geometrical property on dynamical features. It is shown that the lack of knowledge on the arching height of the top and back plates of a cello has a strong impact on the computed dynamical properties of the cello. Secondly, the model is considered with and without repair cleats and defects like galleries excavated by wood-boring insects. It is observed that the bridge admittance exhibits discrepancies above 220 Hz which is in the low frequencies domain of the model and quantify the impact of repairs. This model capability is a starting point for further simulations accounting for material and geometrical uncertainties and to assess the confidence level of a model for restoration issues.

Keywords Musical acoustics · Virtual prototyping · Dynamical modelling · Cultural heritage conservation · Finite element model

25.1 Introduction

Generally applied in industrial and research domains, model-based decision support has been used for decades as a powerful tool. Considering uncertainties and finely modeled geometries, it can be used for the virtual prototyping of parts and structures. In the musical instrument domain, these methods can be used as a support for the design of new instruments. Moreover, it can also be used for the conservation and restoration of antique and valuable instruments. Many models of musical instruments have been developed for decades, especially violins since the 1980s [1]. More recently, models have been developed for the reverse engineering of a violin [2] or the study of dynamics and acoustics of violin body [3] and the way geometric properties interacts. Models have also been developed to screen material properties of the wooden constituents of the violin [4] and as a decision support tool for violins and guitars [5].

It must be highlighted that curators deal with unique and irreplaceable instruments, which represents a main difference with usual industrial products, for which the critical aspects mostly deal with security and cost concerns. Musical instruments are made with different pieces of wood whose mechanical properties may be hard to evaluate and represent a considerable

R. Viala (✉) · V. Placet · S. Cogan

Department of Applied Mechanics, University of Bourgogne-Franche-Comté, FEMTO-ST Institute, CNRS/UFC/ENSMM/UTBM, Besançon, France

e-mail: romain.viala@univ-fcomte.fr

S. Le Conte · S. Vaiedelich

Equipe Conservation Recherche, Musée de la musique, Paris, France

Centre de Recherche sur la Conservation (CRC), Muséum National d'Histoire Naturelle, CNRS, Ministère de la Culture, Paris, France

lack of knowledge. In the same manner, the fine knowledge of the geometry can be either impossible or costly, involving experiments and devices [6, 7].

So, a major concern must be pointed out about the geometrical and material uncertainties, and the way they can affect the results of a model. Moreover, the climatic conditions that an instrument can undergo have to be considered for such problematics, as musical instruments constantly undergo relative humidity and temperature changes when outside the showcase [8]. In this study, a cello is modeled using the finite element method, and a geometrical characteristic is changed, the height of the top and back plates, while the material properties are unchanged. Secondly, the impact of repairs and defaults on the dynamical response of the model is evaluated, as a potential starting point for a decision support tool for restoration of musical instruments. The object of study of this work is an antique cello which exhibits many previously repaired cracks, and galleries produced by xylophagous insects, whose activity can be experimentally detected by acoustic emission [9].

The cello is made of different species of wood: spruce, maple, ebony and sometimes rosewood that are assembled together. Different experimental studies in the dynamical fields have been focused on several parts of the cello, such as the tailpiece dynamics [10, 11] and studied wolf notes [12]. The body of the instrument is here the main object of concern and is made of carved maple back and bent sides, and a carved spruce soundboard. The aim of the study is to evaluate the impact of an incorrect geometrical modeling on the dynamical response. For this purpose, the geometry of the cello is finely modeled using computer aided design and the finite element method, described below.

25.2 Analysis

The studied structure is a cello, made by *Pietro Guarneri* in the eighteenth century and kept at the musée de la musique, Paris, under the label E.1555. The nominal model is made using the template of a model given in [13] and the data collected by curators and instrument makers about some properties of the E1555 cello. The Computer aided design (CAD) of the cello model has been made using the software SOLIDWORKS and is shown in the Fig. 25.1.

The repair cleats and galleries are schematized in the Fig. 25.2. The geometry has been meshed with tetrahedral elements with quadratic interpolation, the number of nodes is approximately equal to 350,000, which leads to a value close to one million degrees of freedom. Most of the parts are made of wood (maple, spruce an ebony species). The wooden parts are modelled under the linear elastic hypothesis, with an orthotropic definition of the elastic parameters. The material properties identified are taken from [14, 15] and given in the Table 25.1. For the latter, three models will be considered: the first model made with nominal values obtained in [13], labelled as V1 and the one with the correct arch height of both back and top, which corresponds to an increase of 10 mm and a corresponding global shape change, labelled as V2. The photogrammetry method has been used for the measurements of the arch dimensions. In addition, a model is created based on the model V2 without cleats and gallery, labelled as V2_2, to evaluate the impact of repairs or defaults on the behavior of the cello.

The bent parts orientation has been considered by changing the orientation of the local coordinate frames of the corresponding elements. The modal basis computation of 100 modes lasts one hour. Once the modes are computed, the comparison between each case is made with a modal assurance criterion, proposed in [16]. To highlight the capability of the finite element models, the bridge admittances of each case are computed. The admittance is computed with the application of an input force and an observation of either the displacement velocity and acceleration at the same point in the same direction,

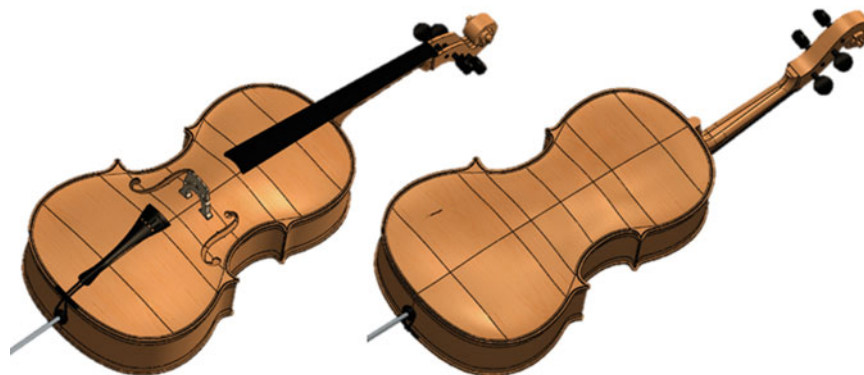


Fig. 25.1 Computer aided design, (CAD) of the cello model; left: front view, right: back view

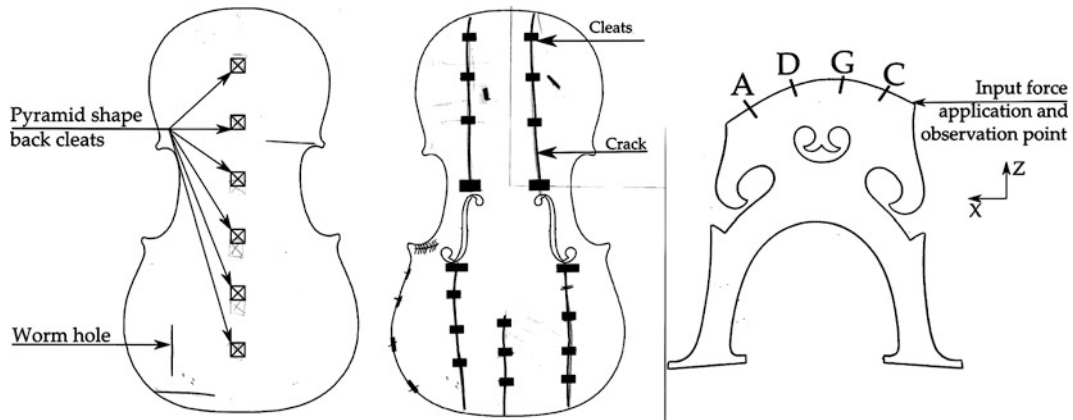


Fig. 25.2 Left: scheme of the cleats and cracks of the cello, based on radiographs provided by the laboratory of the Musée de la musique, Paris, right: bridge excitation and measurement point and direction on a Belgian cello

Table 25.1 Orthotropic material properties for maple, spruce and ebony species, taken from [14, 15]

	Maple	Spruce	Ebony
Specific gravity [-]	0.64	0.44	1.09
E_L [MPa]	12,200	12,840	18,000
E_R [MPa]	1820	1000	2450
E_T [MPa]	1060	650	1520
ν_{LR}, ν_{RL} [-]	0.37, 0.05	0.37, 0.03	0.56, 0.07
ν_{RT}, ν_{TR} [-]	0.65, 0.37	0.48, 0.3	0.95, 0.7
ν_{LT}, ν_{TL} [-]	0.45, 0.03	0.4, 0.02	0.7, 0.06
G_{LR} [MPa]	1375	810	1660
G_{RT} [MPa]	430	46	540
G_{TL} [MPa]	1010	790	1300

as shown in the Fig. 25.2, right part. The bridge admittances are often considered as a signature of the soundboard musical instrument dynamics and has been widely measured [17] but never modeled previously on a numerical model of a cello. The synthesis of the admittance of a cello can unlock some issues that are common in experiments, such as the reproducibility of the measure [18] and the interpretation of the results in the case of geometrical and material differences between instruments, since numerical models can change each parameter at once.

25.3 Results

The computed modal bases are rich and only low frequency canonical modes will be considered. These modes, labeled as T1, C2, C3 and C4 according to usual nomenclature [19], are shown in the Fig. 25.3 and the evolution of the eigenfrequencies for the corresponding modes for each model V1, V2 and V2_2 are given in the Table 25.2.

It is shown that changing the arch height can lead to a variation of the eigenfrequencies of up to 8% for low frequencies mode. In addition, for higher frequencies, the computed and experimental modal bases are not correlated above the 20th modes which states for a completely different behavior above 250 Hz. Thus, such geometrical parameters like arch heights and thickness are keys for the good correlation of a model and a real instrument and need to be characterized.

The admittances at the bridge for the cases V2 (without repairs) and V2_2 (without repairs) are given in the Fig. 25.4. First, the usual A0 acoustic mode is not displayed on the admittance since the fluid-structure interaction was not implemented in the model. The admittance shape below 230 Hz is like the one given in [19] (with lower frequencies) and, under this point, no significative differences are shown between the repaired and not repaired cases. Above this frequency, differences occur in the admittances' shapes, and increase with increasing frequencies, which highlights the facts that repairs affect the dynamical behavior of the cello, even in the low and mid-frequency domains.

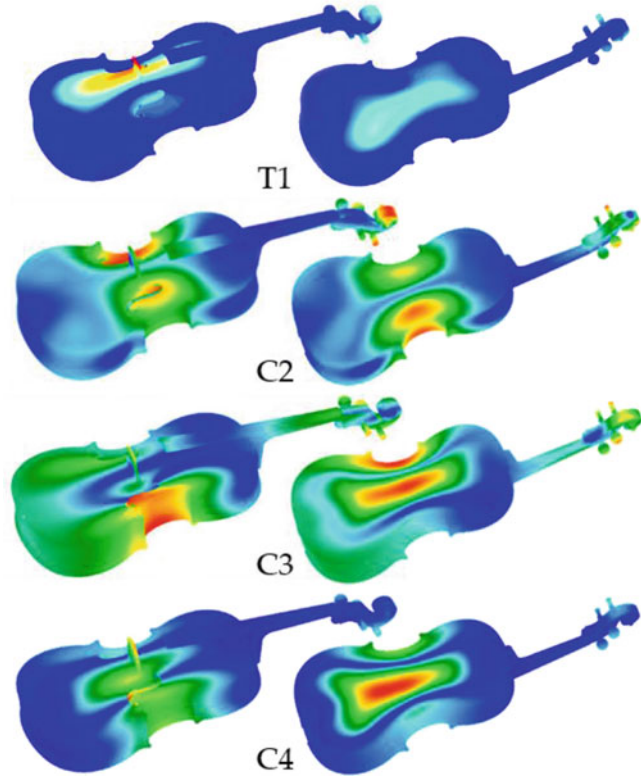


Fig. 25.3 Normalized eigenvectors of the eigenmodes modes of interest (blue = 0, red = 1; left side: top view, right side: back view)

Table 25.2 Eigenfrequencies of the first three modes of interest of the cello and their evolution for three difference cases: nominal model V1, modified model V2, and modified model V2 without repairs

Eigenmode	V1	V2	V2_2
T1 [Hz]	191.3	179.4 (-6.2%)	179.4
C2 [Hz]	179	164.2 (-8.2%)	164.5
C3 [Hz]	207	222.1 (+7.3%)	221.8
C4 [Hz]	213	212.2 (-0.4%)	212.1

Relative changes between V1 and V2 are given in brackets

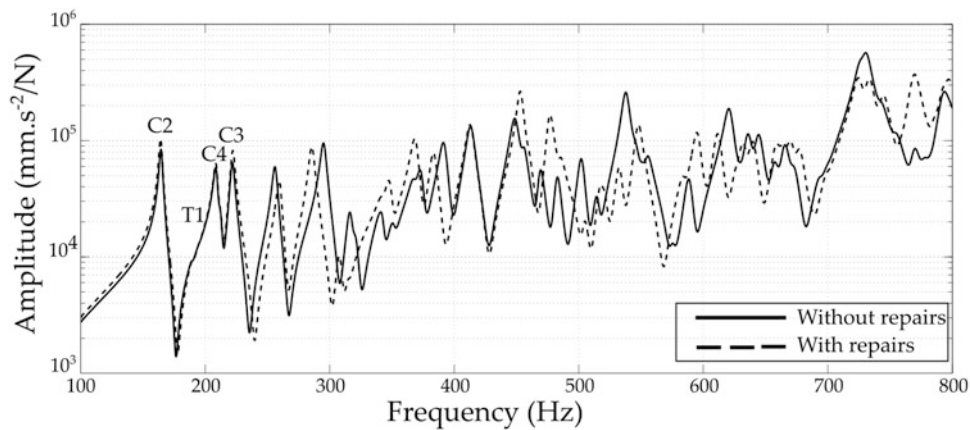


Fig. 25.4 Bridge admittance (acceleration) at the bridge with and without cleats and wormholes

25.4 Conclusion

The numerical models created have highlighted two main facts. Firstly, the geometry accuracy is a key for the predictive capability of a cello, and geometrical properties like arch shape and height are essential for the accuracy of the model. Nowadays, such geometrical features are evaluated effectively with photogrammetry and CT scans means. Secondly, the effects of repairs like cleats and defaults like insect galleries can modeled with such models. The effects of these elements are important on the dynamical behavior of the cello, and this can be considered as an effective tool for more refined and dedicated studies, like the design of repairs cleats that would affect as lower as possible the behavior of the musical instruments, when such repairs are inevitable for the structural integrity of the instrument. In conclusion, this study shows that the numerical models can simulate the effect of restorers and instrument maker's decisions on the dynamical behavior, which can be a starting point for a decision support tool in both static and dynamical domains. The perspective proposed is to evaluate the impact of geometric and material uncertainties on the static response of the cello, when undergoing prestresses due to assembly and strings.

References

1. Knott, G.A.: A Modal Analysis of the Violin Using MSC/NASTRAN and PATRAN. Naval Postgraduate School, Monterey, CA (1987)
2. Pyrkosz, M.A.: Reverse engineering the structural and acoustic behavior of a Stradivari violin. Dissertation, Michigan Technological University (2013)
3. Gough, C.: Vibrational Modes of the Violin Family. In: SMAC 13 Stockholm, 66–74 (2013)
4. Viala, R., Placet, V., Cogan, S., Foltête, E.: Model-based effects screening of stringed instruments. In: Conference Proceedings of the Society for Experimental Mechanics Series, vol. 3, pp. 151–157 (2016)
5. Viala, R.: Towards a model-based decision support tool for stringed musical instrument making. Dissertation, Université Bourgogne Franche-comté (2018)
6. Van den Bulcke, J., Van Loo, D., Dierick, M., Masschaele, B., Van Hoorebeke, L., Van Acker, J.: Nondestructive research on wooden musical instruments: from macro- to microscale imaging with lab-based X-ray CT systems. *J. Cult. Herit.* **27**, S78–S87 (2015)
7. Sirr, S., Waddle, J.: X-ray CT measurements of the internal corpus volume and a new soundpost – corpus volume relationship for stringed instruments of the violin family. *J. Violin Soc. Am.* **XXII**(1), 1–12 (2009)
8. Le conte, S., Vaiedelich, S., François, M.L.M.: A wood viscoelasticity measurement technique and applications to musical instruments: first results. *J. Violin Soc. Am.* **21**, 1–7 (2007)
9. Le Conte, S., Vaiedelich, S., Thomas, J.H., Muliava, V., De Reyer, D., Maurin, E.: Acoustic emission to detect xylophagous insects in wooden musical instrument. *J. Cult. Herit.* **16**(3), 338–343 (2015). Elsevier Masson SAS
10. Fouillhé, E., Houssay, A.: String “After-Length” and the Cello Tailpiece: Acoustics and Perception. In: SMAC 13, April 2014, 0–5 (2013)
11. Fouillhé, E., Goli, G., Houssay, A., Stoppani, G.: Vibration modes of the cello tailpiece. *Arch. Acoust.* **36**(4), 713–726 (2011)
12. Firth, I.A.N.M., Buchanan, J.M.: The wolf in the cello. *J. Acoust. Soc. Am.* **53**, 457–463 (1971)
13. Wake, H.S.: A ‘Strad’ Mode. Wake Publishing, Glastonbury (1975)
14. Viala, R., Placet, V., Cogan, S.: Identification of the anisotropic elastic and damping properties of complex shape composite parts using an inverse method based on finite element model updating and 3D velocity fields measurements (FEMU-3DVF): application to bio-based composite violin soundboard. *Compos. A: Appl. Sci. Manuf.* **106**, 91–103 (2018)
15. Guitard, D., El Amri, F.: Modèles prévisionnels de comportement élastique tridimensionnel pour les bois feuillus et les bois résineux. *Ann. Sci. For.* **44**(3), 335–358 (1987)
16. Allemand, R.J., Brown, D.L.: A correlation coefficient for modal vector analysis. In: First International Modal Analysis Conference, pp. 110–116 (1982)
17. Zhang, A., Woodhouse, J., Stoppani, G.: Motion of the cello bridge. *J. Acoust. Soc. Am.* **140**(4), 2636–2645 (2016)
18. Zhang, A., Woodhouse, J.: Reliability of the input admittance of bowed-string instruments measured by the hammer method. *J. Acoust. Soc. Am.* **136**(6), 3371–3381 (2014)
19. Askenfelt, A.: Quarterly progress and status report eigenmodes and tone quality of the double bass. *STL-QSPR.* **23**, 149–174 (1982)



Chapter 26

Optimal Sensor Placement for Response Predictions Using Local and Global Methods

Costas Argyris, Costas Papadimitriou, and Geert Lombaert

Abstract A Bayesian framework for model-based optimal sensor placement for response predictions is presented. Our interest lies in determining the parameters of the model in order to make predictions about a particular response quantity of interest. This problem is not adequately explored since the majority of currently available literature is focused on parameter inference, rather than prediction inference. The model parameters are inferred by collecting experimental data which depends on the chosen sensor locations. The parameter values are uncertain and their uncertainty is described by a prior probability density function. The measured quantity, or data, is a quantity that can be predicted by the model which depends on both parameters and sensor locations. A prediction error equation is used to describe the discrepancy between the model-predicted measured quantity and the actual data collected from the experiment. The sensor locations are optimized with respect to prediction inference, while the case of parameter inference is derived as a special case under a more general framework. The posterior covariance matrix is used as a measure of uncertainty in the predictions. Two approaches are developed for its calculation, one global and one local. The local approach is based on sensitivities at a fixed value of the parameters, while the global approach uses Monte Carlo sampling and explores the full range of uncertainty in the parameters. A simple numerical example is presented in order to illustrate and verify the two approaches.

Keywords Optimal sensor placement · Bayesian inference · Robust predictions · Uncertainty quantification · Monte Carlo integration

26.1 Introduction

Model-based optimal sensor placement is concerned with finding which is the best way to perform an experiment such that a specific purpose is achieved, using a model of the system as a guide. Common purposes include parameter inference and making predictions using the model [1]. Herein we are interested in optimizing the design for prediction inference, and recover parameter inference as a special case. The parameters are uncertain, as are the experimental data, since no experiment has taken place at the time of design. These uncertainties are treated within the Bayesian framework for uncertainty quantification [2], by assigning a prior probability density function (PDF) for the parameters and a probabilistic model for the difference between model predictions and data, known as the prediction error.

Following the Bayesian method, the posterior represents our updated state of uncertainty about the parameters or predictions given the data. In order to formulate the objective function one needs to chose a scalar measure to describe posterior uncertainty. The seminal paper of Lindley [3] suggests using the expected gain in Shannon information from prior to posterior as a measure of the information provided by an experiment. Information theory measures, based on scalar measures of the Fisher Information Matrix (FIM) [4, 5] and on information entropy [6–8] have been proposed in the past for structural parameter estimation problems.

Much of the currently available literature is focused on designing the experiment for parameter inference. However, when trying to derive both parameter and prediction inference under the same framework, information-theoretic quantities such as the entropy can be troublesome to work with due to the complicated relation between the posterior PDF of parameters and predictions. In this work we use the posterior covariance matrix to describe uncertainty and specifically its determinant as a

C. Argyris (✉) · G. Lombaert
Department of Civil Engineering, KU Leuven, Leuven, Belgium
e-mail: costas.argyris@kuleuven.be

C. Papadimitriou
Department of Mechanical Engineering, University of Thessaly, Volos, Greece

scalar measure. This enables us to formulate the problem for the general case of prediction inference, and recover parameter inference as a special case. The posterior covariance matrix is found using two different approaches, one global that uses Monte Carlo sampling [9, 10] and one local that uses sensitivities.

First we present the general formulation, then develop the two approaches, and finally we verify the methodology using a simple linear example.

26.2 OED Formulation for Response Predictions

Throughout the text all involved quantities are real-valued vectors whose size is denoted when they are first introduced. For clarity purposes, no specific vector notation is used. Let $\mathcal{M} = \mathcal{M}(\theta)$ represent a parametrized model of a structure, which depends on parameters $\theta \in \mathbb{R}^{N_\theta}$ whose values are uncertain. Model $\mathcal{M}(\theta)$ can be used to calculate two different quantities, namely the measured and predicted quantities, both of which depend on parameters θ . These two quantities represent the forward problem. The former is the quantity that is going to be measured when the experiment is performed, and the latter is the quantity that we would like to predict accurately after having collected the experimental data. Let $g = g(\theta) \in \mathbb{R}^{N_g}$ represent the predicted quantity of interest. It depends on the uncertain model parameters θ and therefore it is also uncertain. Our goal is to perform the experiment in such a way that the estimate of $g(\theta)$ is as accurate as possible. Knowledge about $g(\theta)$ comes through knowledge of parameters θ , which in turn is obtained through the measured data collected from the experiment. The inference of parameters θ from measured data constitutes the inverse problem. Then the updated uncertainty in θ is propagated to uncertainty in the predicted quantity $g(\theta)$ (uncertainty propagation).

We assume that the experiment can be performed for N_D different designs. Each design, denoted by $m = 1, \dots, N_D$, can be conceived as a different sensor setup with N_m sensors which would lead to a different measured data set. However, this data set is not known in advance before the experiment takes place. In order to model the process of data collection we consider the two main reasons for mismatch between measured data and model predictions for the measured data: (1) imperfect knowledge about model parameters θ and (2) imperfect model coupled with random measurement error (prediction error). Both sources of uncertainty are taken into account in the prediction error equation which models the measured data set under design m as:

$$\hat{d}_m \sim d_m(\theta) + e_m \quad (26.1)$$

where $d_m(\theta) \in \mathbb{R}^{N_m}$ is the model prediction for the measured data under design m for parameters θ , and $e_m \in \mathbb{R}^{N_m}$ is the prediction error term, considered to be a multivariate zero-mean Gaussian random vector with covariance matrix Σ_{e_m} . Following the Bayesian framework for uncertainty quantification, parameter uncertainty is modelled by assigning a prior PDF to the parameters, namely $p(\theta)$. Then the posterior is given by Bayes' rule as:

$$p(\theta|\hat{d}) = \frac{p(\hat{d}|\theta)p(\theta)}{p(\hat{d})} \quad (26.2)$$

where $p(\hat{d}|\theta)$ is the Gaussian likelihood defined through the prediction error equation (26.1), $p(\theta)$ is the prior and $p(\hat{d})$ is the evidence.

The flow of information from measured data to parameters and to predictions can be seen schematically in Fig. 26.1.

The goal is to find which of the N_D possible experimental designs will result in the most accurate posterior prediction about $g(\theta)$. This is formulated as a discrete optimization problem:

$$m_{opt} = \arg \min U_m, \quad m = 1, \dots, N_D \quad (26.3)$$

where the objective function U_m reflects the uncertainty in the estimate of $g(\theta)$ resulting from data collected from experimental design m . Note that if we set $g(\theta) = \theta$ the problem reduces from inference of predictions to inference of model parameters. Hence, the problem of optimizing the design for parameter inference can be seen as a special case of optimizing for prediction inference, where the predictions are set equal to the parameters. However, the choice of objective function U_m must also reflect that possibility.

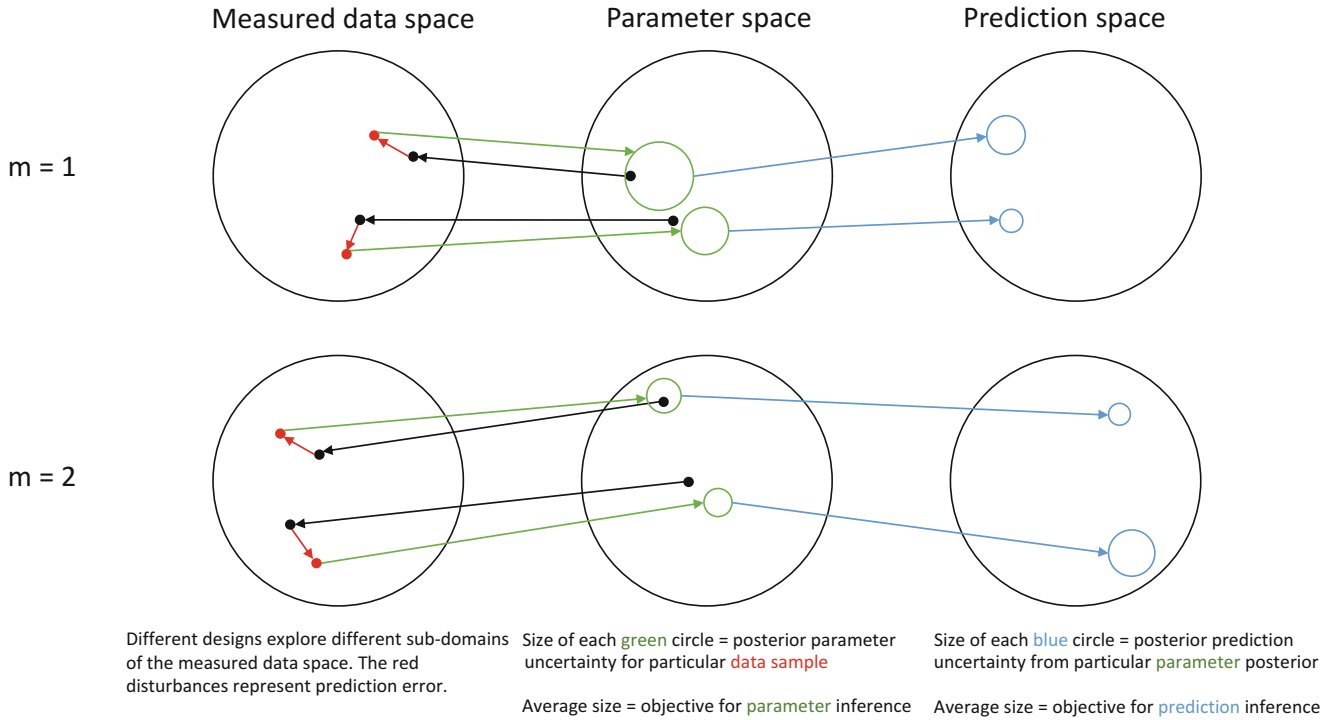


Fig. 26.1 Flow of information from measured data to parameters and predictions

Our choice of objective function U_m is motivated by the fact that we wish to develop both parameter and prediction inference under the same framework. As already stated in the introduction, using the entropy (or any other related information-theoretic quantities such as Kullback-Leibler divergence or Mutual Information) has the drawback of requiring knowledge of the full posterior PDF for the quantity we wish to infer. For parameter inference from measured data (inverse problem), the posterior is given by Bayes' rule (26.2). However, for prediction inference the posterior PDF of predictions g is required which is related to the posterior PDF of parameters through the known formula of transformation of variables from θ to $g(\theta)$:

$$p(g|\hat{d}) = p(\theta(g)|\hat{d}) |J_{g^{-1}}| \quad (26.4)$$

where the posterior of the parameters $p(\theta(g)|\hat{d})$ in the right-hand side is written solely as a function of g using the inverse transformation g^{-1} from g to θ , and $J_{g^{-1}}$ is the Jacobian matrix of the inverse transformation. The transformation needs to be a unique mapping representing a one-to-one relation between g and θ . The inverse transformation g^{-1} from g to θ and its Jacobian can be calculated only for very simple relations between g and θ . These factors severely limit the applicability of the method to very simple cases.

For that reason we turn to the posterior covariance matrix to describe posterior uncertainty in a quantity, and specifically to its determinant as a scalar measure of uncertainty. Using the covariance matrix sidesteps the above mentioned issues because it does not require knowledge of the full functional form of the posterior PDF of the predicted quantity, but only the forward relation $g = g(\theta)$. Also, its calculation is relatively straightforward and can easily accommodate for both prediction and parameter inference. Therefore, we chose the objective function U_m in (26.3) to be the determinant of the posterior covariance matrix of the prediction g , after measured data \hat{d}_m have been collected from design m :

$$U_m = |\Sigma_{g|\hat{d}_m}| \quad (26.5)$$

Next we demonstrate how the posterior covariance matrix can be evaluated using two different approaches, one global and one local.

26.3 Global Sampling-Based Approach

Since we do not know the measured data before the experiment takes place, we follow the strategy of averaging over the unknown, using the prior and likelihood in order to draw possible “data” samples. Following the theory of expected objective function for optimal experimental design [3] the expected objective is the average determinant over all possible data sets that can result from design m :

$$V_m = E[U_m] = \int p(\hat{d}_m) U_m d\hat{d}_m \quad (26.6)$$

Next we demonstrate how the posterior covariance matrix of (26.5) can be evaluated. In the following we temporarily drop the dependence of the posterior covariance matrix of g on the specific set of data \hat{d}_m for notational convenience. Similarly for the dependence of g on θ . Then the element (i, j) of Σ_g , representing the posterior covariance between the i and j elements of the predicted vector g is given by:

$$\Sigma_g^{i,j} = cov(g_i, g_j) = E[(g_i - E[g_i])(g_j - E[g_j])] = E[g_i g_j] - E[g_i]E[g_j] \quad (26.7)$$

where the expectations are evaluated using the known theorem for the expectation of a function of a random variable as:

$$E[g_i g_j] = \int_{\Theta} g_i g_j p(\theta|\hat{d}) d\theta \quad (26.8)$$

$$E[g_i] = \int_{\Theta} g_i p(\theta|\hat{d}) d\theta \quad (26.9)$$

where the posterior is used as the density for θ in order to reflect our updated state of knowledge about the parameters after having observed the data. Substituting the posterior from Bayes’ rule (26.2) results in the following integrals over the prior:

$$E[g_i g_j] = \frac{1}{p(\hat{d})} \int_{\Theta} g_i g_j p(\hat{d}|\theta) p(\theta) d\theta \quad (26.10)$$

$$E[g_i] = \frac{1}{p(\hat{d})} \int_{\Theta} g_i p(\hat{d}|\theta) p(\theta) d\theta \quad (26.11)$$

where the evidence term is given by the total probability theorem as:

$$p(\hat{d}) = \int_{\Theta} p(\hat{d}|\theta) p(\theta) d\theta \quad (26.12)$$

Analytic calculation of the above integrals is possible only for very simple models. Numerical quadrature is efficient only for a very small number of parameters and data points which result in low-dimensional integrals. For the general case of multiple parameters and data points, Monte Carlo integration is the only possible solution. Herein we introduce Monte Carlo importance sampling similar to [9] to approximate the objective function.

26.4 Local Sensitivity-Based Approach

In the sensitivity-based method the posterior covariance matrix of θ is derived from the Gaussian approximation of the posterior:

$$\Sigma_{\theta|\hat{d}_m}^{-1} = [\nabla_{\theta} d_m(\theta)]^T \Sigma_{e_m}^{-1} [\nabla_{\theta} d_m(\theta)] + \Sigma_{\theta}^{-1} \mid_{\theta=\theta^*} \quad (26.13)$$

where $\nabla_{\theta} d_m(\theta)$ is the $N_m \times N_{\theta}$ matrix of sensitivities of the measured quantity with respect to model parameters (Jacobian matrix). The second term, Σ_{θ} , is the covariance matrix of the Gaussian prior for θ .

Expression (26.13) is a local approximation because it is derived from a Taylor series expansion of the log-posterior around the “optimal” value $\theta = \theta^*$ of the model parameters, which minimizes the fit with the data. However, since the data are not available during this stage, a nominal value of θ is selected based on engineering judgement. The Gaussian approximation is exact for the case of linear models.

Then the posterior covariance matrix of predictions g is given by:

$$\Sigma_{g|\hat{d}_m} = [\nabla_\theta g(\theta)] \Sigma_{\theta|\hat{d}_m} [\nabla_\theta g(\theta)]^T \mid_{\theta=\theta^*} \quad (26.14)$$

where $\nabla_\theta g(\theta)$ is the $N_g \times N_\theta$ matrix of sensitivities of the predicted quantity with respect to model parameters (Jacobian matrix). Again the above expression is accurate for predicted quantities that are linear with respect to model parameters. Note that for both methods (global and local) the case of optimizing the design for parameter inference can be recovered as a special case by setting $g(\theta) = \theta$.

26.5 Application: Simple Linear Model

We demonstrate and verify the two approaches using a simple linear model. For this problem the required integrals can be evaluated analytically due to the simple form of the likelihood function, and therefore the analytical form of the objective function is found. Next we approximate the objective function with the sampling method and compare with the analytical solution as the number of samples is increased. Finally we also calculate the objective function using the sensitivity method. Due to the linearity of the problem we anticipate the sensitivity method to be exact.

We consider the simple case of the single-parameter linear model for the measured quantity:

$$d_x(\theta) = \theta x \quad (26.15)$$

where θ is the uncertain parameter and x is the measured location specifying the experimental design. The prediction error equation is then:

$$\hat{d}_x = \theta x + e \quad (26.16)$$

where the error term e is assumed to follow a zero-mean univariate Gaussian distribution $N(0, \sigma_e^2)$. Three cases are examined for the standard deviation of the error σ_e :

1. Constant: $\sigma_e = \sigma'_e$
2. Proportional to location: $\sigma_e = \sigma'_e x$
3. Inversely proportional to location: $\sigma_e = \sigma'_e / x$

The likelihood function then takes the known form:

$$p(\hat{d}_x | \theta, x) = \frac{1}{\sqrt{2\pi\sigma_e^2}} \exp\left(-\frac{1}{2}\frac{(\hat{d}_x - \theta x)^2}{\sigma_e^2}\right) \quad (26.17)$$

We also assume a Gaussian prior for θ , $p(\theta) = N(m_p, \sigma_p^2)$. Since we have only one parameter the predicted quantity is the parameter itself ($g = g(\theta) = \theta$) and therefore the expected utility function is simply the expected posterior variance of θ . So our objective is to find the optimal measure location x^* such that we learn the most about θ .

The integrals of Eqs. (26.10)–(26.12) simplify to:

$$E[\theta^2 | \hat{d}_x] = \frac{1}{p(\hat{d}_x)} \int_{-\infty}^{+\infty} \theta^2 p(\hat{d}_x | \theta) p(\theta) d\theta \quad (26.18)$$

$$E[\theta | \hat{d}_x] = \frac{1}{p(\hat{d}_x)} \int_{-\infty}^{+\infty} \theta p(\hat{d}_x | \theta) p(\theta) d\theta \quad (26.19)$$

$$p(\hat{d}_x) = \int_{-\infty}^{+\infty} p(\hat{d}_x | \theta) p(\theta) d\theta \quad (26.20)$$

which are evaluated analytically for the given form of the likelihood and prior distributions. Then the posterior variance of θ is given by (26.7) as:

$$Var(\theta|\hat{d}_x) = E[\theta^2|\hat{d}_x] - E[\theta|\hat{d}_x]^2 \quad (26.21)$$

and the final objective function is given by the integral over the data:

$$U_x = \int_{-\infty}^{+\infty} p(\hat{d}_x) Var(\theta|\hat{d}_x) dy \quad (26.22)$$

Carrying out all the integrations analytically for the three cases of error standard deviation results in the following forms for the objective function respectively:

$$U_x^1 = \frac{\sigma_e'^2 \sigma_p^2}{\sigma_e'^2 + \sigma_p^2 x^2} \quad (26.23)$$

$$U_x^2 = \frac{\sigma_e'^2 \sigma_p^2}{\sigma_e'^2 + \sigma_p^2} \quad (26.24)$$

$$U_x^3 = \frac{\sigma_e'^2 \sigma_p^2}{\sigma_e'^2 + \sigma_p^2 x^4} \quad (26.25)$$

Next we interpret the resulting objective functions. In the absence of measurement error e , any location x would be equally good to find the value of θ simply by solving the model equation for θ : $\theta = y/x$. This intuitive notion is reflected in all the objective functions by reducing to zero for $\sigma_e' = 0$ independently of the value of x . A zero objective function means zero expected posterior variance for θ , which means that we learn the value of θ exactly with no uncertainty at all. Also note that the objective functions reduce to zero for $\sigma_p = 0$ independently of the value of x again. This is because a zero prior uncertainty implies that we already know exactly the value of θ and no additional data can change that; that is, the posterior is always dominated by the prior.

However, for non-zero values of σ_e' and σ_p there is dependence on the measured location x in objective functions U_x^1 and U_x^3 which correspond to the constant and inversely proportional error cases respectively. Specifically, we see that the objective function decreases (posterior uncertainty in θ decreases) as x increases. This is because the farther away we measure the less important is the measurement error compared to the actual model value. In the constant error case, the error remains the same as the model output is increased when we increase x and therefore the signal-to-noise ratio gets larger. Therefore we have more accurate data \hat{d}_x which is contaminated with less noise, which in turn leads to greater accuracy in the identified value of θ . The same principle holds in the inversely proportional error case but even stronger since the error does not remain constant, but it actually decreases with x , and this results in an even faster reduction of the objective function as x increases (x^4 compared to x^2). Finally note that for the trivial case of $x = 0$, U_x^1 and U_x^3 reduce to the prior variance σ_p^2 . This is because at $x = 0$ the model output is zero and we only measure noise which has no valuable information about θ , and therefore the prior uncertainty remains unchanged.

In the proportional error case we see that U_x^2 does not depend on x at all. This is due to the fact that the signal-to-noise ratio remains the same regardless of x , since the noise is always proportional to x . Small model outputs have small error, and large model outputs have large error, and therefore there is no preference to a specific x so the objective function is constant and independent of x .

Finally note how the objective functions do not depend on the Gaussian prior mean m_p but only on its variance σ_p^2 since what matters is the posterior variance and not the mean.

26.5.1 Comparison with Monte Carlo Integration

Next we solve the same problem (constant error case) using Monte Carlo integration for an increasing number of samples in order to check the convergence. The exact analytical solution U_x^1 is known in this case and is also shown for comparison purposes. The values of σ_e' , σ_p and x which were used are shown in the titles of Fig. 26.2.

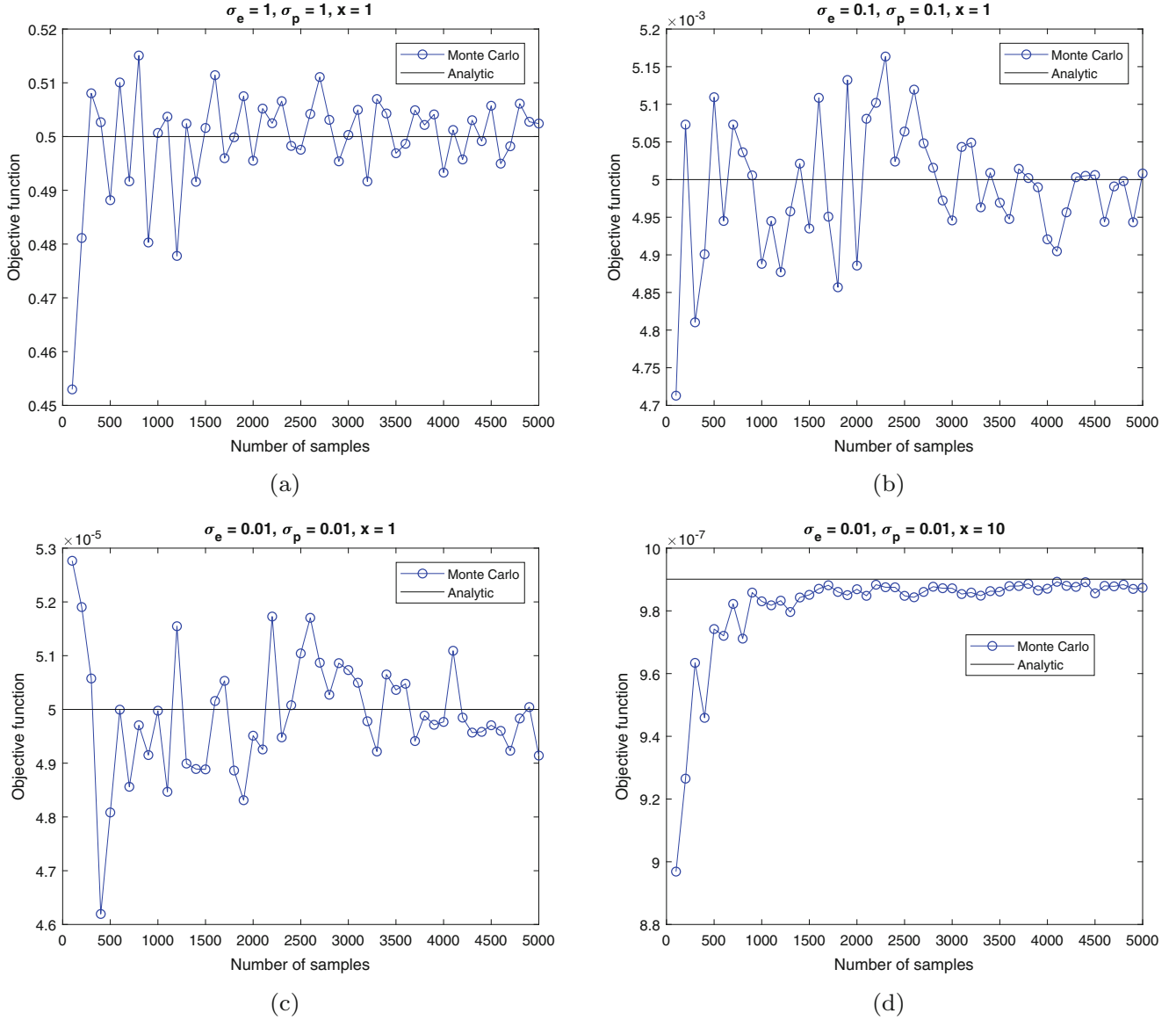


Fig. 26.2 Comparison between Monte Carlo (blue circles) and analytical solutions (black line) for different values of σ'_e , σ'_p and x . Monte Carlo objective function values are normalized by the analytical value for each case of σ'_e , σ'_p and x . Case (a): $\sigma'_e = 1$, $\sigma'_p = 1$, $x = 1$, Case (b): $\sigma'_e = 0.1$, $\sigma'_p = 0.1$, $x = 1$, Case (c): $\sigma'_e = 0.01$, $\sigma'_p = 0.01$, $x = 1$, Case (d): $\sigma'_e = 0.01$, $\sigma'_p = 0.01$, $x = 10$

We can observe how the Monte Carlo solution converges to the true analytical solution as the number of samples is increased (unbiased estimator). We can also see the associated noise (variance) when moving from one number of samples to the next, which is introduced due to the random sampling. The variance is due to both the random sampling of parameter values from the prior and due to the random data samples from the likelihood. For each objective function evaluation a new batch of parameter and data samples is drawn, which leads to slightly different results. The average error in the first three sub-figures ($x = 1$) is about 2% while in the fourth ($x = 10$) is about 0.5%. Also in the case of $x = 10$ the Monte Carlo estimator stabilizes much more quickly compared with $x = 1$. This is due to the fact that there is a much greater signal-to-noise ratio for $x = 10$ and the uncertainty introduced in the estimator through data noise has a much smaller contribution than with $x = 1$. This leads to a better convergence behaviour.

Next we evaluate the objective function with the sensitivity-based method, using the derivative of the measured quantity.

26.5.2 Sensitivity-Based Method

Substituting the linear measured quantity from Eq. (26.15) to (26.13) we obtain:

$$\begin{aligned}
 \sigma_{\theta|\hat{d}_x}^{-2} &= \nabla_\theta(\theta x) \sigma_e'^{-2} \nabla_\theta(\theta x) + \sigma_p^{-2} \\
 &= \frac{x^2}{\sigma_e'^2} + \frac{1}{\sigma_p^2} \\
 &= \frac{x^2 \sigma_p^2}{\sigma_e'^2 \sigma_p^2} + \frac{\sigma_e'^2}{\sigma_e'^2 \sigma_p^2} \\
 &= \frac{x^2 \sigma_p^2 + \sigma_e'^2}{\sigma_e'^2 \sigma_p^2} \\
 \sigma_{\theta|\hat{d}_x}^2 &= \frac{\sigma_e'^2 \sigma_p^2}{\sigma_e'^2 + \sigma_p^2 x^2}
 \end{aligned} \tag{26.26}$$

which has exactly the same form as the one obtained analytically with the global approach in Eq. (26.23), and therefore the same analysis of the results holds here as well. The reason why the sensitivity-based approach gives the exact solution is because the measured quantity is linear with respect to the parameter and this makes the method exact and not approximate.

26.6 Conclusions

A model-based Bayesian optimal sensor placement framework was presented where the interest lies in using the experimental data for making predictions using the model. The posterior covariance matrix of the predictions was used as a measure of uncertainty. Two methods were presented for evaluating the covariance matrix, one global and one local. The global method uses Monte Carlo sampling to evaluate the required integrals while the local method uses Gaussian approximation of the posterior and is based on the sensitivities of the measured and predicted quantities with respect to parameters. A simple linear numerical application was used where the analytical solution is known, in order to demonstrate how the two methods can be applied.

Acknowledgement This work was performed within the frame of the project C16/17/008 “Efficient methods for large-scale PDE-constrained optimization in the presence of uncertainty and complex technological constraints” funded by KU Leuven.

References

- Chaloner, K., Verdinelli, I.: Bayesian experimental design: a review. *Stat. Sci.* **10**, 273–304 (1995)
- Beck, J.L., Katafygiotis, L.S.: Updating models and their uncertainties. I: Bayesian statistical framework. *J. Eng. Mech.* **124**, 463–467 (1998)
- Lindley, D.V.: On a measure of the information provided by an experiment. *Ann. Math. Stat.* **27**, 986–1005 (1956)
- Shah, P.C., Udwadia, F.E.: A methodology for optimal sensor locations for identification of dynamic systems. *J. Appl. Mech.* **45**, 188–196 (1978)
- Udwadia, F.E.: Methodology for optimum sensor locations for parameter identification in dynamic systems. *J. Eng. Mech.* **120**, 368–390 (1994)
- Papadimitriou, C., Beck, J.L., Au, S.K.: Entropy-based optimal sensor location for structural model updating. *J. Vib. Control* **6**, 781–800 (2000)
- Yuen, K.-V., Katafygiotis, L.S., Papadimitriou, C., Mickleborough, N.C.: Optimal sensor placement methodology for identification with unmeasured excitation. *J. Dyn. Syst. Meas. Control* **123**, 677 (2001)
- Ye, S.Q., Ni, Y.Q.: Information entropy based algorithm of sensor placement optimization for structural damage detection. *Smart Struct. Syst.* **10**, 443–458 (2012)
- Ryan, K.J.: Estimating expected information gains for experimental designs with application to the random fatigue-limit model. *J. Comput. Graph. Stat.* **12**, 585–603 (2003)
- Huan, X., Marzouk, Y.M.: Simulation-based optimal Bayesian experimental design for nonlinear systems. *J. Comput. Phys.* **232**, 288–317 (2013)



Chapter 27

Incorporating Uncertainty in the Physical Substructure During Hybrid Substructuring

Connor Ligeikis and Richard Christenson

Abstract In hybrid substructuring, a structural system is partitioned into a numerical substructure and a physical substructure. Typically, the physical substructure consists of a system component whose behavior is difficult to model while the numerical substructure consists of a computational model of the remainder of the system. Hybrid substructuring has previously been shown to be an effective method to quantify the effect of parametric uncertainties in the numerical substructure on the response of the system. This paper proposes and implements a methodology where the effect of parametric uncertainty can also be incorporated into the physical substructure. This idea is implemented in a series of small-scale Real-Time Hybrid Substructuring (RTHS) tests on a magneto-rheological fluid damper used to control a two degree-of-freedom mass-spring system. The physical current supplied to the damper is treated as a random variable. Using the RTHS test results, a metamodel of the system's frequency domain behavior is developed using Principal Component Analysis and Kriging. This metamodel is then used to evaluate probabilistic system performance.

Keywords Real-time hybrid substructuring · Metamodelling · Kriging · Vibration control · Magneto-rheological dampers

27.1 Introduction

Real-Time Hybrid Substructuring (RTHS) is a cyber-physical form of dynamic testing which interfaces numerical modeling with physical experiments in real time [1]. In RTHS, a system is partitioned into a numerical substructure and a physical substructure. The physical substructure is typically a rate-dependent physical component of the system which is difficult to model and the numerical substructure consists of a computational model of the remainder of the system. In a typical RTHS test, a simulated numerical loading is applied to the numerical substructure of the system. A numerical displacement is then computed and applied to the physical substructure via a transfer system such as a hydraulic actuator. Physical loading may also be applied directly to the physical substructure. Restoring forces produced by the physical substructure are measured using sensors and those forces are then fed back to the numerical substructure. This cycle repeats during each time step of the test. Thus, RTHS provides a cost-effective method to study the performance of the full system during the early stages of the design process while only physically testing a single component of that system.

RTHS has been shown to be an effective way to evaluate structural system performance when that system contains parametric uncertainty in the numerical substructure. Abbiati et al. proposed a method called Adaptive Kriging-Hybrid Simulation (AK-HS) which combines a non-parametric statistical interpolation method called Kriging (Gaussian process regression), an adaptive machine learning algorithm, and hybrid substructuring to efficiently estimate a structural system's probability of failure based on a given failure criteria [2]. In this method, a relatively small number of hybrid substructuring tests are used to build a computationally efficient metamodel of the system response. Monte Carlo (MC) simulations are then performed using this metamodel to quantify probabilistic system behavior. This proposed method was experimentally validated using RTHS tests on a system that consisted of two adjacent six degree-of-freedom (DOF) base-isolated structures connected with a viscous damper [3]. It was shown that probabilities of failure can be accurately estimated for a system containing up to 24 random variables using a reasonable number of RTHS tests.

The authors propose an RTHS-based method which can be used to evaluate a structural system's frequency domain behavior when parametric uncertainties are present in both the numerical *and* physical substructures. To demonstrate how

C. Ligeikis · R. Christenson (✉)
Department of Civil and Environmental Engineering, University of Connecticut, Storrs, CT, USA
e-mail: rchriste@engr.uconn.edu

Fig. 27.1 Two DOF mass-spring system

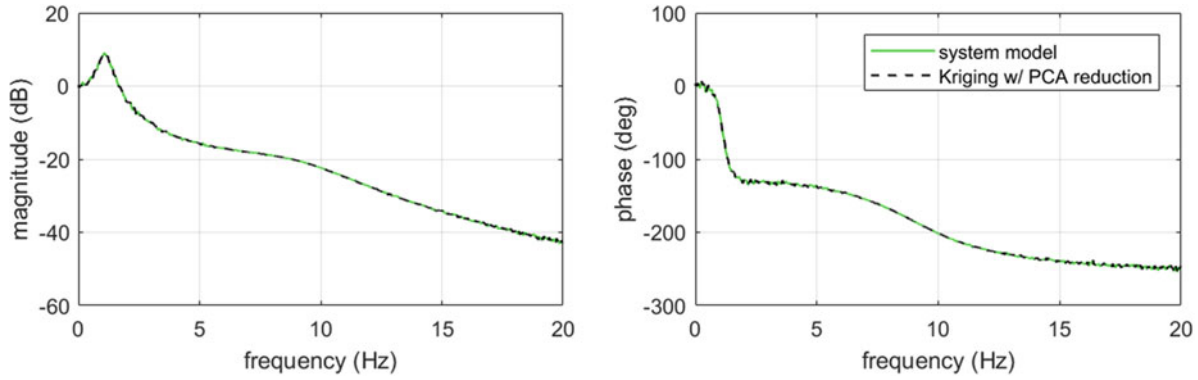
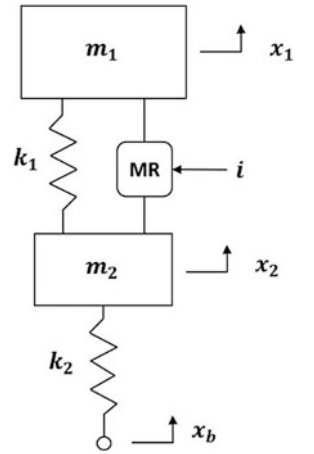


Fig. 27.2 Mean (magnitude and phase) of the FRFs evaluated at 500 sample points by the true system model and the metamodel

this methodology works, a numerical example is provided. The system in question is the two DOF quarter car model shown in Fig. 27.1.

Vibrations are suppressed using a magneto-rheological (MR) fluid damper. MR dampers are devices with variable damping characteristics that are controlled by adjusting a supplied current. In this system, the sprung mass m_1 and the current supplied to the damper i are treated as uniformly distributed random variables ranging from 400 to 600 kg and 0–0.25 amps, respectively. The un-sprung mass m_2 and the spring stiffnesses k_1 and k_2 are considered to be deterministic with values of 50 kg, 25,000 N/m, and 150,000 N/m, respectively. The MR damper is simulated using the hysteretic model proposed by Kwok et al. [4]. In a real RTHS implementation, the MR damper would be the physical substructure and the two DOF system would be the numerical substructure. The system is excited by a 20 Hz band-limited white noise base displacement x_b input. Using Latin hypercube sampling on the random input parameters m_1 and i , 50 simulations are performed using Simulink. Next, the frequency response functions (FRFs) relating the input base displacement x_b to the output sprung mass displacement x_1 are estimated for each of the 50 simulations using the *tfeestimate* function in MATLAB. These FRFs represent the vector-valued response output of the model. The goal is to predict the FRF for a given m_1 and i pair without having to conduct an additional RTHS test. This is accomplished via a statistical metamodel.

First, following the methodology proposed by Yaghoubi et al., the size of the response output vector is reduced by Principal Component Analysis (PCA) [5]. PCA is used to transform the very long (>1000 points) FRF vectors of correlated system outputs into much shorter (<10 points) vectors of uncorrelated variables that represent the core statistical features of the response output. The MATLAB based uncertainty quantification software framework UQLab is then used to build independent Kriging metamodels for each of these uncorrelated PCA variables [6]. Using these metamodels, a vector of PCA variables can be predicted for a desired set of random inputs. These variables are then transformed back into the full length FRF output vector for the unknown m_1 and i pair. To evaluate the effectiveness of this methodology, a mean FRF is computed for 500 MC samples using both the full system model and the metamodel as shown in Fig. 27.2. These mean FRFs are almost identical. Further, Fig. 27.3 shows the full FRFs found using the true model and metamodel for these 500 samples along with the means shown in black. These results demonstrate that this approach is effective at accurately predicting this system's probabilistic behavior.

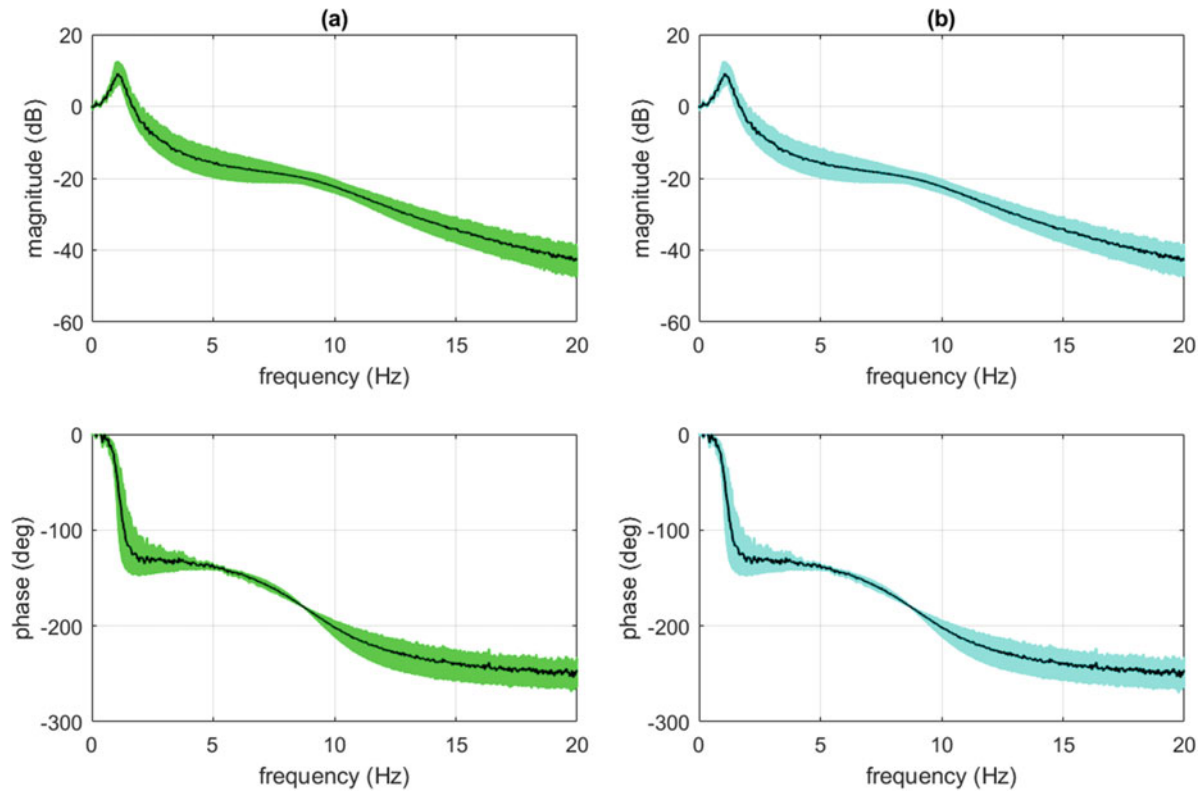


Fig. 27.3 All FRFs obtained by evaluating at 500 sample points: (a) the true system model; and (b) the metamodel

Full RTHS tests to validate the proposed method will be conducted in the Shock and Vibration Laboratory at the University of Connecticut. The physical substructure is a Lord Corporation MR damper (Model RD-1005-3). This damper is attached to a servo-hydraulic actuator system which consists of a Quincy-Ortman Cylinder with a MOOG servo-valve. The actuator is controlled with a Parker Hannifin Corporation analog controller (Model 23-7030). A PCB force sensor (Model 208C04) will be used to measure the damper force. The dynamic equations of the numerical substructure will be solved by a Speedgoat performance real-time target machine. The Speedgoat machine will also provide displacement commands to the servo-hydraulic actuator system. A Data Physics SignalCalc Mobilyzer dynamic signal analyzer will be used to collect numerical and physical data and compute the signal power spectral densities, frequency response functions, and coherence functions automatically.

References

1. Blakeborough, A., Williams, M.S., Darby, A.P., Williams, D.M.: The development of real-time substructure testing. *Philos. Trans. R. Soc. A Math. Phys. Eng. Sci.* **359**(1786), 1869–1891 (2001)
2. Abbiati, G., Schöbi, R., Sudret, B., Stojadinovic, B.: Structural reliability analysis using deterministic hybrid simulations and adaptive kriging metamodeling. In: 16th World Conference on Earthquake Engineering, paper no. 595 (2017)
3. Ligeikis, C., Freeman, A., Christenson, R.: Assessing structural reliability at the component test stage using real-time hybrid substructuring. In: 36th International Modal Analysis Conference (2018)
4. Kwok, N.M., Ha, Q.P., Nguyen, T.H., Li, J., Samali, B.: A novel hysteretic model for magnetorheological fluid dampers and parameter identification using particle swarm optimization. *Sensors Actuators A Phys.* **132**(2), 441–451 (2006)
5. Yaghoubi, V., Marelli, S., Sudret, B., Abrahamsson, T.: Sparse polynomial chaos expansions of frequency response functions using stochastic frequency transformation. *Probab. Eng. Mech.* **48**, 39–58 (2017)
6. Marelli, S., Sudret, B.: UQLab: A framework for uncertainty quantification in Matlab. In: 2nd International Conference on Vulnerability, Risk Analysis and Management (ICVRAM2014), pp. 2554–2563 (2014)



Chapter 28

Applying Uncertainty Quantification to Structural Systems: Parameter Reduction for Evaluating Model Complexity

Robert Locke, Shyla Kupis, Christopher M. Gehb, Roland Platz, and Sez Atamturktur

Abstract Different mathematical models can be developed to represent the dynamic behavior of structural systems and assess properties, such as risk of failure and reliability. Selecting an adequate model requires choosing a model of sufficient complexity to accurately capture the output responses under various operational conditions. However, as model complexity increases, the functional relationship between input parameters varies and the number of parameters required to represent the physical system increases, reducing computational efficiency and increasing modeling difficulty. The process of model selection is further exacerbated by uncertainty introduced from input parameters, noise in experimental measurements, numerical solutions, and model form. The purpose of this research is to evaluate the acceptable level of uncertainty that can be present within numerical models, while reliably capturing the fundamental physics of a subject system. However, before uncertainty quantification can be performed, a sensitivity analysis study is required to prevent numerical ill-conditioning from parameters that contribute insignificant variability to the output response features of interest. The main focus of this paper, therefore, is to employ sensitivity analysis tools on models to remove low sensitivity parameters from the calibration space. The subject system in this study is a modular spring-damper system integrated into a space truss structure. Six different cases of increasing complexity are derived from a mathematical model designed from a two-degree of freedom (2DOF) mass spring-damper that neglects single truss properties, such as geometry and truss member material properties. Model sensitivity analysis is performed using the Analysis of Variation (ANOVA) and the Coefficient of Determination R^2 . The global sensitivity results for the parameters in each 2DOF case are determined from the R^2 calculation and compared in performance to evaluate levels of parameter contribution. Parameters with a weighted R^2 value less than .02 account for less than 2% of the variation in the output responses and are removed from the calibration space. This paper concludes with an outlook on implementing Bayesian inference methodologies, delayed-acceptance single-component adaptive Metropolis (DA-SCAM) algorithm and Gaussian Process Models for Simulation Analysis (GPM/SA), to select the most representative mathematical model and set of input parameters that best characterize the system's dynamic behavior.

Keywords Sensitivity analysis · Analysis of variation · Uncertainty quantification · Bayesian inference · MCMC

28.1 Introduction

The field of structural dynamics requires mathematical models to simulate the static and dynamic behaviors of engineered systems under an assortment of loading and boundary conditions. Simulated responses can assess the structural stability and health of a system, or they can evaluate a system's performance for untested operational and environmental conditions. This methodology helps support high consequence decision making that affects public policy, safety and national security

R. Locke (✉)
Clemson University, Glenn Department of Civil Engineering, Clemson, SC, USA
e-mail: wrlocke@g.clemson.edu

S. Kupis
Clemson University, Department of Environmental Engineering and Earth Sciences, Clemson, SC, USA

C. M. Gehb
Technische Universität Darmstadt, System Reliability, Adaptive Structures, and Machine Acoustics SAM, Darmstadt, Germany

R. Platz
Fraunhofer Institute for Structural Durability and System Reliability LBF, Darmstadt, Germany

S. Atamturktur
Penn State, Department of Architectural Engineering, University Park, PA, USA

procedures [1]. However, a fundamental divide exists between physical systems and numerical solutions to mathematical models from the uncertainty introduced from the design stage, manufacturing processes, and material variability; this uncertainty is classified as aleatory or irreducible uncertainty [2, 3]. This theoretical chasm is further worsened from uncertainty introduced by the surrounding environment (experimental uncertainty), inaccurate solutions to differential equations (numerical uncertainty), the unknown value and variability of parameters (parameter uncertainty), and poor engineering judgment (bias error) [3]. If this uncertainty is left unaccounted, the accuracy of predicted results can drastically decrease and lead to ill-informed decision making. Verification and validation (V&V) studies, therefore, must be performed to evaluate the uncertainty in these predictive models.

This paper will investigate a structural system composed of a coupled modular active spring-damper system and space truss (German acronym MAFDS). The MAFDS was developed in the collaborative research center SFB 805 “Control of Uncertainty in Load-Carrying Structures in Mechanical Engineering” at the Technische Universität Darmstadt, its general functionality is comparable to the front landing gear of an aircraft. The main goal of the MAFDS is to study uncertainty in dynamic stability, vibration behavior, and load distribution, and, eventually, to find ways to control or compensate uncertainty with different measures (e.g. active vibration control technology). The test rig of the MAFDS, as shown in Fig. 28.1, is subjected to a variety of loading and boundary conditions to monitor the impact they have on the uncertainty from stability, strength and vibrational behavior [4]. In this contribution, the MAFDS has been evaluated during the process of model selection and validation to quantify uncertainty in the dynamic outputs from Fig. 28.2 for different sets of inputs. An idealized two-degree-of-freedom (2DOF) model, as shown in Fig. 28.4, was implemented to characterize the mechanics and physics of the spring-damper system only, neglecting single truss properties (e.g. truss geometry and member material properties). The 2DOF model was then solved for the dynamic outputs in Fig. 28.2 using the average acceleration Newmark- β method with numerical integration techniques that minimize numerical uncertainty from a conditionally stable step size and, hence, improved the numerical solutions [5]. Experimental uncertainty was also reduced significantly by correctly calibrating the sensors prior to performing tests under controlled environmental conditions.

The primary focus of this research is to investigate parameter uncertainty and bias error, commonly referred to as model-form uncertainty, introduced by assumptions about model complexity [6, 7]. As model complexity increases, the functional relationship between input parameters (e.g. linear or nonlinear) varies and the number of parameters required to represent a physical system increases. Increasing model complexity reduces the uncertainty associated with output response features due to the modeling form, but also increases response uncertainty due to a lack of knowledge of the input parameters [8]. The inherent difficulty in this problem is identifying what levels of model-form and parameter uncertainty can be included within a model while still capturing the fundamental physics and providing reliable results. Minimizing model-form and parameter uncertainty of multiple models requires addressing under what conditions and circumstances a simple model will reproduce outputs from the MAFDS compared to a more complex model [4]. Thus, the difficulty in predictive modeling is constructing

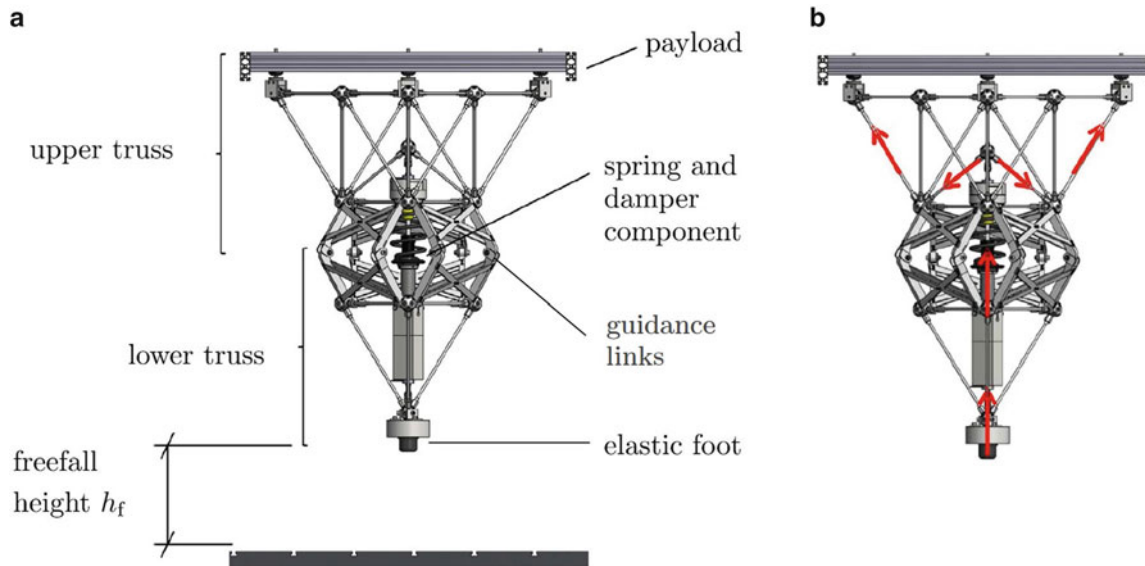


Fig. 28.1 The structural design in (a) displays components of the MAFDS, and (b) demonstrates how the load path will be distributed after a free fall drop test

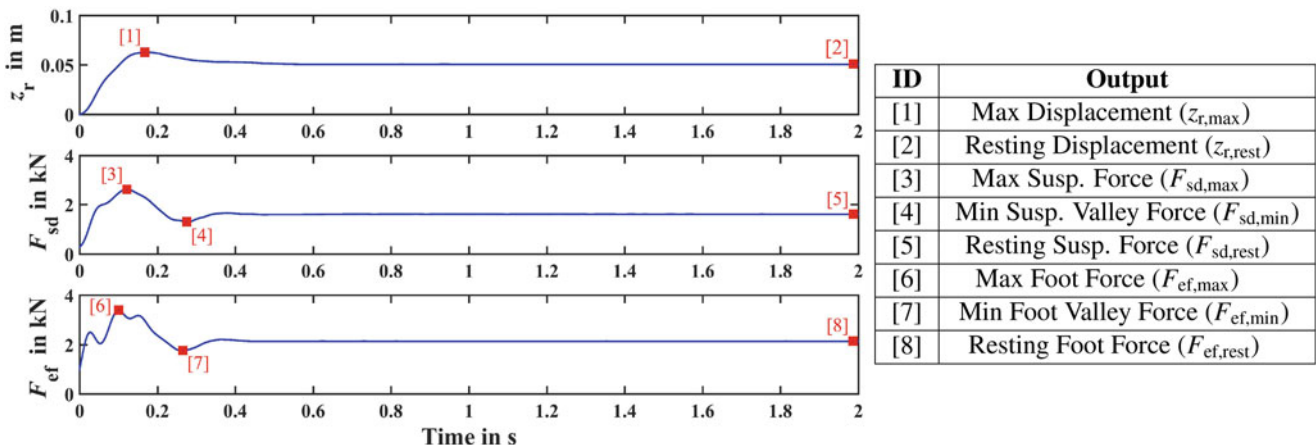


Fig. 28.2 Dynamic outputs of interest from the MAFDS. Left: The top image shows the average relative displacement z_r over time; the middle image shows the force F_{sd} measured at the upper force sensor over time; and the bottom image shows the force F_{ef} measured at the elastic foot over time. Right: Outputs associated with IDs in Left images

a simple mathematical representation that can reduce computational time of more complex models while capturing the governing physics and mechanics of the system. In this study, there are three unique cases for modeling suspension stiffness and two unique cases for modeling the damping force for a total of six 2DOF cases (refer to Table 28.5). These cases have been developed to reproduce the static and dynamic outputs of the MAFDS with varying levels of complexity, similar to [4]. The quantify uncertainty from their simulated outputs, evaluate model-form uncertainty, and, the main goal, to determine which input parameters need to be calibrated in order to capture the data's variability for each 2DOF case.

In this paper, a sensitivity analysis study was performed to determine which input variables contributed the least to the variability of output responses and could be removed of the calibration space, or, in other words, which inputs could be held constant during inversion of the 2DOF MAFDS mathematical model. A statistical screening method that utilized The Analysis of Variation (ANOVA) and the Coefficient of Determination R^2 was employed to evaluate each set of input variables from the six 2DOF cases for their contribution to the variability in the output response features. The weighted R^2 value for each set of parameters were compared against each other, and inputs with a R^2 less than 0.02 were identified as having low sensitivity. This form of parameter reduction is expected to improve parameter estimation for the six 2DOF cases, reduce model-form uncertainty, and ameliorate computational efforts.

28.2 Modular Active Spring-Damper System Description

The MAFDS, as seen in Fig. 28.1, is a large-scale suspension strut system, analogous to an aircraft landing gear, that consists of: an upper space truss structure and added payload; a suspension system with both stiffness and damping components; a lower space truss structure; guidance links that enable kinematic motion between the lower and upper space trusses; an elastic foot with both stiffness and damping components; and a user-specified drop height h_f . The purpose of the MAFDS is not to serve as an aircraft landing gear, but rather as an academic devise to study, in a general sense, the uncertainty in a suspension strut's dynamic outputs [4]. In this paper, there are a total of eight outputs of interest, these are identified by Fig. 28.2. These outputs are calculated using data from the displacement and force sensors shown in Fig. 28.3. The displacement sensors operate under the linear displacement variable transformer (LVDT) principle, while the elastic foot and suspension forces are recorded using a three axial strain gauge and a single axial strain gauge, respectively.

In this study, the MAFDS is represented numerically by an equivalent 2DOF model, Fig. 28.4 indicates the MAFDS components and the free body force diagram for this model. In the 2DOF system, the upper and lower space trusses are idealized as two lumped masses with an upper mass m_u and a lower mass m_l . The mass values for the 2DOF system were determined to be 180 kg and 40 kg, respectively. The suspension system is represented by a spring with stiffness k_s and a dash-pot with viscous damping b_s . The elastic foot is also represented by a spring with stiffness k_{ef} and a dash-pot with damping b_{ef} . Additionally, as indicated in Fig. 28.4, the upper and lower masses have a degree-of-freedom associated with local translational displacements, z_u and z_l , respectively. The six 2DOF cases represent the stiffness and damping forces of the 2DOF mathematical model with varying functional relationships and number of parameters, or, in other words,

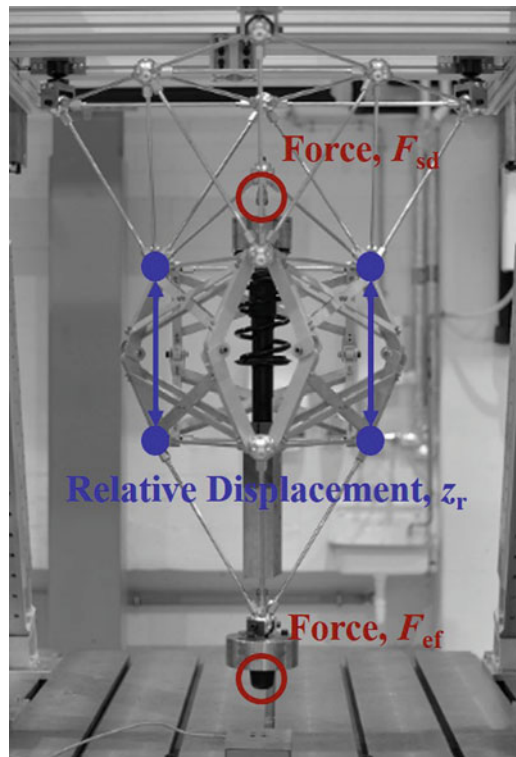


Fig. 28.3 Location of MAFDS force, F_{sd} and F_{ef} , and relative displacement, z_r , sensors

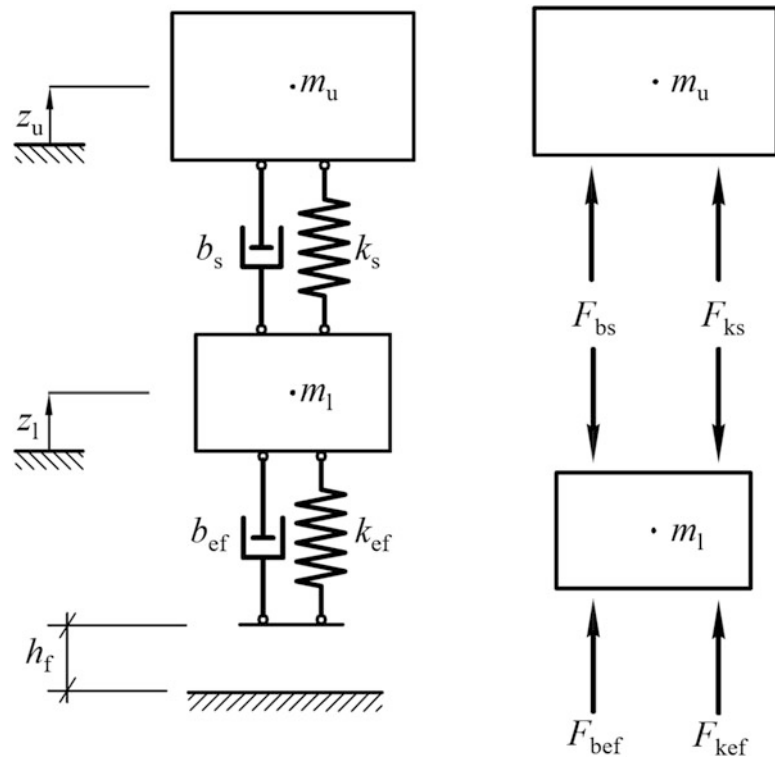


Fig. 28.4 Equivalent 2DOF MAFDS model

differing levels of complexity. These cases serve the purpose of assessing what degree of model complexity is required to effectively represent the MAFDS in the 2DOF mathematical model. The system is assumed to be subjected to a free and full homogeneous field of gravitational acceleration g . When dropped from a height h_f , the initial time step t measurement does not occur until right before the system hits the ground, meaning the initial displacements, $z_u(t)$, $z_l(t)$, and velocities, $\dot{z}_u(t)$, $\dot{z}_l(t)$, at time $t = 0$ are:

$$z_u(0) = z_l(0) = 0, \dot{z}_u(0) = \dot{z}_l(0) = \sqrt{2gh_f}. \quad (28.1)$$

The dynamic outputs of interest, as indicated in Fig. 28.4 are calculated using the equations below.

Relative Displacements z_r $z_{r,\max} = \max z_u - z_l $ $z_{r,\min} = (z_{u,\text{end}} - z_{l,\text{end}}), t = t_{\text{end}}$	Suspension Forces F_{sd} $F_{sd,\max} = \max F_{k_s} + F_{b_s} $ $F_{sd,\min} = \min F_{k_s} + F_{b_s} , t_{\max} < t \leq t_{\text{end}}$ $F_{sd,\text{rest}} = F_{k_s} + F_{b_s}, t = t_{\text{end}}$	Elastic Foot Forces F_{ef} $F_{ef,\max} = \max F_{k_{ef}} + F_{b_{ef}} $ $F_{ef,\min} = \min F_{k_{ef}} + F_{b_{ef}} , t_{\max} < t \leq t_{\text{end}}$ $F_{ef,\text{rest}} = F_{k_{ef}} + F_{b_{ef}}, t = t_{\text{end}}$
--	--	--

(28.2)

The stiffness F_{ks} and damping F_{bs} forces are calculated by Mallapur and Platz [9]:

Suspension $F_{ks} = k_s(z_u - z_l) = k_s z_r$ $F_{bs} = b_s(\dot{z}_u - \dot{z}_l) = b_s \dot{z}_r$	Elastic Foot $F_{kef} = k_{ef} z_l$ $F_{bef} = b_{ef} \dot{z}_l$
---	---

(28.3)

28.3 Stiffness Regression Models

Before creating a variety of different mathematical models to represent the behavior of the entire MAFDS, data from the static system first had to be obtained to model the stiffness behavior of the suspension system. In this study, a series of static tests were performed by increasing the added payload from 0 to 200 kg in increments of 10 kg. During each incremental increase, measurements for the upper force F_{sd} and relative displacements z_r were recorded using the sensors illustrated in Fig. 28.3. For each test, the recorded force was divided by the average relative displacement to calculate the suspension system's stiffness.

Figure 28.5a displays the relation between the measured force F_{sd} and relative displacements z_r . The resulting $F_{ks}(z_r)$ curve indicates that the linear relationship between force and relative displacement transitions when z_r is approximately 0.068 m. This bi-linear relationship, also observed in previous studies [4, 9], indicates there are two potential slope values

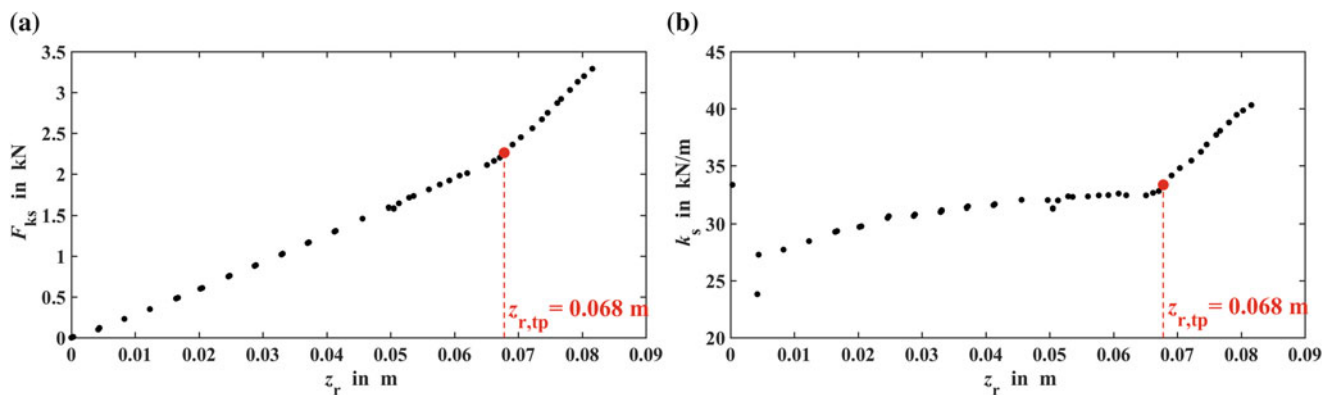


Fig. 28.5 Experimental stiffness (a) force and (b) coefficient curves of the spring-damper system

that can describe the stiffness behavior of the system. On the contrary, Fig. 28.5b indicates that the upper suspension stiffness varies non-linearly with the relative displacement, and, as a result, there are more than two potential values for modeling the system. It was determined that this nonlinear behavior was not observed in the previous studies [4, 9] as a result of biased data produced from improper sensor calibration, and because of this, new suspension stiffness models needed to be developed. Three new independent models of varying complexity were fitted to the stiffness coefficient curve to address the linearity-nonlinearity discrepancy: (1) the most simple model was a piecewise function composed of two linear polynomials; (2) the intermediate model was a cubic polynomial; and (3) the most complex model was a piecewise function composed of two power functions. The following subsections discuss how each method in (1)–(3) was developed.

28.3.1 Piecewise Linear Polynomials

The first and most simple stiffness case was fit to the experimental data in Fig. 28.5b with a piecewise function composed of two linear polynomials. The function is founded on the assumption that the stiffness curve varies bi-linearly with relative displacement at the transition point $z_{r,tp}$ when $z_r \in [0 \text{ m}, 0.068 \text{ m}]$ and $z_r \in [0.068 \text{ m}, 0.082 \text{ m}]$. Each polynomial consisted of two unknown coefficients, which resulted in a total of four unknown stiffness coefficients. The transition point $z_{r,tp}$ is the location where the rate of change in the stiffness coefficient curve increases and is used to derive the fitted suspension stiffness $\hat{k}_{s,a}(z_r)$ as a function of relative displacement z_r in Eq. (28.4).

$$\hat{k}_{s,a}(z_r) = \begin{cases} a_{0,1} + a_{1,1}z_r, & z_r \leq 0.068 \text{ m} \\ a_{0,2} + a_{1,2}z_r, & z_r > 0.068 \text{ m} \end{cases} \quad (28.4)$$

To determine the values for the coefficients in Eq. (28.4), the data in Fig. 28.5b was divided at the transition point $z_{r,tp}$ and a linear regression analysis was performed on each individual set of data. Table 28.1 indicates the calculated mean and standard deviation for each of the subject parameters.

28.3.2 Cubic Polynomial

For the second stiffness case, the complexity of the regression increased as the model form changed from linear polynomials to a third order polynomial. Model complexity did not increase from the number of unknown variables that had to be solved, but rather from the assumption that the stiffness coefficient curve is continuously smooth and nonlinear. Similar to the piecewise linear polynomials case, the cubic polynomial case had a total of four unknown coefficients from fitting a third order polynomial to the stiffness coefficient data. The fitted model $\hat{k}_{s,b}(z_r)$ is developed in Eq. (28.5).

$$\hat{k}_{s,b}(z_r) = b_0 + b_1z_r + b_2z_r^2 + b_3z_r^3 \quad (28.5)$$

Similar to the piecewise linear polynomials case, the mean and standard deviation values for the cubic polynomials were calculated by performing a polynomial regression analysis on the experimental data in Fig. 28.5b. Table 28.2 indicates the mean and standard deviation for each of the cubic polynomial parameters in Eq. (28.5).

Table 28.1 Piecewise first-order polynomial stiffness coefficients, $\hat{k}_{s,a}(z_r)$

Polynomial coefficients	Mean	Standard deviation
$a_{0,1}$, in $\frac{\text{kN}}{\text{m}}$	28	0.50
$a_{1,1}$, in $\frac{\text{kN}}{\text{m}^2}$	73	11.56
$a_{0,2}$, in $\frac{\text{kN}}{\text{m}}$	-1.58	0.95
$a_{1,2}$, in $\frac{\text{kN}}{\text{m}^2}$	516	12.50

Table 28.2 Cubic polynomial stiffness coefficients, $\hat{k}_{s,b}(z_r)$

Polynomial coefficients	Mean	Standard deviation
b_0 , in $\frac{\text{kN}}{\text{m}}$	23	0.52
b_1 , in $\frac{\text{kN}}{\text{m}^2}$	601	48
b_2 , in $\frac{\text{kN}}{\text{m}^3}$	$-1.49e+04$	$1.25e+03$
b_3 , in $\frac{\text{kN}}{\text{m}^4}$	$1.24e+05$	$9.45e+03$

Table 28.3 Piecewise power function stiffness coefficients, $\hat{k}_{s,c}(z_r)$

Polynomial coefficients	Mean	Standard deviation
$c_{0,1}$, in $\frac{\text{kN}}{\text{m}}$	6.55	0.33
$c_{1,1}$, in $\frac{\text{kN}}{\text{m}^2}$	17	0.42
$c_{2,1}$, unitless	0.10	$2.50e-03$
$c_{0,2}$, in $\frac{\text{kN}}{\text{m}}$	4.43	0.13
$c_{1,2}$, in $\frac{\text{kN}}{\text{m}^2}$	0.19	$4.83e-03$
$c_{2,2}$, unitless	1.19	$3.70e-03$

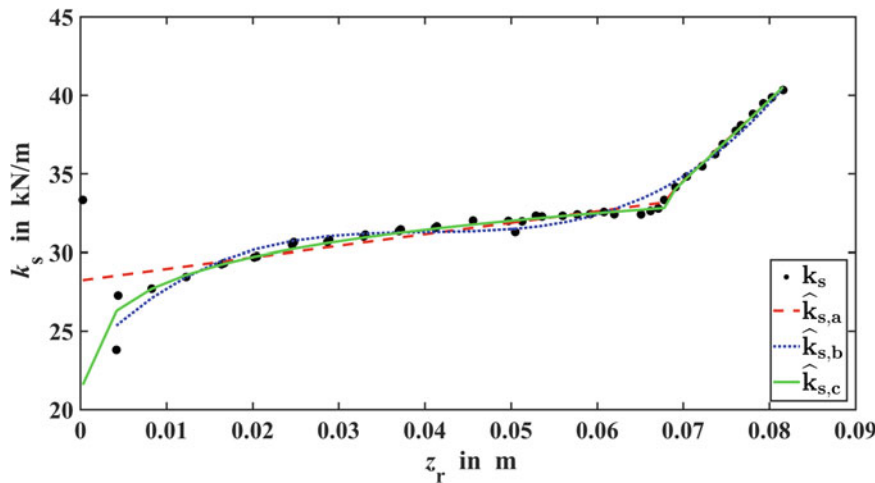


Fig. 28.6 Three fitted regression model to stiffness coefficient data when $z_r \leq z_{r,tp}$ and $z_r > z_{r,tp}$

28.3.3 Piecewise Power Functions

The third stiffness model is the final and most complex case, consisting of a piecewise function composed of two power functions and a total of six unknown stiffness coefficients. The fitted model $\hat{k}_{s,c}(z_r)$ is developed in Eq. (28.6), and again, the mean and standard deviations of the parameters were calculated through a regression analysis of the data in Fig. 28.5b. Table 28.3 indicates the values for each coefficient in Eq. (28.6). During the regression analysis, the power functions had the lowest residual error of all three stiffness model cases, which strongly implies that the suspension stiffness data behaved most like a power function.

$$\hat{k}_{s,c}(z_r) = \begin{cases} c_{0,1} + c_{1,1}z_r^{c_{2,1}}, & z_r \leq 0.068 \text{ m} \\ c_{0,2} + c_{1,2}z_r^{c_{2,2}}, & z_r > 0.068 \text{ m} \end{cases} \quad (28.6)$$

The results in Fig. 28.6 shows how well the three regression models fit the experimental stiffness coefficient data before and after the transition point $z_{r,tp} = 0.068$ m. Initially, the first piecewise power function and the third-order polynomial underestimate the stiffness coefficient data when z_r is approximately less than 0.018 m. The first piecewise linear polynomial, however, overestimates the stiffness coefficient data when $z_r < 0.018$ m. Once $z_r \geq 0.018$ m, the third-order polynomial overestimates the data while the first piecewise linear polynomial underestimates when $z_r \in [0.018 \text{ m}, 0.048 \text{ m}]$. From $z_r \in [0.048 \text{ m}, 0.082 \text{ m}]$, all models closely approximate the stiffness data before and after the transition point $z_{r, tp}$.

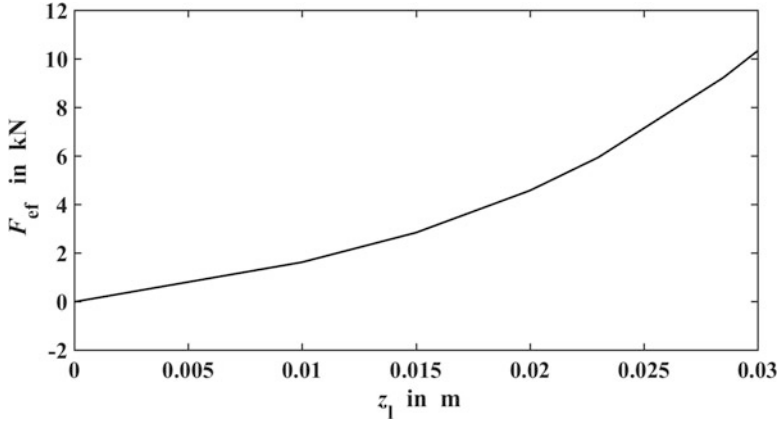


Fig. 28.7 Elastic foot force curve from manufacturer's data

Table 28.4 Elastic foot stiffness coefficients, $k_{ef}(z_1)$

Polynomial coefficients	Mean
d_0 , in $\frac{\text{kN}}{\text{m}}$	148
d_1 , in $\frac{\text{kN}}{\text{m}^2}$	-1717
d_2 , in $\frac{\text{kN}}{\text{m}^3}$	$7.45e+5$

28.3.4 Elastic Foot Stiffness

To reduce the number of unknown calibration parameters, and because the manufacturer provided the stiffness force versus displacement data, the stiffness coefficients for the elastic foot were treated as known parameters [10]. The coefficient values were calculated by taking the derivative of the force versus displacement curve seen in Fig. 28.7, Eq. (28.7) displays the resulting equation for $k_{ef}(z_1)$. Table 28.4 indicates the stiffness coefficient values for $k_{ef}(z_1)$.

$$k_{ef}(z_1) = d_0 + d_1 z_1 + d_2 z_1^2 \quad (28.7)$$

28.4 Damping Regression Models

To determine the damping coefficient b_s of the suspension system, a series of 35 dynamic tests were performed by varying the drop height between 0 and 0.1 m and the added payload between 0 and 100 kg. Similar to the static tests, total force F_{sd} and relative displacement z_r measurements were recorded using the upper suspension force sensor and the displacement sensors illustrated in Fig. 28.3. For each test, the damping force F_{bs} was computed by taking the difference between the total measured force F_{sd} , and the stiffness force \hat{F}_{ks} fitted to each stiffness case (see Eq. (28.8)). Figure 28.8 provides a purely figurative example to illustrate how a damping force curve is developed from the combination of 35 experimental drop tests. As can be seen in Fig. 28.8, a characteristic hysteresis curve is formed, which is assumed to be attributable to the compressibility of oil and/or cavitation within the suspension [11, 12]. In this study, these effects are ignored, and single curve models are fitted to the experimental data via regression analysis to “average” out the effect of hysteresis.

$$\hat{b}_s(\dot{z}_r) = \frac{\hat{F}_{bs}}{\dot{z}_r} = \frac{F_{sd} - \hat{F}_{ks}}{\dot{z}_r} \quad (28.8)$$

Two different cases of varying model complexity were used to model the relationship between the damping force F_{bs} versus relative velocity \dot{z}_r , which are a (1) piecewise function with two linear polynomials, $\hat{F}_{bs,d}$, and (2) cubic polynomial, $\hat{F}_{bs,e}$. All together, there are a total of six 2DOF cases that vary in complexity for modeling suspension stiffness and damping (refer to Table 28.5). The following three subsections further discuss the development of each damping case with respect to its subject stiffness case.

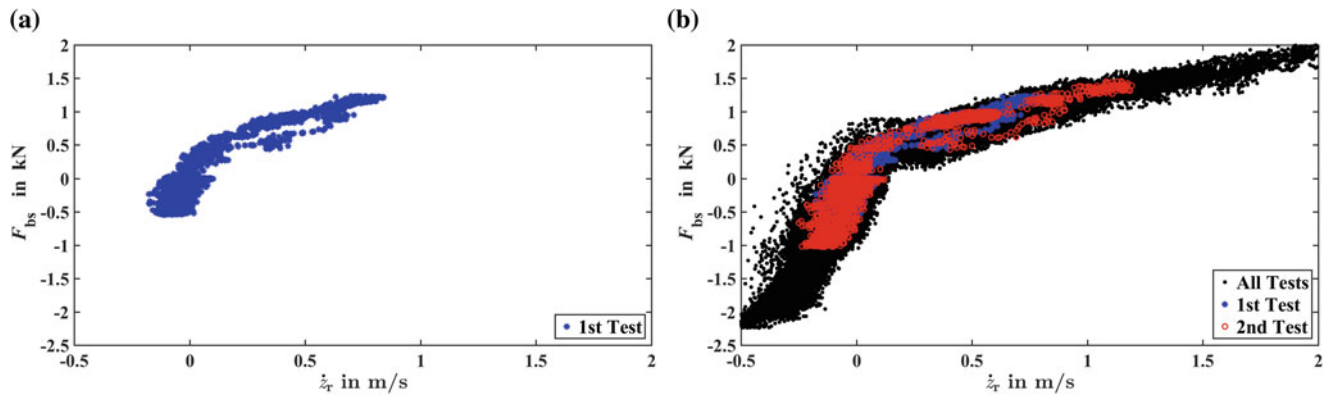


Fig. 28.8 An illustrative example showing the development of the experimental damping force curve of the suspension strut system for (a) one and (b) all thirty-five experimental drop tests

Table 28.5 Cases for suspension stiffness and damping force curves

	2-Piecewise damping, $\hat{F}_{bs,d}$	Third order damping, $\hat{F}_{bs,e}$
2-Piecewise stiffness, $\hat{F}_{ks,a}$	Case 1	Case 2
Third order stiffness, $\hat{F}_{ks,b}$	Case 3	Case 4
Power 2-piecewise stiffness, $\hat{F}_{ks,c}$	Case 5	Case 6

Table 28.6 Piecewise first-order polynomial damping coefficients, $\hat{b}_{s,d}(\dot{z}_r)$

Polynomial coefficients	Mean	Standard deviation	Polynomial coefficients	Mean	Standard deviation	Polynomial coefficients	Mean	Standard deviation
<i>Case 1</i>			<i>Case 3</i>			<i>Case 5</i>		
$m_{1,1}^{(a)}$, in $\frac{kNs}{m}$	4.81	$4.50e-02$	$m_{1,1}^{(b)}$, in $\frac{kNs}{m}$	4.92	$4.82e-02$	$m_{1,1}^{(c)}$, in $\frac{kNs}{m}$	4.86	$4.39e-02$
$m_{1,2}^{(a)}$, in $\frac{kNs}{m}$	1.09	$1.88e-02$	$m_{1,2}^{(b)}$, in $\frac{kNs}{m}$	1.08	$1.93e-02$	$m_{1,2}^{(c)}$, in $\frac{kNs}{m}$	1.08	$1.83e-02$

28.4.1 Piecewise Linear Polynomials

The first case for modeling damping involved fitting two linear polynomials in Eq. (28.9a) to the damping force data F_{bs} at the transition point $\dot{z}_r = 0 \frac{m}{s}$. This is the simplest case because it assumes damping does not exhibit hysteretic behavior, and changes linearly at different rates when $\dot{z}_r < 0 \frac{m}{s}$ and $\dot{z}_r \geq 0 \frac{m}{s}$. There are two unknown polynomial coefficients, which are the slopes of the first-order polynomials in Eq. (28.9a). Because the damping force should be zero at $\dot{z}_r = 0 \frac{m}{s}$, it was assumed that the intercepts $m_{0,1}^{(j)}, m_{0,2}^{(j)} = 0$, $j = a, b, c$ for all stiffness cases. In other words, by taking the first derivative of $F_{bs,d}(\dot{z}_r)$, the damping coefficients $b_{s,d}(\dot{z}_r)$ of the system in Eq. (28.9b) can be calculated from Eq. (28.9a).

$$\hat{F}_{bs,d}^{(j)}(\dot{z}_r) = \begin{cases} m_{0,1}^{(j)} + m_{1,1}^{(j)}\dot{z}_r, & \dot{z}_r < 0 \frac{m}{s} \\ m_{0,2}^{(j)} + m_{1,2}^{(j)}\dot{z}_r, & \dot{z}_r \geq 0 \frac{m}{s} \end{cases} \quad j = a, b, c \quad (28.9a)$$

$$\hat{b}_{s,d}^{(j)}(\dot{z}_r) = \begin{cases} m_{1,1}^{(j)}, & \dot{z}_r < 0 \frac{m}{s} \\ m_{1,2}^{(j)}, & \dot{z}_r \geq 0 \frac{m}{s} \end{cases} \quad j = a, b, c \quad (28.9b)$$

Table 28.6 displays the mean values for $m_{1,1}^{(j)}, m_{1,2}^{(j)}$, $j = a, b, c$ and their standard deviations that were used to construct $\hat{b}_{s,d}(\dot{z}_r)$.

Table 28.7 Cubic polynomial damping coefficients, $\hat{b}_{s,e}(\dot{z}_r)$

Polynomial coefficients	Mean	Standard deviation	Polynomial coefficients	Mean	Standard deviation	Polynomial coefficients	Mean	Standard deviation
<i>Case 2</i>			<i>Case 4</i>			<i>Case 6</i>		
$v_{1,1}^{(a)}$, in $\frac{kNs}{m}$	3.05	$2.08e-02$	$v_{1,1}^{(b)}$, in $\frac{kNs}{m}$	3.16	$2.25e-02$	$v_{1,1}^{(c)}$, in $\frac{kNs}{m}$	3.06	$2.07e-02$
$v_{2,1}^{(a)}$, in $\frac{kNs^2}{m^2}$	-2.62	$4.57e-02$	$v_{2,1}^{(b)}$, in $\frac{kNs^2}{m^2}$	-2.91	$4.95e-02$	$v_{2,1}^{(c)}$, in $\frac{kNs^2}{m^2}$	-2.66	$4.54e-02$
$v_{3,1}^{(a)}$, in $\frac{kNs^3}{m^3}$	0.89	$2.60e-02$	$v_{3,1}^{(b)}$, in $\frac{kNs^3}{m^3}$	1.03	$2.81e-02$	$v_{3,1}^{(c)}$, in $\frac{kNs^3}{m^3}$	0.91	$2.58e-02$

28.4.2 Cubic Polynomial

For the second damping case, the complexity of the system increased as the model form changed from linear polynomials to a third order polynomial. A third order polynomial $\hat{F}_{bs,e}(\dot{z}_r)$ was selected for the nonlinear damping coefficient curve because it was better at capturing the transient behavior with a smoothly varying curve from $\dot{z}_r < 0 \frac{m}{s}$ to $\dot{z}_r \geq 0 \frac{m}{s}$. A total of four unknown polynomial coefficients must be optimized to fit a curve $\hat{F}_{bs,e}(\dot{z}_r)$ to $F_{bs}(\dot{z}_r)$ in Eq. (28.10a). The intercept parameter $v_{0,1}^{(j)}$, $j = a, b, c$, however, was assumed to be zero based on the assumption that the damping force should be zero at $\dot{z}_r = 0 \frac{m}{s}$. Table 28.7 displays the mean values for $v_{1,1}^{(j)}$, $v_{2,1}^{(j)}$, $v_{3,1}^{(j)}$, $j = a, b, c$ and their standard deviations that were used to construct $\hat{b}_{s,e}(\dot{z}_r)$.

$$\hat{F}_{bs,e}^{(j)}(\dot{z}_r) = v_{0,1}^{(j)} + v_{1,1}^{(j)}\dot{z}_r + v_{2,1}^{(j)}\dot{z}_r^2 + v_{3,1}^{(j)}\dot{z}_r^3, \quad j = a, b, c \quad (28.10a)$$

$$\hat{b}_{s,e}^{(j)}(\dot{z}_r) = v_{1,1}^{(j)} + 2v_{2,1}^{(j)}\dot{z}_r + 3v_{3,1}^{(j)}\dot{z}_r^2, \quad j = a, b, c \quad (28.10b)$$

The six damping models for each test case are the damping force plotted against the relative velocity in Fig. 28.9a–c. These results display $\hat{F}_{bs}(\dot{z}_r)$ from the two damping cases, $\hat{F}_{bs,d}^{(j)}$ and $\hat{F}_{bs,e}^{(j)}$, $j = a, b, c$, which were derived from the stiffness cases $\hat{F}_{ks,a}$, $\hat{F}_{ks,b}$ and $\hat{F}_{ks,c}$.

28.4.3 Elastic Foot Damping

Because damping data was not provided by the elastic foot manufacturer, the damping coefficient \hat{b}_{ef} was assumed to be a constant viscous damping coefficient. The prior value for the damping coefficient \hat{b}_{ef} was approximated to follow a uniform probability distribution with values ranging from $0 \frac{Ns}{m}$ to $1000 \frac{Ns}{m}$.

28.5 Solving the Equation of Motion

Once the stiffness and damping properties were approximated for both the suspension and elastic foot for each of the regression cases in Table 28.5, they were indexed into the equation of motion for the 2DOF system,

$$[\mathbf{M}] \begin{Bmatrix} \ddot{z}_u \\ \ddot{z}_l \end{Bmatrix}_{t+\Delta t} + [\mathbf{B}] \begin{Bmatrix} \dot{z}_u \\ \dot{z}_l \end{Bmatrix}_{t+\Delta t} + [\mathbf{K}] \begin{Bmatrix} z_u \\ z_l \end{Bmatrix}_{t+\Delta t} = \{\mathbf{F}\}, \quad (28.11)$$

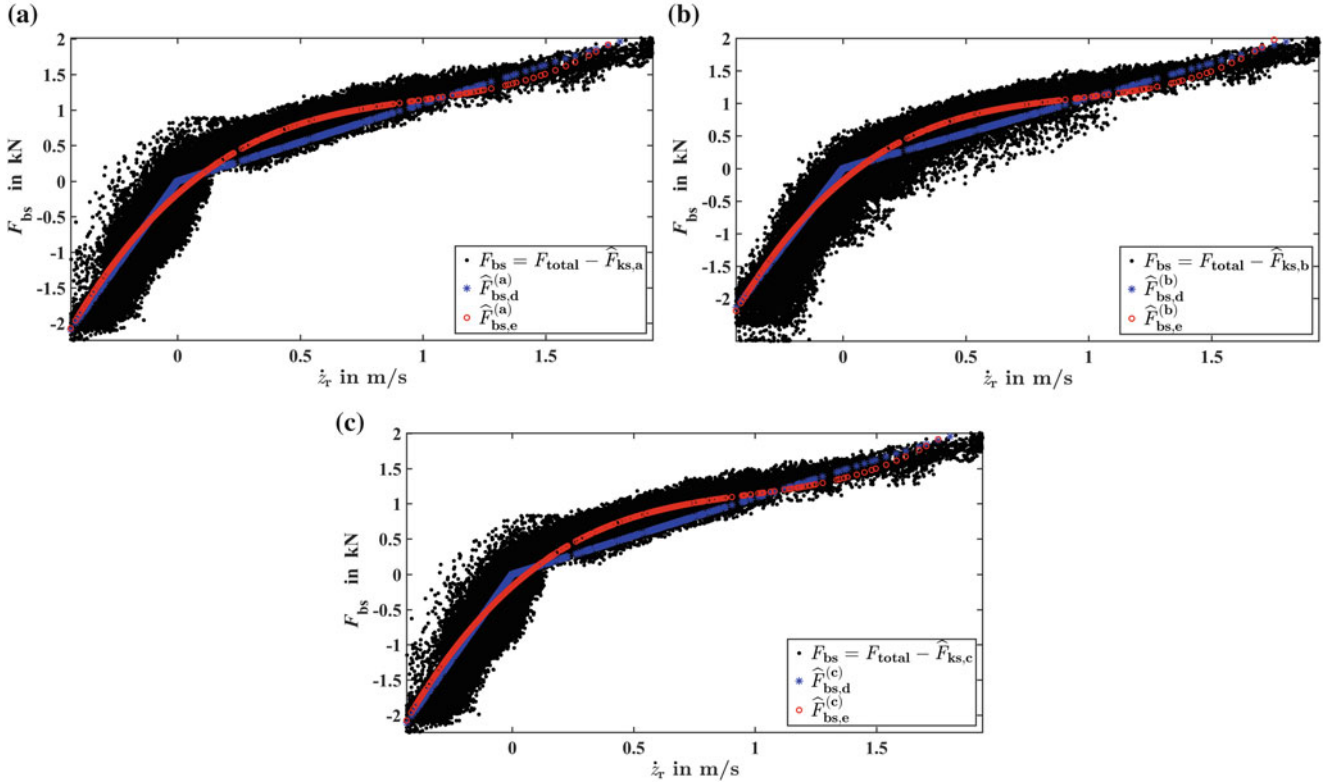


Fig. 28.9 Two damping models, $\widehat{F}_{bs,d}^{(j)}$ and $\widehat{F}_{bs,e}^{(j)}$, were fit to F_{bs} , and both models were calculated using the (a) piecewise linear polynomials $\widehat{F}_{ks,a}$ when $j = a$, (b) cubic polynomial $\widehat{F}_{ks,b}$ when $j = b$, and (c) piecewise power functions $\widehat{F}_{ks,c}$ when $j = c$

where $[\mathbf{M}]$, $[\mathbf{B}]$, $[\mathbf{K}]$, and $\{\mathbf{F}\}$ are the mass matrix, damping matrix, stiffness matrix, and force vector, respectively. The mass, damping, and stiffness matrices and force vector were composed, such that

$$\mathbf{M} = \begin{bmatrix} m_u & 0 \\ 0 & m_l \end{bmatrix} \quad \mathbf{B} = \begin{bmatrix} \widehat{b}_s(\dot{z}_r) & -\widehat{b}_s(\ddot{z}_r) \\ -\widehat{b}_s(\dot{z}_r) & \widehat{b}_s(\dot{z}_r) + \widehat{b}_{ef} \end{bmatrix} \quad \mathbf{K} = \begin{bmatrix} \widehat{k}_s(z_r) & -\widehat{k}_s(z_r) \\ -\widehat{k}_s(z_r) & \widehat{k}_s(z_r) + k_{ef}(z_l) \end{bmatrix} \quad \{\mathbf{F}\} = \begin{cases} g(m_u + m_n) \\ gm_l \end{cases}, \quad (28.12)$$

where g represents the gravitational acceleration constant (i.e. $9.81 \frac{\text{m}}{\text{s}^2}$), and m_n represents the additional payload ranging between 0 and 100 kg added to the upper mass of the 2DOF system. The index $(t + \Delta t)$ in Eq. (28.11) indicates the future time step values for the acceleration $\{\ddot{z}\}$, velocity $\{\dot{z}\}$, and displacement $\{z\}$ vectors, which are unknown and must be solved using numerical integration.

In this study, Newmark- β numerical integration was leveraged to solve the 2DOF equation of motion in Eq. (28.11) and, therefore, the dynamic outputs of interest in Eq. (28.2). Because the initial conditions of the system are known (see Eq. (28.1)), the future time step value $(t + \Delta t)$ for the acceleration, velocity, and displacement vectors must be calculated. Equations (28.13)–(28.15) indicate how the future acceleration, velocity, and displacement vector values are calculated as a function of the present vector values.

$$\{\ddot{z}\}_{t+\Delta t} = e_0\{\Delta z\} - e_1\{\dot{z}\}_t - e_2\{\ddot{z}\}_t \quad (28.13)$$

$$\{\dot{z}\}_{t+\Delta t} = \{\dot{z}\}_t + e_3\{\ddot{z}\}_t + e_4\{\ddot{z}\}_{t+\Delta t} \quad (28.14)$$

$$\{z\}_{t+\Delta t} = \{z\}_t + \{\Delta z\} \quad (28.15)$$

Subscript t indicates the present vector values for acceleration, velocity, and displacement. The change in displacement from the present time step t to the future time step $(t + \Delta t)$ is represented by $\{\Delta z\}$. The parameters $e_0 - e_4$ are numerical integration constants; these values, and others, are determined using the equations below:

$$\begin{aligned} e_0 &= \frac{1}{\beta \Delta t^2} & e_1 &= \frac{1}{\beta \Delta t} & e_2 &= \frac{1}{2\beta} - 1 & e_3 &= (1 - \gamma) \Delta t \\ e_4 &= \gamma \Delta t & e_5 &= \frac{\gamma}{\beta t} & e_6 &= \frac{\gamma}{\beta} - 1 & e_7 &= \frac{\Delta t}{2} \left(\frac{\gamma}{\beta} - 2 \right). \end{aligned} \quad (28.16)$$

The parameters β and γ represent the variation in acceleration during the incremental time step Δt , and numerical or artificial damping introduced by discretization in the time domain, respectively. For this study, the average acceleration Newmark method was utilized, meaning $\beta = \frac{1}{4}$ and $\gamma = \frac{1}{2}$. As previously mentioned, the average acceleration method was ideal for this study because it is conditionally stable for any size time step, and provides accurate results for a “small enough” time step [5]. In this study the numerical time integration step was $\Delta t = 0.0005$ s.

Once the equations for the future acceleration, velocity, and displacement vectors were known, they were entered into Eq. (28.11) and matrix algebra was performed to solve for the unknown change in displacement $\{\Delta z\}$. Equation (28.17) indicates the new equation of motion derived to solve for $\{\Delta z\}$.

$$\{\Delta z\} = [\Psi]^{-1} \{q\}_t \quad (28.17)$$

$$[\Psi] = e_0 [\mathbf{M}] + e_5 [\mathbf{C}] + [\mathbf{K}] \quad (28.18)$$

$$\{q\}_t = \{\mathbf{F}\} + [\mathbf{M}] (e_1 \{\dot{z}\}_t + e_2 \{\ddot{z}\}_t) + [\mathbf{C}] (e_6 \{\dot{z}\}_t + e_7 \{\ddot{z}\}_t) - [\mathbf{K}] \{z\}_t \quad (28.19)$$

When the change in displacement $\{\Delta z\}$ was calculated in Eq. (28.17), it was entered back into Eqs. (28.13)–(28.15) to solve for the future acceleration, velocity, and displacement vector values. After these values were known, the integration process started over with the future time step $(t + \Delta t)$ now becoming the present time step t . This process was repeated until the system entered a steady state at a total simulation time of $t = 2$ s. During this process, the total suspension force F_{sd} and total foot force F_{ef} were calculated for each time step using the equations in Eqs. (28.2)–(28.3).

28.6 Uncertainty Quantification

28.6.1 Sensitivity Analysis

As mentioned, the primary focus of this research project was to investigate uncertainty in the six 2DOF cases that are mathematical representations of the MAFDS. The purpose of having multiple cases is to identify the minimum level of model complexity required to capture the governing physics and mechanics of the physical system in the dynamic outputs. Before solving this problem, however, it was necessary to first perform a sensitivity analysis on each model to identify the parameters that had the least impact on output response variations. In this study, sensitivity analysis methodologies were employed to identify parameters that contributed an insignificant variance to the output response features and eliminate them from the calibration space (i.e. hold at a constant mean value). Low sensitivity variables were eliminated from the calibration space to prevent numerical ill conditioning and to reduce computational costs associated with statistical inversion algorithms [3].

Analysis of Variation (ANOVA) and the Coefficient of Determination R^2 were utilized as statistical screening methodologies in this paper to evaluate the sensitivity of each coefficient in Sects. 28.3 and 28.4. The later R^2 value provided a measure for how varying an independent parameter between its L bounds affects the variability in the output response, which is expressed in Eq. (28.20) as

$$R_{p,n}^2 = 1 - \frac{\sum_{i=1}^L \sum_{j=1}^{L^{N-1}} (y_{p,ij} - \hat{y}_{p,i})^2}{\sum_{k=1}^{L^N} (y_{p,k} - \bar{y}_p)^2}, \quad (28.20)$$

where p is a vector from one to eight representing the response features of interest in Fig. 28.2, and n is a vector from $\{1, 2, \dots, N\}$ representing the parameters from a subject model. The overall mean value for a given response p is represented

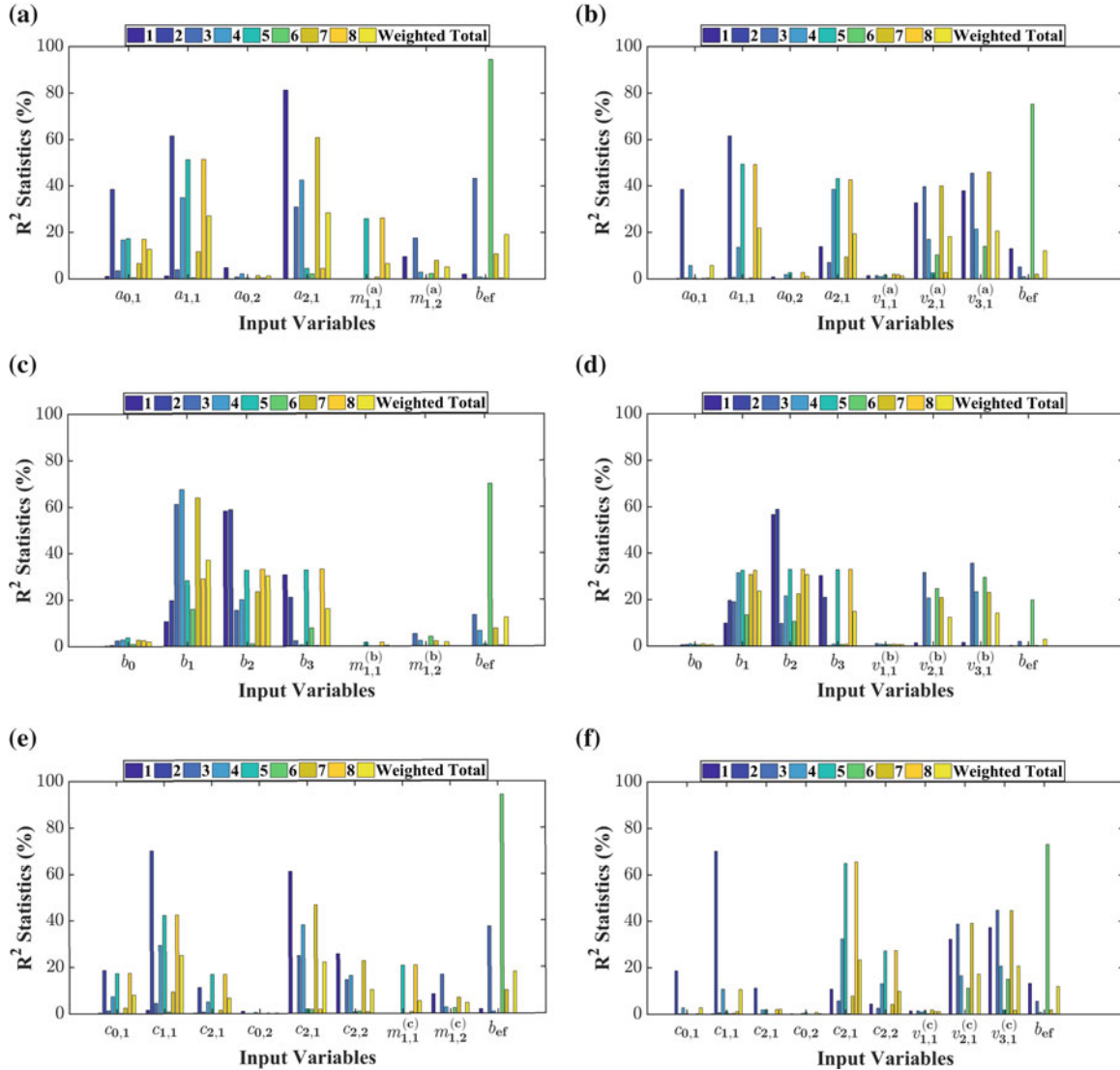


Fig. 28.10 The R^2 results from (a–f) for cases 1–6, respectively, and the colors labeled 1–8 represent the outputs from Fig. 28.2

by \bar{y}_p , while the mean response value for a given parameter level i is represented by $\hat{y}_{p,i}$. The full-factorial level L is used to evaluate the sensitivity of the response features to a given parameter. In this study, a two-level full-factorial design $L = 2$ was performed by sampling a single value at both the 2.5% lower and 97.5% upper limits from each variable's 95% confidence bound. The confidence bounds for each regression coefficient were calculated using the standard deviation values provided in Tables 28.2, 28.3, 28.6, and 28.7. As a result, this design frame has L^N numerical evaluations with a scaled output $R^2 \in [0, 100]$ provided for each of the eight response features. The value of R^2 was then used to evaluate if a parameter could be kept constant using its mean value or if it needed to vary based on R^2 . For example, $R^2 = 0$ indicated that a variable had negligible or no influence on the value of a selected response feature; whereas, a value of $R^2 = 100$ indicated that a variable contributed all of the variability to the selected response feature. For consistency, the additional payload m_n and drop height h_f were held constant for all full-factorial evaluations.

Figure 28.10 indicates the results for all the cases in Table 28.5. The columns presented in Fig. 28.10 indicate the R^2 sensitivity of all the response features to each set of parameters. As can be seen, each parameter for each case appears to have some influence on at least one of the subject outputs. To evaluate which parameters exhibited the least influence, a weighted total was calculated by taking the average R^2 for each parameter. If a parameter was found to have a weighted R^2 value of less than 2%, that parameter was considered to be non-influential and thrown out of the calibration space (i.e. held constant at its mean value). As can be seen in Table 28.8, each of the cases from Table 28.5 has at least one parameter that

Table 28.8 Average R^2 value

Param	Case 1	Param	Case 2	Param	Case 3	Param	Case 4	Param	Case 5	Param	Case 6
$a_{0,1}$	12.62	$a_{0,1}$	5.73	b_0	2.02	b_0	0.63	$c_{0,1}$	8.13	$c_{0,1}$	2.77
$a_{1,1}$	27.03	$a_{1,1}$	21.88	b_1	36.99	b_1	23.68	$c_{1,1}$	25.04	$c_{1,1}$	10.58
$a_{0,2}$	1.26	$a_{0,2}$	1.05	b_2	30.41	b_2	30.72	$c_{2,1}$	6.53	$c_{2,1}$	2.15
$a_{2,1}$	28.35	$a_{1,2}$	19.33	b_3	16.07	b_3	14.95	$c_{0,2}$	0.23	$c_{0,2}$	0.29
$m_{1,1}^{(a)}$	6.61	$v_{1,1}^{(a)}$	1.19	$m_{1,1}^{(b)}$	0.41	$v_{1,1}^{(b)}$	0.62	$c_{1,2}$	22.00	$c_{1,2}$	23.40
$m_{1,2}^{(a)}$	5.12	$v_{2,1}^{(a)}$	18.14	$m_{1,2}^{(b)}$	1.76	$v_{2,1}^{(b)}$	12.42	$c_{2,2}$	10.16	$c_{2,2}$	9.90
b_{ef}	19.00	$v_{3,1}^{(a)}$	20.60	b_{ef}	12.35	$v_{3,1}^{(b)}$	14.17	$m_{1,1}^{(c)}$	5.26	$v_{1,1}^{(c)}$	1.05
		b_{ef}	12.07			b_{ef}	2.83	$m_{1,2}^{(c)}$	4.58	$v_{2,1}^{(c)}$	17.24
								b_{ef}	18.05	$v_{3,1}^{(c)}$	20.74
										b_{ef}	11.88

Table 28.9 Reduced set of input parameters for cases 1–6 of the suspension stiffness and damping coefficients

	Number of full set of input parameters	Number of reduced set of input parameters
Case 1, $\widehat{F}_{\text{bs},a}^{(d)}$	7	6
Case 2, $\widehat{F}_{\text{bs},a}^{(e)}$	8	6
Case 3, $\widehat{F}_{\text{bs},b}^{(d)}$	7	4
Case 4, $\widehat{F}_{\text{bs},b}^{(e)}$	8	6
Case 5, $\widehat{F}_{\text{bs},c}^{(d)}$	9	8
Case 6, $\widehat{F}_{\text{bs},c}^{(e)}$	10	8

could be removed from the calibration space and held constant. Table 28.9 indicates the size of the reduced parameter space for each case.

28.6.2 Uncertainty Quantification Frameworks

Moving forward, inverse modeling will be applied to the 2DOF mathematical model for the six 2DOF cases. Inverse modeling or inversion is the process of using the known dynamic outputs to solve for the set of input variables in Table 28.8 when their true values are unknown. As part of inverse modeling, two Bayesian frameworks will be presented and deployed in a later study to evaluate model-form uncertainty for each of the six 2DOF cases using the output responses in Eq. (28.2) and the reduced set of input variables based on the results from Fig. 28.10 and Table 28.8. The foundations of their methodologies are derived from Bayes' theorem,

$$P(m|d) = \frac{P(\{d_{\text{output}}\}|\{x_{\text{input}}\})P(\{x_{\text{input}}\})}{P(\{d_{\text{output}}\})} \propto P(\{d_{\text{output}}\}|\{x_{\text{input}}\})P(\{x_{\text{input}}\}), \quad (28.21)$$

where $\{x_{\text{input}}\}$ is vector of input variables to the 2DOF mathematical model; $\{d_{\text{output}}\}$ is the vector of dynamic outputs; $P(\{x_{\text{input}}\}|\{d_{\text{output}}\})$ is the posterior distribution; $P(\{d_{\text{output}}\}|\{x_{\text{input}}\})$ is the likelihood function, $P(\{x_{\text{input}}\})$ is the prior distribution; and, $P(\{d_{\text{output}}\})$ is the data distribution, which is held constant for the fixed data set. The posterior distribution $P(\{x_{\text{input}}\}|\{d_{\text{output}}\})$ is the probability that the given set of input variables produced the data set $\{d_{\text{output}}\}$, and the likelihood function $L(\{x_{\text{input}}\}|\{d_{\text{output}}\})$ or $P(\{d_{\text{output}}\}|\{x_{\text{input}}\})$ is the probability $\{d_{\text{output}}\}$ produced the given set of input variables $\{x_{\text{input}}\}$. Finally, $P(\{x_{\text{input}}\})$ is the prior knowledge about the distribution of the input variables, such as its shape, and lower and upper limits. The prior distribution of the input variables from Table 28.8 influences how the parameters are expected to vary in the model space, like a uniform or multivariate Gaussian distribution, and if they are treated as dependent (correlated) or independent (uncorrelated) variables. The first case (1) will be a delayed-acceptance single component adaptive Metropolis (DA-SCAM) algorithm with ordinary kriging of the likelihood, and the second case (2) will be the Gaussian Process Model

for Simulation Analysis (GPM/SA) developed at Los Alamos National Laboratories. Both of these statistical frameworks will predict the probability distribution of how well the N number of model inputs from each 2DOF case will reproduce the experimental response features, such as relative displacement. Before these frameworks are employed, results from the sensitivity analysis study in Fig. 28.10 will eliminate low sensitivity variables contributing less than 2% to all output response features and set them to their mean value using Tables 28.2, 28.3, 28.6, and 28.7.

The first DA-SCAM algorithm is based on a two-stage Metropolis-Hastings (MH) algorithm proposed by Christen and Fox [13] that predicts variables during statistical inversion. Calculating the 2DOF MAFDS forward model every iteration can be computationally expensive. The research from [13] by Fox and Christen proposed using an inexpensive approximation to the forward operator, like the 2DOF MAFDS model, based on an algorithm from [14]. Instead of randomly walking through the model space, a single component adaptive Metropolis algorithm (SCAM) from [15] was introduced to improve sampling in high dimensions for all of the variables in cases 1–6. The initial phase of this algorithm runs a single component adaptive Metropolis algorithm to account for the burn-in time of the Markov chain for each 2DOF case. For the preliminary acceptance decision stage, the delayed acceptance portion of the DA-SCAM algorithm begins with computing an inexpensive likelihood estimate to the 2DOF MAFDS model via ordinary kriging or linear interpolation with de-clustering. The DA-SCAM algorithm is one approach for solving the 2DOF MAFDS model for stiffness and damping cases 1–6.

The Bayesian model calibration approach from [16–18] that implements a multivariate simulator with the goal of reducing the computational expense and time during statistical inversion similarly to the DA-SCAM algorithm. The regression model, $\eta(X, \theta)$, $X = \{h_f, m_n\}$, where X is the set of control variables for drop height and added mass, and θ is the calibration parameters or the input variables at an optimal setting, will capture the random spatial effects from the physics of the data. It is assumed to behave as a multivariate Gaussian distribution with a mean and variance that must be trained to represent the observed training and testing data, which essentially allows the GP model to capture the underlying physical processes of the MAFDS. Since the pdf of the multivariate Gaussian distribution is continuously differentiable, this property of the GP model provides a smoothly varying and continuous simulator $\eta(X, \theta)$ to represent the physics of the MAFDS. By applying the GP model for $\eta(X, \theta)$ in a Markov chain Monte Carlo (MCMC) based algorithm, this algorithm develops a statistical representation of the physically informed system that can be used with any observed data set. This approach will be compared to the results from DA-SCAM algorithm for the six 2ODF cases.

In short, two Bayesian frameworks have been introduced as the first paper in a series. The main purpose of this paper is to introduce the MAFDS 2DOF forward model, address model-form uncertainty through six 2DOF cases, and perform suspension stiffness and damping analysis. In the next study, the GPM/SA and DA-SCAM algorithms will solve the 2DOF MAFDS inverse problem presented in this paper to evaluate model-form uncertainty.

Acknowledgements The authors gratefully acknowledge the support of the National Science Foundation under grant #1633608, and the German Research Foundation (DFG) SFB 805 project grant for funding this research. In particular, the authors acknowledge Maximilian Schäffner and Robert Feldmann for their assistance during this project.

References

1. Farajpour, I., Atamturktur, S.: Error and uncertainty analysis of inexact and imprecise computer models. *J. Comput. Civ. Eng.* **27**, 407–418 (2013)
2. Roy, C.J., Oberkampf, W.L.: A comprehensive framework for verification, validation, and uncertainty quantification in scientific computing. *Comput. Methods Appl. Mech. Eng.* **200**, 2131–2144 (2011)
3. Atamturktur, S., Hemez, F.M., Laman, J.A.: Uncertainty quantification in model verification and validation as applied to large scale historic masonry monuments. *Eng. Struct.* **43**, 221–234 (2012)
4. Mallapur, S., Platz, R.: Quantification and evaluation of uncertainty in the mathematical modelling of a suspension strut using Bayesian model validation approach. In: Conference Proceedings of the Society for Experimental Mechanics Series, vol. 3, pp. 113–124 (2017)
5. Chopra, A.K.: Dynamics of Structures, Technical Report, Pearson/Prentice-Hall, Upper Saddle River (2012)
6. Barnard, G.A.: New methods of quality control. *J. R. Stat. Soc.* **126**, 255–258 (1963)
7. Zhang, R., Mahadevan, S.: Model uncertainty and Bayesian updating in reliability-based inspection. *Struct. Saf.* **22**, 145–160 (2000)
8. Eck, V.G., Donders, W.P., Sturdy, J., Feinberg, J., Delhaas, T., Hellevik, L.R., Huberts, W.: A guide to uncertainty quantification and sensitivity analysis for cardiovascular applications. *Int. J. Numer. Methods Biomed. Eng.* **32**, e02755 (2016)
9. Mallapur, S., Platz, R.: Uncertainty quantification in the mathematical modelling of a suspension strut using bayesian inference. *Mech. Syst. Signal Process.* **118**, 158–170 (2019)
10. ContiTech: Schwingmetall die original gummi-metall- verbindung 28–29 (2011)
11. Czop, P., Gnilka, J.: Reducing aeration and cavitation effect in shock absorbers using fluid-structure interaction simulation, Technical Report (2016)
12. Duym, S.W., Stiens, R., Baron, G.V., Reybrouck, K.G.: Physical modeling of the hysteretic behaviour of automotive shock absorbers, Technical Report, SAE Technical Paper (1997)

13. Christen, J., Fox, C.: Markov chain Monte Carlo using an approximation. *J. Comput. Graph. Stat.* **14**, 795–810 (2005)
14. Fox, C., Nicholls, G.: Sampling conductivity images via MCMC, Technical Report, University of Leeds (1997)
15. Haario, H., Saksman, E., Tamminen, J.: Component wise adaptation for high dimensional MCMC. *Comput. Stat.* **20**, 265–273 (2005)
16. Higdon, D., Gattiker, J., Williams, B., Rightley, M.: Computer model calibration using high-dimensional output. *J. Am. Stat. Assoc.* **103**, 570–583 (2008)
17. Gattiker, J.R.: Using the Gaussian process model for simulation analysis (GPM/SA) code, Technical Report, Los Alamos National Laboratory (2005)
18. Kennedy, M.C., O'Hagan, A.: Bayesian calibration of computer models. *J. R. Stat. Soc. Ser. B Stat. Methodol.* **63**, 425–464 (2001)



Chapter 29

Non-unique Estimates in Material Parameter Identification of Nonlinear FE Models Governed by Multiaxial Material Models Using Unscented Kalman Filtering

Mukesh Kumar Ramancha, Ramin Madarshahian, Rodrigo Astroza, and Joel P. Conte

Abstract Bayesian nonlinear finite element (FE) model updating using input and output measurements have emerged as a powerful technique for structural health monitoring (SHM), and damage diagnosis and prognosis of complex civil engineering systems. The Bayesian approach to model updating is attractive because it provides a rigorous framework to account for and quantify modeling and parameter uncertainty. This paper employs the unscented Kalman filter (UKF), an advanced nonlinear Bayesian filtering method, to update, using noisy input and output measurement data, a nonlinear FE model governed by a multiaxial material constitutive law. Compared to uniaxial material constitutive models, multiaxial models are typically characterized by a larger number of material parameters, thus requiring parameter estimation to be performed in a higher dimensional space. In this work, the UKF is applied to a plane strain FE model of Pine Flat dam (a concrete gravity dam on King's River near Fresno, California) to update the time-invariant material parameters of the cap plasticity model, a three-dimensional non-smooth multi-surface plasticity concrete model, used to represent plain concrete behavior. This study considers seismic input excitation and utilizes numerically simulated measurement response data. Estimates of the multi-axial material model parameters (for the single material model used in this study) are non-unique. All sets of parameter estimates yield very similar and accurate seismic response predictions of both measured and unmeasured response quantities.

Keywords Non-unique estimates · Bayesian parameter estimation · Unscented Kalman filter · Nonlinear FE model · Cap plasticity model · Concrete gravity dams

29.1 Introduction

Finite element (FE) model updating is an important component of structural health monitoring (SHM) of complex civil engineering systems such as dams, buildings and bridges [1]. The system response measured using sensors mounted on the real system differs from the response predicted using a mechanics-based FE model, thus raising the need for model updating. The discrepancy between measured and FE predicted responses are mainly due to noisy input and output measurements, uncertainty in model parameters and model uncertainties (the selected model class does not contain the real structure) [2]. The current state-of-the-art in model updating involves updating the system state vector and the vector of unknown parameters of the FE model using measured input and output data. This is achieved by minimizing the error between the predicted and measured responses [3]. Once updated, the FE model acts as a digital twin (or cyber model) of the real system and can thus be used for structural health monitoring, damage diagnosis and prognosis purposes.

The input and output measurements pertaining to structural/civil engineering systems are often noisy and sparse (not sufficient to completely determine the unknown state and parameter vector of the FE model). In such systems, there often exists a prior knowledge (or degree of belief), expressed as prior probability distribution, about the unknown parameter vector. For example, if the parameter of interest is “the tensile strength of concrete at a certain location of the structure”, then its nominal value can be used as a mean of the prior probability distribution of that parameter. In this regard, the

M. K. Ramancha (✉) · R. Madarshahian · J. P. Conte

Department of Structural Engineering, Jacobs School of Engineering, University of California, San Diego, La Jolla, CA, USA
e-mail: mramanch@eng.ucsd.edu; jconte@ucsd.edu

R. Astroza

Facultad de Ingeniería y Ciencias Aplicadas, Universidad de los Andes, Santiago, Chile

Bayesian approach to model updating is attractive because it allows combining prior knowledge with a noisy and incomplete measurement data set to update the unknown state and parameter vector [4].

In this paper, the Bayesian FE model updating framework is applied to the Pine Flat dam, a concrete gravity dam on the King's river near Fresno, California. In this respect, a 2D plane strain nonlinear FE model of the dam is developed in an FE analysis software framework (*OpenSees*) with the cap plasticity model, a classical 3D non-smooth multi-surface plasticity model [5–7], used to represent the behavior of plain concrete. The FE model characterized by a set of realistic material parameter values is subjected to seismic input excitation to numerically simulate the output response data. The simulated input and output response data with added Gaussian white noise (to mimic the measurement noise) are then used to update only the time-invariant material parameters of the multiaxial material model using unscented Kalman filtering (a nonlinear Bayes filter). This paper investigates the issue of convergence in FE response prediction (to the true response) in the absence of convergence of the parameter estimates to their true values due to parameter non-identifiability issues. Note that this study accounts only for the sources of uncertainty related to the input-output measurement noise and the material parameters. Moreover, the same FE model is used to simulate the response and to perform the model updating, thereby disregarding the effects of modeling uncertainty.

29.2 FE Model Updating as Parameter-Only Estimation Problem

In general, FE model updating aims at jointly estimating the unknown system state and parameter vector of the nonlinear FE model using sparse and noisy input-output measurement data [8]. The state vector \mathbf{x} for an FE model includes the displacement and velocity at every degree of freedom of the model. In addition, for nonlinear FE models, the state vector also contains all history-dependent variables (material history variables) at each integration point of the model [3]. The parameter vector $\boldsymbol{\theta}$ comprises of all unknown FE model parameters such as geometric, damping, constraint and material (time-invariant) parameters. The input measurement data can consist of an earthquake recorded by a seismograph (or seismometer) in the vicinity of the structure while the output measurement data are typically provided by accelerometers mounted at various locations on the structure. Note that the input and output measurement data are noisy and often insufficient to completely estimate the joint state and parameter vector of the nonlinear FE model.

In this study, the FE model with realistic values of model parameters is assumed to predict realistically the actual response of the structure. In other words, the selected FE model class has the capability to represent reasonably well the actual nonlinear behavior of the real structure. With this assumption, the FE model updating problem (joint state and parameter estimation) boils down to a parameter-only estimation problem. Therefore, the input and output measurement data are used to estimate the unknown parameter vector $\boldsymbol{\theta}$ only as the updated nonlinear FE model is relied upon to provide satisfactory estimates of the state of the system.

29.3 Bayesian Parameter Estimation

At time t_k , let $\mathbf{y}_k \in \mathbb{R}^{n_y}$ be the measurement vector and $\mathbf{y}_k^F = \mathbf{h}_k(\mathbf{u}_{1:k}; \boldsymbol{\theta}) \in \mathbb{R}^{n_y}$ denote the response predicted by the FE model \mathbf{h}_k parameterized by vector $\boldsymbol{\theta} \in \mathbb{R}^{n_\theta}$ when subjected to input time history $\mathbf{u}_{1:k}$. The error between the measured response and the FE estimated response at time t_k can be written as $\mathbf{e}_k = \mathbf{y}_k - \mathbf{h}_k(\mathbf{u}_{1:k}; \boldsymbol{\theta})$. The goal of parameter estimation is to estimate the parameter vector $\boldsymbol{\theta}$ by minimizing the error \mathbf{e}_k at time t_k ($k = 0, 1, 2, \dots$) while accounting for the pertinent sources of uncertainty. The Bayesian parameter estimation framework can be used to solve this mathematical inverse problem. This framework can be employed to recursively, over the time steps t_k ($k = 0, 1, 2, \dots$), estimate the parameter vector $\boldsymbol{\theta}$ by using the following discrete-time state-space representation of the system dynamics:

$$\begin{aligned} \text{State Equation : } & \boldsymbol{\theta}_k = \boldsymbol{\theta}_{k-1} + \mathbf{w}_{k-1} \\ \text{Measurement Equation : } & \mathbf{y}_k = \mathbf{h}_k(\mathbf{u}_{1:k}; \boldsymbol{\theta}_k) + \mathbf{v}_k \end{aligned} \quad (29.1)$$

In this framework, the unknown parameter vector $\boldsymbol{\theta}$ at each time step t_k is modeled as random vector denoted by $\boldsymbol{\Theta}_k$. The state equation governing the parameter vector $\boldsymbol{\theta}_k \in \mathbb{R}^{n_\theta}$ is driven by the artificial process noise $\mathbf{w}_k \in \mathbb{R}^{n_\theta}$. The measurement noise $\mathbf{v}_k \in \mathbb{R}^{n_y}$ is assumed to be additive to the FE predicted response $\mathbf{h}_k(\mathbf{u}_{1:k}; \boldsymbol{\theta}_k)$ in the measurement equation.

29.3.1 Unscented Kalman Filtering

The process of recursive Bayesian filtering involves sequentially computing the probability distribution of Θ_k given the current and previous measurements $\mathbf{y}_{1:k} = \{\mathbf{y}_1, \mathbf{y}_2, \dots, \mathbf{y}_k\}$: $\Theta_{k|k} \sim p(\Theta_k | \mathbf{y}_{1:k}), k = 1, 2, 3, \dots$. This involves initializing the filter with an initial probability distribution of the unknown parameter vector $\Theta_{0|0} \sim p(\Theta_0)$ to sequentially compute $p(\Theta_k | \mathbf{y}_{1:k})$ for every k , i.e., recursively update the probability distribution of unknown parameter vector considering new measurements. At each time k , the process of recursive updating involves computing $p(\Theta_k | \mathbf{y}_{1:k-1})$, referred to as predicted parameter distribution at time step t_k , using $p(\Theta_{k-1} | \mathbf{y}_{1:k-1})$ and then updating the predicted distribution to $p(\Theta_k | \mathbf{y}_{1:k})$, referred to as the posterior probability distribution of Θ_k given measurements $\mathbf{y}_{1:k}$ or updated parameter distribution at time step t_k , after observing measurement vector \mathbf{y}_k . Note that the FE model \mathbf{h}_k is a nonlinear function of Θ_k . Therefore, the nonlinear Kalman filter, a nonlinear Bayesian filtering technique, is used in this study to compute the probability distribution of the random vectors $\Theta_{k|k}, k = 1, 2, 3, \dots$.

The nonlinear Kalman filter is a special type of nonlinear Bayes filter for which:

1. The initial distribution of the unknown parameter vector is modeled as Gaussian. Therefore, initial parameter vector $\Theta_{0|0}$ is modeled as a Gaussian random vector with estimated mean vector $\hat{\Theta}_{0|0}$ and estimated covariance matrix $\hat{\mathbf{P}}_{0|0}^{\Theta\Theta}$, i.e., $\Theta_{0|0} \sim \mathcal{N}(\hat{\Theta}_{0|0}, \hat{\mathbf{P}}_{0|0}^{\Theta\Theta})$.
2. Both the process noise and measurement noise are modeled as zero-mean Gaussian white noise processes, i.e., $\mathbf{w}_k \sim \mathcal{N}(\mathbf{0}, \mathbf{Q}_k)$ and $\mathbf{v}_k \sim \mathcal{N}(\mathbf{0}, \mathbf{R}_k)$ for all k , where \mathbf{Q}_k and \mathbf{R}_k are the process and measurement noise covariance matrices, respectively, at time step t_k .
3. The process noise, \mathbf{w}_k , and measurement noise, \mathbf{v}_k , across all time steps t_k ($k = 0, 1, 2, \dots$), along with the initial parameter vector, $\Theta_{0|0}$, are assumed to be mutually statistically independent.
4. The posterior distribution of the unknown parameter vector Θ is assumed to be Gaussian. Therefore, $\Theta_{k|k}$, at any time t_k , is a Gaussian random vector with estimated mean vector $\hat{\Theta}_{k|k}$ and estimated covariance matrix $\hat{\mathbf{P}}_{k|k}^{\Theta\Theta}$.

The unscented Kalman filter (UKF) is a special type of nonlinear Kalman filter which uses a minimal set of deterministically chosen sample points $\mathcal{V}^{(i)}$, also known as sigma-points (SPs), to represent a random vector $\mathbf{E} \in \mathbb{R}^{n\mathbf{E}}$ (Gaussian or non-Gaussian). The SPs are selected such that they accurately capture the true mean vector and the true covariance matrix of the random vector \mathbf{E} . These SPs when propagated through any nonlinear function, $\mathbf{F} = g(\mathbf{E})$, capture the true mean vector and covariance matrix of the transformed random vector \mathbf{F} accurately up to second order (third order if \mathbf{E} follows a Gaussian distribution) [9]. A deterministic sampling technique known as scaled Unscented transformation (SUT) is used in this paper. Figure 29.1 summarizes the algorithm to recursively estimate the mean vector and the covariance matrix of the unknown parameter vector of a nonlinear FE model using the UKF.

29.4 Application Example

Parameter estimation or system identification of concrete gravity dams is a subject of interest to many researchers [10]. Such studies were conducted by Chopra and co-workers using forced vibration test data to estimate the linear elastic material parameters such as Young's modulus of concrete [11] but without accounting for uncertainty. In the present work, the multiaxial material model parameters which govern both the elastic and plastic behavior of the concrete of a dam are estimated using numerically simulated seismic response data contaminated with added Gaussian white noise (to mimic real-world data). The uncertainty due to the input and output measurement noise and the unknown model parameters is accounted for, but the effects of modeling uncertainty are not considered here. To achieve this, an idealized 2D model of Pine Flat dam is developed in *OpenSees* and the FE simulated noisy seismic response data are used to recursively estimate the time-invariant parameters of the cap plasticity material model (used to model the plain concrete of the dam) using the UKF.

Figure 29.2 shows a picture of Pine Flat dam and illustrates the 2D plane strain nonlinear FE model developed. In this FE model, the dam is assumed to be sitting on a rigid foundation, i.e., the boundary conditions at the bottom of the dam are assumed fixed. The concrete is assumed to be isotropic and homogeneous (i.e., characterized by the same material model and same set of material parameter values) over the entire cross-section of the dam. Each finite element consists of a bilinear quadrilateral element with material behavior at each integration point governed by the cap plasticity model (see Fig. 29.3). The dynamic interaction between the water reservoir and the dam (i.e., fluid-structure interaction) is not accounted for in this study; the hydrostatic water pressure distribution along the upstream face of the dam, see Fig. 29.2, is applied statically and kept constant during the dynamic seismic response analysis.

```

Initialize:  $\Theta_{0|0} \sim N(\hat{\Theta}_{0|0}, \hat{P}_{0|0}^{00})$ 
for  $k = 1, 2, 3, \dots$ 
    Generate SPs based on  $\hat{\Theta}_{k-1|k-1}$  and  $\hat{P}_{k-1|k-1}^{00}$ :  $V_{k-1|k-1}^{(i)}, i = 1, 2, \dots, 2n_0 + 1$ 
    Propagate each  $V_{k-1|k-1}^{(i)}$  through the state equation:  $V_{k|k-1}^{(i)} = V_{k-1|k-1}^{(i)}, i = 1, 2, \dots, 2n_0 + 1$ 
    Mean and covariance prediction:  $\hat{\Theta}_{k|k-1} = \hat{\Theta}_{k-1|k-1}, \hat{P}_{k|k-1}^{00} = \hat{P}_{k-1|k-1}^{00} + Q_{k-1}$ 
    Propagate each  $V_{k|k-1}^{(i)}$  through the measurement equation:  $Y_k^{(i)} = h_k(V_{k|k-1}^{(i)}, u_{1:k})$ 
    Measurement prediction:  $\hat{y}_{k|k-1} = \sum_{i=1}^{2n_0+1} W_m^{(i)} Y_k^{(i)}, \hat{P}_{k|k-1}^{yy} = \sum_{i=1}^{2n_0+1} W_c^{(i)} [Y_k^{(i)} - \hat{y}_{k|k-1}] [Y_k^{(i)} - \hat{y}_{k|k-1}]^T + R_k$ 
    Cross covariance of  $\Theta$  and  $Y$ :  $\hat{P}_{k|k-1}^{0y} = \sum_{i=1}^{2n_0+1} W_c^{(i)} [V_{k|k-1}^{(i)} - \hat{\Theta}_{k|k-1}] [Y_k^{(i)} - \hat{y}_{k|k-1}]^T$ 
    Kalman gain:  $K_k = \hat{P}_{k|k-1}^{0y} (\hat{P}_{k|k-1}^{yy})^{-1}$ 
    Mean and covariance update:  $\hat{\Theta}_{k|k} = \hat{\Theta}_{k|k-1} + K_k (y_k - \hat{y}_{k|k-1}), \hat{P}_{k|k}^{00} = \hat{P}_{k|k-1}^{00} - K_k \hat{P}_{k|k-1}^{yy} K_k^T$ 
end

```

Fig. 29.1 Unscented Kalman Filter Algorithm using scaled unscented transformation

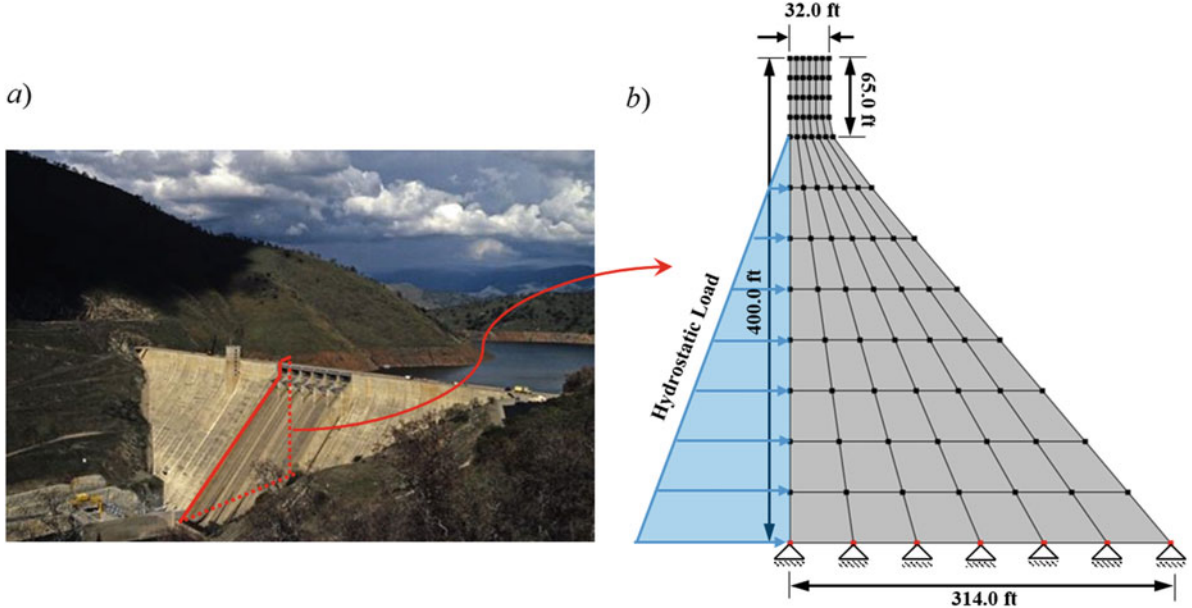


Fig. 29.2 (a) Pine Flat Dam, and (b) 2D FE model of the dam

The cap plasticity material model is a sophisticated three-dimensional non-smooth multi-surface plasticity model intended to capture realistically the multi-dimensional behavior of plain concrete [6, 12], see Fig. 29.3c. The cap plasticity model is characterized by a set of eleven (11) time-invariant material parameters (i.e., material constants) [5]. Two of these parameters (shear modulus, G , and bulk modulus, K) are linear elastic parameters, while the other nine parameters (T , X_0 , R , α , λ , D , W , β and θ) characterize the yield surfaces, the flow rule and the hardening law of the cap plasticity model. The three yield surfaces are: an ideal plasticity failure envelope $f_1(\sigma) = 0$ defined by α , λ , β and θ ; a strain hardening ellipsoidal cap $f_2(\sigma, \kappa) = 0$ (κ is the hardening parameter acting as a material history variable) defined by X_0 and R ; and an ideal plasticity tensile-cutoff surface $f_3(\sigma) = 0$ defined by T . Parameters D and W characterize the hardening law. Here, σ is the stress tensor with s and $(I_1/3)\mathbf{I}$ denoting its deviatoric and volumetric components such that $\sigma = s + (I_1/3)\mathbf{I}$ (I_1 is the first invariant of the

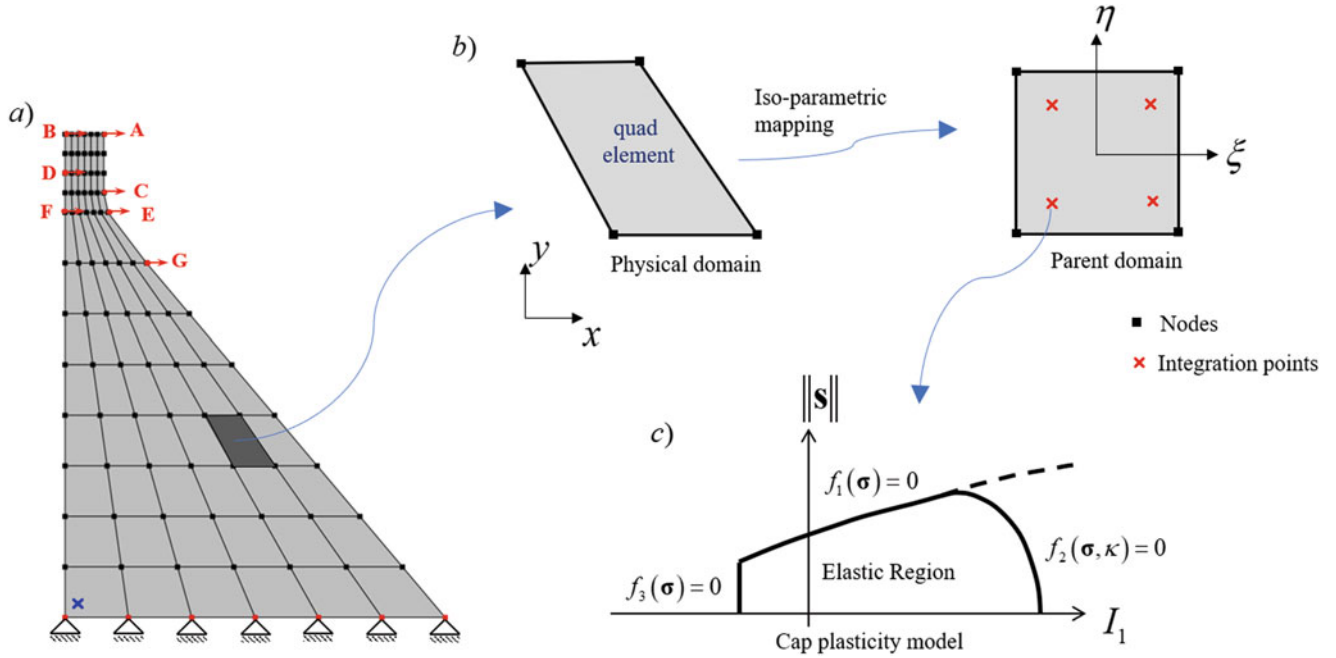


Fig. 29.3 FE model hierarchy: (a) Structure level, (b) Element level, and (c) Material level

stress tensor, and \mathbf{I} denotes the fourth order identity tensor). In this paper, the eleven time-invariant parameters of the cap plasticity model define the unknown parameter vector $\boldsymbol{\theta}$ as $\boldsymbol{\theta} = [G, K, X_0, D, W, R, \lambda, \theta, \beta, \alpha, T]^T \in \mathbb{R}^{11 \times 1}$.

29.4.1 Simulation

The numerically simulated seismic response data with added Gaussian white noise (to simulate measurement noise) is assumed to represent the data measured from a real-world dam and is used in developing and validating the Bayesian filtering framework considered herein. In the simulation (data generation) phase, the 2D FE model of the dam characterized by a realistic set of material parameter values (obtained through calibrating the cap plasticity model to the Colorado concrete test data [7] at the material level) is subjected to the first 20 s of the 360° horizontal component of the 1994 Northridge earthquake (M6.7) recorded at Sylmar Hospital station scaled by factor 2. The set of material parameter values used in the simulation phase are referred to as $\boldsymbol{\theta}^{true}$ from here on and are reported in Eq. (29.2).

$$\boldsymbol{\theta}^{true} : \left[\begin{array}{l} G = 1700 \text{ ksi}, \quad K = 2100 \text{ ksi}, \quad D = 0.0032 \text{ ksi}^{-1}, \quad W = 0.42, \quad X_0 = 16 \text{ ksi}, \\ R = 4.43, \quad \lambda = 1.16 \text{ ksi}, \quad \beta = 0.44 \text{ ksi}^{-1}, \quad \theta = 0.11, \quad \alpha = 3.86 \text{ ksi}, \quad T = -0.3 \text{ ksi} \end{array} \right] \quad (29.2)$$

Then, the absolute acceleration and relative displacement (with respect to the base of the dam) response time histories at locations A–G (see Fig. 29.3a) are obtained from the dynamic seismic response analysis. These response data are referred to as true measured responses and are now polluted with Gaussian white noise of root mean square (RMS) 1.0% g and 0.075 in, for the acceleration and displacement responses, respectively, to simulate the measurement noise. Therefore, the output response vector is defined as $\mathbf{y} = [\mathbf{a}_A, \mathbf{a}_B, \dots, \mathbf{a}_F, \mathbf{d}_A, \mathbf{d}_B, \dots, \mathbf{d}_F]^T \in \mathbb{R}^{14 \times N}$, where N denotes the number of time steps (or sample points) in the simulated response histories, \mathbf{a}_i and \mathbf{d}_i are a vector of the absolute acceleration and the relative displacement response, respectively, at location $i \in [A, B, \dots, F]$ (see Fig. 29.3a). The input (ground motion record) is also polluted with 1.0%g RMS Gaussian white noise to simulate measurement noise. Note that this input white noise transforms to a colored noise at the system output. Therefore, the total output noise (transformed input noise together with the added output measurement noise) is non-white which violates the white noise assumption for \mathbf{v}_k in Eq. (29.1) and may result in biased estimation of the model parameters [2]. Therefore, heterogeneous sensors (absolute acceleration and relative displacement response histories) are considered in this study to enhance the estimation accuracy.

Note that, in this study, the input earthquake ground motion record is appropriately scaled to drive the dam into adequate levels of constitutive nonlinearity. A simple FE response sensitivity analysis using the direct differentiation method (DDM), a local sensitivity analysis, is then performed to ensure that the resulting measured responses are sufficiently sensitive to all the eleven material parameters governing both linear and non-linear behavior of the dam. Low sensitivity of a measured response to a certain parameter implies that the parameter cannot be estimated in the context of a parameter estimation problem.

29.4.2 Estimation

The noisy input and output data set, generated in the simulation phase, are used in the estimation phase to recursively estimate the unknown parameter vector θ using the UKF. The same FE model of the dam, as the one used to simulate the response in the simulation phase, is employed in the parameter estimation phase.

The probability distribution of the initial value ($\theta_{0|0}$) of the unknown parameter vector θ is assumed as

$$\theta_{0|0} \sim \mathcal{N}(\hat{\theta}_{0|0}, \hat{\mathbf{P}}_{0|0}^{\theta\theta}) \rightarrow \begin{cases} \hat{\theta}_{0|0} = \begin{bmatrix} 1.40 & G^{true} & 0.55 & K^{true} & 0.85X_0^{true} & 1.20D^{true} & 0.80W^{true} \\ 0.80R^{true} & 1.15\lambda^{true} & 1.05\theta^{true} & 0.95\beta^{true} & 0.80\alpha^{true} & 0.60 & T^{true} \end{bmatrix}^T \\ \hat{\mathbf{P}}_{0|0}^{\theta\theta} = [0.25 \times \text{diag}(\hat{\theta}_{0|0})]^2 \end{cases} \quad (29.3)$$

The mean parameter values $\hat{\theta}_{0|0}$ in Eq. (29.3) are defined in terms of the true parameter values θ^{true} . However, in a real-world problem, the data are obtained from the sensors mounted on the real system (not simulated numerically); therefore, the true parameter values are unknown and do not even exist (since the selected FE model class may not contain the real structure). The diagonal elements of the covariance matrix of the artificial process noise \mathbf{Q} are assumed to be equal to $(10^{-3} \times \theta_{0|0}^{(i)})^2$, $i = 1, 2, \dots, 11$. The choice of \mathbf{Q} governs the convergence and tracking performance of the filter [9]. In real-world problems, the characteristics of the noise in the measurement data are not known exactly. Therefore, the covariance matrix of the measurement noise \mathbf{R} is set different than that of the (known) added noise to account for the unknown noise level.

The time histories of the posterior mean estimates of all eleven parameters obtained using the UKF and normalized with respect to their corresponding true values are shown in Fig. 29.4. The blue line in each plot represents the normalized mean estimate ($\hat{\theta}_{k|k}$, $k = 1, 2, 3, \dots$) and the grey shaded region represents the estimation uncertainty ($\hat{\mathbf{P}}_{k|k}^{\theta\theta}$, $k = 1, 2, 3, \dots$) in the corresponding mean estimate, namely the mean \pm two standard deviations. The estimates of the two linear-elastic concrete material parameters, G and K , and of a nonlinear-material parameter, the tensile strength of concrete (T), converge smoothly to their corresponding true values (see blue lines in Fig. 29.4). In addition, their estimation uncertainty decreases asymptotically and very fast (see grey shaded areas in Fig. 29.4) as more information about these parameters is assimilated step by step from the measured input and output response. Even though the sensitivity of the measured responses to all parameters is high, it is observed in Fig. 29.3 that the estimates of other parameters controlling the nonlinear concrete behavior, X , R , α , λ , D , W , β and θ , do not converge to their corresponding true values. However, it is important to note that the measurement responses predicted by the FE model characterized by the parameter estimates obtained at the last step of the filter ($t_k = 20s$) are in excellent agreement with the true measurement responses.

In this study, the FE predicted seismic response of the dam obtained using the posterior mean estimates of the parameters is compared to the true response, obtained from the FE model using $\theta = \theta^{true}$, and the relative-root-mean-square error (RRMS) [3] is used as metric to measure the discrepancy between two time series. The evolution of the RRMS error for each sensor (\mathbf{a}_A , \mathbf{a}_B , \dots \mathbf{a}_F , \mathbf{d}_A , \mathbf{d}_B , \dots \mathbf{d}_F) during filtering is shown in Fig. 29.5. In this figure, the RRMS error at each time step t_k is computed by comparing the entire time history of FE predicted response obtained using the posterior mean estimates of the material parameters θ at t_k ($\hat{\theta}_{k|k}$) and the entire time history of the true response (obtained using $\theta = \theta^{true}$). As expected, at the start of filtering (i.e., at $k = 0$), the error between the predicted response (obtained using $\hat{\theta}_{0|0}$) and the true response (obtained using θ^{true}) is very high (with a RRMS error of over 100%). During filtering, the UKF adjusts the estimates of the material parameters to decrease the error between the predicted response and the true response. It is important to observe that although the estimates of some material parameters, X , R , α , λ , D , W , β and θ , do not converge to their corresponding true values, the RRMS errors between the predicted responses and the corresponding true responses decrease progressively to very small values. This implies that the filter finds different sets of parameter values (non-true) that each yields a very good match of the time histories of the measured response quantities. In addition, a very good agreement between predicted and

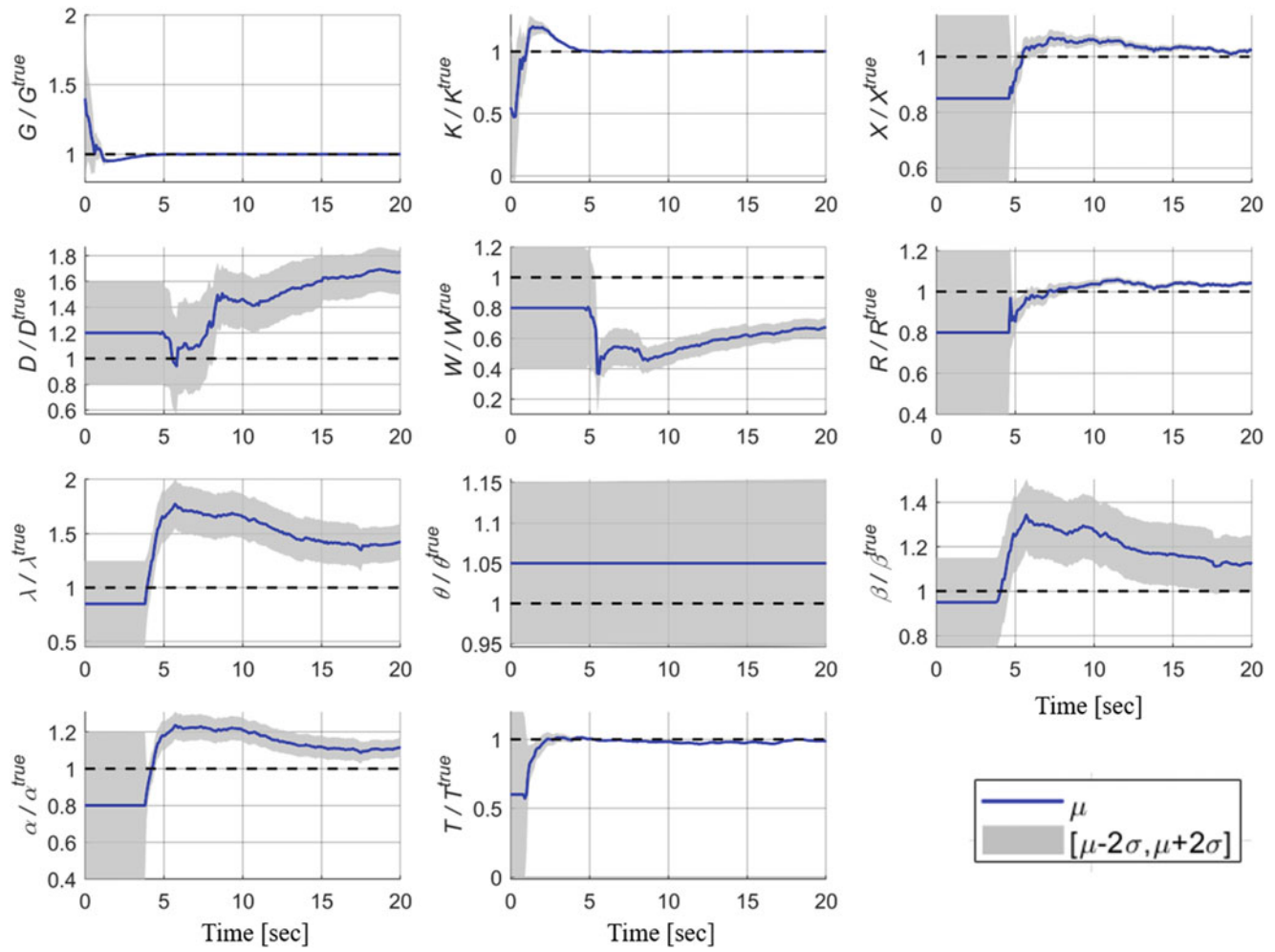


Fig. 29.4 Time history of normalized posterior estimates of all eleven time-invariant material parameters

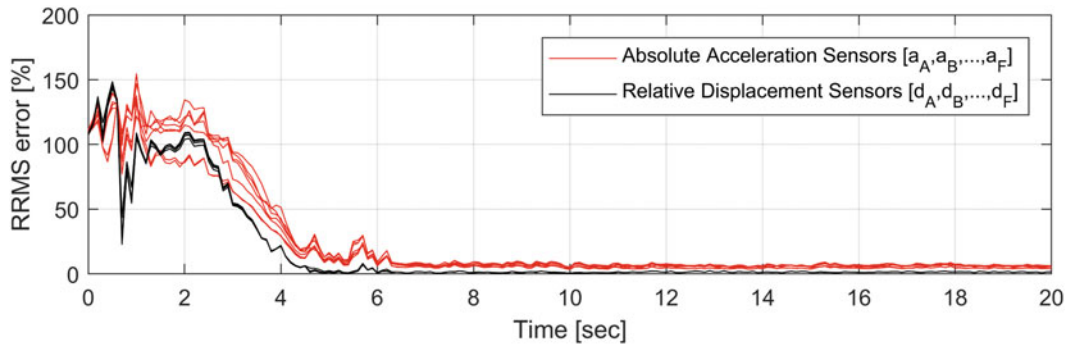


Fig. 29.5 Evolution of RRMS error for all sensors during filtering

true response time histories was also observed for non-measured response quantities. To illustrate this, the predicted response history (using the posterior mean estimate of the material parameters at the last time step, $t_k = 20$ s) and the corresponding true response time history are shown in Fig. 29.6 for the first invariant of the stress tensor (I_1) and the Frobenius norm of the deviatoric stress tensor, respectively, at an integration point close to the heel of the dam (see Fig. 29.3a).

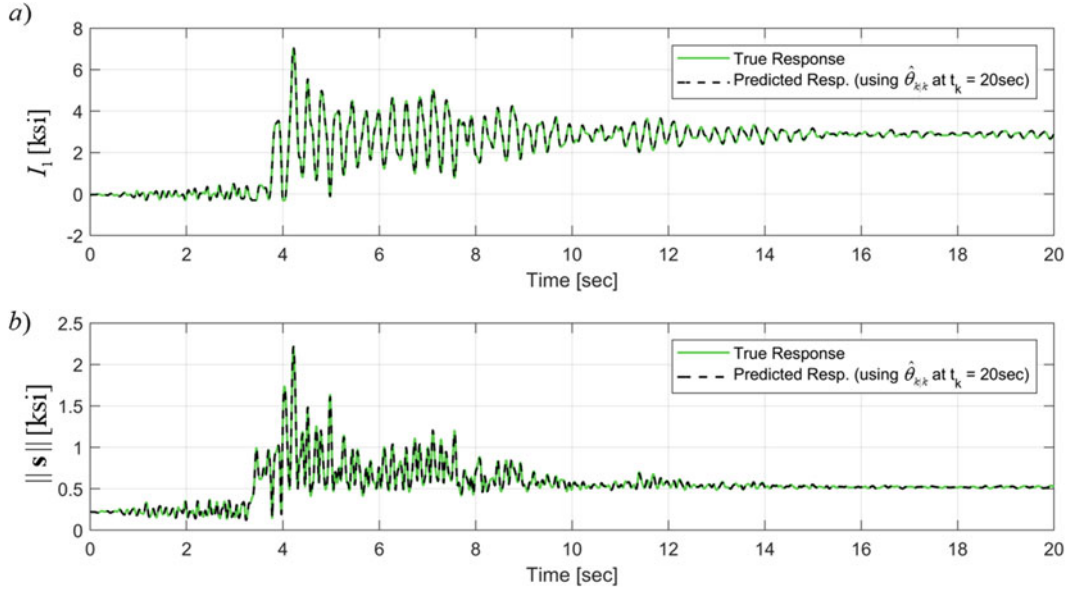


Fig. 29.6 Time histories of (a) First invariant of the stress tensor, and (b) Frobenius norm of the deviatoric stress tensor at heel of the dam

29.4.3 Validation

For validation purposes, the posterior mean estimates of the material parameters at different time steps ($t_k = 0$ s, 3 s, 10 s, 20 s) are used to predict the seismic response of the dam to an earthquake ground motion (the North-South component of the 1940 El Centro earthquake recorded at the El Centro station scaled by a factor of two) significantly different from the one (1994 Northridge earthquake recorded at the Sylmar station) used in the parameter estimation stage of this study. The predicted response and true response histories of the horizontal displacement at the top of the dam are compared in Fig. 29.7. It is observed (see Fig. 29.7a) that the predicted response using $\hat{\theta}_{k|k}$ at $t_k = 0$ s (initial mean estimate of the unknown parameter vector) is in bad agreement with the true response. The response predicted using $\hat{\theta}_{k|k}$ at $t_k = 3$ s matches the true response in the linear elastic range (in the time window 0–4 s, see Fig. 29.7b) since the estimation of the parameters governing the linear elastic response (G and K) is converged by $t_k = 3$ s (see Fig. 29.4). However, the match between this predicted response and the true response is found to degrade when the dam enters its nonlinear range of behavior (after 4 s). The predicted response histories obtained using $\hat{\theta}_{k|k}$ at $t_k = 10$ s and $t_k = 20$ s are found to follow very closely the entire true response histories (see Fig. 29.7c, d). In fact, it was observed that the response predicted using any set of parameter estimates after $t_k = 7$ s agrees with the true response equally well and is confirmed by the low RRMS error in Fig. 29.5: Evolution of RRMS error for all sensors during filtering after $t_k = 7$ s. This confirms that the predicted response converges to the true response even though the parameter estimates do not converge to their true values, due to parameter non-identifiability issues.

29.5 Conclusions

This paper studies the application of the unscented Kalman filter, an advanced nonlinear Bayesian filtering technique, to recursively estimate, using earthquake input and output response data, the time-invariant material parameters of a multiaxial multi-surface plasticity model characterizing the concrete behavior of a nonlinear FE model of a dam. This study is based on numerically simulated dam seismic response data and does not consider the effects of modeling error/uncertainty. The input earthquake ground motion record is appropriately scaled to drive the dam into adequate levels of constitutive nonlinearity and a local sensitivity analysis is performed to ensure that the resulting output measured responses (using the scaled ground motion as input) are sufficiently sensitive to all the material parameters. It is observed that, although the estimates of some parameters do not converge to their corresponding true values, the predicted responses (for both measured and unmeasured response quantities) match the respective true responses extremely well (i.e., with a low relative root-mean-square error). In other words, the filter finds different sets of parameter values (non-true) that yield a very good match between the FE

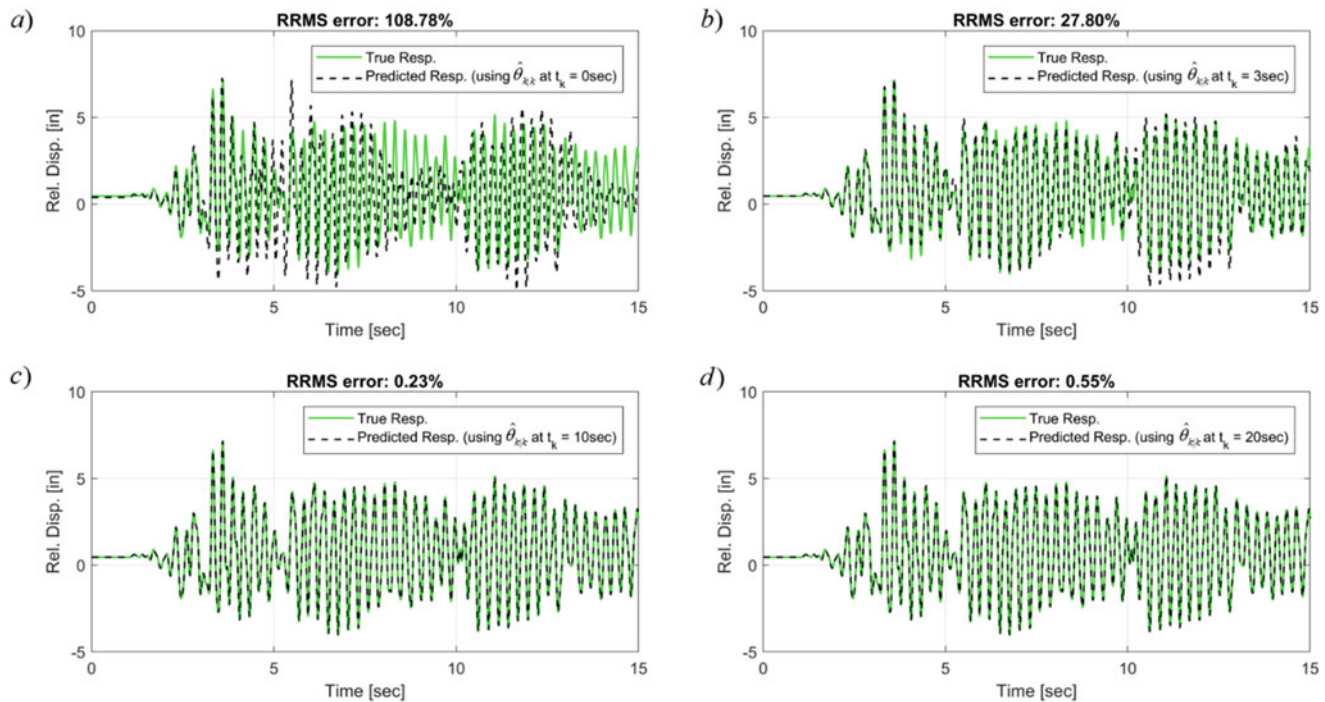


Fig. 29.7 Predicted versus true response using $\hat{\theta}_{k|k}$ at (a) $t_k = 0$ s, (b) $t_k = 3$ s, (c) $t_k = 10$ s, and (d) $t_k = 20$ s

predicted (using the material parameter estimates) and true response time histories. This implies that the set of all eleven material parameters defining the cap plasticity model is not identifiable. In other words, the mathematical inverse problem involves a many-to-one function, i.e., many sets of parameter values result in the same FE predicted response. Therefore, for all practical purposes, any such set of parameter estimates can be used for dam (structural) response prediction, damage diagnosis and prognosis. In the future, structural and practical identifiability analysis of such multiaxial plasticity models should be performed to investigate non-identifiability, if any, of parameters before solving a parameter estimation problem.

Acknowledgements Funding for this work was provided by the U.S. Army Corps of Engineers through the U.S. Army Engineer Research and Development Center Research Cooperative Agreement.

References

1. Friswell, M., Mottershead, J.E.: Finite Element Model Updating in Structural Dynamics. Springer Science & Business Media, Berlin (2013)
2. Ebrahimian, H., Astroza, R., Conte, J.P., de Callafon, R.A.: Nonlinear finite element model updating for damage identification of civil structures using batch Bayesian estimation. *Mech. Syst. Signal Process.* **84**, 194–222 (2017)
3. Astroza, R., Ebrahimian, H., Conte, J.P.: Material parameter identification in distributed plasticity FE models of frame-type structures using nonlinear stochastic filtering. *J. Eng. Mech. ASCE*. **141**(5), 04014149–04011/17 (2014)
4. Yuen, K.-V.: Bayesian Methods for Structural Dynamics and Civil Engineering. John Wiley & Sons, New York, NY (2010)
5. Hofstetter, G., Simo, J.C., Taylor, R.L.: A modified cap model: closest point solution algorithms. *Comput. Struct.* **46**(2), 203–214 (1993)
6. Sandler, I.S., Dimaggio, F.L., Baladi, G.Y.: Generalized cap model for geological materials. *J. Geotech. Eng. Div. ASCE*. **102**(7), 683–699 (1976)
7. Simo, J.C., Ju, J.-W., Pister, K.S., Taylor, R.L.: Assessment of cap model: consistent return algorithms and rate-dependent extension. *J. Eng. Mech. ASCE*. **114**(2), 191–218 (1988)
8. Hemez, F.M., Farrar, C.R.: A brief history of 30 years of model updating in structural dynamics. *Special Topics Struct. Dynam.* **6**, 53–71., Springer (2014)
9. Van Der Merwe, R.: Sigma-point Kalman filters for probabilistic inference in dynamic state-space models. Ph.D. Thesis, Department of Electrical and Computer Engineering, OGI School of Science & Engineering, Oregon Health & Science University, Beaverton, Oregon (2004)
10. Hall, J.F.: Study of the earthquake response of Pine Flat dam. *Earthq. Eng. Struct. Dynam.* **14**(2), 281–295 (1986)
11. Rea, D., Liaw, C.Y., Chopra, A.K.: Mathematical models for the dynamic analysis of concrete gravity dams. *Earthq. Eng. Struct. Dynam.* **3**(3), 249–258 (1974)
12. Chen, W.-F., Saleeb, A.F.: Constitutive equations for engineering materials. In: *Elasticity and Modeling*, vol. 1, Revised edn. Elsevier, Amsterdam (2014)



Chapter 30

On Key Technologies for Realising Digital Twins for Structural Dynamics Applications

D. J. Wagg, P. Gardner, R. J. Barthorpe, and K. Worden

Abstract The term digital twin has gained increasing popularity over the last few years. The concept, loosely based on a virtual model framework that can replicate a particular system for contexts of interest over time, will require the development and integration of several key technologies in order to be fully realised. This paper, focusing on vibration-related problems in mechanical systems, discusses these key technologies as the *building blocks* of a digital twin. The example of a simulation digital twin that can be used for asset management is then considered. After briefly discussing the building blocks required, the process of data-augmented modelling is selected for detailed investigation. This concept is one of the defining characteristics of the digital twin idea, and using a simple numerical example, it is shown how augmenting a model with data can be used to compensate for the inherent model discrepancy. Finally the implications of this type of data augmentation for future digital twin technology is discussed.

Keywords Digital twin · Dynamics · Mechanical · Virtualisation · Vibration

30.1 Introduction

The digital twin concept is based on creating a virtual model framework that can replicate a particular system for contexts of interest over time. For example, a digital twin can be considered as a process, a product or some combination of both. At the most basic level, a digital twin is defined as a virtual duplicate of an engineering system built from a combination of models and data. In this sense the digital twin is more than just a computer-based simulation of the system of interest. Most importantly, the digital twin should have the ability to be used as a predictive tool to inform key engineering decisions, and it will be argued that this is one of its defining characteristics. A good introduction to the idea of the digital twin, including the background and history of the topic, is given by Datta [1–3].

There are multiple other examples of using the digital twin concept for engineering applications in the literature. For example, improving manufacturing processes [4–6], additive manufacturing [7, 8], aerospace engineering [2, 9], offshore drilling [3], product design [10–13] and nuclear fusion [14]. All these applications can be categorised into broad classes of tasks that the digital twin is being asked to achieve (with considerable overlap). In the context considered here, this will specifically be to make predictions for condition or structural health monitoring (SHM) purposes, and to understand the current state of the physical twin.

The aim of this paper is to show an example of how a digital twin can be built for engineering applications which have time-dependent (dynamic) behaviour. The key building blocks required to create a simulation digital twin will be discussed. A key characteristic of a digital twin is the ability to bring together models and data, in order to give more accurate predictions. To demonstrate one approach to achieving this, the process of data-augmented modelling is considered in detail. To illustrate the concepts described an engineering based example is presented. A companion paper to this one presents a mathematical framework for the digital twin paradigm [15].

D. J. Wagg (✉) · P. Gardner · R. J. Barthorpe · K. Worden
Dynamics Research Group, Department of Mechanical Engineering, University of Sheffield, Sheffield, UK
e-mail: david.wagg@sheffield.ac.uk

30.2 Building a Digital Twin

The primary aim of creating a digital twin is to enable the user to have as much information as possible about the current status and future behaviour of the physical twin. To set the context for this, a schematic hierarchy of possible capabilities for a digital twin is shown in Fig. 30.1. Here it can be seen that there are currently five levels of sophistication for a digital twin, starting at the lowest level of sophistication with Level 1, and increasing to Level 5, with each level incorporating the functionality of all previous levels. In fact three key requirements of a digital twin, namely *supervision*, *learning* and *management* are captured by Levels 3 to 5 respectively. To capture the historical time evolution, Levels 1 and 2 are included, but not considered further.

An key distinguishing feature of a digital twin (and hence the dividing line between Levels 2 and 3 in Fig. 30.1) is that it can be used as a predictive tool. Furthermore, despite the focus on asset management tasks, all types of digital twin should evolve over the life-time of the physical twin. As a result they can be used in different contexts, depending on the life stage of the physical twin, whilst remaining a close one-to-one mapping from physical to digital. For example, if required, a digital twin can be used in the design phase of the physical twin, as described in Tuegel et al. [2]. Following that, the digital twin can be used in the manufacture and commissioning stage. Then, the digital twin can be used for asset management through operation and maintenance of the physical twin right through to end of life and decommissioning. Finally it is noted that the optimum final embodiment of the digital twin is in the form of a piece of software with highly informative graphical outputs.

30.2.1 Objectives of a Digital Twin

The precise objectives of the digital twin will depend on the context that is required, but a typical simulation-twin should allow the user to:

- understand the outputs quickly, in real-time if required, with visualisation of results;
- incorporate and update the geometry of the digital twin through integrated computer-aided-design (CAD) and data processes with a clear measure of fidelity;
- tunnel through the full-system CAD to specific components or sub-assemblies of interest and perform isolated tasks;
- navigate a hierarchical representation of physical behaviour at different length scales;
- interrogate the current state of the structure, whether in real-time or historically and perform data analysis (diagnosis);
- test multiple scenarios to predict likely future outcomes (prognosis and decision support);
- design controllers, perform hardware-in-the-loop simulation and/or set control processes for the physical twin;
- quantify a level of confidence (trust) that the user should ascribe to given outputs;
- generate test strategies if the digital twin needs additional data in order to increase the confidence level of a particular task.

Note that the ability to predict future outcomes, and quantify the level of confidence in these predictions are particularly important features. This is now considered by using an example layout for a simulation digital twin.

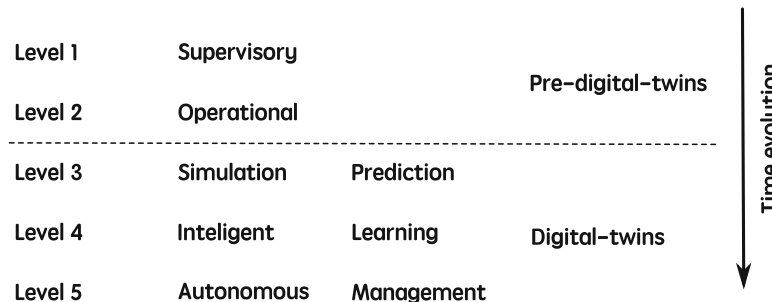


Fig. 30.1 A capabilities hierarchy for digital twins, where each level incorporates all the previous capabilities of the levels below

30.2.2 Example Layout of Simulation Digital Twin

A schematic representation of a simulation digital twin during an asset management phase of a wind turbine structure is shown in Fig. 30.2. Here, data sets are recorded from the physical twin, and control and scheduling commands fed back as required (enabling supervision and operation). The recorded data (potentially in real-time and from similar or legacy sources) are used for tasks in combination with the numerical model(s) and physical test-bed(s) (which can include further online devices, systems or databases) to give the required simulation capability. The interaction of these different elements is coordinated by a *workflow*, which also provides the user with visualisation and quantitative outputs.

As noted above, the exact formulation of a digital twin is context dependent, and so the elements shown inside the digital twin box in Fig. 30.2 are called the *building blocks* required for this specific context. In this example the building blocks are data sets; control and scheduling; numerical models; physical test-beds; workflow; visualisation; and quantitative output data.

The workflow has a central role in providing all the *required processes* that the digital twin is expected to perform. The workflow must also have a user interface enabling commands to be received from the users, and the quantitative and visual outputs to be provided. The workflow will coordinate and sequence the required processes based on the aims and objectives of the digital twin. The required processes themselves can be constructed from a series of “building blocks” within the workflow. The example considered here is of a simulation-twin requiring uncertainty Quantification (UQ), and so it shall be assumed that the required building blocks are:

- physics-based modelling;
- software integration and management;
- verification & validation (V & V);
- uncertainty quantification (UQ);
- quantification of predictive confidence and diagnostics;
- output visualisation (virtual inspection).

In addition to a workflow process related to each building block, it is possible that additional workflow processes can be created by combining and further augmenting these underlying building blocks. For the current example, of a simulation-twin, the process related to data-augmented modelling is now considered.

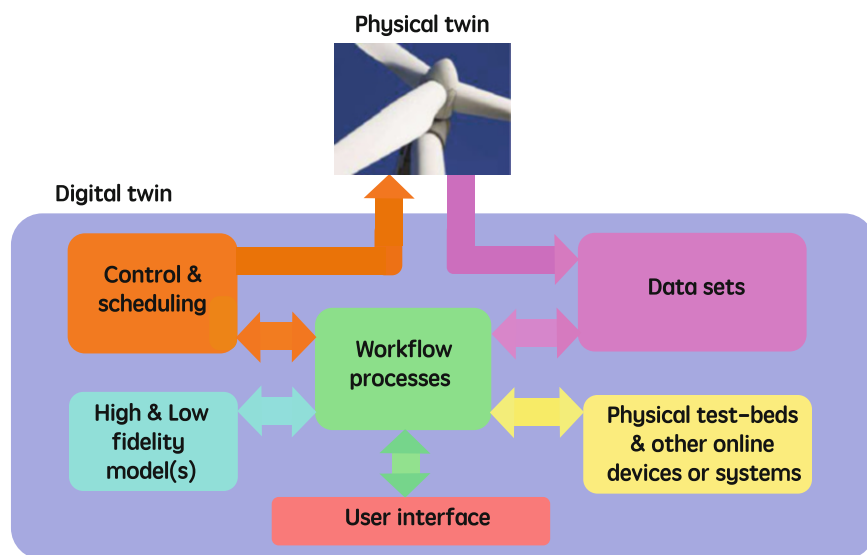


Fig. 30.2 Schematic representation of a simulation digital twin during an assessment management phase, showing the required elements for the simulation-twin and their interrelations

30.2.3 Data-Augmented Modelling

Computer models, regardless of the level of fidelity, are typically not able to capture all possible physics exhibited by an engineering system. As a consequence, a digital twin will augment the outputs from computer models with data to get closer to providing *ultra-realistic* predictions. One way to begin to quantify this is to define the *model discrepancy*. This is simply the mismatch between the computer model output and the measured process from the physical twin (assuming for simplicity there is no observational uncertainty). Two points are worthy of note here. First, model discrepancy it usually quite straightforward to measure (or estimate in the presence of observational uncertainty) even if the physical twin and/or computer model(s) are very complex. Second, even when the parameters are treated as deterministic and considered to be “truly” known, there will typically still be a mismatch, and hence some level of model discrepancy.

Therefore, based on the fact that computer modelling alone will be inadequate, models will be augmented by information from physically recorded data in order to create a digital twin. In fact this augmentation process is one of the core attributes of a digital twin, and for the purpose of demonstrating the concept it will be assumed that the digital twin has just a single computer model. Then, following the approach of Kennedy and O’Hagan [16], the computer model in the digital twin will be represented as

$$\mathbf{z}(\mathbf{x}) = \mathbf{y}(\mathbf{x}) + e = \eta(\mathbf{x}, \boldsymbol{\theta}) + \delta(\mathbf{x}) + e, \quad (30.1)$$

where $\mathbf{z}(\mathbf{x})$ and $\mathbf{y}(\mathbf{x})$ are respectively the observational and bias (or model discrepancy)-corrected computer model outputs based on the given inputs \mathbf{x} . The bias-corrected computer model output is equal to the sum of the computer model $\eta(\mathbf{x}, \boldsymbol{\theta})$ and the model discrepancy $\delta(\mathbf{x})$, where $\boldsymbol{\theta}$ are parameters of the computer model. The observations are assumed to be uncertain, and this is represented in the model by the addition of error, e .

The definitions in Eq. (30.1) allow us to build a digital twin in which firstly, data sets are used to quantify the model discrepancy, $\delta(\mathbf{x})$. Then secondly, this information is used to add a correction (i.e. calibrate) the computer model so that the augmented outputs, $\mathbf{z}(\mathbf{x})$, properly reflect the measured outputs from the physical twin. In the next section a numerical example of this process will be presented.

30.2.4 Numerical Example

The importance of the model discrepancy term is demonstrated for a simple numerical example; a mass, tension wire system, shown schematically in Fig. 30.3. The objective is to predict the natural frequency of the system f (in Hz), given different tensions T , where the mass m is unknown. To reflect the concept of model discrepancy it is assumed that the “true” system has an off-centred mass where, $L = 1\text{ m}$ $a = 0.2\text{ m}$ (Eq. (30.2) and Fig. 30.3a) and that the “true” mass is 5.45 kg. However, the model of the system does not include the ability in incorporate an offset, instead modelling the system with a centred mass, representing a level of missing physics (Eq. (30.3) and Fig. 30.3b), we have

$$f_{true} = \frac{1}{2\pi} \left(\frac{T(a+b)}{mab} \right)^{\frac{1}{2}} \quad (30.2)$$

$$f_{model} = \frac{1}{\pi} \left(\frac{T}{mL} \right)^{\frac{1}{2}} \quad (30.3)$$

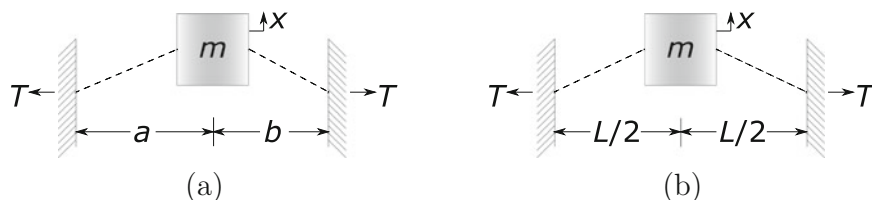


Fig. 30.3 Mass, tensioned wire system schematic. Panel (a) shows the model; centred mass, tensioned wire and panel (b) the ‘true’ system; off-centred mass, tensioned wire ($L = 1\text{ m}$ $a = 0.2\text{ m}$)

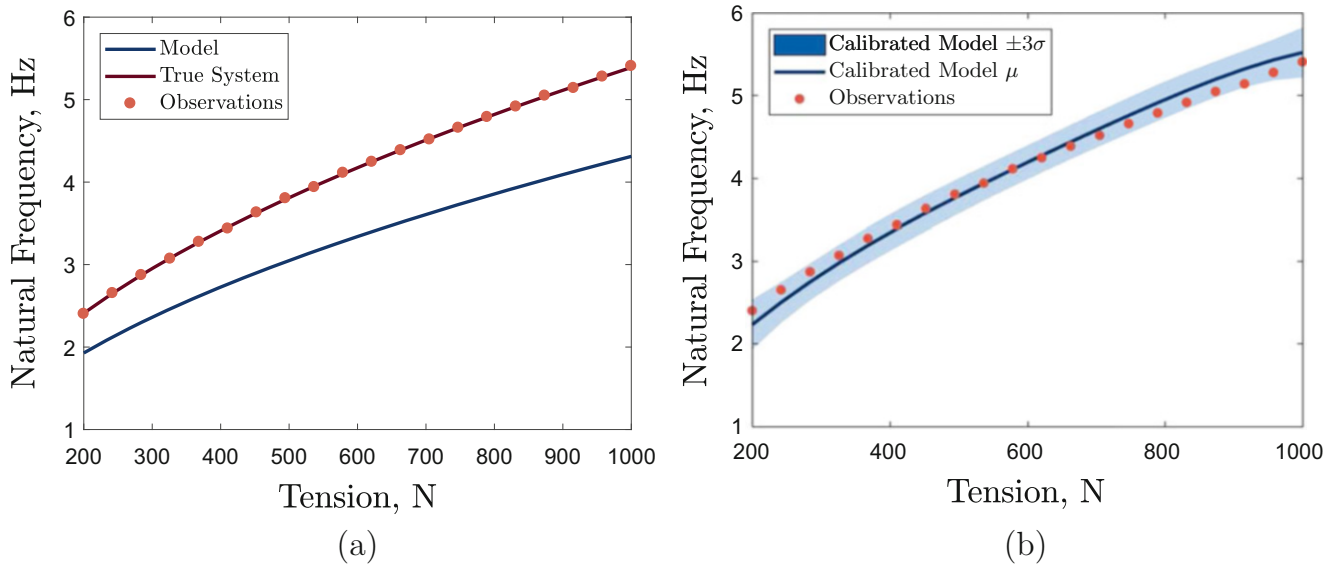


Fig. 30.4 Mass tension wire system example. Panel (a) indicates the model discrepancy between the model and “true” system when the “true” parameter value is used. Panel (b) presents the results of Bayesian calibration

Clearly when the computer model uses the “true” value of m there will be model discrepancy, as shown in Fig. 30.4a, where the computer model, true system and experimental observation (with $e \sim \mathcal{N}(0, 0.01^2)$) are compared when $m = 5.45$ kg. If calibration is performed (here Bayesian calibration is utilised) without considering model discrepancy the estimated parameter value will be biased and there is no guarantee the functional form of the output will be correct. Figure 30.4b presents the outcome of Bayesian calibration for the model (with a prior $M \sim \mathcal{N}(5.45, 0.55^2)$) where the maximum *a posteriori* probability (MAP) estimate is $M = 5.01$ kg. The result also demonstrates the difficulty in replicating the output correctly as model form errors are apparent (for further examples on the importance of model discrepancy see [17]).

30.2.5 Implications for Digital Twin Technology

It should be noted that the example presented is highly simplified compared to the intended application for digital twin technology. However, the intention is to demonstrate the power of data augmentation applied to models containing unmodelled physics. A more general interpretation of the process is that of grey-box modelling. The grey box model is formed by combining a white box (the physics-based model) with a black box (a machine learning or statistical process) in order to capture model discrepancy.

Without quantifying model discrepancy, parameters inferred during an uncertainty quantification process will typically be biased or potentially “over-confident”, leading to inaccurate predictions [17]. In a digital twin where biased parameters at a low-level model are then combined with other augmented models, this may lead to considerable errors at a full-system level. This effect could be compounded in a digital twin which includes multiple models, particularly with modelling issues such as mesh mismatches, which will result in several sources of model form errors, that if propagated to the next model/level will compound further. Trivially, bias will occur in calibrated parameters across the complete set of models, if discrepancy isn’t accounted for. As a result, in contrast to the case of a single validated model, it will be essential for digital twins attempting to join multiple models to incorporate mechanisms for inferring and compensating for model discrepancy.

Once quantified model discrepancy should be used to inform model improvements. By interrogating where the largest sources of model discrepancy exist and the functional form of the bias, improvement to the physical models can be made. This aids building confidence in predictions by ultimately leading to a reduction in uncertainty, where the digital twin will systematically improve and evolve over the life-cycle of the structure.

30.3 Conclusions

In this paper the *building blocks* of a simulation digital twin have been briefly outlined. In order to fuse the building blocks together a series of workflow processes are required, and the process of data-augmented modelling was considered in more detail. This concept is a key defining characteristic of the digital twin idea, and it was shown using a simple numerical example how augmenting a model with data can be used to compensate for the inherent model discrepancy.

There are multiple approaches for inferring model discrepancy, all of which use a data augmentation process, where model form errors are compensated for. The choice of a digital twin does not prescribe a single strategy for inferring model discrepancy, however it will not be possible to ignore this form of uncertainty and bias. General approaches may incorporate grey-box modelling via machine learning components, or fully statistical methods; this is a challenge to the implementation of a digital twin.

Acknowledgement The support of the UK Engineering and Physical Sciences Research Council (EPSRC) through grant EP/R006768/1 is greatly acknowledged.

References

1. Grieves, M., Vickers, J.: Digital twin: mitigating unpredictable, undesirable emergent behavior in complex systems. In: *Transdisciplinary Perspectives on Complex Systems*, pp. 85–113. Springer, Cham (2017)
2. Tuegel, E.J., Ingraffea, A.R., Eason, T.G., Spottswood, S.M.: Reengineering aircraft structural life prediction using a digital twin. *Int. J. Aerosp. Eng.* **2011**, 1–14 (2011). Article ID 154798
3. Datta, S.P.A.: Emergence of Digital twins—is this the march of reason? *J. Innov. Manag.* **5**, 14–33 (2017)
4. Lee, J., Ni, J., Djurdjanovic, D., Qiu, H., Liao, H.: Intelligent prognostics tools and e-maintenance. *Comput. Ind.* **57**, 476–489 (2006)
5. Cerrone, A., Hochhalter, J., Heber, G., Ingraffea, A.: On the effects of modeling as-manufactured geometry: toward digital twin. *Int. J. Aerosp. Eng.* **2014**, 1–10 (2014). Article ID 439278
6. Brenner, B., Hummel, V.: Digital twin as enabler for an innovative digital shopfloor management system in the ESB Logistics Learning Factory at Reutlingen-University. *Procedia Manuf.* **9**, 198–205 (2017)
7. Knapp, G., Mukherjee, T., Zuback, J., Wei, H., Palmer, T., De, A., DebRoy, T.: Building blocks for a digital twin of additive manufacturing. *Acta Mater.* **135**, 390–399 (2017)
8. DebRoy, T., Zhang, W., Turner, J., Babu, S.: Building digital twins of 3D printing machines. *Scr. Mater.* **135**, 119–124 (2017)
9. Li, C., Mahadevan, S., Ling, Y., Choze, S., Wang, L.: Dynamic Bayesian network for aircraft wing health monitoring digital twin. *AIAA J.* **55**(3), 930–941 (2017)
10. Schleich, B., Anwer, N., Mathieu, L., Wartzack, S.: Shaping the digital twin for design and production engineering. *CIRP Ann.* **66**, 141–144 (2017)
11. Söderberg, R., Wärmejord, K., Carlson, J.S., Lindkvist, L.: Toward a digital twin for real-time geometry assurance in individualized production. *CIRP Ann.* **66**, 137–140 (2017)
12. Uhlemann, T.H.J., Schock, C., Lehmann, C., Freiberger, S., Steinhilper, R.: The digital twin: demonstrating the potential of real time data acquisition in production systems. *Procedia Manuf.* **9**, 113–120 (2017)
13. Tao, F., Sui, F., Liu, A., Qi, Q., Zhang, M., Song, B., Guo, Z., Lu, S.C.Y., Nee, A.: Digital twin-driven product design framework. *Int. J. Prod. Res.* 1–19 (2018)
14. Iglesias, D., Bunting, P., Esquembri, S., Hollocombe, J., Silburn, S., Vitton-Mea, L., Balboa, I., Huber, A., Matthews, G., Riccardo, V., et al.: Digital twin applications for the JET divertor. *Fusion Eng. Des.* **125**, 71–76 (2017)
15. Worden, K., Cross, E.J., Gardner, P., Barthorpe, R.J., Wagg, D.J.: On digital twins, mirrors and virtualisations. In: *Proceedings of the 37th IMAC Conference* (2019, to appear)
16. Kennedy, M., O'Hagan, A.: Bayesian calibration of computer models. *J. R. Stat. Soc. Ser. B Stat. Methodol.* **63**, 425–464 (2001)
17. Brynjarsdóttir, J., O'Hagan, A.: Learning about physical parameters: the importance of model discrepancy. *Inverse Problems* **30**, 114007 (2014)



Chapter 31

Hygro-mechanical Modelling of Wood and Glutin-based Bond Lines of Wooden Cultural Heritage Objects

Michael Kaliske and Daniel Konopka

Abstract A comprehensive modelling of the transient hygro-mechanical behaviour of complex wooden structures by finite element method is targeted. New methods and material models for glutin-based bond lines are developed, since bond lines proved to have significant influence on moisture transport and fracture behaviour. The models are validated and applied to the structural analysis of wooden music instruments exposed to mechanical and hygric loadings.

Keywords Finite element analysis · Hygro-mechanical coupling · Multi-Fick'ian moisture transport · Transient structural analysis · Wood-adhesive joint

31.1 Introduction

In many cases, museums with collections of historical music instruments have the conflict between conservation of the original substance and maintenance of original use. Especially playable stringed keyboard instruments are complex wooden structures under heavy mechanical loading. Hygric loadings as alternating climate conditions induce additional mechanical loadings and influence the physical properties enforcing damages to the structure like large deformations and cracks. In a recent research project, the Institute for Structural Analysis is developing an objective simulation tool for museums, conservators and instrument makers in order to be able to evaluate wooden structures.

The complexity of the investigated structures and materials need to be modelled in an efficient and reliable manner. Simplifications and assumptions have to be included. But often, oversimplifications are applied in recent numerical structural analyses of wooden structures. The time- and moisture-dependent material behaviour of wood as well as the mechanical and hygric characteristics (e.g. water transport) of bond lines and surface coatings, which have a significant direct or indirect contribution on the load bearing behaviour of the whole structure, need to be considered properly.

In this paper, a short overview is given on the numerical models utilised in the software for the simulation of the load bearing behaviour at coupled mechanical and hygric loading.

31.2 Methods

For the comprehensive structural-mechanical investigation of the whole construction of a complex wooden structure, like wooden music instruments, numerical methods are required. Therefore, the finite element method (FEM) [1] is utilised.

In the following, the developed methods and time- and moisture-dependent material models of wood and bond lines are briefly introduced. They are used for the investigation of the moisture distribution, the state of deformation and the load bearing behaviour.

The properties of loaded wood essentially depend on the type and direction of loading, respectively the material directions radial (r), tangential (t) and longitudinal (l). Compressively loaded wood, especially perpendicular to the grain, leads to ductile failure with plastic deformations beyond the elastic range. For the numerical simulation, a multi-surface plasticity model has been developed [2] and expanded to moisture dependency [3]. The elastic behaviour bases on the theory of orthotropic elasticity [4]. Exposed to tensile or shear loading, wood shows distinctive brittle failure. This property can be captured by interface-elements and corresponding moisture dependent material models [3, 5].

M. Kaliske (✉) · D. Konopka
Institute for Structural Analysis, Technische Universität Dresden, Dresden, Germany
e-mail: michael.kaliske@tu-dresden.de

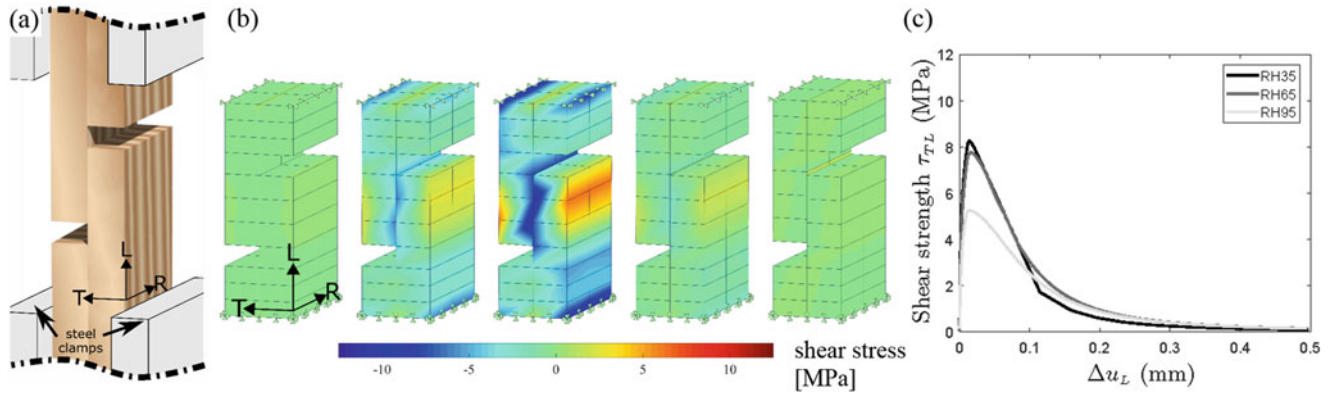


Fig. 31.1 Shear test of adhesive-wood joints (glutin-based glue and European beech): (a) experimentally tested specimen [9]; (b) shear stress (τ_{TL}) propagation from initial condition ($u_L = 0 \text{ mm}$) over peak condition before failure ($u_L = 0.145 \text{ mm}$) until final condition ($u_L = 0.5 \text{ mm}$); (c) effect of three different moisture levels (RH = 35% MC = 6.8%, RH = 65% MC = 12.1%, RH = 95% MC = 23.8%) on the shear stress-relative displacement relation in the joint [11]

When wooden structures are exposed to water vapour, moisture is absorbed via the surface and transported inside the material. Different models with different simulation effort and accuracy exist. A realistic model with a two phase, i.e. multi-FICK'ian moisture transport of vapour and bound water is applied for the investigated sensitive objects [6].

The mechanical and hygric effects are mutually dependent. The processes of swelling and shrinkage (hygro-expansion) take place in every wooden construction and can cause decisive stresses, when the free hygro-expansion is constrained. The effect is modelled with differential swelling/shrinkage values (percent swelling/shrinkage per percent moisture change). Another effect is the change of material properties with changing moisture content, which is as well considered for the material models. With increasing moisture content, elastic and strength values decrease. Since the material properties of wood are defined by the microstructure, all input quantities of the models additionally depend on the wood species.

The surface resistance with respect to the emission of water vapour is considered by hygric convective surface elements. Models for the influence of the buffering effect, based on the boundary layer theory as well as models for shellac varnish with specific permeabilities are available and applied in the simulations [7, 8]. The contribution of the surface coatings on the mechanical load bearing behaviour of the structure is rather marginal, due to their small thickness. It might become relevant for the analysis of grounded (gesso layer) panel paintings with thicker coatings.

Recent investigations deal with the development of multi-FICK'ian hygro-mechanical models for glutin-based bond lines. A cohesive element model, based on [5] is modified by adding features to simulate the mechanical behaviour of and the moisture transport in the joint.

The joint, which includes one layer of adhesive and two layers of transition zones, is simplified by using a single layer of cohesive elements. The material properties of the adhesive and the transition zones are assigned to the cohesive element. This method decreases computational effort with a lesser number of material and element layers, while still maintain the reliability of the model. The investigated glues are gelatine-based adhesives, which are often used in wooden cultural heritage objects found in museums and collections. The hygro-mechanical properties of gelatine-based adhesives base on experimental investigations in [9, 10]. The element and material formulations are described in [11].

The new bond line model is validated by numerical investigations of two wood species, European beech (*Fagus sylvatica* L.) and Norway spruce (*Picea abies* L.), based on own and further experimental studies available in the literature. The simulated specimens contain a single bond line of animal adhesive. Hygro-mechanical shear tests (Fig. 31.1) and diffusion experiments are simulated and compared to the experimental results.

Finally, the methods are applied on the hygro-mechanical structural analysis of a clavichord. The structure is mechanically loaded by the tensioned strings and the pins that carry the string load into the instrument. With respect to the hygric loading, an alternating climate with a changing ambient relative humidity (RH) is simulated.

31.3 Results and Discussion

The results of the validations show that under mechanical loading, the numerical simulation of fracture under tension and shearing are in agreement with the experimental results. Under moisture loading, however, the numerical results are diverse in comparison to the experimental results. The reason for this difference is primarily due to the incomplete experimental data which are served as the input parameter in the numerical simulation.

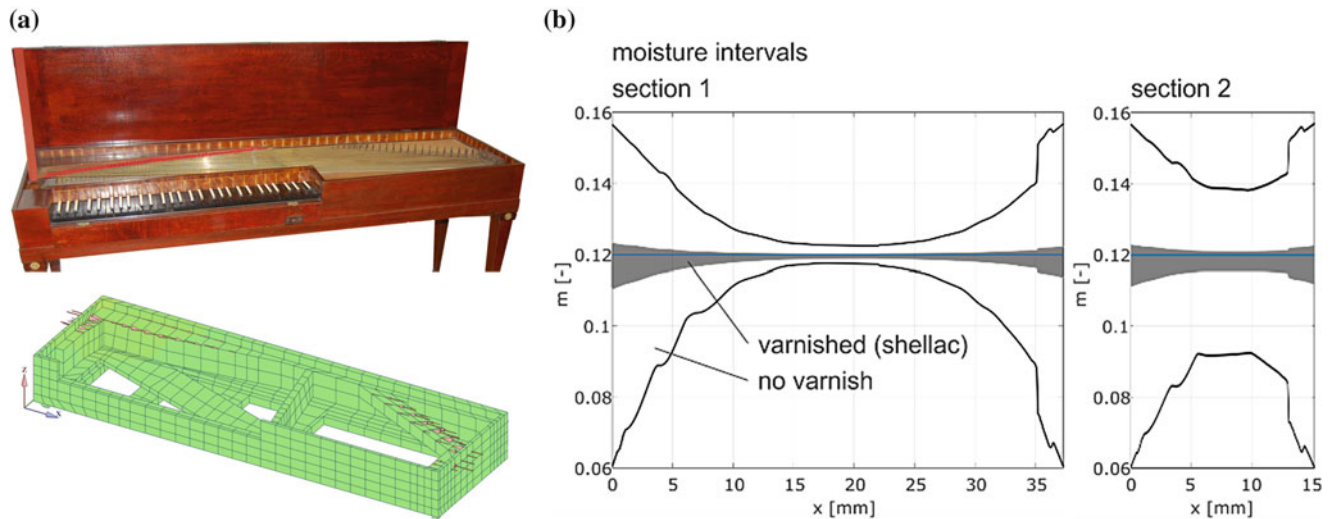


Fig. 31.2 Clavichord: (a) original instrument and discretised FE-model; (b) two discretised cross-sections of the side wall and simulated moisture intervals $m(x,t)$, with and without shellac coating at alternating climate (30%/80%RH, period $\tau = 2$ weeks)

Exemplarily, the results of internal wood moisture distributions in two cross sections of a side wall of the clavichord are shown in Fig. 31.2. Especially in case of unvarnished surfaces the barrier effect of the bond lines is visible. The large moisture gradient leads to internal hygro-expansional constraints at the adhesive layer and might provoke cracks around the bond line.

31.4 Conclusion and Outlook

The new bond line model enables to consider the influence of adhesive layers on the fracture behaviour and the resistance on moisture transport within structural analysis of wooden music instruments. In a first step, the long-term behaviour under consideration of visco-elastic and mechano-sorptive creep [12, 13] is not considered, but will be investigated in the recent research. Moreover, further experimental research on hygro-mechanical fracture behaviour and moisture transport in all members of the investigated structures are required to enhance the accuracy of the simulation results.

Keeping in mind that every model is limited, simulation results can help conservators to evaluate constructions, detect overloaded structural members in a non-destructive way and with that develop conservation measures and define climate conditions.

Acknowledgement The authors would like to acknowledge the cooperation with the Institute for Building Materials (IfB, ETH, Zurich) and the Stiftung Händel-Haus Halle, and the financial support of their research by the German Research Foundation under grant KA 1163/25.

References

1. Bathe, K.-J.: Finite Element Procedure. Prentice Hall, Upper Saddle River, NJ (1996)
2. Resch, E., Kaliske, M.: Three-dimensional numerical analyses of load-bearing behavior and failure of multiple double-shear dowel-type connections in timber engineering. *Comput. Struct.* **88**, 165–177 (2010)
3. Saft, S., Kaliske, M.: Numerical simulation of the ductile failure of mechanically and moisture loaded wooden structures. *Comput. Struct.* **89**, 2460–2470 (2011)
4. Bodig, J., Jayne, B.A.: Mechanics of Wood and Wood Composites. Krieger Publishing, Malabar (1993)
5. Schmidt, J., Kaliske, M.: Simulation of cracks in wood using a coupled material model for interface elements. *Holzforschung*. **61**, 382–389 (2007)
6. Konopka, D., Kaliske, M.: Transient multi-Fickian hygro-mechanical analysis of wood. *Comput. Struct.* **197**, 12–27 (2018)
7. Konopka, D., Gebhardt, C., Kaliske, M.: Numerical modelling of wooden structures. *J. Cult. Herit.* **27S**, S93–S102 (2017)
8. Reichel, S.: Modellierung und Simulation hygro-mechanisch beanspruchter Strukturen aus Holz im Kurz- und Langzeitbereich. PhD Thesis, Technische Universität Dresden (2015)

9. Bachtiar, E.V.: Material characterization of wood, adhesive and coating of cultural heritage under various climatic conditions, PhD Thesis, ETH Zürich (2017)
10. Zumbühl, S.: Proteinische Leime – Ein vertrauter Werkstoff? Aspekte zum feuchtephysikalischen Verhalten von Gelatine. Zeitschrift für Kunsttechnologie und Konservierung. **17**, 95–104 (2003)
11. Bachtiar, E.V., Konopka, D., Schmidt, B., Niemz, P., Kaliske, M.: Hygro-mechanical analysis of wood-adhesive joints. Eng. Struct. In Press (2019)
12. Reichel, S., Kaliske, M.: Hygro-mechanically coupled modelling of creep in wooden structures, Part I: Mechanics. Int. J. Solids Struct. **77**, 28–44 (2015)
13. Reichel, S., Kaliske, M.: Hygro-mechanically coupled modelling of creep in wooden structures, Part II: Influence of moisture content. Int. J. Solids Struct. **77**, 45–64 (2015)



Chapter 32

Modelling of Sympathetic String Vibrations in the Clavichord Using a Modal Udwadia-Kalaba Formulation

J.-T. Jiolat, J.-L. Le Carrou, J. Antunes, and C. d'Alessandro

Abstract The vibratory and acoustic modeling of musical instruments is important for several purposes in cultural heritage preservation, performance studies and musical creation. On the one hand, building a model helps understanding the key features of an instrument, and then is useful for evaluation, documentation and preservation of historical models. On the other hand, modeling and simulation can help for improving existing instruments, or even designing new instruments by extension of the model. The clavichord is an early keyboard instrument equipped with a very simple mechanics. The strings are excited by small metal wedges or blades (the tangents) placed at the end of the keys. The tangent remains in contact with the strings for the duration of the note, defining the vibrating length of the string. All strings are coupled at a same bridge. A string is divided into three sections: a damped section (DS) between the hitch-pin and the tangent; the played section (PS), excited by the tangents, between the tangent and the bridge; and the resting section (RS) between the bridge and the tuning pin. Because of the coupling through the bridge of the PS and RS, the RS is set into vibration, acting as sympathetic strings. The vibratory responses of the RS is modelled using a modal approach based on the Udwadia-Kalaba formulation. Firstly, a review of the method is presented, accompanied with measurements performed on an instrument (copy of a Hubert 1784 fretted clavichord), which include an experimental modal analysis at the instrument bridge and measurements of string motions. Then, simulation results are reported and compared with experimental measurements.

Keywords Sympathetic vibration · Clavichord · Udwadia-Kalaba formulation · String coupling · Modal analysis

32.1 Introduction

The sound of string instruments results of the vibratory behavior of coupled mechanical subsystems. These couplings can be studied by using physical modeling of several kinds. For instance, in the case of the concert harp, the coupling of the strings and the soundboard has been modeled by means of transfer matrices [5]. Also, it could be modeled by using finite element methods or experimental modal analysis, in particular using substructure techniques. In the case of the guitar, the couplings have been modeled by extracting the modal parameters of the soundboard at the bridge locations where the strings and the structure motions are coupled [1]. In the clavichord, a string is divided into three functional sections: a damped section (DS) between the hitch-pin and the tangent; the played section (PS), excited by the tangents, between the tangent and the bridge; and the resting section (RS) between the bridge and the tuning pin (see Fig. 32.1). The RS of the string is not directly excited by the tangent but is subjected to the motion constraint at the bridge. Then it is set into vibration, acting as sympathetic strings. Our objective is to predict the vibratory response of the RS of strings, set indirectly into vibration as a consequence of the excitation of one PS. To proceed accordingly, we first present the Udwadia-Kalaba (U-K) formulation and its modal extension, in order to compute the vibratory responses of a set of coupled mechanical substructures. Then, having extracted the necessary experimental modal parameters from our studied clavichord, we present some results from our numerical simulation.

J.-T. Jiolat (✉) · J.-L. Le Carrou · C. d'Alessandro
Sorbonne Université, CNRS, Institut Jean Le Rond d'Alembert, Equipe LAM, Paris, France

J. Antunes
Centro de Ciencias e Tecnologias Nucleares, Instituto Superior Técnico, Universidade de Lisboa, Bobadela LRS, Portugal

32.2 Model U-K

The U-K formulation was originally obtained from the Gauss principle of least action. Then, in the papers by Arabyan and Wu [2] and Laulusa and Bauchau [4], an original algebraic approach was found for deriving the U-K formulation for constrained systems from the classical formulation with Lagrange multipliers [1]. Let us consider a mechanical system with mass matrix \mathbf{M} which is subjected to an external force vector $\mathbf{F}_e(t)$, which includes all constraint-independent internal and external forces. This system is also subjected to a set of P holonomic and non-holonomic constraints which depend on the system displacement $\mathbf{x}(t)$ and velocity $\mathbf{v}(t)$. Denoting the dynamical solution $\mathbf{x}_u(t)$ of the unconstrained system and the one $\mathbf{x}(t)$ of the constrained system, which depends on the constraining forces $\mathbf{F}_c(t)$, and following [2], one obtains the motion equations of the constrained system proposed by Udwadia and Kalaba [1, 2]:

$$\ddot{\mathbf{x}} = \ddot{\mathbf{x}}_u + \mathbf{M}^{-1/2} \mathbf{B}^+ (\mathbf{b} - \mathbf{A} \ddot{\mathbf{x}}_u). \quad (32.1)$$

$$\ddot{\mathbf{x}}_u = \mathbf{M}^{-1} \mathbf{F}_e(t) \quad (32.2)$$

where \mathbf{A} is the constraint matrix, \mathbf{b} is a known constrained vector, \mathbf{B}^+ is the Moore-Penrose inversion of matrix $\mathbf{B} = \mathbf{A}\mathbf{M}^{1/2}$. The original character of this approach is that it can be used for conservative or dissipative, linear or non-linear systems. Moreover, the generalized inverse \mathbf{B}^+ can be rendered numerically robust, even when the constraint matrix is singular. For a particular excitation $\mathbf{F}_e(t)$, we can solve these equations using a suitable time-step integration scheme. Next, we adapt the U-K formulation in order to deal with continuous flexible systems whose dynamics will be described in terms of modal coordinates. We assume a set of S vibrating subsystems, each one defined in terms of its unconstrained modal basis and being coupled through P kinematic constraints. Then, using the usual modal equations that govern the physical motion of the subsystems, we end up with similar equations of motion, which are described now in terms of modal parameters [1].

$$\ddot{\mathbf{q}} = \mathbf{W} \tilde{\mathbf{M}}^{-1} (-\tilde{\mathbf{C}} \dot{\mathbf{q}} - \tilde{\mathbf{K}} \mathbf{q} + \mathbf{F}_{\text{ext}}) \quad (32.3)$$

where \mathbf{q} represent the vector of modal displacements, $\tilde{\mathbf{M}}$, $\tilde{\mathbf{K}}$, $\tilde{\mathbf{C}}$ are respectively the modal mass matrix, modal stiffness matrix, and modal damping matrix, while $\mathbf{W} = \mathbf{I} - \tilde{\mathbf{M}}^{-1/2} \mathbf{B}^+ \mathbf{A}$ is a convenient global transformation matrix (which is computed before the time loop), where \mathbf{A} is the modal constraint matrix, and \mathbf{F}_{ext} are the external modal forces applied on the system. In order to proceed to the computation of the vibratory response of the constraint system, for a given external force vector, we need to obtain the modal parameters of each unconstrained subsystem. For the strings, we consider the classical mode shapes that we find theoretically for a flexible string. We also use a theoretical formulation for the damping of the string [3]. For the simulation, we decide to take 50 modes for each strings, covering a frequency range up to 24.5 kHz. Concerning the modal parameters of the instrument soundboard, which were measured at the bridge, these were obtained through experimental modal identification, using 37 points for the discretization along the bridge. Once we measured the vibratory frequency response functions (between a reference location and each point of the bridge), we proceeded to the modal identification using a frequency-domain approach called LSRF (Least-squares rational function estimation method), implemented in Matlab [6]. This modal analysis was performed within a frequency band going from 40 to 800 Hz, leading to 12 identified modes.

32.3 Results and Conclusion

To compare our model with experimental data, we used a vibrometer to measure the vibratory velocity of the RS of the C5 string, at two centimeters from the bridge, induced by the tangent excitation of PS of the F3 string (i.e. playing the F3 key), all the other strings being muffled. The vibratory response is only measured in the vertical polarization of the motion of the string, since the model developed gives the response in just one polarization of motion. Our first step was to model the F3 PS and the G4 and C5 RS being coupled with the bridge (see Fig. 32.1). We choose these two strings because their RS have harmonic frequency relations with the harmonics of the PS of the F3 string: therefore a significant vibratory coupling should be expected. We produced numerically a realistic string excitation such that the response of the played string was as close as possible to the experimental response. In Fig. 32.2, we compare the spectral response of the C5 RS given by the numerical simulation with the measured one. In both results, we see the fundamental frequency peak of the F3 string which is at 328 Hz and all its harmonics, which are the partials transmitted to the C5 RS by means of the coupling with the bridge. Also, we

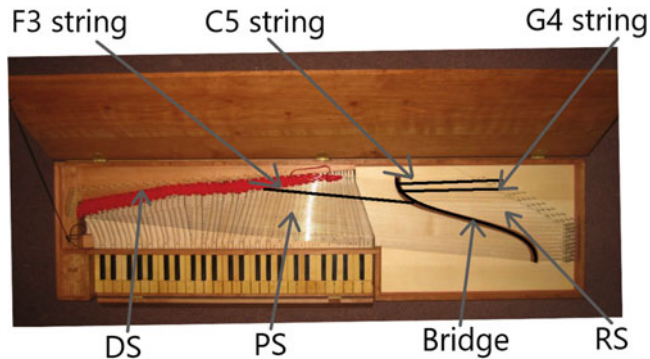


Fig. 32.1 Photo from above of the Hubert clavichord, with indications as to the substructures being modeled in our numerical simulations

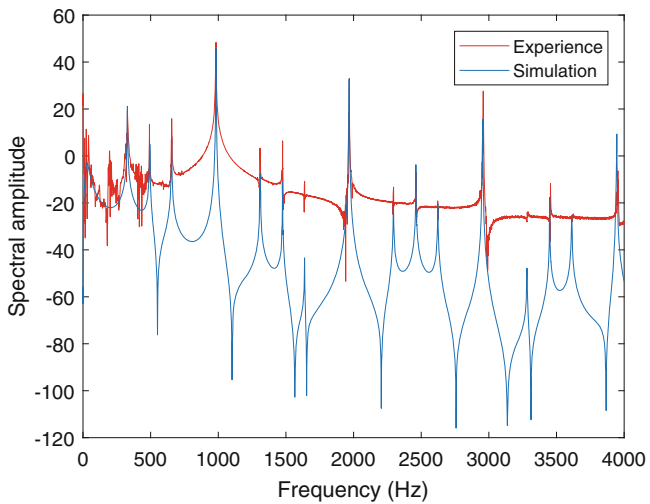


Fig. 32.2 Spectral comparison between the experimental signal measured with the vibrometer and the simulation of the C5 string having excited the F3 string of the Hubert clavichord

note the presence of the fundamental frequency peak of the C5 RS which is at 491 Hz and its harmonics, being present because of the impulse response given to all substructures by the tangent excitation. Figure 32.2 shows a good agreement between the numerical simulation and measurement. So with this simplified model, we can take account of much of the physics being involved despite of the complexity of this instrument. For example, the coupling of the string with the bridge is quite simplified in the model. However, some spectral components do not have the same spectral amplitudes. In particular, we see that the partial at 200 Hz is absent in the simulation. We conjecture that this frequency peak comes from a soundboard mode of the clavichord which was not taken into account in the model. As for the other partials, their lack of spectral energy is probably due to a lack of precision in the estimation of the damping of the strings, and/or from some inaccuracy of the simulated string excitation. To further improve the model, we should consider all the 74 sympathetic strings of the Hubert clavichord in our simulation, which implies much longer computations. However, repeating the same measurement with all strings being free, the vibratory response of the RS of the C5 string remains quite unchanged. So we may not need to consider all the strings in the model to obtain a better result. Also, to improve our results, we should proceed to a more precise study of the damping of the strings and of the excitation features, to have a better estimation of the spectral amplitude of each partial of the computed response.

References

1. Antunes, J., Debut, V.: Dynamical computation of constrained flexible systems using a modal Udwadia-Kalaba formulation: application to musical instruments. *J. Acoust. Soc. Am.* **141**(2), 764–778 (2017)
2. Arabyan, A., Wu, F.: An improved formulation for constrained mechanical systems. *Multibody Syst. Dyn.* **2**(1), 49–69 (1998)
3. Cuesta, C., Valette, C.: Mécanique de la Corde Vibrante, p. 520. Hermès, Paris (1993)
4. Laulusa, A., Bauchau, O.A.: Review of classical approaches for constraint enforcement in multibody systems. *J. Comput. Nonlinear Dyn.* **3**(1), 011004 (2008)
5. Le Carrou, J.L., Gautier, F., Dauchez, N., Gilbert, J.: Modelling of sympathetic string vibrations. *Acta Acust. Acust.* **91**(2), 277–288 (2005)
6. Ozdemir, A.A., Gumussoy, S.: Transfer function estimation in system identification toolbox via vector fitting. *IFAC-PapersOnLine* **50**(1), 6232–6237 (2017)



Chapter 33

Modeling and Stochastic Dynamic Analysis of a Piezoelectric Shunted Rotating Beam

Zhenguo Zhang, Ningyuan Duan, Jiajin Tian, and Hongxing Hua

Abstract This work presents a variational based stochastic electromechanical coupling model for response analysis of a rotating cantilever beam with piezoelectric patches surface-mounted. The resonant shunt circuits are connected to the piezoelectric elements to reduce vibrations of some specific resonance frequencies. The deterministic equations of motion are derived by the generalised form of Hamilton's principle for electromechanical systems and Rayleigh-Ritz modeling method based on the orthogonal polynomial bases, while the Penalty method is adopted to connect the beam and piezoelectric patches. The parameter uncertainties are taken into account in both the structural and electric components. The generalized polynomial chaos expansion (gPCE) is employed to represent propagation of parameter uncertainties and to estimate the statistical characteristics of the responses. Various results are presented and compared with the Monte Carlo simulation (MCS) in order to validate the efficiency of the proposed formulation. Uncertainty analyses are carried out to ascertain the effects of probabilistic parameters on the responses. The results reveal that both the structure and piezoelectric uncertainty can affect the vibration behaviors, and consideration of parameter uncertainties is needed in dynamic designs in order to minimise the vibration response at resonance frequencies.

Keywords Rotating beam · Vibration · Stochastic dynamic · Electromechanical

33.1 Introduction

Rotating beams provide basic components of many common engineering applications, such as turbine blades [1]. In the realistic applications, the turbine blades are subjected to high dynamic forces which can lead to high cycle fatigue failures. An effective vibration control of rotating beams is one of the most essential tasks for relevant designs of such systems. The shunted piezoelectric damping technique is a potentially applicable method to reduce the vibrations of turbine blades.

In the applications of the piezoelectric damping to the turbine blades, most researches have been performed in the non-rotational frames and the rotational effects have been always neglected [2]. The main differences between the rotating and non-rotating beams are the additional Coriolis effects and centrifugal force due to the rotational motion, which will result in the considerable coupling of the vibration modes in different directions. When the aero-elasticity are involved, those effects may significantly influence the dynamic behaviors of rotating beam systems [3]. However, in most studies of rotating beams, only the bending and stretching deformations were considered, the Coriolis effects as well as the coupling among the elastic deformations of various directions, such as bending-stretching and bending-twist have been neglected.

Moreover, in practice input parameters are always submitted to dispersions due to inherent uncertainties involving in manufacturing process and intrinsic properties of materials [4], so the response may also alter in the uncertain way. Thus, in order to accurately estimate the system performance, the consideration of effects of input uncertainties into the system modelling is necessary. However, little research exists regarding the rotating beams with uncertain parameters, and the effects of uncertainty propagation into uncertain responses remain misunderstood.

Thus, the goal of this work is to (1) to develop multiphysics model of rotating beam with piezoelectric patches surface-mounted, and (2) allow a prediction of uncertain responses generated by uncertainties in both the structural and electric components based on a probabilistic framework.

Z. Zhang (✉) · N. Duan · J. Tian · H. Hua
Department of Mechanical Engineering, Shanghai Jiao Tong University, Shanghai, China
e-mail: zzgjtx@sjtu.edu.cn

33.2 Background

To achieve an effective computational procedure, a stochastic variational method is proposed. Firstly, a variational formulation of a rotating beam with piezoelectric patches is derived from the generalised form of Hamilton's principle for electromechanical systems, which involves the structural displacements and electrical voltage of piezoelectric patches. Then an inductance-resistance-shunt is included in the voltage variable by using the Kirchhoff's second law. In order to accurately predict vibration characteristics of the rotating beam, the fully geometrically nonlinear beam theory is employed. The deterministic equations of motion are derived by Rayleigh-Ritz method based on the orthogonal polynomial bases. The generalized polynomial chaos expansion (gPCE) [5] is then employed to represent propagation of uncertainties (such as the resistance and the rotating speed) and to estimate the statistical characteristics of the responses.

33.3 Analysis

Figure 33.1a shows the effect of Coriolis effects on the first in-plane natural frequency against the rotational speed. For small values of rotational speed, the Coriolis force has little influence on the dynamic characteristics. With the increase of the rotational speed, the influence becomes large and the Coriolis effects are counterbalance the stiffening effect of the centrifugal force due to the rotating motion. Figure 33.1b shows the twist displacement of the cantilever rotating beam with a tip force along the vertically bending direction. Due to the Coriolis effects and nonlinear effects, the in-plane and torsional motions are coupled with vertically bending and axial vibrations. The generalized-time integration method [6] is adopted to obtain the transient nonlinear dynamic responses for the rotating beam. It is found that the introducing the series single-mode shunt damping can significantly reduce the resonant magnitude of the selected resonant frequency. That is mainly due to that the strain energy in the beam and piezoelectric patch is transformed into the electrical energy of shunt, which will finally dissipate into heat. Uncertainty analysis is then performed to ascertain the influence of random parameters on responses. The results reveal that both the structure and piezoelectric uncertainties can affect the dynamic behaviors and hence the consideration of input uncertainties is necessary in analyses.

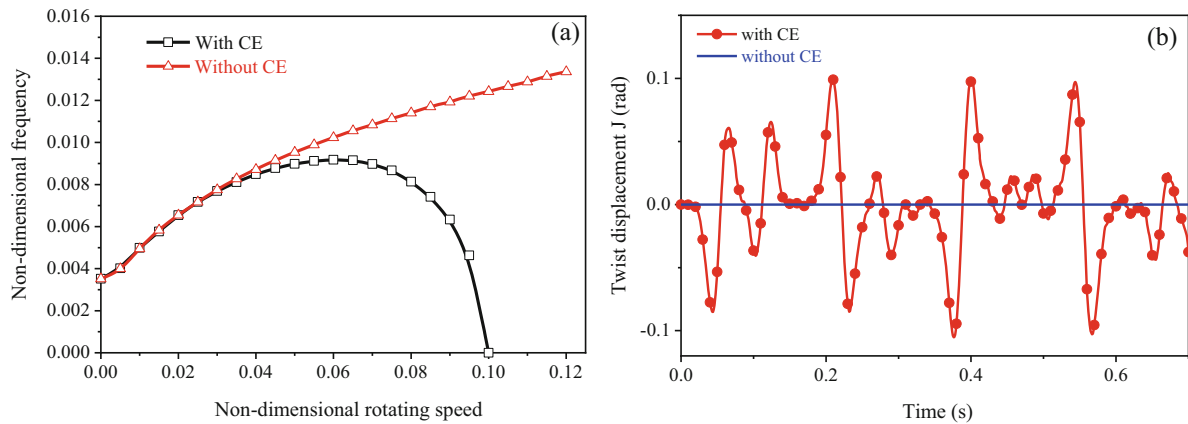


Fig. 33.1 Effects of rotational speed on the dynamic characteristics of the rotating beam

33.4 Conclusion

A coupled electromechanical model is developed for the a rotating beam with piezoelectric patches surface-mounted. The passive inductance-resistance-shunt damping is employed to attenuate the vibration of the rotating beam at the selected resonant frequency. Both the Coriolis effect and nonlinear effects arising from the couplings of bending-stretching, bending-twist and twist-stretching are taken into account. The effect of input uncertainties into the system modelling is considered. The efficiency and accuracy of the given model is tested and validated. Novelty of this work includes the combination of the power of non-intrusive gPCE for prediction of uncertain responses and the flexibility of the generalised form of Hamilton's principle for modeling of the complex electromechanical rotating beam.

Acknowledgements The authors gratefully acknowledge the financial support provided by the National Natural Science Foundation of China (NSFC, Grant No. 51505281).

References

1. Yoo, H.H., Shin, S.H.: Vibration analysis of rotating cantilever beams. *J. Sound Vib.* **212**, 807–828 (1998)
2. Tian, J., Su, J., Zhou, K., Hua, H.: A modified variational method for nonlinear vibration analysis of rotating beams including Coriolis effects. *J. Sound Vib.* **426**, 258–277 (2018)
3. Manolas, D.I., Riziotis, V.A., Voutsinas, S.G.: Assessing the importance of geometric nonlinear effects in the prediction of wind turbine blade loads. *J. Comput. Nonlinear Dyn.* **10**, 041008–041001 (2015)
4. Yuan, J., Scarpa, F., et al.: Efficient computational techniques for mistuning analysis of bladed discs: a review. *Mech. Syst. Signal Process.* **87**, 71–90 (2017)
5. Xiu, D., Karniadakis, G.E.: Modeling uncertainty in flow simulations via generalized polynomial chaos. *J. Comput. Phys.* **187**, 137–167 (2003)
6. Bauchau, O.A.: Flexible multibody dynamics. Springer Science & Business Media, Berlin (2010)



Chapter 34

On Digital Twins, Mirrors and Virtualisations

K. Worden, E. J. Cross, P. Gardner, R. J. Barthorpe, and D. J. Wagg

Abstract A powerful new idea in the computational representation of structures is that of the *digital twin*. The concept of the digital twin emerged and developed over the last two decades, and has been identified by many industries as a highly-desired technology. The current situation is that individual companies often have their own definitions of a digital twin, and no clear consensus has emerged. In particular, there is no current mathematical formulation of a digital twin. A companion paper to the current one will attempt to present the *essential* components of the desired formulation. One of those components is identified as a rigorous representation theory of models, how they are validated, and how validation information can be transferred between models. The current paper will outline the basic ingredients of such a theory, based on the introduction of two new concepts: *mirrors* and *virtualisations*. The paper is not intended as a passive wish-list; it is intended as a *rallying call*. The new theory will require the active participation of researchers across a number of domains including: pure and applied mathematics, physics, computer science and engineering. The paper outlines the main objects of the theory and gives examples of the sort of theorems and hypotheses that might be proved in the new framework.

Keywords Digital twins · Mirrors · Virtualisations · Verification and validation (V&V)

34.1 Introduction

The *digital twin* has emerged in the last two decades as a highly sought-after generalisation of the computational models routinely used by industry and academia in attempts to understand the behaviour of real structures, systems and processes and to make predictions in previously unseen circumstances [1–3]. There is currently no real consensus on what the necessary and sufficient ingredients of a digital twin are, although a sister paper to this one [4] will attempt to bring some order to the subject. What is inarguable, is that because the digital twin extends the concept of a computational model, such a model must be a core ingredient. Furthermore the model must be *validated*; it must be demonstrated to be in correspondence with reality, at least in the context of immediate engineering importance. Because of the problems which a digital twin will be required to address, it will also potentially need to extrapolate or generalise to predictions on different structures or the same structure in different contexts. This paper will argue that, in order to ensure the correct operation of digital twins, a mathematical framework is needed in order to quantify the likely fidelity of validated models when used to generalise or extrapolate. This paper will propose that what is needed is a type of *algebra* of models, which can be used in order to extend current concepts of *verification and validation* (V&V).

For the purposes of this paper, the fundamental problem of V&V will be regarded as the need to answer two questions:

1. What is the lowest-cost model that will allow predictions of the required accuracy for the structure of interest in the context of interest?
2. What is the lowest-cost programme of experimental testing that will validate the model with prescribed confidence?

Note that in answering these questions, one does not need a model that represents the whole structure across its entire range of possible behaviours; one only needs a model that matches in the *context of interest*.¹ In a machine learning context,

¹Some would argue that a true ‘digital twin’ has to match the structure of interest in *all* contexts. This viewpoint does not make complete sense, as the physics of a given structure is unlikely to be known at all scales and in all contexts; this means that modelling would not be possible.

K. Worden (✉) · E. J. Cross · P. Gardner · R. J. Barthorpe · D. J. Wagg
Dynamics Research Group, Department of Mechanical Engineering, University of Sheffield, Sheffield, UK
e-mail: k.worden@sheffield.ac.uk



Fig. 34.1 Fraternal (non-identical) twins (publicity still from 1988 film *Twins*)

the question is essentially of generalisation; having learned from model data, can one say something meaningful about the structure twinned with the model?

The use of the word ‘twin’ in the context of modelling is actually interesting semantically. Clearly the idea is to suggest a one-to-one relationship or *identity* between a structure and a model; however, this is unjustified if one refers to biology. According to recent statistics,² roughly one in 65 births results in twins; of these, the vast majority are fraternal—or *non-identical* twins (see Fig. 34.1). Furthermore, opposite-sex twin pairs make up roughly 33% of fraternal twins. In fact, identical twins result from only one in 285 births, and even identical twins have distinct teeth marks and fingerprints. Finally, twins may look identical, but behave in *completely* different ways.

In order to establish an over-arching mathematical framework, one will need to be precise and meaningful in one’s terminology. The use of the term ‘twin’ is inconsistent with this goal for two reasons discussed above; the first is that there is already widespread and disparate use of the term in the engineering community; the second is that it doesn’t really make sense as an analogy anyway. The view taken in this paper, will be that a more meaningful term is provided by the word *mirror*. A mirror is an instrument that faithfully reflects reality in terms of the aspects of an object that are *mirror-facing*; it provides no ‘information’ about aspects that are not mirror-facing. The idea of ‘mirror-facing’ will be formalised in the following as a *context*. Finally, if the object moves, the movement will be reflected perfectly, in the mirror—at least as far as those aspects that are mirror-facing. This paper then, will attempt to motivate a mathematical basis for understanding *mirrors*.³ As such, it will have the opportunity to develop independently of current conceptions as to what a ‘digital twin’ is, but leaving the possibility for engineers to adopt the technology in developing whatever their favoured definition of a digital twin actually is.⁴

Enough of levity; it is important to remember that everything here is motivated by the desire to construct meaningful validated models of structures and systems; if one were to do nothing more than rearrange the terminology and dress the problem in pretty mathematical trappings, then that would be ultimately empty. This paper is motivated by the belief that a general mathematical theory of models and their validation will be of value; however, the current paper will not be able to go beyond development of the basic terminology and theory and some attempts to convince the reader of the ultimate possibilities. One might argue that general frameworks have already been proposed in terms of the formulation and evaluation of models, and that there is no need to propose another one until the existing ones have been fairly evaluated. This is a fair

Furthermore, a lot of the motivation for digital twins comes from industry, and it is not conceivable that a profit-driven enterprise would require a model to function outside the immediate context of interest if that extended functionality came at an increased cost.

²Twin statistics from <http://www.twinsuk.co.uk>—accessed 30th June 2018.

³The term *digital mirror* is already in use to define an item of technology; the items being exactly what one might imagine them to be. One could use the term with complete confidence that the two meanings are unlikely to be confused; however, for simplicity the objects of interest will just be referred to as ‘mirrors’, although different kinds of mirrors will be introduced.

⁴As a final observation on biological twins, there is an interesting link between twins and mirrors. Twenty five percent of identical twins are *mirror-image twins*; their hair falls in different directions, their fingerprints are mirror images of each other and, if one of them is right-handed, the other will be left-handed.

point; however, the authors here would argue that the current proposal is more sympathetic to the needs of the digital twin concept, because of the explicit attention given to context and environment. There is no intention here to play down any previous works on general methodologies, the assumption is that the tools already proposed will play important roles. One example of a general framework for V&V is provided in [5]. That publication provides a methodology for estimating the uncertainty in system-level predictions, where system-level parameters are estimated in terms of lower-level experiments. The paper is largely concerned with calibration and uncertainty propagation, and introduces tools for estimating the reliability of models. Perhaps more importantly for the current discussion, the paper introduces a concept of ‘relevance’ which quantifies the relationship between the system-level model and lower-level models, and potentially allows a ‘confidence’ measure in terms of extrapolating from lower levels to the system level. The paper by Nagel and Sudret [6], proposes a Bayesian unified framework which provides a ‘... toolkit for statistical model building. It forms some kind of superstructure that embeds a variety of stochastic inverse problems as special cases’. (There are of course, many other papers one could cite; however, there is no intention here to provide a survey.) Another fair criticism of the current paper is that the new term ‘mirror’ is not needed either, it refers simply to a validated model; however, it is introduced here because it refers to a specific class of models and because, as discussed above, there is a need to distinguish the idea from the more overarching digital twin.

The layout of the paper is as follows. The next section will make the main series of definitions of the important concepts in the framework: contexts, mirrors etc. The section will also define the concepts of *environments* and *virtualisations* which are central to the idea of a digital twin. Section 34.3 will discuss a number of example problems in which the idea of a mirror would be fruitful, assuming that the appropriate mathematical underpinnings of the theory can be provided. The paper finishes with some discussion and conclusions.

34.2 Mirrors

34.2.1 Basic Definitions

To start with the *simplest* situation, the discussion will initially consider only physics-based models; data-based and hybrid models⁵ will be brought in later.

One must begin with a structure (or system) S ; this is the *physical* object of interest. It will be interpreted as having an objective reality independent of its surroundings i.e. it is possible to think of it in a vacuum remote from any other matter. Temporal changes in the confirmation and behaviour of the structure will be summarised in a *state vector* $\underline{s}(t) = \{s_1(t), \dots, s_{N_S}(t)\}$, which consists of a set of N_S instantaneous measurements (at time t) which completely characterise its state.

Now, the environment of the structure could be considered as all physical reality exterior to it; however, that is too general. Considering the fact that the environment could also be characterised by a state vector; the *environment* E of S will be defined as the set of environmental variables that can actually affect S i.e. a change in a variable will evoke a change in the state $\underline{s}(t)$. With this in mind, one will have an environmental state vector $\underline{\varrho}(t) = \{e_1(t), \dots, e_{N_E}(t)\}$.

Recognising that one will generally only wish to model some aspects of the behaviour of S , a *context* C for S will be defined as a set of variables $C = \{e_i^C \in E, s_j^C \in \underline{s}; i, j\}$. The subset $\{e_i^C\}$ will be referred to as the *environmental context*, and the subset $\{s_j^C\}$ as the *response* or *predictive context*.

Now, a *schedule* W_C for the context C will be a set of time series $\{\underline{e}_W^C(t_i); i = 1, \dots, N_t; t_i \in [0, T]\}$. (In principle, the set $\{t_i\}$ could be continuous or discrete.) The *response* $\underline{r}_W^C(t)$, to a schedule W_C is defined as the measurement sequence resulting from testing the structure and imposing the schedule as inputs. As the process will generally be dynamic, it will be denoted by the functional,

$$\underline{r}_W^C(t) = S[\underline{e}_W^C(t)] \equiv W_C \quad (34.1)$$

One can now define the *test* T_W^C associated with the schedule W_C in the context C , as the set $T_W^C = \{\underline{\varrho}_W^C, \underline{r}_W^C\}$. In general, tests will be carried out for multiple purposes; for the moment, it will be observed that data are captured for training of models and for testing of models. For this reason, it is useful to divide data accordingly. Supposing that tests have been

⁵Hybrid models are also referred to in the literature as *grey-box* or *data-augmented* models. In the statistics literature, the addition of a data-based model in order to correct a physics-based model is commonly called model *bias correction* or *model discrepancy* correction; the most influential framework is probably that proposed in [7].

carried out multiple times, one can define the *training schedule* (resp. *testing schedule*) as the set of schedules associated with acquiring data for training (resp. testing); the set being denoted by D_{tr} (resp. D_t). (Of course, these sets are specific to a context and a schedule, but the notation will become too unwieldy if this is made explicit.)

Now, a *model* of S for a context C will be defined as a mathematical function M^C which attempts to predict the behaviour of S for any schedule specific to the context C . Depending on the environmental and predictive variables, this may be a multi-scale and/or multi-physics model, and it will almost always be implemented in computer code in some appropriate language.⁶ A *simulation* for a context C under a schedule W_C is then defined as,

$$\underline{m}_W^C(t) = M^C[\underline{\epsilon}_W^C(t) \equiv W_C] \quad (34.2)$$

Now, it is clear that one can obtain the simulation $\underline{m}_i^C(t)$ corresponding to a test $T_i^C = \{\underline{e}_i^C, \underline{r}_i^C\}$ (with i now a schedule label), so that one can attempt to assess the fidelity of the model by comparing its predictions to reality.

A *metric* on a given context C will be defined here simply as a function $d^C(\underline{x}, \underline{y})$ such that $d^C(\underline{x}, \underline{y}) \geq 0$, with the zero only if $\underline{x} = \underline{y}$. (This is only one of the conditions for a true mathematical *metric*, but it will do here for now.)

Finally, the main definitions of the paper are possible:

Definition 2.1 (ϵ -Mirror) A model M_ϵ^C for a given context C is an ϵ -mirror if and only if

$$d^C(\underline{m}_W^C(t), \underline{r}^C(t)) \leq \epsilon \quad (34.3)$$

for all scheduled tests in D_t .

Definition 2.2 (Fitness-for-Purpose) A model M_ϵ^C is *fit-for-purpose* in a given context C iff it is an ϵ -mirror for C and $\epsilon \leq \epsilon_T$ where ϵ_T is a critical threshold based on engineering judgement and/or context requirements.

34.2.2 Hybrid Models and Uncertainty

So far, only pure physics-based models have been considered; models sometimes termed *white-box models*. At the other end of the modelling spectrum are *black-box models* which are formed by taking a model basis with a universal approximation property, and tuning the parameters of the model to a set of observed data; examples of such models are artificial neural networks or support vector machines [8, 9]. One can also make use of *hybrid* or *grey-box* models, which combine some element specified by physics with an element of learning from data.

Suppose that it is desirable or necessary to form or update a model based on data. The model will be established using data acquired from a training schedule D_{tr} and tested on data from a test schedule D_t .⁷ The resulting model $M^{hC}(D_{tr})$ is then an ϵ -mirror if it satisfies the conditions of Definition 2.1 on D_t .

There is no distinction here on how $M^{hC}(D_{tr})$ is obtained. One might start with a white-box model and learn the parameters via system identification, or one might adopt a grey-box structure where a physics-based model is augmented with a nonparametric machine learner [10].

As the use of machine learning has been raised, it would seem to be an appropriate point to discuss *uncertainty*. This is because many modern machine learning algorithms are probabilistic and accommodate uncertainty directly. For example, Bayesian approaches to parameter estimation can characterise the entire density functions of parameters, rather than simply producing point estimates [11, 12]. Furthermore, nonparametric learners like Gaussian process regression can produce a natural confidence interval on predictions [13].

So, under the circumstances, one might allow the possibility that the model $M^{hC}(D_{tr})$ is a function that returns a random variable, i.e. the simulation responses are stochastic processes,

$$M_t^C = M^{hC}[\underline{\epsilon}_W^C(t)](D_{tr}) \quad (34.4)$$

⁶In fact, it may be the case that different models are needed in order to completely cover the context of interest. For notational simplicity, it is assumed here that M^C represents the set of relevant models, returning the values required by the overall context C ; there is no overall loss of generality at this point.

⁷Following best practice in machine learning, different data sets are potentially required in order to fit parameters and establish hyperparameters [8]. In order to keep the notation simpler here and avoid confusion about the term ‘validation’, it is assumed that the modeller simply partitions D_{tr} appropriately.

The simulation might provide the whole density function for M_t^C , or just low-order moments. In the first case, suppose that the model returns the predictive mean of the process $\bar{m}^C(t) = E[M_t^C]$ (where E is an expectation), then, $\bar{m}^C(t)$ can be used to determine whether $M^{hC}(D_{tr})$ is an ϵ -mirror *in the mean*.

Alternatively, suppose that the model returns enough information to determine confidence intervals on the prediction. In this case, then if $\underline{r}^C(t) \in ([\bar{m}^C(t) - \alpha\sigma_r^C(t)], [\bar{m}^C(t) + \alpha\sigma_r^C(t)])$ with probability determined by α , and for all schedules in D_t , then one can define $M^{hC}(D_{tr})$ as an α -mirror. Note that a given stochastic model can be both an ϵ -mirror and an α -mirror.

It would be possible to define various metrics for comparison in the uncertain case; the one based on low-order moments described above is related to the reliability metric discussed in [5], which is in turn related to a formulation of validation as an outlier analysis problem, as discussed in [14]. If the comparison were made on the whole predictive or parameter density functions, one might define a distance measure defined in terms of Kullback-Liebler divergence, for example, and this would lead to the definition of a KL-mirror etc.

34.2.3 The Environment and Virtualisation

Raising the question of uncertainty means that one must reconsider the status of the *environment*.

Recall that the environment is comprised of all those variables which can have a causal influence on S , the structure of interest. In general, this set will be composed of variables that can be controlled (e.g. forces applied to the structure) and variables that can not (or can not be controlled with any precision). In an operational modal analysis context for example, even the forces may not be controllable. It is therefore necessary to separate the variables (in context) accordingly into \underline{e}_u^C and \underline{e}_c^C (uncontrolled and controlled, respectively). This distinction is very important if one wishes to use the model to make true predictions i.e. to determine what the structure might do at some point in the future, under a given (controlled) forcing, but when the \underline{e}_u^C are unknown.

In this situation, what is needed is a generative model M_u^{EC} , that will make some best estimate of $\underline{e}_u^C(t)$,

$$\hat{\underline{e}}_u^C = M_u^{EC}(t) \quad (34.5)$$

This model itself will need to be validated appropriately, as far as possible. Given training data for the \underline{e}_u^C , it might be possible to establish a nonparametric black-box model that is an ϵ - or α -mirror, or one could substitute mean values for the variables and treat variations as uncertainty that needs to be propagated. In any case, one can now make predictions (in the given context),

$$\underline{p}^C(t) = M[\underline{e}_c^C(t), \hat{\underline{e}}_u^C] = M_u^{EC}(t) \quad (34.6)$$

It is now possible to make another important definition: a *virtualisation* for a given context C is a pair,

$$V^C = (M_{\epsilon_1}^{hC}, M_{\epsilon_2}^{EC}) \quad (34.7)$$

where the two models concerned are ϵ -mirrors with the fidelities specified. The importance of the virtualisation is that it can be used to examine what-if scenarios for the structure of interest in previously unseen circumstances. Of course, one can make a similar definition with α -mirrors. Finally, it is important to note that a virtualisation, is itself a model, and as such can also be an ϵ - or α -mirror; this will prove to be of interest later, when the use of virtualisations for design is discussed.

The problem of the ‘environment’ is discussed in [6]; however, there it appears to have been condensed into the estimation/calibration of a further parameter set.

34.2.4 The Turing Mirror

One can also think of a semi-philosophical means of defining a mirror; this parallels the *Turing test* in the field of artificial intelligence, which is a test of the ability of a machine to perform in a manner indistinguishable from a human [15].

The test will involve two protagonists: an *interrogator* and an *oracle*. The two people can only interact in a very limited way, the interrogator is allowed to present questions to the oracle about the structure of interest via a remote interface. The

oracle is equipped with a model of the structure of interest, which is the candidate mirror and also has facilities for carrying out physical testing on the structure. The interrogator is allowed to present the oracle with a set of schedules e_W^C from some given context, and the oracle is required to return either the test responses of the structure r_W^C , or simulations from the model m_W^C .⁸ If the interrogator is unable to decide which option the oracle has taken in any case, then the model in question is a *Turing-mirror* or *T-mirror*.

While this may seem like nothing more than an amusing digression, there is the possibility that the work over the years in terms of implementing the Turing test could be used in order to derive rigorous methods of testing mirrors.

This is enough of basic definitions for now; in the next section, the potential uses of the technology are explored via a number of example cases.

34.3 Examples

34.3.1 A Simple Example: Context Change

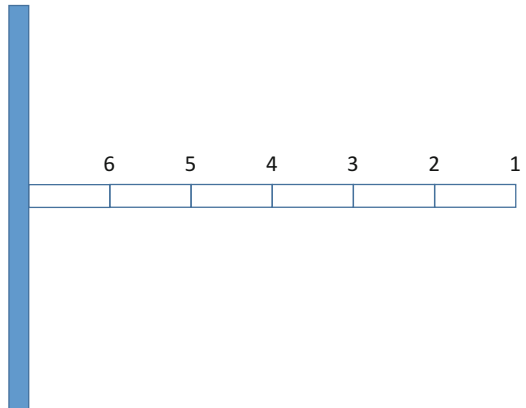
One of the simpler problems one can imagine in the context of mirrors, is how to analyse the performance of a given model, when asked to make predictions outside its original context C . This problem is interesting because it can be made to include the case of *extrapolation*, although that will not be discussed in great detail here. Extrapolation for a data-based or hybrid model occurs, when the model $M^{hC}(D_{tr})$ is used to make predictions outside the range of data encompassed by the training set D_{tr} . Even if the model $M^{hC}(D_{tr})$ is an ϵ -mirror on schedules in the training set, this may not hold if the model extrapolates. One simple way to make the problem of context change encompass the problem of extrapolation, would be to extend the definition of context C , so that it not only specifies the variables under investigation, but also the ranges of those variables encountered in training data.

This example will consider a different problem, where a model M_ϵ^C is required to make predictions on different variables to its context C . Suppose the model is modified in order to predict in a context C' , with the new model denoted $M'^{C'}$. Furthermore, assume that there are no training or test data available for the context C' . The interesting question is:

Given that a model M^C is an ϵ -mirror for the context C ; following modification to $M'^{C'}$, is the new model an ϵ' -mirror for C' for any ϵ' , and if so, what is the minimum value of ϵ' for which this holds? (Note that, with the extended definition of context discussed above, this is the extrapolation problem if $M = M'$).

Consider a simple example. Suppose one has constructed a Finite Element (FE) model M^C , of a cantilever beam (as in Fig. 34.2). The model has been validated on test data measured as the displacement responses $y_i(t)$ at points $i = 1, 3, 5$, so that the predictive context is $\{y_1, y_3, y_5\}$. Suppose that M^C has been established as an ϵ -mirror on the context C . Now, further suppose that one wishes to make predictions of the response at points 2, 3 and 4, so the predictive context for C' is

Fig. 34.2 Simple FE model for illustrating context change



⁸Clearly, there are subtleties. For example, if the necessary test programme in a given case were to take 10 days, while running the model would only take 10 h, the oracle would only return the results after the greater time.

$\{y_2, y_4, y_6\}$. In this situation, there are two simple ways to establish M' :

- The trivial approach is to simply change the output deck of M^C , so that the model outputs the required variables (if it didn't before).
- One can add a numerical interpolation step to the process in order to estimate the variables in C' from those in C .

In the first case, it should be a fairly straightforward matter to establish that the model is an ϵ' -mirror based on the existing theory of error estimates for FE models [16, 17], and one would expect that $\epsilon' \approx \epsilon$. In the second case, one should be able to use error estimates from the numerical analysis of interpolation, combined with some reasonable assumptions about the continuity of the beam profile. One could also bound the errors based on much coarser assumptions e.g. one could estimate how far y_4 could get from y_3 and y_5 before the induced stresses in the beam exceeded the yield stress. Although the latter approach would likely work, it would probably yield an $\epsilon' \gg \epsilon$, so conservative that one would find the value impractical in terms of model trust. In an exercise like this, the objective would be to find the lowest bound on ϵ' possible.

A more interesting problem arises in the case of the extended definition of context. Suppose C covered points 1, 3 and 5 at low levels of excitation, and C' covered points 2, 4 and 6 at a higher level of excitation; there would be two different answers to this question, depending on whether M^C was linear or nonlinear.

34.3.2 An Example Concerning Assembly

This example concerns a very important objective of any programme of ‘virtualisation’. Suppose one could validate a model of a full-scale assembled structure using only test data acquired from substructure testing. The cost savings in the design/production cycle would be potentially very high. It is important that the ‘algebra’ of models being developed covers this situation, and this will entail an understanding of how to model joints and joining processes.

For the sake of simplicity, consider the case of two substructures (but note that this is not a real restriction, as the substructure assembly can be considered recursively). The substructures, denoted S_1 and S_2 , will be assumed to have individual contexts C_1 and C_2 respectively. It will be assumed that the substructures will be joined using some technology, which can itself be modelled; in the general case, one assumes that the joint may itself be a substructure S_J . With a small abuse of mathematical notation, the assembled structure S_A will be denoted by,

$$S_A = S_1 \underset{S_J}{\oplus} S_2 \quad (34.8)$$

For simplicity, it will be assumed that all the responses from the substructures can still be measured; in this case one can denote the new context by $C_A = C_1 \oplus C_2$. (In this case, the \oplus is largely just a direct sum with some reordering of symbols and deletion of copies of symbols that appear in the environment context twice.) In general, one would have to allow for the fact that the joining process might eliminate a possible measurement point on the substructure, and thus change the context by removing a variable.

It is assumed that each substructure S_i has a model M_i^C associated with it, and that the models have been validated using test data from the individual structures, and it has been established that M_i^C is an ϵ_i -mirror in each case. Furthermore, assume that the joint/joining process has a model M_J , and that this model may or may not have been validated. The model of the assembled structure is denoted,

$$M_A = M_1 \underset{M_J}{\oplus} M_2 \quad (34.9)$$

The key question is now,

Given the assumptions stated, is it possible to show that there exists any ϵ_A such that M_A is an ϵ_A -mirror for S_A in the context C_A , in the absence of any test data for the assembly S_A ? If so, then what is the smallest ϵ_A for which this is true?

Of course, one could also attempt to accommodate uncertainty, and frame the question in terms of α -mirrors. This is the most difficult question so far, but it also offers the highest returns, if it can be answered. The problem also depends on whether a validated model for M_J is available. For example, consider the case when the joint is a weld, and that coupon tests have established some of the material properties of the weld material (perhaps with a high degree of uncertainty). Even allowing for the fact that the issue is not just about material properties, one would expect ϵ_A to be a monotonically-increasing function of the weld parameter uncertainties. One might also model the weld as a hybrid model, given that the physics of the joint are not perfectly understood. From first principles, one might approach the problem from the same viewpoint as before; one could make reasonable/trusted assumptions about the real joint and the model joint, and try to determine how far they can diverge.

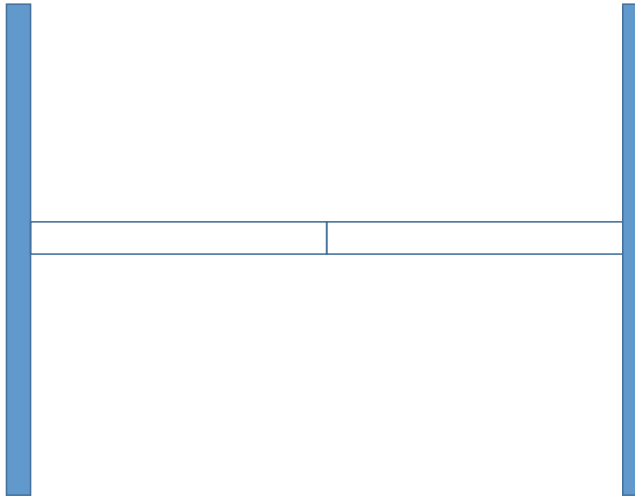


Fig. 34.3 Ecastré beam as sum of two cantilevers

In a general theory, one would hope to prove theorems that were general, perhaps across particular classes of joint models; consider for example the reasonable conjecture:

Suppose that given models $M_i^{C_i}$ ($i = 1, 2$) are ϵ_i -mirrors for structures S_i in contexts C^i , then $M^A = M_1^{C^1} \underset{M_J}{\oplus} M_2^{C^2}$ is an ϵ -mirror for the structure $S_1 \underset{S_J}{\oplus} S_2$ in the context $C_1 \oplus C_2$ with $\epsilon \geq \max(\epsilon_1, \epsilon_2)$ (where $\delta = \epsilon - \max(\epsilon_1, \epsilon_2) \geq 0$ is defined as the *joining deficit*).

Finally, it is important to mention another use of the idea of joining models. One might simply wish to represent a complex structure in terms of substructures, even if there is no physical joining process involved (a situation that arises in hybrid testing [18]). A simple example will suffice. Suppose one wished to model a fixed-fixed beam, and to validate the model. However, suppose that one had no validation data for the beam, but one did possess a validated model for a cantilever beam; in fact the cantilever model had been established as an ϵ -mirror. Clearly, one can regard the fixed-fixed beam as two cantilevers joined *perfectly* at their tips. One could now attempt to answer the question above, as to whether joining two copies of the cantilever beam is an ϵ_A -mirror for the fixed-fixed beam. In this case, one might assume that the joint model M_J is *perfect*; in practice a perfect joint when joining two FE models would be accomplished by seamlessly merging the meshes at the joint so that material continuity is as good at the joint as anywhere else. Perfect or idealised joints of this nature will be denoted by the symbol $\overset{\oplus}{P}$.

Even in the case of a perfect joint, one should be aware of a *caveat*, and this relates to *context*. Suppose that the cantilever model was *linear* and had been validated on test data showing small or moderate deflections of the cantilever tip. When the cantilevers are joined, and the cantilever tips become the mid-point of the beam, the response of the real beam will become nonlinear for much smaller values of mid-point displacement than the values measured at the cantilever tip (Fig. 34.3).

Many of the ideas discussed here are covered by the *multilevel* framework discussed in [5], and it may be that the ideas of *reliability* and *relevance* applied in that framework can be adopted in order to prove hypotheses like those pointed out in the current paper.

34.3.3 An Example Concerning Structural Health Monitoring

One of the major problems with data-based Structural Health Monitoring (SHM) is that data from damaged structures is scarce. Although damage detection is possible even if one only have data from the normal condition of the structure of interest, using unsupervised learning [19]; higher-level diagnostics like locating damage or assessing its type or severity can only be accomplished if one has data from all the damage states of interest. It is inconceivable that one might carry out a test programme that systematically involved damaging numbers of high-value structures, so one has to turn towards modelling as a means of providing the necessary data.

The context responses in an SHM problem are usually going to be features for machine learning. Given the importance of the specific context, new notation will be introduced; the SHM context will be denoted F .

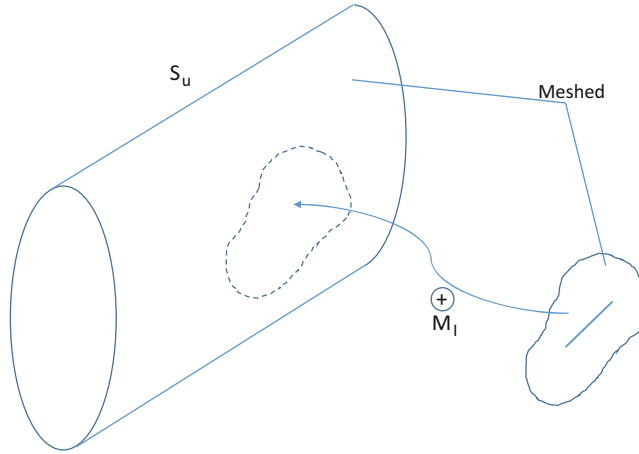


Fig. 34.4 Insertion of a local damage model into an undamaged structure model

Assume two ingredients: the first is a validated model of the undamaged structure of interest S^u , denoted by M^{uF} . Further assume a set of data $\{D_{Tr}^u, D_T^u\}$ which has been used to validate the data. Further assume that M^{uF} is an ϵ^u -mirror, according to some appropriate metric.

The second ingredient is a *local* damage model M^d , which has been validated in a context C_l using data from coupon tests. The model may have been updated on the basis of test data and may well be a hybrid (grey-box) model. Assume that under the circumstances M^{dC_l} is an ϵ^d -mirror for the context C_l according to some appropriate metric. Finally, we assume that there are *no validation data* for the damaged structure S^d .

The problem is essentially a joining problem; however, it is of a specific type and merits a little more new notation. An *insertion* model M_l is defined as an algorithm or prescription for embedding the model M^{dC_l} in M^{uF} , in such a way that the result is a model for S^d . This differs from the previous joint definitions in that there is no new physics associated with the join. M_l could be a very simple process i.e. if the two component models are FE models, insertion will only really mean harmonising the two meshes along the boundary of the join. One can think of the process as a type of *surgery*⁹ i.e. one cuts out a healthy region of M^{uF} and replaces in with M^{dC_l} , as in Fig. 34.4, and then harmonises the meshes at the boundary.¹⁰ Clearly this means that there will need to be compatibility conditions which guarantee some degree of smoothness/continuity across the boundary.¹¹

There is another compatibility condition required here by the theory; the models M^u and M^d must exchange information in such a way that the dynamics evolves appropriately i.e. the response context of C_l must overlap with the environmental context of F i.e. $C_l \cap F \neq \emptyset$. In fact, in a general assembly model $M^{C_1} \underset{M_l}{\oplus} M^{C_2}$, it will usually be necessary that $C_1 \cap C_2 \neq \emptyset$ and $C_1 \cap C_2 \neq \emptyset$ (where \emptyset represents the empty set here).

As a fairly simple example, consider the problem of modelling a crack in a pressure vessel (Fig. 34.4). The undamaged model M^{uF} represents the vessel; the damage model M^{dC_l} , represents a through crack in a section of plate. By joining the two models, one can embed a crack of arbitrary location, length or orientation in the vessel (the process might require some care near the boundaries). A subtlety here is that the crack model might have been validated for flat specimens, in which case a modification might be needed for compatibility with the curved surface of the vessel. A more important issue is the following. The behaviour of the structure will usually be modelled using macroscopic physics, while the detailed crack model will require microscopic physics; this means that the features have to be chosen very carefully so that the behaviour of the crack is communicated over the boundary effectively.

⁹Surgery is a mathematical technique for building complicated topological spaces from simpler ones [20]. It may be that the technique can be applied in the context of joining models.

¹⁰This is similar to the situation in real-time hybrid testing where coordinate sets are defined in each domain, which need to be synchronised in order to form the join. Errors in the synchronisation process then give a measure of how imperfect the joint is.

¹¹Note that this is rather perverse version of surgery, where undamaged tissue is replaced by damaged.

Given all of the above, the mathematical question of interest is:

Given all of the above, is $M^{C_1} \oplus_{M_I} M^{C_2}$ an ϵ -mirror for S^d , and if so, what is the smallest value of ϵ for which this is true?

This will usually be a probabilistic problem where the metrics are quantities like probability of misclassification or probability of detection, in which case it will probably be more appropriate to frame the problem in terms of α -mirrors.

34.3.4 Multi-Fidelity Models: Refinement and Relaxation

This section considers the situation when one has multiple models of the same structure S , in a fixed context C . Suppose that a model M^C is an ϵ -mirror for S . A modified model $M'^C = \text{Ref}[M^C]$ is a *refinement* of M^C , if it is an ϵ' -mirror with $\epsilon' < \epsilon$. Similarly, A modified model $M'^C = \text{Rel}[M^C]$ is a *relaxation* of M^C , if it is an ϵ' -mirror with $\epsilon' > \epsilon$. For finite element models, these operations can be carried out by refining or coarsening the mesh. In this simplest of situations, one might estimate the values of ϵ' using analytical error estimates.

This idea is one that can be used in order to answer Question (1) in the introduction. In principle one starts with a model M^C which is provably fit-for-purpose and then relaxes the model until one arrives at M'^C with $\epsilon' = \epsilon_T$.

Now, it is possible to consider what sort of propositions one might wish to prove in the theory i.e. consider the hypothesis:

Assume a model $M^A = M_1^{C_1} \oplus_{M_J} M_2^{C_2}$ is an ϵ_A -twin for a joined structure $S^1 \oplus_{S_J} S^2$. Further suppose that $M_1^{C_1}$ is an ϵ_1 -mirror. Now, if $M'^A = M_1'^{C_1} \oplus_{M_J} M_2^{C_2}$ is obtained by refining the first submodel, then M'^A is an ϵ'_A -mirror, with $\epsilon'_A < \epsilon_A$.

Another strategy for answering Question (1) would then be to relax submodels in an assembly until the result is marginally fit-for-purpose.

34.3.5 An Example Concerning Design

This is one of the potential applications of digital twin technology that would produce large cost savings for industry.

Suppose one has a existing structure S and a context C ; further suppose that a virtualisation $V^C = (M_{\epsilon_1}^{hC}, M_{\epsilon_2}^{EC})$ exists which has been validated and shown to be an ϵ -mirror for S^C .

Imagine now that one wished to design a new structure S' and thus wanted to know how it would behave (either in the old context C , or in a new context C'). In a situation where one wished to avoid building a prototype for S' , there is no direct means of validating a new visualisation $V'^C = (M'^{hC}, M'^{EC})$, even though this would be ideal for conducting ‘what-if’ games for the new structure. The question of immediate interest is:

Given a virtualisation $V^C = (M_{\epsilon_1}^{hC}, M_{\epsilon_2}^{EC})$, which is an ϵ -mirror for S^C ; is $V'^C = (M'^{hC}_{\epsilon'_1}, M'^{EC}_{\epsilon'_2})$ a mirror for S'^C for any values of ϵ'_1 and ϵ'_2 , and if so, what are the smallest possible values for which this true?

34.4 Discussion and Conclusions

This paper proposes some ingredients for a mathematical theory which would allow a general framework for measuring the fidelity of computational models and for understanding the consequences of combining validated models or using them outside their original context. Such a theory would be invaluable in the design and construction of digital twins, because one of the main uses of digital twins will be to make predictions in circumstances where their core models have not been explicitly validated, and it will be critical to obtain estimates of how much models can be trusted when they are used to extrapolate or generalise; i.e. when they are used to make inferences about different structures or in different contexts.

As discussed in the introduction, there are already attempts to define a unifying framework for model calibration and validation. In fact, these papers already go into greater detail on specific technical points than the current paper e.g. they go as far as to propose a Bayesian framework and define appropriate priors, likelihoods etc. [5, 6]. The techniques proposed can very much form part of the armoury of the more general methodology proposed here. The current paper deliberately draws back from some details because the authors believe that important discussions are still to be had. For example, it is not agreed within the broader V&V and uncertainty quantification communities that probability theory is the correct way to

approach model bias, or epistemic uncertainty in general. For this reason, some of the definitions given here are independent of whatever uncertainty theory ultimately dominates in a given context. As long as an uncertainty theory singles out some *most highly indicated* model from the population of possible choices, one can base the analysis on the ϵ -mirror for that single model. For example, in a Bayesian framework, one can apply the idea to the *Maximum a Posteriori* (MAP) model. Of course, any theorems in the general theory will have to be proved independently for each uncertainty specification.

In many ways, the paper presents a *wish list*; however, it does so in the real hope that the wishes can come true—that the required theory can come together. The paper presents only the sketchiest arguments as to how the various ‘theorems’ might be proved, or how the relevant estimates could be made; this is because the current authors do not have anything like the complete range of abilities/skills that will be needed in order to assemble the theory. In many ways the paper is intended as a rallying call to the academic community; the skills needed will come from a range of disciplines: pure and applied mathematics, physics, computer science (particularly machine learning) and engineering. The authors here believe that a framework can come together which is more than the sum of its parts and that can be of lasting value in the pursuit of effective computer models, and particularly in the construction of digital twins.

Acknowledgement The authors would like to acknowledge the support of the UK Engineering and Physical Sciences Research Council (EPSRC) through grant reference numbers EP/J016942/1 and EP/K003836/2.

References

1. Tuegel, E.J., Ingraffea, A.R., Eason, T.G., Spottswood, S.M.: Reengineering aircraft structural life prediction using a digital twin. *Int. J. Aerosp. Eng.* **2011**, 154798 (2011)
2. Datta, S.P.A.: Emergence of digital twins - is this the march of reason. *J. Innov. Manag.* **5**, 14–33 (2017)
3. Grieves, M., Vickers, J.: *Digital-Twin: Mitigating Unpredictable, Undesirable Emergent Behavior in Complex Systems*, pp. 85–113. Springer, Switzerland (2017)
4. Wagg, D.J., Gardner, P., Barthorpe, R.J., Worden, K.: On key technologies for realising digital-twins for structural dynamics applications. In: *Proceedings of the 37th IMAC, the International Modal Analysis Conference*, Orlando (2019)
5. Li, C., Mahadevan, S.: Role of calibration, validation and relevance in multi-level uncertainty integration. *Reliab. Eng. Syst. Saf.* **148**, 32–43 (2016)
6. Nagel, J., Sudret, B.: A unified framework for multilevel uncertainty quantification in Bayesian inverse problems. *Probab. Eng. Mech.* **43**, 68–84 (2015)
7. Kennedy, M.C., O'Hagan, A.: Bayesian calibration of computer models. *J. R. Stat. Soc. Ser. B Stat. Methodol.* **63**, 425–464 (2001)
8. Bishop, C.M.: *Pattern Recognition and Machine Learning*. Springer, New York (2007)
9. Cherkassky, V., Mulier, F.M.: *Learning from Data: Concepts, Theory and Methods*. Wiley, Hoboken (1998)
10. Worden, K., Barthorpe, R.J., Cross, E.J., Dervilis, N., Holmes, G.R., Manson, G., Rogers, T.J.: On evolutionary system identification with applications to nonlinear benchmarks. *Mech. Syst. Signal Process.* **112**, 194–232 (2018)
11. Worden, K., Hensman, J.J.: Parameter estimation and model selection for a class of hysteretic systems using Bayesian inference. *Mech. Syst. Signal Process.* **32**, 153–169 (2012)
12. Abdessalem, A.B., Dervilis, N., Wagg, D.J., Worden, K.: Model selection and parameter estimation in structural dynamics using approximate Bayesian computation. *Mech. Syst. Signal Process.* **32**, 306–325 (2018)
13. Rasmussen, C.E., Williams, C.K.I.: *Gaussian Processes for Machine Learning*. MIT, Cambridge (2006)
14. Worden, K.: Some thoughts on model validation for nonlinear systems. In: *Proceedings of 3rd International Conference on Identification in Engineering Systems*, Swansea, pp. 142–154 (2002)
15. Turing, A.: Computing machinery and intelligence. *Mind* **236**, 433–460 (1950)
16. Ladeveze, P., Leguillon, D.: Error estimate procedure in the finite element method and applications. *SIAM J. Numer. Anal.* **20**, 485–509 (1983)
17. Ainsworth, M., Tinsley, J.: A posteriori error estimation in finite element analysis. *Comput. Methods Appl. Mech. Eng.* **142**, 1–88 (1997)
18. Gawthrop, P., Neild, S., Wallace, M., Wagg, D.J.: Robust real-time substructuring techniques for lightly-damped systems. *Struct. Control. Health Monit.* **14**, 591–600 (2007)
19. Farrar, C.R., Worden, K.: *Structural Health Monitoring: A Machine Learning Perspective*. Wiley, Hoboken (2012)
20. Cappell, S., Ranicki, A., Rosenberg, J.: *Surveys on Surgery Theory: Volume 1*. Princeton University, Princeton (2000)



Chapter 35

Applications of Reduced Order and Surrogate Modeling in Structural Dynamics

Alexandros A. Taflanidis, Jize Zhang, and Dimitris Patsialis

Abstract Despite recent advances in computational science, the adoption of computationally intensive, high-fidelity simulation models remains a challenge for many structural dynamics applications, especially those within the domain of uncertainty quantification (UQ), requiring repeated calls to a computationally intensive simulator. Reduced order and surrogate models offer an attractive alternative to circumvent this challenge. This contribution investigates how these modeling principles can be leveraged for different UQ applications. For both types of approximate models, the development of the corresponding (reduced order or surrogate) model is directly informed through simulations of the high-fidelity numerical model. The tuning of the approximate model aims to improve accuracy for the specific UQ task at hand, rather than targeting a globally accurate approximation. The specific applications discussed correspond to seismic loss estimation (for reduced order modeling) and posterior sampling for Bayesian inference (for surrogate modeling).

Keywords Reduced order modeling · Surrogate modeling · Structural dynamics · Uncertainty quantification · Seismic loss estimation · Adaptive tuning · Posterior density approximation · Bayesian inference

35.1 Introduction

Reduced order and surrogate models have emerged as powerful computational statistics tools for supporting UQ tasks in different structural dynamics applications [1–6]. Their objective is to replace the original, high-fidelity simulation model with an approximate one that has significantly smaller computational burden (therefore accelerating relevant computations), but can still provide adequate accuracy for the UQ task of interest. This accuracy can be enhanced through tuning, perhaps with adaptive characteristics, tailored to that specific task, instead of trying to accomplish a globally accurate approximation.

Reduced order models simplify the physics-based description of the original system through some form of condensation of the initial degrees of freedom and equations of motion [7], sometimes coupled with an approximation of the nonlinear response characteristics [3]. In the latter case, which is the one emphasized in this contribution, the calibration of the nonlinear properties of the reduced order model can be performed using data from the original, high-fidelity simulation model, with ultimate objective that the reduced order approximate model matches closely the high-fidelity one [1] for excitation (and therefore operating conditions) similar to the ones entailed in the UQ task of interest. On the other hand, surrogate models (also frequently referenced as metamodels) offer an entirely data-driven mathematical approximation of the input/output relationships of the high-fidelity model. The characteristics of the metamodel are tuned using explicitly simulation data from the original model [8]. Among the different classes of surrogate models, Gaussian Process Metamodels (GPMs) have gained wide popularity for UQ applications. This can be attributed (1) to the fact that they correspond to a statistical emulator, providing also a local estimate for the metamodel prediction error, a feature that fits well within the broader UQ setting, and (2) to their computational efficiency in simultaneously providing, through vectorized algebraic manipulations, estimates for multiple input samples, a feature well aligned with stochastic simulation algorithms used frequently in UQ applications. For accurate UQ estimation, the selection of the database informing the metamodel development, what is formally known as Design of Experiments (DoE) [8], plays always a critical role.

This contribution reviews some recent advances for the implementation of reduced order and surrogate modeling in structural dynamics applications. Discussion for each type of approximation model are couched within a specific application; seismic loss estimation for reduced order modeling and posterior sampling in Bayesian inference for surrogate modeling.

A. A. Taflanidis (✉) · J. Zhang · D. Patsialis

Department of Civil and Environmental Engineering and Earth Sciences, University of Notre Dame, Notre Dame, IN, USA

e-mail: a.taflanidis@nd.edu

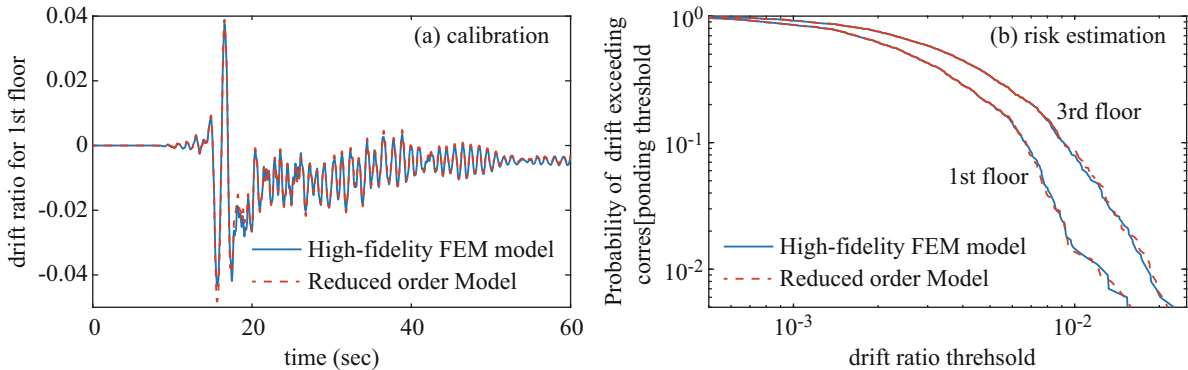


Fig. 35.1 (a) Calibration results (time-history comparisons for one of the six excitations used in the calibration) for a reduced order model matching a high-fidelity FEM model (developed in OpenSees modeling environment) for a three-story benchmark structure and (b) comparison of seismic risk estimates from the reduced order and high-fidelity models considering an ensemble of 1000 ground motions

35.2 Reduced Order Modeling in Seismic Loss Assessment

Modern seismic loss estimation practices (and more broadly seismic risk assessment) require simulation of structural behavior for different levels of earthquake shaking through time-history analysis. Under moderate and strong excitations this behavior is strongly inelastic/hysteretic and evaluating it through high-fidelity Finite Element Models (FEMs) introduces a significant computational burden. Reduced order modeling has been suggested to alleviate this burden [1, 3]. The reduced order model in this setting is developed using data from the original high-fidelity model. Modal analysis (or static condensation) is first leveraged to condense the initial equations of motion to a specific set of degrees of freedom per story. For planar structural models, which is the focus here, this can be established by using one degree of freedom per story. The restoring forces prescribed by the linear stiffness matrix are then substituted with hysteretic ones, equivalently viewed as nonlinear springs connecting different degrees of freedom. Hysteretic models that can be considered for this task include piecewise-linear models, Massing models [1] or Bouc-Wen models [3]. The characteristics of these models that describe the initial (linear) response are selected directly based on the modal analysis results to match exactly the condensed stiffness matrix. Characteristics that describe the nonlinear response can be subsequently calibrated [3] by comparing the reduced order model time-history to the time-history of the original FEM for a range of different excitations. This is posed as a model parameter identification problem with data coming from the high-fidelity FEM simulations. The excitations used in this calibration should be carefully chosen to facilitate identification of all relevant model parameters, something accommodated when nonlinearities associated with all degrees of freedom can be observed in the available data. Earlier work in this field used simplified excitations for this purpose [3] while recent work by the first and third authors has demonstrated how this can be more efficiently accomplished using seismic excitations with different intensity levels and frequency content. As shown in Fig. 35.1, the calibrated model can be then used to efficiently provide loss assessment estimates.

35.3 Surrogate Modeling for Posterior Sampling

The importance of Bayesian inference in the analysis of engineering systems has dramatically increased over the past few decades. For applications with complex posterior Probability Density functions (PDFs) this inference needs to rely on stochastic sampling techniques for approximating this PDF. To alleviate the computational burden for applications entailing complex numerical models, the implementation of surrogate modeling techniques for approximating the likelihood function, involved in the posterior PDF definition, has been investigated [9]. The strategy by Angelikopoulos et al. [9] relied on use of the metamodel for local approximation and only for samples for which its predicted metamodel accuracy was sufficiently high (exact numerical model was used for samples that did not satisfy this requirement). The first two authors recently developed [10] the adaptive Kriging stochastic sampling and density approximation algorithm (AK-SSD) for approximating target densities using metamodeling techniques. AK-SSD utilizes solely metamodel predictions for all calculations within the stochastic sampling task and establishes high computational efficiency by leveraging a global metamodel that is iteratively developed to provide higher accuracy in domains of interest. AK-SSD assumes a sequential sampling setting, using a series

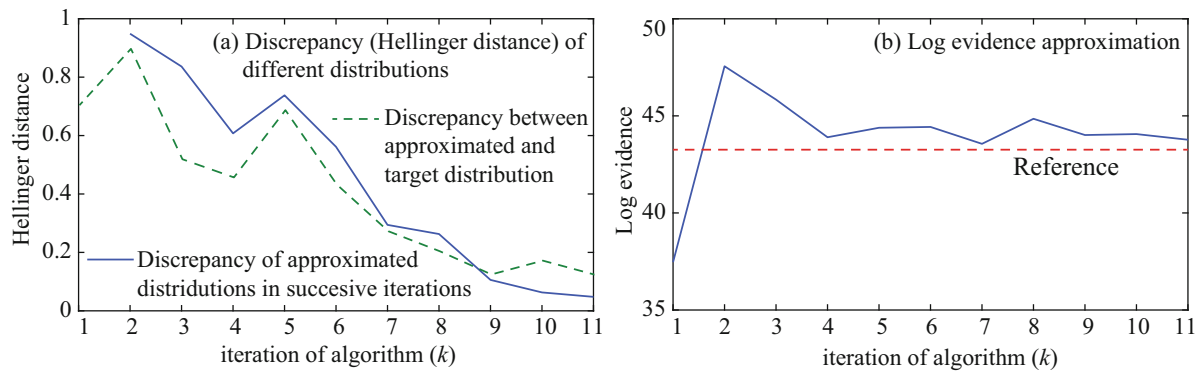


Fig. 35.2 Results for implementation of AK-SSD algorithm for a modal synthesis problem; (a) discrepancy between different distributions across iterations and (b) approximation of log evidence

of intermediate densities to approximate gradually the target density. At each AK-SSD iteration, the current metamodel is used to approximate the intermediate and target densities and if convergence is not achieved knowledge gained from current iteration is leveraged, primarily through an adaptive design of experiments, to update the metamodel formulation and proceed to the next iteration. The Hellinger distance between the approximated densities in consecutive iterations is used to quantify convergence, whereas new experiments are obtained using a hybrid DoE strategy that balances goals of improvement of global metamodel accuracy and addition of experiments in critical regions for the posterior sampling. AK-SSD was initially formulated for rare event estimation but can be seamlessly extended to Bayesian posterior sampling as shown in Fig. 35.2 for a modal synthesis problem of an eight story structure, updating stiffness characteristics through eigenfrequency and modal information for the first three modes of vibration. Part (a) of Fig. 35.2 shows the Hellinger distance discrepancy between the approximated target densities in consecutive iterations or between the approximated and actual target density, while part (b) shows the iteration-wise metamodel-based evidence estimate versus the reference one. As the iteration number k increases discrepancy reaches a plateau, facilitating an efficient convergence to the target density, something further validated by the agreement of the estimated evidence.

References

1. Gidaris, I., Taflanidis, A.A.: Parsimonious modeling of hysteretic structural response in earthquake engineering: calibration/validation and implementation in probabilistic risk assessment. *Eng. Struct.* **49**, 1017–1033 (2013)
2. Jensen, H.A., Muñoz, A., Papadimitriou, C., Millas, E.: Model-reduction techniques for reliability-based design problems of complex structural systems. *Reliab. Eng. Syst. Safe.* **149**, 204–217 (2016)
3. Tehrani, M., Harvey Jr., P., Gavin, H., Mirza, A.: Inelastic condensed dynamic models for estimating seismic demands for buildings. *Eng. Struct.* **177**, 616–629 (2018)
4. Gidaris, I., Taflanidis, A.A., Mavroeidis, G.P.: Kriging metamodeling in seismic risk assessment based on stochastic ground motion models. *Earthq. Eng. Struct. Dynam.* **44**(14), 2377–2399 (2015)
5. Mai, C.V., Spiridonakos, M.D., Chatzi, E.N., Sudret, B.: Surrogate modeling for stochastic dynamical systems by combining nonlinear autoregressive with exogenous input models and polynomial chaos expansions. *Int. J. Uncertain. Quantif.* **6**, 4 (2016)
6. Bakalis, K., Vamvatsikos, D., Fragiadakis, M.: Seismic risk assessment of liquid storage tanks via a nonlinear surrogate model. *Earthq. Eng. Struct. Dynam.* **46**(15), 2851–2868 (2017)
7. Jensen, H., Millas, E., Kusanovic, D., Papadimitriou, C.: Model-reduction techniques for Bayesian finite element model updating using dynamic response data. *Comput. Methods Appl. Mech. Eng.* **279**, 301–324 (2014)
8. Sacks, J., Welch, W.J., Mitchell, T.J., Wynn, H.P.: Design and analysis of computer experiments. *Stat. Sci.* **4**(4), 409–435 (1989)
9. Angelikopoulos, P., Papadimitriou, C., Koumoutsakos, P.: X-TMCMC: adaptive kriging for Bayesian inverse modeling. *Comput. Methods Appl. Mech. Eng.* **289**, 409–428 (2015)
10. Zhang, J., Taflanidis, A.A.: Adaptive Kriging stochastic sampling and density approximation and its application to rare-event estimation. *ASCE-ASME J. Risk Uncertain. Eng. Syst. A Civil Eng.* **4**(3), 04018021 (2018)